Etudes in situ et ex situ par rayonnement synchrotron de la croissance d'îlots de Ge sur substrats de Si(001) nominaux et préstructurés.

Marie-Ingrid Richard

Université Joseph Fourier – Grenoble 1

THÈSE

présentée par

Marie-Ingrid RICHARD

pour obtenir le titre de

Docteur de l'Université Joseph Fourier
Discipline : Physique

Etude *in situ* et *ex situ* par rayonnement synchrotron de la croissance d'îlots de Ge sur substrats de Si(001) nominaux et pré-structurés.

soutenue publiquement le 14 décembre 2007

Composition du jury :

Rapporteurs :	Dr. Isabelle BERBEZIER
	Pr. Václav HOLY
Examinateurs :	Pr. Günther BAUER
	Pr. Yves GARREAU
	Dr. Armando RASTELLI
Codirecteurs de thèse :	Dr. Till-Hartmut METZGER
	Dr. Gilles RENAUD
	Pr. Hubert RENEVIER

European Synchrotron Radiation Facility (ESRF)
Département de Recherche Fondamentale sur la Matière Condensée - CEA Grenoble

Contents

Acknowledgements **vii**

Summary **ix**

Résumé **xi**

Introduction **xiii**

1 Growth of Ge islands on Si(001). **1**
1.1 Crystallographic structure . . . 1
1.2 Growth techniques . . . 1
1.3 Growth modes . . . 2
1.3.1 Growth thermodynamics. . . . 2
1.3.2 Growth kinetics. . . . 3
1.4 Growth process: Si(001) surface reconstruction, wetting layer and three dimensional growth. . . . 4
1.5 Intermixing . . . 6
1.6 Self-organization of Ge islands on Si(001). . . . 7
1.7 Defects and dislocations . . . 11
1.7.1 Planar defects in Si and Ge bulks. . . . 11
1.7.2 Formation of defects during the Ge growth on Si(001). . . . 11
1.8 Conclusions and perspectives . . . 14

2 Characterization methods **19**
2.1 Introduction . . . 19
2.2 X-ray characterization methods. . . . 19
2.2.1 Surface sensitive X-ray scattering. . . . 19
2.2.2 X-ray scattering. . . . 23
2.2.3 The Distorted Wave Born Approximation for grazing incidence scattering . . . 25
2.2.4 Grazing incidence small angle scattering. . . . 26
2.2.5 Multiwavelength Anomalous Diffraction . . . 32
2.3 Other techniques. . . . 35
2.3.1 Atomic force microscopy. . . . 35
2.4 Conclusion . . . 35

3 Elastic simulations and X-ray scattering. **39**
3.1 Strain and composition in SiGe nanoscale islands studied by elastic simulations and X-ray scattering. . . . 39
3.1.1 Theoretical model. . . . 40
3.1.2 Diffraction from a strained crystal. . . . 40
3.1.3 Study of the relaxation state of pyramids and domes with and without wetting layer. . . . 41

3.1.4 Impact of the wetting layer on the diffracted signal and relaxation state of islands. 42
3.1.5 Impact of intermixing on the diffracted signal and relaxation state of islands. . 44
3.1.6 Study of the effect of the distorted wave Born approximation on the scattered intensity. 45
3.1.7 Conclusion 51

4 Experimental set-ups **55**
4.1 Introduction 55
4.2 The ID01 beamline 55
4.2.1 ID01 optics hutch 55
4.2.2 ID01 experimental hutch 56
4.3 The BM32 beamline 58
4.3.1 The ultra high vacuum chamber 58
4.3.2 The diffractometer 60
4.3.3 The GISAXS set-up 60
4.4 Complementary between the BM32 and ID01 set-ups 61
4.5 Measure of the intensity 62
4.5.1 Scans and resolution function 62
4.5.2 Correction factors 62

5 Defects in implanted Si and in Ge islands. **67**
5.1 Introduction 67
5.2 Defects in implanted Si 68
5.2.1 Sample preparation 68
5.2.2 Signature of defects at an allowed reflection 68
5.2.3 Signature of defects at a basis-forbidden reflection 71
5.2.4 Conclusion: Allowed vs quasi-forbidden reflection 79
5.3 Defects in Ge islands 80
5.3.1 Defects in ordered self-assembled Ge quantum dots (SAQD). 80
5.3.2 Description of the SAQDs sample. 81
5.3.3 Strain and ordering analysis of the SAQDs. 81
5.3.4 Detection of lateral ordering of the Ge nanostructures: GISAXS vs GIXD. . . . 83
5.3.5 Composition of the SAQDs. 85
5.3.6 Comparison with transmission electron microscopy study. 86
5.3.7 Simulation of the strain of the Ge QDs using finite difference method (FDM). . 87
5.3.8 Looking at the (200) forbidden reflection: analysis of the nature and size of defects. 89
5.4 Synthesis 95

6 Atomic ordering and stacking faults in Ge islands on Si(001). **99**
6.1 Introduction 99
6.2 Atomic ordering in Ge islands on Si(001) 100
6.2.1 Origin of the atomic ordering 100
6.2.2 Understanding the formation of anti-phase boundaries 101
6.2.3 The different classes of reflections. 102
6.2.4 Determination of the size and number of ordered domains. 103
6.2.5 X-ray diffraction analysis of the atomic ordering on patterned and nominal samples. 109
6.2.6 Synthesis and discussion on the origin of the scattering around the (200) reflection. 112
6.2.7 Annealing effect on the atomic ordering: atomic ordering, a *metastable* phenomenon. 112
6.3 Defects in Ge islands on Si(001) 114
6.3.1 *In situ* study of the formation of stacking-faults inside Ge islands 114

6.4 Atomic ordering vs defects . . . 122
6.4.1 *Ex situ* studies of atomic ordering and defects in 15 ML grown Ge islands. . . . 123
6.4.2 *Ex situ* studies of atomic ordering and defects in Ge islands on Si(001) as a function of growth temperature, growth rate and annealing. . . . 126
6.5 Conclusion . . . 132

7 *In situ* results of the growth of Ge islands on nominal Si(001). 135
7.1 Introduction . . . 135
7.2 Impact of growth rate and growth interruption. . . . 136
7.3 *In situ* anomalous scattering: determination of the composition of Ge islands on Si(001) using X-ray scattering methods. . . . 139
7.4 In situ investigation of the island nucleation of Ge on Si(001) using X-ray scattering methods . . . 146
7.5 In situ X-ray study of the evolution of island morphology and relaxation during a slow growth rate of Ge on Si(001): early transition to superdomes . . . 153
7.5.1 Experiments . . . 153
7.5.2 Experimental results . . . 154
7.5.3 GISAXS analysis . . . 158
7.5.4 Analysis and discussion . . . 161
7.5.5 Conclusion . . . 165
7.6 Coalescence of domes or superdomes: towards the formation of "flat-top superdomes". 165
7.7 Conclusion . . . 172

8 *In situ* study of the growth of Ge islands on pre-patterned Si(001) substrates. 177
8.1 Laterally ordered growth of Ge islands on a nano-patterned Si(001) surface obtained by lithography: An *in situ* study. . . . 177
8.1.1 Sample preparation and X-ray characterization. . . . 177
8.1.2 Morphology of the ordered pits after the growth of a Si buffer layer. . . . 179
8.1.3 Degree of ordering of the pits after the growth of the Si buffer layer. . . . 180
8.1.4 Morphology and strain state of the Ge deposit during the initial stage of Ge growth on the pre-patterned substrate. . . . 180
8.1.5 Formation of 3D islands . . . 182
8.1.6 Summary of the growth on the lithographically pre-patterned substrate. . . . 184
8.2 Organized growth of Ge quantum dots on a nano-patterned Si(001) surface obtained by direct wafer bonding followed by chemical etching: An *in situ* X-ray study. . . . 186
8.2.1 Sample preparation and X-ray characterization. . . . 186
8.2.2 Experimental results . . . 189
8.2.3 Synthesis on the growth of Ge islands on nano-patterned Si(001) surfaces obtained by wafer bonding. . . . 204
8.3 Conclusion . . . 204

9 Ex-situ comparison between the growth of Ge islands on pre-patterned and nominal Si(001). 207
9.1 Introduction . . . 207
9.1.1 Sample description . . . 208
9.1.2 AFM and SEM analysis . . . 208
9.1.3 GISAXS analysis . . . 210
9.1.4 Strain state analysis . . . 212
9.1.5 MAD analysis . . . 214
9.1.6 Summary of the GI-MAD analysis . . . 218
9.1.7 Grazing-incidence diffraction anomalous fine structure (GI-DAFS) analysis . . 220
9.1.8 GI-MAD on asymmetric reflection. . . . 225
9.2 Lateral composition of the islands. . . . 228

9.2.1 Lateral composition of the patterned sample Z576. 228
9.2.2 Lateral composition of the nominal and pre-patterned parts of sample $Z25$. . . 234
9.2.3 Direct evaluation of strain profile and morphology of Ge islands on Si(001) investigated by X-ray scattering 238
9.2.4 Observation of the edges of cristallines nano-islands. 241
9.3 Conclusion 244

Conclusion and outlook **247**
9.4 Conclusion 247
9.5 Future perspectives. 248

Abbreviations **253**

List of symbols **255**

Acknowledgements

I would like to thank my supervisors for their help and support in this work. I am thus extremely grateful to Dr. Gilles Renaud and Dr. Till-Hartmut Metzger who kindly shared their knowledge with me and helped me during my thesis. I really appreciated their pedagogy, their extraordinary good mood, their precious advices and the freedom they gave me during my thesis and also the nice and positive atmosphere of their group. I also warmly thank Dr. Tobias Schülli who spared his precious time to explain me the diffraction and the growth under ultra-high vacuum. Thank you Tobias for all your help and support. It was really a pleasure at working with them.

I want to specially thank Pr. Václav Holý. It was impressive and a real pleasure to work with him. I recognize the chance I had to meet Vaclav during my thesis and I want to thank him for all the things he brang to me.

I also had the chance to work with Pr. Günther Bauer who has exceptional scientific knowledge and human qualities. His impressive knowledge on the Si/Ge system and the discussions with him were always very fruitful. I really thank him for his interest and kindly advice in the interpretation of x-ray measurements.

I want to acknowledge Dr. Isabelle Berbezier (L2MP Marseille), Dr. Armando Rastelli (IFW Dresden) and Pr. Yves Garreau (Synchrotron Soleil) for their presence in the exam committee, and for fruitful discussions.

I would also like to acknowledge Pr. Hubert Renevier (LMGP-Minatec) and Dr. Maria Grazia Proietti (University of Zaragoza) for their help during experiments on BM02 and for the EDAFS data evaluation.

I want to thank Dr. Angelo Malachias for his collaboration. He has been a continuous source of ideas, learning and motivation.

The help on the theory and especially on simulations was really appreciated from Vincent Favre-Nicolin (CEA-Grenoble), Catherine Priester (IEMN-Villeneuve d'Ascq), Kai Nordlund (Accelerator Laboratory, Finlande) and Frédéric Lançon (CEA-Grenoble).

From the CEA/DRFMC and CEA-Léti, I'd like to thank Dr. Alexis Bavard, Dr. Alina Pascale, Dr. Franck Fournel and Dr. Joel Eymery for the preparation of the twisted wafers, for their suggestions and help with the data interpretation..

I must thank all the ID01 team: Dr. Oier Bikondoa (thanks for your help during experiments and your impressive good mood), Dr. Luciana Capelli (thanks for all the knowledge on defects you shared with me), Dr. Barbel Krause, Dr. Cristian Mocuta, Kiran Mundboth, Dr. Dina Carbone, Dr. Ana Diaz. I want to thank them for the interesting scientific discussions I had with them. Thanks Dr. Peter Boesecke and Hamid Djabouli for bringing successful, immediate and efficient solutions to all technical problems at beamline ID01.

The whole staff of the beamline BM32 has to be acknowledged indeed for its help during the experiments and the friendly daily support. They deserve to be mentioned: Olivier Ulrich, Marion Noblet-Ducruet, Odile Robach, Jean-Sébastien Micha, François Rieutord, Xavier Ulrich, Odile Robach and Frédéric Larizza.

From the University of Linz, I acknowlege Dr. Zhenyang Zhong and Dr. Gang Chen for the interesting discussion and sample preparation. I also acknowledge the group of Pr. Xie from the University of California for sample preparation. For the TEM images, I'd like to thank Dr. Valier Poydenot and Dr. Jean-Luc Rouvière, from the CEA-Grenoble.

I'd like to also thank the former PhD students: Dr. Johann Coraux and Dr. Romain Dujardin for their help during experiments and for data evaluation.

Merci à ma famille pour tout le bonheur qu'elle m'apporte.

Summary

The work presented in this manuscript focuses on the structural (size, strain, defects, composition) investigation of Ge nano-islands grown on both nominal and pre-patterned Si(001) substrates by Molecular Beam Epitaxy, using grazing incidence (anomalous) X-ray diffraction and scattering at the European Synchrotron Radiation Facility (ESRF). The samples were either prepared in independent MBE chambers and then characterized *ex situ* on the ID01 ESRF beamline, or they were characterized *in situ* during their MBE growth, using the BM32 ESRF beamline setup. The dynamical scattering effects occurring in grazing incidence have been studied on the basis of finite element simulations of the strain fields in nano-islands, revealing the strong influence of the incident angle on the intensity scattered by large islands. A novel X-ray method has been developed to detect the presence of defects and to study the structure of their core by concentrating on measurements along rods of scattering by defects passing through bulk forbidden reflections. In order to obtain new insight into the dynamics of growth phenomena, the shape, size, growth mode, composition and possible defects and/or atomic ordering inside all islands were characterized, as a function of deposition, deposition temperature, flux and possible annealing. The evolution of strain, the transition from elastic to plastic relaxation, the intermixing and the correlation of these internal paramtres with the different morphologies of the island have been addressed using *in situ* scattering methods. This study sheds light on the early transition to superdomes during a slow growth rate of Ge on Si(001) and reports a new shape of superdomes, which is the result of island coalescence. At last, the growth on nominal Si(001) surfaces was compared to growth on Si(001) surfaces that were patterned according to different procedures: e-beam lithography or wafer bonding followed by chemical etching. It has been shown that by tuning the surface curvature, it is possible to change the relaxation state and the overall elastic energy of islands without modifying their mean Ge composition. These results show new insight about the intermixing process which does not appear to be strain-driven but induced by surface-mediated diffusion processes.

Keywords: Ge - Si(001) - Strain - MAD - anomalous diffraction - GISAXS - GIXD - grazing incidence X-ray diffraction and scattering - nano-islands - finite element simulations - defects - stacking faults - atomic ordering - implanted Si - lithography - intermixing - MBE - lateral organization - wafer bonding - pre-patterning - DAFS - DWBA.

Résumé

Les travaux présentés dans ce manuscrit sont consacrés à l'étude structurale (taille, déformation, défauts, composition) d'îlots de Ge sur substrats de Si(001) nominaux et pré-structurés durant ou après croissance par épitaxie par jet moléculaire, en utilisant la diffraction (anomale) des rayons X en incidence rasante à l'Installation Européenne de Rayonnement Synchrotron (ESRF). Les échantillons ont été caractérisés soit *ex situ* après croissance sur la ligne de lumière ID01, soit *in situ* durant leur croissance par EJM grâce au dispositif dédié sur la ligne BM32. Les effets dynamiques associés à l'utilisation de l'incidence rasante ont été étudiés sur la base de simulations des champs de déformations dans les nanostructures de Ge. Les résultats ont montré l'influence majeure de l'angle d'incidence sur l'intensité diffusée par les nano-objets de taille de l'ordre de la centaine de nanomètres. Une nouvelle technique de rayons X a été développée pour détecter leur présence et étudier la structure de leur coeur en se concentrant sur l'intensité diffusée par les défauts autour de réflexions interdites. Pour comprendre les dynamiques de croissance, la forme, la taille, le mode de croissance, la composition et la présence éventuelle de défauts et/ou d'ordre atomique à l'intérieur des nanostructures ont été caractérisés en fonction du dépôt, de sa température, de la vitesse de croissance et du recuit. L'évolution des déformations, la transition élastique-plastique, l'interdiffusion et leur relation avec les différentes morphologies des îlots ont été étudiés grâce à l'utilisation de techniques in situ de rayons X. L'étude a mis en évidence l'apparition précoce des dislocations dans les îlots durant la croissance lente de Ge sur Si(001) et la formation d'un nouveau type de superdomes qui résulte de la coalescence d'îlots. Enfin, les croissances sur surfaces Si(001) nominales et pré-structurées ont été comparées. La structuration a été obtenue soit par lithographie électronique soit par collage moléculaire et attaque chimique. Ces études ont permis de montrer qu'en modulant la surface, il est possible de changer l'état de relaxation et l'énergie élastique totale des îlots sans modifier leur composition moyenne en Ge. Ces résultats ont aussi révélés que le processus d'interdiffusion n'est pas induit par la contrainte mais plutôt par les phénomènes de diffusion de surfaces.

Mots clés: Ge - Si(001) - Déformation - MAD - diffraction anomale - GISAXS - GIXD - diffraction et diffusion des rayons X en incidence rasante - îlots nanométriques - simulations par élément finis - défauts - fautes

Introduction

By late 1960's, the advent of novel epitaxial growth techniques, *e.g.* molecular beam epitaxy (MBE) or chemical vapor deposition (CVD), enabled the fabrication of semiconductor nanostructures, in which free carriers are restricted to an extremely small space in the range of 1-100nm. The confinement of the carrier motion is achieved by embedding a low band gap material (*e.g.* Ge, band gap = 0.67eV) in a high band gap material (*e.g.* Si, band gap = 1.11eV), *i.e.* by potential barriers. This confinement in one, two, or three dimensions, in the case of quantum wells, quantum wires and quantum dots (QDs), respectively, leads to a modified density of states with respect to bulk solids. Quantum wells and superlattices were mainly investigated in 1970's and 1980's. The main requirement for their applications was the smoothness of the material interfaces. Their growth modes are at present well controlled in many systems [1, 2]. Nowadays, we encounter them in daily life, e.g. in laser diodes [3, 4, 5] of CD players, in optical waveguides or in light emitting diodes [6]. In quantum wells or superlattices, electrons and holes are not at fixed energy levels but distributed according to the Fermi-Dirac distribution. Thus, they present the weakness to possibly loose excitons (electron-hole pairs) by their recombination at a wavelength different than the working wavelength of a laser for instance. This requires the reinjection of electrons and holes in the quantum wells.

QDs as quasi-zero-dimensional objects attracted the interest of researchers since the late 1980's. The main motivation was to complete spatial carrier confinement resulting in atom-like energy spectra and higher density of states when compared to quantum wires and quantum wells. Three-dimensional carrier motion confinement takes place also in nano-islands. QDs should present small size and dispersion and a huge density to be more attractive than quantum wells for opto-electronic applications. To avoid parasite emission, the energy between the fundamental and excited levels should be larger than $2k_BT$. In a simple model, the total energy of an electron confined in three directions (see Fig. 1) can be written as $E_{n_x,n_y,n_z} = (\hbar\pi)^2/(2m^*)((n_x/d_x)^2 + (n_y/d_y)^2 + (n_z/d_z)^2)$, where m^* is the effective electron mass, d_x, d_y and d_z are the sizes of the potential barrier and n_x, n_y and n_z the quantum numbers. If we suppose $E_{211} - E_{111} \geq 2k_BT$, then this implies $d_{max} = \sqrt{3(\hbar\pi)^2/(4m^*k_BT)}$. For Ge, $m^* = 0.55m_e$, where m_e is the electron mass, then $d_{max} \sim 7nm$.

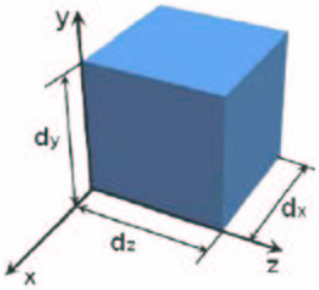

Figure 1: Model of the squared box: the electron is confined in three directions.

This means that the gap between two levels decreases when the number of atoms in the solid increases. The size dispersion modifies the energy of confinement and widens the density of states of

carriers. To avoid these effects, the size dispersion (σ/d) should be smaller than 20% [7].

Nowadays, among a variety of nanofabrication techniques, e.g. lithographic techniques, molding, embossing, the process of self-assembly in Stranski-Krastanow growth mode seems to be the most promising for producing defect free semiconductor QDs and nano-islands on a large scale.

For instance, InAs/GaAs QD lasers have already outperformed properties of quantum well lasers [8]. They show lower threshold currents at room temperature. Their main advantage is the operation in transmission windows of the optical waveguides, i.e., at wavelengths of 1.3 μm and possibly also 1.5 μm. One of the emerging applications of quantum dots is in the field of quantum information processing. InAs self-assembled QDs embedded in an optical microcavity can be used as single photon sources [9] and sources of polarization correlated photons [10], which are potential components of photon-based quantum information applications. QDs can also provide an environment for storing qubits in the form of exciton, *i.e.* electron-hole pair, or electron spin [11, 12, 13].

Concerning Si/Ge nanostructures, the possibility of achieving laterally ordered islands and of modifying the band structure in a capping layer through the strain fields of buried dots has led to the concept of the Dot-FET, a dot-based field-effect transistor on Si [14]. It will allow both to enhance the electron mobility and their maximum device frequency. Si-Ge structures offer the advantage of compatibility with well-established Si technology. One of the aims of incorporating Ge in Si is to improve the poor performances of Si as absorber and emitter of light, due to the indirect nature of the Si band-gap. Ge islands incorporated in Si have been proved to enhance the absorption of near- and mid-infrared radiation, leading to possible applications in photodetectors [15]. Photoluminescence and electroluminescence at a wavelength of ~ 1.5 μm observable up to room temperature have been demonstrated [16, 17]. The reader can refer to Ref. [18] for an extended discussion of the structural properties and applications of self-organized semiconductor nanostructures.

Better understanding of the physics of QDs and nano-islands formation, the control of their structural properties, and their precise positioning is a prerequisite for their application on large scale. In particular, size, shape, defects and chemical composition of these nanostructures are important factors influencing their optical and electric performances. These properties can be characterized in detail using the grazing incidence X-ray scattering technique, applied both *in situ*, during growth and *ex situ* after growth. Indeed, X-rays provide information on: (1) the strain state, that influences semiconductor band alignment and the quantum efficiency of nanostructures; (2) the composition, that changes the confining profile by changing the energy bandgap; (3) the morphology and size distribution, which are directly related to the width of spectral and electronic response of these materials (4) the atomic ordering that can also affect the band alignement (5) the defects which decrease the quantum efficiency of nanostructures.

This manuscript present the results of several X-ray scattering studies of the morphological, structural and compositional properties of Ge islands grown on Si(001) by MBE, according to the Stranski-Krastanow growth mode. The samples were either prepared in remote MBE chambers and then characterized *ex situ* on the ID01 ESRF beamline, or they were characterized *in situ*, during their MBE growth, using the BM32 ESRF beamline setup. In all cases, the shape, size, growth mode, composition and possible defects and/or atomic ordering inside the islands were characterized, as a function of amount deposited, deposition temperature, flux and possible annealing. The growths on Si(001) surfaces were compared to those on Si(001) surfaces that were patterned according to different procedures: e-beam lithography or wafer bonding followed by chemical etching.

The manuscript is organized into eigth chapters. The **first chapter** describes the properties of the Si and Ge elements and the characteristics of the self-assembled growth of Ge using molecular beam epitaxy.

The **second chapter** presents the different characterization techniques and especially the different X-ray techniques used to study the atomic and cristallographical properties of Ge nanostructures on Si(001). Grazing Incidence Small Angle X-ray Scattering (GISAXS) experiments allow to study the morphology and ordering during the *in situ* growth of Ge nanostructures on Si(001). The Multiwavelength Anomalous Diffraction (MAD) technique is presented in the framework of the Born Approximation. The composition distribution within nanostructures has to be measured precisely in all three dimensions as intermixing is a prevalent phenomenon in Si/Ge system. To fulfill these re-

quirements, diffraction has been combined with simulations with the Finite Difference Method (FDM), which is exposed in the **third chapter**. Using the calculated strain field, the diffraction pattern is simulated in the framework of the Distorted-Wave Born Approximation (DWBA).

The **fourth chapter** describes the experimental set-ups, and especially describes the two beamlines of ESRF where this work has been performed: ID01 and BM32.

The **fifth chapter** focuses on a novel X-ray method to study the structure of the core of the defects by concentrating on measurements along rods of scattering by defects, passing through bulk forbidden reflections. The technique will be exposed in the case of defects in implanted Si and in Ge islands.

The **sixth chapter** will present what can be learnt by looking at a forbidden reflection during the growth of Ge nanostructures on Si(001). This chapter demonstrates the importance of scanning around the (200) forbidden reflection to characterize defects or atomic ordering inside these nanostructures.

The **seventh chapter** focuses on the *in situ* growth of Ge islands on nominal Si(001). The impact of growth rate and growth interruption on the island morphology and composition is studied. The composition of Ge islands during their *in situ* growth is determined as a function of growth temperature. *In situ* X-rays allow to study the evolution of island morphology and relaxation as a function of deposited Ge monolayers (ML). New insight into the dynamics of growth phenomena can be obtained. Then, an AFM study evidences the formation of superdomes with a new shape.

An interesting development for devices applications is the positioning of islands and the improvement of size monodispersity. One way to achieve these goals is the growth of regular islands by a combination of patterning techniques and self-assembly. The *in situ* evolution of the morphology and relaxation of the pre-patterned surface and ordered islands has been studied in **chapter eight** by combining (anomalous)-grazing incidence X-ray diffraction (GIXD) and (anomalous)-grazing incidence small angle X-ray scattering (GISAXS).

The **ninth chapter** deals with the *ex situ* comparison between the growth of Ge islands on pre-patterned and nominal Si(001). The combination of MAD that allows to extract the scattering amplitude of the Ge and Si atoms and diffraction anomalous fine structure (DAFS) spectroscopy allows to determine the local environment of atoms. It is a powerful approach to disentangle strain and composition.

Bibliography

[1] P. Schwander, C. Kisielowski, M. Seibt, F. H. Baumann, Y. Kim and A. Ourmazd, Phys. Rev. Lett. **71**, 4150 (1993)

[2] C. Lamberti, Surface Science Reports **53**, 1 (2004).

[3] Y. Arakawa and H. Sakaki, Appl. Phys. Lett. **40**, 939 (1982).

[4] M. Kondow, K. Uomi, A. Niwa, T. Kitatani, S. Watahiki and Y. Yazawa, Japanese J. of Appl. Phys. **35**, 1273 (1996).

[5] S. Hooper, M. Kauer, V. Bousquet, K. Johnson, J. M. Barnes and J. Heffernan, Electronics Letters **40**, 33 (2004).

[6] S. Nakamura, T. Mukai and M. Senoh, Appl. Phys. Lett. **64**, 1687 (1994).

[7] J. M. Gérard, Master courses.

[8] Y. H. Liu, I. R. Sellers, T. J. Badcock, D. J. Mowbray, M. S. Skolnick, K. M. Groom, M. Gutierrez, M. Hopkinson, J. S. Nig, J. P. R. David, and R. Beanland, Appl. Phys. Lett. **85**, 704 (2004).

[9] E. Moreau, I. Robert, J. M. Gérard, I. Abram, L. Manin, and V. Thierry-Mieg, Appl. Phys. Lett. **79**, 2865 (2001).

[10] C. Santori, D. Fattal, M. Pelton, G. S. Solomon, and Y. Yamamoto, Phys. Rev. B **66**, 045308 (2002).

[11] M. Friesen, M. P. Rugheimer, D. E. Savage, M. G. Lagally, D. W. van der Weide, R. Joynt, and M. A. Eriksson, Phys. Rev. B **67**, 121301 (2003).

[12] L. Koppens, J. A. Folk, J. M. Elzerman, R. Hanson, L. H. W. von Beveren, I. T. Vink, H. P. Tranitz, W. Wegscheider, L. P. Kouwenhoven, and L. M. K. Vandersypen, Science **309**, 1346 (2005).

[13] J. R. Petta, A. C. Johnson, J. M. Taylor, E. A. Laird, A. Yacoby, M. D. Lukin, C. M. Marcus, M. P. Hanson, and A. C. Gossard, Science **309**, 2180 (2005).

[14] O.G. Schmidt and K. Eberl, IEEE Trans. Electron Devices **48**, 1175 (2001).

[15] W. Wu, J. Liu, J. Wan, and K. L. Wang, Superlattices and Microstructures **26**, 219 (1999).

[16] T. Brunhes *et al.*, Appl. Phys. Lett. **77**, 1822 (2000).

[17] L. Vescan *et al.*, J. Appl. Phys. **87**, 7275 (2000).

[18] J. Stangl, V. Holý, and G. Bauer, Reviews of Modern Physics **76**, 725 (2004).

Chapter 1

Growth of Ge islands on Si(001).

Ce chapitre présente une revue de la litterature sur la croissance d'ilots de Ge elabore par epitaxie par jets moleculaires sur substrats de Si(001). Les proprietes morphologique, structurale et chimique des ilots de Ge sont presente. La croissance conduit a une diversite de taille, de forme, de contraintes et d'interdiffusion dans les ilots; ce qui peut s'expliquer par l'interaction entre thermodynamique et cinetique. En outre, les differentes techniques et Une revue est realise This chapter presents an overview of the literature on the growth of Ge islands on Si(001) using molecular beam epitaxy. A review is made of the morphological, structural and chemical properties of Ge/Si(001) nanostructures. The growth leads to a diversity of island size, shape, strain and intermixing profiles, which can be explained by the interplay between thermodynamics and kinetics. In addition, the different techniques and processes involved in the lateral ordering of such nanostructures at the mesoscopic scale are discussed. Different types of defects observed inside Ge islands are presented.

This chapter presents an overview of the literature on the growth of Ge islands on Si(001) using molecular beam epitaxy. A review is made of the morphological, structural and chemical properties of Ge/Si(001) nanostructures. The growth leads to a diversity of island size, shape, strain and intermixing profiles, which can be explained by the interplay between thermodynamics and kinetics. In addition, the different techniques and processes involved in the lateral ordering of such nanostructures at the mesoscopic scale are discussed. Different types of defects observed inside Ge islands are presented.

1.1 Crystallographic structure

Crystalline silicon and germanium have the same lattice structure, *i.e.* that of diamond. The cubic unit cell (Fig. 1.1) contains eight atoms. However, the lattice constant of Ge is about 4.16% larger than that of Si. The difference is called misfit and is defined as $\epsilon = (a_{Ge} - a_{Si})/a_{Si}$, where a_{Si} =5.4309Å and a_{Ge} =5.6461Å are the lattice constants of Si and Ge, respectively. The diamond structure consists of two face centered cubic (FCC) lattices shifted by a vector of $\frac{1}{4}[111]$. The primitive unit cell is defined by the vectors: $a'_1 = \frac{1}{2}[101], a'_2 = \frac{1}{2}[110], a'_3 = \frac{1}{2}[011]$.

1.2 Growth techniques

The most common used deposition techniques for semiconductors are Chemical Vapor Deposition (CVD) and Molecular Beam Epitaxy (MBE). Several variants of these basic techniques have been developed to meet specific needs. The main difference between CVD and MBE is that in the former, the deposited atoms are introduced as gases (for instance silane SiH_4 and germane GeH_4 for the growth

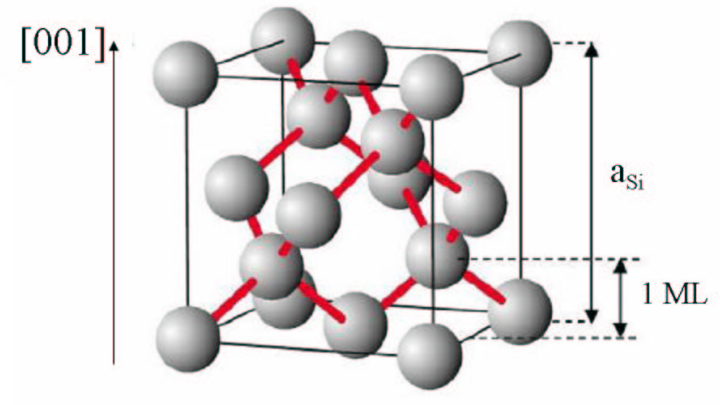

Figure 1.1: Diamond unit cell of Si or Ge.

of Si, Ge) which crack on the hot surface, releasing hydrogen in the growth chamber. In MBE atoms are generated by evaporation and focused on the substrate as atomic beams. In CVD, at substrate temperatures relevant for SiGe/Si heteroepitaxy, the growth rate (i.e. the thickness increase of a flat epilayer per unit time) is strongly influenced by the substrate temperature T_s, since the cracking probability is a function of T_s while in MBE growth, T_s and growth rate can be tuned separately, rendering this system more suitable for fundamental studies.

1.3 Growth modes

1.3.1 Growth thermodynamics.

Epitaxial growth is generally classified according to the following basic three modes [1]: layer-by-layer or Frank-Van der Merwe (FM) growth [2], island growth (Volmer-Weber (VW)), or layer-plus-island growth (Stranski-Krastanow (SK) [3]) (see Fig. 1.2). A simple distinction between the FM and VW modes can be done on the basis of surface and interface tensions, assuming that growth occurs in vacuum. In the FM mode the interaction between neighboring A atoms in the film is weaker than that with the B atoms of the substrate:

$$\gamma_B \geq \gamma_A + \gamma_{IF} \tag{1.1}$$

where γ_A and γ_B are the film/vacuum and substrate/vacuum surface tensions and γ_{IF} is the film/substrate surface tension. In this case, the increase of the free surface of the deposited film decreases the overall energy of the system. The deposited material wets the surface and grow in a two dimensional (2D) mode. A new layer will be formed after the completion of the previous one. That's why the growth is called layer by layer growth. The opposite occurs for the VW growth mode. The increase of the free surface of the deposited film increases the total energy of the system. To maintain free surfaces for the substrate, three dimensional (3D) islands will form. Of course, kinetic limitations can modify this simple view.

For the mixed SK growth mode, the driving force for the island formation on top of an ultrathin layer during heteroepitaxial growth is the misfit (*e.g.* 4.16% for the SiGe system) between the crystal lattice of the growing layer and that of the substrate, which creates strain in the growing layer. In the first stage of growth, a pseudomorphic thin layer called wetting layer (WL) is created, which is elastically distorted. During growth the elastic energy stored in this layer increases. In general, either *plastic* or *elastic relaxation* of this internal elastic energy is possible. From the linear elastical theory, the energy per surface unit stored by a layer is:

$$E = M(\frac{\Delta a}{a})^2 h + \gamma_B + \gamma_{IF}, \tag{1.2}$$

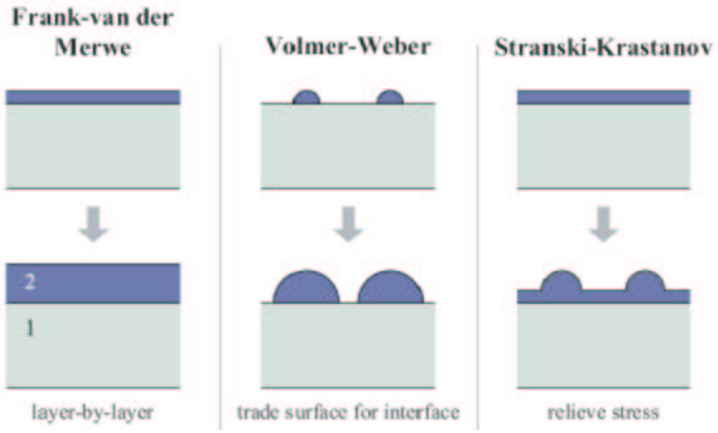

Figure 1.2: Heteroepitaxial growth modes [40].

where M is the Young modulus of the film, $\frac{\Delta a}{a}$ is the misfit and h the layer height. If $\frac{\Delta a}{a} < 1\%$, the 2D growth will proceed until the formation of dislocation in the layer [5, 6]. These dislocations are called misfit dislocations. If $2 < \frac{\Delta a}{a} < 10\%$ (as it is the case for the SiGe system), a thin pseudomorphic layer will form until the elastic energy stored by the 2D layer will become too high. The system will elastically relax by the formation of 3D islands. The strain energy release is all the more efficient as the aspect ratio of the 3D islands is high. The increase of the aspect ratio implies an increase of the free surface of the island and thus an increase of its surface energy. The SK growth is thus the result of the competition between strain energy release and surface energy increase. If the growth of the strained material goes on, the islands will reach a size for which elastic relaxation is not enough to release the strain energy and dislocations will form. The mean island parameter will tend towards its free lattice parameter.

1.3.2 Growth kinetics.

Kinetic parameters such as the growth rate and time can affect the morphological evolution of islands. This can influence the critical thickness for the 2D-3D transition [7], the island nucleation [8, 9] and island density [9, 10]. Fig. 1.3 describes the different atomistic processes that occur during the crystal growth.

At thermodynamic equilibrium, all processes proceed in opposite directions at equal rates, as required by consideration of a 'detailed balance'. For instance, surface processes such as adsorption and desorption should counterbalance (Fig. 1.3). By contrast, crystal growth is an inherent non-equilibrium process and the final macroscopic state depends on the route taken through various reaction paths. To describe the route, an important parameter is the atomic diffusion length (L_D) which depends on the surface diffusion coefficient D and the growth rate. The diffusion coefficient is thermally activated and follows an Arrhenius law:

$$D = D_0 \mathrm{e}^{-\frac{E_A}{k_B T}}, \tag{1.3}$$

where E_A is the activation energy, T the growth temperature, D_0 a constant and k_B the Boltzmann constant. The deposited atoms will preferentially attach on atomic steps or on surface inhomogeneities depending on their diffusion length. On a surface without defects, they will coalesce to nucleate 2D 'islands', which will then be a preferential site for atom attachment. This will result in the formation of a 2D layer. For the island growth, the same process occurs. Above a critical thickness, it is energetically favorable to form 3D islands and to incorporate atoms in the islands.

During island growth, Ostwald ripening may occur. This supposes that atoms detach more readily from smaller islands and condense faster on larger ones. For a fixed amount of material, larger islands

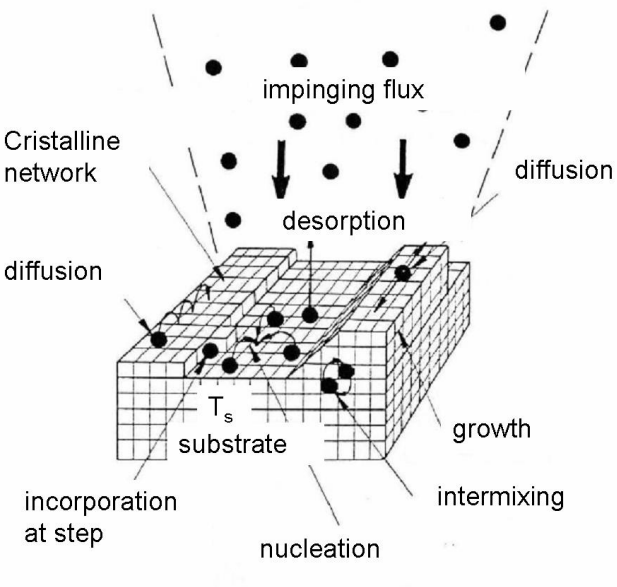

Figure 1.3: Schematic of different atomistic processes that occur during crystal growth [11].

grow at the expense of smaller ones. It can be demonstrated that the average island size should increase as $t^{\frac{3}{4}}$ if Ostwald ripening occurs [12, 13] as the only growth process. By contrast, in a condition of thermodynamic equilibrium the average island size should remain constant.

Influence of the deposition rate.

If we consider a growth where atoms are deposited on a surface at a constant deposition rate F, then the ratio D/F determines the average distance that an adsorbed species has to travel to meet another adsorbate, either for nucleation of a new aggregate or by attachment to an already formed island. The ratio of deposition to diffusion rate D/F is thus the key parameter characterizing growth kinetics. If deposition is slower than diffusion (large values of D/F), growth occurs close to equilibrium conditions, the adsorbed species have enough time to explore the potential energy surface so that the system reaches a minimum energy configuration. If deposit is fast, growth is essentially determined by kinetics; individual processes leading to metastable structures are important [14].

1.4 Growth process: Si(001) surface reconstruction, wetting layer and three dimensional growth.

As previously mentioned, elastic energy relief explains the formation of 3D nanostructures and depends on the layer thickness. For layer thicknesses below and about one monolayer (ML), the elastic energy is reduced by *surface reconstruction* [15]. On the Si(001) surface, a 2x1 surface reconstruction is observed, which is due to the atomic rearrangement of the broken (or dangling) bonds of the atoms on the surface. The reconstructed dimer bonds are oriented parallel to the $< 110 >$ direction (see Fig. 7.12). Generally, the surface normal is not perfectly aligned along a crystallographic direction and presents a *miscut* of typically 0.1° - 1°. Thus, the surface consists of atomically flat (001) terraces separated by monolayer steps. The dimer orientations at neighboring terraces are mutually perpendicular. For a general miscut orientation the monolayer steps consist of microscopic S_A and S_B portions, oriented parallel and perpendicular to the dimer rows of the upper terrace, respectively. Dimeriza-

tion strains the surface. For increasing Ge coverage, the surface reconstruction type changes to 2xN. This can be described as a periodic sequence in which every N^{th} dimer is missing. With increasing Ge coverage, N decreases [16]. After a coverage of two monolayers of Ge, the 2xN reconstruction evolves to a MxN reconstruction [17, 18]. It appears from experimental and theoretical studies that an exchange of Ge adatoms with Si atoms in the substrate is possible, since the corresponding energy barrier is rather low [19, 20, 21]. This phenomenon is important to understand atomic ordering. If the step-flow growth of a SiGe alloy can be described as a movement of closely spaced T_A, T_B terraces, compositional ordering is observed [22].

The two-dimensional film growth adopts a step-flow growth if the mean free path for adatom diffusion across the terrace is larger than the mean step distance. The step-flow growth describes epitaxial growth as a lateral movement of monolayer steps via attachment of adatoms at their steps and their kinks. During SiGe/Si heteroepitaxy, the step-flow mode is unstable against the bunching of S_A and S_B steps. Recently, step bunching during SiGe heteroepitaxy on Si(001) was investigated for several Ge concentrations [23], the resulting bunch morphology depends mainly on growth temperature. Beside step bunching, other instability mechanisms can lead to quasiperiodic structures during step-flow growth. Step meandering can be explained by a different adatom mobility towards the step at upper and lower terraces (T_A, T_B), this results in a wavy step morphology.

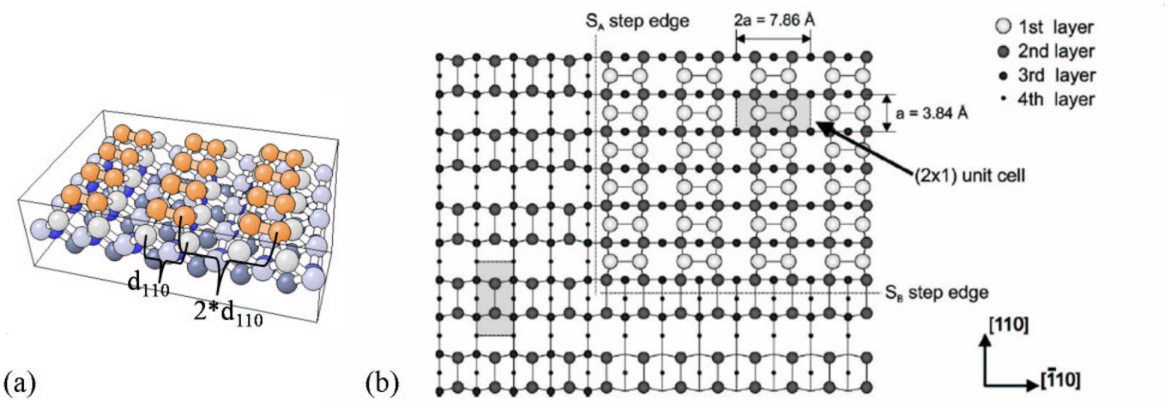

Figure 1.4: (a) and (b) Schematic models of the atomic configuration of the (2x1) reconstructed Si(001) surface. The upper terrace is separated by a S_A and S_B step from the lower terrace. On each of the two terraces a (2x1) unit cell is indicated by a gray shading. Due to the crystal symmetry of the diamond lattice, the unit cell is rotated by 90° on the two terraces [17].

Depending on the experimental conditions, the critical thickness of the reconstructed wetting layer is around 3 to 5 monolayers (ML) (1ML(Ge) corresponds to a thickness of $a_{Ge}/4$, where a_{Ge} is the lattice parameter of Ge). After that, islands are formed as a result of the competition between strain energy release and surface energy increase. In SiGe/Si, essentially five forms of islands are observed: shallow mounts (prepyramids), "hut clusters"-elongated pyramids with {105} facets (see Fig. 1.5), square pyramids with {105} facets, domes with {105}, {113}, {15 3 23} crystallographic facets and a top (001) facet parallel to the substrate surface [24], "barns" with additional {111} and {4 20 23} facets and finally dislocated "superdomes" with the same facets as coherent barns.

In the first stage of growth, shallow prepyramids appear that later convert to hut clusters or pyramids. Hut clusters were proved to be metastable by Medeiros-Ribeiro *et al.* [26] as they tend to disappear during annealing experiments, contrary to pyramids and domes. They are usually observed only in samples grown at low temperature. As pyramids reach a critical volume, they undergo a morphological change to multifacetted islands, called domes, while islands smaller than a critical size are in the process of shrinking [27]. This transition leads to a bimodal size and shape distribution of islands [28] and occurs at a critical volume proportional to ϵ^{-6} [29], where ϵ is the strain between the epilayer and the substrate. Then, large domes evolve to coherent barns and finally plastically

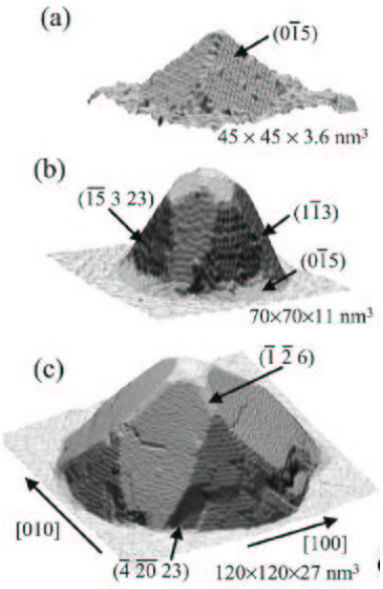

Figure 1.5: STM images of a Ge pyramid (a), a dome (b) and a superdome (c). The Miller indexes of the facets is indicated (from Ref. [25]).

relaxed superdomes with misfit dislocations at their bases. The formation of "barns" is observed for temperatures higher than 620°C [30]. The Si-Ge intermixing is expected to play a significant role in stabilizing the {4 20 23} facets.

1.5 Intermixing

Si-Ge intermixing generally takes place during growth or post-growth annealing as a mechanism of strain release. Intermixing is a crucial point in the SiGe system. What is largely accepted is that, if the deposition temperature is high enough, strong intermixing changes the composition, size (islands tend to become larger [31]) and shape of islands. Besides, with increasing growth temperature, Si-Ge intermixing becomes more larger [8]. In addition, if intermixing is strong enough, domes can transform back to pyramids [33, 34]. However, the alloying mechanisms are still not completely understood.

Eight years ago, atomistic elastic models ([35, 36]) have shown that the intermixing in 3D islands is driven by strain energy enhancement near the island perimeter, where the strain has a maximum. In 2003, experimental results by Denker *et al.* [37] revealed that strain energy relief is not the only driving force for Si-Ge intermixing in Ge pyramids. After applying a selective etching procedure, they showed that pyramids grown at 560°C have a variable lateral composition with a Ge rich center and highly Si intermixed corners. The observed Si enrichment of the corners could be reproduced by numerical simulations based on surface diffusion.

The composition has also been studied by other techniques such as energy-filtering transmission electron microscopy and X-ray energy dispersive spectrometry [38] or anomalous X-ray diffraction [39]. The results show a nonuniform composition distribution inside the quantum dots (QDs), alternatively showing a Si-rich center [39] or perimeter [37], depending on the growth temperature.

Recently, Katsaros *et al.* [40] have investigated the dependence of the composition of self-organized islands on the temperature, the growth rate, and the annealing time. They demonstrated that pyramids grown at 560°C and 580°C can either present a Si rich core or a Ge rich core with a characteristic cross shape (see Fig. 1.6 (a)-(b)). The periphery of domes grown at low temperatures (560°C-600°C) has a higher Si content compared to the center, whereas domes grown at 620°C show a Si rich core

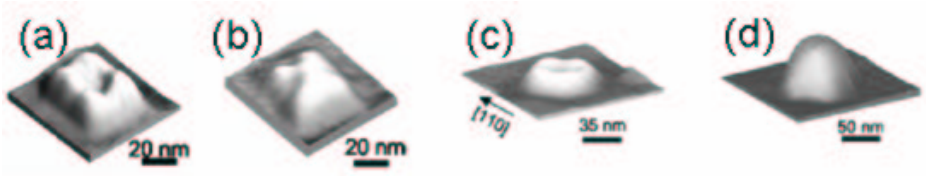

Figure 1.6: 65% Ge isocompositional profiles of pyramids without apex (a) and with protruding apex (b) grown at 580°C and of domes grown at 580°C (c) and 620°C (d) (from Ref. [40]). The remaining material has a Ge composition lower than 65% and is thus Si rich.

(see Fig. 1.6 (c)-(d)). All the observed composition profiles were explained by a simple model that is of kinetic origin and relies just on surface diffusion phenomena. The inhomogeneous Si distribution of islands grown at lower temperatures is produced by kinetic limitations. Besides, Katsaros *et al.* [40] showed the impact of growth rate which modifies the composition inside domes and the impact of annealing. After growth interruption or annealing during 10 minutes, the domes grown at 580°C display a completely different compositional profile with a strongly asymmetric Si rich core. This can be explained by the lateral movement of Ge islands during annealing [41]. Nevertheless, it has been recently proposed that, in addition to surface diffusion, volume exchange events may play a role in shaping up the composition profiles, and that stress-driven intermixing is needed for global interpretation of experimental results [42].

From recent works, it thus appears that the island growth is substantially determined by the interplay between thermodynamics and kinetic constraints. Understanding the mechanisms which are relevant to explain the Si incorporation inside the wetting layer and the islands is the core of the current debate on intermixing in the Si/Ge system. Pure bulk diffusion (*i.e.* atomic motion events in regions that are far enough from the surface) can be considered as practically absent due to its high potential barriers [43]. Sub-surface processes can be relevant as the strain stored during the growth of Ge on Si substrates could significantly increase the atom mobility in the sub-surface region [44]. Surface diffusion (*i.e.* migration of Si and Ge adatoms at the surface) must be regarded as the most active process as diffusion events are faster than bulk and sub-surface processes by more than 20 and 8 orders of magnitude, respectively [45].

For a short review of the most relevant concepts developed in recent years on the subject of alloying in self-organized semiconductors see Ref. [45].

To highlight the mechanism of Si intermixing inside Ge islands grown on Si(001), the Ge composition of the islands will be followed monolayer by monolayer during their *in situ* growth (see chapter 6). To answer the question whether intermixing is induced by strain energy relief or by a surface mediated diffusion process, the Ge composition of two families of domes grown at the same temperature but differently relaxed will be compared (see chapter 9).

1.6 Self-organization of Ge islands on Si(001).

Spontaneous self-organization of nanostructures has been studied extensively during the past years. It is shown that nucleation of Ge dots on nominal Si(001) is mainly random without preferential sites [4, 17]. To steer lateral self-organization, two general methods have been proposed, using either an inhomogeneous stress field [47] or a specific morphology [48, 2, 50] at the surface. The local variations in the surface chemical potential induced by these inhomogeneities may act as nucleation or coalescence center for deposited atoms. These inhomogeneities can be added to the expression of the chemical potential μ. The chemical potential is a fundamental parameter in thermodynamics and allows to describe the change of the Helmotz free energy H of the system when the number of particles N is changed [51], $\mu = [\partial H/\partial N]_{T,\epsilon}$, with T the temperature and ϵ the deformation. According to Refs.

[52, 53], the evolution of the chemical potential along the surface can be described by

$$\mu = \mu_0 + \Omega\gamma\kappa(x,y) + \Omega E_s(x,y), \tag{1.4}$$

where μ_0 is the chemical potential for the unstressed planar surface, $\Omega\gamma\kappa$ is the contribution of the surface curvature, κ, where γ is the surface free energy per unit area, and ΩE_s is the contribution of tangential stress; here E_s is the local strain energy at the surface and Ω is the atomic volume of the species. The driving-force in a growth regime depends on the local gradient of μ according to the Nernst-Einstein relation $J = -D_s grad\mu$, where D_s is the coefficient of surface diffusion. Nucleation of islands is controlled by the adatom velocity on the surface v which can be expressed as [54]:

$$v = -\frac{D_s}{kT}\frac{\delta\mu}{\delta s}, \tag{1.5}$$

where kT is the thermal energy and $\delta\mu/\delta s$ is the derivative of the chemical potential along the surface.

This simplified model shows that, in the case of an *homoepitaxial* growth:

- the curvature dependent surface energy $\Omega\gamma\kappa$ term favors the diffusion of ad-atoms towards concave morphologies (pits, holes, trenches...) via the capillarity force;
- the elastic energy ΩE_s favors the nuclation on convex morphologies (edges, apex,...) due to a reduction of the amount of compressive strain, which allows a higher relaxation of the elastic energy. It also favors dot positioning on tensile-strained surface areas.

For *hepitaxial* heterostructures, the local surface curvature and the mechanical relaxations strongly influence the island shape and position. The local minimization of chemical potential will be defined by a competition between the surface and strain energy terms. The elastic energy will take into account the misfit between the substrate and deposited elements. The island relaxation will depend on the surface curvature. For instance, when Ge islands are located on convex morphologies, the lattice parameter inside the islands will be larger than the one at the Si/Ge interface. The reverse will be observed on concave morphologies (see Fig. 1.7). In addition, the critical thickness of the wetting layer can be reached earlier in specific regions of the patterned surface.

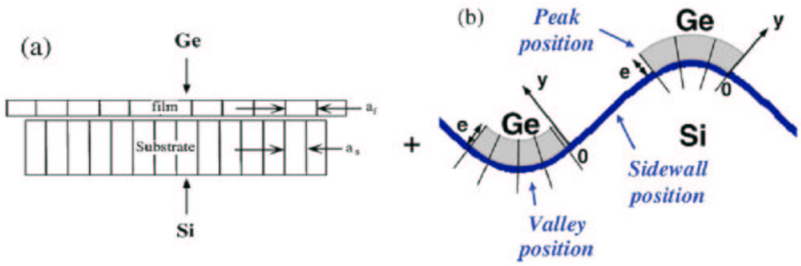

Figure 1.7: Schematics of biaxial elastic strain of a flat (a) and bent Ge island (b), from [55].

To sum up, the preferential nucleation sites are determined by the local minima of the chemical potential, which results from a competition between surface energy and elastic energy. By introducing regular inhomogeneities on the surface, it is then possible to control the growth towards preferential nucleation sites. The periodic modulation of the chemical potential will allow a lateral long range ordering.

In the following part, we will describe how to organize islands, either by using the intrinsic surface properties or by artificially creating a periodic patterning which will favour nucleation at preferential sites.

Specific morphologies of the surface, such as step bunches [56], reconstruction [57] and nano-facets can result in a preferential nucleation of dots. Remarkable Ge dots ordering can be obtained through

self-organized growth instability (see Fig. 1.8 (a)-(b)). Nevertheless, this does not result in true long-range ordering and the periodicity is not easily controlled on these surfaces.

Several ordering effects induced by the stress have been demonstrated, such as, for instance, the vertical correlated growth of semiconductor quantum dots [58]. Besides, stress driven instabilities which develop during the growth of Ge on vicinal Si substrates allow to create periodic nanopatterns [56]. But the organization is again more or less at long range distance and this allows only a one dimensional organization. Ge islands have also been shown to nucleate on dislocation lines [28, 16] (see Fig. 1.8 (c)).

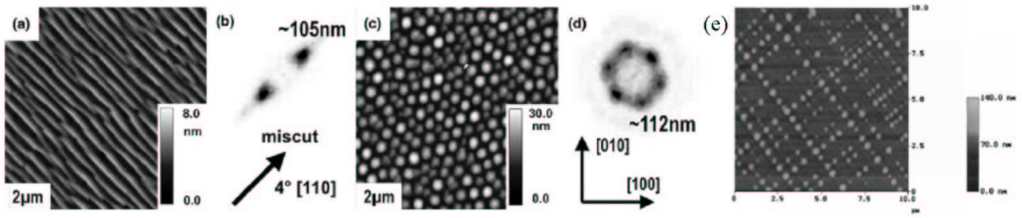

Figure 1.8: (a) AFM data of a thick Si buffer grown at 425°C and at a Si-rate of 0.2 Å/s on a Si(001) substrate with 4° miscut along [110]. The epilayer exhibits pronounced step bunching with ripple periods of 100±10 nm, which is depicted in the corresponding Fourier transform (b) [59] (c) SiGe islands grown on top of such a rippled buffer results in a fair degree of 2D face-centered rectangular ordering and (d) Fourier transform of (c). (e) AFM image of Ge islands grown on a Si layer strained by a relaxed SiGe layer. The Ge islands are aligned on the strain field induced by the burried misfit dislocation network [58].

But generally the dislocations are not totally periodic and the organization is only at short range distance. Then, it has been demonstrated that finely tuned elastic fields can be created by molecular bonding [60]. Use of buried arrays of dislocations (Fig. 1.9 (a)) artificially made by molecular bonding of two crystals combines the advantages of crystalline strained surfaces with the quasi-perfect periodicity of dislocation networks. Nevertheless, such strain-patterned templates have yielded to only short-range ordering [61] (Fig. 1.9 (b)). To overcome this problem, an alternative has been developped which use strain-driven etching to pattern the morphology of the surface (Fig. 1.9 (c)-(d)). The growth of Ge islands on such substrates will be studied in chapter 8.

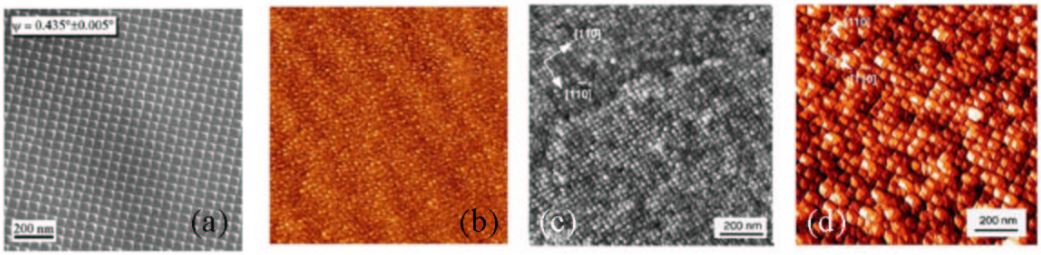

Figure 1.9: (a) TEM plane-view image of the burried dislocation network obtained after the molecular bonding of two Si(001) wafers [62]. (b) STM image of Ge islands grown on sample shown in Fig. (a). The burried dislocation network only induces short-range ordering. (c) STM image of the Si surface after strain-driven etching. (d) STM image of Ge islands grown on the etched surface. A lateral ordering of the Ge islands is observed [61].

To control the periodic morphology of the surface, different lithography techniques are used (holographic or e-beam lithography) which are then followed by transfer processes ('lift-off', reactive ion etching, ...). These controlled surface structurations induce a periodic modulation of the chemical

potential and allow a long range ordering. As an example, Fig. 1.10 shows ordered Ge islands grown on Si surfaces pre-patterned by holographic lithography [63] or focused ion beam [64].

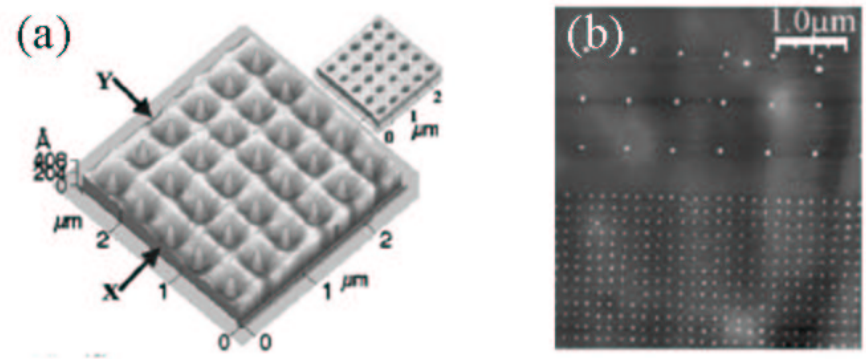

Figure 1.10: (a) AFM image of a pre-patterned surface after holographic lithography and after a deposit of 6ML of Ge at 700°C [63]. (b) AFM image of Ge islands on a Si substrate pre-patterned by focused ion beam [64].

The islands are preferentially localized inside the pits as a result of a competition between surface and elastic energies. The island localisation strongly depends on the aspect ratio and morphology of the surface. Numerous experimental [65, 66] or theoretical [67, 68] studies show the impact of the local chemical potential on the localisation of the Ge islands on Si surfaces. As an example, Fig. 1.11 shows that the competition between the surface-energy and strain-energy terms leads to multiple local minima in the chemical potential. The surface energy term produces chemical-potential minima in concave regions at the foot of stripes [52] and the strain relaxation term produces local chemical potential minima in the most convex regions on the top of the stripes. The strain-relaxation term thus has a strong impact on the position of the Ge islands on pre-patterned Si surfaces. The strain relaxation term is highly attenuated in the case of Ge islands grown on a pre-patterned SiO_2 surface [69].

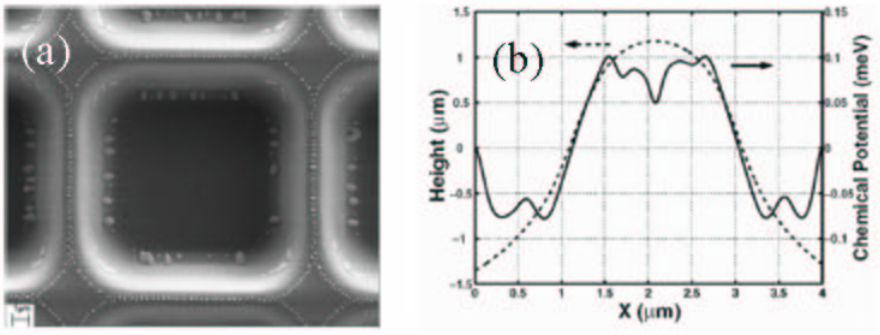

Figure 1.11: (a) Scanning electron microscope image of Ge 3D islands grown on patterned stripes on Si(001). (b) Variation of the local surface chemical potential of stripe structures with position X. The dashed line is the surface profile measured by AFM. From [52].

The Ge growth on Si surfaces pre-patterned by lithography will be presented in chapter 8.

1.7 Defects and dislocations

1.7.1 Planar defects in Si and Ge bulks.

The {111} and {100} planes are dense planes of Si and Ge cubic diamond structures. {111} planes show an hexagonal symmetry and present a periodic stacking sequence AaBbCcAaBbCc (see Fig. 1.12). Thereby, large planar defects (such as stacking faults) can be formed with closed partial dislocations at their boundaries in Si and Ge. Stacking faults can be either *intrinsic* (ISF) or *extrinsic* (ESF). ISFs are formed when an atomic layer is removed from the stacking sequence, whereas for ESFs an additional layer is inserted into the lattice (Fig. 1.12). Both can be bound by Frank partial dislocation loops, which have a Burgers vector $\mathbf{b}=a/3\langle 111\rangle$, a being the lattice constant.

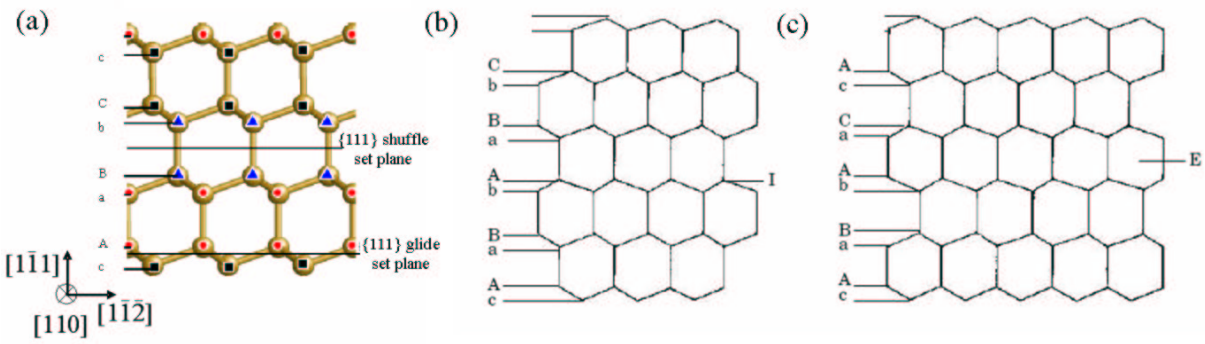

Figure 1.12: (a) Projection of the diamond structure on the (110) plane. (b) Intrinsic stacking fault (I) and (c) Extrinsic stacking fault. The diamond structure is projected on the (110) plane.

Another type of planar defects is twin faults. They appear when the original sequence *AaBbCcAaBbCc* is reverse into *CcBbAaCcBbAa* (see Fig. 5.33 (c)).

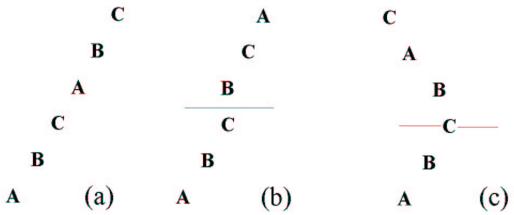

Figure 1.13: Sequences of 111 layers expressed in terms of A, B and C positions. The layers a, b and c have been omitted. (a) Correct sequence. (b) A deformation fault: an intrinsic stacking fault. (c) A growth or twin fault.

The characteristics of planar defects and especially of planar core defects (*i.e.* distortion, size) will be studied in chapter 5.

1.7.2 Formation of defects during the Ge growth on Si(001).

As previously mentioned, the growth of Ge on Si(001) is coherent until the formation of large islands for which elastic relaxation is not enough. A competing strain relief mechanism appears which is based on the creation of misfit dislocations at the island/substrate interface.

Defects in Ge islands have been extensively studied theoretically [70, 71] and experimentally by transmission electron microscopy (TEM) [72, 73]. Different kinds of defects can be present: either screw dislocations ($\mathbf{b}//[\mathbf{110}]$), 90° misfit dislocations, 60° misfit dislocations (see Fig. 1.14) or stacking

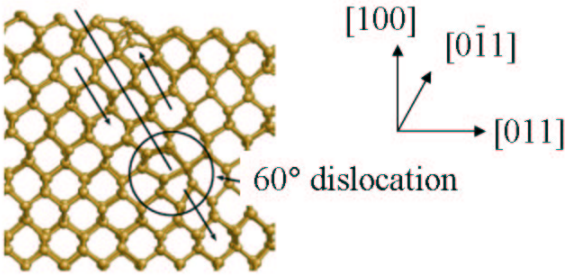

Figure 1.14: Scheme of a 60° perfect dislocation [74].

faults. The 60° dislocations are the most common dislocations in Ge islands. In semiconductors with the diamond structure, glide is confined to {111} planes. Because the 90° dislocations cannot glide on the allowed {111} planes, they are generally far less involved in plastic relaxation than the 60° dislocations. 60° dislocations have their Burgers vector **b**=a/2[101] which is inclined at an angle of 60° to the dislocation line unit vectors along [110] or [1-10] [75], and thus they can relieve strain in both [110] and [1-10] directions. The Burgers vector has a component which couples to the lateral [1-10] misfit stress; but it also has a [001] 'tilt' component, which couples to the shear stress in the island. The island presents a minimum of energy when the [101] dislocation is displaced towards one side of the island [76]. 60°-dislocations can glide down to the interface on their {111} type glide planes. They are often called glissile 60°-dislocations.

Sessile 90° Lomer type-dislocations are pure edge dislocations with Burgers vector **b**=a/2[110] parallel to the interface. They have minimum energy at the center of the island-substrate interface. Both of them accomodate misfit strain at the Ge/Si interface as dislocations at the interface reduce the total free energy of a growing strained island [77]. Both of them can be dissociated into two partial dislocations and a stacking fault.

The growth and relaxation of Ge islands depends significantly on the temperature, *i.e.* they exhibit different kinds of dislocations according to the growth temperature. At high temperatures, 60° type-dislocations are introduced. However, in the low-temperature regime, the islands grow relaxed from the outset with pure edge dislocations [73]. Whatever the temperature, incoherent islands also present {111}-type stacking faults originating at the Ge/Si interface [78].

The insertion of misfit dislocations partially depends on growth kinetics. Dislocation introduction drastically lowers the island chemical potential, causing growth acceleration at the coherent-to-incoherent transition [79]. It is also recognized that slow Ge deposition rates allow Ge/Si islands to adopt the height, width and distribution of dislocations required to minimize their energy [72].

As observed by LeGoues [72], dislocated islands grow almost vertically, except for a sudden periodic lateral expansion each time a new misfit dislocation is formed. Thus, dislocated islands undergo a complex cyclic growth. The use of chemical etching and atomic force microscopy (AFM) has recently confirmed this complex cyclic growth by revealing a tree-ring structure below dislocated SiGe islands [80] (see Fig. 1.15 (a)-(b)). Figure 1.15 (c) explains the mechanism of dislocation incorporation. Trenches surround the island base. Once a dislocation has been introduced, the island becomes a sink for material as it is more strain-relaxed and will rapidly expand in the lateral direction covering a part of the trench. The covered trench is preserved, while the remaining part is subject to further erosion. The process is repeated for each additional dislocation.

Using this technique, Merdzhanova *et al.* [80] show that the critical volume for which it becomes energetically favorable for an island to incorporate a dislocation increases when the growth temperature increases (see Fig. 1.15 (d)). This result is consistent with an interpretation of increased Si interdiffusion and island alloying reducing the island-substrate misfit. They clearly show that island coalescence is the dominant pathway towards dislocation nucleation at low temperatures, while at higher temperature anomalous coarsening is effective: the strain-relaxed superdomes grow at the expense of nearby smaller islands.

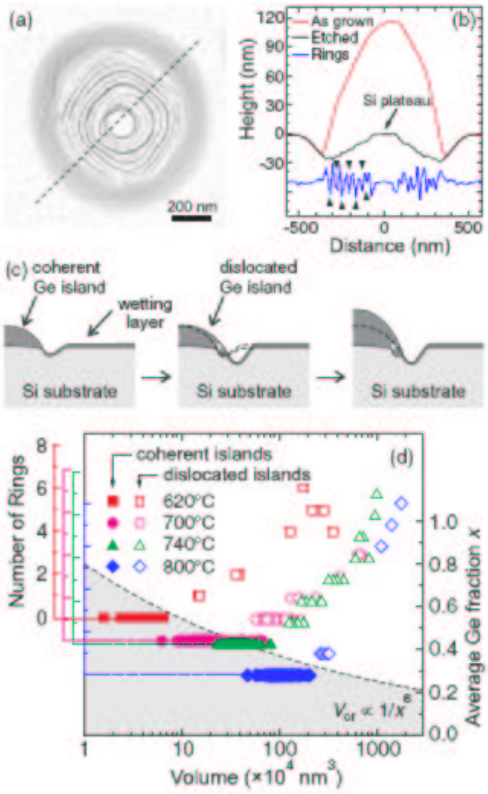

Figure 1.15: (a) AFM scan of the tree-ring structure left over by a single superdome (grown at 800°C) after etching. (b) Cross-sectional profile of the same superdome before and after etching along the dashed line shown in (a). (c) Schematic representation of the mechanism. (d) Number of rings vs island volume and extimated Ge fraction x for different temperatures [80].

All the mentioned methods to detect defects are *ex situ* techniques except *in situ* TEM measurements. These methods do not allow to give statistical information on the formation of defects during the *in situ* growth of Ge on Si(001) and to link these information with island relaxation and composition. Chapters 5 and 6 will present a novel method to follow the formation of defects (size, localization) as a function of island growth.

1.8 Conclusions and perspectives

Despite the wide knowledge acquired in this system, there are still some open questions concerning the evolution of the strain, the elastic to plastic transition, the intermixing and their relations with the different shapes of the island. These questions will be investigated in the next chapters.

Bibliography

[1] E. Bauer, Z. Kristallogr. **110**, 372 (1958).

[2] F. C. Frank, J. H. Van der Merwe, Proc. Roy. Soc. London Ser. A **198**, 213 (1949).

[3] I. N. Stranski, L. Krastanow, Ber. Akad. Wiss. Wien, Math.-Naturwiss. K1, Art. IIb **146**, 797 (1938).

[4] R. J. Wagner, *Growth energetics of germanium quantum dots by atomistic simulations*, PhD thesis, University of Michigan (2004).

[5] J. W. Matthews and A. E. Blakeslee, J. Cryst. Growth **27**, 118 (1974).

[6] B. W. Dodson and J. Y. Tsao, Appl. Phys. Lett. **51**, 1325 (1987).

[7] C. W. Snyder, J. F. Mansfield, B. G. Orr, Phys. Rev. B **46**, 9551 (1992).

[8] K. E. Kohr, S. Das Sarma, Phys. Rev. B **62**, 16657 (2000).

[9] B. Voigtländer, M. Kawamura, N. Paul, V. Cherepanov, J. Phys.: Cond. Matter **16**, S1535 (2004).

[10] P. Kratzer, M. Scheffler, Phys. Rev. Lett. **88**, 036102 (2002).

[11] R. Dujardin, *Epitaxie par jets moléculaire de nanostructures isolées de germanium sur silicium*, PhD thesis, Joseph Fourier University (2006).

[12] B. K. Chakraverty, J. Phys. Chem. Solids **28**, 2401 (1967).

[13] B. K. Chakraverty, J. Phys. Chem. Solids **28**, 2413 (1967).

[14] J. V. Barth, G. Costantini, K. Kern, Nature **437**, 671 (2005).

[15] A. Zangwill, Physics at Surfaces, Cambridge University, Cambridge, England(1988).

[16] C. Teichert, C. Hofer, K. Lyutovich, M. Bauer and E. Kasper, Thin Solid Films **380**, 25 (2000).

[17] B. Voigtländer, Surf. Sci. Rep. **43**, 127 (2001).

[18] A. Rastelli, H. von Känel, B. J. Spencer and J. Tersoff, Phys. Rev. B **68**, 115301(2003).

[19] Z. Y. Lu, F. Liu, C. Z. Wang, X. R. Qin, B. S. Swartzentruber, M. G. Lagally and K. M. Ho, Phys. Rev. Lett. **85**, 5603 (2000).

[20] X. R. Quin, B. S. Schwartzentruber and M. G. Lagalli, Phys. Rev. Lett. **85**, 3660, (2000).

[21] X. R. Quin, B. S. Schwartzentruber and M. G. Lagalli, Phys. Rev. Lett. **84**, 4645, (2000).

[22] D. E. Jesson, S. J. Pennycook, J. Z. Tischler and J. D. Budai, Phys. Rev. Lett. **70**, 2293 (1993).

[23] M. Mühlberger, C. Schelling, G. Springholz and F. Schäffler, Surf. Sci. **532**, 721, (2003).

[24] A. Rastelli, and H. von Känel, Surf. Sci. **515**, L493, (2002).

[25] A. Rastelli, E. Müller, and H. von Känel, Appl. Phys. Lett. **80**, 1438, (2002).

[26] G. Medeiros-Ribeiro, A. M. Bratkowski, T. I. Kamins, D. A. A. Ohlberg, and R. S. Williams, Science **279**, 353, (1998).

[27] A. Rastelli, M. Stoffel, J. Tersoff, G. S. Kar, and O. G. Schmidt, Phys. Rev. Lett. **95**, 026103 (2005).

[28] F. M. Ross, R. M. Tromp, M. C. Reuter, Science **286**, 1931 (1999).

[29] A. Rastelli, PhD thesis, Dipartimento di Fisica 'A. Volta', Università degli Studi di Pavia (2002).

[30] M. Stoffel, A. Rastelli, J. Tersoff, T. Merdzhanova and O. G. Schmidt, Phys. Rev. B **74**, 155326, (2006).

[31] G. Capellini, M. D. Seta, F. Evangelisti, Appl. Phys. Lett. **78**, 303 (2001).

[32] T. U. Schülli, M. Stoffel, J. Stangl, R. T. Lechner, E. Wintersberger, M. Sztucki, T. H. Metzger, O. G. Schmidt and G. Bauer, Phys. Rev. B. **71**, 035326 (2005).

[33] T. I. Kamins, R. S. Williams, Appl. Phys. Lett. **71**, 1201 (1997).

[34] W. Henstrom, C.-P. Liu, J. M. Gibson, T. Kamins, and R. S. Williams, Appl. Phys. Lett. **77**, 1624 (2000).

[35] S. A. Chaparro, J. Drucker, Y. Zhang, D. Chandrasekhar, M. R. MacCartney, and D. J. Smith, Phys. Rev. Lett. **83**, 1199 (1999).

[36] P. Sonnet, and P. C. Kelires, Phys. Rev. B **66**, 205307 (2002).

[37] U. Denker, M. Stoffel and O. Schmidt, Phys. Rev. Lett. **90**, 196102 (2003).

[38] X. Z. Liao, J. Zou, D. J. H. Cockayne, J. Wan, Z. M. Jiang, G. Jin, and K. L. Wang, Phys. Rev. Lett. **65**, 153306 (2002).

[39] A. Malachias, S. Kycia, G. Meideros-Ribeiro, R. Magalhaes-Paniago, T. I. Kamins, R. S. Stanley, Phys. Rev. Lett. **91**, 176101 (2003).

[40] G. Katsaros, G. Costantini, M. Stoffel, R. Esteban, A. M. Bittner, A. Rastelli, U. Denker, O. G. Schmidt, and K. Kern, Phys. Rev. B **72**, 195320 (2005).

[41] Y. Tu and J. Tersoff, Phys. Rev. Lett. **98**, 096103 (2007).

[42] G. Hadjisavvas, and P. C. Kelires, Phys. Rev. B **72**, 075334 (2005).

[43] N. Sugii, J. Appl. Phys. **89**, 6459 (2001).

[44] F. Rosei, P. Raiteri, Appl. Surf. Sci. **195**, 16 (2002).

[45] F. Ratto, G. Costantini, A. Rastelli, O. G. Schmidt, K. Kern, and F. Rosei, Journal of Experimental Nanoscience **1**, 279 (2006).

[46] J. M. Baribeau, X. Wu, N. L. Rowell, and D. J. Lockwood, J. Phys.: Condens. Matter **18**, R139 (2006).

[47] J. Tersoff, C. Teichert, M. G. Lagally, Phys. Rev. Lett. **76**, 1675 (1996).

[48] T. Kamins, G. Meideros-Ribeiro, D. Ohlberg, and R. S. Williams, Appl. Phys. A **67**, 727 (1998).

[49] Z. Zhong and G. Bauer, Appl. Phys. Lett. **84**, 1922 (2004).

[50] R. Songmuang, S. Kuravittaya, O. G. Schmidt, Appl. Phys. Lett. **82**, 2892 (2003).

[51] A. Pimpinelli, J. Villain, *Physique de la croissance cristalline*, Collection Alea-Saclay (1995).

[52] B. Yang *et al.*, Phys. Rev. Lett. **92**, 025502 (2004).

[53] M. Borgström, V. Zela, and W. Seifert, Nanotechnology **14**, 264 (2003).

[54] D. J. Slorovitz, Acta Metall. **37**, 621 (1989).

[55] A. Bavard, J. Eymery, A. Pascale and F. Fournel, Phys. Stat. Sol. (b) **243**, 3963 (2006).

[56] I. Berbezier, A. Ronda, Phys. Rev. B **75**, 195407 (2007).

[57] V. Repain, G. Baudot, H. Ellmar, S. Rousset, Europhys. Lett. **58**, 730 (2002).

[58] Q. Xie, A. Madhukar, P. Chen, N. P. Kobayashi, Phys. Rev. Lett. **75**, 2542 (1995).

[59] Z. Zhong, H. Lichtenberger, G. Chen, M. Mülberger, C. Schelling, J. Myslivecek, A. Halilovic, J. Stangl, G. Bauer, W. Jantsch, and F. Schäffler, Micro. Eng. **83**, 1730 (2006).

[60] A. Bavard, PhD Thesis: University of Grenoble (2007).

[61] F. Leroy, J. Eymery, P. Gentile, F. Fournel, Surf. Sci. **545**, 211 (2003).

[62] F. Fournel, H. Moriceau, B. Aspar, K. Rousseau, J. Eymery, J. L. Rouvière, N. Magnéa, Appl. Phys. Lett. **80**, 793 (2002).

[63] Z. Zhong, A. Halivovic, T. Fromherz, F. Schäffler, G. Bauer, Appl. Phys. Lett. **82**, 4779 (2003).

[64] A. Portavoce, M. Kammler, R. Hull, M. C. Reuter, F. M. Ross, Nanotechnology **17**, 4451 (2006).

[65] Z. Zhong, A. Halivovic, M. Mühlberger, F. Schäffler, G. Bauer, Appl. Phys. Lett. **93**, 6258 (2003).

[66] A. Karmous, A. Cuenat, A. Ronda, I. Berbezier, S. Atha, R. Hull, Appl. Phys. Lett. **85**, 6401 (2004).

[67] R. V. Kukta, D. Kouris, J. Appl. Phys. **97**, 033527 (2005).

[68] M. Bavencoffe, E. Houdart, C. Priester, J. Cryst. Growth **275**, 305 (2005).

[69] A. L. Giermann, C. V. Thompson, Appl. Phys. Lett. **86**, 121903 (2005).

[70] B. J. Spencer and J. Tersoff, Appl. Phys. Lett. **77**, 2533 (2000).

[71] B. J. Spencer and J. Tersoff, Phys. Rev. B **63**, 205424 (2001).

[72] F.K. LeGoues, M. C. Reuter, J. Tersoff, M. Hammar and R. M. Tromp, Phys. Rev. Lett. **73**, 300 (1994).

[73] M. Hammar, F. K. LeGoues, J. Tersoff, M. C. Reuterand R. M. Tromp, Surface Science. (**349**), 129 (1996).

[74] J. Godet, *Etude par simulations et calculs atomistiques, de la formation de dislocations aux défauts de surface dans un cristal de silicium soumis à des contraintes.*, University of Poitiers (2004).

[75] J. P. Hirth and J. Lothe, *Theory of Dislocations* , (Krieger 1992).

[76] B. J. Spencer, J. Tersoff, Appl. Phys. Lett. (**77**), 16 (2000).

[77] H. T. Johnson and L. B. Freund, J. Appl. Phys. **91**, 9 (1997).

[78] D. J. Smith, D. Chandrasekhar, S. A. Chaperro, P. A. Crozier, J. Drucker, M. Floyd, M. R. McCartney, and Y. Zhang, J. Cryst. Growth **259**, 232 (2003).

[79] M. Krishnamurthy, J. S. Drucker and J. A. Venables, J. Appl. Phys. **69**, 6461 (1991).

[80] T. Merdzhanova, S. Kiravittaya, A. Rastelli, M. Stoffel, U. Denker, and O. G. Schmidt, Phys. Rev. Lett. **96**, 226103 (2006).

Chapter 2

Characterization methods

2.1 Introduction

As the characteristic dimensions of semiconductor devices decrease into the regime of nanostructures with sizes of the order of 100 nm or less, advanced characterization tools are strongly needed to understand and control nanostructure properties. The physical properties of semiconductor heterostructures of reduced dimensions strongly depend on their structural properties, *i.e.* ***their morphology, their composition and structure at atomic level. Their morphology includes their shape, size and organization on a substrate. The atomic structure includes their strain, their composition and very importantly the presence of defects such as point defects, dislocations or stacking faults. It is thus essential to characterize these properties as deeply as possible, in order to predict and understand their physical properties. In this work, these morphological and structural properties are mainly addressed by X-ray techniques using synchrotron radiation. The basic problem in X-ray scattering is the weak scattering signal due to the small amount of material which forms the nanostructures. In order to enhance the scattering signal from the nanostructures, grazing incidence techniques have been used. In the first section, the scientific background for the grazing incidence techniques, in which the refraction of X-rays at an interface is of fundamental importance, is described. In section 2.1.2, the basis of X-ray scattering and grazing incidence X-ray diffraction (GIXD) will be presented. In the following section, an approximation for the description of grazing incidence phenomena at surfaces is presented. In section 2.1.4, the grazing incidence small angle scattering (GISAXS) technique is described. The missing part, the chemical composition is revealed by performing multiwavelength anomalous diffraction (GI-MAD), which adds chemical sensitivity, is described in section 2.1.5. X-ray scattering has the drawback that the information is obtained in reciprocal space. It is thus most useful to combine it with others techniques, such as Atomic Force Microscopy (AFM), Transmission Electron Microscopy (TEM),..., which are shortly presented in the last section.***

2.2 X-ray characterization methods.

2.2.1 Surface sensitive X-ray scattering.

To investigate heterostructures such as quantum dots or islands, most of the time, the incident X-ray wave vector $\mathbf{k_i}$ is kept at grazing incidence with respect to the sample surface. This minimizes the unwanted elastic or inelastic background scattering from the bulk, while promoting the near-surface scattering.

Figure 2.1 shows the schematic drawing of different X-ray measurements at grazing incident scattering geometry. The X-ray beam impinges on the surface with the incident angle α_i. The scattered beam of wave vector $\mathbf{k_f}$ makes the in-plane scattering angle 2θ with respect to the incident beam. It is detected at a direction defined by slits and makes an angle α_f with respect to the sample surface and an in-plane angle δ with respect to the transmitted beam. The momentum transfer is defined as $\mathbf{Q} = \mathbf{k_f} - \mathbf{k_i}$ and is decomposed into two components $\mathbf{Q}_{//}$ and $Q_\perp$, respectively parallel and perpendicular to the surface. The absolute value of $Q_\perp$ is a function of α_i and α_f: $Q_\perp = k_0(\sin\alpha_i + \sin\alpha_f)$ with $k_0 = 2\pi/\lambda$, where λ is the wavelength.

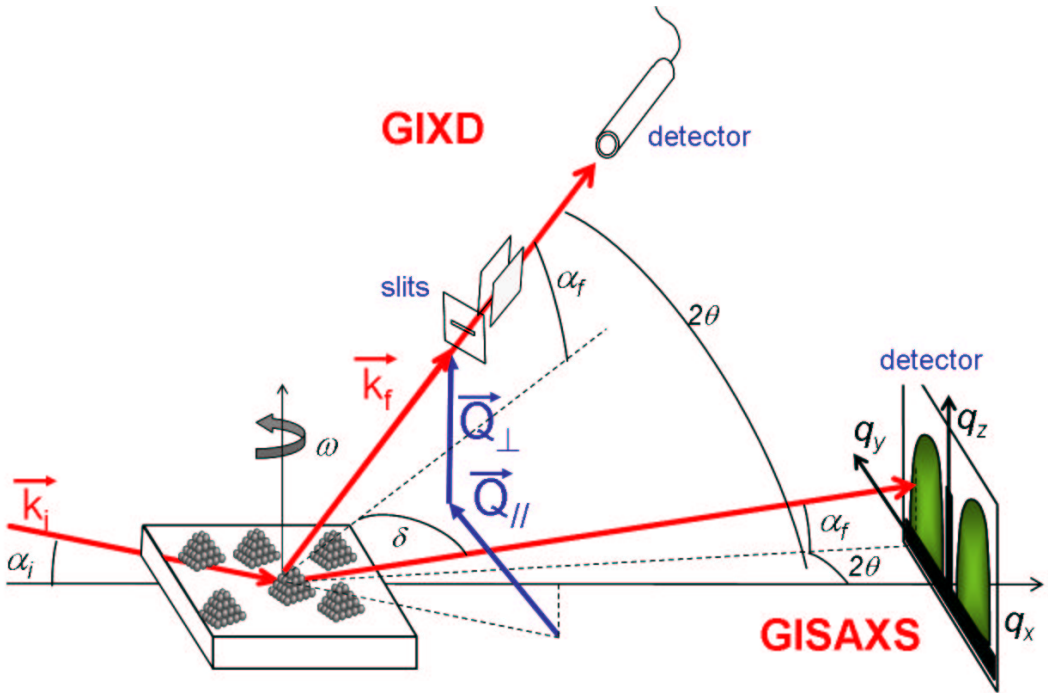

Figure 2.1: Schematic representation of the reciprocal space of nano-islands with corresponding X-ray techniques.

When all angles are small, the momentum transfer is also small ($\sim 0 - 1nm^{-1}$). Hence large dimensions are probed in real space. One corresponding technique is Grazing Incidence Small Angle Scattering (GISAXS) which is used to probe the morphology parallel to the surface (along Q_y) and perpendicular to it (along Q_z), at intermediate length scales (typically between a few nm and a few hundreds of nm). Large scattering angles 2θ allow probing the atomic scale using for instance Grazing Incidence X-ray Diffraction (GIXD), which is the typical technique to probe the crystallographic lattice of nanostructures.

Because the incident angle is small, it is necessary to consider the effects of refraction at the interface [1].

Refraction of X-rays at an interface

As X-rays are electromagnetic waves, they obey Maxwell's equations. In a medium characterized by a refractive index n, the Helmholtz propagation equation for the electric field amplitude $\phi(\mathbf{r})$ can be written as:

$$[\nabla^2 + k_0^2 n^2]\phi(\mathbf{r}) = \mathbf{0} \tag{2.1}$$

n depends on the wavelength λ and on the position $\mathbf{r}$. k_0 is the vacuum wave vector modulus, corresponding to the vacuum wavelength $\lambda = 2\pi/k_0$. For X-rays in condensed matter, n can be

atoms	δ	β	α_c ($\circ$)
Ge	$6.428\text{x}10^{-6}$	$1.316\text{x}10^{-7}$	0.21°
Si	$4.034\text{x}10^{-6}$	$5.068\text{x}10^{-8}$	0.163°

Table 2.1: Values of δ, β, α_c evaluated at 11keV for Ge and Si.

decomposed into its mean value and its spatial fluctuation [2, 3],

$$n(\mathbf{r}) =< n(\mathbf{r}) > +\Delta n(\mathbf{r}) = 1 - \delta + i\beta + \Delta n(\mathbf{r}) \tag{2.2}$$

with:

$$\delta = \frac{r_e N_A}{2\pi}(\frac{hc}{E})^2 \sum_{i=1}^{n}(f_{0,i} + f_i^{'})\frac{\rho_i}{A_i} \tag{2.3}$$

$$\beta = \frac{r_e N_A}{2\pi}(\frac{hc}{E})^2 \sum_{i=1}^{n}(f_i^{"})\frac{\rho_i}{A_i} \tag{2.4}$$

where ρ_i is the volumic mass of the element i, A_i is its atomic mass, N_A is Avogadro's number and r_e the classical electron radius.

δ and β correspond to the dispersion and absorption phenomena. Like f' and f" (the real and imaginary part of the dispersion correction, respectively), δ and β vary near the absorption edges.

In the X-ray region, δ is always positive and its value is $\sim 10^{-5} - 10^{-6}$ (see Table 2.1). β is usually one or two orders of magnitude smaller [4]. Thus, the real part of the refractive index is slightly smaller than 1 for X-rays (contrary to visible wavelengths for which $n > 1$).

The incident $\vec{k_i}$ and reflected $\vec{k_r}$ wave vectors are defined by:

$$\vec{k_i} = k_0 \begin{pmatrix} cos\alpha_i \\ 0 \\ sin\alpha_i \end{pmatrix} \tag{2.5}$$

$$\vec{k_r} = k_0 \begin{pmatrix} cos\alpha_i \\ 0 \\ -sin\alpha_i \end{pmatrix}, \tag{2.6}$$

where α_i is the incident angle of the X-ray beam.

Neglecting the detailed structure of an atom, $n(\mathbf{r})$ can be spatially averaged and assimilated to $< n(\mathbf{r}) >$, simply noted n. The Snell-Descartes law relates the incident angle α_i to the refracted angle α_t in the case of a vacuum/matter interface:

$$cos\alpha_i = ncos\alpha_t \quad i.e. \text{ for small } \alpha_i \text{ and } \alpha_t{:}\alpha_t^2 = \alpha_i^2 - 2\delta + 2i\beta \tag{2.7}$$

As the real part of the index of refraction is slightly smaller than 1 for X-rays, a total external reflection occurs for incident angles α_i smaller than the critical angle α_c. This angle is defined by α_t=0 $i.e.$ from the Snell-Descartes law,

$$\alpha_c \sim \sqrt{2\delta} \tag{2.8}$$

Since $\delta \sim 10^{-6}$, α_c is of the order of the tenth of a degree and depends on the photon energy (E) ($\alpha_c \sim \frac{1}{E} \sim \lambda$). The transmitted wave vector $\vec{k_t}$ is expressed as:

$$\vec{k_t} = k_0 \begin{pmatrix} cos\alpha_i \\ 0 \\ A_i - \mathrm{i}B_i \end{pmatrix} \tag{2.9}$$

In the small angle approximation ($\alpha_i \ll 1$):

$$A_i = \frac{1}{\sqrt{2}}(\sqrt{(\alpha_i^2-\alpha_c^2)^2+4\beta^2}+\alpha_i^2-\alpha_c^2)^{1/2} \quad (2.10)$$

$$B_i = \frac{1}{\sqrt{2}}(\sqrt{(\alpha_i^2-\alpha_c^2)^2+4\beta^2}+\alpha_c^2-\alpha_i^2)^{1/2} \quad (2.11)$$

The amplitude of the transmitted wave in the matter is expressed as:

$$\varphi_t(\mathbf{r}) = t(\mathbf{k_i}e^{-i\mathbf{k_t}\cdot\mathbf{r}}) \quad (2.12)$$

$$= t(\mathbf{k_i}e^{-iRe(\mathbf{k_t})\cdot\mathbf{r}})e^{-|z|/l_i}, \quad (2.13)$$

where t is the transmission coefficient. The amplitude of the transmitted wave is exponentially dumped and its penetration depth l_i is defined by [5]:

$$l_i = \frac{1}{Im(k_{tz})} \sim \frac{1}{2kB_i} \quad (2.14)$$

Following Helmholtz's reciprocity principle [6] "if the source and the point of observation are interchanged the same amplitude would result". The previous equations are also valid in the case of a matter/vacuum interface. The incident angle α_i can be replaced by the exit angle α_f. As the scattered intensity is measured at the exit of the material, the scattering depth Λ depends both on α_i and on the exit angle α_f and is given by

$$\Lambda = \frac{1}{2k(B_i+B_f)} \quad (2.15)$$

Neglecting absorption ($\beta = 0$), the real part of k_{tz}, perpendicular to the interface is null for $\alpha_i \leq \alpha_c$: the transmitted wave propagates only parallel to the surface with an amplitude decaying rapidly in the material on the nm-scale. For α_i and α_f near the critical angle, the scattering depth is typically limited to 10-100 Å. By choosing the incident angle, the probed depth can be adjusted and controlled; X-rays can become a surface probe [7]. In the vicinity and above the critical angle, the penetration depth strongly depends on the X-ray energy as does the critical angle.

Based on the continuity of the electric and magnetic fields at the interface (z=0), the coefficients for the reflected and transmitted waves, r and t respectively are thereby obtained by the Fresnel formula [8, 9].

$$r_F = \frac{k_{iz}-k_{tz}}{k_{iz}+k_{tz}};\ if\ \alpha_i \ll 1 :\ r_F = \frac{\alpha_i-\alpha_t}{\alpha_i+\alpha_t} \quad (2.16)$$

$$t_F = \frac{2k_{iz}}{k_{iz}+k_{tz}};\ if\ \alpha_i \ll 1 :\ t_F = \frac{2\alpha_i}{\alpha_i+\alpha_t} \quad (2.17)$$

Hence the intensity transmission coefficients are $R_F = |r_F|^2$ and $T_F = |t_F|^2$. If the surface is rough with a gaussian distribution σ, P. Croce [10] demonstrated that these coefficients are modified according to:

$$R = R_F e^{-2\sigma^2 k_{iz}k_{tz}}\ and\ T = T_F e^{-\frac{1}{2}\sigma^2(k_{tz}^2-k_{iz}^2)} \quad (2.18)$$

For $\alpha_i \leq \alpha_c$, neglecting the absorption, $R = 1$ (see Fig. 2.2): it corresponds to the domain of total external reflection. The transmission coefficient has a maximum for $\alpha_i = \alpha_c$, $T = 4$. This property is sometimes used in grazing incidence diffraction by fixing α_i and/or α_f at α_c, in order to enhance the surface scattering. The main advantage of the use of grazing incidence scattering methods is the enhancement of the experimental signal from the scatterers located in the near-surface layer. The scattering signal arising from the substrate is minimized. This method enables to study the structural properties from layers of nanometric thickness, and requires a brilliant X-ray beam. This condition dictates the preferential application of grazing-incidence scattering methods using synchrotron radiation.

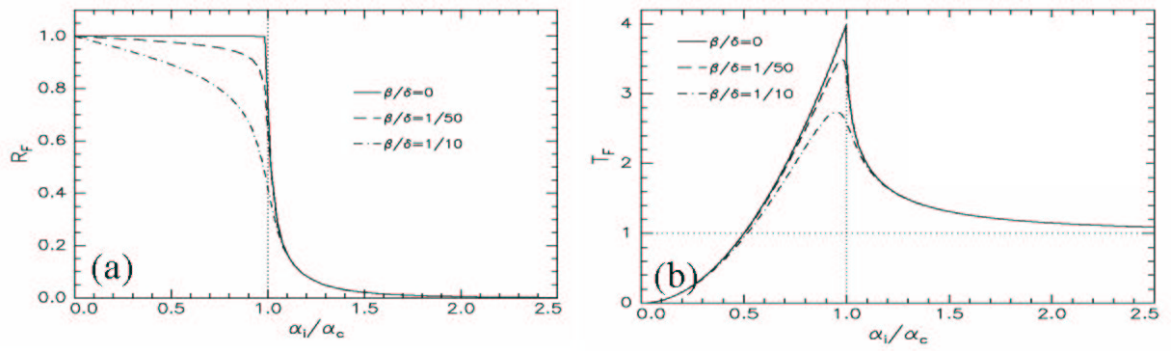

Figure 2.2: Evolution of the coefficients for the reflected and transmitted waves, R_F and T_F respectively.

2.2.2 X-ray scattering.

Since the interaction of hard X-rays with matter is weak, the kinematical approximation of single scattering, called Born approximation is valid in most cases [11]. In the case of an ensemble of N atoms j positionned at $\mathbf{R_j}$ and characterized by an atomic scattering factor f_j, the amplitude of the diffracted beam can be written:

$$A(\mathbf{Q}) = \sum_{j=1}^{N} f_j(\mathbf{Q}) \mathrm{e}^{-\mathrm{i}\mathbf{Q}\cdot\mathbf{R_j}}, \tag{2.19}$$

where the momentum transfer $\mathbf{Q}$ is defined as $\mathbf{Q} = \mathbf{k_f} - \mathbf{k_i}$, $\mathbf{k_i}$ and $\mathbf{k_f}$ are the incident and exit X-ray wave vectors. As generally, the illuminated zone is larger than the coherent length of the X-ray beam $\sim 1\mu m$, and the $\mathbf{R_j}$ positions of the atoms are only statistically known due to thermal motion, the collected intensity is statistically defined and spatially averaged:

$$I(\mathbf{Q}) \propto < \left| \sum_{j=1}^{N} f_j(\mathbf{Q}) \mathrm{e}^{-\mathrm{i}\mathbf{Q}\cdot\mathbf{R_j}} \right|^2 > . \tag{2.20}$$

In the case of a perfect crystal with N_1, N_2 and N_3 unit cells along the three crystal axes defined by the vectors $\mathbf{a_1}$, $\mathbf{a_2}$ and $\mathbf{a_3}$ and supposing that the illuminated zone is of the order of the coherent length of the X-ray beam, the diffracted beam can be written:

$$A(\mathbf{Q}) = \sum_{unit\ cell} f_j \mathrm{e}^{\mathrm{i}\mathbf{Q}\cdot\mathbf{r_j}} \sum_{n_1,n_2,n_3}^{N_1,N_2,N_3} \mathrm{e}^{\mathrm{i}\mathbf{Q}(n_1.\mathbf{a_1}+n_2.\mathbf{a_2}+n_3.\mathbf{a_3})}. \tag{2.21}$$

Thus,

$$I(\mathbf{Q}) \propto \left| \sum_{unit\ cell} f_j(\mathbf{Q}) \mathrm{e}^{-\mathrm{i}\mathbf{Q}\cdot\mathbf{r_j}} \right|^2 \frac{\sin(N_1\mathbf{Q}.\mathbf{a_1}/2)^2}{\sin(\mathbf{Q}.\mathbf{a_1}/2)^2} \frac{\sin(N_2\mathbf{Q}.\mathbf{a_2}/2)^2}{\sin(\mathbf{Q}.\mathbf{a_2}/2)^2} \frac{\sin(N_3\mathbf{Q}.\mathbf{a_3}/2)^2}{\sin(\mathbf{Q}.\mathbf{a_3}/2)^2}. \tag{2.22}$$

The three last terms constitute the interference function and the first term is the structure factor $F(\mathbf{Q}) = \sum_{unit\ cell} f_j \mathrm{e}^{\mathrm{i}\mathbf{Q}\cdot\mathbf{r_j}}$, which is expressed as a function of the atomic positions $\mathbf{r_j}$ within the unit cell. The intensity is thus the product of the structure factor, which depends only on the structure within the unit cell, and the form factor related to the shape of the crystal. The interference function tends to a periodic array of Dirac delta functions. The intensity is non-zero only if $\mathbf{Q}.\mathbf{a_1} = 2\pi h$, $\mathbf{Q}.\mathbf{a_2} = 2\pi k$ and $\mathbf{Q}.\mathbf{a_3} = 2\pi l$, with h, k, l integers. The intensity is non-zero only if $\mathbf{Q}$ is a vector of

Reflection	Intensity
h+k+l=4n	F^2_{hkl}=16($2f^2_{Si,Ge}$)
hkl odd	F^2_{hkl}=16($2f^2_{Si,Ge}$)
hkl mixed	F^2_{hkl}=0
h+k+l=2(2n+1)	F^2_{hkl}=0

Table 2.2: Structure factors of a Si or Ge crystal for different reflections.

the reciprocal lattice of basic vectors $\mathbf{b_1}$, $\mathbf{b_2}$ and $\mathbf{b_3}$, which fulfill

$$\mathbf{b_1} = \frac{\mathbf{a_2} \wedge \mathbf{a_3}}{\mathbf{a_1}.\mathbf{a_2} \wedge \mathbf{a_3}} \tag{2.23}$$

$$\mathbf{b_2} = \frac{\mathbf{a_3} \wedge \mathbf{a_1}}{\mathbf{a_1}.\mathbf{a_2} \wedge \mathbf{a_3}} \tag{2.24}$$

$$\mathbf{b_3} = \frac{\mathbf{a_1} \wedge \mathbf{a_2}}{\mathbf{a_1}.\mathbf{a_2} \wedge \mathbf{a_3}}. \tag{2.25}$$

In this case, $\mathbf{Q} = 2\pi(h\mathbf{b_1} + k\mathbf{b_2} + l\mathbf{b_3}) = \mathbf{Q_{hkl}}$. The scattered intensity is thus non-zero for the (h, k, l) points which form a periodic network in the reciprocal space. The crystal can also be seen as a periodic stacking of atomic planes, called (h, k, l) planes. The inter-planar distance between these planes is given by [12]

$$d_{hkl} = 2\pi / \left|\mathbf{Q_{hkl}}\right|. \tag{2.26}$$

The $\mathbf{Q_{hkl}}$ vector is perpendicular to the (h, k, l) plane. From geometrical considerations, it follows that $|\mathbf{Q_{hkl}}| = 4\pi \sin(\theta)/\lambda$, where 2θ is the angle between k_i and k_f. It comes

$$2d_{hkl} \sin(\theta) = \lambda, \tag{2.27}$$

which corresponds to the Bragg law for the (h, k, l) reflection. The Miller indexes correspond to vectors of the reciprocal space unit cells. When the above Laue condition is fulfilled, the intensity can be written

$$I_{hkl} \propto F^2_{hkl} N_1^2 N_2^2 N_3^2. \tag{2.28}$$

The structure factor can be expressed by

$$F_{hkl} \propto \sum_{unit\ cell} f_j(\mathbf{Q}) \mathrm{e}^{-2\pi \mathrm{i} h x_j + k y_j + l z_j}, \tag{2.29}$$

where f_j, x_j, y_j and z_j are respectively the scattering factor of atom j and the fractional coordinates in the unit cell. In the case of a diamond (Si or Ge) structure, the unit cell contains eight atoms with coordinates: (0,0,0), (1/2,1/2,0), (0,1/2,1/2), (1/2,0,1/2), (1/4,1/4,1/4), (3/4,3/4,1/4), (3/4,1/4,3/4) and (1/4,3/4,3/4). The structure factor values for different reflections is indicated in Table 2.2.

Consider now a quasi-two dimensional crystal of finite thickness along Q_3. The Laue condition on $\mathbf{Q_3}$ is relaxed. The reciprocal space is made of rods perpendicular to the surface plane, called crystal truncation rods (CTR) connecting bulk Bragg peaks.

In general, the reflections have a finite width, which is related to the finite width of the crystal. In order to deduce the structure factor, a pertinent measurement is to integrate the intensity of each reflection. The finite size D of the crystal along Q_1 for instance can be simply related to the peak full width at half maximum (FWHM) Δh by:

$$D = a_1/\Delta h \tag{2.30}$$

In the case of a mosaic spread or a distribution of lattice parameters, the Bragg peaks will be broadened.

Figure 2.3 is a schematical drawing of the intensity scattered by nanostructures on top of a substrate as a function of the in-plane and out-of-plane momentum transfer. The semi-infinite crystals yields CTRs. Wide Bragg reflections are from the nanostructures. They are peaked at different $Q_{//}$ and $Q_{\perp}$ values from the substrate one as a result of strain relaxation. This allows the analysis of the nanostructures (composition, relaxation) without interference with the substrate.

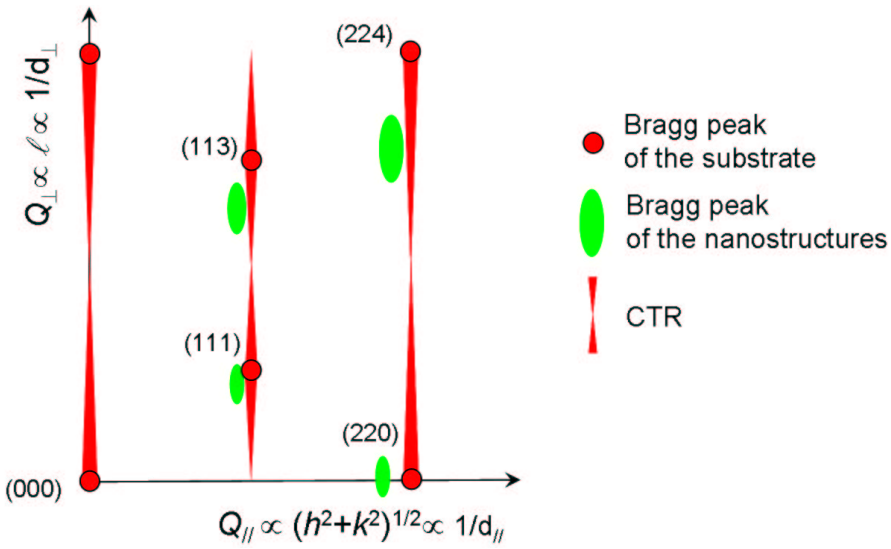

Figure 2.3: Intensity scattered by nanostructures on top of a substrate as a function of the in-plane and out-of-plane momentum transfer.

2.2.3 The Distorted Wave Born Approximation for grazing incidence scattering

The demand for a theoretically simple model for the description of grazing incidence phenomena on surfaces was satisfied by Croce [10] and by Vineyard [13] in 1982 with the Distorted Wave Born Approximation (DWBA), a compromise between kinematic approximation and dynamical theory of X-rays. In 1988, S. K. Sinha *et al.* [6] completed the DWBA theory by using a quantum approach of the DWBA to analyse the scattering from rough surfaces.

The DWBA method starts from the Helmholtz propagation equation (see eq. 2.1). The latter is reduced to a scalar one as the polarization effects can be safely ignored at small angles [14]. In the case of free-standing islands on a surface, the index of refraction $n^2(\mathbf{r})$ can be written as:

$$n^2(\mathbf{r}) = {n_0}^2(z) + ({n_i}^2 - 1)S(\mathbf{r}). \tag{2.31}$$

It includes the index of refraction of the substrate and vacuum,

$$n_0(z) = \begin{cases} 1 & \text{if z>0} \\ n_s = 1 - \delta_s + \mathrm{i}\beta_s & \text{if z<0} \end{cases}$$

and that, $n_i = 1 - \delta_i + \mathrm{i}\beta_i$, of the islands of shapes $S(\mathbf{r})$ [$S(\mathbf{r})$=0 or 1 outside or inside the island, respectively]. As no parallel dependence appears in $n_0(z)$, the Fresnel wave field solution without perturbation (*i.e.* without islands) for a unit incident wave in vacuum $\mathbf{k} = (\mathbf{k}_{//}, k_{z,0})$ is made of upward and downward propagating waves:

$$\phi_0(\mathbf{r},\mathbf{k}) = \mathrm{e}^{\mathrm{i}\mathbf{k}_{//}\cdot\mathbf{r}} \begin{cases} \mathrm{e}^{\mathrm{i}k_{z,0}z} + r_F \mathrm{e}^{-\mathrm{i}k_{z,0}z} & \text{if z>0} \\ t_F \mathrm{e}^{-\mathrm{i}\tilde{k}_{z,0}z} & \text{if z<0} \end{cases}$$

(2.32)

The perpendicular components of the wave vector transfer are $k_{z,0} = -\sqrt{k_0^2 - k_{//}^2}$ in vacuum and $\tilde{k}_{z,0} = -\sqrt{n_s^2 k_0^2 - k_{//}^2}$ inside the substrate. r_F and t_F are the coefficients for the reflected and transmitted waves (see Eqs. 2.16, 2.17). The scattered wave amplitude $\phi_{sc}(\mathbf{r})$ is obtained treating the islands as a first order perturbation [15]. For an incoming plane wave $\mathbf{k_i}$, the total solution $\phi(\mathbf{r})$ reads

$$\begin{aligned} \phi(\mathbf{r}) &= \phi_0(\mathbf{r}, \mathbf{k_i}) + \phi_{sc}(\mathbf{r}, \mathbf{k_i}, \mathbf{k_f}) && (2.33) \\ &= \phi_0(\mathbf{r}, \mathbf{k_i}) + {k_0}^2({n_i}^2 - 1)\frac{\mathrm{e}^{-\mathrm{i}k_0 r}}{4\pi r}\int d\mathbf{r}'\phi_0(\mathbf{r}', -\mathbf{k_f})S(\mathbf{r}')\phi_0(\mathbf{r}', \mathbf{k_i}). && (2.34) \end{aligned}$$

The scattering from the islands acts only for $z > 0$, the introduction of the Fresnel wave field expression of Eqs. 2.32 into Eq. 2.34 leads to the following result

$$\phi_{sc}(\mathbf{r}) = k_0^2(n_i^2 - 1)[\tilde{S}(\mathbf{q}_{//}, q_z) + R_i\tilde{S}(\mathbf{q}_{//}, p_z) + R_f\tilde{S}(\mathbf{q}_{//}, -p_z) + R_i R_f\tilde{S}(\mathbf{q}_{//}, -q_z)], \quad (2.35)$$

with

$$\tilde{S}(\mathbf{q}_{//}, \pm k_{i,z} \pm k_{f,z}) = \int d\mathbf{r}' S(\mathbf{r}')\mathrm{e}^{-\mathrm{i}q_{//}r'_{//}}\mathrm{e}^{-\mathrm{i}(\pm k_{i,z} \pm k_{f,z})r'_z}, \quad (2.36)$$

where $q_z = k_{f_z} - k_{i_z}$, $p_z = k_{f_z} + k_{i_z}$ and R_i, R_f are the reflectivities of the incident and scattered waves. Each term is related to one of the scattering processes shown in Fig. 2.4. The differential scattering cross-section is then given by

$$\frac{d^2\sigma}{d\Omega^2} = r^2 < |\phi_{sc}(\mathbf{r}, \mathbf{k_i}, \mathbf{k_f})|^2 > \sim \frac{k_0^4\left|n_i^2 - 1\right|^2}{16\pi^2} < \left|\Phi(\mathbf{q}_{//}, \mathbf{k_i}, \mathbf{k_f})\right|^2 >, \quad (2.37)$$

where Φ is the DWBA form factor of one island:

$$\Phi_(\mathbf{q}_{//}, \mathbf{k_i}, \mathbf{k_f}) = \tilde{S}(\mathbf{q}_{//}, q_z) + R_i\tilde{S}(\mathbf{q}_{//}, p_z) + R_f\tilde{S}(\mathbf{q}_{//}, -p_z) + R_i R_f\tilde{S}(\mathbf{q}_{//}, -q_z)]. \quad (2.38)$$

The first term corresponds to the kinematical scattering of the incident wave by the islands (case of the Born approximation (BA)). The three other terms imply reflections on the substrate and are known as multiple scattering paths. The four terms corresponds to the Distorted Wave Born Approximation (DWBA). Figure 2.5 compares the evolution of the scattered intensity as a function of α_f in the kinematical approach and DWBA. The first difference is the Yoneda [16] peak at α_f=α_c, which results from the interplay between the four events and the Fresnel reflection coefficients in the DWBA process. Then, an angular shift is observed along α_f between the kinematical approach and DWBA. This shift strongly depends on the incident angle. Figure 2.6 shows the modulus square of the four terms for a cylinder as function of α_f for various α_i. If α_i=α_c and α_i=$\alpha_c/2$, the first and second paths ($\tilde{S}(\mathbf{q}_{//}, q_z)$, $R_i\tilde{S}(\mathbf{q}_{//}, p_z)$) have similar intensities shifted by an angle of $2\alpha_i$. The third and fourth terms can not be neglected if $\alpha_f \leq \alpha_c$. If α_i and α_f are much larger than α_c, the coefficients for the reflected waves are very weak. Only one term remains in the equation, corresponding to the Born approximation. The DWBA approximation is thus necessary when α_i and/or α_f are near the critical angle.

2.2.4 Grazing incidence small angle scattering.

The GISAXS (Grazing Incidence Small Angle X-Ray Scattering) technique has emerged as a powerful tool ([18, 19, 20, 21, 22]), yielding morphological information and allowing to characterize an assembly of nanoparticles. The scattered intensity is recorded on a 2D detector as a function of the exit angle α_f with respect to the in-plane scattering angle $2\theta_f$. These angles allow to define the reciprocal space coordinates $Q_\perp = Q_z$ and $\mathbf{Q}_{//} = (Q_x, Q_y)$, respectively perpendicular and parallel to the surface (see Fig. 2.7).

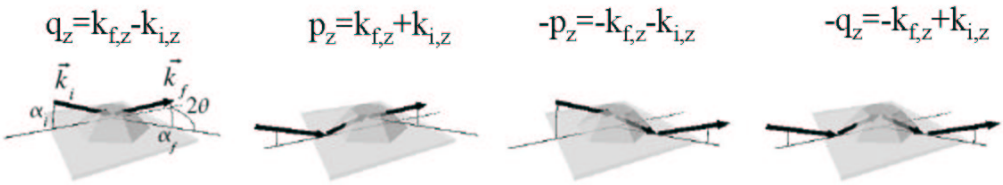

Figure 2.4: Four multiple scattering paths in the DWBA approximation, in grazing incidence geometry. 2θ is the in-plane scattering angle, α_i and α_f are the incident and exit angles.

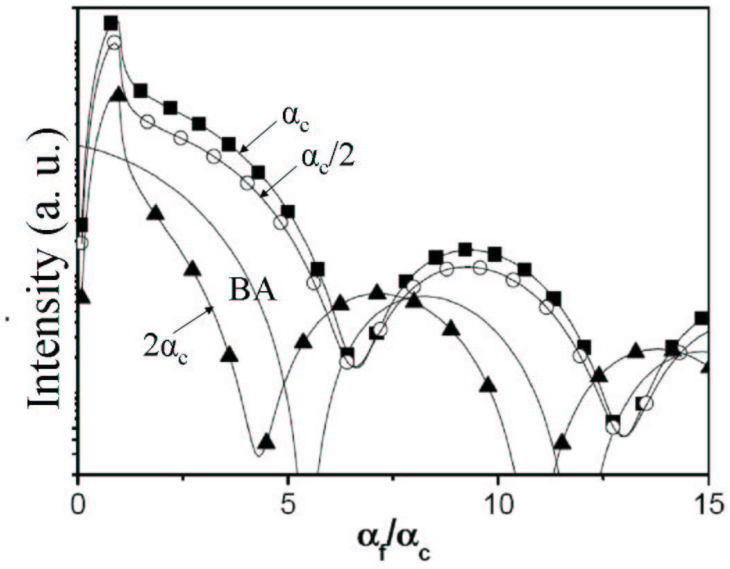

Figure 2.5: The interference fringes for the form factor of a cylinder of height H=5nm as a function of the exit angle α_f normalized by the angle of total external reflection α_c within the various approximations: BA, DWBA(α_i=α_c/2, α_c, 2α_c) [17].

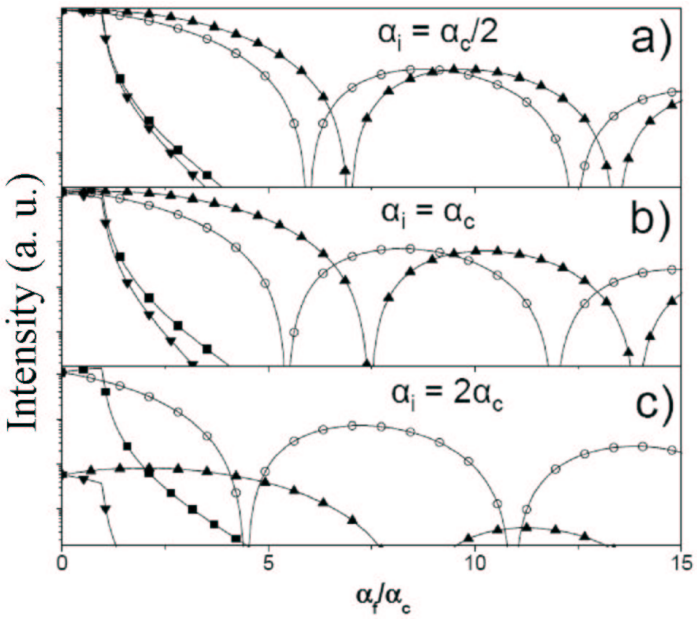

Figure 2.6: The modulus square of the four terms for a cylinder as function of α_f for various α_i: Term 1 (open circle)-Term 2 (black triangle)-Term 3 (black square)-Term 4(black inverted triangle) (same parameters as in Fig. 2.6) [17].

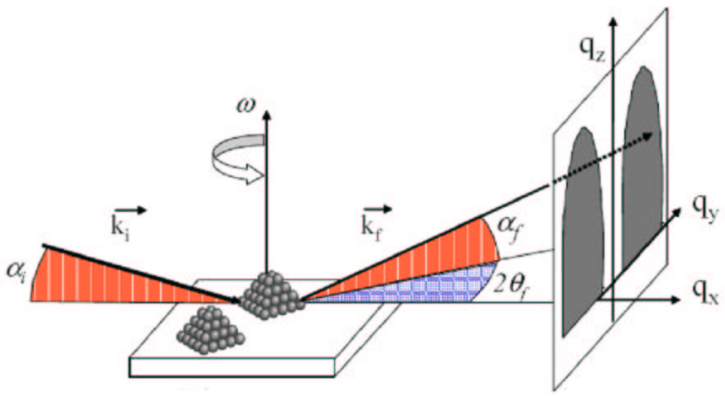

Figure 2.7: GISAXS geometry.

$$Q_x = k_0[cos(\alpha_f)cos(2\theta_f) - cos(\alpha_i)] \quad (2.39)$$
$$Q_y = k_0[cos(\alpha_f)sin(2\theta_f)] \quad (2.40)$$
$$Q_z = k_0[sin(\alpha_f) + sin(\alpha_i)] \quad (2.41)$$

As these angles are small, Q_x is small and often neglected. The scattered intensity is measured around the direct and reflected beams with $\mathbf{Q}_{//} \sim k_0 \sin 2\theta_f$ and $Q_z \sim k_0(\sin\alpha_f + \sin\alpha_i)$. Two-dimensional GISAXS patterns are recorded using a CDD detector placed perpendicular to the incident beam. In a first approximation, the GISAXS intensity for a homogeneous ensemble of islands on a surface is given by:

$$I(\mathbf{Q}) = F(\mathbf{Q}) \cdot S(\mathbf{Q}), \quad (2.42)$$

where F and S are the Fourier transform of the particle shape and the island-island pair correlation function, which depends on the lateral positions of the islands and which can be written as:

$$S(\mathbf{Q}_{(\mathbf{x},\mathbf{y})}) = 1 + \rho_s \int [g(\mathbf{r}) - 1]\mathrm{e}^{-\mathrm{i}\mathbf{Q}_{(\mathbf{x},\mathbf{y})}\cdot\mathbf{r}} d\mathbf{r}, \quad (2.43)$$

where ρ_s is the particles mean density and $g(\mathbf{r})$ the island-island pair correlation function. In the Born approximation, the island form factor is given by the Fourier transform of its electron density:

$$F(\mathbf{Q}) = \int_V \rho(\mathbf{r})\mathrm{e}^{-\mathrm{i}\mathbf{Q}\cdot\mathbf{r}} dV. \quad (2.44)$$

As a first approximation, the average lateral particle size d and height h are thus inversely proportional to the spread of the scattering parallel and perpendicular to the surface, respectively. The average island separation D is inversely proportional to the distance between the main correlation peaks along the parallel direction (see Fig. 2.8).

In the Distorted Wave Born Approximation, the form factor is the coherent sum of four terms (see Eq. 2.38), which correspond to diffuse scattering reflections on the sample surface:

$$F(\mathbf{Q}_{(\mathbf{x},\mathbf{y})}, \mathbf{k_i}, \mathbf{k_f}) = F(\mathbf{Q}_{(\mathbf{x},\mathbf{y})}, q_z) + R_i F(\mathbf{Q}_{(\mathbf{x},\mathbf{y})}, p_z) + R_f F(\mathbf{Q}_{(\mathbf{x},\mathbf{y})}, -p_z) + R_i R_f F(\mathbf{Q}_{(\mathbf{x},\mathbf{y})}, -q_z). \quad (2.45)$$

Figure 2.9 shows a GISAXS image recorded from germanium islands grown on a Si(001) surface. The islands have the shape of domes exposing different kind of facets: {105} facets at the apex, {113} and {15 3 23} facets at the island basis. These facets are two-dimensional objects in real space, their Fourier transform yields 1D intensity rods perpendicular to the facets, called facet streaks. If the incident beam is parallel to the $[\bar{1}10]$ direction, the detector plane becomes the (110) reciprocal plane, which contains the [113] and $[\bar{1}\bar{1}3]$ rods perpendicular to the (113) and $(\bar{1}\bar{1}3)$ facets, respectively. Their intensity is characteristic of the facet sizes as will be shown in chapter 7. Besides, not only facets but also island edges can give intensity rods in the GISAXS image. Island edges are one-dimensional object in real space; their Fourier transform corresponds to 2D planes. The intersection of the 2D planes with the detector plane yields 1D intensity rods perpendicular to the island edge, which are less intense than facet streaks. Along the edge rod, the intensity falls down as $\left|Q_\perp^{-4}\right|$ [3], where $Q_\perp$ is the component of $\mathbf{Q}$ perpendicular to the edge. Along the facet streak, the intensity drops as $\left|Q_\perp^{-2}\right|$ [3]. In the case of a non-faceted island with a rounded surface, for instance a sphere, the intensity decreases as $\left|Q_\perp^{-4}\right|$, which corresponds to the Debye-Porod law [23]. In the case of a pyramid, the intensity perpendicular to the streaks drops as $\left|Q_{//}^{-6}\right|$ [3], whereas for a dome, this drops as $\left|Q_{//}^{-3}\right|$, where $Q_{//}$ is perpendicular to the streak (see Fig. 2.9). Whatever the approximation (BA, DWBA) used, the intensity is proportional to the square modulus of the form factor of the particles for high momentum transfer $\mathbf{Q}$. For a sample with a large size distribution, the asymptotic intensity drops as $|Q^n|$, where n depends only on the islands shape. From the asymptotic intensity decrease, it is then possible to identify islands shape or scattering edges. This will be demonstrated in chapter 7.

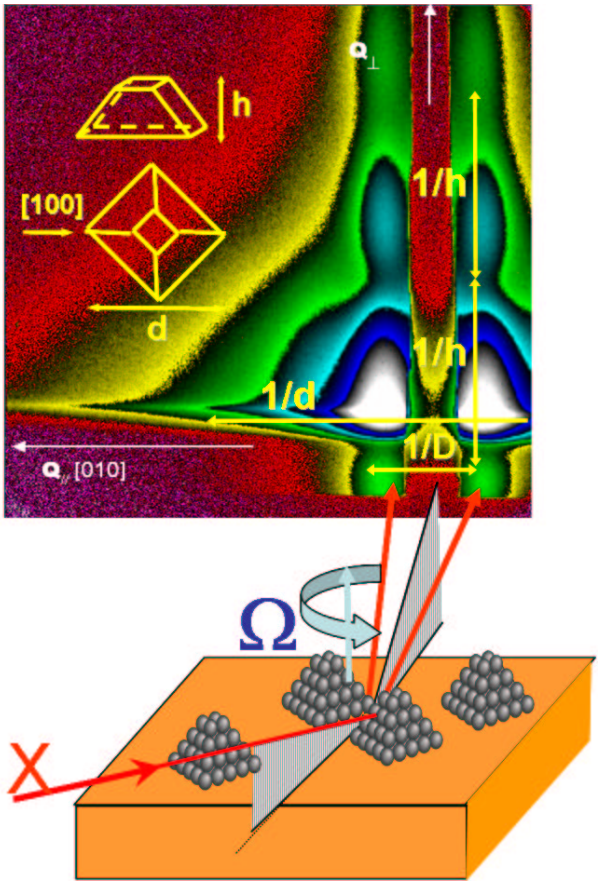

Figure 2.8: Two dimensional GISAXS pattern. The average particle lateral size d and height h and the average island separation D are indicated.

In Fig. 2.9, a sharp intensity increase is observed for $\alpha_f = \alpha_c$, which corresponds to the Yoneda peak. For each facet, an additional streak is observed. The GISAXS image was collected with $\alpha_i = \alpha_c$, the critical angle. The 'two streaks' result from the first two terms of equation 2.45. The rod with the smaller Q_z value comes from a single scattering event by the {113} facets (BA). This corresponds to the first scattering process of the DWBA, with a Q_z component given by $Q_z = k_f - k_i = (2\pi/\lambda)[sin(\alpha_f) + sin(\alpha_i)]$. The other streak comes from the second scattering process which takes into account the reflection of the incident beam on the substrate. Along Q_z, the two scattering streaks are separated by $\Delta = q_z - p_z = (4\pi/\lambda)sin(\alpha_i)$ (see Fig. 2.9).

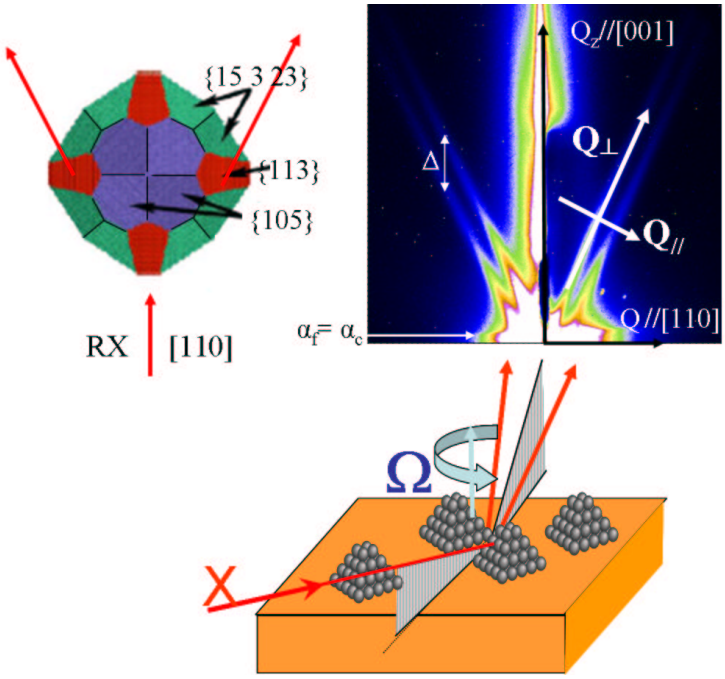

Figure 2.9: Two dimensional GISAXS pattern performed on germanium domes (see the schematic drawing), with {105}, {113} and {15 3 23} facets. The X-ray beam is parallel to the < 110 > azimuth to probe the scattering from the {113} facets. {113} facets yield intensity rods of scattering perpendicular to them.

More precisely, the intensity $I(\mathbf{Q})$ scattered by an ensemble of islands is given by the sum of a coherent and a diffuse term [23]

$$I(\mathbf{Q}) = S(\mathbf{Q}) < |F(\mathbf{Q})| >^2 + \sum_m \Phi_m(\mathbf{Q}) \mathrm{e}^{-\mathrm{i}\mathbf{Q}\cdot\mathbf{r_m}} \tag{2.46}$$

The first term is a coherent term. It comes from the interferences between the waves scattered by the islands. The signal is characterized by correlation peaks which reveal the ordering between neighboring islands. The coherent term is minimum at Q=0. The second term corresponds to the incoherent scattering and is the signature of island shape, size and orientation fluctuations. This term shows a maximum at Q=0. The $\Phi_m(\mathbf{Q})$ coefficients describes the correlation between island sizes:

$$\Phi_m(\mathbf{Q}) =< [F_n(\mathbf{Q}) - < F(\mathbf{Q}) >][F_{n+m}(\mathbf{Q}) - < F(\mathbf{Q}) >]^* >^n, \tag{2.47}$$

where F_n is the form factor of island n. Two approximations are commonly used to evaluate the incoherent scattering. The Decoupling Approximation (DA) assumes that the nature of the scatterers and their positions are independent, *i.e.* $\Phi_m = 0$ for $m \neq 0$. The Local Monodisperse Approximation (LMA) assumes that the neighbouring islands have the same size and shape over the coherent area

of the X-ray beam. In the LMA, the intensity is the sum of the intensity scattered by domains with islands of same morphology:

$$I(\mathbf{Q}) = S(\mathbf{Q}) \cdot < F(\mathbf{Q})^2 > . \tag{2.48}$$

The LMA is generally used as it gives better results than the DA. In the case of Ge islands on Si(001), the assembly of islands is not dense, so that $S(\mathbf{Q})$ is approximatively equal to one. The GISAXS measurements is in this case only sensitive to the island shape: $I(\mathbf{Q}) =< F(\mathbf{Q})^2 >$. In the case of a dense system of correlated particles, another approximation is needed: the size-spacing coupling approximation (SSCA) [24]. To perform a quantitative analysis, the IsGISAXS program [25] needs to be used.

2.2.5 Multiwavelength Anomalous Diffraction

X-ray diffraction is a powerful technique for measuring strain. Nevertheless, strain is related to composition in a complicated way and Vegard's law is usually not valid as the composition depends also on the nanostructure shape, aspect ratio, and on the mutual stress that nanostructures and substrate apply to each other. This can be partially overcomed by exploiting the chemical sensitivity that X-ray techniques can provide. The idea is to tune the X-ray energy to the absorption edge of the atomic species that belongs to the nanostructures, *i.e.* to modify their atomic scattering factor by exciting resonant scattering. This is the basic principle of anomalous (resonant) diffraction [26]. In the case of an electron bound to an atom, a dispersion and an absorption terms $f'(E)$ and $f"(E)$ should be added to the expected normal scattering power $f_0(\mathbf{Q})$ of an atom:

$$f = f_0(\mathbf{Q}) + f'(E) + \mathrm{i}f"(E) \tag{2.49}$$

$f_0(\mathbf{Q})$ is generally proportional to the number of electrons of an atom. $f_0 = Z$ at $\mathbf{Q}$=0 and decreases for higher scattering angles or momentum transfers Q.

Theoretical values of $f_0(\mathbf{Q})$, as well as for $f'(E)$ and $f"(E)$ are tabulated or can be calculated [27, 28] (Fig. 2.10).

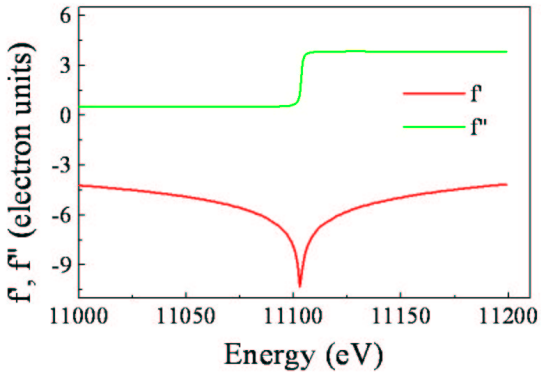

Figure 2.10: Theoretical values of $f'(E)$ and $f"(E)$ for Ge as a function of energy around the Ge K absorption edge.

Supposing two types of atoms and the photon energy in the vicinity of the absorption edge of one element (the anomalous or resonant atom), the atomic scattering factor of all anomalous (A) or non anomalous (N) atoms can be written as $f_{A/N}(\mathbf{Q}, E) = f^0_{A/N}(\mathbf{Q}) + f'_{0,A/N}(E) + \mathrm{i}f"_{0,A/N}(E)$, where $f'_{0,A/N}(E) + \mathrm{i}f"_{0,A/N}(E)$ represents the anomalous scattering of anomalous atoms (A) or non anomalous atoms (N). According to the schematic representation in figure 2.11, in the Born approximation, the structure factor F_0 is the sum of (1) the partial structure factor of all anomalous atoms (A) of phase

ϕ_A: $F_A(\mathbf{Q},E) = \sum_j^{N_A} f_A^0(\mathbf{Q})\mathrm{e}^{\mathrm{i}\mathbf{Q}\cdot\mathbf{r_j}} = |F_A|\,\mathrm{e}^{\mathrm{i}\phi_A}$, (2) the partial structure factor of all non anomalous atoms (N) of phase ϕ_N: $F_N(\mathbf{Q},E) = \sum_j^{N_N} f_N(\mathbf{Q})\mathrm{e}^{\mathrm{i}\mathbf{Q}\cdot\mathbf{r_j}} = |F_N|\,\mathrm{e}^{\mathrm{i}\phi_N}$, and (3) the anomalous scattering of all atoms A.

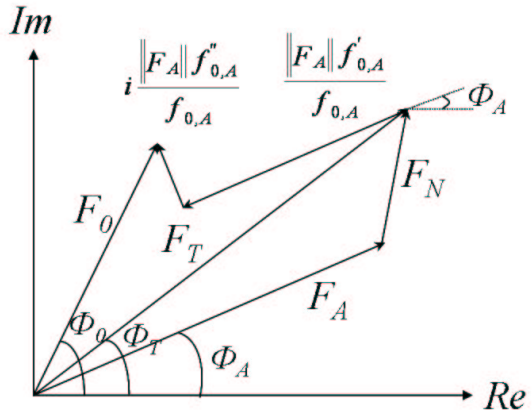

Figure 2.11: Schematic representation of the structure factor F_0, and its relationship with F_T, F_A and F_N in the complex plane.

For a given $\mathbf{Q}$ value and energy, one can write [29]:

$$F_0(\mathbf{Q},E) = F_T(\mathbf{Q},E) + \frac{F_A(\mathbf{Q},E)}{f_A^0(\mathbf{Q})}[f'_{0,A/N}(E) + \mathrm{i}f''_{0,A/N}(E)], \tag{2.50}$$

where $F_T = F_A + F_N$. By looking at figure 2.11, it can be shown that:

$$\begin{aligned} |F_0|^2 &= |F_T|^2 + \left(\frac{|F_A|}{f_A^0}\right)^2 \left({f'_{0,A}}^2(E) + {f''_{0,A}}^2(E)\right) \\ &\quad +2\frac{|F_T||F_A|}{f_A^0}\left[f'_{0,A}(E)\cos(\varphi_T-\varphi_A) + f''_{0,A}(E)\sin(\varphi_T-\varphi_A)\right] \end{aligned} \tag{2.51}$$

The modulus $|F_T|$, $|F_A|$, $|F_N|$ and phases $\phi_T - \phi_A$, $\phi_N - \phi_A$ are not energy dependent. Then, by using tabulated or experimental $f'_{0,A}$ and $f''_{0,A}$ values, the intensity variation of $I_0 = |F_0(E)|$ can be fitted as a function of energy. One can recover $\Delta\phi = \phi_T - \phi_A$, $|F_T|$ and $|F_A|$ with at least three energies and without any structural model, at a given $\mathbf{Q}$ vector. Then, it is possible to deduce $\phi_T - \phi_N$ and $|F_N|$.

The `NanoMAD` program

The `NanoMAD` program developped by V. Favre-Nicolin allows to extract the partial structure factors $|F_A|$ and $|F_N|$ and the phase difference $\phi_N - \phi_A$ at a given (h, k, l) point of reciprocal space where the intensity has been measured at several energies. The only known parameter is the cristallographic unit cell, which is the diamond unit cell in the case of Ge nanostructures. For each (h, k, l) point, the fluorescence can be evaluated and substracted from the experimental intensities.

The program evaluates without any structural hypothesis the parameters $|F_T|$, $|F_A|$ and $\Delta\phi$. They are then refined by adjusting the new calculated intensity expressed by equation 2.51 with the experimental intensities through a least-squares minimization. The starting parameters ($|F_T|$, $|F_A|$ and $\Delta\phi$) are thus varied to minimize the factor

$$\chi^2 = \frac{N_{in}}{N(N_{in}-N_{var})}\sum_i^N \left(\frac{I_{calc}(E_i) - I_{exp}(E_i)}{\sigma_i}\right)^2, \tag{2.52}$$

where N_{in}, N_{var}, I_{calc}, I_{exp} and σ_i are the number of independent experimental points, the number of independent parameters, the calculated intensity, the experimental intensity and the uncertainties for each measured intensity. The refinement is satisfactory if $\chi^2 \sim 1$. The uncertainties σ of $|F_T|$, $|F_A|$ and $\Delta\phi$ and their covariant terms (σ_{F_T,F_A}, $\sigma_{F_T,\Delta\phi}$ and $\sigma_{F_A,\Delta\phi}$) are then evaluated. After the extraction of the parameters F_T, F_A and $\Delta\phi$, F_N and $\phi_T - \phi_N$ are deduced from the formula $F_N = F_T - F_A$. The errors on $|F_T|$, $|F_A|$ and $\Delta\phi$ are propagated on those of F_N and $\phi_T - \phi_N$ via the relation:

$$\sigma_y^2 = \sum_i (\frac{\partial y}{\partial x_i})^2 \sigma_{x_i}^2 + 2 \sum_{i \neq j} \frac{\partial y}{\partial x_i} \frac{\partial y}{\partial x_j} \sigma_{x_i x_j}^2, \tag{2.53}$$

where x=$|F_T|$, $|F_A|$, $\Delta\phi$ and y=F_N, $\phi_T - \phi_N$.

Choice of the energies and accuracy of the measurement of the energy spectrum.

The structural parameters $|F_T|$, $|F_A|$ and $\Delta\phi$ can be determined using a minimum of three energies. Nevertheless, it is important to increase and to carefully choose [30, 31] the number of energies to minimize the reduced merit factor. It has been shown [32] that a better refinement is obtained when the energies are chosen at the maximum of the absorption edge, (50-100eV) below the absorption edge when $f_A^{'}$ is minimum and 50eV above the absorption edge. Generally, ten to twelve energies are used. Fig. 2.12 shows a judicious choice of energies, which was demonstrated to be as optimal as the choice of more than 100 energies [32].

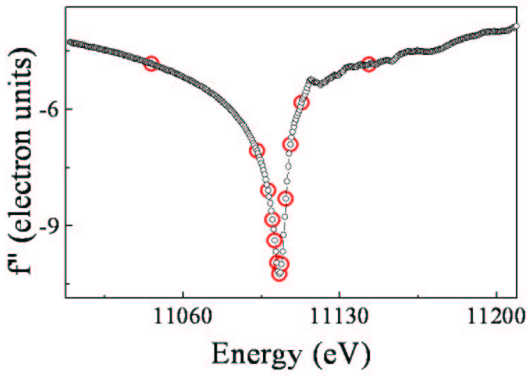

Figure 2.12: Choice of energies for a MAD experiment around the Ge K edge, in order to maximize the phasing power and precision in the extraction of $|F_T|$, $|F_A|$ and $\phi_T - \phi_A$.

Chemical composition.

In the case of Ge dots on an Si substrate, the experiment is conducted at the Ge K-edge, and we can extract from the MAD experiment $|F_A|$=$|F_{Ge}|$ and $|F_N|$=$|F_{Si}|$ through a least-square minimization. Then, the Ge_xSi_{1-x} content can be deduced using the relation:

$$\frac{|F_{Ge}|}{|F_{Si}|} = \frac{x f_{Ge}^0}{|(1-x) f_{Si}|} \tag{2.54}$$

One must notice that the knowledge of F_A, F_N and $\phi_N - \phi_A$ is not sufficient to conclude about the actual nanostructure chemical composition. Only in the case of an iso-strain *homogeneous binary alloy*, the F_A/F_N ratio gives the exact intermixing amount ($\phi_N - \phi_A = 0$), without any crystallographic model. The method can still be applied for any *homogeneous alloy* providing that the crystallographic

structure is known *a priori*. It can be noted, that, in the most general case, the scattering signal results from the contribution of anomalous and non anomalous atoms that are strained in different ways and/or are located in different crystallographic sites or sample regions ($\phi_N - \phi_A \neq 0$).

2.3 Other techniques.

However, X-ray scattering also has drawbacks. The information is obtained in reciprocal space, and thus has to be 'translated' in the real world. It is thus useful to combine it with others techniques such as for instance atomic force microscopy (AFM), transmission electron microscopy (TEM) or medium energy ion scattering (MEIS). MEIS experiments have been previously performed to determine the strain state of Si-Ge QDs [33] or Ge nanowires deposited on Si [34]. TEM experiments allow to determine the strain strain, defects and composition inside dots. But they presents the drawback that the sample needs to be prepared. The preparation, which is a random cut of the sample, can entail a partial deformation of the strain field. In the following, we will shortly describe AFM measurements.

2.3.1 Atomic force microscopy.

Atomic force microscopy (AFM) measures the force between the sample surface and a fine tip with a radius less than 10 nm. The force can be measured by the bending of the cantilever on which the tip is mounted (contact mode). The tip is in direct contact with the sample surface and the force is due to hard-sphere repulsion between the tip and the sample surface. In addition, the force can be determined by measuring the change in resonance frequency due to it (tapping) mode. The AFM presents a typical resolution of several nm laterally and several Åvertically. It is well suited to characterize *ex situ* the shape of islands.

Deconvolution of island sizes.

The dimensions of surface corrugations measured by AFM is influenced by the finite size of the probe tip. Not only the apex of the tip but also its sidewalls interacts with the surface. This effect is enhanced when the sample topography is abrupt. The measured topography is thus a convolution of the real surface and the tip shape. The deconvolution requires the knowledge of both the surface and the tip shape. A correction Δl of the lateral size l of an island can be simply obtained assuming a spherical tip with radius R. For an island of height h defined by facets with an angle α, the measured size will be enlarged by:

$$\Delta l = \sqrt{h(2R-h)} - h\cot\alpha \qquad h < R(1-\cos\alpha) \tag{2.55}$$

$$\Delta l = R[\sin\alpha - (1-\cos\alpha)\cot\alpha] \qquad h \geq R(1-\cos\alpha) \tag{2.56}$$

Typical apex radii of commercial AFM tips are of the order of 5nm. Using the facet angle of 25° observed for {113} facetted domes, we obtain $R(1-\cos\alpha)$=0.47nm. Then, a constant value of Δl=2.5 nm can be used to correct the diameter measured by AFM of such domes.

2.4 Conclusion

The progress in nanoscience and nanotechnology asks for tools to characterize the structure of objects both at mesoscopic and atomic levels. The strength of X-ray technique are: the high resolution on the strain, the possibility to probe all correlation length scales, i.e. morphology and atomic structure, their average over several square millimeters which provides statistically average information. The measurements usually require no special sample environment or preparation: it is a non-destructive probe and the penetration depth can be varied between a few nanometers to micrometers, thus probing both surface or near surface structures and bulk. The chemical contrast of a given element can be

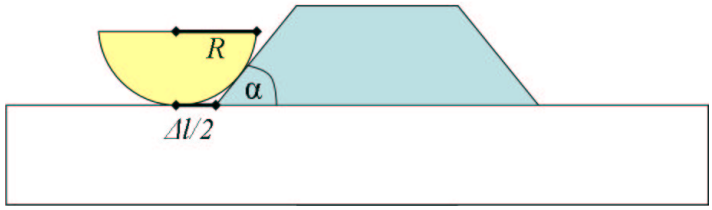

Figure 2.13: Increase of lateral island size as measured by AFM with respect to the real size of the tip. The real island diameter can be approximatively obtained by subtracting Δl of the measured island size.

enhanced by performing anomalous scattering close to a specific absorption edge, yielding compositional information. X-ray can also be applied in situ in Ultra-High-Vacuum (UHV) during the growth of nanostructures. However X-ray scattering has the drawback to give information in the reciprocal space and to require beamtime at the synchrotron. It is thus useful to combine X-rays with imaging in the real space. In the following chapter, we will describe how the strain and composition can be determined combining X-ray scattering and elastic simulations.

Bibliography

[1] . M. Born, and E. Wolf, *Principles of optics*, 5^{th} edition, Pergamon (Eds).

[2] H. Dosch, *Critical Phenomena at Surfaces and Interfaces*, Springer-Verlag, Berlin (1992).

[3] R. W. James, *The optical principles of the diffraction of X-rays*, Cornell University Press, New-York (1965).

[4] *http://www-crxo.lbl.gov/*

[5] R. Feidenhans'l, Surf. Sci. Rep. **10**, 105 (1989).

[6] S. K. Sinha, E. B. Sirota, S. Garoff and H. B. Stanley, Phys. Rev. B **38**, 2297 (1988)

[7] H. Dosch, B. W. Batterman and D. C. Wack, Phys. Rev. Lett. **56**, 1144 (1986).

[8] A. Fresnel, *Mémoire de l'académie* **11**, 393 (1823).

[9] M. Born and E. Wolf, *Principles of Optics*, Pergamon, New-York (1980).

[10] P. Croce and L. Névot, Revue Phys. Appl. **11**, 113 (1976).

[11] D. Bohm, Quantum theory, Prentice-Hall (1951).

[12] C. Kittel, *Introduction à la physique de l'état solide*, Dunod (1970).

[13] G. H. Vineyard, Phys. Rev. B **26**, 4146 (1982).

[14] S. Dietrich and A. Haase, Phys. Rep. **260**, 1 (1995).

[15] M. Rauscher, R. Paniago, T. H. Metzger, Z. Kovatz, J. Domke, J. Peisl, H.-D. Pfannes, J. Schulze and I. Eisele, J. Appl. Phys. **86**, 6763 (1999).

[16] Y. Yoneda, Phys. Rev. B **131**, 2010 (1963).

[17] F. Leroy, Ph. D. Thesis: Joseph Fourier University, Grenoble, France (2004).

[18] G. Renaud, R. Lazzari, Ch. Revenant, A. Barbier, M. Noblet, O. Ulrich, F. Leroy, J. Jupille, Y. Borensztein, C. R. Henry, J.-P. Deville, F. Scheurer, J. Mane-Mane, and O. Fruchart, Science **300**, 1416 (2003).

[19] B. Lairson, A. Payne, S. Brennan, N. Rensing, B. Daniels and B. Clemens, J. Appl. Phys **78**, 4449 (1995).

[20] V. Holý, T. Roch, J. Stangl, A. Daniel, G. Bauer, T. H. Metzger, Y. Zhu, K. Brunner and G. Abstreiter, Phys. Rev. B **63**, 205318 (2001).

[21] T. H. Metzger, I. Kegel, R. Paniago and J. Peisl, J. Phys. D : Appl. Phys. **32**, A202 (1999).

[22] O. Robach, G. Renaud, and A. Barbier, Phys. Rev. B **60**, 5858 (1999).

[23] A. Guinier and G. Fournet, *Small Angle Scattering of X-rays*, Wiley, New York (1955).

[24] R. Lazzari, F. Leroy, and G. Renaud, Phys. Rev. B **76**, 125411 (2007).

[25] R. Lazzari, J. Appl. Cryst. **35**, 406 (2002).

[26] J. L. Hodeau, V. Favre-Nicolin, S. Bos, H. Renevier, J. E. Lorenzo, and J. F. Bérar, Chem. Rev. **101**, 1843 (2001).

[27] S. Sasaki, *Numerical tables of anomalous scattering factors calculated by cromer and liberman method*, KEK Report **88**, 1 (1989).

[28] D. Waasmaier, A. Kirfel, Acta Cryst. **A51**, 416 (1995)

[29] V. Favre-Nicolin, *Développement de la diffraction anomale dispersive, application à l'étude de structures modulées inorganiques et de macromolécules biologiques.*, Ph. D. Thesis: Joseph Fourier University, Grenoble, France (1999).

[30] J. C. Phillips, K. O. Hodgson, Acta Cryst. A **36**, 856 (1980).

[31] R. Narayan, S. Ramaseshan, Acta Cryst. A **37**, 181 (1981).

[32] J. Coraux, *Etude par spectroscopie X en condition de diffraction de la croissance et de l'encapsulation de boites quantiques GAN/AlN*, Ph. D. Thesis: Joseph Fourier University, Grenoble, France (2006).

[33] D. W. Moon, H. I. Lee, B. Cho, Y. L. Foo, T. Spila, S. Hong, and J. E. Greene, Appl. Phys. Lett. **83**, 5298 (2005).

[34] K. Sumitomo, H. Omi, Z. Zhang, and T. Ogino, Phys. Rev. B **67**, 035319 (2003).

Chapter 3

Elastic simulations and X-ray scattering.

This chapter presents Finite Difference Method (FDM) calculations of the strain in islands of different compositions coherently grown on Si(001) and the simulation of the corresponding diffraction profiles using the Born and Distorted Wave Born Approximations. The effects of this later are discussed. This will be useful to help understanding the experimental data.

3.1 Strain and composition in SiGe nanoscale islands studied by elastic simulations and X-ray scattering.

As previously mentioned in chapter one, during the beginning of layer by layer growth of Ge/Si heterostructures, the lattice parameter difference leads to a linear increase of elastic energy with the number of deposited monolayers. After a critical layer thickness, it is energetically favorable to relax the lattice strain by forming islands. This partial relaxation is elastic. The remaining strain field influences the band structure and consequently the electronic properties of the system. The knowledge about the elastic properties and the strain field in quantum dots (QD) is of interest for better understanding and controlling of the electronic characteristics. The strain distributions used in this work have been calculated for a single island. The analysis of the strain profile of nanoscale semiconductors by X-ray diffraction has been demonstrated by I. Kegel *et al.* [1]. In order to understand the trends observed in X-ray experiments it appears helpful to use a theoretical model of the strain distribution in the SiGe or Ge quantum dots.

The use of numerical finite element modelling (FEM) to calculate the strain field in mesoscopic structures down to structure sizes of a few tens of nanometers has become successfully established [2, 3]. The results obtained by FEM can be used for X-ray diffuse scattering simulations. We will follow the same iterative approach developed by Wiebach *et al.* [3]: (i) creation of a specific structure model in real space that includes island size, shape, and chemical composition; (ii) FEM calculation of the three-dimensional strain field inside the island and the surrounding substrate and wetting-layer; (iii) numerical calculation of diffuse scattering; (iv) comparison to experimental data; and (v) further improvement of the model (i) and calculation of diffuse intensities from a new model until satisfactory agreement is achieved. This approach cannot be used as a true fitting procedure because there are too many free parameters in the model (shape, size, chemical composition, and spatial correlation) and calculations are lengthly. Therefore, it is necessary to include knowledge obtained by other methods, *e.g.*, information on the shape and size obtained by AFM. The FEM calculation is done for a single island and its environment. The subsequent simulation of the diffuse intensity is performed numerically, *i.e.*, on a regular grid consisting of base cells. The dimensions of the base cells can be

chosen larger than the crystal unit cells. This depends on the size of the sample and on the memory of the computer.

3.1.1 Theoretical model.

The crystal lattice can be distorted due to externally imposed constraints on the dimensions of the crystalline unit cell. These externally imposed distortions can be decomposed into a volumetric and a distortional component [4]. The volumetric component comes when for instance, alloys are grown in bulk form or when epitaxial films are grown on a lattice-matched substrate. The distortional component becomes important when epitaxial films are coherently grown on a lattice-mismatched substrate.

If the substrate is an unstrained $Si_{1-x}Ge_x$ alloy crystal (bulk) whose Ge composition is x and whose mean lattice parameter $a_{SiGe(sub)}$ is a weighted average (Vegard's law) of the two endpoint lattice parameters, then $a_{SiGe(sub)} = (1\text{-}x)a_{Si} + xa_{Ge}$. If an epitaxial $Si_{1-y}Ge_y$ film is grown on top of the $Si_{1-x}Ge_x$ substrate then its lattice parameter parallel to the interface must be the same as the substrate. The lattice parameter perpendicular to the interface will change to approximately keep the unit cell volume constant. A quantitative description of the volumetric and distortional components of externally imposed strains can be done writing the generalized Hooke's law for cubic crystals:

$$\begin{pmatrix} \sigma_x \\ \sigma_y \\ \sigma_z \\ \tau_{xy} \\ \tau_{yz} \\ \tau_{zx} \end{pmatrix} = \begin{pmatrix} \mathrm{c}_{11} & \mathrm{c}_{12} & \mathrm{c}_{12} & 0 & 0 & 0 \\ \mathrm{c}_{12} & \mathrm{c}_{11} & \mathrm{c}_{12} & 0 & 0 & 0 \\ \mathrm{c}_{12} & \mathrm{c}_{12} & \mathrm{c}_{11} & 0 & 0 & 0 \\ 0 & 0 & 0 & \mathrm{c}_{44} & 0 & 0 \\ 0 & 0 & 0 & 0 & \mathrm{c}_{44} & 0 \\ 0 & 0 & 0 & 0 & 0 & \mathrm{c}_{44} \end{pmatrix} \cdot \begin{pmatrix} \epsilon_x \\ \epsilon_y \\ \epsilon_z \\ \gamma_{xy} \\ \gamma_{yz} \\ \gamma_{zx} \end{pmatrix} \tag{3.1}$$

where the ϵ_i's and σ_i's are the normal strains and stresses and the γ_i's and τ_i's are the shear strains and stresses, respectively. For a film and substrate that are in cube on cube epitaxy ($(001)_F//(001)_S$ and $[100]_F//[100]_S$), the last matrix is reduced to:

$$\begin{pmatrix} \sigma_{//} \\ \sigma_{\perp} \end{pmatrix} = \begin{pmatrix} \mathrm{c}_{11} + c_{12} & \mathrm{c}_{12} \\ 2\mathrm{c}_{12} & \mathrm{c}_{11} \end{pmatrix} \cdot \begin{pmatrix} \epsilon_{//} \\ \epsilon_{\perp} \end{pmatrix} \tag{3.2}$$

In the case of an epitaxial film with a free surface (e.g. uncapped films and/or islands) the perpendicular stress vanishes. Hence

$$\sigma_{\perp} = 2C_{12}\epsilon_{//} + C_{11}\epsilon_{\perp} = 0. \tag{3.3}$$

The perpendicular strain in the film is then given by:

$$\epsilon_{\perp} = \frac{-2C_{12}}{C_{11}}\epsilon_{//} = \frac{-2\nu}{1-\nu}\epsilon_{//}, \tag{3.4}$$

ν is the Poisson's ratio, defined as the negative of the ratio between lateral and longitudinal strain constants under uniaxial longitudinal stress ($\nu = C_{12}/[C_{11} + C_{12}]$). The term that multiplies $\epsilon_{//}$ is the equivalent Poisson's ratio for a biaxial strain.

3.1.2 Diffraction from a strained crystal.

In a strained crystal, the position of atom i will be changed from its ideal position $\mathbf{r_i}$ to $\mathbf{r_i} + \mathbf{u_i}$. The amplitude of the diffracted beam will be changed into:

$$A(\mathbf{Q}) = \sum_{atoms\ i} f_i(\mathbf{Q}) \mathrm{e}^{-\mathrm{i}\mathbf{Q}\cdot(\mathbf{r_i}+\mathbf{u_i})}. \tag{3.5}$$

The crystal was modeled as a finite array of $N_x\mathrm{x}N_y\mathrm{x}N_z$ unit cells. The displacement vector u_j associated to each point of the array, *i.e.* to each unit cell j was calculated by numerical finite

element simulation. If we assume that atoms in each unit cell have the exact same deformation (a reasonable approximation for small deformations and only to compute scattering close to non-forbidden reflections), then we can factorize the scattering for a full unit cell. The scattered amplitude is then equal to:

$$A(\mathbf{Q}) = \sum_{atoms\ i} f_i \mathrm{e}^{-\mathrm{i}\mathbf{Q}\cdot\mathbf{r_i}} \sum_{unit\ cell\ j} \mathrm{e}^{-\mathrm{i}\mathbf{Q}\cdot(\mathbf{R_j}+\mathbf{u_j})}, \tag{3.6}$$

where $\mathbf{R_j}$ is the position of the j_{th} unit cell and $\mathbf{u_j}$ is its displacement from its ideal position (in the unstrained crystal), $\mathbf{r_i}$ is the ideal position of atom i within the unit cell. The first term in Eq. 3.6 is the structure factor F of the ideal unit cell. In our case, two types of atoms are studied, Ge and Si. If x_{Ge} is the occupancy factor of Ge in a given unit cell (1 if the Ge atom is in the QD, 0 if it is outside), the amplitude can be written as:

$$A(\mathbf{Q}) = F_{Ge}(\mathbf{Q}) \sum_{unit\ cell\ j} x_{Ge} \mathrm{e}^{-\mathrm{i}\mathbf{Q}\cdot(\mathbf{R_j}+\mathbf{u_j})} + F_{Si}(\mathbf{Q}) \sum_{unit\ cell\ j} (1 - x_{Ge}) \mathrm{e}^{-\mathrm{i}\mathbf{Q}\cdot(\mathbf{R_j}+\mathbf{u_j})} \tag{3.7}$$

The two last equations do not allow to calculate *e.g.* the (200) scattering, which is due to the unit cell distortions. The calculation is made possible and time consuming using the following formula, which assums that atoms in each unit cell are displaced from their ideal positions by a vector $\mathbf{u_{ij}}$, which is linearly interpolated knowing the ideal position of the atom in its unit cell and the displacement of the neighbouring unit cells:

$$A(\mathbf{Q}) = \sum_{unit\ cell\ j} \sum_{atoms\ i} f_i(\mathbf{Q}) \mathrm{e}^{-\mathrm{i}\mathbf{Q}\cdot(\mathbf{R_j}+\mathbf{r_i}+\mathbf{u_{ij}})}. \tag{3.8}$$

The calculations were performed using the Born or the distorted wave Born approximation, either using Eq. 3.7 or Eq. 3.8. The Fourier transform (FT) of a finite box of Si is a peak with oscillations. In the experiment, the sample can be considered as infinite because the lattice parameter of Si and Ge are much smaller than the sample dimension, so no oscillations are actually observed. To avoid these fringes, we do not calculate the Fourier transform (FT) of the nanostructure, but only the difference (calculated over the finite box) with an ideal infinite Si crystal. The simulated box TF(B) is then obtained with: TF(B)=TF(B∞)+TF(ΔB). TF(B∞) is the Fourier transform of the infinite Si crystal, *i.e.* a Dirac-peak that can be neglected. The term TF(ΔB) is the difference of the FT of the real Si matrix with the strain field, the FT of the real Ge dot and the FT of the simulated finite box consisting of a perfect Si lattice. It follows that in the final result the FT of the perfect infinite crystal from the simulated structure is missing.

Finite Difference Method (FDM) program.

The FDM program used in this work was first developed by C. Priester [5]. The program is not strictly a finite element program. The strain is calculated using three-dimensional (3D) finite-difference technique in elasticity theory. Using the FDM program, it is possible to simulate different island shapes such as {105} facetted pyramids, facetted domes (Fig. 3.1 (b)) or domes inside facetted pits (Fig. 3.1 (d)).

Different models which allow variation of intermixing along the island height have been implemented. Figure 3.2 (a) displays three possibilities: (1) an increasing exponential Ge content from the bottom to the apex of the island, (2) a linear increase of the Ge content and (3) a decreasing exponential Ge content. In addition, different intermixing profiles can be calculated. Figure 3.2 (b) gives the example of a Si rich core dome with a higher Ge content at its periphery as observed by A. Malachias [6].

3.1.3 Study of the relaxation state of pyramids and domes with and without wetting layer.

A model of one island in a box is used. The island is located directly on the Si substrate. Using the FDM modelling, the strain field of a {105} facetted pyramid of 70nm length and a dome shaped

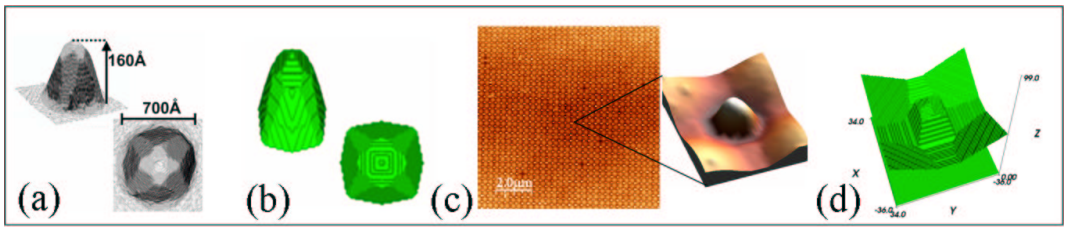

Figure 3.1: (a) Facetted domes observed by STM by A. Rastelli [7]. (b) Facetted domes simulated by the FDM program. (c) AFM image of domes inside laterally ordered pits. (b) Facetted domes inside pits simulated by the FDM program.

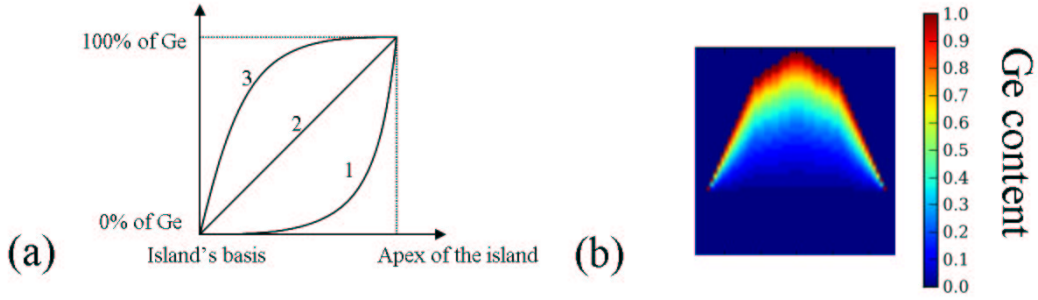

Figure 3.2: (a) Three models of intermixing along the island height. (b) Example of an intermixing profile.

island of 115 nm length has been calculated. The shape was chosen in agreement with that reported in literature [7]. Figure 3.3 displays the in-plane strain **with respect to the Si substrate**: ${\epsilon^{Si}}_{xx} = (a_{i,j} - a_{Si})/a_{Si}$, where a_{Si} and $a_{i,j}$ are the in-plane lattice parameters of Si bulk and (i,j) cell of the Si substrate or Ge island, respectively. The in-plane strain with respect to the Ge bulk will be ${\epsilon^{Ge}}_{xx} = (a_{i,j} - a_{Ge})/a_{Ge}$, where a_{Ge} is the in-plane lattice parameter of Ge bulk. The mean ${\epsilon^{Si}}_{xx}$ in the Ge pyramid and Ge dome equals 0.88% and 1.84%, respectively. The Ge dome presents a larger volume and thus a larger relaxation. The Ge is deformed in the plane (${\epsilon^{Ge}}_{xx} \sim 2.3\%$ (dome)-3% (pyramid)) to get closer to the lattice parameter of Si and to insure a continuity of the strain field (ϵ_{xx}, ϵ_{yy}) at the Si/Ge interface. To compensate the compression in the xy plane, the Ge positively deforms (expansion) in the z direction (see zone 1 in Fig. 3.3). As the mean in-plane lattice parameter of the pyramid ($\bar{a}$=5.48 Å) is smaller than that of the dome ($\bar{a}$=5.52 Å), the expansion along z of the Ge unit cell of the pyramid (${\epsilon^{Si}}_{zz} = (c_{i,j} - c_{Si})/c_{Si} = 6.59$ %) is higher than that of the dome (${\epsilon^{Si}}_{zz} = 5.87$ %), c_{Si} and $c_{i,j}$ are the out-of-plane lattice parameters of the Si bulk and (i,j) cell of the Ge island, respectively. In both cases, the mean in-plane strain of the Si substrate is ${\epsilon^{Si}}_{xx} = 0\%$. The Si substrate is composed of two regions: underneath the islands, the Si lattices are compressed (zone 2 in Fig. 3.3) and at the periphery of the islands, the Si lattices are dilated (zone 3 in Fig. 3.3).

3.1.4 Impact of the wetting layer on the diffracted signal and relaxation state of islands.

Figure 3.4 shows the simulated Ge and Si intensities using the atomic displacement field calculated from FDM for the pure Ge pyramid and dome shaped islands, with or without pure Ge wetting layer. Tiny differences can be observed between the curves simulated with or without wetting layer. The wetting layer has a small impact on the diffracted signal.

A component of the Si signal can be observed in the right part of the Si(400) Bragg peak. This corresponds to the scattering from compressed parts of the Si substrate (zone 2 in Fig. 3.3). The

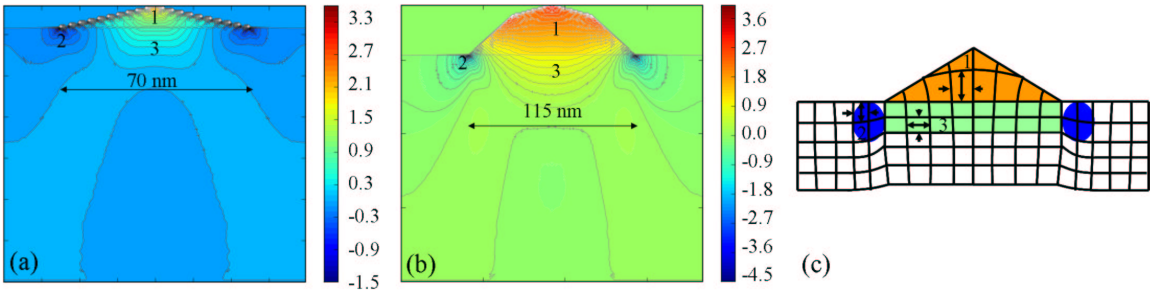

Figure 3.3: $\epsilon^{Si}{}_{xx}$ values in the xz plane of a pure Ge pyramid (a) and dome-shaped (b) island without wetting-layer. $\epsilon^{Si}{}_{xx} = 4.13\%$ means that the Ge atoms are no more strained. When $\epsilon^{Si}{}_{xx}$ <0, the Si lattices are compressed (zone 2). This happens in both cases for Si unit cells at the periphery of the pyramid and dome. This can explain the formation of trenches around domes. When $\epsilon^{Si}{}_{xx}$ >0, the Si lattices are dilated (zone 3). This is generally observed underneath the islands. (c) Sketch of strain and lattice parameter in a Ge island.

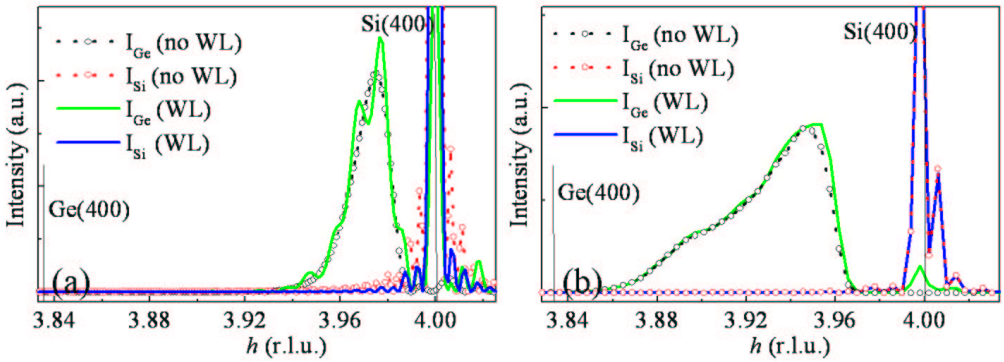

Figure 3.4: Simulated Ge and Si intensities using Eq. 3.6 for the pure Ge pyramid (a) and dome (b) shaped islands, with or without pure Ge wetting layer.

maximum of Ge scattered intensity I_{Ge} is displaced towards lower h values for the dome shaped island. For a given shape, the strain depends on the aspect ratio between height and diameter. Generally, the smaller the aspect ratio between height and diameter, the more compressed the island in its plane. This explains why the in-plane lattice relaxation is larger for domes than for pyramids. From the h position of the maximum of I_{Ge}, the mean in-plane lattice parameter $a_{//}$ of the island can be determined: $a_{//} = a_{Si}(2 - h/h_{Si})$, where a_{Si} is the lattice parameter of the Si bulk and h_{Si} is the position of the Si Bragg peak. Two components of the Ge diffuse signal are observed for the dome shaped island (see Fig. 3.4 (b)). This can be related to the scattering from two regions of the island: the basis composed of {113} and {15 3 23} facets and the apex composed of the four {105} facets.

Increasing the Ge volume, the maximum of the Ge intensity goes towards the position of the Ge bulk Bragg peak and the intensity of the Si signal increases (not shown here), showing that the higher the Ge volume, the higher the strain inside the Si substrate.

3.1.5 Impact of intermixing on the diffracted signal and relaxation state of islands.

The Si and Ge diffuse scattering signals around the (220) reflection are simulated (Fig. 3.5) in the case of two domes of identical size (∼100 nm width), but one of pure Ge and the other being a SiGe alloyed dome with a Ge content increasing linearly: from 0% at the center of the basis to 100% at the apex. For the pure Ge dome, the Ge scattering intensity is positioned at lower h values, close to that of bulk Ge (h ∼1.92). It is well known that intermixing reduces the mean strain inside the islands [8]. In addition, there is an asymmetry between the left and right parts of the Si scattering signal around the (220)Si Bragg peak. The substrate presents a more compressed Si part. A tail of the Si scattering signal is observed for the intermixed dome at lower h value. The Ge and Si signals are well separated for pure Ge domes, which is not the case for the intermixed island. The absence or presence of this separation can thus help qualitatively determining if there is or not intermixing.

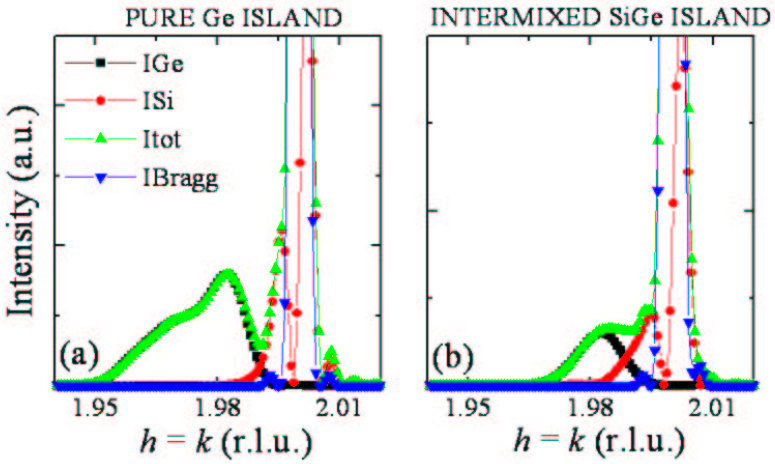

Figure 3.5: Simulated Ge and Si intensities for a pure Ge (a) and a GeSi intermixed (b) domes.

3.1.6 Study of the effect of the distorted wave Born approximation on the scattered intensity.

In the following, the studied samples will be separated into two subsystems: the first one is the islands QD and the second one is the substrate S_0. The interaction potential between X-rays and matter is thus divided into two terms related to the islands and the substrate. The scattering operators related to the islands and substrate are $\hat{T}_{QD}$ and $\hat{T}_{S0}$. In the Fraunhofer approximation, the scattered wave amplitude is proportional to [9]:

$$< \phi_f|\hat{T}_{S0}|\phi_i > + < \phi^-_{0,f}|\hat{T}_{QD}|\phi^+_{0,i} >, \tag{3.9}$$

where the primary wave $|\phi_i >$ is scattered dynamically by S_0, and the wave field $|\phi^+_{0,i} >$ is created. Similarly, $|\phi^+_{0,f} >$ is the time-reversed wave field with primary wave $|\phi_f >$ [10]. Provided that the structure of S_0 is simple enough, the first term of Eq. 3.9 can be calculated in the frame of the dynamical theory [9]. The calculation of the second term of Eq. 3.9 is more difficult as the second term involves multiple scattering of the distorted waves in the islands. Anyway, supposing that the islands are only a small deviation with respect to S_0, the scattered wave amplitude of the second term of Eq. 3.9 can be expressed in the frame of the DWBA. The whole scattering from the islands can thus be written as [10]

$$\begin{aligned} F_{QD} \quad = \quad & \sum_{j\in QDs} f_j \mathrm{e}^{\mathrm{i}(\mathbf{k_f}-\mathbf{k_i})\cdot\mathbf{r_j}} + r(\mathbf{k_i},E)\sum_{j\in QDs} f_j \mathrm{e}^{\mathrm{i}(\mathbf{k_f}+\mathbf{k_i})\cdot\mathbf{r_j}} \\ & + r(\mathbf{k_f},E)\sum_{j\in QDs} f_j \mathrm{e}^{-\mathrm{i}(-\mathbf{k_f}-\mathbf{k_i})\cdot\mathbf{r_j}} + r(\mathbf{k_i},E)r(\mathbf{k_f},E)\sum_{j\in QDs} f_j \mathrm{e}^{-\mathrm{i}(-\mathbf{k_f}+\mathbf{k_i})\cdot\mathbf{r_j}}, \end{aligned} \tag{3.10}$$

where f_j is the atomic scattering factor of all the atoms j in the island (Ge + intermixed Si), $\mathbf{k}_i$ and $\mathbf{k}_f$ are the incoming and outcoming waves, $r(\mathbf{k_f},E)$ are the reflectivities of the incident and scattered waves and $\mathbf{r_j}$ is the position of atom j. In the following, we will define q_z and p_z as $q_z = k_{f_z} - k_{i_z}$ and $p_z = k_{f_z} + k_{i_z}$. Provided that the scattering from S_0 (first term in Eq. 3.9) is neglected, the total complex scattering amplitude is given by Eq. 3.10. Note that we did not take into account dynamical diffraction in S_0 [12], but only refraction at the S_0 interface. This is justified by the negligible scattering from S_0 as compared to that of the islands close to the island scattering peak in reciprocal space. The first term in Eq. 3.10 corresponds to the kinematical scattering of the incident wave by the islands (case of the Born approximation). The three other terms imply reflections on the substrate and are known as multiple scattering paths.

The aim of the present section is to check the relative importance of the four paths of the Distorted Wave Born Approximation (DWBA) as a function of energy and incident angle. For the model, a dome with 115 nm diameter has been chosen. The size of the island corresponds to that observed after a deposit of 6-7 ML at ∼650°C on nominal substrates (see chapter 9). Figure 3.6 shows the contribution of the four paths and the overall scattered intensity around the (400)Si reflection in the scattering region of the Ge islands (h=3.98) as a function of α_f and α_i. The simulations have been performed at 11 keV for $\alpha_i = \alpha_c$ and $\alpha_i = 1.86\alpha_c$. The four paths interfere constructively at $\alpha_f = \alpha_c$. The observed maximum is known as the Yoneda peak. The oscillations observed for the two first paths come from the finite size of the island. A shift along α_f is observed between the first and second paths. In the sub-critical regime, the amplitudes of the two first paths are nearly identical as the coefficient for the reflected wave is ∼1. In the second regime, the first path is predominant, except for $\alpha_f < \alpha_c$, where the third path is also dominant. Besides, it can be observed that the maximum of the DWBA signal is not positioned at $\alpha_f = \alpha_c$ as an effect of multiple scattering. From the α_f position of this maximum $\alpha_{f,max}$, it is possible to determine the mean height z of the iso-strain area of the island which scattered at h=3.98 [1]:

$$z = \frac{\lambda}{2\pi\alpha_{f,max}} arccos(\frac{\alpha_{f,max}}{\alpha_c}). \tag{3.11}$$

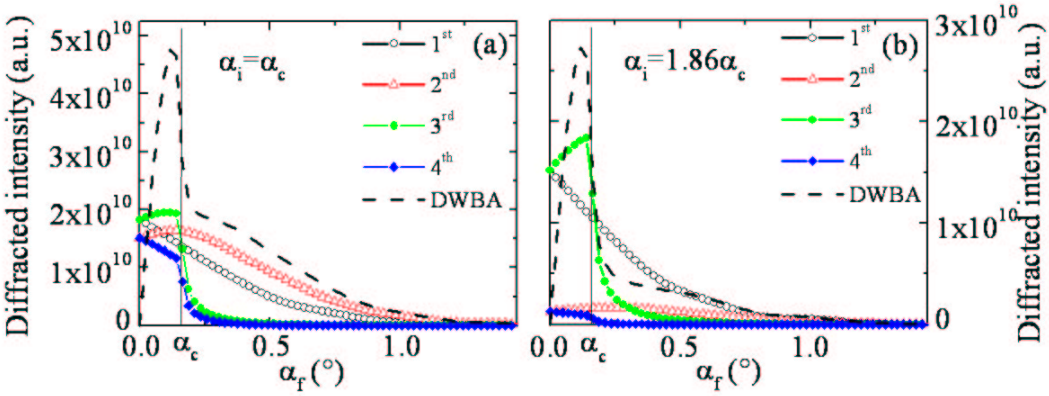

Figure 3.6: Diffracted intensity by a 115nm dome calculated in the region of maximum of Ge intensity around the (400) reflection as a function of α_f for the four paths and for all the paths, in the case of α_i=α_c (a) and α_i=1.86α_c (b).

Scattering path	Prefactor	Out-of-plane scattering vector	h	k	$l(\alpha_i$=0.161°)	$l(\alpha_i$=0.28°)
First	1	q_z	4	0	0	0
Second	$r(\mathbf{k_i})$	p_z	4	0	0.027	0.047
Third	$r(\mathbf{k_f})$	-p_z	4	0	0.027	0.047
Fourth	$r(\mathbf{k_i})r(\mathbf{k_f})$	-q_z	4	0	0	0

Table 3.1: The four scattering paths, their prefactors, their out-of-plane scattering vector, and the position of their maximum along the h, k and l reciprocal space directions for the (400) reflection at α_i=0.161° and α_i=0.28° at 11keV.

A complete analysis of the strain inside the islands can be outlined by correlating the in-plane strain ($\epsilon_{//}$) and the out-of-plane strain ($\epsilon_\perp$). In order to well separate these strain contributions in reciprocal space, two dimensional out-of-plane mapping can be performed at the (602) reflection (see chapter 9). In the following, we will check the relative importance of the four paths at the (602) reflection as a function of the incident angle. In the BA, which corresponds to the first term in Eq. 3.10, the (h,k,l) positions in reciprocal space are explored by adjusting the modulus and direction of the scattering vector $\mathbf{Q}$=$\mathbf{k}_f$-$\mathbf{k}_i$. Depending on the scattering paths, the maximum position of the Ge scattering factor along l is modified. It has been demonstrated [10] that for an in-plane reflection such as (400), the exact Bragg condition occurs for the first path with $Q_z = q_z = 2\pi(sin\alpha_f + sin\alpha_i)/\lambda = 0 = 2\pi l/c_{Si}$, c_{Si} being the out-of-plane lattice parameter of the Si substrate, when (h,k,l)=(400). For the second path, $Q_z = p_z = 2\pi(sin\alpha_f - sin\alpha_i)/\lambda$. Consequently, the intensity maximum is shifted along l and the position of the intensity maximum is (h,k,l)=(40l), with l=$2c_{Si}sin\alpha_i/\lambda$. For the third path, $Q_z = -p_z = 2\pi(-sin\alpha_f + sin\alpha_i)/\lambda$. Consequently, the position of the intensity maximum is (h,k,l)=(40l), with l=$2c_{Si}sin\alpha_f/\lambda$ and α_i=α_f. Finally, for the fourth path, the position of the intensity maximum is (h,k,l)=(400).

Table 3.1 summarizes the prefactors, the out-of-plane scattering vector, and the maximum position along the h, k and l of the four scattering paths in Eq. 3.10 for the (400) reflection at α_i=0.161° and α_i=0.28° and at 11keV. All four scattering maxima are superimposed along the h and k directions, while slightly shifted along l. In the case of the asymmetric (602) reflection, shifts are expected along

the l direction. Refraction of the X-ray beam causes a change in the direction of the incident wave vector $\mathbf{k}_i$ at the air-sample interface and of the exit wave vector $\mathbf{k}_f$ at the sample-air interface. It has been demonstrated [10] that, for an asymmetric reflection, when $\alpha_i \leq \alpha_c$ and α_f large, the out-of-plane projection of the scattering vector in the sample is $Q'_z \sim 2\pi sin\alpha_f \lambda$, while $Q_z = 2\pi(sin\alpha_f + sin\alpha_i)/\lambda$ in vacuum. The refraction effects cause a $c_{Si} sin\alpha_i/\lambda$ shift along l of the scattered signals. At 11 keV, this corresponds to a 0.014 l *global* shift of the scattered signals towards larger l values at α_i=α_c. Figure 3.7 shows the simulated scattering contributions, $|F_{Ge}|$ of the four paths and in the DWBA along the in- and out-of-plane h and l directions, close to the (602) at α_i=0.161° and at 11 keV for the 115 nm wide dome shaped island (see Fig. 3.3). Note that the 3^{rd} and 4^{th} paths are negligible compared to the 1^{st} and 2^{nd} paths as α_f is large ($l \sim 2$). The simulated scattering contributions of the 1^{st} and 2^{nd} paths and in the DWBA are represented with the same scale contrary to those of the 3^{rd} and 4^{th} paths. Shifts of the scattering contribution are observed for the second and third paths as expected theoretically (see the different positions of the black and red circles in Fig. 3.7). Contrary to a work performed on 40 nm width GaN QDs [10], the shifts are not negligible with respect to the finite size spreading of the scattering peaks. Differences such as the spreading along h of the Ge scattering contribution are then observed between the simulation in the BA and in the DWBA. In particular, significant intensity is present around (h,l)=(5.87,1.96) (see black circles) in the BA case, which is absent in the DWBA one. In some regions, a factor higher than two can be obtained for the ratio value between the 1^{st} path (BA) and the DWBA. To explain this phenomenon, the last image of Fig. 3.7 displays the difference of phases $\Delta\phi = \phi_2 - \phi_1$ between the 1^{st} and 2^{nd} paths (the other paths have a negligible contribution on the scattering signal). In the circled region, $\Delta\phi$ oscillates between π and $-\pi$. In this region, the first and second paths interfere thus destructively and explain the absence of intensity in this region. It should be stressed that the total intensity is not the sum of the intensity from each scattering path as a result of the interferences between the different paths [11].

In the critical incident angle regime, there are thus noticeable differences between the Ge contribution simulated in the BA and in the DWBA. Figure 3.8 shows the Ge contribution simulated in the BA and in the DWBA in the case of the subcritical (α_i=0.10°), critical (α_i=0.161°) and supercritical (α_i=0.28°) incident angle regime for a highly intermixed 115 nm wide dome. In all cases, variations between the BA and DWBA are observed. Drastic differences are observed at the critical angle. At α_i=0.10°, it remains only one intensity maximum. At α_i=0.28°, the intensity of the maximum positioned at low l values is higher than the one positioned at higher l values; this is the reverse in the BA. Besides, the maxima of intensity are not located at the same position as in the BA. This implies that for large domes (∼100nm width and ∼20nm height), the out-of-plane and in-plane strain measured at an asymetric reflection should be investigated using a Distorted Wave Born Approximation treatment.

We previously showed that the scattered amplitude in the DWBA and for each scattering path are not similar at an asymmetric reflection. We will now investigate the difference of the Ge scattered intensity at an in-plane reflection such as the (400) as a function of the incident angle. Fig. 3.9 displays the Ge scattered amplitude variations for each scattering path and in the DWBA with the four terms. This was simulated close to the Si(400) reflection for different incident angle and as a function of small l values.

As previously mentioned, the third and fourth paths are almost negligible; except when $\alpha_f > \alpha_i$, the third path has to be taken into account. What clearly appears is that the simulated signal in the DWBA differs from that of the different paths. The simulated signal in the DWBA is not superimposed to that in the first path (BA). To clearly identify the variations between the DWBA and BA signals, we summed up the scattered intensity between α_f ∼0° and α_f ∼1.5° to properly account for the experimental setup (see Fig. 3.10). Using the position sensitive detector (PSD), the intensity is generally integrated from α_f ∼0° to α_f ∼1.5°. For the model, a dome with 115 nm diameter and a 70 nm wide pyramid have been chosen. The integrated intensity around the in-plane (400) reflection for the dome shaped island drastically varies for the first path (BA) and in the DWBA depending on the incident angle. The generalized Eq. 3.10 not only influences the intensity distribution along Q_z or α_f but through an indirect mechanism also that of Q_r or h. If we restrict the equation Eq. 3.10 to

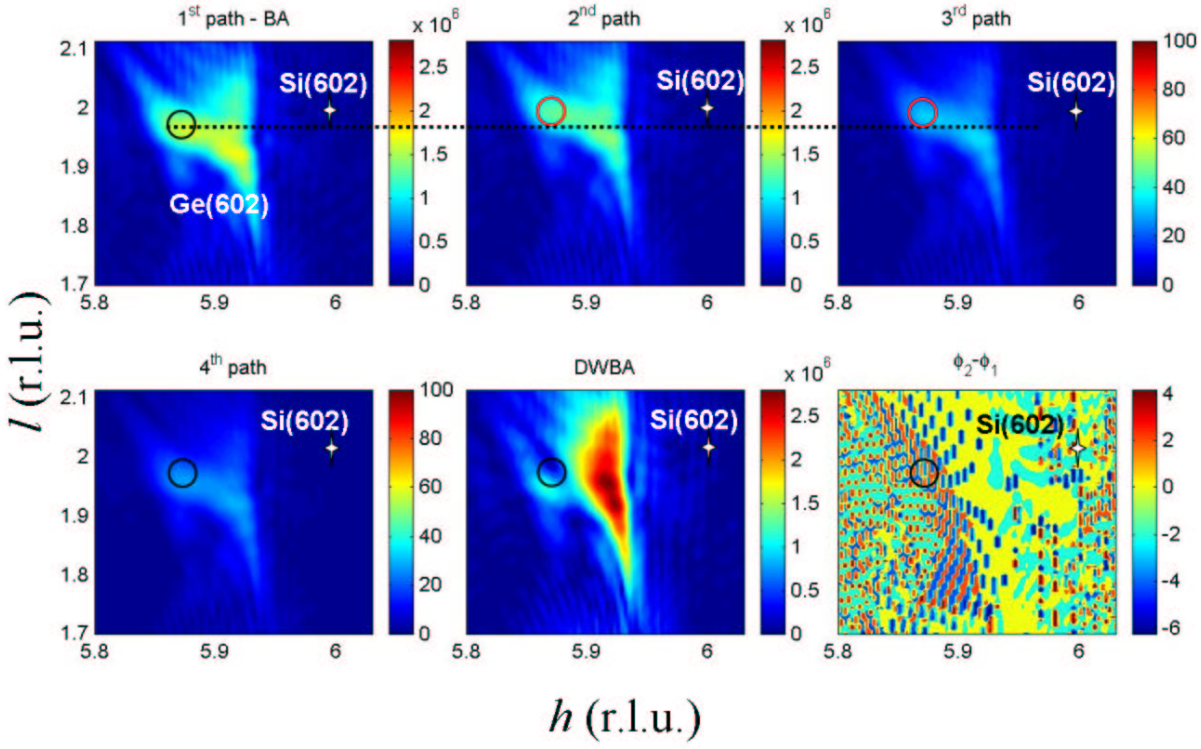

Figure 3.7: Simulated scattering contributions, $|F_{Ge}|$ of the four paths and in the DWBA along the in- and out-of-plane h and l directions, close to the (602) at α_i=0.161° and at 11 keV. Note that the 3^{rd} and 4^{th} paths are negligible compared to the 1^{st} and 2^{nd} paths as α_f is large. The last image shows the difference of phases between the 1^{st} and 2^{nd} paths.

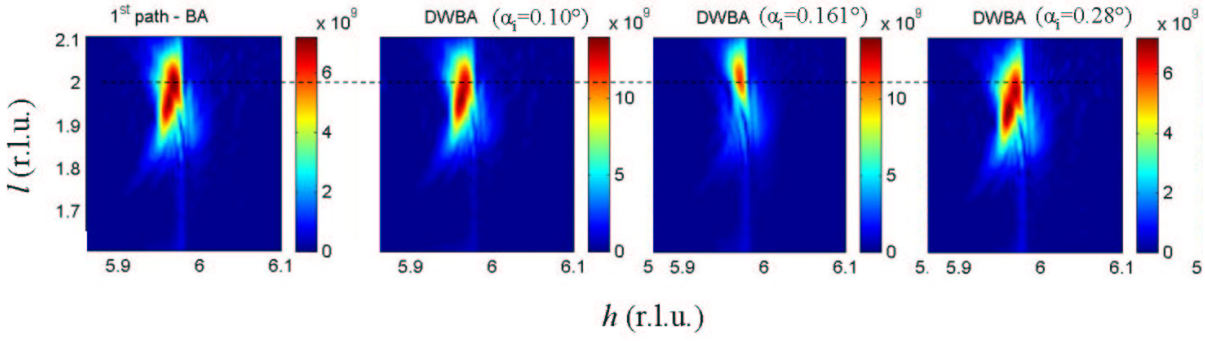

Figure 3.8: Simulated scattering contributions, $|F_{Ge}|$ of the 1^{st} path (BA) and in the DWBA in the case of the subcritical (α_i=0.10°), critical (α_i=0.161°) and supercritical (α_i=0.28°) incident angle regime for a SiGe intermixed dome.

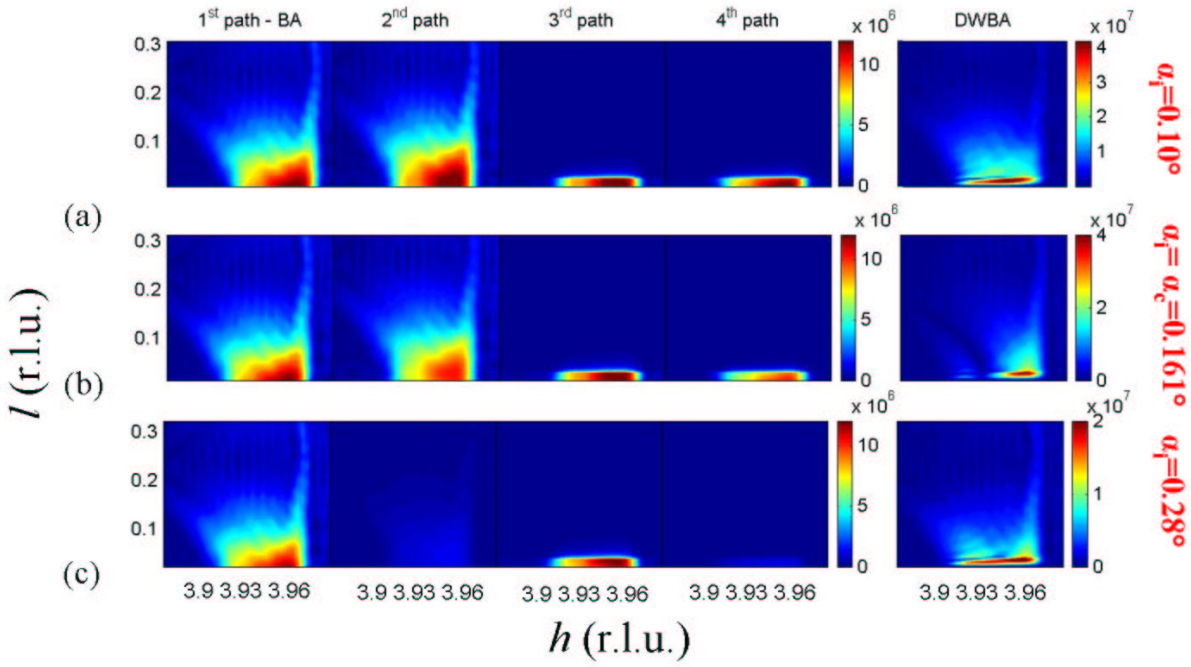

Figure 3.9: Simulated scattering contributions, $|F_{Ge}|$ of the four paths and in the DWBA along the in- and out-of-plane h and l directions, close to the (400) at 11 keV in the case of the subcritical (α_i=0.10°) (a), critical (α_i=0.161°) (b) and supercritical (α_i=0.28°) (c) incident angle regime.

cases where the iso-strain areas are sufficiently large, the total scattered amplitude can be written as:

$$F_z^t(\alpha_i, \alpha_f) = F_z(q_z)t(\alpha_i, z)t(\alpha_f, z), \tag{3.12}$$

where $t(\alpha, z) = 1 + r(\alpha)\mathrm{e}^{-4\pi \mathrm{i}\alpha z/\lambda}$, which is known as the general optical function [13]. In addition, it has been demonstrated [13] that different values of Q_r corresponds to different heights z. Figure 3.11 displays this phenomenon. The decrease of the α_f or l position of the global maximum is related to the general optical function and indicates lower heights for decreasing strain. Hence, the optical function varies along the radial direction.

If the value of α_i is below the critical angle of the substrate α_c, there may be a certain height z and a corresponding radial position Q_r or h where the optical function has its maximum exactly at α_i. Around that Q_r, the intensity will be enhanced and may lead to a local maximum. Such a maximum can be easily mistaken as a prevalent strain state inside the islands [13]. Figure 3.10 (a) clearly shows one maximum at α_i below the critical angle which is displaced compared to the real maxima of the strain state given by the 1^{st} path, which does not take into account the optical effects induced by the reflection on the substrate. At the critical angle and above, the position of the maxima of intensity is near the real position of the maxima of the strain state. The measurement of the strain state inside such 100 nm wide dome requires extreme accuracy in the adjustment of the angle of incidence. This phenomenon is well observed when the iso-strain conditions are fulfilled:

$$r(z)H_{nc}\,|\mathbf{h}|\,d\epsilon_{//}(z)/dz|_{z=z_0} \gg 1, \tag{3.13}$$

where H_{nc} is the height of the nanocrystal and $\epsilon_{//}(z)$ is the out-of-plane strain state. This implies that this phenomenon is observed for high enough islands. As an example, for smaller islands such as 70nm pyramid of 7 nm height, this phenomenon is not observed.

In figure 3.10 (b), the Ge integrated intensity can be superimposed in the BA and in the DWBA. In addition, for large domes, the BA and DWBA signals can be superimposed when the contribution

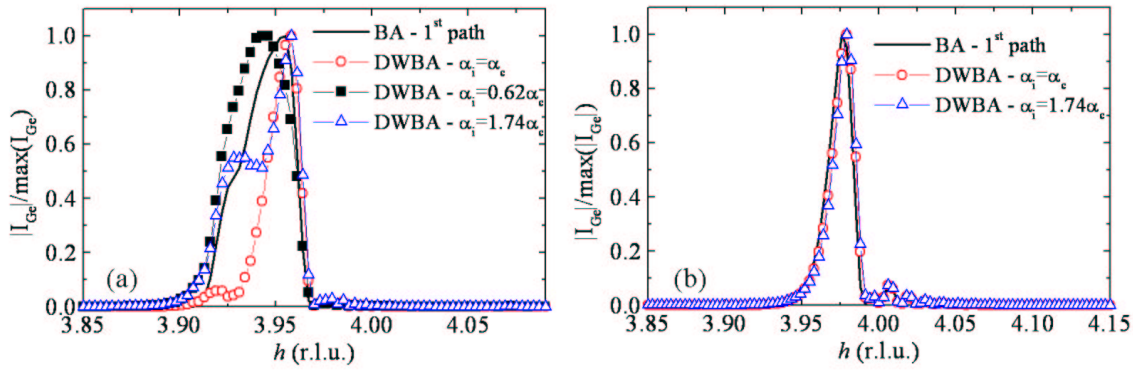

Figure 3.10: Ge scattered intensity integrated between α_f ~0° and α_f ~1.5° for the 1^{st} path (BA) and the DWBA in the case of the subcritical (α_i=0.10°), critical (α_i=0.161°) and supercritical (α_i=0.28°) incident angle regime for a 115 nm wide dome (a) and a 70 nm wide pyramid (b).

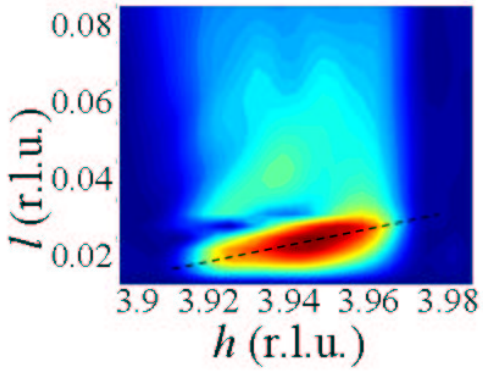

Figure 3.11: Simulated scattering contributions, $|F_{Ge}|$ around the (400) reflection in the DWBA at α_i=0.10°. An increase of the maximum position of $\alpha_{f,max}$, which is related to the maximum intensity observed along l, appears with decreasing strain.

of the 2^{nd}, 3^{rd} and 4^{th} paths are negligible, *i.e.* at high α_i values such as $\alpha_i = 0.5°$ (see Fig. 3.12). But in this case, the background arising from the substrate is enhanced and may overcome the signal diffracted from the islands, which in addition is reduced (see Fig. 3.6).

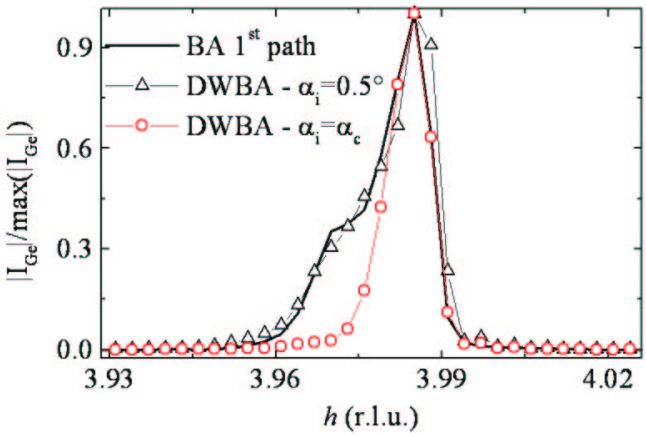

Figure 3.12: Ge scattered intensity integrated between α_f ~0° and α_f ~1.5° for the 1^{st} path (BA) and the DWBA in the case at α_i=α_c and α_i=0.5° for an intermixed SiGe 115 nm wide dome.

3.1.7 Conclusion

In this chapter, the impact of the wetting layer and intermixing on the diffracted signal and relaxation state of the islands have been estimated. The absence or presence of a separation between the Ge and Si scattering signals can help qualitatively determining if there is or not intermixing. Then, the relative importance of the four paths of the Distorted Wave Born Approximation (DWBA) as a function the incident angle for large islands such as domes are shown. For large islands fulfilling the iso-strain conditions, the Born approximation is no more valid in the region of exit angles between zero and twice the critical angle. The observed maxima could be mistaken as prevalent strain state inside the islands. This phenomenon is not observed for small islands, as recently shown by J. Coraux [10]. In addition, varying the incident angle around the critical angle α_c also allows to determine if the signal arises from small or high islands. In case of bimodal growth with pyramids and domes, the corresponding signals can be distinguished.

Bibliography

[1] I. Kegel, T.-H. Metzger, A. Lorke, J. Peisl, J. Stangl, G. Bauer, J. M. Garcia and P. Petroff, Phys. Rev. Lett. **85**, 1694 (2000).

[2] T. Benabbas, P. Francios, Y. Androussi, and A. Lefebvre, J. Appl. Phys. **80**, 2763 (1996).

[3] T. Wiebach, M. Schmidbauer, M. Hanke, H. Raidt, R. Kohler, and H. Wawra, Phys. Rev. B **61**, 5571 (2000).

[4] L. D. Landau, *Theory of Elasticity*, Pergamon Press (1959).

[5] V. Ranjan, G. Allan, C. Priester and C. Delerue, Phys. Rev. B (**68**) 115305 (2003).

[6] A. Malachias, S. Kycia, G. Meideros-Ribeiro, R. Magalhaes-Paniago, T. I. Kamins, R. S. Stanley, Phys. Rev. Lett. **91**, 176101 (2003).

[7] A. Rastelli, PhD thesis, Dipartimento di Fisica 'A. Volta', Universit*à* degli Studi di Pavia (2002).

[8] T. U. Schülli, M. Stoffel, J. Stangl, R. T. Lechner, E. Wintersberger, M. Sztucki, T. H. Metzger, O. G. Schmidt and G. Bauer, Phys. Rev. B. **71**, 035326 (2005).

[9] U. Pietsch, V. Holý, and T. Baumbach, *High-Resolution X-Ray Scattering: From Thin Films to Lateral Nanostructures*, (Springer 2004).

[10] J. Coraux, V. Favre-Nicolin, M. G. Proietti, B. Daudin, and H. Renevier, Phys. Rev. B. **75**, 235312 (2007).

[11] Kegel I., Metzger T.-H., Lorke A., Peisl J., Stangl J., Bauer G., Nordlund K., Schoenfeld W.V. and Petroff P., Phys. Rev. B **63**, 035318 (2001).

[12] M. Schmidbauer, D. Grigoriev, M. Hanke, P. Schafer, T. Wiebach, and R. Kohler, Phys. Rev. B **71**, 115324 (2005).

[13] I. Kegel, *X-ray diffraction from semiconductor quantum dots*, PhD thesis: Universty of M*ünchen*(2000).

Chapter 4

Experimental set-ups

All X-ray measurements presented in this work have been performed using synchrotron radiation at the ESRF. Part of this work has been performed using ID01, which is a very powerful beamline to characterize nanostructures ex situ. It has been complemented by in situ experiments using BM32, in which the same kind of X-ray measurements are performed (although with less intensity) while growing the nanostructures in ultra-high-vacuum by molecular beam epitaxy. In this chapter, the main characteristics of the two setups and how to perform X-ray experiment are described.

4.1 Introduction

Many remarkable properties characterize synchrotron radiation, such as energy tunability, high photon flux, low X-ray beam divergence, coherence and pulsed emission [1].

Brilliance is defined as:

$$brilliance = \frac{Photons/second}{mrad^2 mm^2 (0.1\% bandwith)}. \tag{4.1}$$

A high brilliance is needed to obtain a sufficiently high signal-to-background ratio. The reader can refer to Refs. [1, 2] for an extended discussion of the physics of synchrotron radiation.

4.2 The ID01 beamline

The beamline is dedicated to combine small-and wide-angle X-ray scattering techniques with anomalous scattering [3, 4].

4.2.1 ID01 optics hutch

On the ID01 beamline (see Fig. 4.1), three undulators select an X-ray beam with an energy variable from 2.1 to 70 keV. For the majority of experiments, one or two 42 mm undulator(s) are used. The X-ray energy is selected by changing the gap between the magnets of the insertion device, by choosing one of its harmonics and by selecting the monochromator angle. The double-crystal Si(111) monochromator allows for the fine tuning of the desired energy with an energy resolution $\Delta E/E$ of 10^{-4}. This allows scanning the X-ray energy around the absorption edge with a resolution of $\sim$1 eV. But the 'monochromatic' X-ray beam still contains higher harmonics [3]. Two Si mirrors in the optics hutch located before and after the monochromator, are used to reject these harmonics and maintain the focal spot fixed at the sample position, during the tuning of the energy. In addition, due to the wide energy range accessible at ID01, the mirrors offer coatings of Pt and Rh, that can be selected by a simple translation. The fact that the critical angle for total external reflection changes significantly

with the X-ray energy allows to choose an incident angle on the mirror that is below the critical one for the 1^{st} harmonic, but well above the critical angle for the 3^{rd} harmonic for instance. In order to increase the photon flux at the sample position, the X-ray beam is focused both in horizontal and vertical directions. The horizontal focussing is achieved by sagitally bending the second crystal of the monochromator, while the vertical focussing is obtained by bending the second mirror along the direction of the beam. The expected flux of photons at the sample position is $\sim 10^{13}$ ph.s^{-1} at a storage ring current of 200 mA in a spot of ∼0.1 mm(H)x0.1 mm(V) at 11 keV.

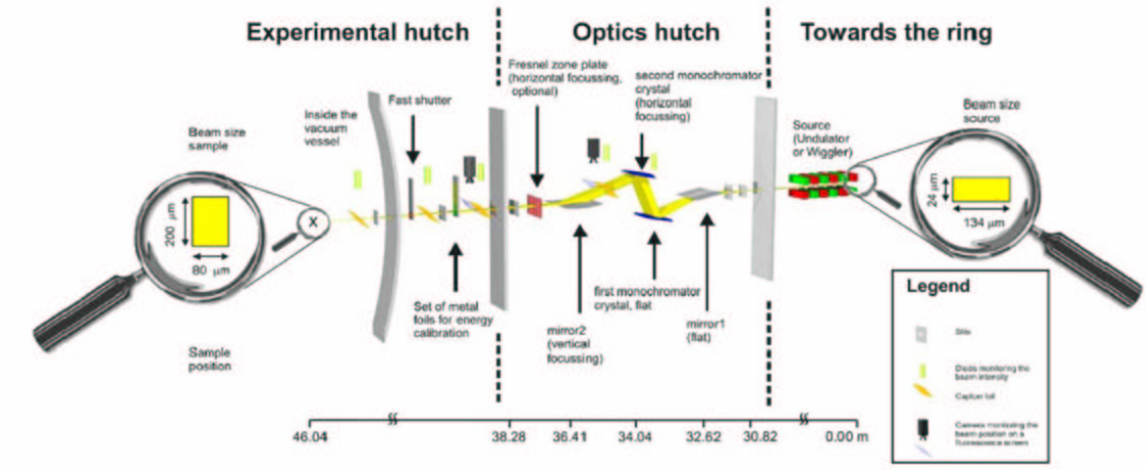

Figure 4.1: Scheme of the optics of the beamline ID01 from the X-ray source to the sample position. The insertion devices from ID01 (a wiggler and an undulator) are located in the storage ring. The main components of the optics hutch are the double-crystal monochromator and the two Si mirrors. Courtesy of B. Krause.

4.2.2 ID01 experimental hutch

The 4+2 circle diffractometer of ID01 (see Fig. 4.2) is located in a huge vacuum vessel with a diameter of 2.8 m. A four circle diffractometer (η, χ, δ and ϕ) is combined with two additional horizontal rotations (ν and μ) [5]. The sample is mounted on a sample holder and fixed on a motorised goniometer head. The head is positioned at the center of rotation of the diffractometer. A kapton cone, flushed with He, covers the sample. It reduces air scattering and protects the sample surface from ozone, which is formed by X-ray induced ionisation of air. The standard energy used for the experiments reported in this work is 11 keV. In order to reduce the air scattering and absorption along the X-ray path, tubes under vacuum are used. The sample surface was usually oriented vertically (*i.e.* χ=90°) (see Fig. 4.3). This configuration presents the advantage that the X-ray beam divergence is smaller than in the horizontal direction allowing for the highest angular resolution parallel to the sample surface. Besides, the polarisation factor of the synchrotron radiation is $P = 1$ in the vertical scattering plane. The size of the X-ray beam at the sample position is defined by slits located as close as possible to the sample with a tuneable aperture of $\sim$ 0.5 mmx0.2 mm, vertically and horizontally, respectively. In the horizontal direction, the aperture is small in order to illuminate only the sample. The intensity of the X-ray beam is monitored between the slit and the sample to enable the normalisation of the scattered intensity, which is useful for the data analysis, and to check the correct alignment of the beamline optics.

The Bragg condition for *i.e.* the *hkl* Si lattice node is fulfilled when the Bragg angle θ_{hkl} and the scattering angle $2\theta_{hkl}$ are set by using ϕ (sample rotation) and δ (detector arm vertical rotation), respectively. In reciprocal space, scans in the radial direction q_r are carried out by maintaining the θ-2θ condition between the detector and sample rotation by moving both δ and ϕ motors. The angular

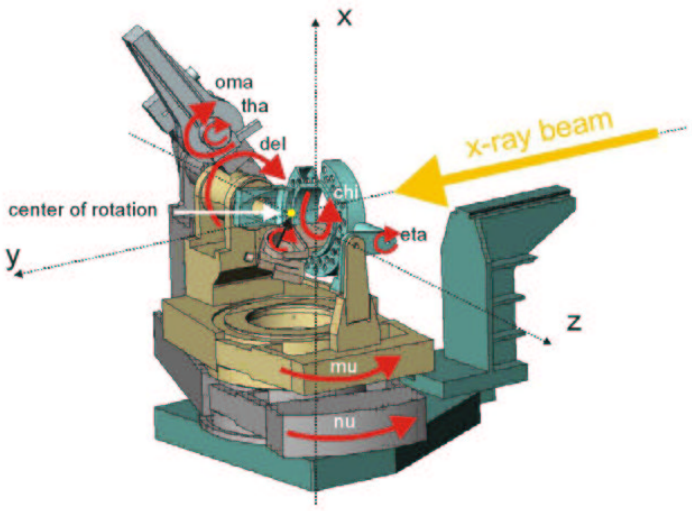

Figure 4.2: The 4+2 diffractometer of the ID01 beamline. The axes of the four circles (η, χ, δ and ϕ) and the two independent horizontal circles (ν and μ) are indicated. The motors *oma* and *tha* are used only when the analyser crystal is mounted. The center of rotation of the diffractometer is indicated by a yellow dot.

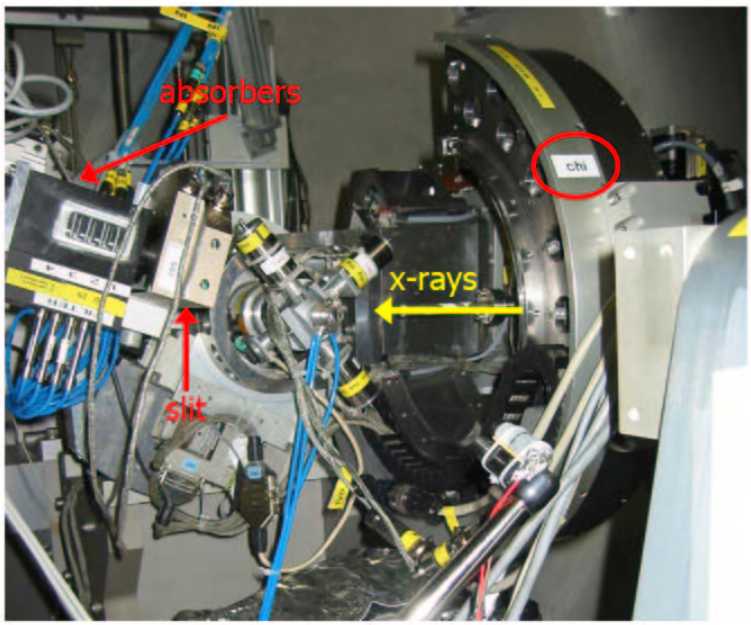

Figure 4.3: Picture of the ID01 diffractometer showing the sample mounted on the sample holder and on the motorised goniometer head in the position corresponding to χ=90°. This scattering set-up is used to perform grazing incidence experiments. The box containing the dynamical absorbers is visible on the left side of the picture together with the slit located after the sample.

(or transversal) scans in the q_a direction are performed by rotating the sample only with the ϕ motor, while keeping the detector position fixed at the $2\theta_{hkl}$ value selected for the hkl Bragg peak. The α_i angle is defined with an accuracy of 0.001° as for all angles.

After the interaction with the sample, the scattered photons are collected by a linear position sensitive detector (PSD), which is mounted perpendicularly to the sample surface at a distance of $\sim$ 1m from the sample. This orientation of the detector is well suited to record α_f-resolved spectra. The Vantec PSD is a Xe gas filled linear detector with a length of 50 mm. It presents a good efficiency in the photon energy range 3 keV to 17 keV. Its measured spacial resolution is about ~ 134 μm. It has a delay-line of 100 ns, which allows a high count-rate per seconds ($\sim 10^6$ cps integrated intensity). Two sets of slits, one just after the sample and the other just before the detector, define a collimation path for the scattered beam and a small footprint of the X-ray beam on the sample surface. This configuration allows for an angular resolution of $\sim 0.1^\circ$, achieved with a vertical opening of the detector slit parallel to the surface of 2 mm.

4.3 The BM32 beamline

The SUV ('Surface Ultra Vide' in French) instrument of the CRG (Collaborating Research Group)-BM32 beamline at the ESRF is dedicated to the study of surfaces and interfaces *insitu* under ultra high vacuum and during growth. The small amount of probed matter and the weak interaction between matter and X-rays imply the use of synchrotron radiation. Two main techniques are combined on this instrument: Grazing Incidence Small Angle X-ray Scattering (GISAXS) and Grazing Incidence X-ray Diffraction (GIXD). The characteristics of the GIXD set-up are explained in the Refs [6, 7, 8]. In this section, the specifities of the GISAXS set-up will be underlined.

Contrary to the ID01 beamline, a bending magnet produces a white spectrum of emitted X-rays. The optics consist of a Si(111) monochromator between two mirrors to select the X-ray energy, to reject the harmonics and to sagitally (by bending the second crystal of the monochromator) and vertically (by bending the second mirror) focus the beam. The beam energy can be selected between 5 and 30 keV with 10^{-4} resolution. The size of the focused beam on the sample is $\sim$0.25 mm(H)x0.18 mm(V) with a divergence of $\sim$1 mrad(H)x0.1 mrad(V) and the flux is $\sim 10^{11}$ photons.s^{-1}.

4.3.1 The ultra high vacuum chamber

The UHV chamber (see Fig. 4.4 and 4.5) presents a complete equipment to prepare surfaces, to perform growth and to characterize surfaces. It is equipped with a 180 l/s turbomelecular pump, a 400 l/s ion pump and a titanium sublimation pump wich can be cooled by liquid N_2. After a bake-out at 160°C, the base pressure is a few 10^{-11} mbar.

The X-ray beam enters and leaves the vacuum chamber through a large Be window. The chamber is equipped with standard surface-science tools. It is possible to perform reflection high-energy electron diffraction (RHEED) measurements. This allows a quick characterization of the state of the surface (roughness, reconstruction) and changes occuring during deposition. RHEED in itself is a useful analytical technique, but in the present set-up it is mainly used to prepare X-ray diffraction experiments. An electron-energy analyser can be used for Auger electron spectroscopy (AES). AES allows to determine the chemical composition of a surface. A mass spectrometer permits to characterize the residual gas composition. The sample is mounted on a molybdenum holder which allows to transfer it in the ultra high vacuum chamber. It is introduced via two successive chambers to reduce pollution during transfert. Different methods of sample heating are possible: the sample can be heated by a direct current up to 700°C or by electron bombardment up to 2000°C. Ion bombardment can be performed to clean surfaces. The chamber can be equipped with six evaporation cells: three Knudsen cells and three electron bombardment cells. The cells have shutters that are remotely controlled. A quartz microbalance allows to calibrate the evaporation fluxes.

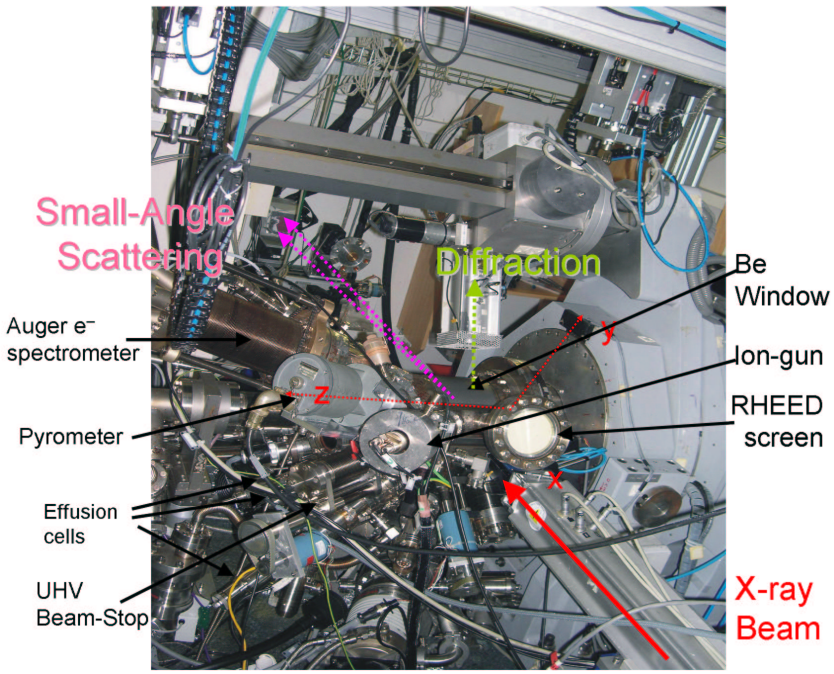

Figure 4.4: Ultra high vacuum chamber connected to the diffractometer.

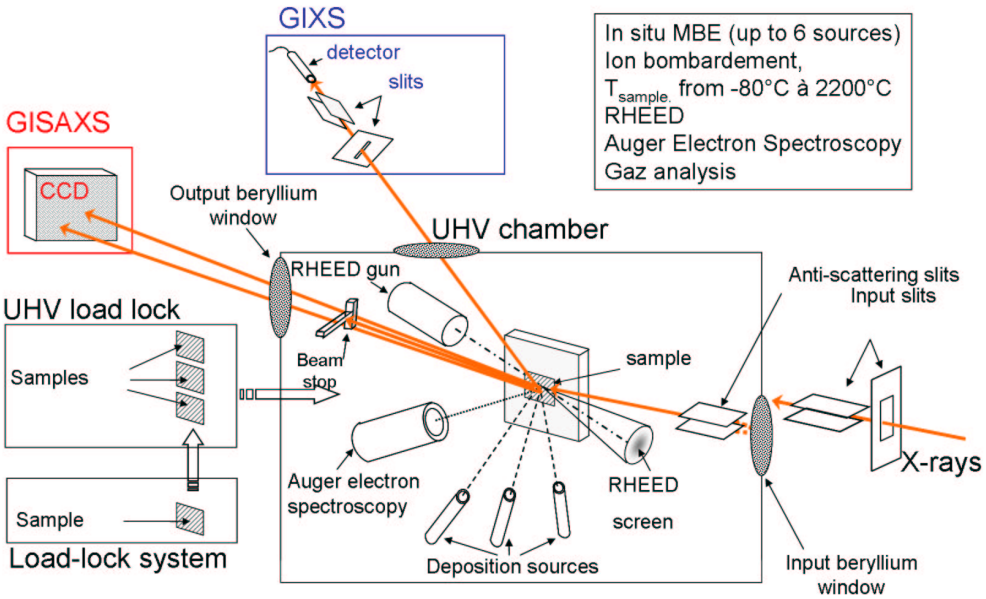

Figure 4.5: Scheme of the experimental set-up on BM32.

4.3.2 The diffractometer

The UHV chamber is mounted on a 'z-axis' 6-circle diffractometer [9, 10, 11, 12]. Synchrotron radiation

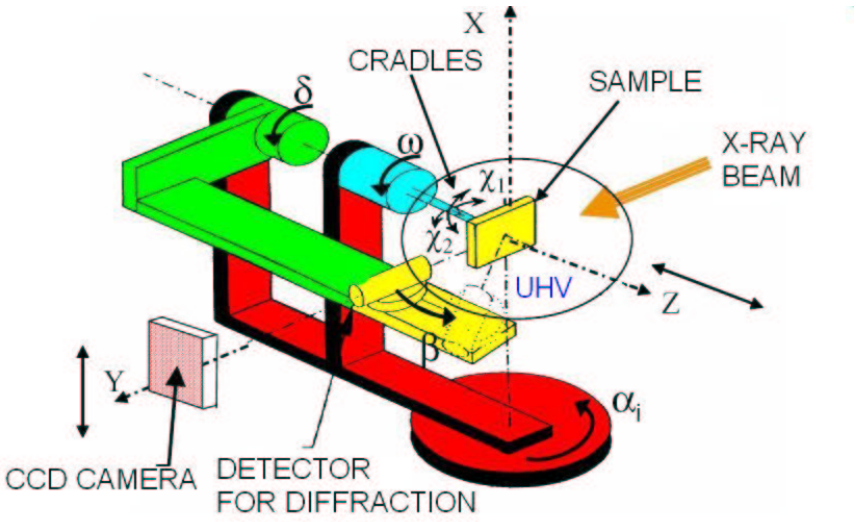

Figure 4.6: SUV-diffractometer.

is highly polarized in the horizontal plane. The sample is positionned vertically in order to avoid near-zero polarization factors for scattering angles around 90°. The incident angle α_i is defined by a rotation of the whole diffractometer and chamber around a vertical axis. The ω rotation of the sample around the horizontal z-axis is made possible by two separate differentially pumped stages which allow a rotation of 360° of the goniometer head while preserving the UHV inside the chamber, and keeping the incident angle α_i fixed. Two cradles (χ_1 and χ_2) allow the alignement of the surface of the sample perpendicularly to the ω axis of the diffractometer. This allows a rotation over a range of $\pm 3°$ with a resolution of 0.001°. A translation along the z-axis allows a sample positioning in the beam with a resolution of 10 μm. When GISAXS measurements are performed, a charged coupled device (CCD) camera is used to record the scattered intensity in the low-Q range. Then, only the α_i and ω angles vary. For surface diffraction at higher angles (GIXD), two angles characterize the detector position: δ is its in-plane angle, and β is its out-of-plane angle.

4.3.3 The GISAXS set-up

The signal scattered at small angles is located near the primary beam. It is necessary to reduce the diffuse background coming from the optical elements of the beamline, from the beryllium windows and from the beam-defining slits. The beam needs to be optimized to reduce as much as possible its divergence. Parasitic scattering from the beryllium window and from air should be eliminated. An anti-scattering slit is thus located in UHV, just after the entrance beryllium window. A beam-stop or knife edge, located in UHV and before the sample allows to reduce the signal coming from the direct beam (see Fig. 4.7). Two beam-stops positionned after the sample in the vacuum chamber and outside block the reflected and refracted beams induced by the surface scattering. All the beam-stops and the anti-scattering slits are made of tungsten or tantalum and motorised to adjust their position with a resolution of ~5 μm. The 2D detector is a CCD camera developped by Princeton Instruments. The acceptance of the camera is 65 mmx65 mm. It is made of 1242x1152 pixels of size 56.5 μmx56.5 μm. Its storage capacity is 3x10^5 electrons/pixel and its background noise 7 electrons/pixel at 100 kHz. The Gd_2O_2 fluorescent screen is optimized in the photon energy range 3 keV to 30 keV. The detector is Peltier cooled down to -60°C to suppress thermal noise. The minimal distance between

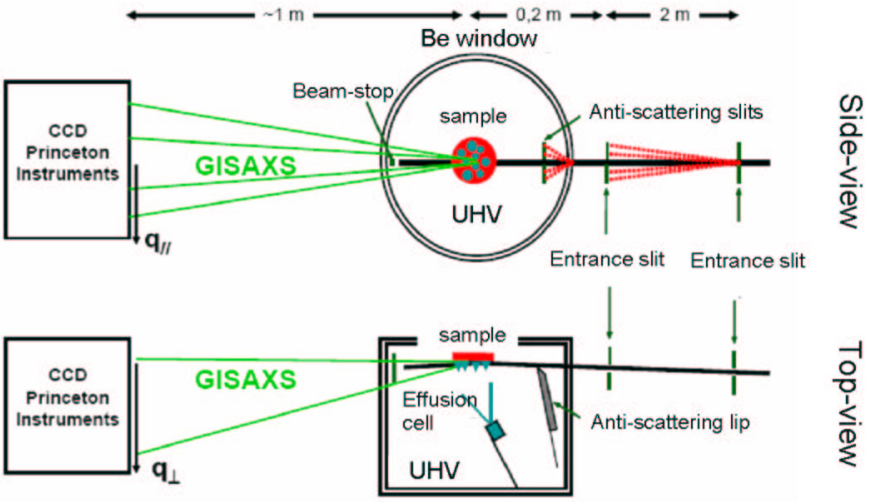

Figure 4.7: Experimental set-up dedicated to GISAXS.

the sample and the CCD is 600 mm and the maxima one is around 2 m. To reduce air scattering, a He filled tube is installed between the vacuum chamber and the detector.

4.4 Complementary between the BM32 and ID01 set-ups

Self-assembled nanostructures are the subject of intense investigations since they present potential applications in future nanoscale devices [13] such as quantum-dot lasers and memories. There is much excitement about new methods of controlling and monitoring the growth of such nanometer-scale particles. The SUV set-up is dedicated to this issue and allows the possibility to follow the average shape and size of nanoparticles during growth and quasi "in real time". A grazing incidence small-angle X-ray experiment can be configured to reveal details of nanoparticle growth *in situ*. Recently, GISAXS [14] was used to analyze the shape and size of growing metallic islands. It has shown to be a powerful tool to analyze the faceting of semiconductor islands and to index their facets [15]. The morphology of islands during their growth has been investigated by several *in situ* methods, such as electron or synchrotron diffraction [16], scanning tunnelling or low-energy electron microscopies [17, 18]. With *in situ* GISAXS, contrary to other *in situ* techniques, not only the average diameter and height of the islands but also the average size of each facet can be directly determined during growth. The strengh of the BM32 beamline is that *in situ* GISAXS is combined with *in situ* grazing incidence diffraction (GIXD), which allows monitoring the island nucleation by the beginning of lattice relaxation and following the evolution of the strain state and composition by use of anomalous-GIXD.

The beamline ID01 presents many advantages. It is easier to change sample. It is well suited to perform anomalous scattering near the Ge K-edge as shown in this work. Its high brilliance and the possibility to use a 1D detector for diffraction allow to probe weak signals (like at the (200) forbidden reflection) and to fasten the collection of X-ray data. Outside the framework of this thesis, the beamline ID01 has demonstrated to be a performant beamline for coherence [19] and micro-diffraction [20].

4.5 Measure of the intensity

4.5.1 Scans and resolution function

Two types of scans are mainly performed in the plane ($\mathbf{Q}_\perp$=0): scans along the $\mathbf{Q}$ direction called radial scans ('θ-2θ') or scans at constant $|\mathbf{Q}|$ called transverse or angular scans ('rocking scans'). Scans along $\mathbf{Q}_\perp$ allow to describe truncation rods. More generally, any kind of scan in the reciprocal space can be performed using the '*hkl*' mode, which requires defining the relationships between the angular space and the reciprocal space. When using GIXD, the knowledge of the resolution function is important. The resolution function depends on:

- the angular divergence of the incident beam,
- the energy resolution, $\frac{\Delta E}{E} = \frac{\Delta k}{k}$,
- the angular acceptance of the detector.

The small integrated volume is always tangential to the Ewald sphere. In this work, we generally studied in-plane Bragg peaks, like (hk0). In this case, only the in-plane projection of the resolution function needs to be taken into account. The resolution function is mainly due to the angular acceptance of the detector. For instance, the in-plane divergence of the incident beam on BM32 is ∼0.13 mrad, while the detector acceptance is ∼ 4mrad. Thus, the resolution function presents an elongated shape tangent to the Ewald sphere at the measured point. The resolution function is approximated by a highly asymmetric parallelepiped, which is tilted by an angle $\delta = 2\theta$ with respect to the momentum-transfer direction. Figure 4.8 shows the resolution function of the detector which is located at the in-plane angle $\delta = 2\theta$. If $\mathbf{Q}_\perp$=0, then the angle between the resolution function and the reciprocal space vector $\mathbf{Q}$ is $\frac{\delta}{2} = \theta = arcsin(\frac{\lambda}{2a}\sqrt{h^2+k^2+l^2})$, where a is the lattice parameter of the studied material.

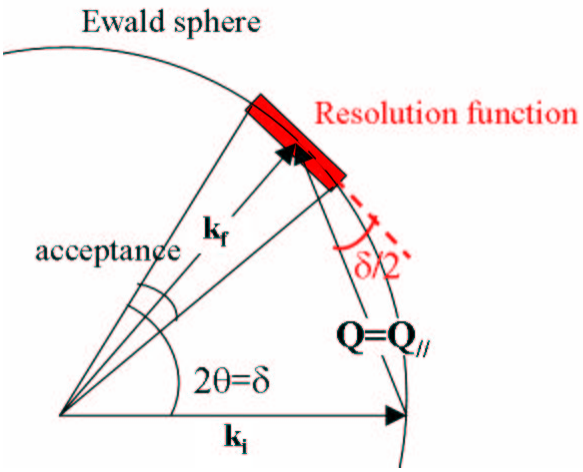

Figure 4.8: Sketch of the in-plane projection of the resolution function. Its main origin is the angular acceptance of the detector.

4.5.2 Correction factors

The collected intensity has to be corrected by general factors:

Polarization factor

The polarization factor, P, is given by $cos^2(\alpha_{pol})$, with α_{pol} the angle between the direction of obervation and the vector p_i indicating the polarization direction. The horizontal polarization can be written [21]

$$P_{hor} = 1 - (sin(\alpha_i)cos(\delta)cos(\beta) + cos(\alpha_i)sin(\beta))^2 \sim 1 - sin^2(\beta) = cos^2(\beta), \tag{4.2}$$

where α, δ and β are the incident angle, the in-plane angle of the detector and the out-of-plane angle of the detector respectively. The vertical polarization is

$$P_{ver} = 1 - sin^2(\delta)cos^2(\beta), \tag{4.3}$$

In the z-axis mode, the vertical polarization component is often neglected because the polarization is almost completely horizontal. For an in-plane reflection, $\beta \sim 0$; thus, $P \sim 1$. In this work, only scans along rods have been corrected by the polarization factor $cos^2(\beta)$.

Area correction

The equation for the integrated intensity contains the active surface area A. This area is usually determined by slits in the incoming beam and in front of the detector (see fig. 4.9). The in-plane illuminated surface area therefore becomes $A{=}A_0C_{area}$, with

$$C_{area} = 1/sin(\delta), \tag{4.4}$$

for a z-axis mode and where $A_0 = s_1s_2$.

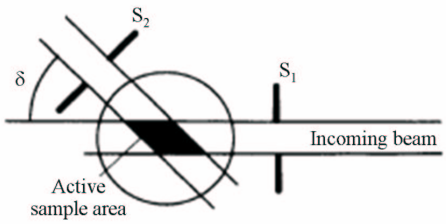

Figure 4.9: View of the surface plane showing the illuminated area defined by slits in the incoming and outgoing beams [21]

If the integrated intensity is needed, it has to be corrected by another factor called Lorentz factor.

Lorentz factor

Indeed, to probe reciprocal space, sample and detector are moving. The different peaks of the reciprocal space intercept the Ewald sphere with a speed which is a function of the relative orientation of the different circles of the diffractometer. This differs from one to another region of reciprocal space [22]. To compare the integrated intensity measured at different regions of reciprocal space, it is necessary to multiply this intensity by a lorentz factor, L.

Bibliography

[1] J. Als-Nielsen, D. McMorrow, *Elements of X-Ray Physics*, J. Winley & Sons, Inc., New-York (2001).

[2] D. Raoux, *Introduction to synchrotron radiation and to physics of storage rings in Neutron and synchrotron radiation for condensed matter studies - theory, instruments and methods-*, Vol. 1, Springer, Berlin (1993).

[3] http://www.esrf.fr/exp_facilities/ID1/user_guide

[4] M. J. Capitan, D. Thiaudiere, L. Goirand, R. Taffut, S. Lequien, Phys. Rev. B **283**, 256 (2000).

[5] H. You, J. Appl. Cryst. **32**, 614 (1999).

[6] R. Baudoing-Savois, G. Renaud, M. De Santis, A. Barbier, O. Robach, P. Taunier, P. Jeantet, O. Ulrich, J. P. Roux, M.-C. Saint-Lager, A. Barski, O. Geaymond, G. Bérard, P. Dolle, M. Noblet, A. Mougin, Nucl. Inst. In Phys. Res. B **149**, 213 (1999).

[7] R. Baudoing-Savois, M. De Santis, M.-C. Saint-Lager, P. Dolle, O. Geaymond, P. Taunier, P. Jeantet, J. P. Roux, G. Renaud, A. Barbier, O. Robach, 0. Ulrich, A. Mougin, G. Bérard, Nucl. Inst. In Phys. Res. B **159**, 120 (1999).

[8] G. Renaud, B. Villette and P. Guénard, Nucl. Inst. In Phys. Res. B **95**, 422 (1995).

[9] J. M. Bloch, J. Appl. Cryst. **18**, 33 (1985).

[10] S. Brenann, P. Eisenberger, Nucl. Inst. Meth. **222**, 164 (1984).

[11] J. W. Chung, K. E. Lutterodt, E. D. Specht, R. J. Birgeneau, P. J. Estruo, A. R. Kortan, Phys. Rev. Lett. **59**, 2192 (1987).

[12] K. Akimoto, J. Mizuki, I. Hirosawa, J. Matsui, Rev. Sci. Instrum. **60**, 2362 (1989).

[13] O.G. Schmidt and K. Eberl, IEEE Trans. Electron Devices **48**, 1175 (2001).

[14] G. Renaud, R. Lazarri, C. Revenant, A. Barbier, M. Noblet, O. Ulrich, F. Leroy, J. Jupille, Y. Borensztein, C. R. Henry, J.-P. Deville, F. Scheurer, J. Mané-Mané, O. Fruchart, Science **300**, 1416 (2003).

[15] T. U. Schülli, M.-I. Richard, G. Renaud, V. Favre-Nicolin, E. Wintersberger and G. Bauer, Appl. Phys. Lett., **89**, 143114 (2006).

[16] M. Takahasi, T. Kaizu, and J. Mizuki, Appl. Phys. Lett. **88**, 101917 (2006).

[17] F. M. Ross, R. M. Tromp, M. C. Reuter, Science **286**, 3 (1999).

[18] O. Kirfel, E. Müller, D. Grützmacher, K. Kern, A. Hesse, J. Stangl, V. Holý, and G. Bauer, Appl. Surf. Sci. **224**, 139 (2004).

[19] S. Ravy, D. Le Bolloc'h, R. Currat, A. Fluerasu, C. Mocuta, and B. Dkhil, Phys. Rev. Lett. **98**, 105501 (2007).

[20] K. Mundboth, Ph.D. Thesis, Linz University (2007)

[21] E. Vlieg, J. Appl. Cryst. **30**, 532-543 (1997).

[22] J. G. McIntyre, R. F. D. Stansfield, Acta Crystallographica A **44**, 257 (1988).

Chapter 5

Defects in implanted Si and in Ge islands.

In this chapter, we describe a novel X-ray method that allows studying defects inside Si implanted substrates and Ge islands. Since these later are planar (along (111) planes), this is done by performing measurements along rods of scattering along $< 111 >$ ***directions, around bulk forbidden reflections.***

5.1 Introduction

Understanding the properties of point defects and dislocations is of great importance in semiconductor technology. For instance, in silicon implantation, the interaction of defects and impurities play a crucial role in the doping of silicon [1, 2]. In device fabrication, an important issue is that the nanostructure interfaces must be kept free of defects in order to obtain the desired electronic properties [3]. For instance, misfit dislocations at interfaces cause increases in the off-leakage current of metal-oxide-semiconductor field effect transistors (MOSFETs) [4]. Defects have to be removed to produce working semiconductor devices.

Defects in silicon have been intensively studied [5, 6, 7]. The most important extended defects observed are stacking faults, "311" defects and perfect dislocation loops [5]. Transmission electron microscopy (TEM) is a technique of choice to determine the structure, nature, and location of these defects [8]. However, TEM experiments remain a destructive analysis and it would be beneficial to have complementary, non destructive means to characterize defects.

Diffuse X-ray scattering is a well-established method for the investigation of defects in crystals [9, 10]. This method is based on the measurement of the distribution of the scattered intensity I in reciprocal space, i.e., as a function of the scattering vector $\mathbf{Q} = \mathbf{K}_f - \mathbf{K}_i$, where $\mathbf{K}_{i,f}$ are the wave-vectors of the primary and scattered radiations. The measured intensity distribution $I(\mathbf{Q})$ is a coherent superposition of two contributions – scattering from the defects core and scattering from the deformed lattice around the defect (displacement-field scattering; see also Ref. [11]). Usually, the displacement-field scattering close to allowed Bragg peaks (the Huang scattering) is used for the defect investigation. However, close to an allowed Bragg peak, the contribution of the defect cores is very weak due to very small number of atoms forming the defect cores and to the high contribution of the Huang scattering, so that the investigation of the structure of the defect core is difficult and only indirect, via the measurement of the displacement field *around* the defect core. Not only diffuse scattering measurements around allowed reflections but also high-resolution TEM (HRTEM) experiments toil in observing the atomic displacement field of the atoms in the core of defects [12].

In this chapter, we demonstrate that grazing incidence diffuse X-ray scattering (GI-DXS) is well suited to investigate defects in implanted Si and in Ge islands. And, we present a novel X-ray method

how to study the defect cores *directly* in concentrating on measurements along rods of scattering by defects, around bulk forbidden reflections.

5.2 Defects in implanted Si

5.2.1 Sample preparation

We have used this approach for the investigation of the core structure of stacking faults generated in Cz p-type Si(001) by Xe-implantation and subsequent annealing. Xe^+ ions were implanted to a dose of 2×10^{14} cm^{-2} at 130 keV, which results in an amorphous layer of about 100 nm thickness and the creation of end-of-range (EOR) excess interstitials beyond the amorphous-to-crystalline interface (Figure 5.1). Implants and annealing processes were performed by AMD, Dresden. The abruptness of the amorphous to crystalline (a/c) interface is determined by the implanted atomic species. Subsequently, As^+ ions were implanted at 3 keV to a dose of 2×10^{15} cm^{-2} in order to generate an ultra-shallow dopant profile. The sample was subsequently spike annealed at 1173 K, close to the processing conditions for industrial devices. The annealing treatments was performed in an atmosphere of 5% O_2 and 95% N_2 to reduce dopant loss. The annealing induces the recrystallization of the amorphous Si. The process begins at the a/c interface and continues until recrystallization of all the Si. Generally a thin layer of amorphous material (2-3 nm) remains, mainly composed of native SiO_2. This kind of recrystallisation is called solid phase epitaxial regrowth (SPER). The crystalline quality of the SPER region is very high: nevertheless, several small defects may be present. Electrically active dopant atoms located at substitutional positions (As_s) are the most common defect in this region. Clusters of electrically inactive dopants (As_{cl}) may be present, together with several defects that cooperate in the diffusion of the dopant atoms. In the case of As implantation, dopants and vacancies V form As_nV_m aggregates. The most stable clusters are As_2V, As_3V and As_4V [13]. A vast majority of defects called end-of-range (EOR) defects are concentrated below the original amorphous-to-crystal interface. They are all of extrinsic nature, *i.e.* formed by a supersaturation of excess Si interstitials [14]. For high temperatures and/or longer annealing times, the 'excess interstitial' population condenses into extended defects, such as {113} defects, faulted (FDLs) and perfect (PDLs) dislocation loops [14]. Faulted dislocation loops are formed by circular extra (111) planes of Si interstitials with two inserted stacking faults bonded by a partial dislocation loop of Burgers vector $\mathbf{b} = a/3 < 111 >$. Perfect dislocation loops (PDL) have (111)-habit planes as well, and are elongated along the $< 110 >$ directions, perpendicular to their Burgers vector $\mathbf{b} = a/2 < 110 >$, with no associated stacking faults.

In order to isolate the defect induced diffuse scattering, a comparison of implanted and non-implanted areas on the same wafer is mandatory for meaningful GI-DXS experiments. To this end the wafers were patterned with photo-resist in stripes of 10 mm before the PAI treatment and stripped prior to the annealing. The samples of 10 mmx20 mm were cleaved from the wafers and consisted of an implanted and a virgin half (Figure 5.2). During the measurement the sample was translated in the X-ray beam from one side to the other, keeping all other settings unchanged. In this way the background intensity from the virgin wafer (mainly thermal diffuse scattering (TDS)) can be subtracted from the total intensity of the implanted part.

5.2.2 Signature of defects at an allowed reflection

DXS (diffuse X-ray scattering) measurements were carried out at the ESRF beamline ID01 with a 8 keV X-ray beam in the grazing incidence geometry (Figure 5.3). An incident angle α_i of 0.35°, slightly larger than the critical angle for Si (*i.e.* 0.13° above the critical angle of total external reflection, $\frac{\alpha_i}{\alpha_c} \sim 1.6$) was used, resulting in a scattering depth of $\lambda \sim$400 nm. Thereby, the X-rays reach the layer of EOR defects left by the pre-amorphisation.

A (q_r, q_a) in-plane reciprocal space map was performed around the (400)Si Bragg peak (Fig. 5.4). The intensity along q_z (*i.e.* the [001] direction) was integrated using a linear position sensitive detector (PSD) perpendicular to the sample surface (see figure 5.3).

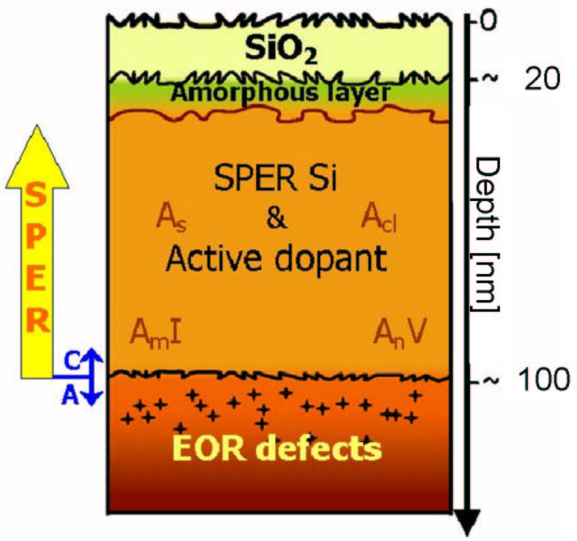

Figure 5.1: Scheme of the structure of the Si substrate after implantation of the ion species A and annealing (see text for details). Courtesy of L. Capello [15].

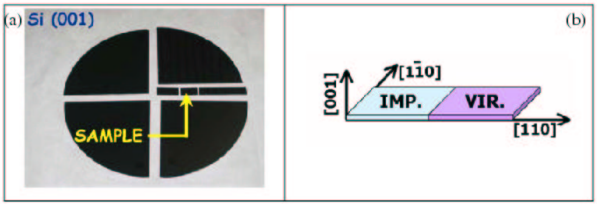

Figure 5.2: (a) Photograph of a Si wafer showing the cleavage of a sample for X-ray scattering experiments. (b) Scheme of the (001) Si 'double-structure' sample with an implanted and a 'virgin' non-implanted area. Courtesy of L. Capello [15].

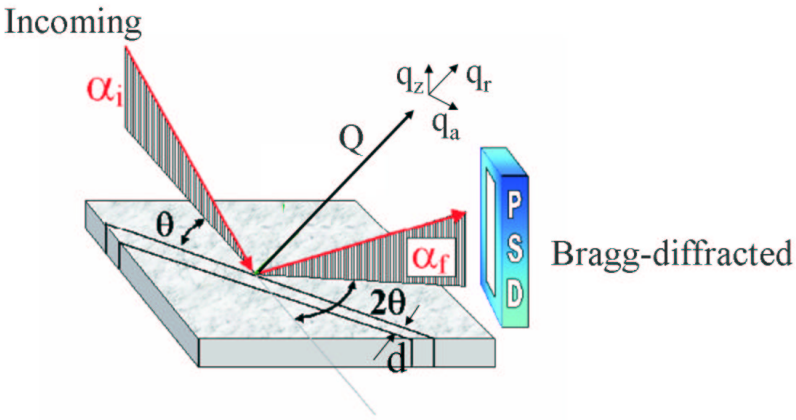

Figure 5.3: Geometry used to measure the diffuse X-ray scattering at grazing incidence α_i and exit α_f angles. The PSD is used for efficient reciprocal space mapping in the $q_{//} - q_z$ plane.

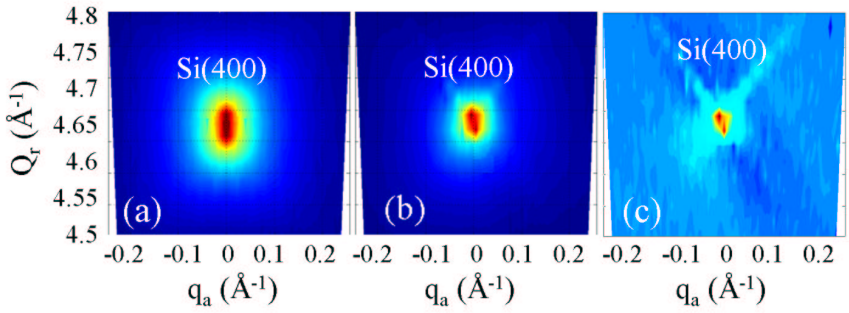

Figure 5.4: $In-plane$ 400 maps of the virgin sample (a) and implanted sample (b). Figure (c) is a (400) map which has been obtained by the substraction of the (400) map of the implanted sample with the (400) map of the virgin sample.

The intensity recorded from the non-implanted area of the sample was subtracted from the total intensity of the implanted area. Thereby, the thermal diffuse scattering (TDS) background was eliminated, resulting in the purely defect-induced DXS. Only this defect-induced diffuse scattering will further be analyzed in the following. The hump-like intensity (Fig. 5.5) follows the $< 111 >$ directions and the projected $< 110 >$ directions in the plane. An angle of 35° can be measured between the [110] and [111] directions. According to previous studies and theoretical predictions, the intensity concentrated in streaks along $< 111 >$ is the characteristic footprint of the presence of FDLs [14, 20]. FDLs are stacking faults (SFs) on {111} planes consisting of a double layer of Si interstitials, bounded by Frank loops with Burgers vectors $\mathbf{b}=a/3< 111 >$. The long-range displacement field caused by the FDLs in the Si matrix points predominantly in $< 111 >$ directions and thus gives rise to a streak-like DXS intensity along the $< 111 >$ directions [17, 20]. PDLs do not result in streaked GI-DXS [18].

The streak width was found to be almost constant along [111] and the integrated intensity along the streaks decays as q^{-2} (see figure 5.5).

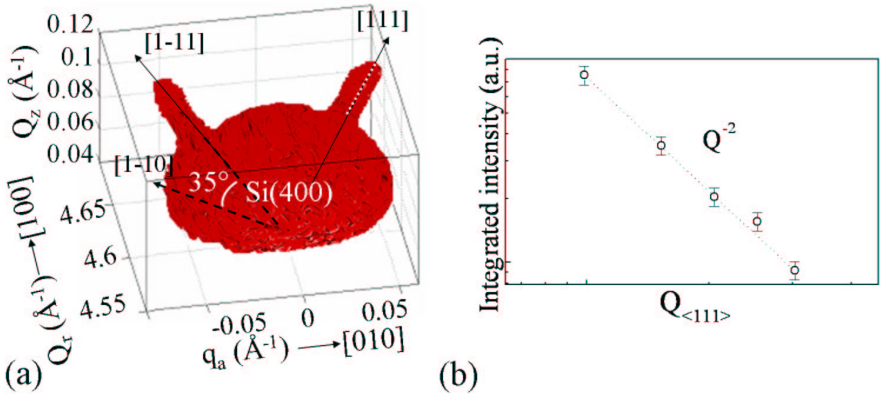

Figure 5.5: (a) 3D reciprocal space map of diffuse scattering measured at $\mathbf{h}$=[400]. $< 111 >$ streaks indicate the presence of stacking faults inside the Si implanted substrate. The angle between the $< 111 >$ streaks and the $< 110 >$ directions is ∼35°. (b) The streak intensity denoted by the white dashed line in figure (a) decays as q^{-2}.

This symmetric part of the diffuse scattering intensity is the so-called Huang diffuse scattering (HDS) [17]. For point defects, a q^{-2} decay and a linear dependence from the defect concentration are expected for the HDS intensity, as observed. This gradual decay changes to a q^{-4} behaviour,

when the point defects form clusters. Fig. 5.4 also clearly shows that the intensity streak is more pronounced on the positive q_r side, [111]. For a momentum transfer along q_r, the measurement is strain sensitive allowing for the determination of the defects, that can either expand or contract the lattice [17]. The scattering from expanding, interstitial-type defects results from a local lattice compression and exhibits a higher diffuse intensity for positive q_r, while the opposite happens for contracting, vacancy-type defects. Thus, the asymmetric intensity distribution of the streaks with higher intensity for poitive q_r proves the extrinsic nature of these SFs. The mean diameter of the SFs was determined using the q-space width of the streaks perpendicular to the [111] direction. From the fit, the mean radius of the faults follows $R_0 = (35 \pm 5)$ nm.

To conclude, DXS is a non-destructive method to investigate the long-range displacement field induced by extrinsic extended defects. Much of what is known about self-interstitial atoms in metals or semiconductors and the interactions of these defects has been gained through measurements of the Huang DXS, which refers to the scattering close to Bragg peaks [19]. We will deal now with what can be learned in looking at forbidden reflections.

5.2.3 Signature of defects at a basis-forbidden reflection

A. Analytical model

Restricting to the kinematical approximation and assuming only one type of atoms present in the crystal (*i.e.* only Si atoms), the amplitude of the wave scattered by a distorted crystal is

$$E(\mathbf{Q}) = \sqrt{N}[E_1(\mathbf{Q}) + E_2(\mathbf{Q})] \tag{5.1}$$

$$= \sum_n \sum_s f(\mathbf{Q}) \mathrm{e}^{-\mathrm{i}\mathbf{Q}.(\mathbf{R}_n + \mathbf{r}_s)} \mathrm{e}^{-\mathrm{i}\mathbf{Q}.\mathbf{u}(\mathbf{R}_n + \mathbf{r}_s)} + \sum_c f(\mathbf{Q}) \mathrm{e}^{-\mathrm{i}\mathbf{Q}.\mathbf{R}_c} \tag{5.2}$$

where E_1 is the amplitude of the scattering from the displacement field aroung a single defect, called displacement-field scattering or Huang scattering if the scattering is close to an allowed Bragg peak and E_2 is the amplitude of the scattering from the defects core. N denotes the total number of irradiated defects. The sum $\sum_n$ runs over the elementary unit cells (with non-disturbed positions $\mathbf{R}_n$), $\sum_s$ describes the sums over the atoms within one unit cell, having the non-disturbed positions $\mathbf{r}_s$. Due to the defects, the atoms are displaced from their ideal positions by $\mathbf{u}(\mathbf{R}_n + \mathbf{r}_s)$, $f(\mathbf{Q})$ is the atomic scattering factor (assumed not to be affected by the disturbance). The second term in Eq. (7.5) expresses the contribution of extra atoms (atoms of the defect cores) at the positions $\mathbf{R}_c$.

If the irradiated sample volume V contains a large number of defects, the measured intensity is averaged over the statistical ensemble of all defect configurations

$$I(\mathbf{Q}) = N(\langle |E_1(\mathbf{Q})|^2 \rangle + \langle |E_2(\mathbf{Q})|^2 \rangle + 2Re[\langle E_1(\mathbf{Q}) E_2^*(\mathbf{Q}) \rangle]). \tag{5.3}$$

The crystal with defects is assumed to be statistically homogeneous, *i.e.* the correlation function of the random displacement field $C(\mathbf{r}, \mathbf{r}') = \langle \mathrm{e}^{-\mathrm{i}\mathbf{Q}.[\mathbf{u}(\mathbf{r}) - \mathbf{u}(\mathbf{r}')]} \rangle$ depends only on $\mathbf{r} - \mathbf{r}'$. This assumption requires that (i) the characteristic parameters of the defects (size, density, etc.) are constant in the sample volume V, and (ii) the volume V is larger than the mean distance between the defects. Expressing the sum $\sum_n$ over the lattice points by the sum $\sum_{\mathbf{g}}$ over the reciprocal lattice points (RELPs) $\mathbf{g}$, the intensity of the displacement field around a single defect can be written

$$I_{11}(\mathbf{Q}) = \langle |E_1(\mathbf{Q})|^2 \rangle \tag{5.4}$$

$$= \frac{|f(\mathbf{Q})|^2}{V_{\mathrm{cell}}^2} \sum_{\mathbf{g}} \sum_{\mathbf{g}'} F_0(\mathbf{g}) F_0^*(\mathbf{g}') C^{FT}(\mathbf{Q} - \mathbf{g}, \mathbf{Q}) \mathbf{C}^{\mathbf{FT}*}(\mathbf{Q} - \mathbf{g}', \mathbf{Q}) \tag{5.5}$$

where $F_0(\mathbf{g}) = \sum_s \mathrm{e}^{-\mathrm{i}\mathbf{g}.\mathbf{r}_s}$ is the structure factor of a *non-deformed* unit cell, $V_{\mathrm{cell}} = a^3$ is the volume of the unit cell, and

$$C^{FT}(\mathbf{Q} - \mathbf{g}, \mathbf{Q}) = \int \mathrm{d}^3\mathbf{r} \mathrm{e}^{-\mathrm{i}(\mathbf{Q} - \mathbf{g}).\mathbf{r}} \left[\mathrm{e}^{-\mathrm{i}\mathbf{Q}.\mathbf{v}(\mathbf{r})} - 1 \right], \tag{5.6}$$

$\mathbf{v}(\mathbf{r})$ is the displacement field around a *single* defect.

Similarly, for the mixed term,

$$I_{12}(\mathbf{Q}) = \langle E_1(\mathbf{Q})E_2^*(\mathbf{Q})\rangle \tag{5.7}$$

$$= \frac{|f(\mathbf{Q})|^2}{V_{\text{cell}}^2}\sum_{\mathbf{g}} F_0(\mathbf{g})\int \mathrm{d}^3\mathbf{r}\mathrm{e}^{-\mathrm{i}(\mathbf{Q}-\mathbf{g}).\mathbf{r}}\langle \mathrm{e}^{-\mathrm{i}\mathbf{Q}.\mathbf{u}(\mathbf{r})}\sum_{\mathbf{c}}\mathrm{e}^{-\mathrm{i}\mathbf{Q}.\mathbf{R_c}}\rangle. \tag{5.8}$$

According to Eq. (7.6, 5.8), the intensity of the displacement-field scattering in a given point $\mathbf{Q}$ in reciprocal space is a coherent superposition of contributions centered in various RELPs $\mathbf{g}$. If we can neglect the overlapping of the contributions from different $\mathbf{g}$'s, in the sum $\sum_{\mathbf{g}}$ only the term with minimum deviation $\mathbf{Q}-\mathbf{g}$ is not negligible (say, the term $\mathbf{g}=\mathbf{h}$, $\mathbf{h}$ the diffraction vector of the considered Bragg reflection). If, in addition, the diffraction $\mathbf{h}$ is forbidden (i.e., $F_0(\mathbf{h})=0$; $\mathbf{h}$=(200) in Si, for instance), the displacement-field scattering intensities I_{11} and I_{12} can be neglected and the diffuse scattering stems only from the defect cores. Even if this overlapping cannot be neglected, the Huang contribution to the diffusely scattered intensity close to a forbidden RELP $\mathbf{h}$ is suppressed and the intensity is mainly influenced by the core term, i.e., by the atomic positions in the defect cores: $I_{22}(\mathbf{Q}) = \langle|E_2(\mathbf{Q})|^2\rangle$. A stacking fault consists of two parallel {111} discs of radius R_0, separated by the distance Δ. If $\Delta << R_0$, the core intensity of small extrinsic stacking faults randomly distributed in a Si crystal is proportional to the number N of irradiated defects and it can be written as [9, 11]

$$I_{22}(\mathbf{Q}) = N|\mathrm{e}^{-\mathrm{i}Q_\perp\Delta}-1|^2|\Omega^{FT}(\mathbf{q})|^2, \tag{5.9}$$

where $Q_\perp$ is the component of $\mathbf{Q}$ perpendicular to the disc plane, $\Omega^{FT}(\mathbf{q})$ is the Fourier transformation of the shape function of the defect core, here a disk with radius R_0

$$\Omega^{FT}(\mathbf{q}) \propto \pi R_0^2\frac{2J_1(q_{//}R_0)}{q_{//}R_0}\cdot\frac{\sin(q_\perp b)}{q_\perp b}, \tag{5.10}$$

$q = Q - h$ is the position vector in reciprocal space relatively to the reciprocal lattice vector $\mathbf{h}$. The faults lie in {111} planes having the Burgers vector $\mathbf{b} = 1/3 < 111 >$ perpendicular to the disc planes [20].

Previous works on diffuse X-ray scattering from defects were restricted to the close vicinity of a RELP, i.e. to $|\mathbf{Q}-\mathbf{h}| \ll |\mathbf{h}|$. For instance, for the allowed reflection $\mathbf{h}$=(400), the main part of the scattering intensity is the Huang term I_{11} depending on the displacement field $\mathbf{v}(\mathbf{r})$ around the defects. In this case, only the asymptotic deformation field of a defect, $\lim_{|\mathbf{r}|\to\infty}\mathbf{v}(\mathbf{r})$ plays a role. The asymptotic field can be derived by means of the elastic Green-function approach [17] and it can be expressed by means of a double-force tensor of the defect. The asymmetry of the intensity distribution is caused by the mixed term I_{12} and, in the case of extrinsic loops, the intensity is larger for $q_r > 0$. As the scattered intensity is far away from a RELP, the asymptotic expression of the deformation field of a defect is not sufficient, since the displacement field $\mathbf{v}(\mathbf{r})$ in the vicinity of the defect becomes important. A more exact Burgers formula [20], describing the displacement field of a faulted loop also in its close neighborhood, needs to be used. It has been demonstrated in Ref. [21] that the intensity of diffuse X-ray scattering calculated by this formula compares well with the result of atomistic simulations.

In order to demonstrate the sensitivity of the scattered intensity to the defect core structure, we have simulated the intensity scattered from a Si crystal containing randomly distributed small circular stacking faults; the faults lie in {111} planes having the Burgers vector $\mathbf{b} = 1/3\langle 111\rangle$ perpendicular to the planes (the Frank loops [20]). For the sake of simplicity, we have assumed that all loops have the same radius R_0. The core of a Frank loop consists of two extra {111} planes (denoted A and a in [20]), having the nominal distance $\Delta_0 = a\sqrt{3}/4$. The atoms in these planes are arranged in a hexagonal array, the distance of nearest atoms in the plane is $a\sqrt{2}/2$. From symmetry considerations it follows that the reciprocal-space distribution of the scattered intensity $I(\mathbf{Q})$ is concentrated along $\langle 111\rangle$ lines perpendicular to the loop planes.

Figure 7.28 represents the distribution of the scattered intensity of the defect cores $|E_2|^2$ calculated along the [111] direction perpendicular to the fault plane around the forbidden RELP $\mathbf{h} = (200)$, at which $\mathbf{q} \equiv \mathbf{Q} - \mathbf{h} = 0$. If the distance Δ of the two $\{111\}$ discs creating the defect core equals Δ_0, the core intensity is proportional to $1 - \cos(q_\perp \Delta_0)$. In this case, the scattered intensity is a symmetric function along $q_\perp$ and is exactly zero for $\mathbf{q} = 0$. If however, the distance Δ differs from its ideal value Δ_0 by $d\Delta$, the scattered intensity is proportional to $1 - \cos(q_\perp \Delta_0 + q_\perp d\Delta)$. The intensity along $q_\perp$ is asymmetric and its minimum is not at $\mathbf{q} = 0$.

From the figure 7.28 it follows that the intensity $I(\mathbf{Q})$ around the forbidden RELP $\mathbf{h} = [200]$ very sensitively depends on small changes in the inter-planar distance Δ, while the intensity close to an allowed RELP (311 or 111, for instance) is almost Δ independent. Figure 7.28 illustrates the origin of this behavior. Around an allowed RELP the term $E_1(\mathbf{Q})$ is dominant and the core term $E_2(\mathbf{Q})$ can be neglected. Around a forbidden RELP $\mathbf{h}$, only more distant allowed RELPs $\mathbf{g} \neq \mathbf{h}$ contribute to $E_1(\mathbf{Q})$ and the resulting term $E_1(\mathbf{Q})$ is comparable or even smaller than the core term $E_2(\mathbf{Q})$. A small change in Δ only slightly affects the intensity $|E_2|^2$ of the core term but it changes substantially its phase and also the total intensity around the forbidden RELP, being proportional to $|E_1(\mathbf{Q}) + E_2(\mathbf{Q})|^2$.

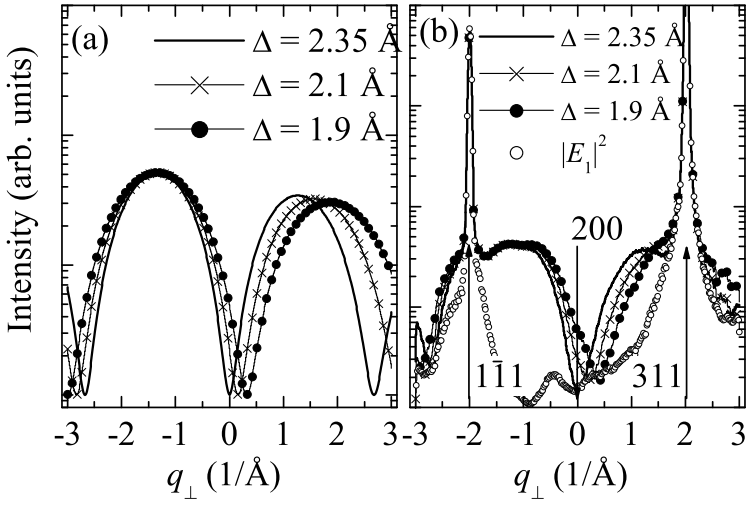

Figure 5.6: The distribution of diffusely scattered intensity from circular stacking faults calculated along the [111] line perpendicular to the loop plane. The loop radius is $R_0 = 30$ nm, the point $q_\perp = 0$ corresponds to the forbidden RELP 200. In figure (a), the contributions of the defect cores are plotted for various distances Δ of the defect (111) planes; figure (b) shows the total intensities as well as the Huang contribution $|E_1|^2$ that does not depend on Δ (points).

B. Experimental results and analysis.

This approach was used for the investigation of the core structure of small stacking faults generated in Si(001) by As-implantation and subsequent annealing.

The scattered radiation was collected by a linear detector perpendicular to the sample surface. A three-dimensional intensity distribution $I(\mathbf{Q})$ around the 200 reciprocal lattice point was recorded. Figure 7.29 shows the in-plane and the three-dimensional distribution of the scattered intensity respectively. The diffuse scattering was concentrated in intensity streaks along $\{111\}$ directions visible in Fig. 7.29. Because of the grazing-incidence geometry used, only half of reciprocal space above the sample horizon ($Q_z > 0$) can be covered. The full width at half maximum (FWHM) $\delta q_\parallel$ of the streak cross-section is $\delta q_\parallel \approx 2\pi/(2R_0)$ and the shape of the cross-section can be approximated by a modified Lorentz function [22].

$$I(q_\parallel) = \text{const} \left[1 + (2q_\parallel/\delta q_\parallel)^2 (2^{2/3} - 1)\right]^{-3/2}. \tag{5.11}$$

$q_\parallel$ is the length of the component of $\mathbf{q}$ parallel to the loop plane. The cross-section of the measured streak along with its fit by Eq. (7.7) are plotted in Fig. 7.30 ; from the fit the mean radius $R_0 = (30 \pm 2)$ nm of the faults follows.

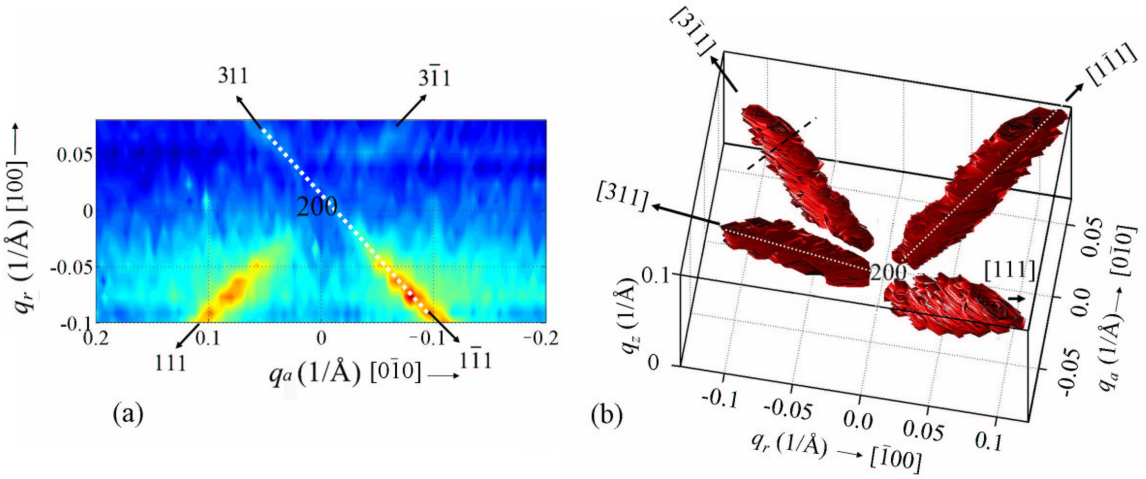

Figure 5.7: (a) Reciprocal space map of diffuse scattering integrating over the linear detector and measured around the forbidden grazing-incidence diffraction $\mathbf{h} = [200]$. The line denotes the trajectory, along which the line scan in Fig. 7.31 was extracted. Figure (b) shows the three dimensional reciprocal-space distribution around $\mathbf{h} = [200]$. The scattered intensity is concentrated in streaks along $\langle 111 \rangle$ perpendicular to the fault planes.

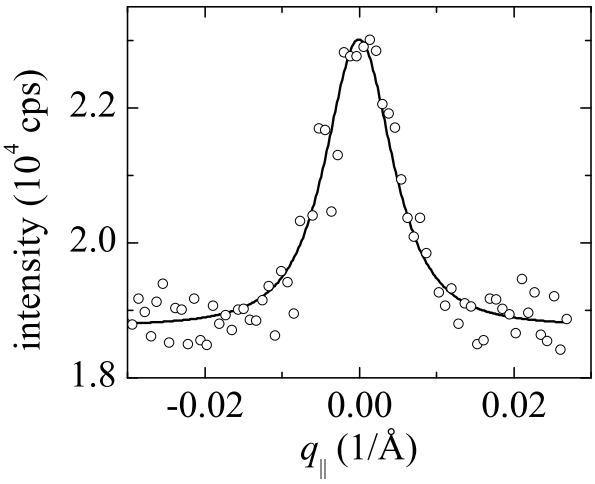

Figure 5.8: Cross-section of the measured intensity streak (points) along the black dashed line (see Fig. 7.28) and its fit by Eq. (7.7) (line).

The intensity distribution along the streaks $I(q_\perp)$ is plotted in Fig. 7.31. The intensity has been corrected by the polarization factor and beam footprint [23] (see previous chapter). The resolution element has been taken into account. Depending on the path in reciprocal space, the resolution element (Fig. 5.10) cuts the streaks in a different way and thus integrates the streak intensity differently. The orientation of the resolution function with respect to Q projected in the plane is simply given by the

Bragg angle of the reflection ($\theta = \frac{2\theta}{2}$). The streaks will be correctly integrated when the resolution function of the detector will be perpendicular to the streaks. As observed in Fig. 5.10, this is not the case along the streak passing through the (200) and going towards the $(3\bar{1}1)$ Bragg peak. That's why the intensity was collected along the streaks passing through the $(1\bar{1}1)$ and (311) Bragg peaks.

In Fig. 7.31, $q_\perp$ is the coordinate of $\mathbf{q}$ along the trajectory depicted in Fig. 7.29 (see white dashed lines); $q_\perp = 0$ corresponds to the forbidden RELP $\mathbf{h} = [200]$. We have fitted this distribution to the theory described above; in the fit we relied on only one free parameter Δ; from the fit, $\Delta = (2.1 \pm 0.2)$ Å follows. Calculating the scattered intensity, we took into account the defect-free surface layer mentioned above and which starts at $z_0 \approx$100 nm, and the dependence of the irradiated sample depth L on the incidence and exit angles, α_i and α_f respectively. The calculated scattered intensity is thus multiplied by the factor $P(\alpha_i, \alpha_f)$ which can be written as

$$P(\alpha_i, \alpha_f) = \int_{-\infty}^{-z_0} \mathrm{e}^{-\frac{|z|}{L(\alpha_i+\alpha_f)}} dz |t(\alpha_i)t(\alpha_f)|^2, \tag{5.12}$$

where t are the transmission coefficients. P varies along the measured rods, as α_f varies.

The correspondence of the measured and fitted intensity distribution is good (see Fig. 7.31, full line). The scattered intensity is larger for $q_\perp < 0$; the discs are thus compressed ($d\Delta = \Delta - \Delta_0 < 0$)

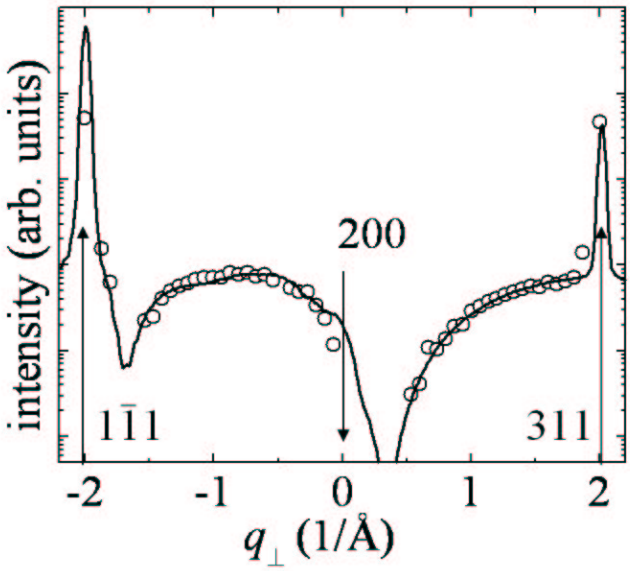

Figure 5.9: Distribution of the measured intensity (points) along the trajectory denoted in Fig. 7.29, along with its theoretical fit (line) with the analytical model.

It is worthy to note that the diffusely scattered intensity cannot be explained only by the core scattering, even if the nearest RELP is forbidden. Since the defects are very thin in the direction perpendicular to the loop plane, of the order of the interplanar spacing, the extension of the $|E_1(\mathbf{Q})|^2$ term in this direction is comparable to the distance between nearest RELPs, and this term is not negligible even around a forbidden RELP. If we neglect completely $E_1(\mathbf{Q})$, the asymmetry of the experimental intensity distribution around (200) can be explained only by a non-realistically small value of Δ.

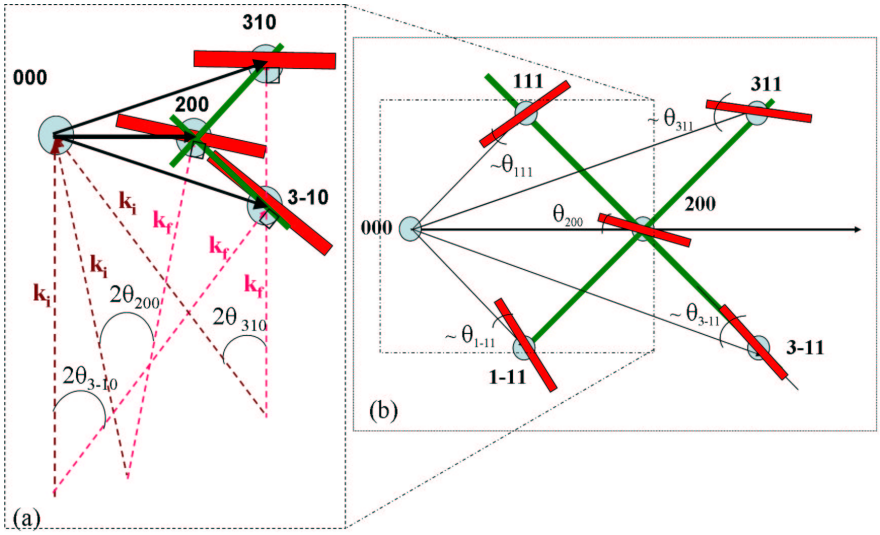

Figure 5.10: Drawing of the in-plane projection of the resolution function (red) as a function of the position along the streaks.

C. Atomistic model.

We have compared the simulated intensity distribution with the result of atomistic simulations [21]. An extrinsic stacking fault was created by adding an extra double (111) atomic plane in the center of a large simulation cell where atoms are at perfect lattice sites. The extra plane had the shape of a regular hexagon bound by dislocation line segment along $\langle 111 \rangle$ crystal directions. We used a length of 20 $\frac{1}{2}[110]a$ (a is the lattice constant) for one side of the hexagon, corresponding to 2282 extra atoms in the stacking fault. Due to computational limitation, the size of the defect is chosen four times smaller than the average measured stacking fault size. The coordinates of all the atoms are then relaxed to the closest potential energy minimum using the well-tested Stillinger-Weber interatomic potential model [24]. The relaxation gives realistic coordinates of atoms $\mathbf{R_i}$ describing the strain field surrounding the defects. Using the positions of atoms following from the atomistic simulations, the X-ray scattering intensity within the kinematical appoximation is obtained by straightforward summation,

$$I(\mathbf{K}) = N(\sigma/a)\left| f_{\mathbf{K}} \sum_i \mathrm{e}^{-\sigma^2 {R_i}^2/(2a^2)} \mathrm{e}^{\mathrm{i}\mathbf{K}.\mathbf{R_i}} \right|^2, \tag{5.13}$$

$\mathbf{K}$ is the reciprocal lattice vector, $\mathbf{R_i}$ the atom position referred to the defect center, a the lattice constant, $f_{\mathbf{K}}$ the atomic form factor, and $N(\sigma/a)$ a normalization factor. The convolution term $\mathrm{e}^{-\sigma^2 {R_i}^2/(2a^2)}$ was first proposed by Keating and Goland [25] who showed that with a convoluting exponential term, the convergence of the sum can be speeded up significantly. The convolution factor σ has the effect of broadening the Bragg peak, but not affecting the qualitative shape of the scattering [5]. The calculations have been carried out using σ=0.4, which was about the smallest value for which no artificial truncation ripples [25] were observed in the scattering patterns.

The sample presents stacking faults with four types of orientations: (111), $(\bar{1}\bar{1}1)$, $(\bar{1}11)$ and $(1\bar{1}1)$. Only one stacking fault with orientation $\mathbf{u}$=(111) has been simulated with the atomistic program. Figure 5.11 corresponds to the results of the DXS around the (200) forbidden peak in the two planes (*i.e.* $\mathbf{p}$=(110) and $(1\bar{1}0)$) for two different possible orientations ($\mathbf{u}$=(111) and $(\bar{1}\bar{1}1)$) of the stacking fault. As observed in fig. 5.11, streaks appear only in the (110) plane. Considering a single $< 111 >$ stacking fault with orientation $\mathbf{u}$. One fault has two streaks perpendicular to its plane in both the positive and negative directions [18]. In order that the streaks from a stacking fault with orientation ($\mathbf{u}$=(111) or $(\bar{1}\bar{1}1)$) lie in a $\mathbf{p}$ plane, the relation $\mathbf{u}.\mathbf{p} \neq 0$ should be verified. This is fulfilled only for

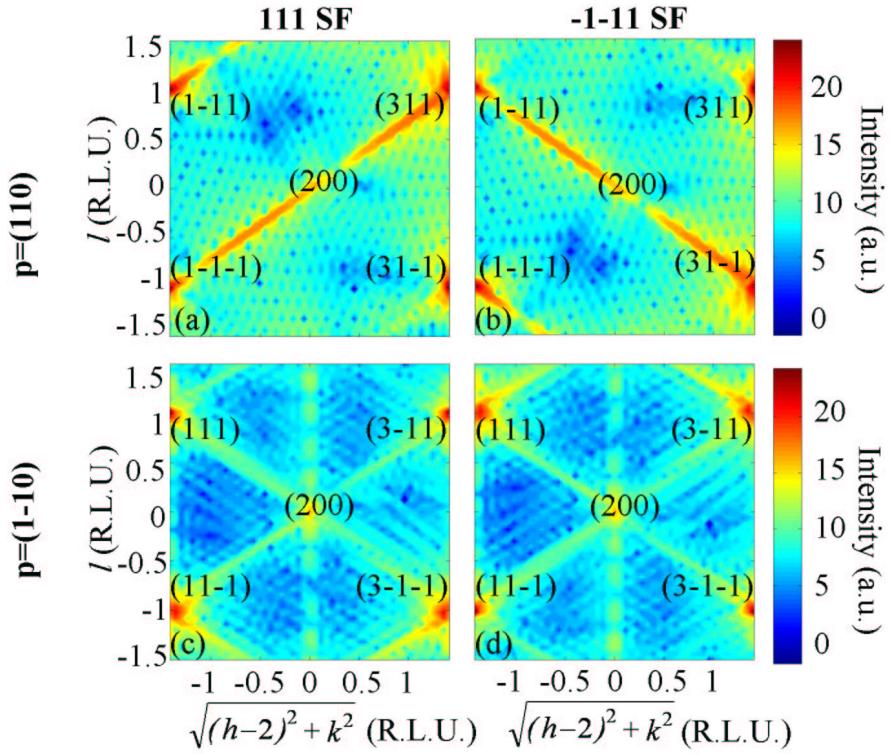

Figure 5.11: Results of the diffuse X-ray scattering calculation around the (200) forbidden peak for two different possible orientations of the 111 stacking fault (**u**=(111) (a) and (c) and **u**=($\bar{1}\bar{1}1$) (b) and (d)) in the two planes: (110) (a)-(b), and ($1\bar{1}0$) (c)-(d).

the (110) plane.

We have calculated the scattered intensity directly using Eq. (5.13), and averaged the scattered intensity over all four possible {111} orientations of a hexagonal stacking fault (Fig. 5.12 (a)). We have compared the experimental results with the results of atomistic simulations (Fig. 5.12 (b)). The red line in Fig. 5.12 (b) exhibits a small sharp maximum also in the forbidden 200 point ($q_\perp = 0$). This maximum is caused by the size truncation of the crystal that was included in the atomistic simulation. Except for this maximum, the correspondence between the measured and simulated curves is very good.

Figure 7.32 schematically depicts the sequence of (111) layers and positions of the atoms obtained by the atomistic simulation in a close vicinity of the defect core (a double layer denoted Aa) inserted between the double layers Bb and Cc of the crystal matrix. For clarity, we have plotted only the atoms with small coordinates along [$\bar{1}\bar{1}2$]. Here we compare the ideal distance Δ_0 of the Aa layers creating the defect core (denoted by a pair of straight full lines) with the distance Δ following from the fit of the measured intensity distribution (dashed straight lines). From the atomistic simulation it follows that the atoms in the defect core close to its periphery are displaced along the [111] Burgers vector so that the inserted Aa discs are not planar. Most likely, this distortion at the edge of the defect core is the reason for the difference between the measured intensity distribution and the intensity profile simulated using the theory in Eqs. (7.5-5.8) (full line in Fig. 7.31), in which no distortion of the inserted Aa planes was assumed. Nevertheless, the value of Δ obtained from the fit corresponds well to the mean distance between the atoms in the A and a core planes in [111] direction.

To study size effects, we compared the intensity simulated for stacking fault lengths of 14 and 20 $\frac{1}{2}$[110]a (Fig. 5.14 (a)).

For the smaller defect, the diffuse intensity is weaker but the shape of the signal remains the same.

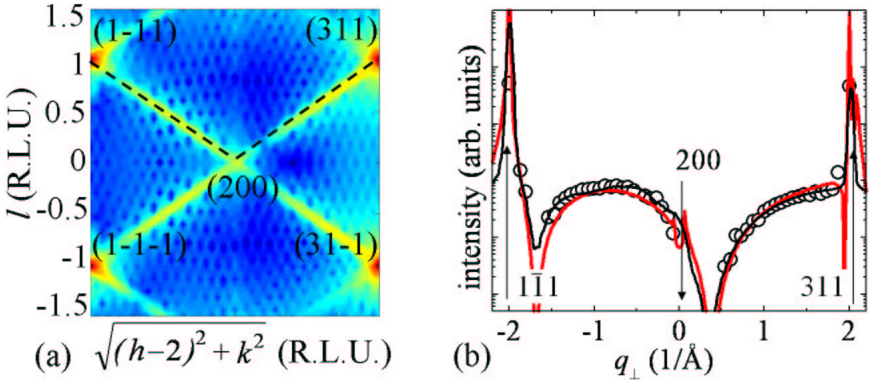

Figure 5.12: Result of the diffuse X-ray scattering calculation around the (200) forbidden averaged over all the four possible {111} orientations of a hexagonal stacking fault. (b) Distribution of the measured intensity (points) along the trajectory denoted in Fig. 5.12 (a), along with its theoretical fit using the analytical model (black line) and atomistic simulations for the displacement field (red line).

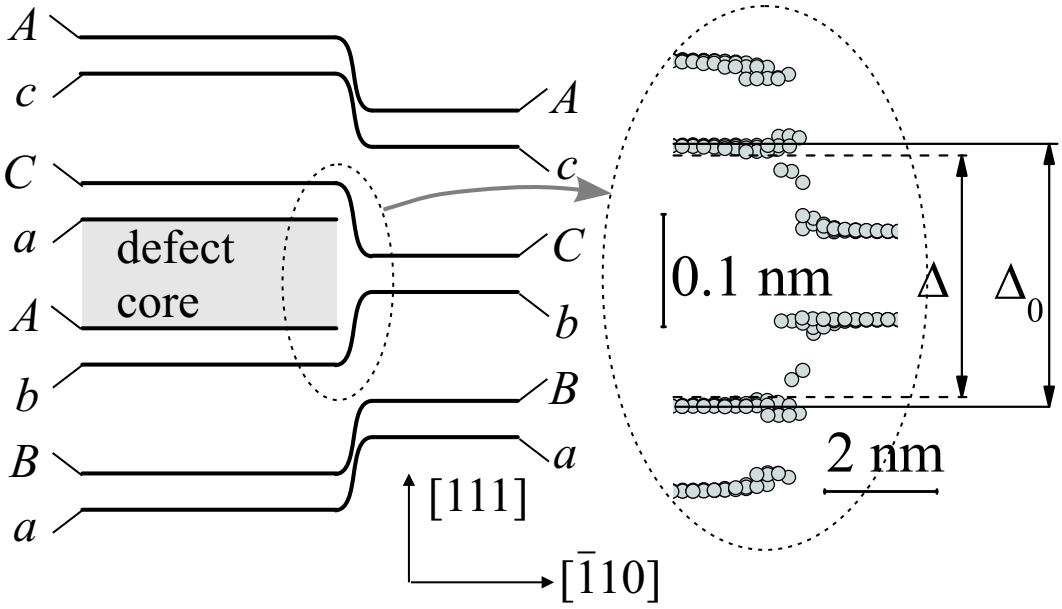

Figure 5.13: Schematical sketch of the stacking of the sequence of (111) layers, the defect core (gray rectangle) is represented by a pair of inserted Aa layers. In the insert, the atomic positions are plotted around the edge of the defect core, following from the atomistic simulations. The full horizontal lines represent the ideal distance Δ_0 of the core planes, the dashed lines denote the distance Δ of these plane following from the fit of the measured intensities (full line in Fig. 7.31).

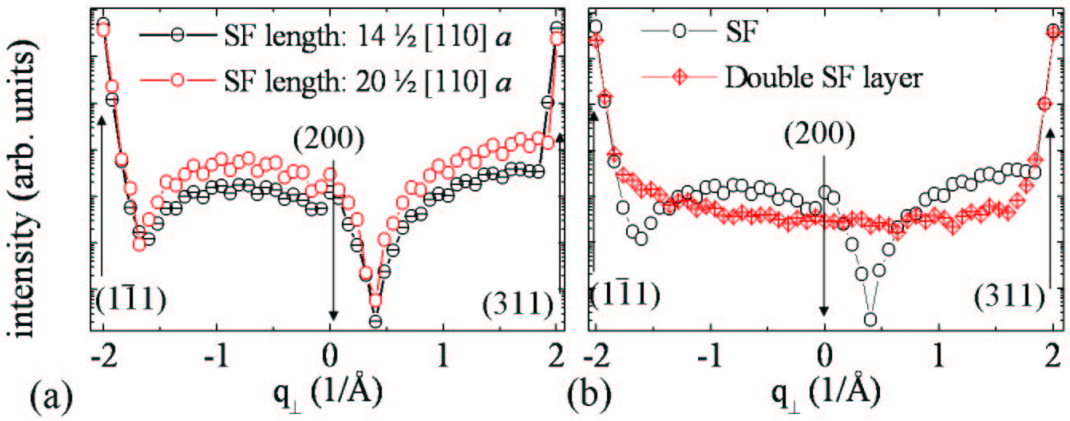

Figure 5.14: (a) Simulated diffuse X-ray scattering around the (200) forbidden peak and along the [111] direction for stacking fault lengths of 14 and 20 $\frac{1}{2}[110]a$. (b) Comparison of the simulated diffuse X-ray scattering for a single and a double stacking fault layer of size 14 $\frac{1}{2}[110]a$.

Thus, the stacking fault size has no impact on the shape of the fault's core signal. Then, we compared the intensity simulated for a single and a double stacking fault layer of size 14 $\frac{1}{2}[110]a$ (Fig. 5.14 (b)). In both cases, the scattered intensity is concentrated in streaks along $< 111 >$ perpendicular to the fault planes (not shown here). The intensity along the streaks present some differences as shown in Fig. 5.14 (b). Thus, collecting the intensity along the streaks also allows to determine the nature of the stacking faults.

We have also calculated the intensity scattered by a stacking fault around other forbidden reflections: **h**=[420] and **h**=[600] (Fig. 5.15). In both cases, a maximum is observed at the position of the forbidden reflection. The maximum is due to two effects: $E_2 \neq 0$ (scattering of the defects core) and $E_1 \neq 0$ (The relaxation of the unit cell breaks its symmetry.). Along the $< 111 >$ streaks, the intensity is not null. Defects scatter everywhere in reciprocal space: the intensity is modulated by the form factor and displacement field of the defects. Several minima are observed. This reveals the higher sensibility on the Δd value for higher $q_\perp$ values.

5.2.4 Conclusion: Allowed vs quasi-forbidden reflection

Defects are composed of different areas. The defect core is the region where the structure appreciably differs from the structure of the matrix. Moreover, a deformed crystalline area surrounds the defect core. Close to the defect core, the lattice distortion is strong. Only calculations performed using a discrete atomistic model for the distortion field can be applied to calculate the DXS from this area. Outside this region, the distortion is weaker and the asymptotic displacement field can be described using linear elasticity theory. The diffusely scattered signal is composed by the coherent superposition of two contributions: the diffuse scattering from the deformed area in the defect neighbourhood (called displacement-field scattering or Huang diffuse scattering if close to an allowed Bragg peak) and the core scattering. Close to an *allowed reflection*, the Huang diffuse scattering is dominant. In this case, the *long-range displacement field* of the defects is probed. A q^{-2} decay is observed. The DXS intensity is stronger for positive values of Δq_r. The scattering comes from lattice *expanding* defects. In contrary, close to the (200) *forbidden reflection*, the intensity is stronger for negative value of Δq_r. The intensity caused by the long-range displacement field of the defect is nearly suppressed. It is mainly influenced by the *core* of the defect which is in local *compression*.

In summary, we have demonstrated that diffuse X-ray scattering around a forbidden reciprocal

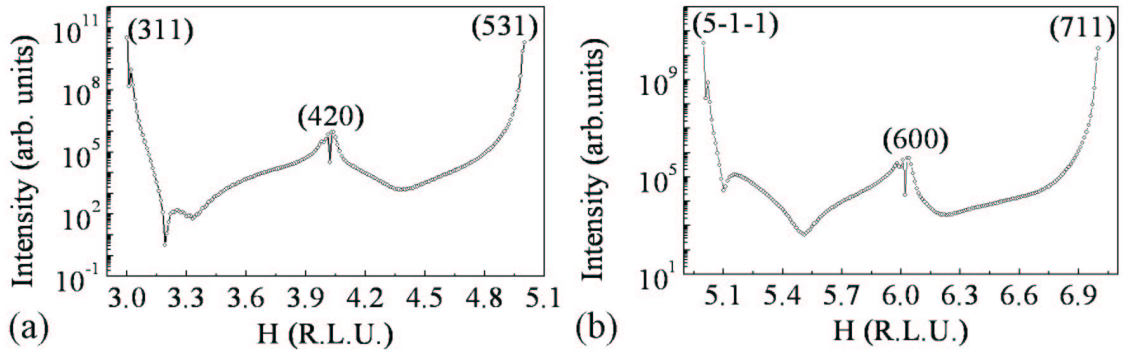

Figure 5.15: Simulated diffuse X-ray scattering by a stacking fault of 14 $\frac{1}{2}$ [110] length around the (420) (a) and (600) (b) forbidden peaks.

lattice point is well suited for the study of the cores of extrinsic stacking faults in Si. We have shown that the diffuse scattering from the distorted neighborhood of the defects is fairly suppressed in this case which makes it possible to study directly the atomic structure of the defect cores. From the comparison of the measured intensity with a simulation based on the continuum displacement model we have revealed a compression of the {111} planes in the defect cores. This finding was supported by atomistic simulations. As the core of defects is small, it diffuses on an extended zone in the reciprocal space. An important point is that the contribution of several allowed reciprocal-space points to the total intensity around the forbidden reflection is needed to analytically simulate the defect core. Thus, diffuse X-ray scattering near forbidden reflection appears as a fine, unique and destruction-free technique to detect stacking faults and characterize their small compression in the core.

The approach above constitutes a pioneer experiment. In most of the cases, the measurement of the properties of defects were performed around allowed reflections. The scattering from the defects core is very weak, so that the investigation of the structure of the defect core was only indirect, using the displacement field around the defect. Transmission electron microscopy is a complementary technique to detect defects. But it remains a destructive method and its resolution does not allow yet to probe the core of defects, notably the distortion and size.

5.3 Defects in Ge islands

5.3.1 Defects in ordered self-assembled Ge quantum dots (SAQD).

The simultaneous control of the localization, density and size uniformity of epitaxial nanostructures is a key parameter for future nanoelectronic devices. To fulfil these requirements, a novel approach has been developed consisting in forming regular self-assembled quantum dot structures (SAQD) by combining the nanoscale patterning with diblock copolymer and the Stranski-Krastanow growth process [26]. This results in the formation of highly-ordered periodic quantum dots less than 100 nm in size. Although electron beam lithography can produce features with size less than 100 nm, this technique is not used for large scale industry products due to the slow fabrication time of the technique. Nano-patterning using di-block copolymer appears as a powerful alternative that not only inherits the advantage, large throughout, of optical lithography but also can routinely create features with sizes down to 10 nm. However, the underlying mechanism for the guided assembly process by patterned topographic surface features remains poorly understood.

Grazing incidence X-ray diffraction (GID) and GI-DXD were used to investigate the strain profile, the defects, composition, and degree of ordering of the grown Ge islands.

5.3.2 Description of the SAQDs sample.

The investigated sample consists of a Si(001) substrate having hexagonally ordered hole patterns on the surface prepared through patterning using diblock copolymer. In a first set, diblock copolymers of PS-PMMA (Polystyrene-b-poly-methylmethacrylate) which form hexagonally organized cylindrical patterns after self-assembly [26] are transferred to the SiO_2 mask layer through reactive ion etching (RIE) with SF_6 etching chemistry (see Fig. 5.16). This creates hexagonally ordered holes in the oxide layer. The pattern size was originally about 30 nm and the center-to-center distance was about 45 nm. The oxide mask layer thickness was 30 nm. Then, Ge quantum dots are selectively grown in the Si openings by molecular beam epitaxy. A two step Ge growth process was employed in which a 0.3 nm thick Ge was first grown at 200°C and then a 0.6 nm thick Ge layer was subsequently grown at 600°C in order to minimize the intermixing between Ge and the Si substrate. The SiO_2 layer was etched away. Figure 5.17 shows the hexagonally ordered structure, which is made of domains. The size of the ordered domains is in the few hundreds nanometer range. The Ge QD size is about 20 nm in width and 4nm in height and the center-to-center distance is about 35nm. The aspect ratio of individual Ge dots remains low ($\sim$ 1:5), the dot size is uniform and the density is high ($\sim$5x10^{10} cm^{-2}) [27].

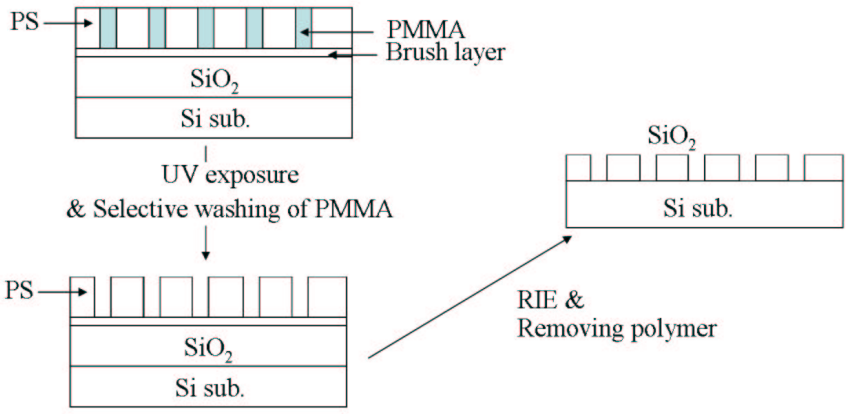

Figure 5.16: Schematic illustration of the nanopatterning process for forming the self-assembled hexagonal cylindrical patterns of exposed Si areas (holes) in the SiO_2 mask layer using self-assembled diblock copolymer of PS-*b*-MMA as template.

5.3.3 Strain and ordering analysis of the SAQDs.

The X-ray experiments were performed in grazing incidence geometry at beamline ID01 (ESRF). The X-ray photon energy was set to 11 keV and the incident angle to 0.16° (i.e. the critical angle for total external reflection of Si at this energy) in order to be sensitive to the surface. GID was used to determine the lateral correlation, size, strain and chemical composition inside the nanostructures.

Angular (figure 5.18) and radial scans (figure 5.19) have been performed near the (220) and (400) reflections. The angular scan (figure 5.18) contains information on the size and on the lateral correlation of the SAQDs. It shows several peaks originating from the lateral ordering of the SAQDs, which reveals a long-range ordering. From the angular distance between the (400)Si Bragg Peak ($n = 0$) and the first ordering peak ($n = 1$), the average "lattice parameter" d of the hexagonal packing of QDs can be deduced (d=38nm), which is in good agreement with the SEM image. The distance between the n^{th} ordering peak and the $(n-1)^{th}$ ordering peak corresponds to an hexagonal ordering averaged in rotation (Fig. 5.18). The full width at half maximum (FWHM) of the correlation peaks is inversely

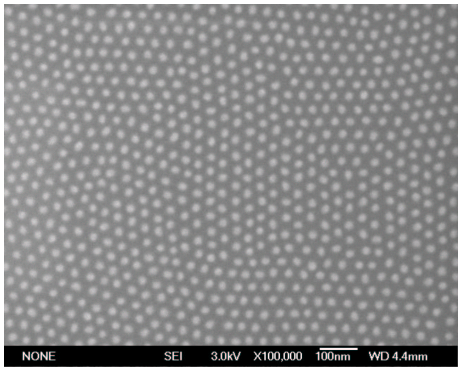

Figure 5.17: SEM image showing the hexagonally ordered quantum dots. The average domain size equals about a few hundred nanometer.

proportional to the domain size. The domain size can be roughly estimated to be $\sim$ 190 nm which is in good agreement with the SEM image.

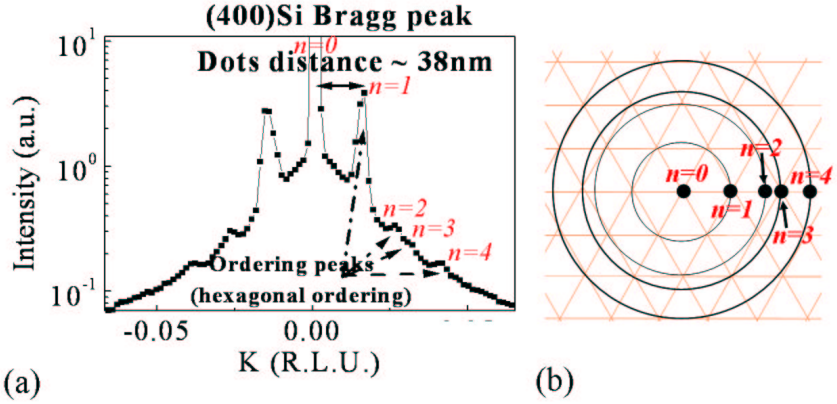

Figure 5.18: (a) Angular scan at the (400)Si substrate reflection. (b) Drawing of the hexagonal packing and theoretical position of correlation peaks (black circles).

On the radial scan along the [110] direction and close to the Si(220) substrate reflection (figure 5.19), ordering peaks are well observed around the Si Bragg peak. This rich peak structure has an intensity profile that is asymmetric with respect to the sharp (220) substrate peak. An ordering peak is observed on the right side of the Si Bragg peak. This indicates strain relaxation towards lattice parameters lower than the one of Si. This signal may come from a highly compressed part of the patterned Si substrate. The shape and correlation functions are modulated by the strain. The distance between the correlation peaks is Δh=0.01. The associated distance is d=$a/\sqrt{2}\Delta h$=38 nm, which corresponds to the inter-dots distance.

The maximum of the signal scattered by the Ge islands is at h $\sim$1.929, which is close to that of fully relaxed Ge (h=1.918). Ge SAQDs are thus nearly fully relaxed corresponding to 3.55% strain with respect to the Si lattice parameter. By measuring the full width at half maximum (FWHM) of the relaxed peak, the lateral size ($D = a/(\sqrt{2}\Delta h)$) of the Ge SAQDs is found to be (14.5$\pm$3.0)nm, which is lower than the size measured by SEM. Indeed, the FWHM of the relaxed peak has two contributions: the finite size of the islands and their deformation fields. To determine the islands size from a radial scan along Q_r, the relaxation state of the islands, *i.e.* the distribution of the inter-planar

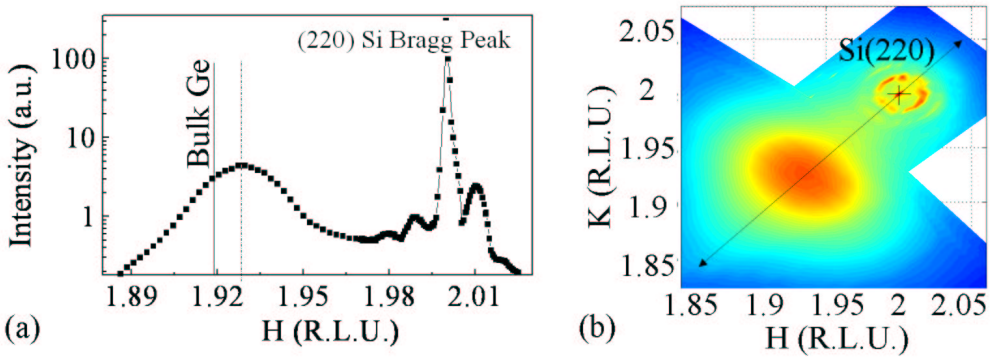

Figure 5.19: (a) Radial scan close to the (220)Si substrate reflection. (b) (220) map of the Ge islands. The arrow corresponds to the direction of the radial scan shown in figure (a).

distances d_{hkl} inside the islands [28] needs to be taken into account:

$$\Delta Q_r = \sqrt{(Q_r \frac{\Delta d_{hkl}}{d_{hkl}})^2 + (\frac{2\pi}{D})^2} \tag{5.14}$$

By measuring ΔQ_{r220} and ΔQ_{r400} (*i.e.* the width of the diffuse signal coming from the QDs) and in resolving the upper equation, the islands size is found to be D ∼19nm, which is consistent with the size deduced from the SEM image. The deformation field broadens the scattering peaks.

The lateral size D of the islands can also be determined by angular scans according to $q_a = 4\pi/\lambda sin(2\Theta/2)\Delta\Theta$. 2Θ is the Bragg angle and $\Delta\Theta$ is the FWHM of the angular scan. The lateral size D verifies:

$$D = \frac{\lambda}{2sin(2\Theta/2)\Delta\Theta} \tag{5.15}$$

At the maximum of diffuse scattering, the mean size of the islands is measured: $D \sim$ 10nm, which again is too small. This underestimation is due to the fact that, in the angular direction, the presence of in-plane mosaic spread M, *i.e.* small desorientation of the island axes with respect to the substrate broadens the scattering peaks as follows:

$$\Delta\Theta^2 = M^2 + \frac{1}{Q_a^2}(\frac{2\pi}{D})^2 \tag{5.16}$$

As the measured D ∼10nm is inferior to its real value (∼20nm), it follows $M \neq 0$. The Ge SAQDs are not coherent; they contain defects. Besides, no size oscillations are observed in the angular scans, despite the fact that the Ge islands are homogeneous in size as observed in the SEM image. This can be understood by the presence of in-plane mosaic spread. Their signals are convoluted with the Fourier Transform of the QD shape. This results in the broadening of the angular signal and thus attenuates the shape oscillations.

5.3.4 Detection of lateral ordering of the Ge nanostructures: GISAXS vs GIXD.

GISAXS images were recorded to determine the shape of the grown islands (Fig. 5.20). Fig. 5.20 (a) shows the measured data as a function of Q_y and $Q_\perp$=Q_z coordinates of the scattering vector, *i.e.*, parallel and perpendicular to the sample surface for the $< 100 >$ crystallographic axis of the Si(001) substrate. The GISAXS map shown in Fig. 5.20 (b) results from 90 GISAXS patterns measured at different azimuths and for which the intensity at Q_z=0 (*i.e.* at the Yoneda peak) has been extracted.

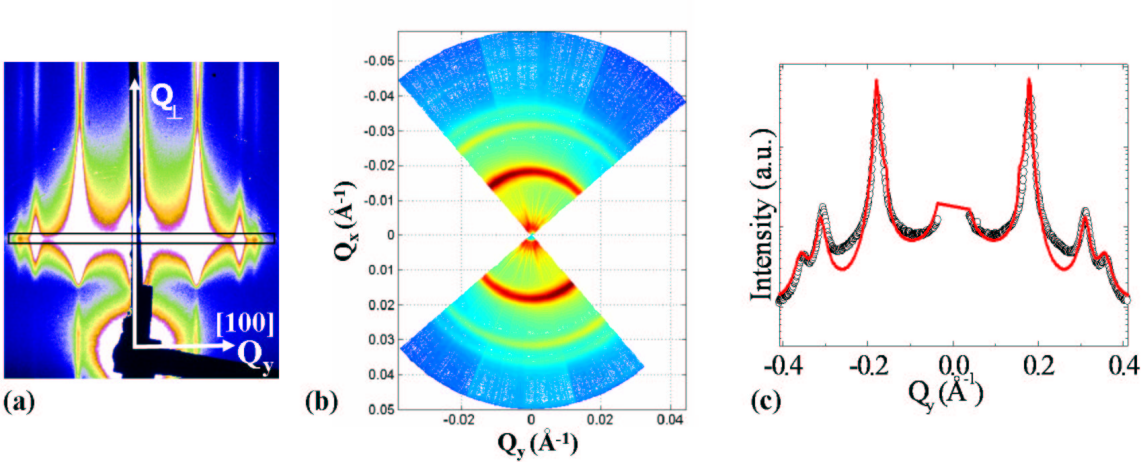

Figure 5.20: (a) GISAXS image of the organized Ge islands along the $< 100 >$ azimuth. (b) GISAXS map showing the correlation rings originating from the interference function of the well-organized Ge islands. (c) Intensity cross section of the GISAXS pattern shown in Fig. 5.20 (a). The cut is made along the Q_y direction at the location of the Yoneda's peak.

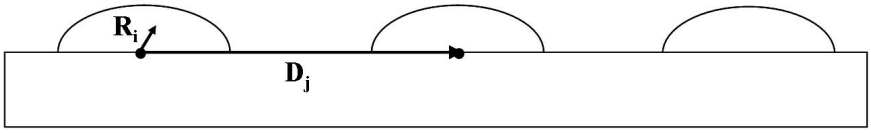

Figure 5.21: Schematic drawing of the islands and the corresponding $\mathbf{R_i}$ and $\mathbf{D_j}$ vectors.

Inter-dots distance	(40±3) nm
Islands diameter	(20.5±1.0) nm
Islands height	(4±3) nm

Table 5.1: Rough estimation of the morphology of the islands.

No facet streaks are observed, obviously hidden by the correlation peaks along Q_y, which reveal the long-range hexagonal ordering of the grown Ge islands.

In the GID geometry, ordering peaks are observed only around the Si Bragg peaks. Despite the fact that the Ge islands are laterally organized, no interference function (*i.e.* no correlation peaks) is observed at the position of the relaxed Ge (see the (220) map on figure 5.19). In supposing $\mathbf{R_i}$ and $\mathbf{D_j}$ the atomic position of the i^{th} atoms inside the islands and the inter-dot vector respectively (Fig. 5.21), the scattered amplitude around $\mathbf{Q}+\mathbf{q}$, $|\mathbf{q}| << |\mathbf{Q}|$ ($\mathbf{Q}$ is the reciprocal space vector) can be expressed as

$$A(\mathbf{Q}+\mathbf{q}) = \sum_{i,j} \mathrm{e}^{-\mathrm{i}(\mathbf{Q}+\mathbf{q})\cdot(\mathbf{R_i}+\mathbf{D_j})}. \tag{5.17}$$

As $\mathrm{e}^{-\mathrm{i}\mathbf{Q}\cdot R_i} = 1$, the previous equation can be written

$$A(\mathbf{Q}+\mathbf{q}) = \sum_{i} \mathrm{e}^{-\mathrm{i}\mathbf{q}\cdot\mathbf{R_i}} \times \sum_{j} \mathrm{e}^{-\mathrm{i}(\mathbf{Q}+\mathbf{q})\cdot\mathbf{D_j}} \tag{5.18}$$

The first term $F(\mathbf{q}) = \sum_{\mathbf{i}} \mathrm{e}^{-\mathrm{i}\mathbf{q}\cdot\mathbf{R_i}}$ corresponds to the form factor of the islands. The second term $\sum_j \mathrm{e}^{-\mathrm{i}(\mathbf{Q}+\mathbf{q})\cdot\mathbf{D_j}}$ can be written differently according to scattering configurations.

- In Grazing Incidence Small Angle X-Ray Scattering (GISAXS), the signal is collected in the vicinity of the origin of the reciprocal space ($\mathbf{Q}=\mathbf{0}$). This implies $\sum_j \mathrm{e}^{-\mathrm{i}(\mathbf{Q}+\mathbf{q})\cdot\mathbf{D_j}} = \sum_j \mathrm{e}^{-\mathrm{i}\mathbf{q}\cdot\mathbf{D_j}}$. Thus, $I(\mathbf{q}) = A.A^* = |F(\mathbf{q})|^2 * S(\mathbf{q})$, where $S(\mathbf{q})$ is the interference function.

- In Grazing Incidence Diffraction (GID), if a parametrical relation exists between the crystallographic networks of the substrate and the islands, $\mathbf{Q}.\mathbf{D_j} \equiv \mathbf{0}\ [\mathbf{2}\pi]$. This implies $\sum_j \mathrm{e}^{-\mathrm{i}(\mathbf{Q}+\mathbf{q})\cdot\mathbf{D_j}} = \sum_j \mathrm{e}^{-\mathrm{i}\mathbf{q}\cdot\mathbf{D_j}}$. Thus, $I(\mathbf{Q}+\mathbf{q}) = A.A^* = |F(\mathbf{q})|^2 * S(\mathbf{q})$, where $S(\mathbf{q})$ is the interference function. The same result is obtained compared to GISAXS: the scattering around the Bragg peak is identical to the signal collected at small angles.

- In Grazing Incidence Diffraction (GID), if the crystallographic networks of the substrate and the islands are incommensurate, $\mathbf{Q}.\mathbf{D_j}$ is random. This implies $\sum_j \mathrm{e}^{-\mathrm{i}(\mathbf{Q}+\mathbf{q})\cdot\mathbf{D_j}} = \sum_j \mathrm{e}^{-\mathrm{i}\mathbf{q}\cdot\mathbf{D_j}}\mathrm{e}^{\mathrm{i}\Psi}$ with Ψ a random phase. The islands do not interfere: $S(\mathbf{Q}+\mathbf{q}) = \mathbf{1}$. Thus, $I(\mathbf{Q}+\mathbf{q}) = A.A^* = |F(\mathbf{q})|^2$.

GISAXS is thus a preferable technique to reveal the lateral ordering of nanostructures. As the interference function is not eliminated by the uncommensurability between the networks of the islands and the substrate.

An intensity cross-section along Q_y and at the location of the Yoneda's peak is displayed in Fig. 5.20 (c). The inter-dot distance and the diameter of the particles are roughly estimated by fitting the intensity cross-section by the form factor of spherical-shaped islands. The results are summarized in the table 5.1. The values are in good agreement with the SEM and AFM images.

5.3.5 Composition of the SAQDs.

In order to determine the composition of the Ge islands, anomalous GID using MAD (Multiwavelength Anomalous Diffraction) was performed, from which the contribution of the Ge and Si atoms are quantitatively extracted.

In principle, the DWBA effects complicate the analysis near the critical angle of total reflection. However, in the case of a non-resonant material under the island, as it is the case for the Si substrate, the MAD analysis without including the DWBA allows to separatly determine the partial structure factors of the Ge atoms $|F_{Ge}|$, of the non-anomalous atoms $|F_{Si}|$ and of all the atoms, $|F_T| = |F_{Ge}| + |F_{Si}|$.

Fig. 5.22 shows $|F_{Ge}|$, $|F_{Si}|$ and $|F_T|$ extracted from MAD measurements using the `NanoMAD` program.

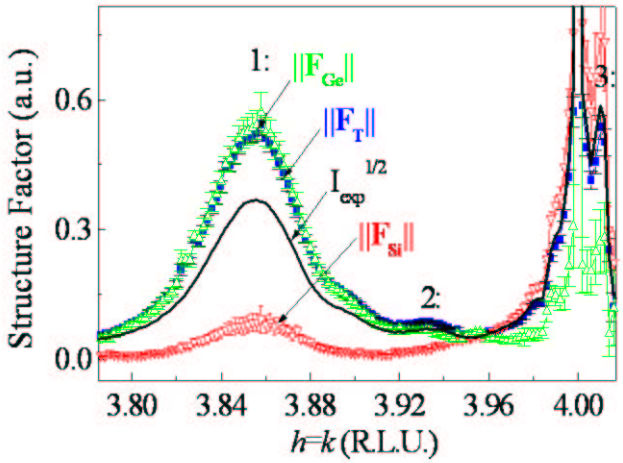

Figure 5.22: Ge, Si and total structure factors $|F_{Ge}|$, $|F_{Si}|$ and $|F_T|$ extracted with the NanoMAD progam from MAD measurements on the Ge SAQDs sample. The numbers correspond to different regions of the sample as explained in the text.

The Si and Ge partial structure factors show a maximum of intensity at $h \sim 3.855$ (position indicated by the number 1 in Fig. 5.22), close to the position of fully relaxed Ge ($h \sim 3.835$). As observed before, the Ge islands are nearly fully relaxed and incoherent. A part of the Si presents the same lattice parameter compared to the relaxed Ge islands (region 1). The Si contribution located at the position 1 is well separated from the one of the Si substrate. This is the signature of interdiffusion inside the incoherent 3D islands. From the knowledge of $|F_{Si}|$ and $|F_{Ge}|$, the Ge concentration (c_{Ge}) inside the Ge islands has been determined: c_{Ge}=73%. The peak labelled 3 corresponds to a correlation peak due to the nano-patterning of the Si substrate. The peak labelled 2 is broader than the correlation peak 3. This might be the signature of defects organized at the Si/Ge interface. A Ge contribution is essentially observed in the region of the peak '2', which could mean that the defects are localized inside the Ge nanostructures.

5.3.6 Comparison with transmission electron microscopy study.

Transmission electron microscopy (TEM) is traditionally used for the characterization of defects. In this section, some TEM and HRTEM cross-section images will be discussed, which were acquired using a JEOL 4000EX field emission microscope. The sample preparation before the analysis is needed to reduce the sample thickness to 100nm using mechanical polishing and a precision ion polishing system. The images were carried out at the microscopy laboratory of the CEA-Grenoble by J.-L. Rouvière.

Figure 5.23 shows HRTEM cross-section images in the [110] zone axis of the grown Ge islands. The images show that the islands are {113} facetted. These facets were not detected by GISAXS as the signal coming from the facets is hidden by the correlation peaks. The images also clearly show the selective growth inside the exposed patterned Si areas, as opposed to over the SiO_2 covered regions

(which was then removed after growth). This explains the origin of the strong ordering peak observed on the right side of the Si Bragg peak in Fig. 5.19. The Si atoms at the edge of the Ge islands are highly compressed.

The determination of the stacking fault type (extrinsic or intrinsic) can be performed by studying the stacking sequence AaBbCcAaBbCc (see Fig. 5.24). A missing double planes (for instance cC) corresponds to an intrinsic stacking fault. Two additional double planes correspond to an extrinsic stacking fault. Thus, after the introduction of an intrinsic stacking fault or an extrinsic stacking fault, a positive translation of a pair or two pairs of {111} planes in the $< 111 >$ directions is observed (Fig. 5.24).

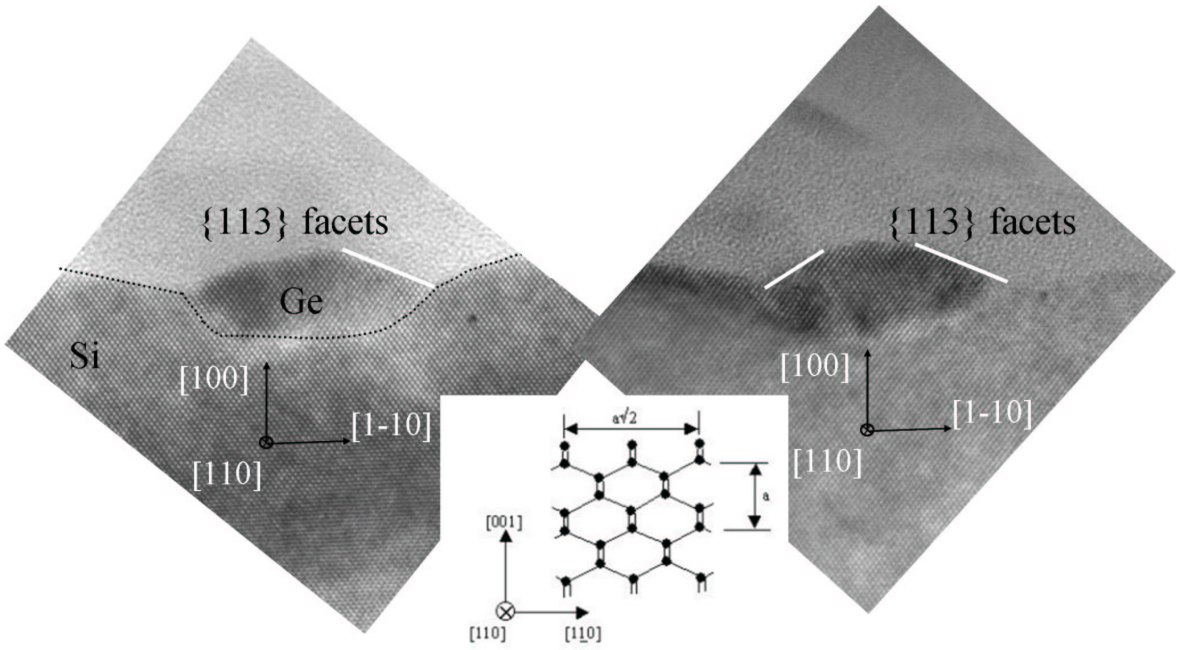

Figure 5.23: HRTEM cross-section images in the [110] zone axis of the grown Ge islands. Each point corresponds to a pair of atoms.

Figures 5.25 show HRTEM cross-section images in the [110] zone axis of several grown Ge islands and a phase diagram of an island. The phase diagram clearly shows the presence of a dislocation at the Ge/Si interface. Intrinsic, extrinsic stacking faults and twins are observed inside the Ge islands, which explain the high relaxation of the Ge islands.

5.3.7 Simulation of the strain of the Ge QDs using finite difference method (FDM).

We performed FDM simulations to compare the island strain field between incoherent islands and islands coherently bound to the Si substrate. If we suppose that the islands are coherent, we can perform finite element simulations. The FDM method used in this work was developed by Catherine Priester [29]. The calculation is done for a single island. Using the continuum elasticity theory (finite difference method), the total elastic energy is minimized with respect to the strain components ϵ_{ij}. To know the positions of all Ge atoms in the dots, the strain field was calculated in the frame of an elasticity model with the FDM method. In the following, we consider 20 nm large times 8 nm high pure ellipsoidal Ge QDs grown on a patterned Si(001) substrate. The island size is in agreement with the HRTEM cross-sections. Figure 5.26 shows the corresponding in- and out-of-plane strain maps along a cross section of the QD through its middle. The strain is defined relatively to the Si substrate.

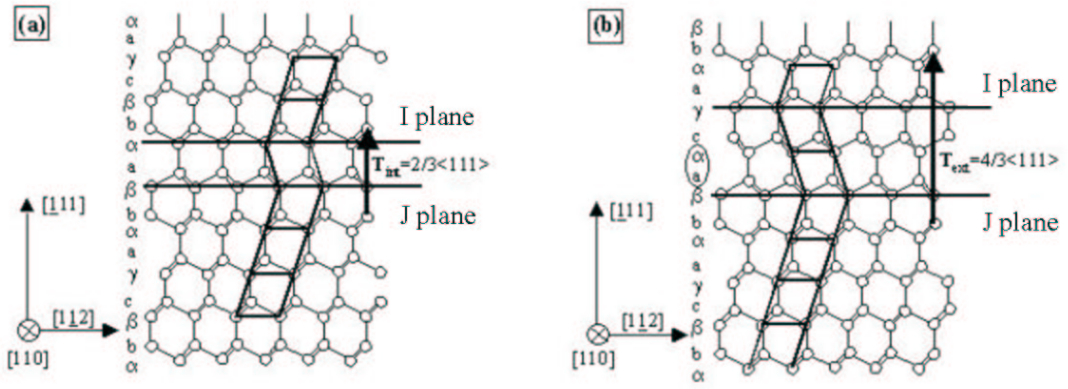

Figure 5.24: Determination of the staking fault type (intrinsic or extrinsic) from the use of two planes, named I and J, which are parallel to the stacking fault.

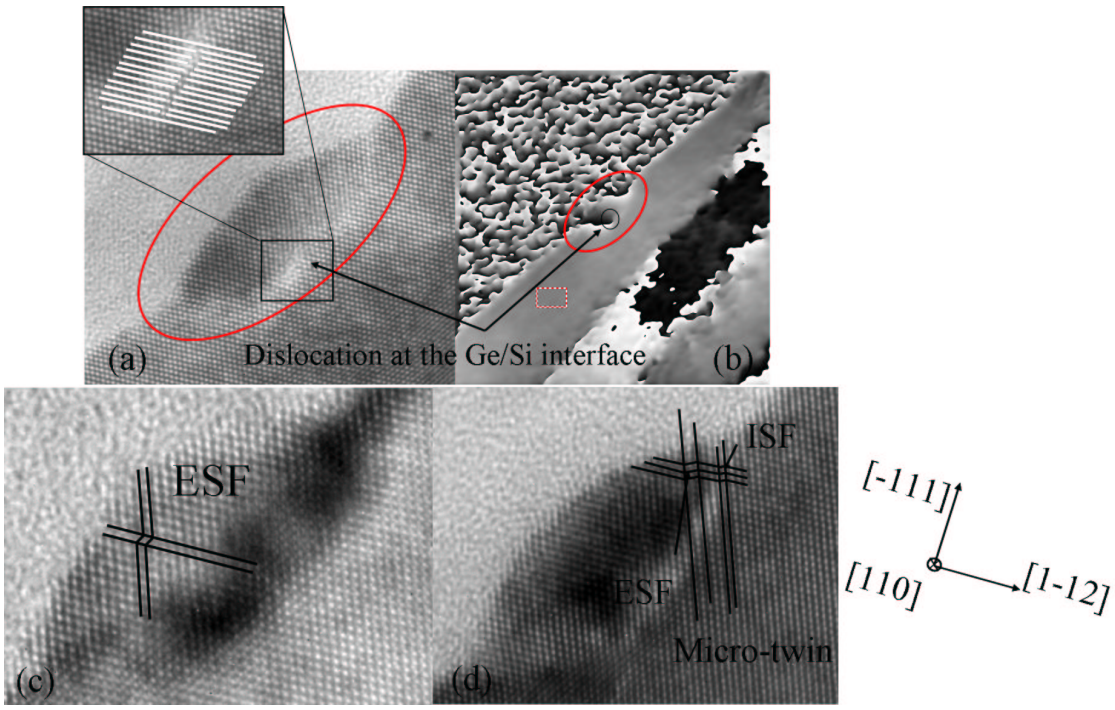

Figure 5.25: (a) HRTEM cross-section image in the [110] zone axis of a grown Ge islands. A dislocation is observed at the Si/Ge interface. (b)Phase diagram revealing an interfacial dislocation going through the island. (c)-(d) HRTEM cross-section images in the [110] zone axis of grown Ge island. Intrinsic, extrinsic stacking faults and twins are observed inside the Ge islands.

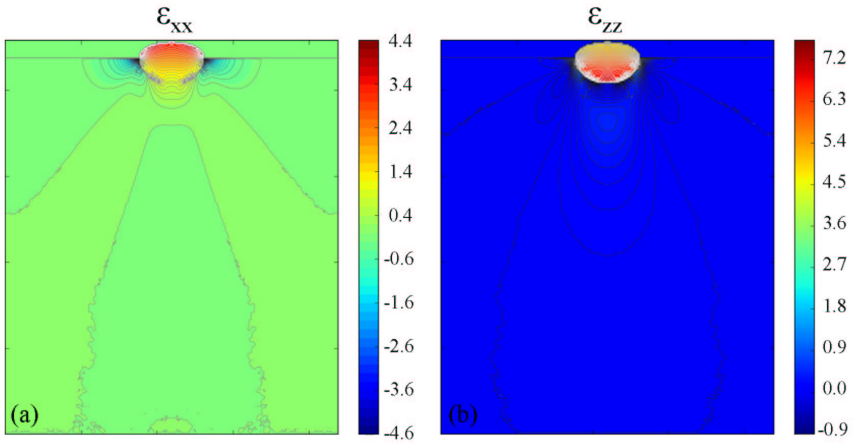

Figure 5.26: (a) In-plane ϵ_{xx} strain and out-plane ϵ_{zz} strain with respect to the Si substrate simulated within an elastic model, using the FDM method, for a 20nm large and 8nm high QD.

Diffraction simulation.

The crystal was modeled as a finite array of N_xxN_yxN_z unit cells. The displacement vector $\mathbf{u_j}$ associated to each point of the array, *i.e.* to each unit cell j was calculated by numerical finite difference simulation. If we assume that atoms in each unit cell have the exact same deformation (a reasonable approximation for small deformations and only to compute scattering close to non-forbidden reflections), then we can factorize the scattering for a full unit cell. The scattered amplitude is then equal to:

$$A(\mathbf{Q}) = \sum_{atoms\ i} f_i \mathrm{e}^{-\mathrm{i}\mathbf{Q}\cdot\mathbf{r_i}} \sum_{unit\ cell\ j} \mathrm{e}^{-\mathrm{i}\mathbf{Q}\cdot(\mathbf{R_j}+\mathbf{u_j})}, \tag{5.19}$$

where $\mathbf{R_j}$ is the position of the j_{th} unit cell and $\mathbf{u_j}$ is its displacement from its ideal position (in the unstrained crystal), $\mathbf{r_i}$ is the ideal position of atom i within the unit cell. The first term in Eq. 3.6 is the structure factor F of the ideal unit cell. In our case, two types of atoms are studied, Ge and Si. If x_{Ge} is the occupancy factor of Ge in a given unit cell (1 if the Ge atom is in the QD, 0 if it is outside), the amplitude can be written as:

$$A(\mathbf{Q}) = F_{Ge}(\mathbf{Q}) \sum_{unit\ cell\ j} x_{Ge} \mathrm{e}^{-\mathrm{i}\mathbf{Q}\cdot(\mathbf{R_j}+\mathbf{u_j})} + F_{Si}(\mathbf{Q}) \sum_{unit\ cell\ j} (1 - x_{Ge}) \mathrm{e}^{-\mathrm{i}\mathbf{Q}\cdot(\mathbf{R_j}+\mathbf{u_j})} \tag{5.20}$$

By using this approach, the Ge and Si structure factors were calculated near the (220) forbidden reflection for a relaxed 3D island (see Fig. 5.27). The simulated diffraction peak is much closer to the Si peak than the experimental data. This shows that an additional relaxation phenomenon is present in addition to elastic relaxation: this is plastic relaxation by defects as confirmed by HRTEM. Thus, the FDM simulations show that the Ge islands are far from being purely elastically relaxed.

5.3.8 Looking at the (200) forbidden reflection: analysis of the nature and size of defects.

By looking at the Si(200) reflection, which is basis-forbidden for pure Si or Ge bulk, A. Malachias *et al.* [30] observed the presence of atomic ordering inside Ge islands. Previously in the case of implanted Si, we have shown that mapping around the (200) forbidden reflection detects defects and allows to study the presence of defects and to determine the core of defects with respect to distortion and size.

A (h, k) in-plane reciprocal space map was performed around the (200)Si Bragg peak. The intensity along l, ([001] direction) was integrated using a linear position sensitive detector (PSD) (see figure

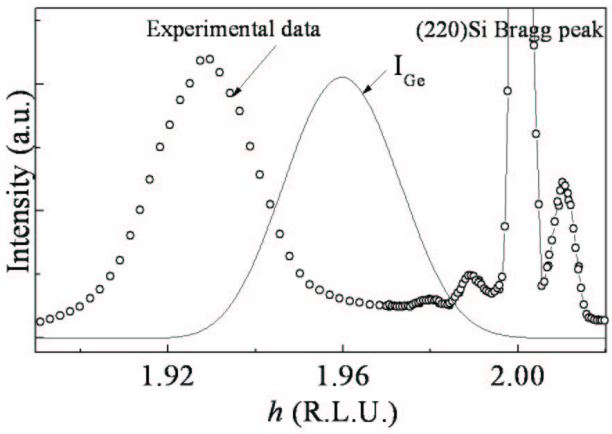

Figure 5.27: Experimental and simulated (I_{Ge}) diffraction patterns of 20nm large and 8nm high QDs near the (220) reflection. The simulation is for an island made of pure Ge.

5.28). The hump-like intensity follows the ⟨111⟩ directions and the projected ⟨110⟩ directions in the plane. According to previous studies and theoretical predictions, the intensity concentrated in streaks along ⟨111⟩ is the characteristic footprint of the presence of faulted dislocation loops (FDLs).

For the first time, by looking at the (200) forbidden reflection, streaks along the < 111 > directions have been observed, revealing the presence of stacking faults inside the Ge islands.

No atomic ordering is thus observed in this sample (see next chapter for more explanation) but stacking faults (SFs) on {111} planes are present. In a diamond structure, extrinsic SFs consist of a double inserted plane, bounded by Frank loops with Burgers vectors **b**=a/3< 111 >. Thus, a stacking fault is made of two parallel {111} discs of radius R, separated by a distance Δ, whose nominal value is $\Delta_0 = a\sqrt{3}/4$.

On the figure 5.28, the four streaks intercept each other at h=1.925. At this position, a maximum of intensity is observed. The intersection of the four streaks corresponds to the position of the maximum of relaxation (h=3.855) of the Ge QDs measured at the (400) reflection. Besides, an asymmetry of the scattered signal is observed at the (200): the scattered intensity is larger for $h < h_{Ge(200)}$.

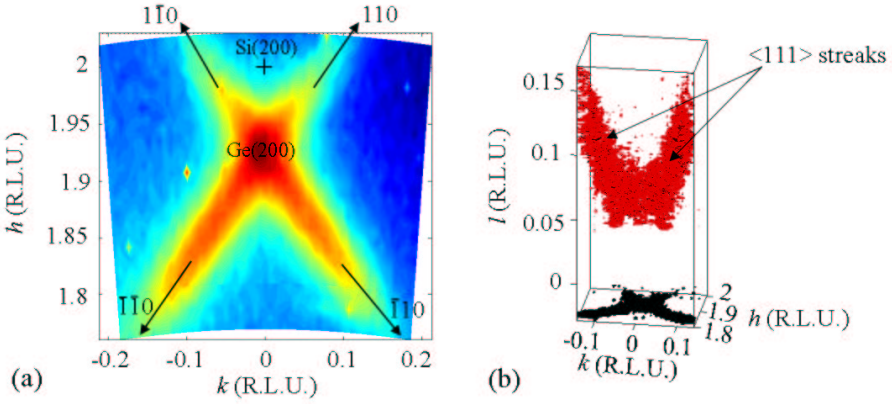

Figure 5.28: (a) Reciprocal space map of diffuse scattering measured around the forbidden reflection **h**=[200]. Figure (b) shows a part of the three dimensional intensity distribution around **h**=[200]. The scattered intensity is concentrated in streaks along ⟨111⟩ directions, perpendicular to the fault planes.

Comparison between the signal induced by defects in implanted Si and in Ge islands.

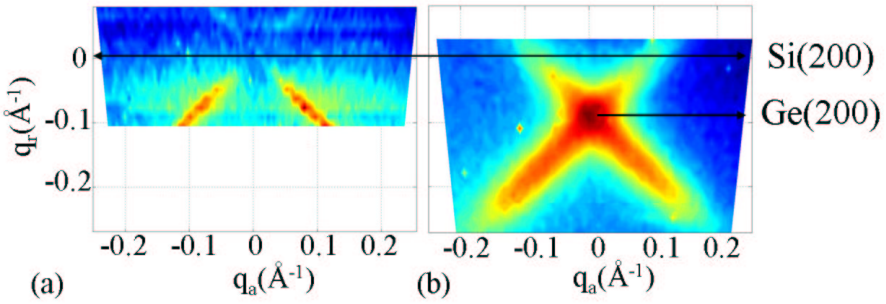

Figure 5.29: Reciprocal space map of diffuse scattering measured around the forbidden reflection **h**=[200] for the Si implanted substrate (a) and for the Ge QDs (b).

The signals induced by defects in implanted Si and in Ge islands (see figure 5.29) present some similarities:

- The scattered intensity is concentrated in streaks along ⟨111⟩ perpendicular to the fault planes.
- The scattered signal is asymmetric: the intensity is maximum for low values of q_r. This is explained by the fact that the two discs which form the extrinsic stacking faults are compressed ($\Delta - \Delta_0 < 0$, where Δ and Δ_0 are the experimental and nominal distances between the two inserted planes forming the stacking fault).

But they present the difference that the intersection of the four streaks shows a minimum of intensity for the implanted Si template and a maximum of intensity for the plastically relaxed Ge islands, which needs to be explained. The (200) reflection is forbidden for pure Ge and Si bulk. Does this statement hold also for 3D confined islands? To answer this question, the diffraction pattern of Ge QDs was calculated around the (200) reflection, using the strain field previously calculated (see Fig. 5.26) and using Eq. 3.8. The *Ge* and *Si* structure factors were determined for a relaxed 20 nm wide and 8 nm high hemispherical Ge island on a Si substrate (see Fig. 5.30 (a)).

In this case, the *Ge* structure factor is not null and presents a maximum at an h position smaller than the position of the (200)Si forbidden Bragg peak. The position of the maximum of scattered amplitude corresponds to the relaxation state of the Ge islands. Thus, relaxed 3D nanostructures yield intensity at basis-forbidden reflections. The h position of the maximum of the scattered intensity is directly linked to the relaxation state of the nanostructures, as h is directly related to the lattice parameter along the [100] direction. The maximum observed at the intersection of the four streaks for the Ge QDs can thus be explained by the scattering of nano-structures which is also strain dependent at a 'basis'-forbidden reflection. The scattering can result either from the *distortion* of the lattice induced by the mismatch, which implies a break of the unit cell symmetry (as shown below), or from *truncated unit cells* at the surface of the QDs. To check the influence of the truncated unit cells on the (200) signal, the *Ge* structure factor of the island has been calculated imposing a null strain field inside the island (see Fig. 5.31 (b)). In this case, the Ge structure factor is not null showing that truncated unit cells give intensity at the (200); the signal is only 10% less intense than the one calculated taking into account the srain field inside the island. The truncated unit cells are thus responsible for 90% of the signal observed at the (200). Compared to the Si implanted substrate, the signal observed at the (200) for Ge dots is not only composed of the scattering induced by defects, but also of the scattering induced by the relaxed nano-structures.

To compare the out-of-plane signal given by defects in Si implanted templates and in Ge dots, the diffuse intensity distribution was measured along q_z (see figure 5.31) at different h or q_r values

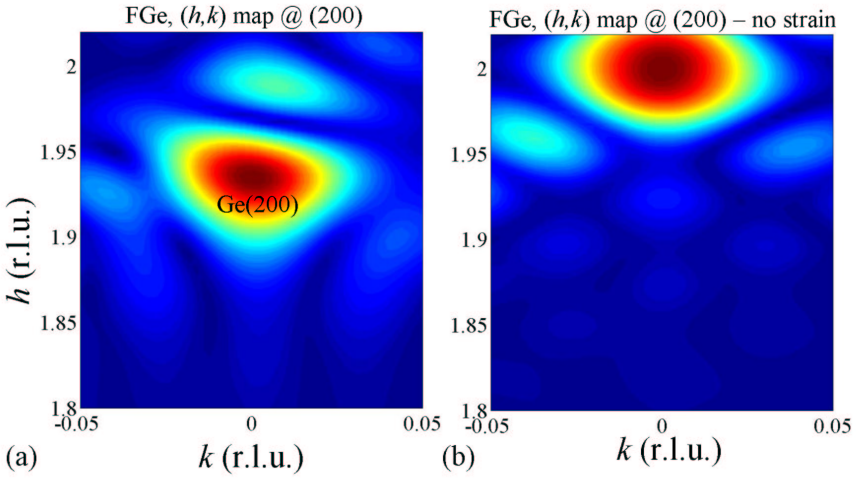

Figure 5.30: *Ge* simulated structure factor of a 20 nm wide and 8 nm high Ge island on a Si patterned substrate taking into account its strain field (a) and with imposing a null strain field inside the Ge island to check the influence of the truncated unit cells at the surface of the island on the (200) signal (b).

along the in-plane projected direction of the {111} streaks and at constant α_i (α_i=1.6α_c for the Si implanted template and $\alpha_i \sim \alpha_c$ for the Ge dots). A hump (1) is observed in the case of the Si implanted substrate. This hump-like intensity is due to the scattering induced by the stacking faults. In the case of the Ge dots, two maxima are observed: (1) a hump-like intensity which is due to the scattering induced by the defects, (2) a peak at $q_{z,critical} = 0.31\text{Å}^{-1}$, $q_{z,critical}$ being the value of q_z for the critical angle α_c. This is due to the grazing incidence geometry, where all scattered intensities are multiplied by the transmission functions T_i and T_f. This peak is not observed in the case of the Si implanted sample. The presence of this peak indicates that the defects are located in a layer close to the surface for the Ge dots. In this case, the DXS is enhanced by the transmission function, which occurs at the critical angle α_f=α_c. In the case of the implanted Si, the intensity enhancement at $q_{z,critical}$ is missing. The absence of the peak indicates that the defects are located in a layer far from the surface. The X-rays first have to pass through the weakly scattering SPER region, before the EOR defects are reached and contribute significantly to the diffuse X-ray scattering (see Fig. 5.1) [15].

To disentangle the contribution of the relaxed nanostructures from the mean contribution of the defects, the integrated intensity of the hump-like intensity, named (1) in figure 5.31(b) was measured along the ⟨111⟩ direction (see figure 5.32). In other words, this is a measurement of the intensity along the rod linking the (1$\bar{1}$1)Ge and (311)Ge Bragg peaks and passing through the (200)Ge Bragg peak. Like the signal observed for the implanted Si, it presents a minimum of intensity around the (200)Ge forbidden reflection. The minimum is displaced towards higher h values. An asymmetry of the signal is also observed. Contrary to the Si implanted template, additional peaks are observed at non integer values of h, k and l: $\frac{1}{3}(5\bar{1}1)$ and $\frac{1}{3}(822)$. This means that the defects are more complex than single stacking faults. We show in the next section that these peaks are a signature of the presence of twins.

The fit of the cross-section of the measured streak gives the mean radius $R_0 = (6.5 \pm 0.5)$nm of the faults (see Fig. 5.31 (b)).

Twin faulting on the {111} planes.

Figure 5.33 shows sequences of 111 layers in the case of no defect, a deformation fault and a twin fault. Since the upper part of Fig. 5.33 (c) is the twin or mirror of the lower part, a growth fault is also a twin fault. In the following, a direct stacking, *AaBb*, *BbCc* or *CcAa* is noted Δ and inversely,

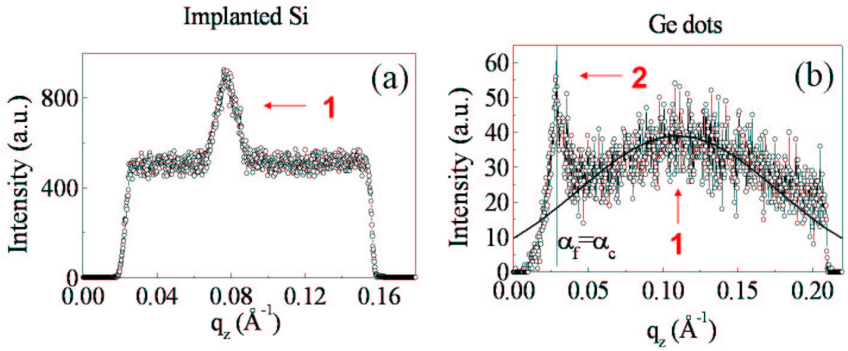

Figure 5.31: Diffuse intensity distribution measured along q_z for a given h value in the region of scattered intensity around the (200) reflection for the Si implanted substrate (α_i=0.35°) (a) and for the Ge QDs (α_i=0.13°) (b).

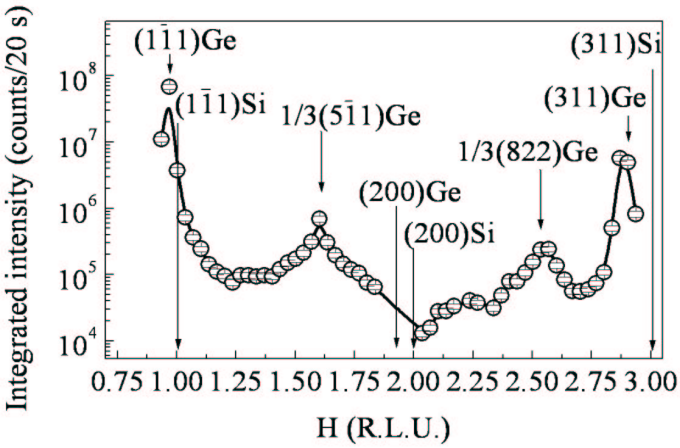

Figure 5.32: Integrated intensity (points) along a < 111 > rod passing through the (1$\bar{1}$1)Ge, (200)Ge and (311)Ge Bragg peaks.

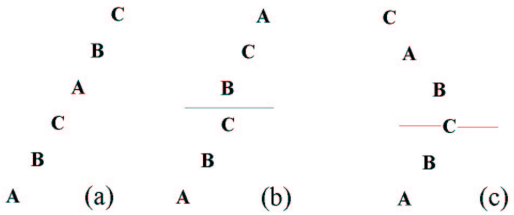

Figure 5.33: Sequences of 111 layers expressed in terms of A, B and C positions. The layers a, b and c have been omitted. (a) Correct sequence. (b) A deformation fault. (c) A growth or twin fault.

an indirect stacking, $AaCc$, $CcBb$ or $BbAa$ is noted ∇. The ...$\nabla\nabla\nabla$... crystal is the symmetric of the ...$\Delta\Delta\Delta$... crystal after a (111) plane symmetry and an inversion. The symmetry is described by the matrix [31, 32]:

$$\begin{pmatrix} -1/3 & 2/3 & 2/3 \\ 2/3 & -1/3 & 2/3 \\ 2/3 & 2/3 & -1/3 \end{pmatrix}$$

In the reciprocal space related to the ...$\Delta\Delta\Delta$... crystal, the diffraction conditions fulfill: $h+k+l = 4n$ or h, k, l odd. For the ...$\nabla\nabla\nabla$... crystal, the (h_1, k_1, l_1) Miller indexes can be written:

$$h_1 = 1/3(-h+2k+2l) \quad (5.21)$$
$$k_1 = 1/3(2h-k+2l) \quad (5.22)$$
$$l_1 = 1/3(2h+2k-l) \quad (5.23)$$

For instance, the(311)+n(111) Bragg peaks of the ...$\Delta\Delta\Delta$... crystal become (022)+(n+1/3)(111) Bragg peaks in the reciprocal space of the ...$\nabla\nabla\nabla$... crystal. The (nnn) peaks are unchanged ($n \in Z$).

Figure 5.34 shows the Bragg peaks of the direct stacking (Δ) and the additionnal Bragg peaks of the indirect stacking (black ∇). Among the additional Bragg peaks, the $\frac{1}{3}(5\bar{1}1)$ and $\frac{1}{3}(822)$ reflections can be observed. The experimental peaks observed in figure 5.32 is thus the result of the presence of twin faults. From the FWHM of the additional peaks along the [111] direction, the size of the twin fault is given by $2\pi/\Delta q_{111}$=58 Å. Hence, on the average, the twin faults are composed of ∼18 {111} planes.

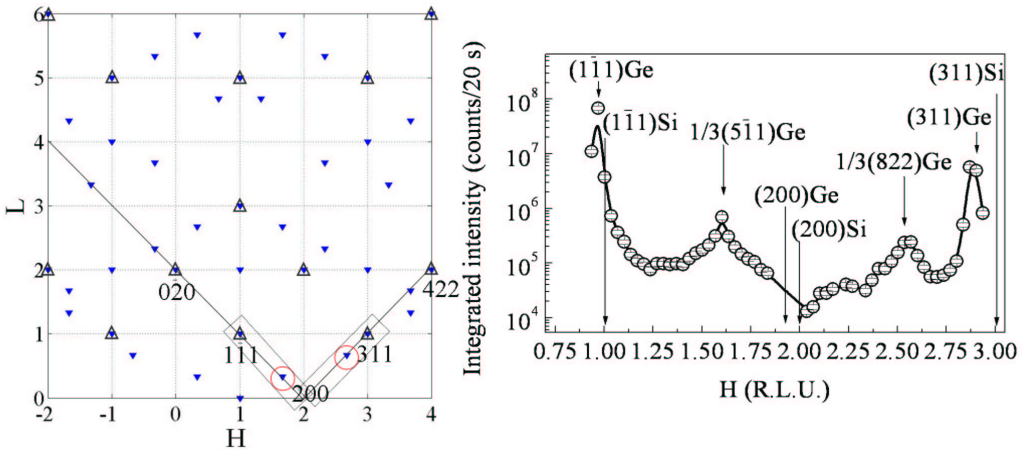

Figure 5.34: Reciprocal space map of a twin crystal. The (1$\bar{1}$0) plane is drawn. All the peaks verify $x-y=2$. The fourfold symmetry around the [001] direction has been taken into account. The Bragg peaks of the direct and indirect stackings are labelled Δ and ∇, respectively. The experimentally observed twin Bragg peaks at $\frac{1}{3}(5\bar{1}1)$ and $\frac{1}{3}(822)$ are circled.

Allowed vs quasi-forbidden reflection in the case of nanostructures.

In implanted Si substrates, the presence of defects were observed by looking at allowed and basis-forbidden reflections and along the {111} rods linking them. Close to an *allowed reflection*, the Huang diffuse scattering is dominant. In this case, the *long-range displacement field* of the defects is probed. By contrast, close to the (200) *forbidden reflection*, the intensity is mainly induced by the *core* of the defect. In the case of nanostrutures, no direct signature of defects such as streaks along the [111] direction is observed near an *allowed* reflection (Figs. 5.35 (b) and (c)), contrary to the case

of the Si implanted substrate (Fig. 5.35 (a)). The streaks coming from the defects are hidden by the intensity scattered by the nanostructures. Indirectly, by simulating the signal observed at an allowed reflection by using the Finite Difference Method, it is possible to detect whether islands are elastically or plastically relaxed, thus to detect the presence of defects inside nanostructures. Nevertheless, contrary to X-rays, the FDM simulations do not allow to directly determine the nature, the density and the average size of the defects and TEM does not provide statistically average information of the size of the defects and the compression of their core.

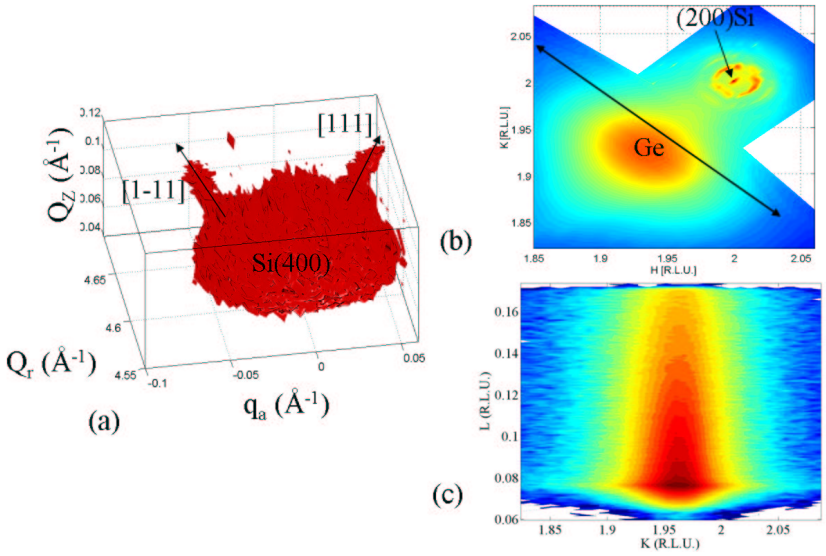

Figure 5.35: (a) 3D reciprocal space map of diffuse scattering measured at **h**=[400] for the Si implanted substrate. $< 111 >$ streaks indicate the presence of stacking faults inside the Si template. (b) (220) reciprocal space map of the Ge QDs. To detect the presence of $< 111 >$ streaks, a scan indicated by the line in figure (b) has been performed by using the PSD. No streaks are observable. The diffuse scattering induced by the Ge islands hides the signal coming from defects.

5.4 Synthesis

In summary, we have demonstrated that diffuse X-ray scattering around a forbidden reciprocal lattice point is well suited for the study of extrinsic stacking faults in Si and Ge bulk and islands. We have shown that the diffuse scattering from the distorted neighborhood of the defects is almost suppressed in this case which makes it possible to access directly to the atomic structure of the core of the defects. Looking at the (200) basis-forbidden reflection directly gives the evidence of the presence of planar defects inside 3D nanostructures or bulk, such as stacking faults parallel to {111} planes. More generally, any defect composed of faulted planes can be characterized by measuring the intensity along rods of scattering perpendicular to these planes. Close to Bragg peaks, the displacement field of the defects is characterized; far from Bragg peaks, and over an extended range, small displacements of the planes in the core of the defects can be determined. From the comparison of the measured intensity with a simulation based on the continuum displacement model we have revealed a compression of the {111} planes in the defect cores for implanted Si. Thus, diffuse X-ray scattering near forbidden reflection appears as a fine, unique and destruction-free technique to detect stacking faults and characterize their small compression in the core. This X-ray method can

be easily combined with in-situ growth [33] to detect, for instance, the formation of stacking faults inside nanostructures. The method can also be used for other defects, as long as the lattice of the defect cores contributes to the scattered intensity close to a reflection that is forbidden for the host lattice. The X-ray scattering profile near forbidden reflections depends on the nature of the defects.

Bibliography

[1] E. Chason, S. T. Picraux, M. Poate, J. O. Borland, M. I. Current, T. Diaz de la Rubia, D. J. Eagleasham, O. W. Holland, M. E. Law, C. W. Magee, J. W. Mayer, J. Melngailis, and A. F. Tasch, J. Appl. Phys. **81**, 6513 (1997).

[2] L. Capello, T. H. Metzger, V. Holý, M. Servidori and A. Malachias, J. Appl. Cryst. **39**, 571-581 (2006).

[3] J. Stangl, V. Holý, and G. Bauer, Rev. Mod. Physics, **76**, (2004).

[4] J. G. Fiorenza, G. Braithwaite, C. W. Leitz, M. T. Currie, J. Yap, F. Singaporewala, V. K. Yang, T. A. Langdo, J. Carlin, M. Somerville, A. Lochtefeld, H. Badawi, and M. T. Bulsara, Semicond. Sci. Technol. **19**, L4 (2004). Fiorenza

[5] K. Nordlund, J. Appl. Phys. **91**, 5 (2002).

[6] K. Nordlund, T. H. Metzger, A. Malachias, L. Capello, P. Calvo, A. Claverie, F. Cristiano, J. Appl. Phys., (**98**) 073529 (2005).

[7] P. Klang, V. Holý,J. Kubena, R. Stoudek and J. Sik, J. Phys. D:Appl. Phys. (**38**) A105-A110 (2005).

[8] A. Claverie, B. Colombeau, B. De Maudit, C. Bonafos, X. Hebras, G. Ben Assayag, F. Cristiano, Appl. Phys. A, (**76**) 1025 (2003).

[9] M. A. Krivoglaz, *X-Ray and Neutron Diffraction in Nonideal Crystals*, (Springer 1996).

[10] U. Pietsch, V. Holý, and T. Baumbach, *High-Resolution X-Ray Scattering: From Thin Films to Lateral Nanostructures*, (Springer 2004).

[11] H. Trinkaus, Phys. Stat. Solidi (b) **51**, 307 (1972), **54**, 209 (1972).

[12] A. Claverie, *private communication*

[13] R. Pinacho, M. Jaraiz, P. Castrillo, J. E. Rubio, I. Martin-Bragado and J. Barbolla, Mater. Sci. Eng. B, (**114 − 115**) 135-140 (2004).

[14] L. Capello, T.H. Metzger, Mat. Sci. and Engineering B,**77 − 81** 114-115 (2004).

[15] L. Capello, *Thesis of the Universty Claude Bernard-Lyon I and of the University of Torino*, Mai 2005.

[16] M. Sztucki, T.H. Metzger, J. Peisl, J.R. Patel, Appl. Phys. Lett., **76** 2698 (2000).

[17] P. H. Dederichs, J. Phys. F: Metal Phys. **3** 471 (1973); P. H. Dederichs, Phys. Rev. B **1**, 1306 (1970); P. H. Dederichs, Phys. Rev. B **4**, 1041 (1971).

[18] P. Ehrhart, T. Trinkaus, B. C. Larson, Phys. Rev. B **25** 834 (1982).

[19] K. Nordlund, P. Partyka, R. S. Averback, I. K. Robinson, P. Ehrhart, J. Appl. Phys., (**88**) 5 (2000).

[20] J. P. Hirth and J. Lothe, *Theory of Dislocations* , (Krieger 1992).

[21] K. Nordlund, U. Beck, T. H. Metzger, and J. R. Patel, Appl. Phys. Lett. **76**, 846 (2000).

[22] M.-I. Richard, T. U. Schülli, G. Renaud, E. Wintersberger, G. Bauer, and V. Holý, Phys. Rev. B, submitted (2007).

[23] E. Vlieg, J. Appl. Cryst. **30**, 532-543 (1997).

[24] F. H. Stillinger and T. A. Weber, Phys. Rev. B **31**, 5262 (1985).

[25] D. T. Keating and A. N. Goland, Acta Cryst. A: Cryst. Phys., Diffr., Theor. Gen. Crystallogr. **27**, 134 (1971).

[26] D. Y. Ryu, K. Shin, E. Drokenmuller, C. J. Hawker, T. P. Russell, Science (**308**), 236 (2005).

[27] T. S. Yoon, Z. Zhao, W. Feng, B. Li, J. Liu, Y.-H. Xie, D. Y. Ryu, T. P. Russell, H.-M. Kim, K. B. Kim, J. Cryst. Growth (**290**), 309 (2006).

[28] G. Renaud, A. Barbier and O. Robach, Phys. Rev. B (**60**), 5872 (1999).

[29] V. Ranjan, G. Allan, C. Priester and C. Delerue, Phys. Rev. B (**68**) 115305 (2003).

[30] A. Malachias, T. U. Schülli, G. Medeiros-Ribeiro, L. G. Cancado, M. Stoffel, O. G. Schmidt, T. H. Metzger and R. Magalhães-Paniago, Phys. Rev. B (**72**), 165315 (2005).

[31] B. E. Warren, *X-ray diffraction*, Dover Publications (1969).

[32] P. Guénard, Thèse de l'Université-Grenoble I (Octobre 1996)

[33] *http://www.esrf.eu/UsersAndScience/Experiments/CRG/BM32*

Chapter 6

Atomic ordering and stacking faults in Ge islands on Si(001).

In this chapter, the impact of growth temperature, growth rate and annealing on the presence of compositional ordering and/or defects inside Ge nanostructures grown on Si(001) is discussed. Before that, we present an X-ray formalism which has been developed to evidence that compositional ordering leads to the observed scattering features at the (200) forbidden reflection.

6.1 Introduction

The presence of atomic ordering inside Ge islands has been recently observed by A. Malachias *et al.* [1]. By measuring basis-forbidden X-ray reflections of Ge:Si(001) islands such as the (200) forbidden reflection, they concluded to the existence of atomically ordered regions inside these nanostructures. Figure 6.1 shows the intensity observed around the allowed Si(400) and around the Si(200) reflection which is forbidden for pure Si or Ge or disordered alloys for a deposit of 6.7 ML of Ge on Si(001) at 620°C [1]. The (200) X-ray scattering map can be well explained and fitted by Si/Ge ordered domains. Contrary to the (400) map, a minimum of intensity can also be observed along $q_a = 0$ in the (200) map. This was interpreted by A. Malachias as arising from ordered domains separated by antiphase boundaries. Thus, mapping around the (200) forbidden reflection can give new insights of the Si/Ge growth.

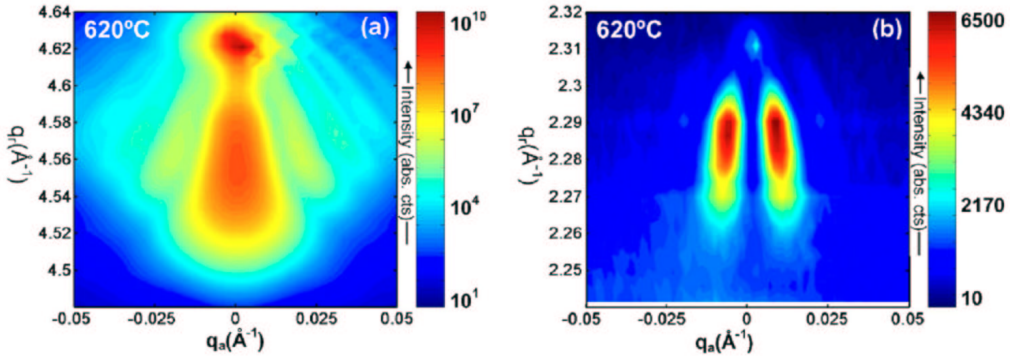

Figure 6.1: Measured $q_r - q_a$ (400) and (200) maps for a sample grown at 620°C [1].

Besides, in the previous chapter, we have also used a forbidden reflection to investigate the structure

of extrinsic stacking faults in implanted Si and in Ge nanostructures. We demonstrated that scanning along the [111] direction around the (200) forbidden reflection allows to reveal the presence of planar defects such as '111' stacking faults. This demonstrates the importance of scanning around the (200) forbidden reflection to highlight defects or atomic ordering inside the nanostructures.

In this chapter, the origin of atomic ordering is discussed. An X-ray formalism is developed to model the atomic ordering. Then, the impact of growth temperature, growth rate and annealing on the presence of compositional ordering and/or defects inside Ge nanostructures grown on Si(001) is presented.

6.2 Atomic ordering in Ge islands on Si(001)

The history of ordering in semiconductor alloys began in 1985 by the surprising discovery of Kuan *et al.* [2] that AlGaAs grown on (110)GaAs at 700°C by molecular beam epitaxy (MBE) spontaneously orders during the growth process. The same year, Ourmazd and Bean [3] reported the formation of {111} ordering in SiGe alloys grown on (001)Si by MBE.

Ordering has extremely important practical consequences. It induces the reduction of the bandgap energy [4]. A benefit of ordering is the use of order/disorder boundaries for the production of heterostructures [5] without any change in the composition.

6.2.1 Origin of the atomic ordering

The ordering phenomena in SiGe thin films were first explained combining strain and thermodynamic arguments [6, 7]. Then, Müller *et al.* [8] showed that strain is not a necessary condition for ordering by observing superstructure reflections from unstrained alloy substrates. By simulating the electron diffraction patterns, they concluded that Ge and Si atoms belong to a pseudo-diamond structure, called RS_2. Thereby, the initially $Fd3m$ cubic symmetry of the random alloy is reduced to the trigonal space group $R3m$. This loss of symmetry can influence the electronic band gap structure. In 1990, LeGoues *et al.* [10] evidenced that ordering is not an *equilibrium* phenomenon. It is linked to surface reconstruction as they did not observe superstructure reflection at the non reconstructed 1x1 film whereas they observed superstructure reflections at the 2x1 reconstructed alloy. Besides, films grown on Si(111) substrates do not exhibit ordering. In addition, the occurence of the ordering in other semiconductor systems such as InGaAs(001) is apparently related to the epitaxial growth process and the prevailing surface reconstructions [14].

A thermodynamic first-principles calculation [15] shows that atomic ordering is unstable with regard to disordering. Kinetic origin of ordering has been continuously corroborated during the last years [11, 12, 13].

In 1989, Kelires and Tersoff [16] simulated the equilibrium alloy properties at the (2x1)SiGe reconstructed surface. They showed that the composition varies non-linearly with depth. A strong segregation of Ge to the top surface layer (called layer 1) was found to occur as Ge atoms have a lower surface energy compared to Si. The first subsurface layer (called layer 2) was strongly composed of Si atoms. The next subsurface layers (called layers 3 and 4) show a different composition compared to the bulk composition: a lateral ordering of Si and Ge atoms was shown to occur to the two different sites of the (2x1) unit cell. These results were explained by taking into account the local stress field beneath the dimerised surface. Atomic sites are either under compression or under tension. Kelires and Tersoff found that sites under compression would favour occupation by the smaller Si atoms, while sites under tension would favour occupation by the larger Ge atoms to lower the strain energy. They thus showed that the surface dimer reconstruction induces subsurface stress ordering. If dimer-induced subsurface stresses are responsible for the ordering, then if one can completely remove or reduce the surface dimers, the ordering should be eliminated or reduced. LeGoues *et al.* [10] demonstated the above effect for SiGe layers using Sb as a surfactant to destroy the (2x1) surface recontruction. The absence of surface dimer bonds resulted in no ordering.

6.2.2 Understanding the formation of anti-phase boundaries

The presence of atomic ordering inside Ge islands grown on Si(001) by molecular beam epitaxy has been previously concluded by A. Malachias [1]. Intensity was observed around the Si(200) reflection which is forbidden for pure Si or Ge (see Fig. 6.1 (b)). A minimum of intensity was also measured along q_a or $k = 0$. This was explained by the presence of anti-phase boundaries along the $< 100 >$ directions between the ordered domains. The waves scattered by the ordered domains interfere thus destructively along k=0. GeSi islands are not only atomically ordered but, moreover, subdivided into domains by antiphase boundaries (APBs). The distances between APBs, being equivalent to the widths of the domains, are strongly dependent on growth temperature and growth rate. APBs are the drawbacks to deteriorate electronic properties, *e.g.* they reduce the carrier mobilities [17].

Several atomic arrangements have been proposed for a SiGe ordered alloy. Some of those are shown schematically in Fig 6.2. and are labelled $MS1$, $RS1$, $RS2$ and $RS3$ [18]. The common features of the ordered structures are the presence of compositional ordering along $< 111 >$ directions and a 2x2x2 superlattice cell. The $RS3$ structure, shown in Fig. 6.2 (d) and proposed in references [18, 11, 12, 13] is more flexible than the others since it incorporates four parameters α, β, γ and δ.

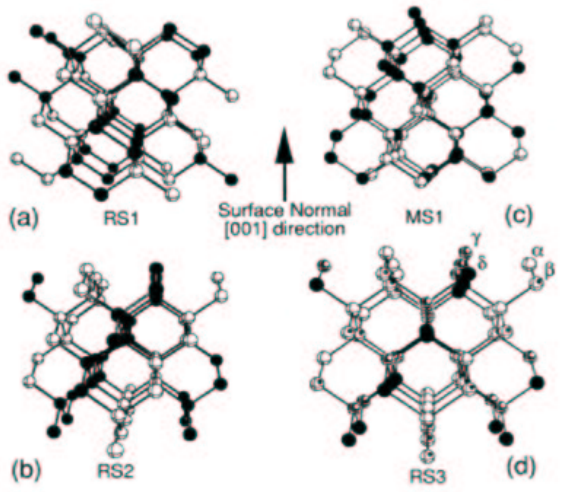

Figure 6.2: Structures for $Si_{0.5}Ge_{0.5}$. The white and black atoms correspond to Ge and Si atoms, respectively. (a) $RS1$ model, (b) $RS2$ model (c) $MS1$ model, (d) RS3 model and (d) Schematic representation of the Si/Ge atomic ordering arrangement in the RS3 model. α and β correspond to the probability of finding Ge atoms in (α, β) sites and δ and γ correspond to the probability of finding Si atoms in (δ, γ) sites.

α and β correspond to the probability of finding Ge atoms in (α, β) sites and δ and γ correspond to the probability of finding Si atoms in (δ, γ) sites (see Fig. 6.3). If $\alpha = \beta$, $\delta = \gamma$, then the model becomes $RS2$. The $RS2$ model can be directly rejected as it fails to explain the presence of intensity at the (200) reflection [18].

As the ordering appears only when (001) or vicinal (001) substrates are used, ordering occurs as a surface phenomenon and cannot be explained solely by bulk crystal thermodynamics. A theory using Monte Carlo simulations on Si_xGe_{1-x} predicted energetic stability of a near-surface structure with larger Ge atoms beneath dangling bonds and smaller Si atoms beneath dimers due to compressive stress caused by the dimer formation [16]. Ordering in Si_xGe_{1-x} shows stacking in $< 111 >$ directions. This is a natural consequence of (2x1) (the ordered directions are [-111] and [1-11]) and (1x2) (the ordered directions are [11-1] and [-1-1-1]) domains coexisting on a (001)SiGe surface. X-ray diffraction analyses have proven the phase relation between the atomic arrangements of Si and Ge and the positions of dimers and dangling bonds for CuPt-type ordering for SiGe [19, 20].

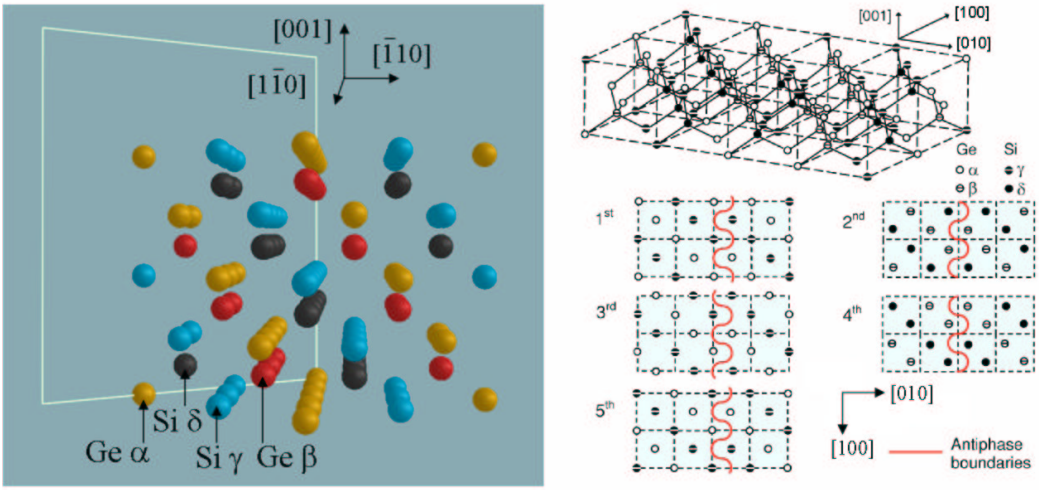

Figure 6.3: (a) and (b) Schematic representation of the Si/Ge atomic ordering arrangement in the RS3 model. Ge-rich sites (α, β) correspond to yellow and red atoms in the left insert and white atoms in the right insert; Si-rich sites (δ, γ) correspond to blue and black atoms in the left insert and black atoms in the right insert. In the right insert, five atomic layers along [001] are shown to indicate antiphase boundaries in each layer.

Jesson *et al.* [Jesson] proposed a kinetic mechanism of SiGe ordering which is associated with dimer formation. The ordering results from a combination of surface segregation and atomic exchange processes at kink sites on the steps. This model which was then used by A. Malachias *et al.* [21] explains how SiGe order arises naturally at monolayer step edges during the growth of coherent 2D islands without the need of atomic rearrangement after the deposition of a complete bilayer. It also explains the formation of anti-phase boundaries along $< 100 >$ directions.

Another simple model of ordering is the zinc-blende type ordering (see Fig. 6.4), which is a particular case of the $RS3$ model ($\alpha = \beta = \gamma = \delta = 1$). This model will be used in the following for numerical simulation of the intensity at the (200) reflection.

6.2.3 The different classes of reflections.

As mentioned in chapter 2, the allowed diamond-sructure reflections possess hkl all even with $h+k+l=4n$ or hkl all odd. The second class of reflections are the integral basis-forbidden reflections for which $h+k+l=4n+2$ all even and nonzero. A small, but nonzero structure factor for basis-forbidden reflections is known to be associated with the radially antisymmetric contribution to the charge distribution in Si and Ge [22]. Note that this structure factor is identically zero when h, k, or l is zero. The third class of reflections includes the lattice-forbidden reflections for which h, k and l are mixed. For these, the structure factor is exactly zero in the diamond structure or in any other fcc-based structure. A non-zero measurements indicates the presence of ordering inside the cubic unit cell [18]. The fourth class of reflections involves the half-integer hkl of the form $(i/2, j/2, m/2)$, where i, j and m are odd integers. These reflections are lattice forbidden. Their presence indicates ordering inside double unit cells.

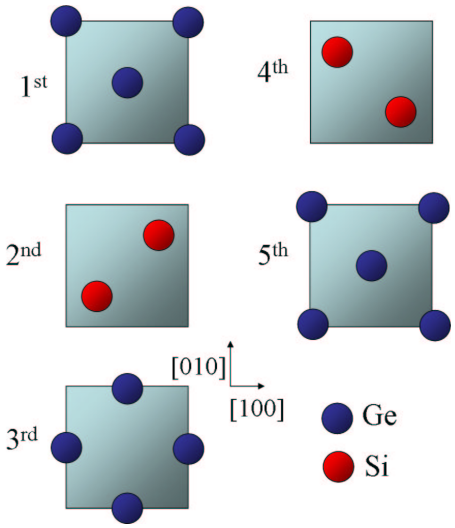

Figure 6.4: The Zinc-blende structure. Five atomic layers along [001] are shown.

6.2.4 Determination of the size and number of ordered domains.

To determine the size and the number of ordered domains separated by antiphase boundaries, an analytical model has been proposed, based on which numerical simulations have been performed.

Analytical model.

For simplicity, let us consider a parallelepipedic island made of ordered domains, consisting of M, N and P unit cells with lattice parameters **a**, **b** and **c** along the x, y and z directions, respectively. Let us also introduce antiphase boundaries along the [010] direction. The islands are thus composed of V domains, shifted from each other by **b**/2. They are present along the y direction, each of equal length $N' = N/V$ unit cells. Then, the scattered amplitude can be written as:

$$\begin{aligned} A &= F_{unit\ cell} \sum_{m=0}^{M-1} \mathrm{e}^{2\mathrm{i}\pi(hm)} [\sum_{n=0}^{N'-1} \mathrm{e}^{2\mathrm{i}\pi(kn)} + \mathrm{e}^{\mathrm{i}\pi} \sum_{n=N'}^{2N'-1} \mathrm{e}^{2\mathrm{i}\pi(kn)} \\ &\quad + \sum_{n=2N'}^{3N'-1} \mathrm{e}^{2\mathrm{i}\pi(kn)} + \ldots + \mathrm{e}^{\mathrm{i}\pi(V-1)} \sum_{n=(V-1)N'}^{VN'-1} \mathrm{e}^{2\mathrm{i}\pi(kn)}] \sum_{p=0}^{P-1} \mathrm{e}^{2\mathrm{i}\pi(lp)} \end{aligned} \tag{6.1}$$

Let us now consider the scattering around the (200) Bragg reflection: $h = 2 = aq_r/(2\pi)$, $k = aq_a/(2\pi)$ and $l = aq_z/(2\pi) = 0$. q_r and q_z are fixed, eq. 6.2 can be simplified to

$$A = M \cdot P \cdot F_{unit\ cell} \sum_{n=0}^{N'-1} \mathrm{e}^{\mathrm{i}q_a na} \sum_{v=1}^{V} (-1)^{v-1} \mathrm{e}^{\mathrm{i}q_a N' a(v-1)} \tag{6.2}$$

$$= M \cdot P \cdot F_{unit\ cell} \sum_{n=0}^{N'-1} \mathrm{e}^{\mathrm{i}q_a na} \sum_{v=0}^{V-1} \mathrm{e}^{\mathrm{i}v(q_a N' a+\pi)} \tag{6.3}$$

The solution for the geometrical series is

$$\sum_{n=0}^{N'-1} x^n = \frac{x^{N'} - 1}{x - 1} \tag{6.4}$$

Thus,

$$A = M \cdot P \cdot F_{unit\ cell} \frac{e^{iq_a N'a} - 1}{e^{iq_a a} - 1} \cdot \frac{e^{iV(q_a N'a+\pi)} - 1}{e^{i(q_a N'a+\pi)} - 1} \tag{6.5}$$

The scattered intensity $I(q_a)$ is given by the absolute square of the amplitude:

$$\begin{aligned} I(q_a) &= AA^* && (6.6)\\ &= cst \cdot \left| \frac{e^{iq_a N'a} - 1}{e^{iq_a a} - 1} \cdot \frac{e^{iV(q_a N'a+\pi)} - 1}{e^{i(q_a N'a+\pi)} - 1} \right|^2 && (6.7)\\ &= cst \cdot \frac{\sin^2(\frac{1}{2}q_a N'a)}{\sin^2(\frac{1}{2}q_a a)} \cdot \frac{\sin^2[\frac{1}{2}V(q_a N'a+\pi)]}{\sin^2[\frac{1}{2}(q_a N'a+\pi)]} && (6.8) \end{aligned}$$

Depending on the parity of the number of domains V, the scattered intensity can be written:

$$\begin{aligned} I(q_a) &\propto \frac{\sin^2(\frac{1}{2}q_a N'a)}{\sin^2(\frac{1}{2}q_a a)} \cdot \frac{\sin^2[\frac{1}{2}V q_a N'a]}{\cos^2[\frac{1}{2}q_a N'a]}\ if\ V = 2n, n \in \aleph && (6.9)\\ &\propto \frac{\sin^2(\frac{1}{2}q_a N'a)}{\sin^2(\frac{1}{2}q_a a)} \cdot \frac{\cos^2[\frac{1}{2}V q_a N'a]}{\cos^2[\frac{1}{2}q_a N'a]}\ if\ V = 2n+1, n \in \aleph && (6.10) \end{aligned}$$

For two domains, the preceding equations can be written

$$I(q_a) \propto \frac{\sin^2(\frac{1}{2}q_a N'a)}{\sin^2(\frac{1}{2}q_a a)} \cdot \sin^2[\frac{1}{2}q_a N'a] \tag{6.11}$$

The above formula reveals that the formula given in Ref. [1] is not correct.

Discussion of the domain size $N'a$.

In the case of a simple zinc-blende ordering, the Ge and Si planes alternate along the [001] direction (see Fig. 6.4) and the size of the unit cell in the [010] direction is a_{Si}, which implies that $a = a_{Si}$. In the case of the complex $RS3$ model for instance, the size of the unit cell in the [010] direction is $2a_{Si}$, which means that in this case a=$2a_{Si}$. In all cases, the domain size is given by $N'a$.

Influence of the number of domains and their sizes.

Using the formula 6.9 or 6.10, it is then possible to determine the influence of the number of domains and their sizes along q_a in the diffraction patterns observed at the (200) forbidden reflection. Figure 6.5 (a) shows the simulated intensity for two, three, four and five domains of equal length of 300 Å. The position of the first maxima depends weakly on the number of domains. The distance between the two intensity maxima increases with the number of domains, while the width of the lobes decreases. The intensity for two domains of equal size have been simulated for different domains sizes $N'a$ (Fig. 6.5 (b)). With increasing domain size, the distance between the two lobes decreases, as well as their widths.

Influence of the size of the ordered domains and of the size pa of the anti-phase boundary in the case of two ordered domains.

In section D.1, we made the hypothesis that the sizes of the ordered domains were identical. In the case of two ordered domains of different sizes Na and $N'a$=$(N + \Delta N)a$, one can write:

$$A(q_a) = cst \cdot \frac{e^{iq_a Na} - 1}{e^{iq_a a} - 1} - e^{iq_a Na} \frac{e^{iq_a (N+\Delta N)a} - 1}{e^{iq_a a} - 1} \tag{6.12}$$

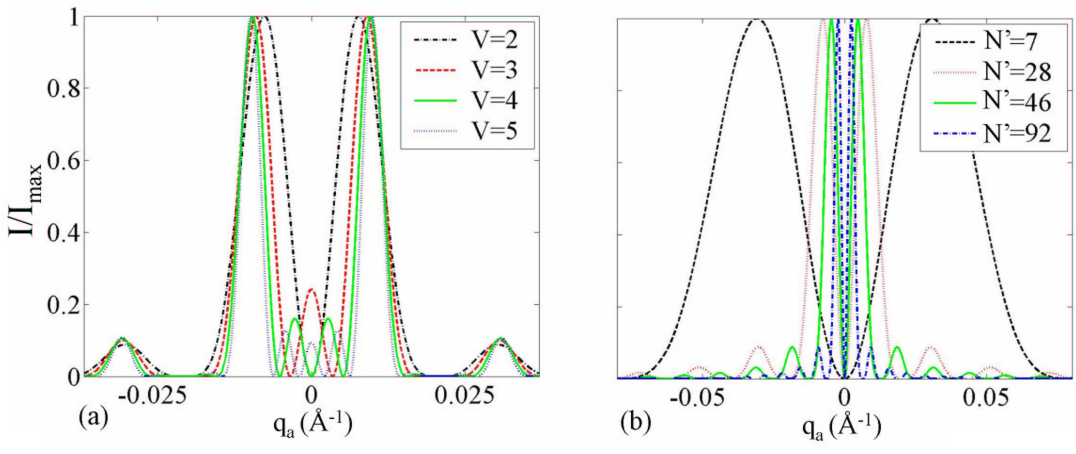

Figure 6.5: (a) Simulated intensity for two, three, four and five domains of 300 Å each, V denotes the number of domains. (b) Simulated intensity for two domains of equal size, for different domain sizes $N'a_{Si}$, where N' is the number of unit cells and a_{Si} is the lattice parameter of Si bulk.

We can also suppose that between two ordered domains, we have the presence of a disorded zone of length pa ($p \in \aleph$) (*i.e.* pa is the size of the antiphase boundary). In this case, the scattered amplitude can be written as:

$$A(q_a) = cst \cdot \frac{e^{iq_a Na} - 1}{e^{iq_a a} - 1} + e^{i(\pi + pq_a a)} e^{iq_a Na} \frac{e^{iq_a (N+\Delta N)a} - 1}{e^{iq_a a} - 1} \tag{6.13}$$

Figure 6.6 shows that with increasing ΔN (N'=N+ΔN) and p (the number of unit cells forming the antiphase boundary), the position and the intensity of the second maxima are modified, as well as the full width at half maximum, which is drastically changed.

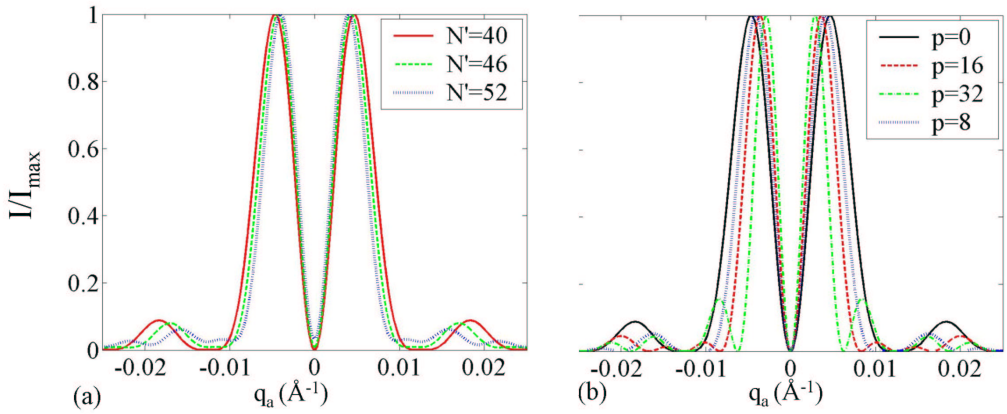

Figure 6.6: (a) Simulated intensity for two ordered domains. One has a size of $40a$ and the size ($N'a$) of the other domain varies: $40a$, $46a$ and $52a$. (b) Simulated intensity for two domains of same size ($40a$) separated by an antiphase boundary of different sizes: $8a$, $16a$ and $32a$. p indicates the number of unit cells forming the antiphase boundary.

With increasing ΔN, the intensity of the second maxima is decreased and their position is displaced towards q_a=0. With increasing length of the disordered zone (pa), the position of the first and second

maxima is displaced towards q_a=0. Depending on p, the intensity of the second maxima can be higher or lower than the intensity for p=0.

To sum up, the width of the first lobes or maxima depends drastically on

- the number of domains and their orientations
- the domain size
- the differences between the sizes of adjacent domains
- the width pa of the antiphase boundary

The model proposed by A. Malachias [1] did not take into account the differences between the sizes of adjacent domains and the width pa of the antiphase boundary, which strongly affect the diffraction patterns.

Numerical simulations.

Numerical simulations were performed to validate the analytical model, to look at the impact of the antiphase boundaries in both [100] and [010] directions, to evaluate the number of ordered domains and to look at the influence of the strain.

The calculation was done for a single 115 nm dome-shaped island. As a first approximation, zinc-blende ordering (see Fig. 6.4) instead of the complex RS_3 ordering was simulated. The choice of this ordering does not affect the in-plane (200) reciprocal space map. The position of the atoms were calculated in the frame of an elastic model with the FDM method.

Two, four or nine cylindrical or parallelepipedic-shaped domains with opposite phases and a size of 270 Å were used to simulate the (200) reciprocal space map.

Angular scans are not sensitive to strain. The scattered intensity is thus directly related to the Fourier transform of the shape of the ordered domains (if neglecting possible mosaic spread). In the case of the numerical simulations, the q_a line scans are at a fixed q_r position corresponding to the q_r position of maximum of Ge intensity observed in the simulated (200) map. Figure 6.7 shows the good agreement between the numerical simulations and the analytical model.

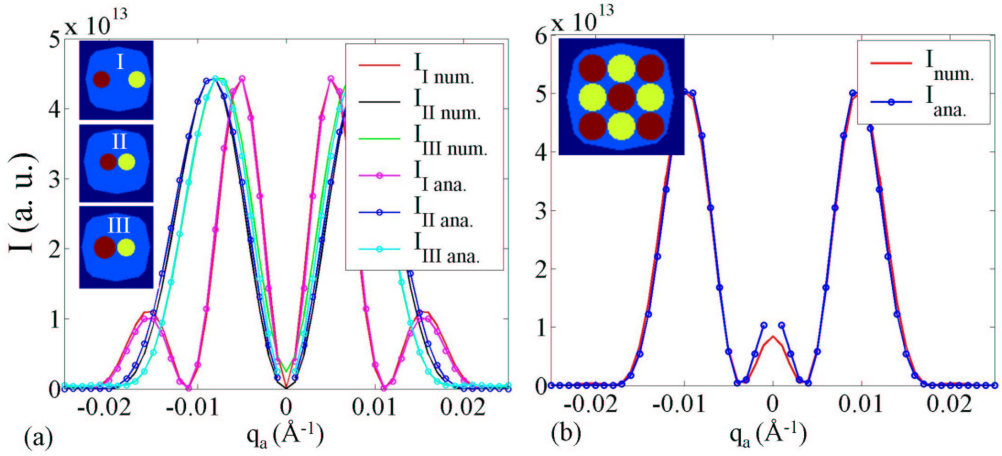

Figure 6.7: (a) Numerical and analytical simulations of two ordered domains of same size (cases I and II) and of **different** sizes (case III). The width of the antiphase-boundary is changed between case I and cases II and III. (b) Numerical and analytical simulations in the case of nine ordered domains of same size.

Figure 6.7 (a) also shows the impact of the width of the antiphase-boundary on the observed signal. As mentioned before, with increasing the width of the antiphase-boundary, the position of the first

and second maxima is displaced towards q_a=0. Figure 6.8 shows the impact of the strain state when the center of mass of the two ordered domains is displaced from the center of the island. The intensity does not exhibit any dependence with this displacement.

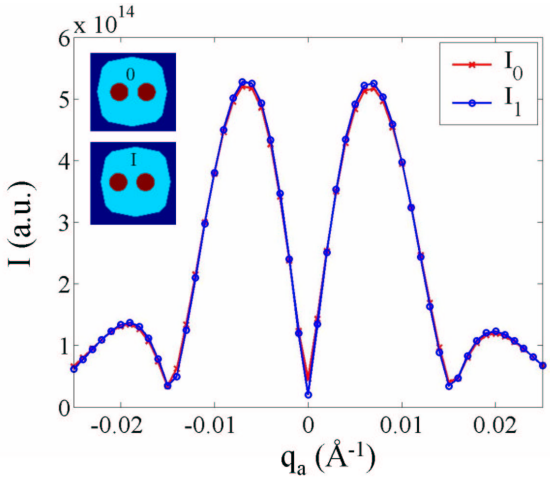

Figure 6.8: (a) Numerical simulations of two ordered domains of same size (cases 0 and I). In the case I, the two domains are displaced from the center of the island.

Figure 6.9 shows the Ge and Si structure factors simulated at the (200) forbidden reflection in the case of four ordered domains separated by anti-phase boundaries. One domain has a different size. And figure 6.10 shows the Ge structure factor and the intensity simulated at the (200) forbidden

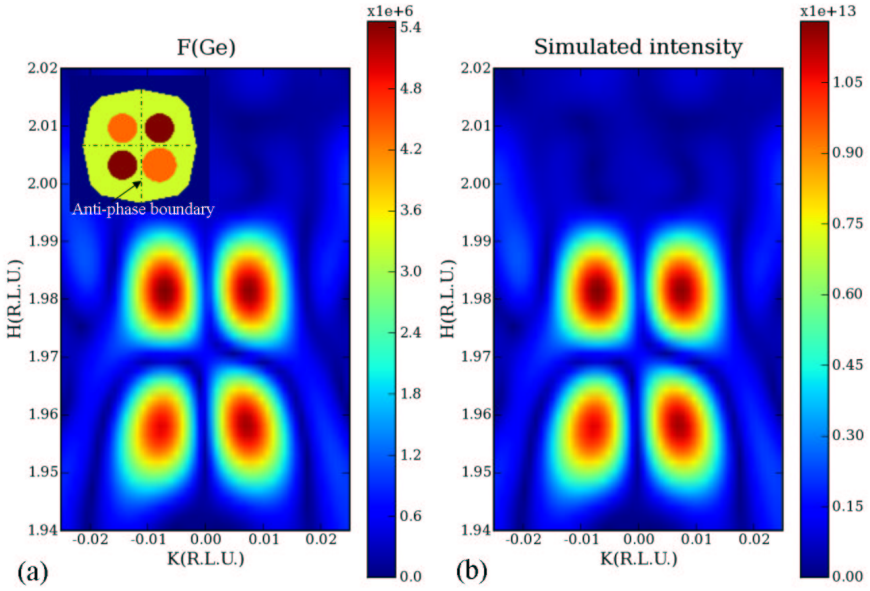

Figure 6.9: Simulated (a) Ge structure factor, $|F_{Ge}|$ and (b) total intensity, $|F_{Ge} + F_{Si}|^2$ at the (200) forbidden reflection in the case of four cylindrical-shaped domains with opposite phases. One domain has a different size to look at its influence on the diffraction pattern.

reflection in the case of nine equal size ordered domains separated by anti-phase boundaries. As experimentally, the same signal has been measured at the (200) and (020) reflections, the ordering

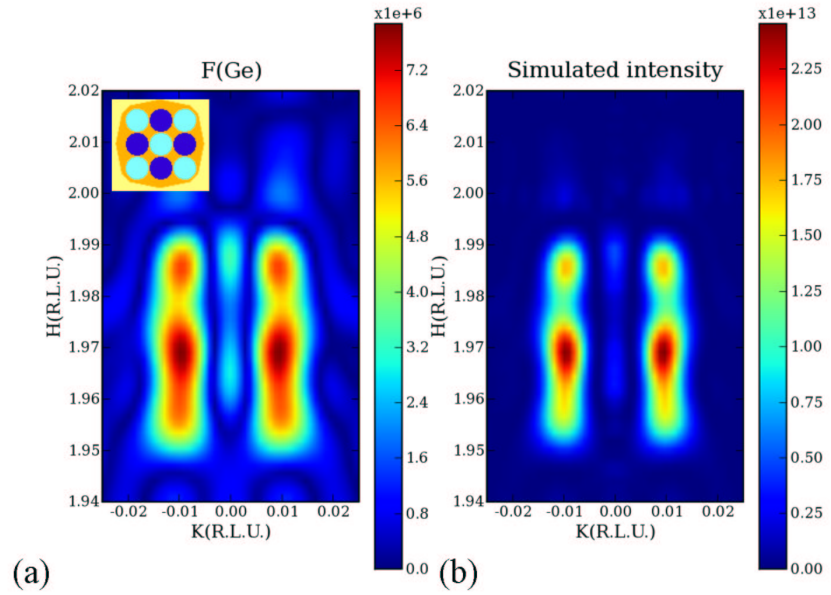

Figure 6.10: Simulated (a) Ge structure factor and (b) total intensity around the (200) forbidden reflection in the case of nine cylindrical-shaped domains with opposite phases. The inset in figure (a) shows an in-plane cut of the dome revealing the 9 domains separated by antiphase-boundaries.

over the sample should present a four-fold symmetry with antiphase boundaries along the [100] and [010] directions. In the radial direction, the simulated F_{Ge} and total intensity I show one or two minima for the four and nine ordered domains, respectively. These minima are explained by the presence of $< 100 >$ anti-phase boundaries. *In the radial direction, no minimum is experimentally observed. In these two examples, the strain alone cannot explain why experimentally no minimum is observed along the radial direction. Nevertheless, in the simulation, we did not take into account the possibility of islands of different sizes and different strain state.* It can be possible that the islands have a random number of ordered domains, which can explain that no minimum of intensity is observed experimentally along the radial direction. Nevertheless, summing the contribution of the (200) Ge structure factors obtained for the simulation of four (see Fig. 6.9) and nine (see Fig. 6.10) ordered domains, in this case, does not remove the minimum of intensity along the radial direction.

Another possibility to obtain two distinct lobes without minima along the radial direction is that the sample is composed of two types of islands with two ordered domains separated by a [100] antiphase boundary (islands of type I) or by a [010] antiphase boundary. As the surface is both 2x1 and 1x2 reconstructed and that atomic ordering may be linked to surface reconstruction, these two types of islands may exist. The incoherent sum of their intensity is shown in figure 6.11 (islands of type II). In this case, no minimum of intensity is observed along the radial direction. This is the only simulation close to the experimental data.

To summarize, the numerical simulations are in good agreement with the developed analytical model. Assuming atomic ordering, the observed diffraction data at the (200) reflection depends drastically on the number of domains and their orientations, on the domain size, on the differences between the sizes of adjacent domains and on the width of the antiphase boundary. This implies that the size of the ordered domains cannot be easily fitted. Or, at least, it is not possible to determine the ordered domain size with only one reflection.

In the following sections, some experimental results on atomic ordering will be presented.

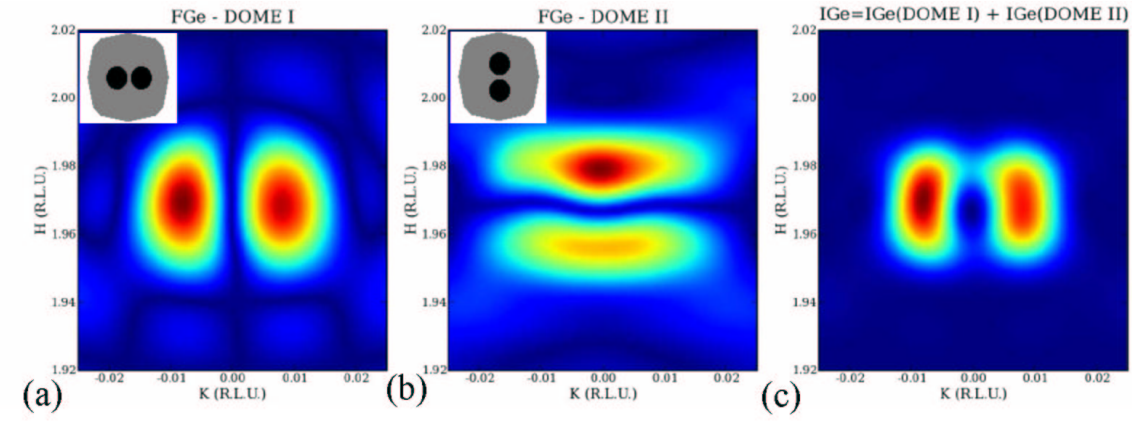

Figure 6.11: Simulated Ge structure factor at the (200) forbidden reflection in the case of two cylindrical-shaped domains with opposite phases separated by a [100] (DOME I) (a) or a [010] (DOME II) (b) anti-phase boundary. The maximum value of the Ge structure factor is higher in the case of DOME I ($\sim$ 2.7E9 a.u.) than in the case of DOME II ($\sim$ 1.2E9 a.u.). (c) shows the incoherent sum of the intensity of the scattering from domes I and II at the (200).

6.2.5 X-ray diffraction analysis of the atomic ordering on patterned and nominal samples.

To determine if islands on both pre-patterned and nominal samples are composed of ordered SiGe alloy, the scattered intensity was measured for several samples in the vicinity of the (200) reflection (see Table 6.1). Figure 6.12 show the corresponding measurements. In contrast to the (400) reflection, around the (200) reflection, a pronounced minimum is observed along k=0. As mentionned above, it is the signature of structures interfering destructively, such as antiphase domains inside the islands.

Samples	Growth temperature	Amount of Germanium
Z576 (nominal and patterned)	620°C	7 MLs
Z25 (nominal and patterned)	650°C	7.2MLs

Table 6.1: Series of sample

The (400) reciprocal space maps allow to determine the size of the islands as a function of the in-plane lattice parameter, while at the (200) the size of the ordered domains is determined. As an example, the (1.9625 k 0) angular scan of the nominal part of sample Z576 (see dashed line 1 in Fig. 6.12) has been fitted supposing 2 or 3 ordered domains along the [010] directions. As shown in figure 6.13 (a), the best fit is obtained in the case of two domains. In the case of three domains, the position of the first maximum is displaced and the distance between the two intensity maxima is larger. This is the case for all the three samples. This demonstrates that the number of ordered domains may be two along the [010] direction. (We cannot exlude a combination of 2, 4, 9 domains inside different islands.) However, in the case of two ordered domains, the positions of the second maxima are not well fitted. An angular scan along the [010] direction and around h=3.985=1.9625x2 gives an island size of (49$\pm$5)nm. The simulated size of the two ordered domains with a narrow antiphase boundary is (27$\pm$4)nm. In this case, the sum of the sizes of the two domains corresponds to the size of the island. If we suppose that the ordered domains are separated by a wide (15 nm) anti-phase boundary, the second maxima are well fitted and the size of the ordered domains is reduced (17 nm). This model, in which the ordered domains would be confined closed to the islands facets, is in agreement with the fact that the atomic ordering is rather stabilized by the reconstruction of the {113} and {15 3 23}

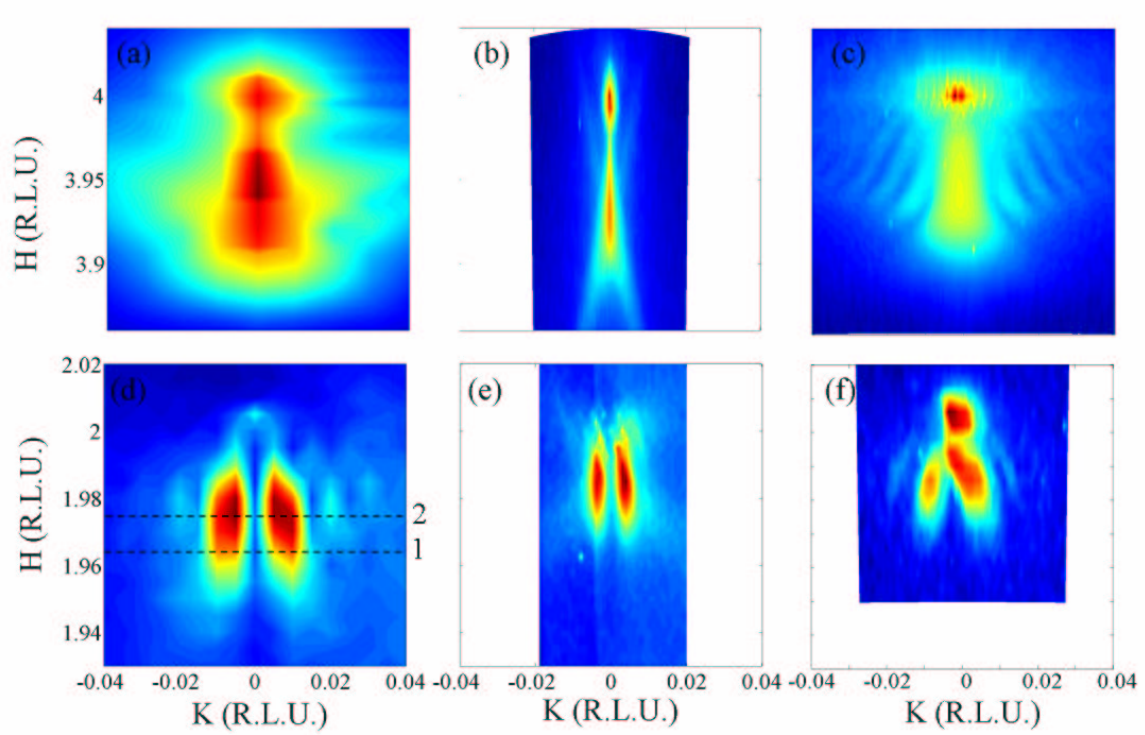

Figure 6.12: (400) reciprocal space maps of sample Z576 nominal (a) and patterned (b) parts and of sample Z25 nominal part (c). (200) reciprocal space maps of samples Z576 nominal (d) and patterned (e) parts and sample Z25 nominal part (f).

facets as shown by Monte Carlo simulations [23].

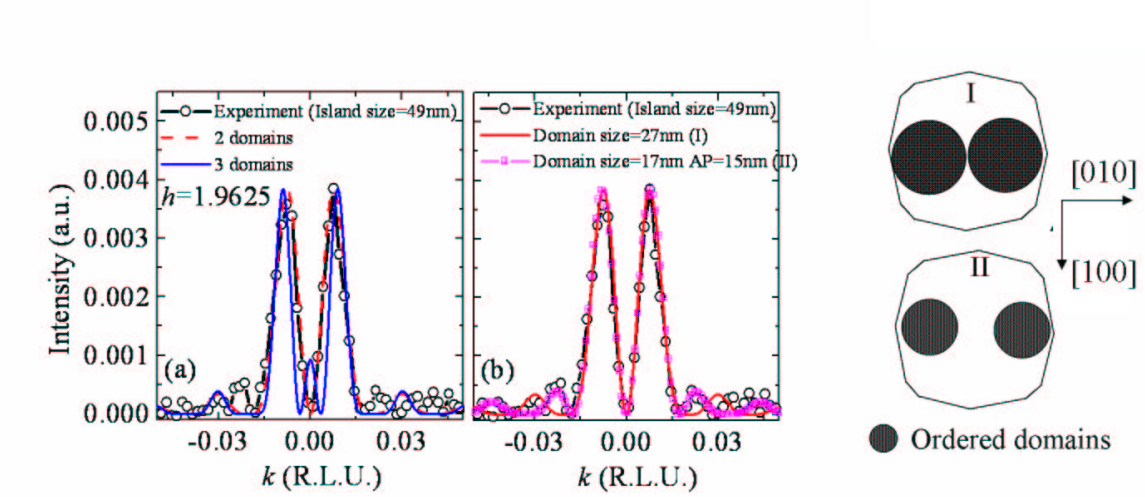

Figure 6.13: (a) Comparison between the experimental and simulated (1.9625 k 0) scans. The simulation is done in the case of two same size domains or nine same size domains, *i.e.* three domains along the [010] direction. (b) Comparison between the experimental and simulated (1.9625 k 0) scans. The simulation is done in the case of two same size domains with a narrow antiphase-boundary or with a large antiphase boundary. Schematic drawing of the ordered domains inside the iso-strain volume of the dome.

The same behaviour is observed fitting the (1.975 k 0) angular scan (see dashed line 2 in Fig. 6.12) of the nominal part of sample Z576 (see Fig. 6.14). In the case of two ordered domains with a narrow antiphase boundary, the position of the second maxima is not well fitted. If we suppose that the ordered domains are separated by a wide (25 nm) anti-phase boundary, the position of the second maxima are well fitted but not the third.

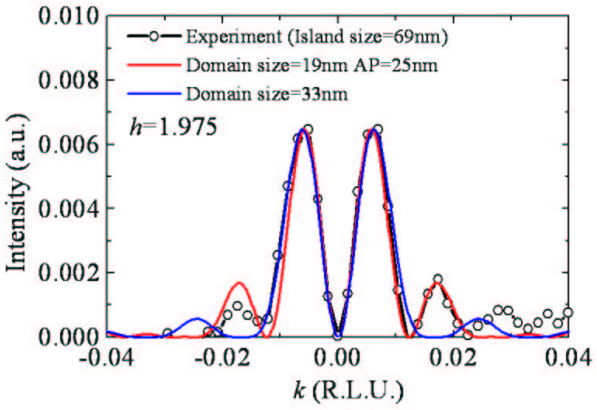

Figure 6.14: Comparison between the experimental and simulated (1.975 k 0) scans. The simulation is done in the case of two same size domains with a narrow antiphase-boundary or with a large antiphase boundary.

6.2.6 Synthesis and discussion on the origin of the scattering around the (200) reflection.

To summarize, the comparison between the experimental data and the analytical model reveals the presence of two ordered domains along the [010] direction. The model with a large antiphase boundary fits the data better. Only the simplest models have been tested. The reality could be much more complex, since islands of different sizes, different strain state, and probably with different numbers of ordered domains might coexist to yield the observed scattered intensity.

The diffuse scattering observed at the (200) reflection in the case of coherent islands may result from:

- *the distortion of the unit cells induced by strain relaxation inside the nanostructures (see the previous chapter)*
- *the truncated lattices at the surface of the nanostructures (see the previous chapter)*
- *the atomic ordering*
- *the relative displacement of the FCC sublattices in diamond unit cell [27].*

This implies that intensity at the (200) is not necessarily induced by atomic ordering. However, if it is not the case, one has to explain the minimum of intensity observed along k=0.

In the previous chapter, we demonstrated that the distortion of the unit cells induced by strain relaxation and truncated lattices at the surface do not yield a minimum of intensity along k=0. In contrast, atomic ordering with the presence of antiphase boundaries can explain the observed features at the (200). To simulate the diffuse scattering observed at the (200) forbidden reflection, we have also tested other models which did not take into account atomic ordering. For instance, we tested if the composition profile can yield the observed scattered intensity. Neither a conventional profile [24] nor a 'rosette' like composition profile [25, 26] yield the minimum of intensity observed at the (200) reflection. Up to now, only atomic ordering explains the observed features at the (200).

In literature, different ordering models have been proposed. The $RS2$ model can be directly rejected as it does not yield intensity at the (200). The $RS3$ model, which is a more general and flexible model can also be rejected. This model yields intensity at the (200) and also at half integral reflections. As reported by A. Malachias [1], half integral reflections such as $(\frac{1}{2}\ \frac{1}{2}\ \frac{1}{2})$ and $(\frac{3}{2}\ \frac{3}{2}\ \frac{3}{2})$ were not observed. This indicates that ordering is not along the $< 111 >$ directions. One ordering model which can explain the intensity at the (200) and its absence at the half integral reflections is the zinc-blende model (see Fig. 6.4), common in compound semiconductor. This model is explained by a dominant surface segregation which allows reduction in dangling bond energies [18].

Only atomic ordering explains the minimum. Nevertheless, the impact of the relative displacement of the FCC sublattices in the diamond unit cells [27] needs to be investigated to check if this displacement can yield a minimum of intensity at the (200). The reader has to remind that the FDM simulations only give the position of one atom per unit cell. In this work, the position of the other atoms of the unit cell have been interpolated linearly. In stressed crystals, the relative displacement of sublattices is different. The position of the atoms in the diamond unit cell should thus not be interpolated linearly. This has been theoretically demonstrated in diamond structures [27]. The relative displacement of sublattices should be taken into account to demonstrate if this can yield the minimum of intensity observed at the (200) for Ge nanostructures.

In the following, we will postulate that the two lobes observed at the (200) are the signature of atomic ordering. The impact of annealing on compositional ordering will be investigated.

6.2.7 Annealing effect on the atomic ordering: atomic ordering, a *metastable* phenomenon.

The sample investigated in this part was grown by molecular beam epitaxy in the BM32 chamber connected to the diffractometer. Germanium was deposited with a fast deposition rate of 36 *sec* for

one Ge monolayer (ML) (∼0.028 ML/s). 9-10 ML of Ge were deposited at a growth temperature of 650°C. At the end of the growth, measurements around the (200) forbidden reciprocal lattice point show intensity lobes which indicate the presence of atomic ordering. The presence of streaks along the < 111 > directions was not observed around the (200) forbidden reflection.

GISAXS measurements were performed along the < 100 >, < 110 > and < 15 3 23 > azimuths, where streaks along the < 105 >, < 113 > and < 15 3 23 > directions were observed. The observed scattering rods correspond to facet streaks of pyramids and domes. No < 111 > facet streaks are observed. This indicates that no superdomes are formed. This is in good agreement with the fact that no signature of defects are seen at the (200) forbidden reflection. In addition, performing angular scans reveals size oscillations (not shown here). Atomic ordering is thus observed inside *monodisperse* domes. Few pyramids are observed on this sample by AFM.

To analyze the influence of annealing on atomic ordering, the grown sample was *in situ* annealed up to a temperature of 835°C. To determine the relaxation state of the Ge islands during annealing, grazing-incidence scans were performed around the (400)Si Bragg peak (see figure 6.15).

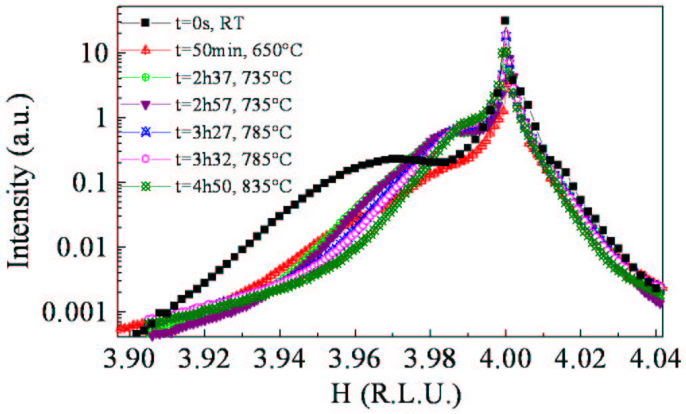

Figure 6.15: Radial scans around the (400)Si Bragg peak for different annealing times and temperatures.

Before annealing, a maximum of diffuse scattering appears around h=3.965. This corresponds to the relaxation state of the Ge domes. During annealing, the position of the maximum of intensity evolves and moves towards the position of the Si-peak. At the annealing temperature of 835°C, the position of the maximum is around h=3.988. The mean relaxation state of the islands evolves during annealing. This is explained by the increase of Si intermixing during annealing.

To determine the ordered domain size during annealing, grazing-incidence scans were performed around the (200)Si Bragg peak (figure 6.16 (a)). To evaluate the tendency of the evolution of the ordered domains size, we suppose that the islands are only composed of two ordered domains along [010] separated by a thin antiphase boundary. The size of the ordered domains, $D = Nd$ is thus given by the formula:

$$I(q_a) \propto \frac{\sin^2(\frac{1}{2}q_a N d)}{\sin^2(\frac{1}{2}q_a d)} \cdot \sin^2(\frac{1}{2}q_a N d), \tag{6.14}$$

where $q_a = \frac{2\pi k}{a}$. With this model, the size of the ordered domains before annealing is evaluated equal to (35±3)nm which is half of the mean island size ((64±1)nm evaluated by grazing incidence reflection around the (400) reflection). Increasing annealing temperature, an increase of the ordered domain size is observed (see black circles in Fig. 6.16(b)). Besides, for a given annealing temperature, the ordered domain size increases with annealing time (see red circles in Fig. 6.16(b)).

Atomic ordering is not an *equilibrium* phenomenon as a random alloy is energetically favorable

[28, 29]. The fact that atomic ordering does not disappear after annealing demonstrates that atomic ordering is a *metastable* phenomenon. As observed above, the size of ordered domains increases with temperature and time. The enlargement of the domains can be either due to material coming from neighboring island, bulk diffusion or to a reorganization of atoms inside the island. The first hypothesis may be prevalent as it is well known that during annealing, 'anomalous coarsening' occurs and induces the increase of the mean island size [30]. Coarsening allows to lower the energy configuration of the system and occurs due to surface diffusion. Atomic ordering appears to be favorized by surface mediated diffusion processes. Then, during annealing at high temperatures and for long times, diffusion of Si from the substrate into the Ge islands has been observed [31] and can explain the enlargement of the ordered domains.

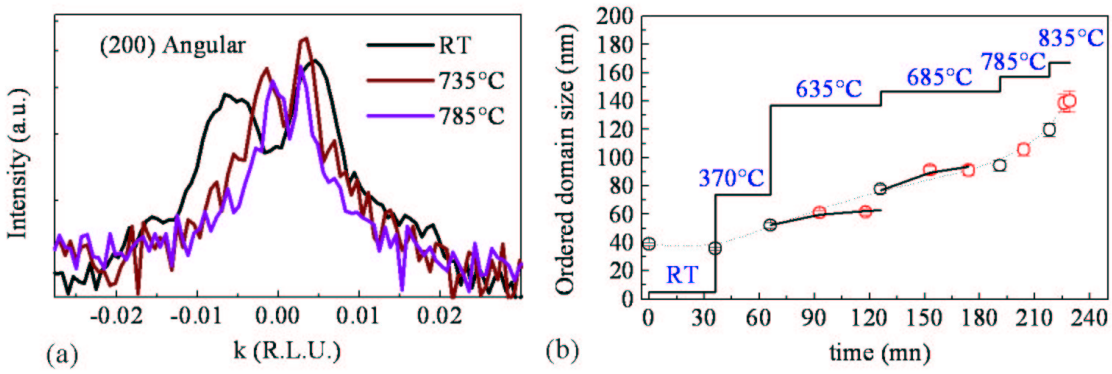

Figure 6.16: (a) Angular scans near the (200)Si Bragg peak (h=1.99) after the growth at room temperature and for different annealing times and temperatures. (b) Evolution of the ordered domain sizes as a function of annealing times and temperatures

Looking at the (200) forbidden reflection can also allow detecting defects inside Ge islands as previously shown in chapter 5. The study was previously performed on Ge islands grown by a combination of nanoscale patterning with diblock copolymer and Stranski-Krastanow growth process. In this section, we will focus on the detection of defects in Ge islands during their *in situ* growth on flat Si(001) substrates.

6.3 Defects in Ge islands on Si(001)

6.3.1 *In situ* study of the formation of stacking-faults inside Ge islands

A. Sample morphology

The sample investigated in this part was grown by molecular beam epitaxy in the BM32 chamber connected to the diffractometer. Germanium was deposited with a slow deposition rate of 170 *sec* for one Ge monolayer (∼0.006 ML/s) at a growth temperature of 650°C. As observed by GISAXS (images not shown here, see chapter 7), domes and superdomes appear after a deposit of 4.8ML and 6ML of Ge, respectively. To determine the relaxation state of the Ge islands during their growth, grazing-incidence scans were performed around the (400)Si Bragg peak (see Fig. 6.17). At 4.3ML, a small increase of the scattering on both sides of the Si peak appears, which corresponds to the formation of strained pyramids. At 5.1ML, the relaxation state increases due to the formation of domes as rods of scattering from {113} and {15 3 23} facets are seen in the GISAXS images. At 6ML, a change of the relaxation state is observed. It can be related to the formation of other islands, called barns or super-domes as rods of scattering from {111} facets are observed in GISAXS images. The island morphology as a function of deposit is summarizes in Tab. 6.2.

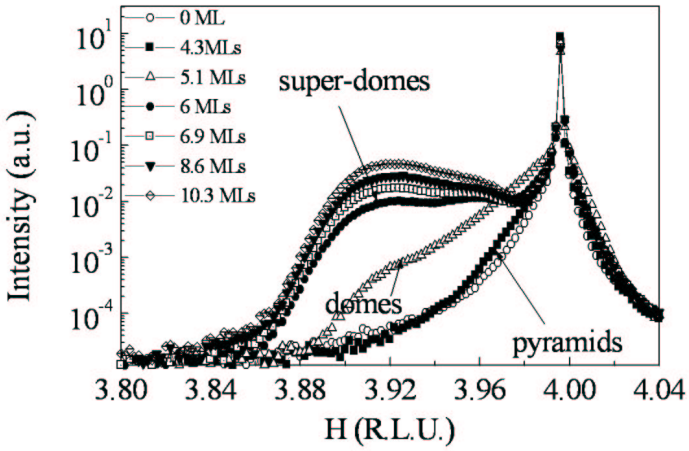

Figure 6.17: Radial scans for several Ge deposits around the (400)Si Bragg peak for a growth temperature of 650°C.

θ	Islands
0-3.5 ML	wetting-layer
4.3 ML	pyramids
5.1 ML	domes
6 ML	coherent barns or superdomes

Table 6.2: Island morphology as a function of deposit θ

B. Detection of the formation of defects.

To determine for which Ge deposit stacking-faults or defects are formed inside the islands, angular scans were performed around the (200) reciprocal lattice point at h=1.94 and h=1.98 (see Figs. 6.18 (a)-(b)).

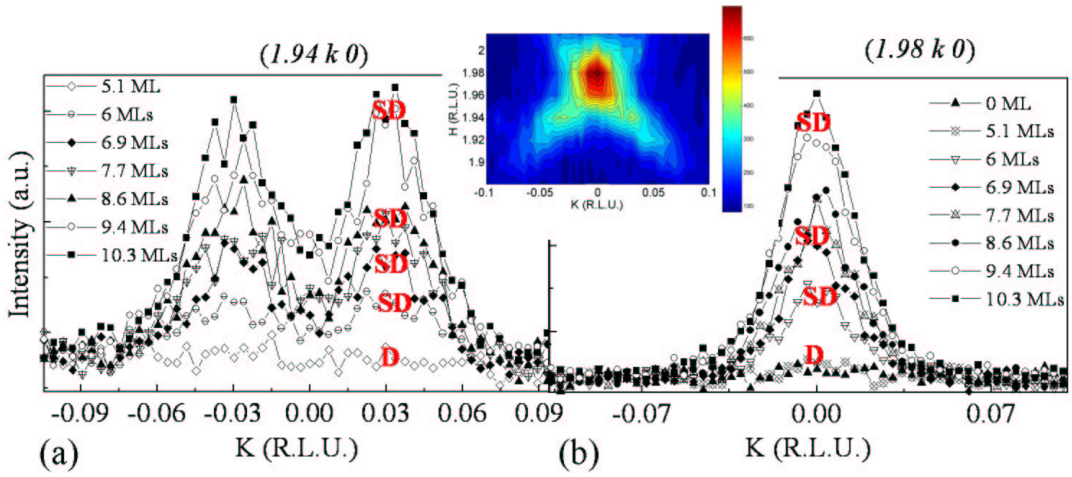

Figure 6.18: Angular scans for several Ge deposit for a growth temperature of 650°C at h=1.94 (a) and h=1.98 (b).

After a deposit of 6ML, narrow streaks along the $< 111 >$ directions appear as observed by the apparition of intensity at h=1.94 and h=1.98. The apparition of $< 111 >$ streaks correspond to the apparition of {111} facetted islands such as barns or superdomes. The $< 111 >$ streaks at the (200) forbidden reflection can either come from {111} stacking faults inside the islands as observed previously (see chapter 5) or from the scattering by {111} facets of either barns or superdomes. To determine whether the $< 111 >$ facet streaks are the signature of the presence of {111} facetted islands, numerical simulations have been performed. They demonstrate that {111} facets scatter at the (200) forbidden reflection. Nevertheless, the signal is weak. To check the intensity of the signal induced by the scattering from {111} facets, we investigate the scattering from 200-nm facetted pyramids grown by Liquid Phase Epitaxy (LPE). Such pyramids present no defects and are thus well suited for this analysis. No $< 111 >$ streaks were observed, which confirms that the scattering from facets at the (200) is weak compared to that of stacking faults.

This has been also confirmed by a combined AFM and *ex situ* study which was performed on four samples. The combination of AFM and *ex situ* X-ray measurements at the (200) will allow to compare the size of the {111} facets with the $< 111 >$ streaks size measured at the (200).

The samples were grown at four different temperatures: 620°C, 700°C, 740°C and 800°C. 15 ML of Ge were deposited with a growth rate of ∼0.03 ML/s by molecular beam epitaxy. AFM images (Fig. 6.19) show the presence of {111} facetted superdomes, noted 1 and 2 for instance. The {111} facets appear at the basis of the superdomes. AFM profiles along the [110] direction were performed to measure the size of the {111} facets (Fig. 6.19 (b)-(c)). For all samples, the (200) reciprocal space maps show the presence of $< 111 >$ streaks (Fig. 6.20 (b)). From these measurements, the size of the stacking faults were determined (Fig. 6.20 (a)). The samples were then etched to observe the tree-ring structure below dislocated SiGe islands [32] (Fig. 6.20 (c)). The tree-ring structure gives the position and the number of dislocations as a consequence of the complex cyclic growth of dislocated islands [33].

Figure 6.20 shows the evolution of the {111} facet lengths of superdomes, of the critical ring width obtained after chemical etching and of the size of the $< 111 >$ streaks observed by X-rays. The size

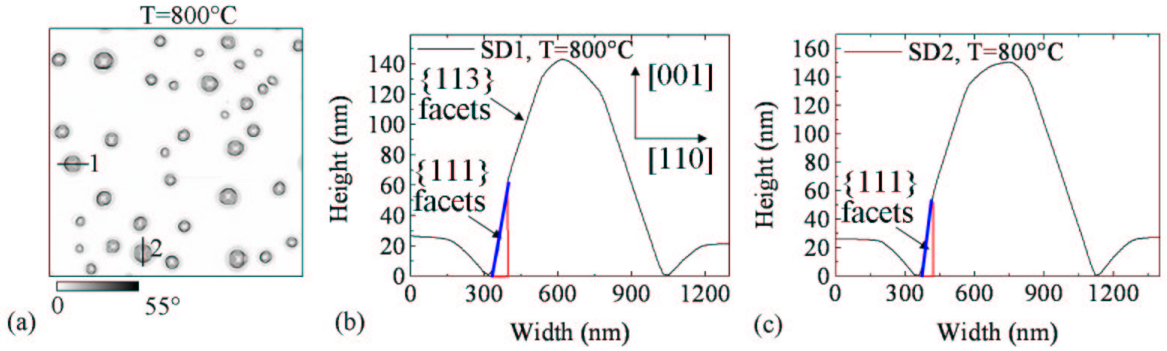

Figure 6.19: (a) AFM image of Ge islands grown at 800°C and after a deposit of 15 ML. Two superdomes are indicated by a line. (b) and (c) AFM profiles along the [110] direction for two superdomes. Courstesy of M. Stoffel.

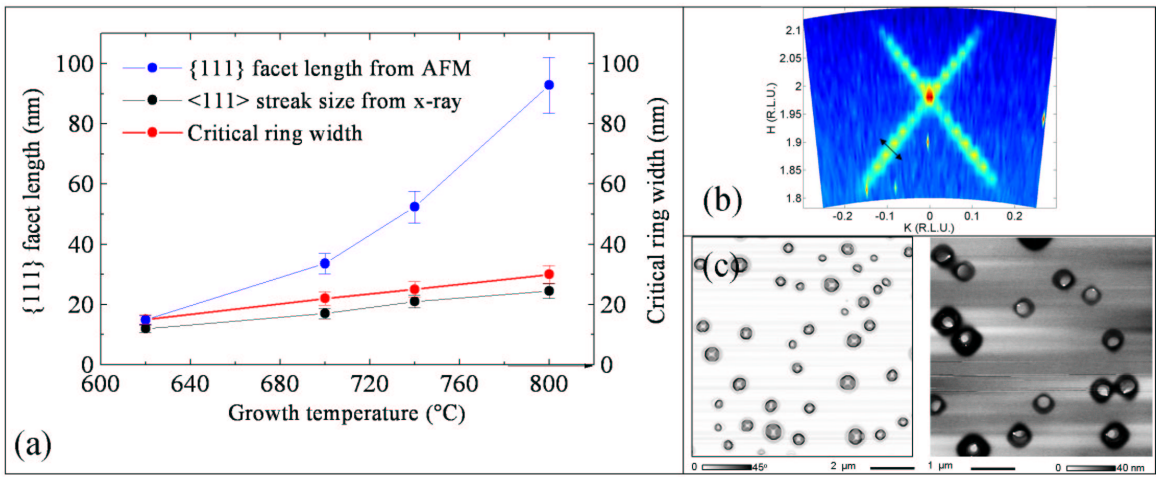

Figure 6.20: (a) Evolution of the {111} facet lengths of superdomes as a function of temperature. Evolution of the critical ring width obtained after etching (c) as a function of temperature. And evolution of the size deduced from the width of the $< 111 >$ streaks observed by X-rays (b). Figure (b) displays a reciprocal space map around the (200) reflection. (c) AFM images before and after etching.

of the < 111 > streaks at the (200) forbidden reflection do not correspond to the {111} facet size of the superdomes. This demonstrates that the < 111 > streaks are not the signature of the scattering by the facets but rather arise from stacking faults. What is interesting is that the size of the < 111 > streaks is well correlated with the critical ring width.

The presence of stacking-faults is thus revealed by the formation of narrow streaks along the < 111 > directions at the (200) forbidden reflection.

For the sample grown on BM32, < 111 > streaks appear after a deposit of 6ML (see Fig. 6.18). A deposit of 6ML corresponds to the formation of barns or superdomes (see Table 5.2). Between 4.3 and 6ML, coherent domes are formed. They are then followed by the formation of incoherent superdomes which contain stacking faults. Thus, looking at the (200) forbidden reflection allows to precisely determine for which deposit defects such as stacking faults appear.

C. Evolution of the average radius and of the density of stacking faults (SFs) as a function of Ge deposit.

Fig. 6.18 shows angular scans performed around the (200) reciprocal lattice point. Narrow streaks along the < 111 > directions are observed. The inserted map in Fig. 6.18 is a projection in the ($hk0$) plane of the intensity integrated along the detector. Thus, in the plane, we measure the projection of the < 111 > sreaks which are then transformed into < 110 > streaks.

Figure 6.18 shows that, with increasing Ge deposition, an increase of the integrated intensity of the streaks is observed. At h=1.98, this increase is related to the increase of the volume of the growing islands with Ge deposit. At h=1.94, the scattering from the islands is reduced; the signal comes nearly entirely from the stacking-faults. The integrated intensity of the streaks at h=1.94 is thus proportional to the total number of the defects tied up in stacking faults. The observed increase of the integrated intensity is linked to the increase of the number of stacking-faults inside superdomes. The analysis of the streaks in the < 111 > directions thus offers the possibility to determine both the *average radius* of the SFs present perpendicular to the Burgers vector from the full width half height of the streaks, and the *total number* of the defects tied up in stacking faults from the integrated intensity of the streaks.

To determine the full width at half maximum of the streaks (in the [111] direction) using a measurement along the angular direction, *i.e.* the [010] direction, the broadening conditioned by the intersection angle at 45° must be taken into account. The diameter of the stacking fault in real space is then

$$D = \frac{a}{cos(45°)\Delta k_{[010]}} \tag{6.15}$$

From 6ML$\leq \theta \leq$10.3ML, the average diameter of the defects is relatively constant (see figure 6.21 (a)): D=(22±3)nm. The area A under the curve of the scattered intensity in an angular direction was determined at h=1.94 (figure 6.21(b)). Assuming a disk shape for the stacking fault, the relative change of the total number of SFs, n_{SF} can be determined from the relation [34]:

$$n_{SF} \propto A/\pi(\frac{D}{2})^2 \tag{6.16}$$

The values obtained are suitable for comparing the total number of defects as a function of Ge deposit. From the fit of the curve, the streak area is revealed to increase linearly with Ge deposition. Supposing the equiprobability of finding the same number of defects in the [100] and [010] directions of the sample, the total number of defects is found to *increase linearly* with Ge deposition. *In situ* GIXD is thus a powerful and non-destructive technique to follow the evolution of defects.

In summary, we precisely follow the formation of stacking-faults during growth. We determine the onset of the nucleation of stacking-faults as a function of Ge deposit. We show that the average diameter of the defects is relatively constant during growth: D=(22±3)nm. The stacking faults appear to have an equilibrium size. In addition, the stacking-fault density is shown to increase linearly with time and with the amount of deposited Ge. Contrary to annealing [35], the introduction of additional dislocations is prefered to relieve strain during growth.

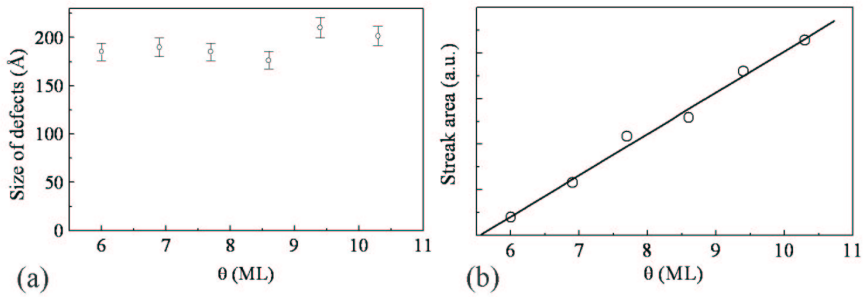

Figure 6.21: (a) Average size of defects as a function of Ge deposit, θ. (b) Streak area measured in one direction at h=1.94 as a function of Ge deposit, θ.

D. Relation between relaxation and insertion of defects during growth

If we consider an incoherent island on Si(001), its mean strain ϵ **with respect to Ge** is reduced from ϵ_0 (0.04 for Ge and Si) to $\epsilon_0 - \frac{nb}{w}$, where b is the in-plane projection of the effective Burgers vector, w its mean width and n its number of dislocations [33]. Taking into account the elastic relaxation of the island, the mean strain can be written as:

$$\epsilon = (0.04 - \frac{nb}{w}) * \sqrt{1-\alpha}, \tag{6.17}$$

where α is the elastic gain in accomodating films strain through the formation of partly relaxed islands [36].

If the island is coherent (n=0), $\epsilon = \epsilon_{coh.} = 0.04 * \sqrt{1-\alpha}$. With increasing Ge deposit and after a deposit of 6 ML, the in-plane deformation of the Ge island ϵ is experimentally observed to remains constant (see Fig. 6.17). The number of dislocations was shown above to increase linearly with θ, and w to evolve as $\theta^{\frac{1}{3}}$ (see chapter 7). This implies that the residual elastic strain is found to decrease during growth. Dislocations partially relax the island, reducing the need for strain energy relief by elastic deformation.

What is surprising is the presence of two Ge scattering peaks when superdomes are formed. One is localized near the Ge bulk Bragg peak and corresponds to the mean relaxation of the Ge superdomes. The second shoulder is positioned at h=3.96, which corresponds to the position of the maximum of the intensity scattered at the (200) forbidden reflection. This intermediate peak can arise from domes not yet transformed into superdomes, and thus much less relaxed, or this peak could be a signature of the defect network. As previously observed by TEM, 60° dislocations or misfit dislocations are generally formed at the Si/Ge interface (Figure 6.22). They are laterally separated by a distance of ∼20-25nm, which corresponds to the critical ring width obtained after etching (see Fig. 6.20). The Ge:Si interdiffusion inside the sample was studied by X-ray anomalous scattering. The Si and Ge structure factors were extracted (Fig. 6.23). It appears that the position h=3.96 is near the interface between Si and Ge.

As already mentionned, the diffuse scattering from defects is localized around h ∼1.98 near the (200) forbidden reflection. If we assume that the effective strain induced by dislocations is given by the mean relaxation observed at the (200) forbidden reflection, then

$$\frac{\bar{a}_{200,Defects} - a_{Si}}{a_{Si}} = 1\% = \frac{nb}{w} = \frac{b}{\lambda}, \tag{6.18}$$

where λ is the in-plane distance between two dislocations, $\bar{a}_{200,Defects}$ is the mean lattice parameter calculated from the position of the maximum intensity of the scattering from defects and a_{Si} is the lattice parameter of Si bulk. Supposing 60° dislocations whose effective Burgers vector is $b = \frac{a_{Si}}{2\sqrt{2}}$, we obtain λ = 19nm, which is in good agreement with literature. Note that two Ge scattering

contributions are observed around the (400) reflection (see Fig. 6.17): at h ∼3.96 and h ∼3.91. Around the (200) reflection, a maximum of intensity is only observed at h ∼1.98=(3.96/2). This implies that only the island region where defects are localized, scatters.

In summary, mapping around the (200) forbidden reflection allows to determine the size of the defects, to evaluate the evolution of the number of defects during the in situ growth and to determine the mean in-plane distance between interfacial dislocations.

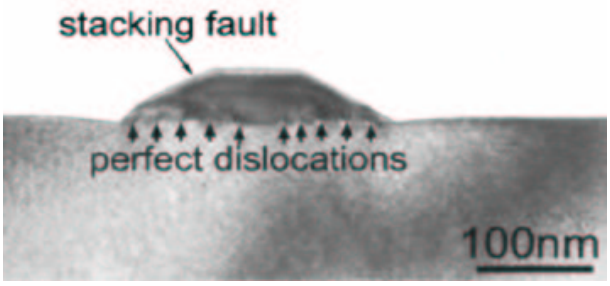

Figure 6.22: Bright-field cross sectional TEM images showing an incoherent island with a stacking fault and periodic misfit dislocations separated by Λ ∼25nm. From [37].

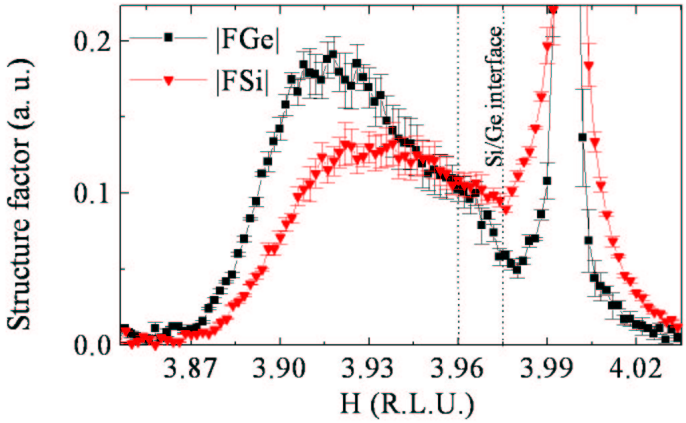

Figure 6.23: Evolution of the Si and Ge structure factors around the (400)Si Bragg peak.

E. Localization of the defects.

The maximum of the intensity scattered at the (200) forbidden reflection is positionned at h=1.98. Diffuse scattering from Ge superdomes appears at h=3.92. Contrary to what has been observed previously in chapter 5, the stacking faults do not scatter at the same h position as the Ge superdomes. In this case, the stacking faults scatter in-between the position of the Ge relaxation and the one of the Si Bragg peak (see Fig. 6.23). The stacking faults are thus positioned at the interface and extend in the Ge islands, as this is usually observed in literature. Nevertheless, some stacking faults can extent in the Si substrate (Fig. 6.24). TEM images 6.25 performed on a similar sample show also the presence of stacking faults inside the Si substrate.

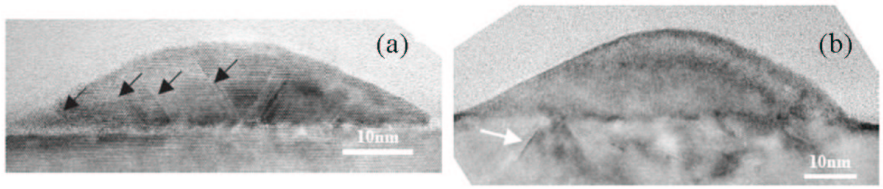

Figure 6.24: Cross-sectional high-resolution electron microcraphs of Ge/Si islands from a sample with 14 ML Ge grown at 400°C (a) and a sample with 8 ML Ge grown at 550°C (b). (a) Note {111}-type stacking defects shown by arrows. (b) The large island shows several {111}-type stacking defects originating at the Ge/Si interface. Also note the strain beneath the island, including a short {111} defect. From [47].

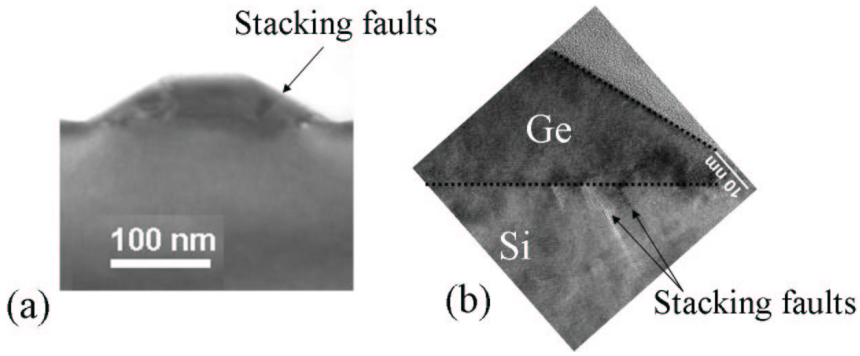

Figure 6.25: Cross-sectional high-resolution electron microcraphs of Ge/Si islands of superdomes grown in the BM32 MBE chamber. Detection of stacking faults inside the island (a) and in the Si substrate (b).

F. Effect of the growth rate on the apparition of defects.

F.1 Slow growth rate

The samples investigated in this section were grown by molecular beam epitaxy in the BM32 chamber with a slow deposition rate of ∼0.006 ML/s. 10-11 ML of Ge were deposited at four growth temperatures: 500°C, 550°C, 600°C and 650°C. AFM images show the presence of superdomes on all samples. The (200) measurements reveal the presence of stacking faults inside the islands. The average size of the stacking faults was determined from the FWHM by fitting the streak cross-section (see Fig. 6.26 (a)).

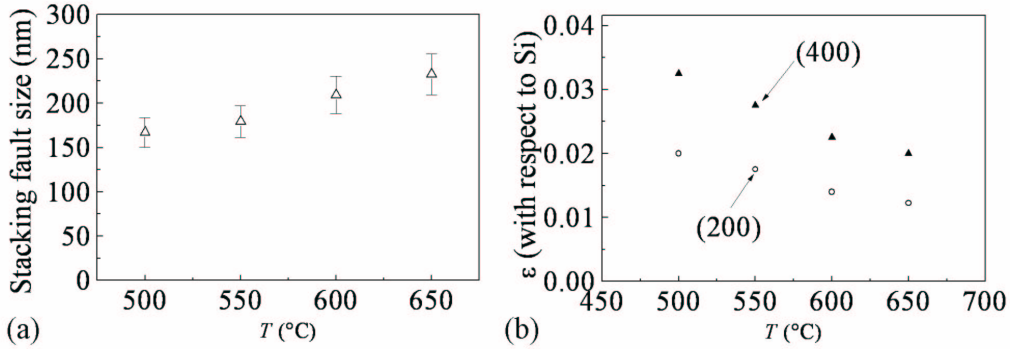

Figure 6.26: (a) Evolution of the average size of stacking faults as a function of the growth temperature T. (b) Evolution of the average strain ϵ (with respect to Si) measured at the (200) and (400) reflections.

With increasing temperature, the mean size of the stacking fault increases, but only slowly, always being of the order of 20 nm. With increasing temperature, the in-plane average strain ϵ of the islands (with respect to Si) decreases as a consequence of the increase of intermixing (see Fig. 6.26 (b)). This is also the case for the strain value ϵ_{200} measured at the (200) forbidden reflection. If we assume that the effective strain induced by dislocations is given by the mean relaxation observed at the (200) forbidden reflection, then $\lambda \propto \frac{1}{\epsilon_{200}}$. Thus, with increasing temperature, the in-plane distance between two dislocations increases. This is in agreement with what is observed after etching. The distance between the tree-ring structures which gives the position of dislocations increases with temperature (see the evolution of the critical ring width in Fig. 6.20). *Intermixing delays the formation of dislocations.*

F.2 Effect of a fast growth rate

Samples were grown by molecular beam epitaxy in the BM32 chamber with a fast deposition rate of ∼0.028 ML/s. 9-10 ML of Ge were deposited at 620°C and 650°C. From GISAXS measurements, no $< 111 >$ streaks have been observed. Besides, no $< 111 >$ streaks have been observed around the (200) forbidden reflection. Contrary to a slow growth rate, no dislocated islands are formed for a deposit of 10 ML. *In summary, not only a slow growth temperature favors the formation of defects but also a slow growth rate.*

6.4 Atomic ordering vs defects

Identifying suitable growth conditions to avoid defects and atomic ordering is of considerable interest, as the atomic-scale and defects ordering has important consequences for the optical and electronic properties.

6.4.1 *Ex situ* studies of atomic ordering and defects in 15 ML grown Ge islands.

The aim of this section is to study atomic ordering and defects as a function of growth temperature, when superdome islands are formed. The X-ray measurements are compared with the results of AFM and selective chemical etching. Atomic ordering will be observed to remain when superdomes are formed.

The samples investigated in this section have been performed in the Max-Planck-Institute for solid state research by M. Stoffel. The X-ray measurements have been performed in collaboration with A. Malachias. 15 ML of Ge were deposited with a growth rate of ~ 0.03 ML/s by molecular beam epitaxy at four different temperatures: 620°C, 700°C, 740°C and 800°C. AFM images (see Fig. 6.19) show the presence of {111} facetted superdomes for all samples. The three-dimensional intensity has been measured around the (200) and (400) reciprocal lattice points (see Fig. 6.27). The scattered intensity was collected by a linear detector perpendicular to the sample surface. The incident angle was kept constant at 0.13°, below the critical angle of total external reflection for the X-ray beam energy used $\sim$ 11 keV. For all three samples, the diffuse scattering was concentrated in intensity streaks along $< 111 >$ directions around the (200) reciprocal space point.

These streaks are visible in Fig. 6.27 (a). They are in the plane along the $< 110 >$ directions after integrating the signal along the [001] direction. As previously observed (see Fig. 6.20 and corresponding explanations), the $< 111 >$ streaks are the signature of the stacking-faults and not the signature of scattering by the {111} facets of the superdomes. With increasing temperature, the width of the streaks decreases. This clearly shows that the size of the stacking faults along the $< 111 >$ directions increases with temperature.

If we assume that the effective strain induced by defects is given by the mean relaxation observed at the (200) forbidden reflection, then the in-plane distance between two dislocations is $\lambda = b/\epsilon_{200}$, where b is the effective Burgers vector of the dislocation. The in-plane distance between two interfacial 60° dislocations evolves from 13 nm to 29 nm with increasing the temperature from 600°C to 800°C. The in-plane distance between two dislocations is displayed in Fig. 6.28. This is in good agreement with what has been observed by selective chemical etching. *This clearly shows that the mean in-plane distance between periodic interfacial dislocations is obtained by mapping around the (200) forbidden reflection.*

Reciprocal space maps around the 400 reciprocal space point allow to determine the relaxation of the grown islands. In Figs. 6.27 (b), a part of the diffuse scattering is concentrated in intensity streaks along the in-plane $< 110 >$ directions. A three-dimensional intensity map (not shown here) revealed that the intensity streaks are along the $< 111 >$ directions. This signal can come from diffuse scattering either from 111 stacking-faults or from {111} facets. With increasing temperature, the streaks along the $< 111 >$ directions appear more and more intense. The intensity distribution along the streaks I(q//[111]) is plotted in Fig. 6.29 (b). The intensity distribution shows a q^{-2} dependence. For defects, the diffuse scattering intensity around an allowed reflection is the so-called Huang diffuse scattering (HDS), for which a q^{-2} decay is expected. Besides, along the facet streaks, the intensity drops a q^{-2}. Thus, the q^{-2} decay does not allow to determine the origin of the $< 111 >$ rods in the (400) reciprocal space maps: either diffuse scattering from 111 stacking-faults or diffuse scattering from {111} facets. From the fit of the width of the $< 111 >$ rods which gives a size of $\sim$39 nm for the sample grown at 700°C, it follows that the diffuse scattering comes from the {111} facets, as the determined value is in good agreement with the facet size measured by AFM (see Fig. 6.19). *At the (400) allowed reflection, the form factor of the islands is observed, whereas the (200) forbidden reflection is sensitive to local breaks of the unit cell symmetry which are induced by defects.*

Fig. 6.30 shows the (200) reciprocal space map for the sample grown at a temperature of 700°C. At the intersection of the $< 111 >$ streaks, two diffuse intensity lobes are observed in Fig. 6.30(b). They reveal the presence of atomic ordering inside the Ge nanostructures. Two intensity lobes are also observed for the other samples, which indicates the presence of atomic ordering in all samples. For all samples, the two diffuse intensity lobes are localized at the same h position as the intersection of the $< 111 >$ streaks. This reveals that the ordered domains are localized inside the same relaxed regions

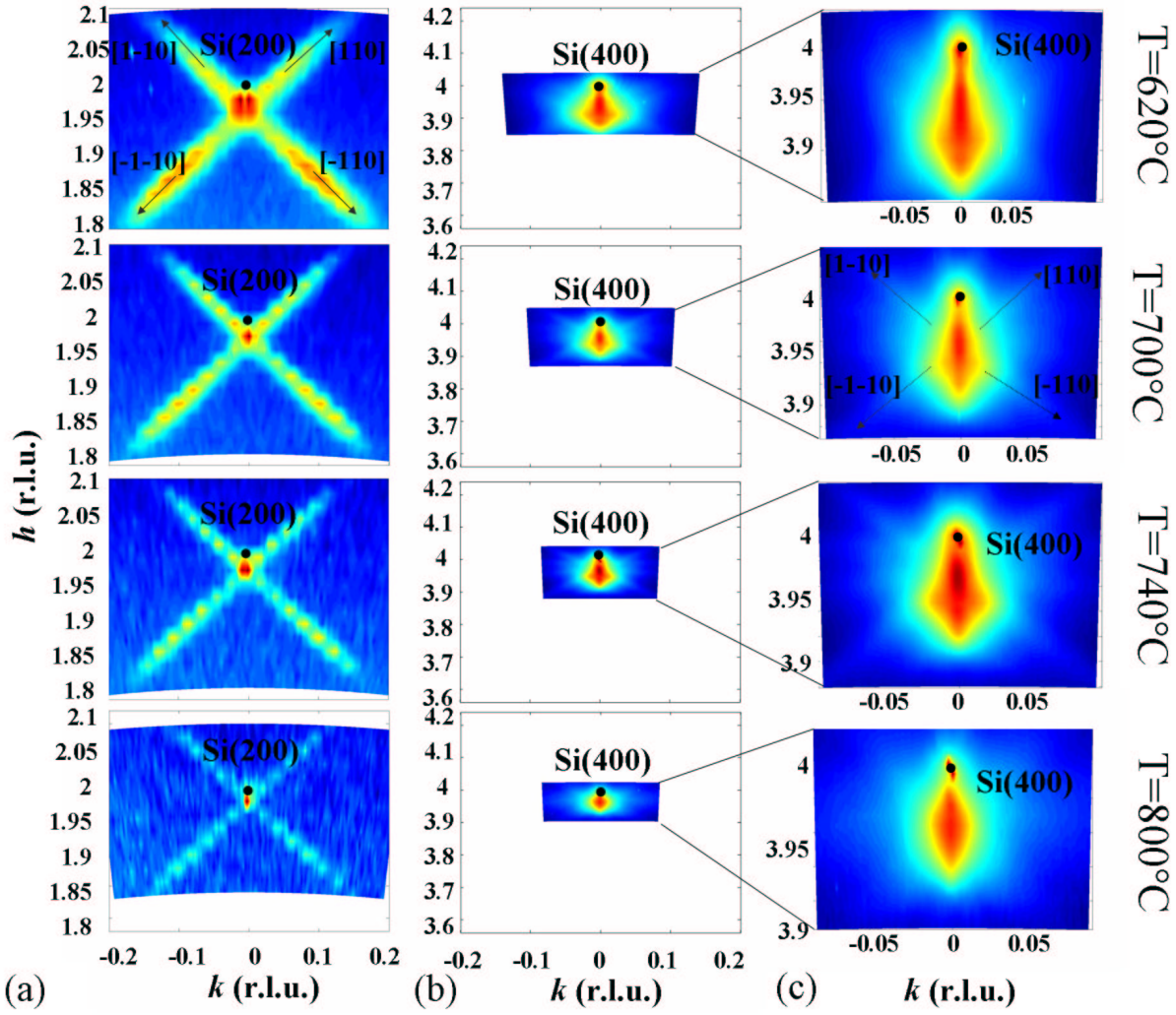

Figure 6.27: (a) (200) reciprocal space maps for the four samples. The signal is concentrated in streaks along $< 111 >$, *i.e.* along $< 110 >$ in the plane after integrating the signal along the [001] direction. (b) (400) reciprocal space maps for the four samples. (c) Zoom around the 400 reciprocal space point. One part of the signal is also concentrated in streaks along $< 111 >$, *i.e.* along $< 110 >$ in the plane after intergrating the signal along the [001] direction.

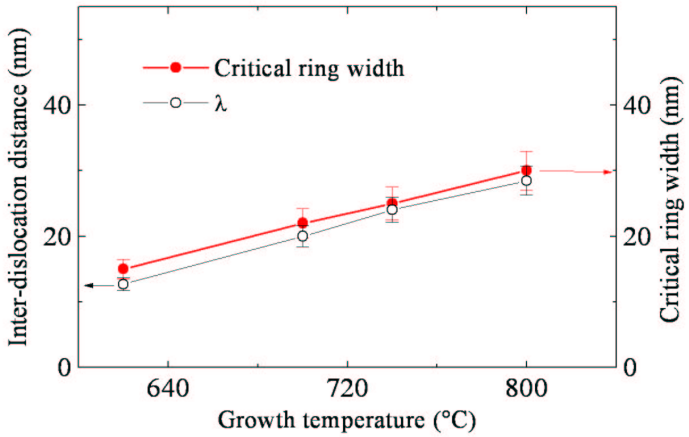

Figure 6.28: Evolution of the critical ring width obtained after etching and of the inter-dislocation distance obtained by X-rays as a function of growth temperature.

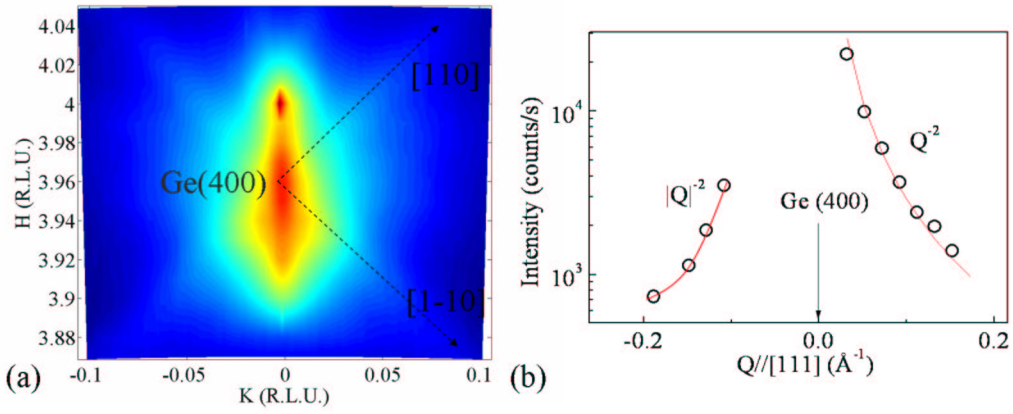

Figure 6.29: (a) (400) reciprocal space map of the sample grown at 700°C. (b) Distribution of the measured intensity along the [111] direction. The in-plane projection of the trajectory is denoted in fig. 6.29 (a).

than the {111} stacking faults. To evaluate the tendency of the ordered domain size, we suppose that the islands are only composed of two ordered domains along [010] separated by a thin antiphase boundary. The size of the ordered domains is fitted by Eq. 6.11. The samples grown at 620°C, 700°C, 740°C and 800°C show ordered domains with a mean size of 32, 66, 76 and 160 nm, respectively. As already observed by A. Malachias *et al.* [1], the size of ordered domains increases with temperature as a consequence of the increase of the island size.

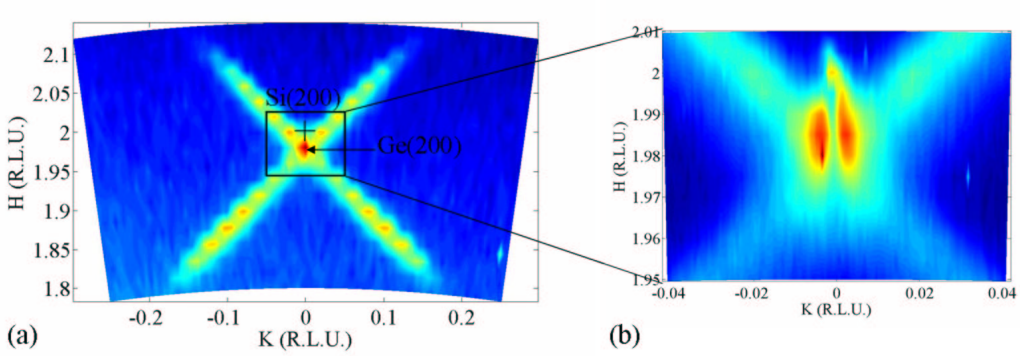

Figure 6.30: (a) (200) reciprocal space map for the sample grown at a temperature of 700°. (b) Zoom on the intersection of the $< 111 >$ streaks.

Fig. 6.31 shows radial scans around the (200) and (400) reflections. The (400) radial scans allow to determine the relaxation of the Ge nanostructures. As previously mentioned, the mean relaxation observed at the (200) can be related to the interfacial 60° dislocation network. Along the [100] direction and around the (400)Si Bragg peak, two or three maxima of diffuse scattering are observed. With increasing temperature, the scattered intensity is centered at much higher h values, close to that of the Si Bragg peak. This is explained by the increase of Si intermixing [39] with temperature. The Ge scattering peaks near the Ge bulk Bragg peak correspond to the mean relaxation of the Ge superdomes. The shoulder nearest the Si Bragg peak can arise from domes which are observed on the AFM images or can be the signature of the defect network. As the position of the shoulder does not correspond to the position of the maximum of intensity scattered at the (200), this signal should be the signature of the relaxation of domes.

To determine the composition of the islands, anomalous scattering has been performed using two energies. The results (not shown here) confirm that with increasing temperature, intermixing increases and reveal that superdomes are less intermixed than domes. This can be understood by the fact that superdomes are preferred with respect to domes for Ge attachment.

6.4.2 *Ex situ* studies of atomic ordering and defects in Ge islands on Si(001) as a function of growth temperature, growth rate and annealing.

The aim of this section is to study the growth conditions (temperature, growth rate, annealing) for which atomic ordering and defects are observed in Ge nanostructures grown on Si(001).

The samples investigated in this work were grown on Si(001) substrates by solid source molecular beam epitaxy (MBE) in the BM32 MBE chamber. 7-10 monolayers (ML) of Ge were deposited on the Si substrates to form domes and/or superdomes. The growth temperature and growth time were varied for each sample. This allows to determine for which growth conditions ordered domains appear and whether ordering is thermodynamically or kinetically driven. Some samples were also annealed to study the effect of the annealing process on the atomic ordering. The three-dimensional intensity

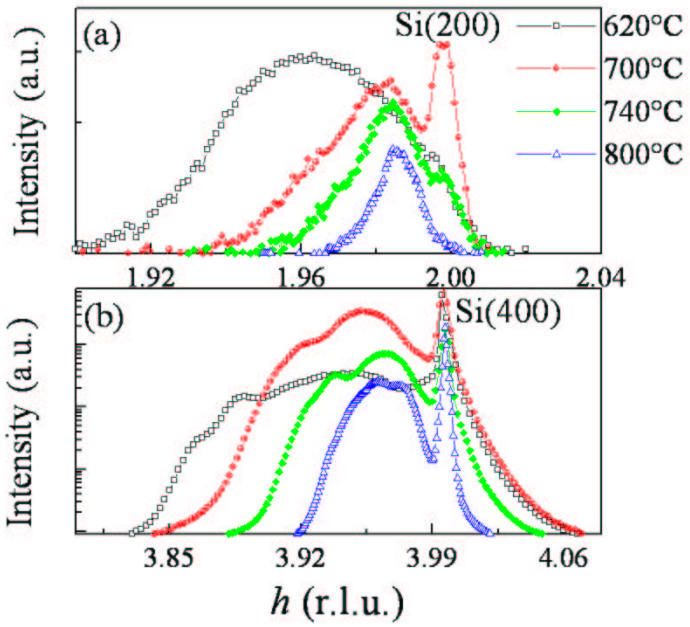

Figure 6.31: Radial scans around the (200) (a) and (400) (b) reflections as a function of growth temperatures.

has been measured around the (200) reciprocal lattice point. The diffuse scattering was sometimes concentrated into scattered intensity lobes which indicate the presence of atomic ordering or/and into narrow streaks along {111} directions which reveal the presence of stacking faults.

Fig. 6.32 shows the mean lateral size of ordered domains as a function of growth temperature and growth rate. The numbers indicate the time spent to deposit ∼8 ML of Ge on the Si(001) substrates. To evaluate the tendency of the variation of the ordered domain size, we suppose that the islands are only composed of two ordered domains along [010] separated by a thin antiphase boundary. With this model, the size of the ordered domains increases with temperature and with lowering the growth rate. For each growth, the mean island size was evaluated by grazing incidence diffraction around the (400) reflection. With this model, the size of the ordered domains is found to be half of the mean island size for the investigated growth temperatures and growth rates. The enlargement of the domains follows the enlargement of the island. For high temperatures (*i.e.* 600°C and 650°C) and slow growth rates (∼ 0.008 ML/s), we observed sometimes the disappearance of atomic ordering. Ordering can disappear by tuning the growth rate. This implies that the formation of ordered domains is not thermodynamically driven. Besides, atomic ordering does not disappear after annealing. This may imply that atomic ordering is kinetically driven by surface diffusion. When superdomes are formed, atomic ordering remains and its relaxation is positioned at the same h value as the intersection of the $< 111 >$ streaks coming from stacking faults. Both atomic ordering and stacking faults are localized in the same relaxed regions of the Ge nanostructures.

We have previously investigated the size of {111} stacking faults as a function of growth temperature. We have shown that, with increasing temperature, the mean size of the stacking fault increases, but only slowly, always being of the order of 20 nm. Fig. 6.33 shows the influence of the growth rate and annealing on the mean size of the stacking faults. The average size of the stacking faults was determined by fitting the full width at half maximum (FWHM) of the streak cross-section. With decreasing the growth rate and with annealing, an increase of the mean size of the stacking faults is observed, which may be related to an increase of the island height. During annealing, the insertion

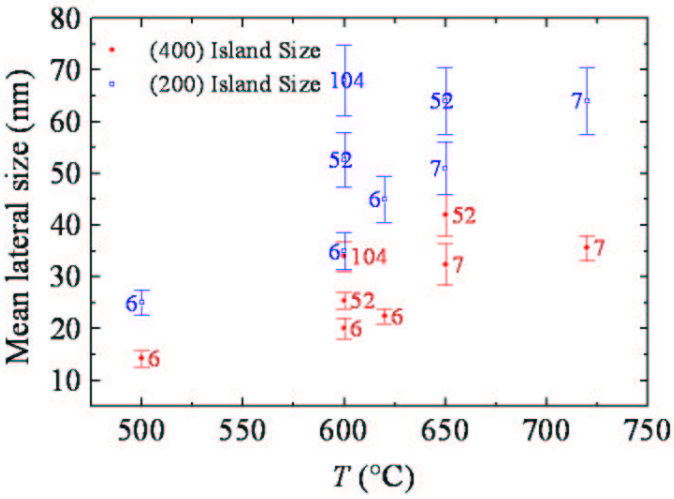

Figure 6.32: Evolution of the mean ordered domain size and of the mean island size as a function of growth temperature and growth rate. The numbers associated with each point indicate the time spent to deposit ∼8 ML of Ge.

of 60° dislocations [35] is not prevalent and the stacking fault size will increase along the $< 111 >$ directions. *The size of the stacking faults is thus time and temperature dependent.*

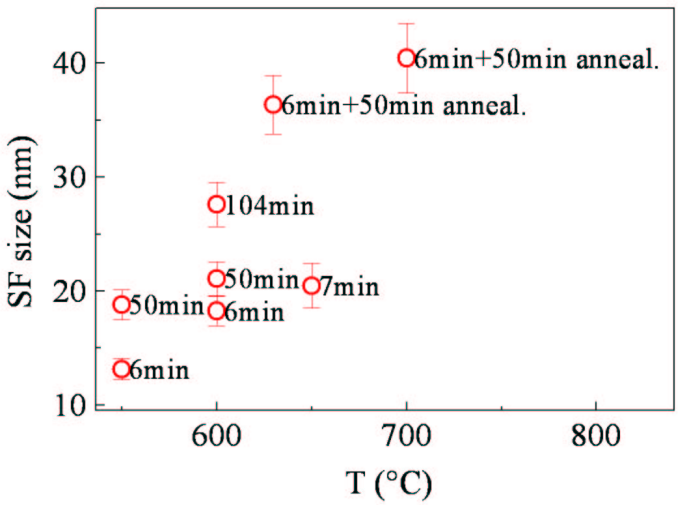

Figure 6.33: Evolution of the mean stacking fault (SF) size as a function of growth temperature, growth rate and annealing. The labels associated with each point indicate the time spent to deposit ∼8 ML of Ge and the annealing time.

To look at the influence of the growth temperature on the formation of stacking faults, we compared three samples grown with the same growth rate but with different growth temperatures. 8 ML of Ge

were deposited during 50 min on samples at 550°C, 600°C and 700°C. The samples grown at 550°C, 600°C show superdomes with stacking faults, whereas the sample grown at 700°C only show atomic ordering. Fig. 6.34 displays the in-plane relaxation of the islands grown on the three samples. The Ge scattered intensity of the sample grown at 700°C is displaced towards the position of the Si bulk Bragg peak, which reveals that the islands on this sample are richer in Si. *Incorporation of more Si into the islands or a larger Si concentration is indeed able to delay the introduction of defects inside the nanostructures.*

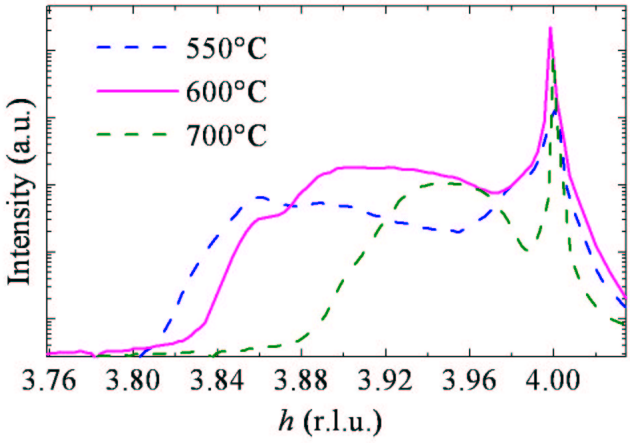

Figure 6.34: Radial scans along the [h00] direction, in the vicinity of the Si(400) reflection for a growth temperature of 500°C, 600°C and 700°C.

To look at the influence of the growth rate, we studied two growth temperatures, 500°C and 650°C, and we tuned the growth rate. First, we deposited 7 ML of Ge at a growth temperature of 500°C with a fast (sample 1), a slow (sample 2) and a very slow (sample 3) growth rates, ∼0.02 ML/s, ∼0.008 ML/s and ∼0.0013 ML/s respectively. Only atomic ordering was observed on sample 1, whereas the (200) reciprocal space maps of the other samples grown with a slower growth rate reveal the presence of stacking faults.

Fig. 6.35 (a) displays GIXD measurements which were performed around the Si(400) Bragg peak. The Ge diffuse scattering is centered at much lower h values, close to the value (h=3.835) of fully relaxed Ge for samples grown with a slower growth rate, *i.e.* for samples 2 and 3. This is the signature of superdomes, whereas the Ge diffuse scattering of sample 1 can arise from domes not yet transformed into superdomes, and thus much less relaxed. *For the first time, it appears that not only low growth temperature but also slow growth rate induces the formation of defects.* The sample grown with a very slow growth rate (sample 3) presents another Ge contribution which scatters near the Si(400) Bragg peak, at h=3.97. This contribution is located above the Si Bragg peak. This scattering around the Si Bragg peak can be identified as the shape factor (squared Fourier transform of the shape) of small islands such as pyramids, strained by the substrate, having an average lattice parameter parallel to the surface very close to the Si one, as well as to possible strain induced by the deposit in the substrate, below its surface. A very slow growth rate may have the same effect as annealing; domes are transformed back into pyramids. The same behaviour is observed for a growth temperature of 650°C and for a deposit of 8-8.5 ML of Ge (see Fig. 6.35 (b)). Contrary to a fast growth rate (∼0.02 ML/s), a slow growth rate (∼0.008 ML/s) or annealing fastens the appearance of defects inside nanostructures. This is revealed by the appearance of {111} streaks at the (200) forbidden reflection. The Ge diffuse scattering is displaced towards the position of the Si Bragg peak as a result

of Si intermixing. It appears thus that annealing and a slow growth rate can fasten the introduction of dislocations inside the nanostructures. To explain this phenomenon, a simple energetic model is proposed.

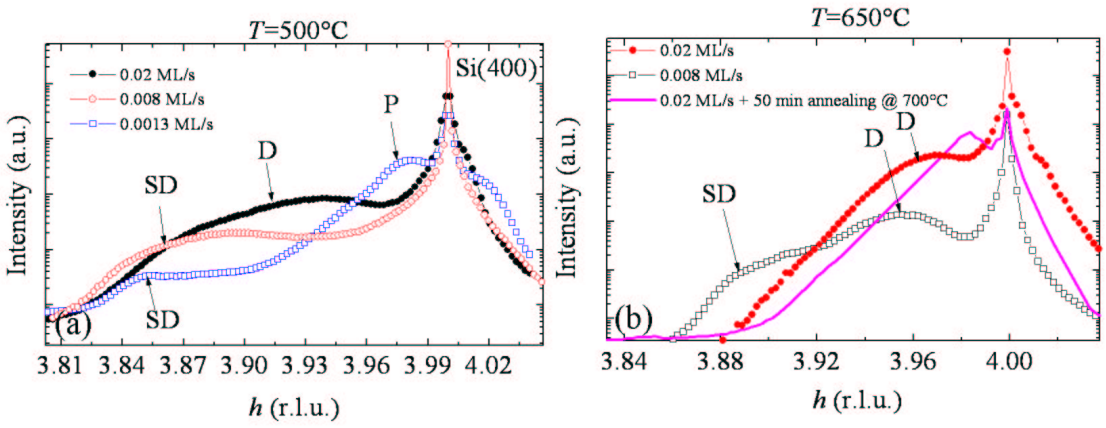

Figure 6.35: Radial scans along the [h00] direction, in the vicinity of the Si(400) reflection for a growth temperature of 500°C (a) and 650°C (b) and for different growth conditions: growth rate and/or annealing.

In a simple energetic model, the total energy stored by an island with volume $V = L^2h$ can be written as follows [44, 33, 45]:

$$E = \frac{1}{2}c\epsilon^2L^2h + E(D) \tag{6.19}$$

$$E = \frac{1}{2}c(x_{Ge}f - N\frac{b}{L})^2L^2h + Gb^2NL, \tag{6.20}$$

where $E(D)$ is the energy to create the interfacial 60° dislocation network, ϵ is the mean island strain [33], x is the Ge content of the islands, f is the Si/Ge misfit (0.042), N the number of dislocations of Burgers vector b, c the elastic coefficient and G the shear modulus. It becomes energetically favorable to introduce a dislocation for an island when $E(N = 1) < E(N = 0)$. This implies that it is energetically favorable to introduce a dislocation when the mean Ge concentration x_{Ge} of an island follows the relation:

$$x_{Ge}L > \frac{b(c\xi + 2G)}{2\xi cf} = const, \tag{6.21}$$

where ξ verifies $h = \xi L$.

To understand the impact of the growth rate and annealing on the introduction of dislocations, the average Ge:Si interdiffusion inside each sample was studied by X-ray anomalous scattering using the multiwavelengths anomalous diffraction (MAD) technique.

Fig. 6.36 shows the Ge concentration calculated from the Ge and Si structure factors extracted from the MAD program. It appears that Si intermixing is enhanced for slower growth rates (see Fig. 6.36 (a)). It has also been observed that the size of islands is increased whereas the density of islands is decreased for slower growth rates [16, 41]. Formation of bigger islands is enhanced by the increase of the surface diffusion length ($l = \sqrt{Dt}$, where D is the diffusion coefficient and t the time). A slow growth rate is thus characterized by an increase of the mean island size whereas the Ge content decreases. From Eq. 6.21, it appears that there is a competition between intermixing and island size to incorporate a dislocation. Assuming that the critical volumes for which it becomes energetically favorable for an island to incorporate a dislocation is proportional to x^{-6} [42, 43, 32],

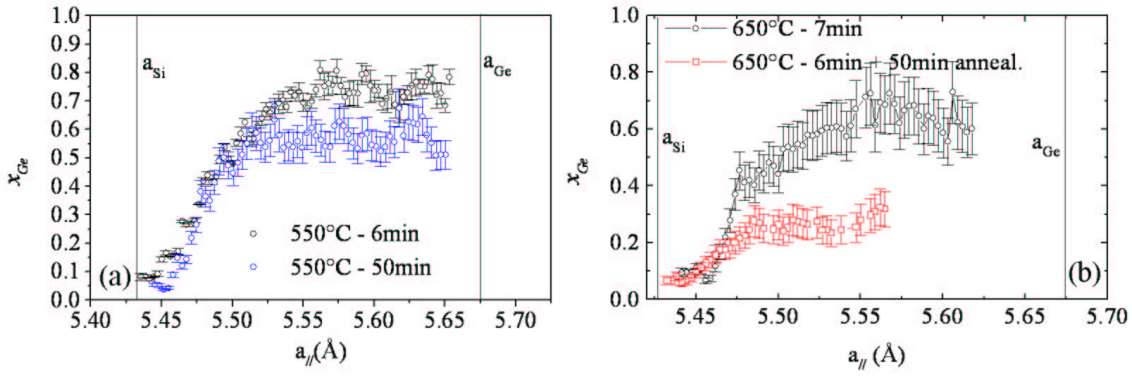

Figure 6.36: Ge content for samples grown at 500°C (a) for a fast and slow growth rate and at 650°C (b) for a fast growth rate and after annealing. The time corresponds to either the time spent to deposit 8 ML on the sample or to the annealing time.

growth temperature (°C)	growth time (min)	ordered domains	stacking faults	average Ge content
500	6	***yes***	no	***0.65***
550	6	no	yes	0.75
550	50	no	yes	0.6
600	6	***yes***	no	***0.5***
650	7	***yes***	yes	***0.56***
650	50	no	yes	0.62
700	50	***yes***	no	***0.46***
720	6	***yes***	no	***0.47 - 0.38***

Table 6.3: Table of studied samples

the $x_{Ge}L$ product is roughly proportional to $\frac{1}{x}$. The slower the growth rate, the smaller the Ge concentration and thus the smaller the criterion ($x_{Ge}L \propto \frac{1}{x}$) for which a dislocation is introduced. Thus the condition $x_{Ge}L > const.$ can be fulfilled for smaller deposit compared to a fast growth rate. This explanation is also valid for annealing. Whereas Si intermixing is enhanced, the volumes of islands increases as a result of intermixing and enhancement of anomalous coarsening. Intermixing delays the introduction of dislocations as the first dislocation will be introduced for an higher volume as mentioned by Merdzhanova *et al.* [32]. As more intermixed systems have a higher volume and as the volume increases faster than the decrease of Ge content, a slow growth rate or annealing will fasten the introduction of dislocations inside Ge nanostructures, *i.e.* dislocations will appear for an earlier deposit of Ge. For the first time, it appears that a slow growth rate can fasten the introduction of defects inside nanostructures; which is explained by a simple energetic model.

Table 6.3 shows the mean Ge composition associated to the appearance of ordered domains or stacking faults. It follows that atomic ordering is observed when the mean Ge composition is $\sim$ 0.5. This corroborates that the diffuse intensity lobes observed at the (200) may come from atomic ordering.

6.5 Conclusion

To conclude, up to now, only atomic ordering explains the two intensity lobes observed at the (200). Mapping the (200) forbidden reflection allows also to detect the presence of {111} stacking faults, to determine their sizes perpendicular to the $< 111 >$ ***directions, to evaluate the number of defects during the*** **in situ** ***growth and to determine the mean in-plane distance between interfacial dislocations. A simple energetic model shows that a slow growth rate can fasten the introduction of dislocations inside the nanostructures.***

Bibliography

[1] A. Malachias, T. U. Schülli, G. Medeiros-Ribeiro, L. G. Cancado, M. Stoffel, O. G. Schmidt, T. H. Metzger and R. Magalhães-Paniago, Phys. Rev. B (**72**), 165315 (2005).

[2] T. S. Kuan, T. F. Kuech, W. I. Wang, and E. L. Wilkie, Phys. Rev. Lett. (**54**), 201 (1985).

[3] A. Ourmazd and J. C. Bean, Phys. Rev. Lett. (**55**), 765 (1985).

[4] A. Gomyo, K. Iobgayashi, S. Kawata, I. Hino, T. Suzuki, and T. Yuasa, J. Crystal Growth (**77**), 367 (1987).

[5] L. C. Su, I. H. Ho, N. Kobayashi, and G. B. Stringfellow, J. Cryst. Growth (**145**), 140 (1994).

[6] J. L. Martins, A. Zunger, Phys. Rev. Lett. (**56**), 1400 (1986).

[7] P. B. Littlewood, Phys. Rev. B (**65**), 153306 (1986).

[8] E. Müller, H.-U. Nissen, M. Ospelt, H. von Känel, Phys. Rev. Lett. (**63**), 1819 (1989).

[9] F. K. LeGoues, V. P. Kesan, S. S. Iyer, Phys. Rev. Lett. (**64**), 40 (1990).

[10] F. K. LeGoues, V. P. Kesan, S. S. Iyer, J. Tersoff, R. Tromp, Phys. Rev. Lett. (**64**), 2038 (1990).

[11] D. E. Jesson, S. J. Pennycook, and J.-M. Baribeau, Phys. Rev. Lett. (**66**), 750 (1991).

[12] D. E. Jesson, S. J. Pennycook, J.-M. Baribeau and D. C. Houghton, Phys. Rev. Lett. (**68**), 2062 (1991).

[13] D. E. Jesson, S. J. Pennycook, J. Z. Tischler, J. D. Budai, J.-M. Baribeau and D. C. Houghton, Phys. Rev. Lett. (**70**), 2293 (1993).

[14] A. Chakrabarti, P. Kratzer and M. Scheffler, Phys. Rev. B (**74**), 245328 (2006).

[15] J. E. Bernard, R. G. Dandrea, L. G. Ferreira, S. Froyen, S.-H. Wei, and A. Zunger, Appl. Phys. Lett. (**56**), 731 (1990).

[16] P. C. Kelires and J. Tersoff, Phys. Rev. Lett. (**63**), 1164 (1989).

[17] S. P. Najda, A. Kean, G. Duggan, J. Appl. Phys. (**82**), 4408 (1997).

[18] J. Z. Tischler, J. D. Budai, D. E. Jesson, G. Eres, P. Zschack, J.-M. Baribeau, and D. C. Houghton, Phys. Rev. B (**51**), 10947 (1995).

[19] N. Ikarashi, K. Akimoto, T. Tatsumi and K. Ishida, Phys. Rev. Lett. (**72**), 3198 (1994).

[20] K. L. Whiteaker, I. K. Robinson, J. E. Nostrand, and D. G. Cahill, Phys. Rev. B (**57**), 12410 (1998).

[21] A. Malachias, T. H. Metzger, M. Stoffel, O. G. Schmidt, V. Holy, Thin Solid Films (**515**), 5587 (2007).

[22] J. Z. Tischler and B. W. Batterman, Phys. Rev. B (**30**), 7060 (1984).

[23] P. Kelires, *private communication*.

[24] A. Malachias, S. Kycia, G. Meideros-Ribeiro, R. Magalhaes-Paniago, T. I. Kamins, R. S. Stanley, Phys. Rev. Lett. **91**, 176101 (2003).

[25] U. Denker, M. Stoffel and O. Schmidt, Phys. Rev. Lett. **90**, 196102 (2003).

[26] M. S. Leite, G. Medeiros-Ribeiro, T. I. Kamins, and R. Stanley Williams, Phys. Rev. Lett. **98**, 165901 (2007).

[27] C. S. G. Cousins, Acta. Cryst. **A 39**, 256101 (2001).

[28] P. Sonnet, and P. C. Kelires, Phys. Rev. B **66**, 205307 (2002).

[29] G. Hadjisavvas, and P. C. Kelires, Phys. Rev. B **72**, 075334 (2005).

[30] A. Rastelli, M. Stoffel, J. Tersoff, G. S. Kar, and O. G. Schmidt, Phys. Rev. Lett. **95**, 026103 (2005).

[31] T. I. Kamins, G. Medeiros-Ribeiro, D. A. A. Ohlberg, and R. Stanley Williams, J. Appl. Phys. **85**, 1159 (1999).

[32] T. Merdzhanova, S. Kiravittaya, A. Rastelli, M. Stoffel, U. Denker, and O. G. Schmidt, Phys. Rev. Lett. **96**, 226103 (2006).

[33] J. Tersoff and R. M. Tromp, Phys. Rev. Lett. **70**, 2782 (1993).

[34] L. Capello, *Thesis of the Universty Claude Bernard-Lyon I and of the University of Torino*, Mai 2005.

[35] M. Stoffel, A. Rastelli, J. Stangl, T. Merdzhanova, G. Bauer and O.G. Schmidt, Phys. Rev. B. **75**, 113307 (2007)

[36] H Mariette, C. R. Physique **6**, 23 (2005).

[37] J. Zou, X. Z. Liao, D. J. Cockayne, Z. M. Jiang, Appl. Phys. Lett. 81, 1996 (2002).

[38] D. J. Smith, D. Chandrasekhar, S. A. Chaperro, P.A. Crozier, J. Drucker, M. Floyd, M. R. McCartney, Y. Zhang, J. of Crystal Growth **259**, 232 (2003).

[39] T. U. Schülli, M. Stoffel, J. Stangl, R. T. Lechner, E. Wintersberger, M. Sztucki, T. H. Metzger, O. G. Schmidt and G. Bauer, Phys. Rev. B. **71**, 035326 (2005).

[40] G. Capellini, M. De Seta, and F. Evangelisti, J. Appl. Phys. **93**, 291 (2003).

[41] B. Cho, T. Schwarz-Selinger, K. Ohmori, D. G. Cahill and J.E. Greene, Phys. Rev. B **66**, 195407 (2002).

[42] J.A. Floro, G.A. Lucadamo, E. Chason, L.B. Freund, M. Sinclair, R.D. Twesten, and R.Q. Hwang, Phys. Rev. Lett. **80**, 4717 (1998).

[43] A. Rastelli *et al.*, Phys. Rev. Lett. **87**, 256101 (2001).

[44] F. Tinjoux, PhD Thesis, University Joseph Fourier (2003).

[45] V. Holý, *private communication*.

Chapter 7

In situ results of the growth of Ge islands on nominal Si(001).

In this chapter, in situ results of the growth of Ge islands on nominal Si(001) is presented. The impact of growth interruption and growth rate on island shape and composition is highlighted. Transport of material during the 2D-3D transition is addressed. The evolution of island morphology and relaxation during a slow growth rate is presented. Finally, a new shape of superdomes is reported.

7.1 Introduction

Growth of semiconductor islands has been studied in great detail on a variety of heteroepitaxial systems [1]-[3]. Due to the modified properties of the band structure and the density of states, such quantum dots promise to supply the basis for new optoelectronic devices. After two decades of research on these systems, the first devices based on zero dimensionally confined objects are commercially exploited [4] as laser diodes with a very low threshold current. This technology requires a certain tunability of structural properties of the quantum dots.

The physical properties of semiconductor nanoparticles depend to a geat extend on their size, shape, internal structure, strain and composition, which thus have to be fully controlled and understood. Semiconductor nanostructures are classically grown by the Stranski-Krastanow (SK) mechanism for which, beyond a critical thickness, islands are formed on a two-dimensional wetting layer. This is the case for the growth of Ge on Si(001) for which the 2D-3D transition is driven by the 4.16% lattice mismatch between Ge and Si, Ge having the larger lattice parameter. The mechanism of the SK growth of Ge layers on Si(001) substrates has been investigated extensively (see *e.g.* Ref. [5] for a review). By increasing the Ge coverage above a critical thickness of ∼4 monolayers (ML), islands that are coherent *i.e.* without defects appear. Square pyramids exposing {105} facets first appear, followed by dome-shaped islands with {105}, {113}, {15 3 23} facets, and a top (001) facet [3, 6]. Another type of coherent islands called 'barns' with additionnal {111} and {20 4 23} facets [7, 8] may follow. Above a thickness between ∼8 and 11 ML [9, 8], the misfit strain can no longer be accomodated coherently, and larger islands named 'superdomes' with interfacial misfit dislocations appear. They expose similar facets as barns, but with different relative sizes.

Despite the wide knowledge acquired in this system, there are still some open questions concerning the evolution of the strain, the elastic to plastic relaxation, the intermixing and their relations with the different shapes of the island. These questions will be investigated in the next sections.

	500°C - slow	650°C - slow	650°C - fast	500°C - fast
No growth int.	S_1 (8 ML)	S_3 (7 ML)	S_5 (7 ML)	
Growth int.	S_2 (8 ML)	S_4 (7 ML)	S_6 (7 ML)	S_7 (8 ML)

Table 7.1: Impact of growth interruption. The words slow and fast mean slow and fast growth rates.

7.2 Impact of growth rate and growth interruption.

To look at the influence of growth rate and growth interruption on the strain relaxation and morphology of the growing islands, 8 ML of Ge were deposited with a slow growth rate (∼0.0048 ML/s) on four Si(001) substrates, named S_1, S_2, S_3 and S_4. This was done in the BM32 MBE/GIXD setup. Samples S_1 and S_2 were grown at 500°C and samples S_3 and S_4 at 650°C. For samples S_2 and S_4, after each deposited monolayer, the growth was interrupted 40 min and the temperature decreased to 450°C for X-ray measurements. No growth interruption was performed for samples S_1 and S_2. This allows to characterize the impact of growth interruption at 500°C and 650°C for a slow growth rate. Three other samples were grown with a fast growth rate (∼0.024 ML/s): samples S_5, S_6 and S_7. Seven monolayers of Ge were deposited at a growth temperature of 650°C for samples S_5, S_6 and eight monolayers of Ge were deposited at a growth temperature of 500°C for sample S_7. Contrary to sample S_6 and S_7, no growth interruption was performed for sample S_5. This allows to study the impact of the growth rate. Table 1 summarizes the growth conditions for each sample.

Figure 7.1 shows the AFM profiles of the different samples. No superdomes are observed on the AFM images of samples S_4, S_5 and S_6. Nevertheless, an extended AFM study (see insets in Fig. 7.1) shows the absence of superdomes only on sample S_5 grown with a fast growth rate without growth interruption. *A fast growth rate will thus delay the appearance of defects inside the Ge islands.*

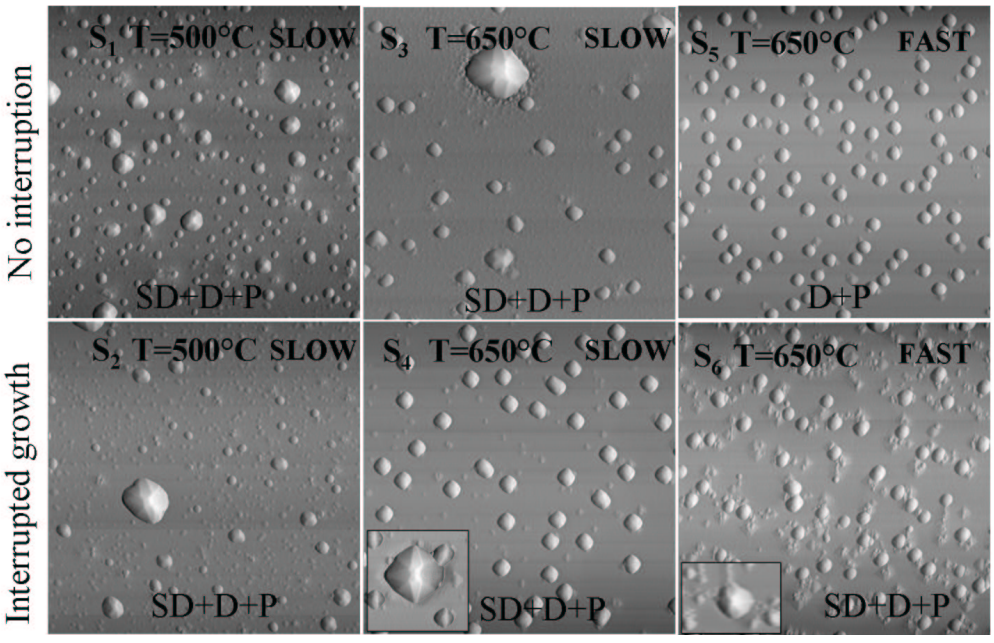

Figure 7.1: AFM images of the six studied samples. The whole scan range is 2μm. The inserted AFM images show a 200 nm wide superdome (S_4) and a 290 nm wide superdome (S_6). The letters P, D and S mean pyramids, domes and superdomes.

Figures 7.2 (a)-(b) show radial scans around the (400)Si Bragg peak, collected with an incident angle α_i of 0.15°, slightly below the critical angle for Si. They allow to compare the relaxation state as a function of growth temperature, growth rate and growth interruption. For a growth temperature of 500°C, one maximum of Ge scattering is displaced towards the position of fully relaxed Ge (h=3.84):h ∼3.855 for S_1 and S_2. For the growth temperature of 650°C, the Ge signal is centered at much larger h values than for T=500°C: h ∼3.9-3.955 for S_3, h ∼3.92-3.96 for S_4 and h ∼3.96 for S_5. On all samples, except on sample S_5, dislocated superdomes are observed. The introduction of dislocations leads to a more complete relaxation. Only the enhancement of intermixing at high temperature [10] can explain the difference of the position of the maximum of diffuse scattering between the growth temperatures of 500°C and 650°C. As previously observed [10], islands are more intermixed at high temperatures.

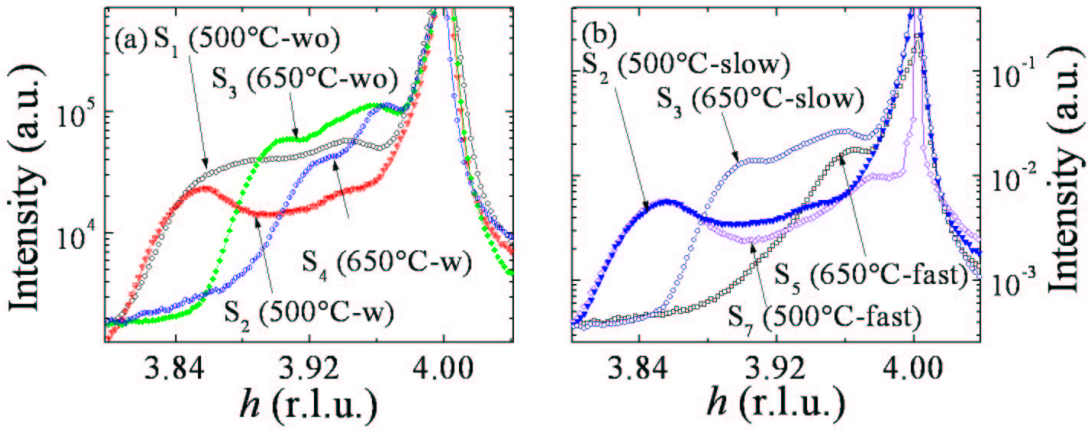

Figure 7.2: Radial scans around the (400)Si Bragg peak. (a) Slow growth rate, impact of growth interruption. The 'w' and 'wo' letters mean with and without interruptions. (b) Impact of the growth rate.

For a growth temperature of 500°C and a deposit of 8 ML, the samples are composed of pyramids, domes and superdomes for a slow growth rate, with and without interruption (S_2 and S_1) and for a fast growth rate with interruption (S_7). For all samples grown at T=500°C, a double shoulder is observed (see Fig. 7.2 (a)-(b)). This indicates at least a bimodal growth for the considered temperatures. The shoulder, closest to the Si-peak is centered at h ∼3.945 (S_1), h ∼3.94 (S_2) and h ∼3.975 (S_7). The second maximum in intensity, close to the position of relaxed Ge, is located at h ∼3.855. It hardly evolves with growth interruption or growth rate. The more relaxed islands correspond to the observed superdomes on the AFM images (see Fig. 7.1). At T=500°C, growth interruption or growth rate have thus a small impact on the relaxation states of the dislocated islands. The other maximum close to the Si-peak corresponds to less relaxed Ge islands, such as domes or pyramids.

For a slow growth rate (see Fig. 7.2 (a)), the position of this maximum (h ∼3.94 at 650°C (S_3, S_4) and h ∼3.93 at 500°C (S_1, S_2)) slightly evolves with or without growth interruption. This maximum is more intense without growth interruption, *i.e.* the density of coherent domes is larger without interruption. This means that the total number of atoms in coherent domes is higher without growth interruption. This coincides with the AFM images which show that the number of domes is higher for S_1 compared to S_2, where superdomes dominate. More facetted pyramids are observed on sample S_2. It has been recently observed [11] that domes can transform back into pyramids during annealing. The

Samples (T=500°C)	Coherent islands size	Samples (T=650°C)	Domes size
S_1 (D)	26±2 nm	S_3	41±3 nm
S_2 (D)	22±2 nm	S_4	63±3 nm
S_7 (P)	17±2 nm	S_5	58±3 nm
		S_6	54±3 nm

Table 7.2: Size of coherent islands for a growth temperature of 500°C and 650°C.

same phenomenon may appear during growth interruption. For a fast growth rate (S_7), the position of the maximum is displaced towards the position of the Si Bragg peak. AFM images (not shown here) reveal the presence of pyramids and superdomes. No domes are observed. During a fast growth rate with interruption, and after a deposit of 7ML, only pyramids and superdomes are observed. Thus, growth interruption may transform domes back to pyramids, which explains why the maximum is displaced towards the position of the Si Bragg peak.

For a growth temperature of 650°C and a deposit of 7 ML, the samples are composed of pyramids, domes and superdomes for a slow growth rate, without and with interruption (S_3 and S_4) and for a fast growth rate with interruption (S_6). As already mentioned, for a fast growth without interruption (S_5), no superdomes are observed. For this sample (S_5), the Ge scattering shows only one maximum located at h ∼3.965. This corresponds to the signal of coherent domes. For the other samples grown at 650°C, the scattered intensity is composed of a double shoulder which coincides well with the bimodal growth observed on the AFM images. The shoulder, closest to the Si-peak is centered at h ∼3.958 (S_3), h ∼3.965 (S_4) and h ∼3.96 (S_6 - GIXD data not shown here). This signal is located close to the same position as the maximum of intensity of the sample (S_5) composed only of domes. Thus, this signal corresponds to the dome islands. The second maximum, closest to the position of relaxed Ge, is located at h ∼3.9 (S_3), h ∼3.92 (S_4) and h ∼3.91 (S_6 - GIXD data not shown here). This signal corresponds to more relaxed islands, such as superdomes. Note that few superdomes are observed on samples S_4 and S_6. Nevertheless, due to their large volume and as the intensity is proportional to the square of the number of atoms, their signal can be observed in diffraction. In addition, it can be noticed that the position of the maxima is displaced towards the position of the Si-peak in the case of samples grown with interruption (S_4 and S_7) compared to sample grown without interruption (S_3). This can be understood for instance by the fact that intermixing is enhanced during growth interruption. Thus, growth interruption and growth rate have a strong impact on the growth mode at T=650°C.

To compare the size of coherent domes as a function of growth temperature, growth interruption or growth rate, the full width at half maximum (FWHM), $\Delta\theta$ of the angular scans related to the position of the maximum of intensity closest to the Si-peak was measured. The lateral size D is determined by:

$$D = \frac{\lambda}{2sin(2\Theta/2)\Delta\Theta}, \tag{7.1}$$

where 2Θ is the Bragg angle. It can be observed that the lateral size of coherent islands grown at T=500°C is smaller than the one of those grown at T=650°C. This can be explained by the surface mobility and by intermixing, which are enhanced at high temperature and which lead to larger islands and lower island density. No clear dependence on the island size appears with or without growth interruption. With growth interruption, an increase of the island size (comparison between S_3 and S_4) can be explained by the increase of intermixing during interruption, a decrease of the island size (comparison between S_1 and S_2 at 500°C and between S_3 and S_4 at 650°C) can be explained by a shape transition from domes to pyramids during interruption, as observed on the AFM images and as already observed during annealing.

Figure 7.3 shows reciprocal space maps around the (400)Si Bragg peak. The circles indicate the relaxation states of domes and superdomes as a function of growth temperature. The effect of intermixing is obvious.

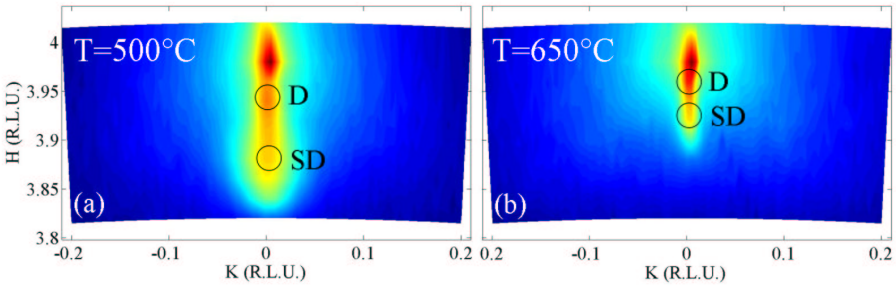

Figure 7.3: (a) (400) reciprocal space map for the sample grown at 500°C with a slow growth rate and without interruption (S_1). (b) (400) reciprocal space map for the sample grown at 650°C with a slow growth rate and with interruption (S_4). The circles indicate the position where domes ans superdomes scatter.

To summarize, only the enhancement of intermixing at high temperature can explain the difference of island relaxation between the growth temperatures of 500° C and 650° C. At T=500° C and after a deposit of 8ML of Ge, growth interruption or growth rate have a small impact on the relaxation states of the dislocated islands. For a growth temperature of 500° C and with growth interruption, more coherent pyramids than domes are observed on the AFM images. This can only be explained by a shape transition from domes to pyramids during growth interruption. At T=650° C, growth interruption and growth rate have a strong impact as a fast growth rate will delay the apparition of superdomes.

7.3 *In situ* anomalous scattering: determination of the composition of Ge islands on Si(001) using X-ray scattering methods.

In this section, the energy dependence of the atomic scattering factor f will be used to determine the chemical composition of the Ge islands. As previously described, the Kramers-Kronig relationships can be exploited for the precise determination of f' and $f"$. Experimentally, an integration over the energy from 0 to ∞ has to be avoided. Nevertheless, we are sensitive to a more detailed structure of $f"$ in the energy regime where a precise information about f' is needed. These energy regimes are usually the edges, and, in our cases, the Ge K-edge. Tabulated values of $f"$ are thus replaced by renormalized experimental values of $f"$ in the energy range across the absorption edge and used as input to calculate f'. The experimental $f"$ values were determined via the fluorescence yield across the Ge K-edge which was measured from 8ML-grown Ge islands. The theoretical and experimental values of the anomalous corrections (f' and $f"$) are plotted in fig. 7.4.

Recording experimental diffraction data for multiple wavelengths across the Ge K-edge, the scattering contributions of Ge and Si can be discriminated. Using the `NanoMAD` program, it is then possible to quantitatively extract $|F_{Ge}|$ and $|F_{Si}|$ through a least-square minimization.

The Ge_xSi_{1-x} content can then be deduced using the relation:

$$\frac{|F_{Ge}|}{|F_{Si}|} = \frac{x f^0_{Ge}}{(1-x)|f_{Si}|} \tag{7.2}$$

$$x = \frac{y|f_{Si}|}{f^0_{Ge} + y|f_{Si}|}, \tag{7.3}$$

where $y = |F_{Ge}|/|F_{Si}|$. The error on y can be written as:

$$\Delta y = y\left(\frac{\Delta F_{Si}}{F_{Si}} + \frac{\Delta F_{Ge}}{F_{Ge}}\right) \tag{7.4}$$

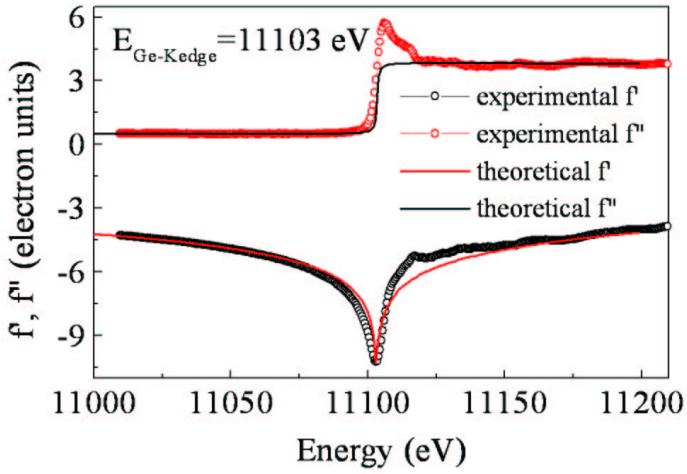

Figure 7.4: Theoretical and measured values of f" close to the Ge K-edge. Values of f' are obtained through the Kramers-Kronig relations.

	Superdomes	Domes	Pyramids
slow growth - no interruption S_1	75%	60%	
slow growth - no interruption S_8	78%		37%
slow growth - interruption S_2	73-80%	65-73%	30-34%
fast growth - interruption S_7	78-83%		34-40%

Table 7.3: Mean Ge composition as a function of island morphology at T=500°C.

The `NanoMAD` program gives a good estimation of the Ge composition in regions which fulfill $F_{Ge} >> 0$ and $|F_{Ge} - F_{Si}| >> 0$, *i.e.* in the scattering region of 3D islands.

For all samples, MAD experiments have been performed after a deposit of θ =8ML (samples S_1, S_2 and S_7 grown at T=500°C), θ =7ML (samples S_3, S_4, S_5 and S_6 grown at T=650°C) and θ =11ML (sample S_8 grown at T=500°C). The Ge, Si and the total structure factors were extracted and allowed to estimate the Ge composition as a function of the island in-plane relaxation. Before the extraction, the scattered intensity has been substracted by the intensity scattered at θ =0ML in order to eliminate the non-anomalous signal coming from the thermal diffuse scattering of the Si substrate. Fig. 7.5 (a) displays the Ge content as a function of the island in-plane relaxation as well as the Ge, Si and the total structure factors extracted for all samples grown at 500°C.

Table 7.3 gives the mean Ge composition as a function of island morphology.

A radial scan is sensitive to the strain relaxation of the islands. By a comparison between the X-ray results and the AFM profiles, it is possible to determine the strain created by pyramids, domes and superdomes and then, to have access to their corresponding composition. The indexation is consistent with finite element simulations. At a growth temperature of 500°C, superdomes, domes and pyramids present a mean Ge composition of (73-83)±25%, (60-71)±15% and (34-40)±15%, respectively. Note that the error bar is larger in the scattering region of superdomes as $|F_{Si}|$ is low (see Eq. 7.4). It appears that superdomes are less intermixed. This is consistent with Ref. [12]. As observed by LeGoues *et al.*, once a dislocation has been introduced, dislocated islands become more relaxed and are thus preferred with respect to domes for Ge attachment. Contrary to what has been previously observed [13], MAD results show that pyramids are more Si intermixed than domes. These results

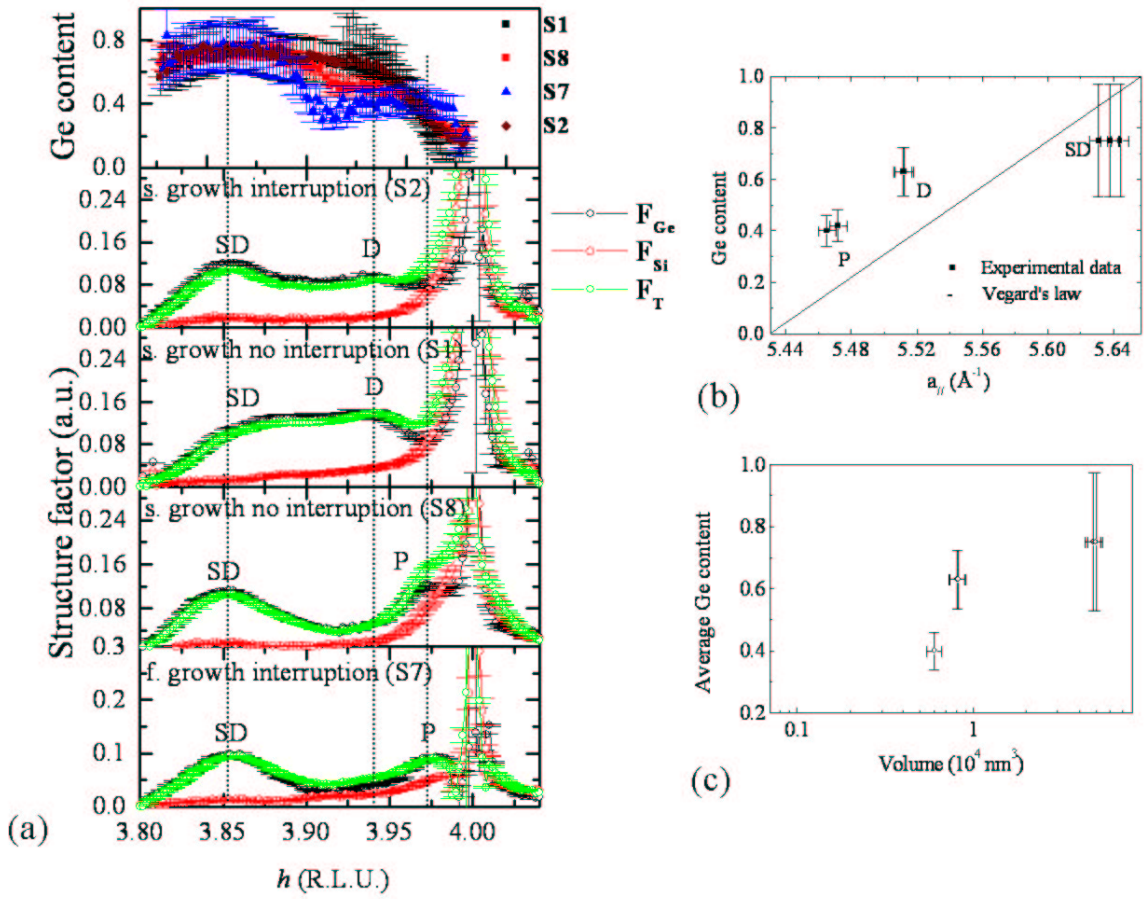

Figure 7.5: (a) Ge content as a function of in-plane relaxation at T=500°C. The structure factors of *Ge*, *Si* and the total structure factors as a function of in-plane relaxation. The maximum relaxation of pyramids, domes and superdomes are labelled 'P', 'D' and 'SD'. Ge content of pyramids, domes and superdomes as a function of (b) in-plane lattice parameter and (c) island volume.

are in good agreement with recent results obtained by A. Rastelli *et al.* using a tomographic approach based on selective etching. Fig. 7.7 (b) and (c) show the average Ge fraction in pyramids, domes, barns and superdomes using this approach. For a very fast, withou interruption growth at 740°C and a deposit of 15 ML of Ge, pyramids are composed on average of 30% of Ge. This is slighlty lower than what we observe as our growth temperatures are lower. A smaller Ge content in pyramids is also in agreement with the recent work of Baribeau *et al.* [14] who used analytical transmission electron microscopy to map the composition of Ge dots grown on Si(001) by molecular beam epitaxy. ∼6 ML of Ge were deposited at 650°C with a growth rate of ∼0.007ML/s. They observed a considerable intermixing in pyramids with a Ge concentration increasing almost linearly from close to 0 at the base to about 50% at the apex of the pyramid. The mean Ge content in the pyramid was about ∼30-35%, whereas in the dome, this was higher than ∼40%. They related the stronger intermixing in the pyramid to strain. Pyramids remain heavily tetragonally distorted in comparison to the domes that adopt a relaxed lattice constant close to that of bulk Ge near the top of the dot.

The Ge composition may be underestimated in the case of pyramids as pyramids scatter near the scattering region of the distorted Si substrate. A small variation of composition (lower than the estimated error bars) can be observed when varying the growth rate or when performing growth

	Superdomes	Domes
slow growth - interruption S_4	58-65%	50%
slow growth - no interruption S_3	61%	57%
fast growth - no interruption S_5		53%
fast growth - interruption S_6	61%	53-55%

Table 7.4: Mean Ge composition as a function of island morphology at T=650°C.

interruptions at 500°C. A slow rate or growth interruption have a small impact on the mean vertical composition of the islands at 500°C. Figs. 7.5 (b) and (c) display the Ge content as a function of in-plane lattice parameter and island volume. This demonstrates that the mean Ge content is far from being given by Vegard's law. The correct value of local in-plane strain with local composition Si_xGe_{1-x} is given by $\epsilon_{//} = \frac{a'}{a(x)} - 1$, where $a(x)$ is the lattice parameter of an unstrained alloy (calculating using the Vegard's law $a(x) = xa_{Si} + (1-x)a_{Ge}$) and a' is the in-plane average lattice parameter which is inversely proportional to the h=h_{Ge} position of the diffuse F_{Ge} peak maximum. Note that $\epsilon_{//} < 0$ for superdomes in Fig. 7.5 (b), which is not physical. This means that the mean Ge concentration inside superdomes has been underestimated. At these lattice parameters, the Si structure factor is small increasing the error on the determination of the Ge content.

The same analysis has been performed for islands grown at T=650°C (see Fig. 7.6 (f)-(j)). Table 7.4 gives the mean Ge composition as a function of island morphology. This shows that the mean Ge composition is lower at a high growth temperature, as observed in literature [10]. As previously observed for T=500°C, superdomes are less intermixed than domes. For these series of samples, a small variation of composition (lower than the estimated error bars) can be observed when varying the growth rate or when performing growth interruptions. This does not discard the possibility of lateral variation of the composition inside islands as a function of growth rate as observed by Katsaros *et al.* [15].

Performing MAD at the end of the growth allows to determine the mean Ge composition inside as grown pyramids, domes and superdomes. The results are in agreement with literature: higher Ge content inside superdomes and small amount of Ge inside pyramids for the two investigated temperatures for both fast and slow growth rates. These results also raise the question how the Ge content evolves inside pyramids, domes and superdomes ***during*** *their growth.* We address these issues using *in situ* multiwavelength anomalous diffraction (MAD) measurements close to the Ge K-edge during the growth, monolayer after monolayer. *In situ* MAD experiments have been performed during growth for three samples (see Fig. 7.8):

- at T=500°C and with a fast growth rate (see Fig. 7.8 (a)) (S_7)
- at T=500°C and with a slow growth rate (see Fig. 7.8 (b)) (S_2)
- at T=650°C and with a slow growth rate (see Fig. 7.8 (c)) (S_4)

After completion of each monolayer, the temperature was decreased to allow X-ray measurements without further kinetic evolution.

In the growth regime of the wetting layer, no variations are observed for F_{Si} and F_{Ge} (not shown here). The wetting layer is thus pseudomorphic. Fig. 7.8 (a) shows GIXD measurements which were performed around the Si(400) Bragg peak at 500°C for a fast growth rate (sample $S7$). At a deposit of 3 ML, a small diffuse scattering appears on the left-hand part of the Si(400) at h ∼3.975 and increases in intensity up to a deposit of 5 ML. The Ge content associated to this scattering region is $\sim (35 \pm 15)$%. As pyramids are strained by the Si substrate and as after growth pyramids are observed on this sample (AFM image not shown here), the scattering measured at this position can be attributed to strained pyramids. As already mentioned, the Ge content inside pyramids may be underestimated as pyramids scatter near the Si substrate. With increasing deposit, the scattering

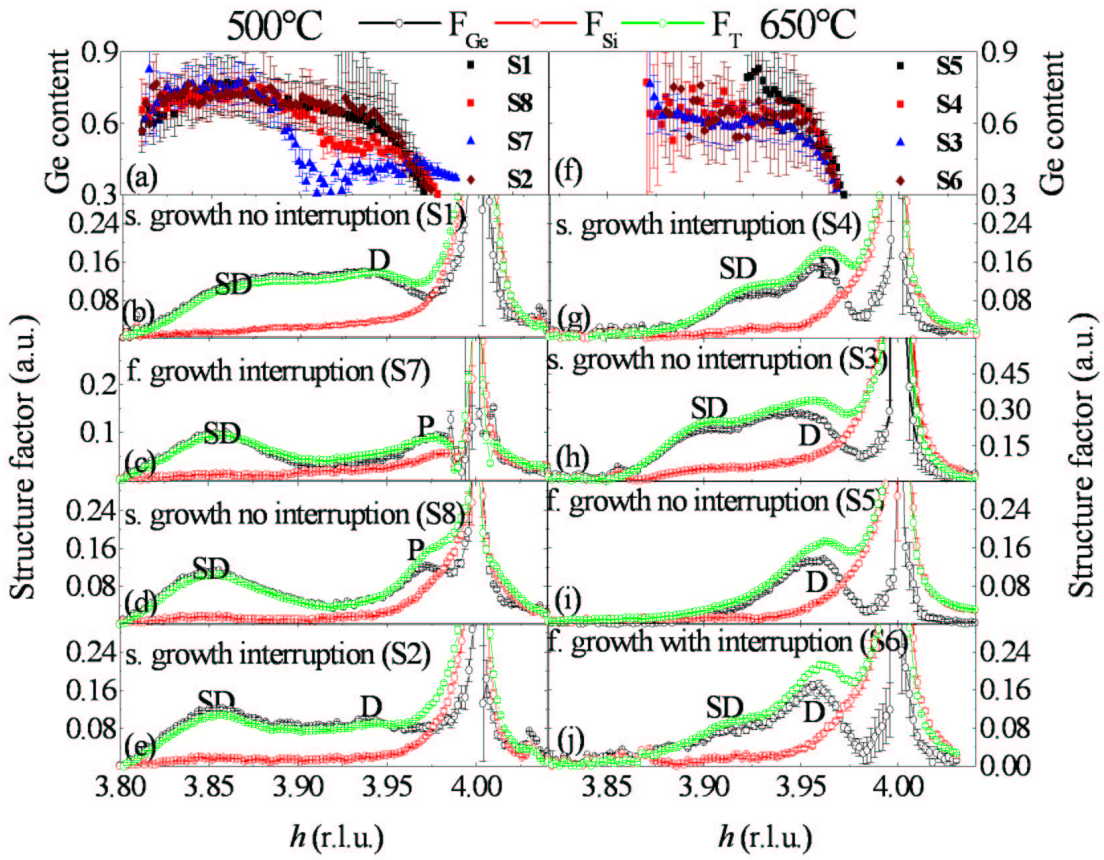

Figure 7.6: Ge content as a function of in-plane relaxation at T=500°C (a) and T=650°C (f). *Ge*, *Si* and the total structure factors as a function of in-plane relaxation (b)-(e) at T=500°C and (g)-(j) at T=650°C. The maximum of relaxation of pramids, domes and superdomes are labelled 'P', 'D' and 'SD'.

from pyramids decreases, while a new component appears at lower h values (h ∼3.855), close to the value of fully relaxed Ge. With increasing deposit, this last component increases. The large lattice parameter of these islands, close to the value for bulk Ge, can only be explained by large, plastically relaxed islands. For a deposit of 5 ML and after, the signal from dislocated islands increases while the one from pyramids decreases indicating the formation of dislocated islands via coalescence of pyramids. The dislocated islands show a mean Ge content of (78±20)%, while pyramids are highly intermixed. MAD is a well suited method to follow the variation of the Ge content inside different scattering regions during the *in situ* growth. *What is remarkable is that the mean Ge content inside pyramids slightly evolves (∼(35±15)%) with Ge deposit.* The growth may be summarized as follows:

- after a deposit of 3 ML of Ge, growth of highly intermixed pyramids;
- at 6 ML, pyramid coalescence resulting in the formation of superdomes with a higher Ge content as superdomes are prefered for Ge attachement.

This implies that intermixing occurs at the beginning of the growthTo confirm this, we performed finite difference method (FDM) simulations. Assuming a coherent ∼55 nm (as measured by GIXD angular scans) wide pyramid of pure Ge, the scattered intensity was simulated around the Si(400)

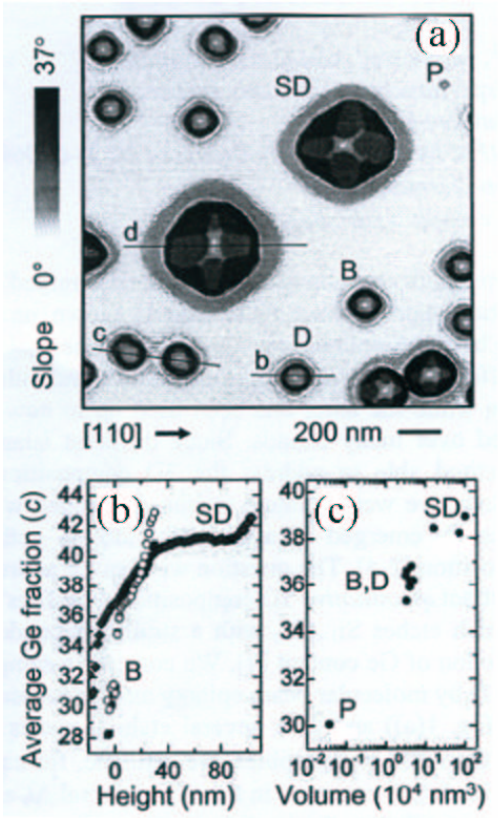

Figure 7.7: (a) AFM scan of a sample obtained upon deposition of 15 ML of Ge at 740°C on Si(001). Superdomes (SD), barns (B), domes (D) and pyramids (P) are observed. (b) Average Ge fraction as a function of height for two barns and a superdome showing the increase of Ge content with increasing distance from the Si substrate. (c) Average Ge fraction as a function of island volume for the islands shown in (a). The composition is determined by selective etching. Courstesy of A. Rastelli.

Bragg peak (see Fig. 7.9). The average relaxation of the simulated island is not centered at the position of the experimental data and is shifted towards the position of the Ge bulk Bragg peak. This confirms that the experimentally observed relaxation cannot be achieved by pure Ge pyramids but by intermixed pyramids.

Note that at 500°C, generally, no intermixing is observed in islands [16]. However, this is for growth rates much larger than here, and of course without interruption. In addition, the temperature may slightly differ from one equipment to another. In the present case, at 500°C, intermixing is observed inside pyramids and superdomes are slightly intermixed.

The same behaviour is observed for a slow growth rate (see Fig. 7.8 (b)). Contrary to the previous growth, an additional diffuse scattering, which is related to domes, appears in-between the signals from pyramids and superdomes. Domes display a composition equal or slightly below that of superdomes. As previously observed, Ge atoms will preferentially attach to superdomes. The Ge composition inside pyramids is rather low and does not evolve during growth.

Fig. 7.8 (c) shows GIXD measurements which were performed around the Si(400) Bragg peak at 650°C for a fast growth rate (sample *S*6). After a deposit of 5 ML, domes and superdomes are formed with on the same average Ge composition, smaller than what has been observed for 500°C. With increasing deposit, the Ge content in superdomes slightly increases.

The measurements are in agreement with literature. The mean Ge composition is higher at a low growth temperature [10]. Superdomes are less intermixed than domes and

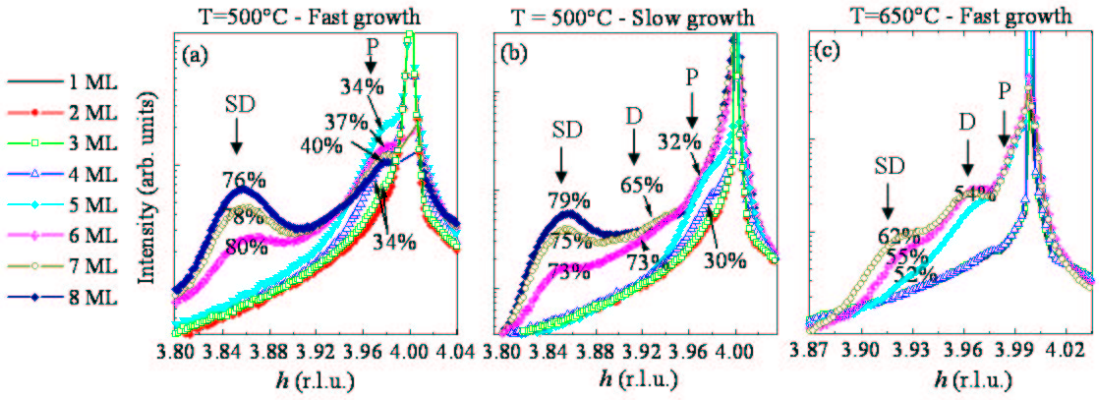

Figure 7.8: Radial scans around the (400) reflection for samples grown (a) at T=500°C with a fast growth rate, (b) at T=500°C with a slow growth rate and (c) at T=650°C and with a slow growth rate. The numbers correspond to the Ge content associated to the different reciprocal space units, h.

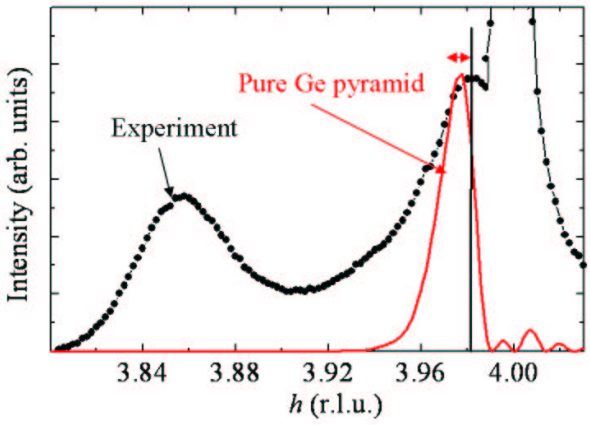

Figure 7.9: Experimental and simulated scattered intensities. Finite difference simulations of the strain state of a $\sim$ 55 nm pyramid of pure Ge show that its lattice parameter is closer to that of Ge than experimentally (sample $S7$ - 8 ML of Ge deposit) observed.

pyramids as Ge atoms will preferentially attach to superdomes. For a growth temperature of 500° C, intermixing has been observed already during the formation of pyramids. In all cases, the intermixing is stronger than in domes and superdomes. This can be related to strain. Pyramids remain heavily tetragonally distorted in comparison to the domes that adopt a relaxed lattice constant close to that of bulk Ge near the top of the island.

7.4 In situ investigation of the island nucleation of Ge on Si(001) using X-ray scattering methods

The origin of interdiffusion is still discussed as experimental data are missing. In particular the role of kinetic effects at different stages of the growth are not yet fully understood. This also raises the question for a possible transport of material from the wetting layer or the substrate into the islands during or after the 2D-3D transition of the SK growth instability. We address these issues in the present section, using scattering methods which do not suffer from restrictions of high temperatures and are thus ideal tools for *in situ* growth studies. The diffraction pattern of reflected high-energy electrons (RHEED) thus often serves for a qualitative analysis of different stages of MBE growth. X-ray scattering methods offer the advantage of much higher resolution and the possibility of quantitative analysis. Furthermore, the exploitation of the small-angle scattering regime together with diffraction at higher angles allows to record data over a broad range of momentum transfers. Typically this range extends from 0.003 to 10 $Å^{-1}$ thus probing lengthscales from several 100 nm down to atomic distances. To answer the above questions, we thus coupled three X-ray techniques, *in situ*, during the MBE growth of Ge on Si(001). The first, grazing incidence small angle X-ray scattering (GISAXS) is sensitive to the morphology of nucleating islands, and can thus easily detect 2D-3D and shape transitions. The second, grazing incidence X-ray diffraction (GIXD), in particular when recording reciprocal space maps in the vicinity of Bragg reflections, allows to follow the lattice relaxation during the nucleation of the islands. It is thus a very sensitive measure of the strain state of the islands and of the 2D-3D transition from wetting layer to island growth. The third, grazing incidence multiple wavelength anomalous diffraction (GI-MAD) allows to separate the Si and Ge contribution to the diffraction, and thus to determine the composition of the growing islands [17].

Figure 7.10 sketches the different probed regions in reciprocal space of such a sample. Close to the reciprocal space origin (000), GISAXS images are recorded with a 2D CCD detector. Morphological features as streaks from facets reveal the island's shape. The splitting of the streaks occurs as a consequence of a fourfold scattering process when working close to the critical angle [18].

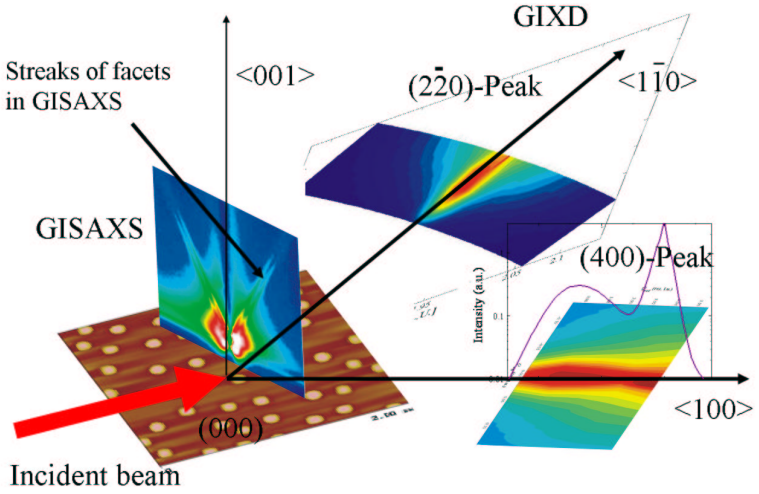

Figure 7.10: Sketch of the *in situ* X-ray scattering setup: Under grazing incidence conditions, the evolution of the sample morphology can be followed in the small-angle regime, the formation of facets is indicated in the GISAXS pattern. The lattice relaxation is monitored by the appearance of Bragg peaks in GIXD.

All Si(001) surfaces where deoxidized at 900°C under UHV conditions and characterized for their surface quality with GIXD and RHEED (Fig. 7.11). The surfaces showed a 2x1 reconstruction (Fig.

7.12) whose average domain size was determined to be about 1 μm.

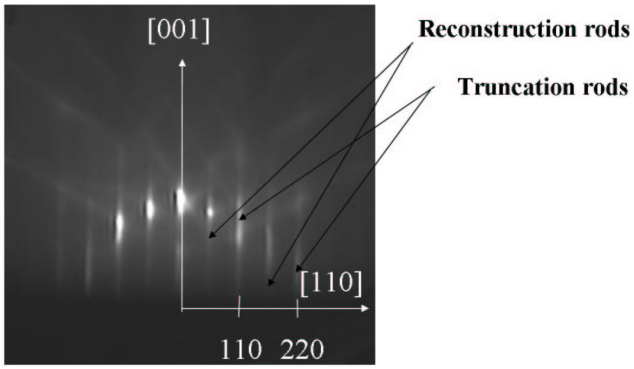

Figure 7.11: RHEED pattern of the 2x1 reconstructed surface.

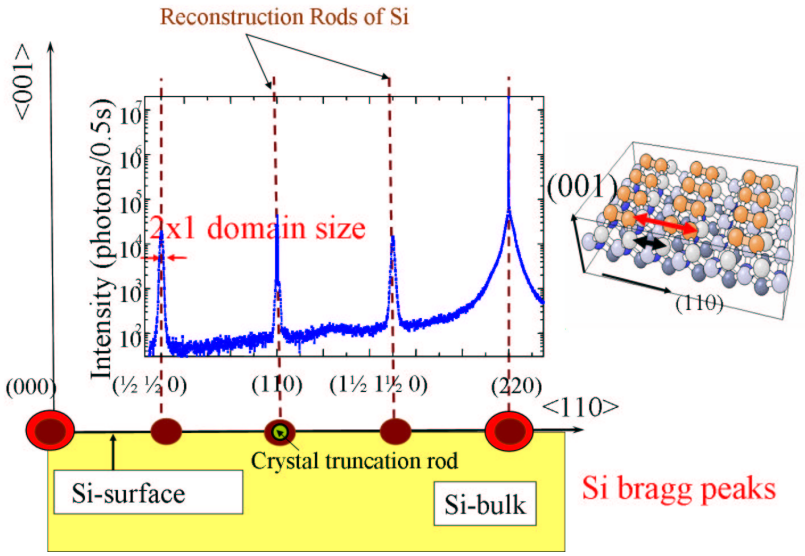

Figure 7.12: Radial scan along the (hh0) direction in the vicinity of the Si(220) reflection. Peaks appear at the Bragg positions (red circles). A peak is observed at the (110) position (green circle). It corresponds to the intersection between the crystal truncation rod passing through the (111) and (11$\bar{1}$(1)) Bragg peaks with the (000) plane. The Si(001) surface shows a 2x1 reconstructed surface (see the inset). The distance along the $< 110 >$ direction between two atoms on the surface is twice bigger than the distance between two atoms in the bulk. In reciprocal space, this gives additional peaks (brown circles), called reconstruction rods of Si

During the growth of Ge, reciprocal space maps were recorded in the vicinity of the (220) and (400) in-plane Bragg reflections of Ge and Si (the Ge lattice parameter is 4.2 % larger than the Si one). For each deposited Ge-monolayer (ML), GISAXS patterns were collected in the azimutal orientations $< 110 >$, $< 100 >$ and $< 15\ 3\ 0 >$.

In this part, we present the results for substrate temperatures of 500°C and 600°C. For a growth temperature of 500°C a series of radial scans across the (400) reflection is shown in Fig. 7.13 (a). Perpendicular dashed lines mark the positions of the lattice parameters of Ge and Si. No lattice

relaxation is visible up to 4 ML coverage. For 5 ML and 6 ML deposit, a double shoulder (indicated as 1 and 2 in the graph) is developping.

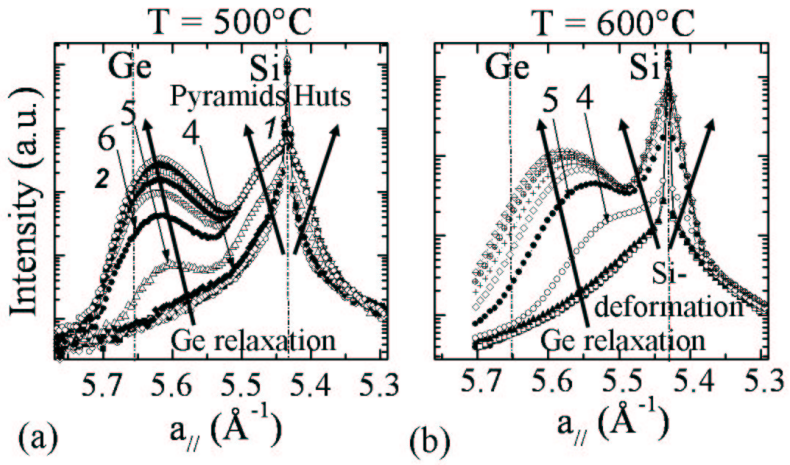

Figure 7.13: Evolution of the lattice relaxation and the Ge concentration during the growth of Ge on Si(001) as a function of lattice parameter at 500°C (a) and 600°C (b).

This indicates a bimodal growth in this temperature regime. The shoulder one, closest to the Si-peak corresponds to highly strained islands that form in very early stages of the nucleation. For depositions higher than 6 ML, only more relaxed islands (shoulder two) continue to grow. The maximum in intensity for these more relaxed islands is located at about 5.64 Å, very close to the Ge bulk value of 5.655 Å. Its position hardly evolves for deposits higher than 6 ML. After a deposit of 11 ML, superdomes, as well as remaining hut clusters can be found in the AFM images (Fig. 7.14(a) and (b)).

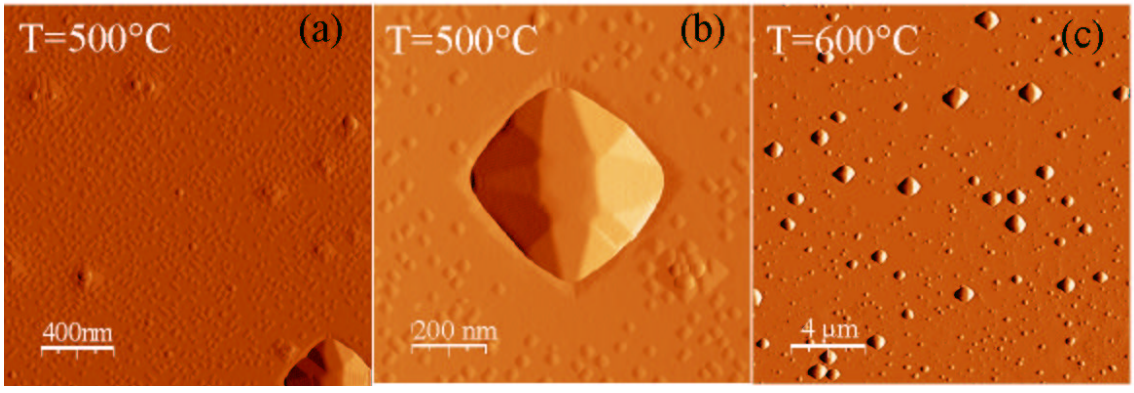

Figure 7.14: AFM images of the samples grown at a temperature of 500°C (a)-(b) and 600°C (c).

Figure 7.15 shows the evolution of the reconstruction as a function of the Ge deposit. Before growth, additional peaks which correspond to reconstruction rods of the 2x1 reconstructed surface appear. With increasing deposit, the intensity of the 2x1 reconstruction rods decreases (see fig. 7.15

(b)) while another peak appears near the Si(220) Bragg peak (see fig. 7.15 (c)). The position of this peak (h_{peak}) evolves with the deposit and it refers to the 2xN reconstruction of the Ge wetting layer, N being equal to $1/(2 - h_{peak})$.

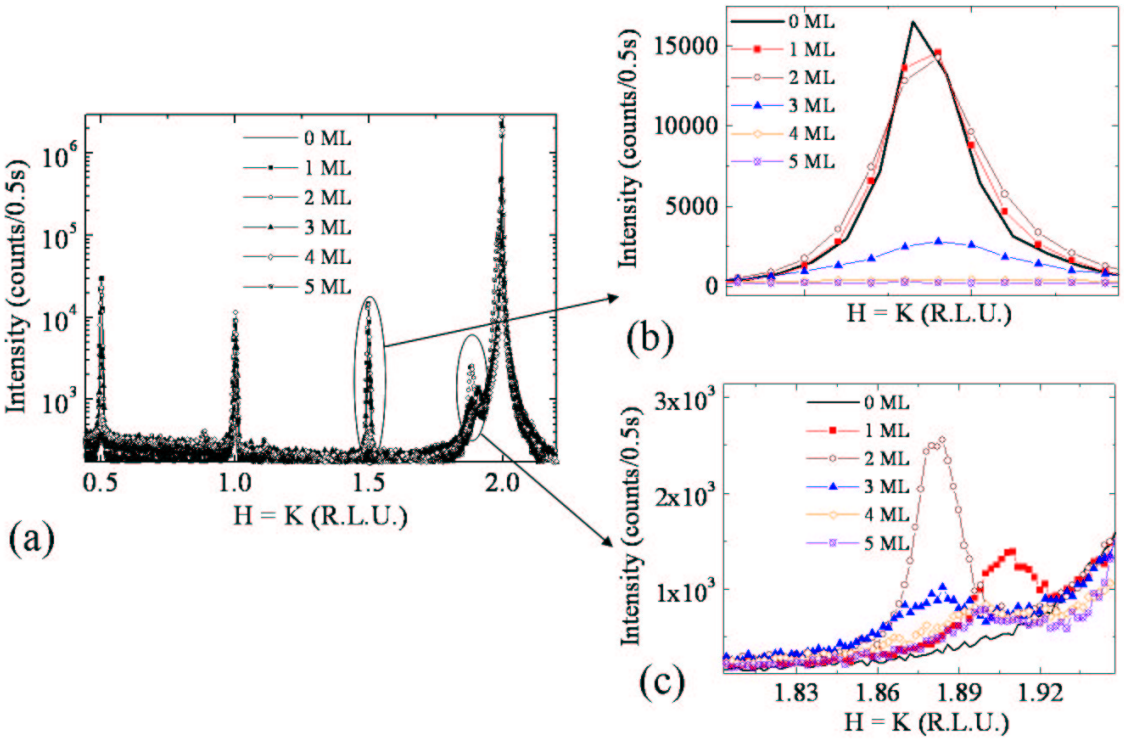

Figure 7.15: Evolution of the reconstructed surface during the growth.

In order to understand this morphological transition in detail, the recorded GISAXS patterns have to be considered [19].

For 0 ML, and thus a perfect Si(001) surface, a typical pattern as measured with our experimental setup is shown in Fig. 7.16 (a). The image is dominated in its lower part by stray radiation originating from the direct beam that is blocked by a beam stop in the lower center. The perpendicular streak in the higher part of the image corresponds to specular diffuse scattering from the surface. To record the appearance of islands and in particular of facets, different low-index azimutal orientations were regarded. Figure 7.16 (b) shows a typical GISAXS image in the $< 100 >$ azimut for early nucleation stages (5ML of Ge) at 500°C. Broad and diffuse streaks in the $< 105 >$ direction (traced by arrows) indicate the formation of {105} facetted pyramids and/or hut clusters. Due to the flat facet orientation (11° with respect to the (001) surface) these islands are highly strained. For the $< 110 >$ azimuth no evolution can be observed for these low deposits: the image in Fig. 7.16 (c) corresponds to a deposit of 5 ML. In the neighboring image, for 6 ML deposition, streaks in $< 113 >$ direction appear. The same behavior is observed for <15 3 0> azimuth, where $< 15323 >$ streaks appear at 6 ML (not shown here). The previously described {105} facets remain almost unchanged at this point. These {105}, {113} and {15 3 23} facets describe the multifacetted dome or superdome shape as reported in earlier works [9]. To obtain a measure for material transport, reciprocal space maps of the scattered intensity in the vicinity of the (220) and (400) Bragg reflections were recorded (Fig. 7.17).

The main probe here is the relaxation of the lattice parameter. Integrating the scattered intensity

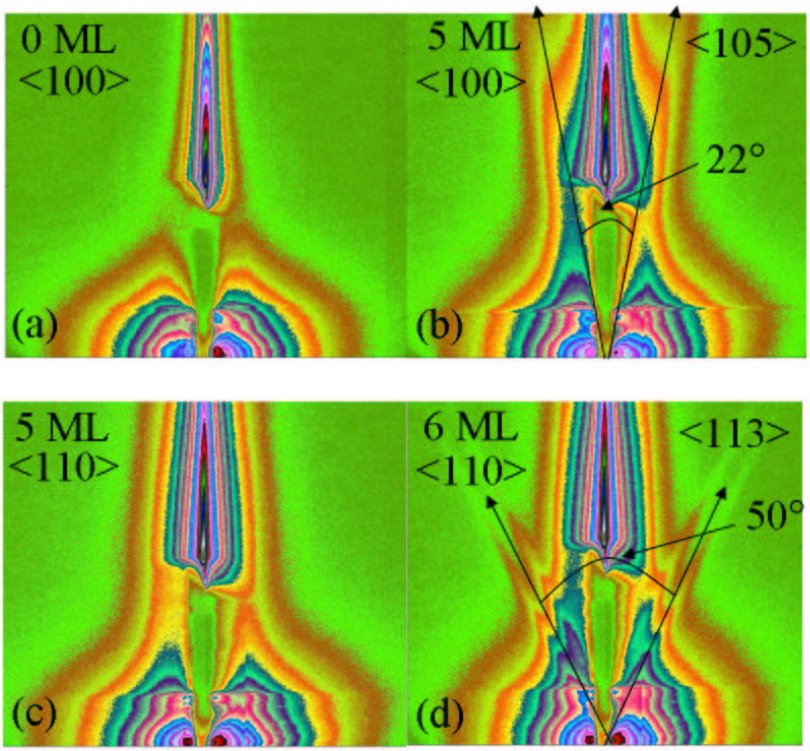

Figure 7.16: GISAXS images for different deposition stages and azimutal orientations for a deposition temperature of T=500°C. (a): Scattering image from a flat surface in the $< 100 >$ sample azimuth; the central beam is blocked by a beam stop. (b): {105} facets attributed to pyramids at 5 deposited ML. (c): The $< 110 >$ azimuth shows facet streaks during the pyramid growth. (d): At 6 ML the sharp pyramid to dome transition is reached and {113} facets appear.

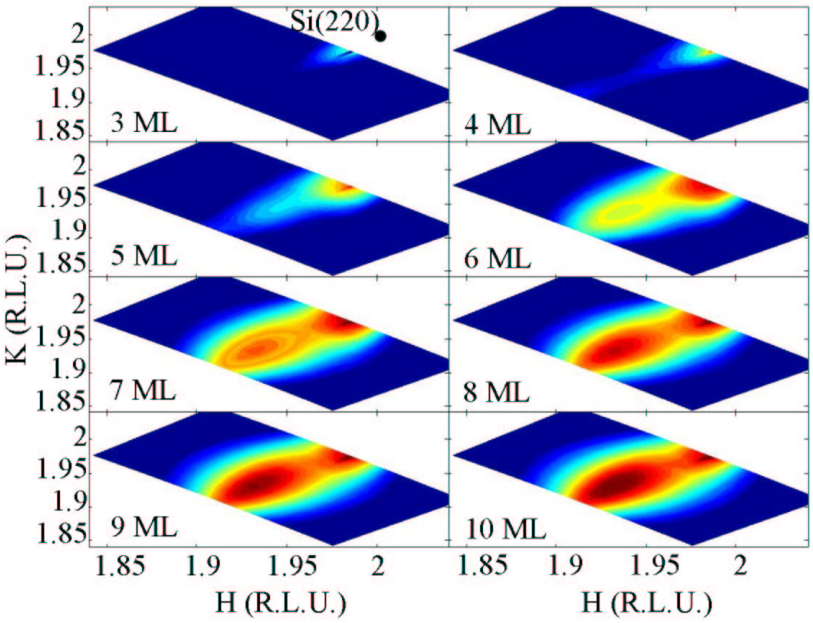

Figure 7.17: Reciprocal space maps of the scattered intensity in the vicinity of the (220)Si Bragg reflections.

over all three dimensions in reciprocal space, one can extract a measure that is directly proportional to the growing scattering volume in the nanostructures. Material deposited to the wetting-layer does not contribute to these intensities, as it remains pseudomorphic to the substrate and thus scatters at the same reciprocal position as the Si peak. For every deposited monolayer, the reciprocal space map for 0ML, thus the pure Si-substrate, was subtracted. The remaining integrated intensity as a function of the deposition is plotted in Fig. 7.18(a) for a deposition temperature of 500°C.

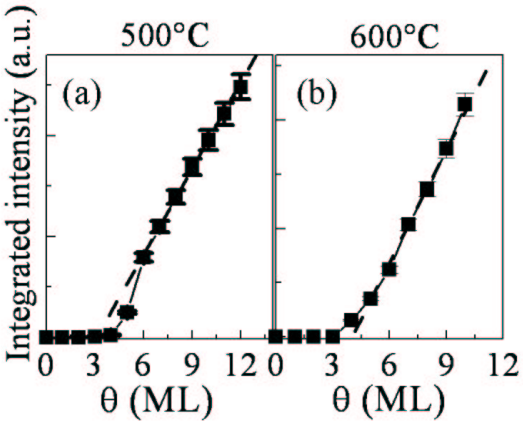

Figure 7.18: Evolution of the integrated intensity as a function of the deposition for a growth temperature of 500°C (a) and 600°C (b).

As expected, for up to 4 ML, no change in the integrated intensity can be observed as the deposited Ge forms a pseudomorphic wetting-layer. The first relaxation leads to a small rise of the intensity at 5 ML. It follows a steeper slope between 6 and 8 ML and a linear evolution for higher deposits. The linear evolution indicated by the dashed line can be understood, if the complete amount of deposited Ge crystallizes in the form of islands. In the transitional region from 5-6 ML, one thus observes a quantity of Ge added to the islands, that is superior to the deposited amount. The additional material is either Ge from the previously deposited wetting layer or Si that migrates into the island.

To distinguish between these two possibilities, we performed GI-MAD to probe for eventual interdiffusion. This method allows for a separation of the contribution from Ge and Si and to determine the composition in reciprocal space.

The diffracted intensity was measured in the vicinity of the (220) and (400) reflections at 12 energies close to the Ge K-edge. Using the known $f'_{Ge}(E)$ and $f"_{Ge}(E)$, it is then possible [20] to quantitatively extract $|F_{Ge}|$ and $|F_{Si}|$ through a least-square minimization. For a deposition of 7 ML the Ge concentration is plotted as a function of lattice parameter in Fig. 7.19(c). No or very weak Si signal can be found inside the islands, excluding interdiffusion effects at 500°C for this sample. Nevertheless, it is possible that at the 2D-3D transition intermixing occurs during the formation of pyramids as previously observed in last section.

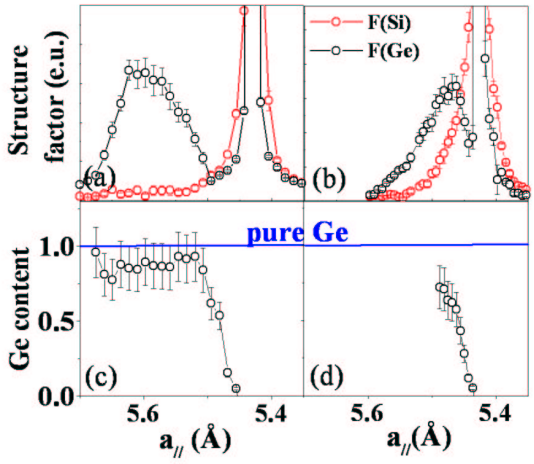

Figure 7.19: *Ge* and *Si* structure factors for a deposition of 7 ML of Ge for a growth temperature of 500°C (a) and 600°C (b) and the corresponding Ge content: (c) and (d).

The combination of the adressed parameters in the data presented in Figs. 7.16, 7.18 (a) and 7.19(a)-(c) allows the following conclusions. The first nucleation step leads to the formation of {105} facetted pyramids and hut clusters. One part of these transform into domes or superdomes for ongoing deposition. During the pyramid formation as well as during the pyramid to dome/superdome transition, thus in the regime of 5-6 deposited monolayers, the steepest rise of intensity observed in Fig. 7.18 (a) indicates that an equivalent of ∼1 ML of Ge is transported from the pure Ge or intermixed wetting layer into the islands. A depletion of the previously formed wetting-layer has been assumed in earlier publications [21, 22]. Our results for the critical thickness as well as for the remaining wettinglayer thickness are in good agreement with recently published simulations [23].

For 600°C interdiffusion effects are known to exist, and we repeated the measurement and data treatment as described above to trace the material transport during the growth. These data are shown in Figs. 7.13 (b) and 7.19(b)-(d). While the morphological states remain qualitatively the same during the growth, the kink in the raise of the integrated intensity of the growing islands cannot be observed. The growing intensity close to the Si substrate peak in Fig.7.13 (b) can be attributed to deformations in the Si substrate as the scattering from silicon strongly dominates in this region and

as its intensity grows with the growth of the SiGe-domes [10]. The relaxation of the lattice parameter during the dome growth was less important in the beginning and grows for ongoing deposition. This can be explained by interdiffusion that is already present in the wetting-layer at 600°C. The material that forms the first domes (at 5 ML at this temperature) consists of a SiGe alloy, that is formed at the surface due to ongoing intermixing at the interface and forms wettinglayer and islands. Ongoing deposition of pure Ge leads to a progressing increase of the Ge concentration and further relaxation of the growing domes or superdomes. The smooth rise of the integrated intensity at 600°C (Fig. 7.18 (b)) shows that no partial de-wetting of the interdiffused wetting layer occurs after the island nucleation. Furthermore the material exchange that takes place between wetting layer and substrate lowers the strain energy per atom in the wetting layer. The comparison of Figs. 7.18(a) and (b) shows that the nuclation occurs at 600°C one ML earlier than at 500°C, preventing the effect of a supersatured wetting layer [22]. The resulting island ensemble consists only of domes and superdomes with a narrower size distribution than for 500°C. We state that our method allows to follow the evolution of Ge-islands during the whole deposition process. Quantitative statements as the amount of Ge remaining in the wetting layer or the presence of Si in the island can be determined during the growth.

7.5 In situ X-ray study of the evolution of island morphology and relaxation during a slow growth rate of Ge on Si(001): early transition to superdomes

The coherent pyramid and dome-shaped islands have been the subject of many very detailed recent studies which deal with their growth [8, 24, 25] as well as with their strain and composition [26, 27, 15]. In contrast, much less work [28] has been done to characterize the superdomes. The kinetics of the superdome growth and of their shape transitions is still not completely understood. In particular, the evolution with the *growth rate*, the *temperature* [29] and the *deposited thickness* of the superdome apparition, size and shape are not fully characterized during growth. This calls for *in situ* investigations as a function of temperature. The morphology of islands during their growth has been investigated by several *in situ* methods, such as electron or synchrotron diffraction [30], scanning tunnelling or low-energy electron microscopies [31, 25]. Recently, grazing incidence X-ray scattering (GISAXS) [19] was used to analyze the shape and size of growing metallic islands. It has been shown to be a powerful tool to analyze the faceting of semiconductor islands and to index their facets [32]. With *in situ* GISAXS, contrary to other *in situ* techniques, not only the average diameter and height of the islands but also the average size of each facet can be directly determined during growth. In addition, *in situ* GISAXS was combined with grazing incidence X-ray diffraction (GIXD), which allows monitoring the island nucleation by the beginning of lattice relaxation and following the evolution of the strain state.

We report in this section on a combined GISAXS-GIXD study performed *in situ*, during the growth of Ge on Si(001) at a slow growth rate and at different temperatures. The transition from the wetting-layer to the dome and superdome formation is detected and quantitatively characterized by both techniques.

7.5.1 Experiments

The samples were grown by molecular-beam epitaxy (MBE) in a dedicated ultra-high vacuum chamber equipped with large beryllium windows and coupled to a surface diffractometer for GIXD and GISAXS measurements, on the BM32 synchrotron beamline at the ESRF. The Si(001) substrates were deoxidized by annealing at 1200 K until a sharp, 2x1 reconstructed, Reflection High Energy Electron Diffraction (RHEED) pattern was observed. Germanium was deposited with a Knudsen cell with a slow deposition rate of 170 sec for one Ge monolayer (ML) (∼0.006 ML/s), which was *in situ* calibrated using both a quartz microbalance and X-ray reflectivity. This rate is about five times smaller than the deposition rate usually used for Ge/Si MBE experiments [24]. Ge was deposited monolayer after

monolayer at four growth temperatures (773 K, 823 K, 873 K and 923 K). We have experimentally determined with GISAXS and GIXD, that no evolution of the island morphology, internal structure or composition happens during annealings below 773K. At 823 K, small changes were found to start only after 30 s of annealing, which confirms the observation of Medeiros-Ribeiro *et al.* [33]. To avoid any evolution of the islands between successive deposits, the samples were immediatly cooled down to 723 K after each added monolayer, reference temperature at which the X-ray measurements were performed. These typically lasted 50 min, after which the temperature was raised again to the deposition temperature. During cooling or heating, the sample never stayed more than 30 s at intermediate temperatures between 773 K and the growth temperature, so that significant morphological evolution or Si-Ge intermixing between successive deposits can be safely neglected [32, 33, 25]. We actually checked that, for a growth temperature of 923 K, the same final state (as probed with GISAXS and GIXD) was obtained for a 7 ML deposit realized with the procedure described above, and a 7 ML deposit without growth interruption. Consequently, our successive deposits are equivalent to a continuous deposit with constant rate, as a function of time: the deposited amount θ is proportional to an equivalent deposition time t.

For all X-ray measurements, the X-ray beam energy was set at 11043 eV, and the incident angle fixed at the critical angle for total external reflection, $\alpha_i = 0.163°$. The incident beam of 1mrad(H)x0.1mrad(V) divergence, was defined by a pair of slits to 0.1mm(H)x0.3mm(V) at the sample position, the horizontal direction being perpendicular to the surface.

For GIXD measurements, the scattered beam direction was defined by a pair of 1mm slits parallel to the surface, and one 8mm slit perpendicular to it. The slit-to-sample distances were 200 and 600mm, respectively. For GISAXS measurements, in vacuum slits and beam-stop were used to avoid background scattering by the beryllium windows. The scattered intensity was detected by a two-dimensional low-noise CCD detector from Princeton (1152x1242 pixels of 56.25 μmx56.25 μm) placed 1.68m away from the sample.

All direct- or reciprocal-space notations refer to the bulk Si unit cell (a=b=c = 5.431Å, α=β=γ=90°). The Miller indexes (h, k, l) are expressed in reciprocal lattice units (r.l.u.) of Si.

GIXD measurements were performed mostly along the ($h0l$) direction (l being small: l=0.04), with finer measurements in the vicinity of the Si(400) and Ge(400) Bragg peaks (Fig. 7.20). These radial scans were recorded *in situ* for each added monolayer. GISAXS measurements consisted in recording two-dimensional GISAXS intensity distributions with the X-ray beam aligned along the substrate's [100], [110] and [15 3 0] directions. The GISAXS maps represent cuts of the three-dimensional intensity distribution in reciprocal space with the Ewald sphere. The scattering vector is defined as $\mathbf{Q} = \mathbf{K}_f - \mathbf{K}_i$ ($\mathbf{K}_{i,f}$ are the wave vectors of the primary and scattered beams, respectively, having the angles $\alpha_{i,f}$ with the mean sample surface). The collected images correspond to ($Q_y Q_z$) planes which are tangential to the Ewald sphere.

7.5.2 Experimental results

A. *In situ* grazing incidence diffraction (GIXD)

Fig. 7.20 shows GIXD measurements which were performed around the Si(400) Bragg peak at 773 K, 823 K, 873 K and 923 K.

For all growth temperatures, the scattering around the Si(400) Bragg peak is found unchanged between 0 and θ_1 ML, which confirms the expected growth of the fully strained wetting layer. Between a deposit of θ_1 and θ_2 ML, a small scattering signal appears on the left-hand part of the Si(400) and increases in intensity. Then, after a deposit of θ_2 ML, this signal shows a huge increase. With increasing deposit, the maximum of intensity is displaced towards lower h values until reaching a fixed h value centered around h_{end}. θ_1 is lower than 3.4 for T=773 K and is lower than 4.3 for the other growth temperatures. For all growth temperatures, θ_2 ∼6. h_{end} has a value of 3.86, 3.89, 3.9 and 3.96 for the growth temperatures of 773 K, 823 K, 873 K and 923 K, respectively. With decreasing temperature, the scattered intensity is centered at much lower h values, close to the value (h=3.835) of fully relaxed Ge.

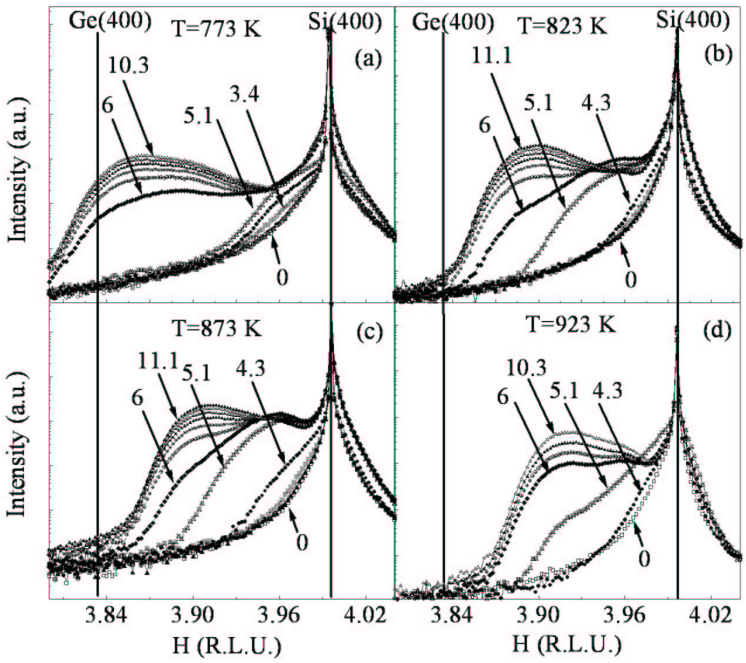

Figure 7.20: Radial scans along the $(h0l)$ direction, with l=0.04, in the vicinity of the Si(400) reflection, for different Ge deposits (in equivalent monolayers ML). Some Ge deposits are indicated on the graphs. The vertical lines show the position of the bulk Si(400) and Ge(400) Bragg peak. a) At 773 K (from 0 to 10.3 ML), b) at 823 K (from 0 to 11.1 ML), c) at 873 K (from 0 to 10.3 ML), and d) at 923 K (from 0 to 11.1 ML).

B. *In situ* grazing incidence small-angle scattering (GISAXS)

GISAXS measurements were combined with GIXD to have access to the morphology of the growing nanoparticles. Figures 7.21 and 7.22 show the measured data for all growth temperatures as function of the Q_y and Q_z coordinates of the scattering vector, *i.e.*, parallel and perpendicular to the sample surface, respectively for the [110] (figure 7.21) and [15 3 0] (figure 7.22) azimuthal directions of the primary beam. The maps measured along the [100] azimuth are not shown because the expected scattering from {105} facets is hardly visible, being too close to the specular rod.

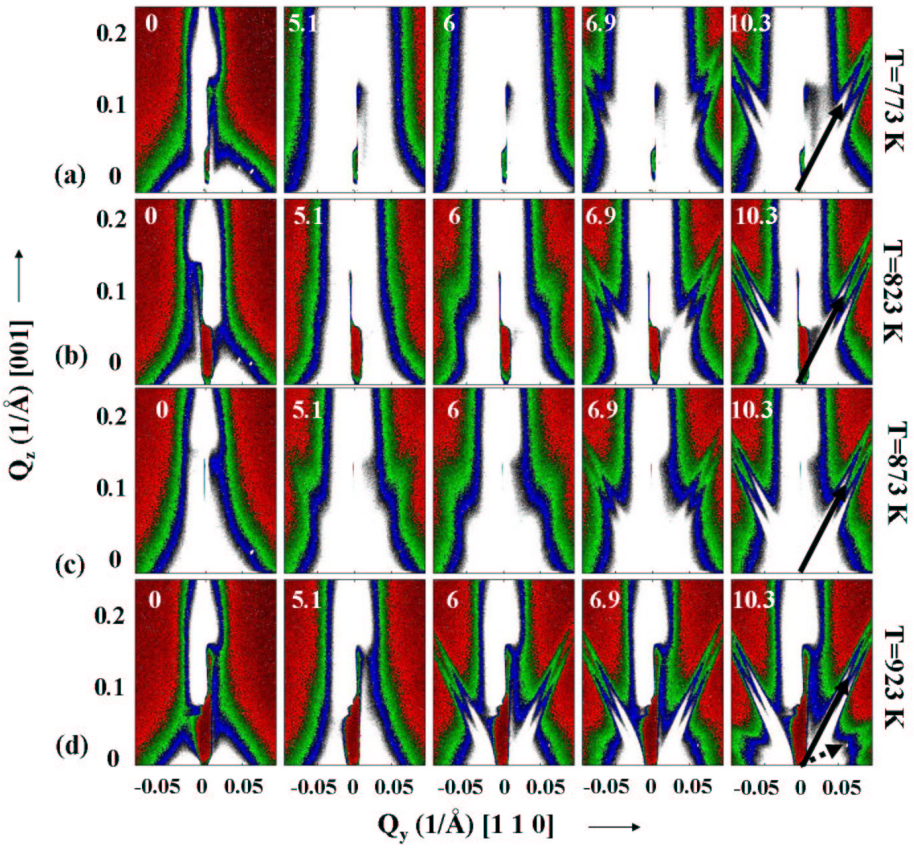

Figure 7.21: GISAXS images along the $< 110 >$ azimuth for different Ge deposits (in equivalent monolayers ML) and a) at 773 K, b) at 823 K, c) at 873 K, and d) at 923 K. The full and dashed black arrow denote $< 113 >$ and $< 111 >$ streaks, respectively.

For all growth temperatures, the intensity maps exhibit nearly no change for nominal Ge coverages θ between 0 and 4-5 ML. The first changes are observable above 6 ML for a growth temperature of 773 K (Fig. 7.21 and 7.22 (a)), and above 5 ML at 823 K (Fig. 7.21 and 7.22 (b)), 873 K (Fig. 7.21 and 7.22 (c)) and 923 K (Fig. 7.21 and 7.22 (d)). These changes are in the form of diffuse intensity streaks along $\langle 113 \rangle$ directions for the maps measured in the [110] azimuth (Fig. 7.21) and along $\langle 15\ 3\ 23 \rangle$ directions (Fig. 7.22) for the maps measured in the [15 3 0] azimuth. Note that all streaks are doubled; this will be explained below. Very weak additional scattering streaks along $< 111 >$ directions can be hardly observed in the [110] azimuth for a deposit of 7-8 ML at 873 K and for a deposit of 10 ML at 823 K. At T=923 K, weak additional streaks along $\langle 111 \rangle$ appear in the [110] azimuth as early as 6 ML. The signal from the $< 111 >$ streaks is clearly visible at 10ML in Fig. 7.21 (d). An onset of $< 20\ 4\ 23 >$ streaks is also visible in Fig. 7.21 (d), where its direction is denoted by a black arrow.

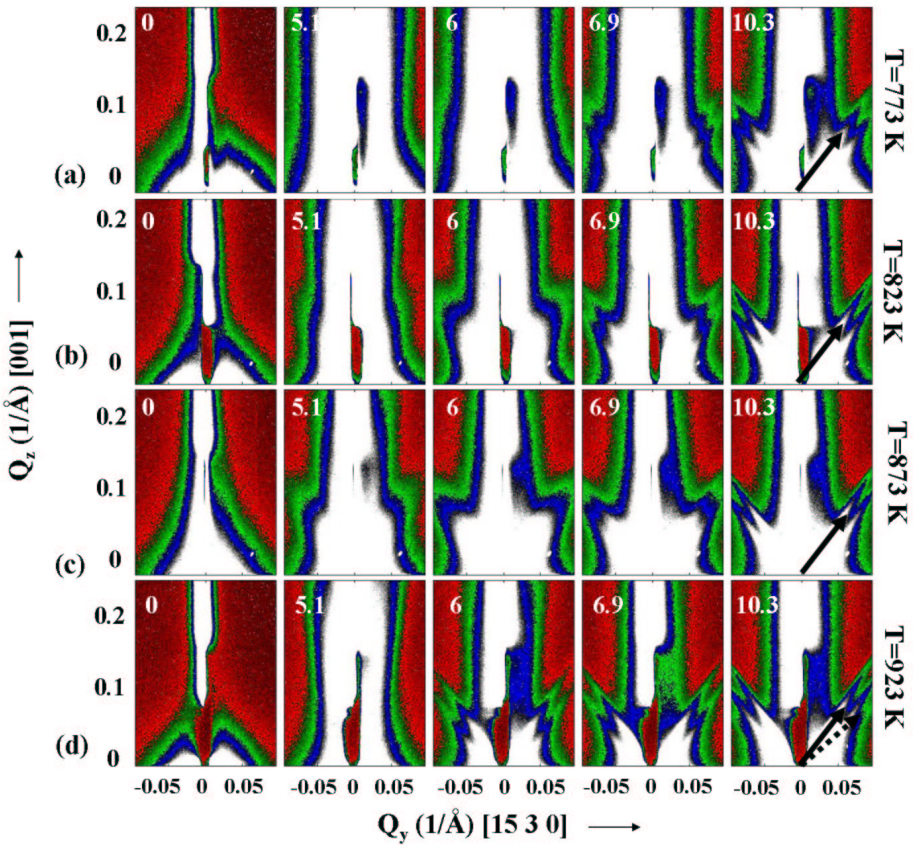

Figure 7.22: GISAXS images along the < 15 3 0 > azimuth for different Ge deposits (in equivalent monolayers ML) and a) at 773 K, b) at 823 K, c) at 873 K, and d) at 923 K. The full and dashed black arrow denote < 15 3 23 > and < 20 4 23 > streaks, respectively.

7.5.3 GISAXS analysis

For the analysis of the measured GISAXS data we have used the distorted-wave Born approximation (DWBA) [18]. From this approach it follows that the intensity scattered by a non-capped island is a coherent superposition of 4 scattering processes. If we assume that the island positions are completely random and that the islands are far apart from each other, the intensity of the scattered radiation is an incoherent superposition of intensities scattered by individual islands

$$I(\mathbf{Q}) = \text{const.} \sum_{n=1}^{4} \sum_{m=1}^{4} A_n A_m^* \left\langle \Omega^{\mathrm{FT}}(\mathbf{Q}_n) \Omega^{\mathrm{FT}*}(\mathbf{Q}_m) \right\rangle , \tag{7.5}$$

where the sums run over the scattering processes, A_n and $\mathbf{Q}_n$ are the amplitude and scattering vector of process n. The direct (kinematical) process $n = 1$ is the scattering of the incident wave, the indirect processes $n = 2, 3, 4$ comprise the scattering of the wave specularly reflected from the flat surface between the islands ($n = 2$), specular reflection of the wave scattered from the island ($n = 3$), and specular reflection of both the primary and the scattered waves ($n = 4$) – see [18] for details. $\Omega^{\mathrm{FT}}(\mathbf{Q})$ is the Fourier transform of the shape function $\Omega(\mathbf{r})$ of a single island and the averaging in Eq. (7.5) is carried out over all island sizes.

In the case of islands with flat facets, it is suitable to convert the volume integral calculating $\Omega^{\mathrm{FT}}(\mathbf{Q})$ into an integral over the island surface $S(\Omega) = \cup_j S^{(j)}$ using the Stokes formula, which yields

$$\Omega^{\mathrm{FT}}(\mathbf{Q}) = \frac{\mathrm{i}}{Q^2} \sum_j Q_\perp^{(j)} \mathrm{e}^{-\mathrm{i}Q_\perp^{(j)} r_\perp^{(j)}} F_j(\mathbf{Q}_\parallel^{(j)}). \tag{7.6}$$

In this equation, if we denote $\mathbf{n}^{(j)}$ the unit vector of the outer normal of the facet j with the area $S^{(j)}$, then $r_\perp^{(j)} = \mathbf{r}.\mathbf{n}^{(j)}$ is the distance of this facet from the origin (the origin is at the center of the bottom of the islands), $Q_\perp^{(j)} = \mathbf{Q}.\mathbf{n}^{(j)}$ is the component of $\mathbf{Q}$ perpendicular to the facet and $\mathbf{Q}_\parallel^{(j)} = \mathbf{n}^{(j)} \times (\mathbf{Q} \times \mathbf{n}^{(j)})$ is the component of $\mathbf{Q}$ parallel to the facet. We have also denoted $F_j(\mathbf{Q}_\parallel^{(j)}) = \int_{S^{(j)}} \mathrm{d}^2\mathbf{r}_\parallel^{(j)} \ \mathrm{e}^{-\mathrm{i}\mathbf{Q}_\parallel^{(j)}.\mathbf{r}_\parallel^{(j)}}$ the Fourier transformation of the shape function of the facet j.

Equation (7.6) makes it possible to analyze the contribution of individual facets to the intensity $I(\mathbf{Q})$. If we neglect tiny interference fringes (that are smeared out by the size averaging anyway), we can simplify the expression for the scattered intensity as follows

$$I(\mathbf{Q}) \approx \text{const.} \sum_j \sum_{n=1}^{4} |A_n|^2 \left(\frac{Q_{\perp n}^{(j)}}{Q_n^2} \right)^2 \left\langle \left| F_j(\mathbf{Q}_{\parallel n}^{(j)}) \right|^2 \right\rangle . \tag{7.7}$$

Within this approximation, the intensity is a sum of the contributions of individual facets. Each facet gives rise to a narrow streak in reciprocal space parallel to $\mathbf{n}^{(j)}$. The width of the streak is inversely proportional to the facet size L (Fig. 7.23).

Along the streak, the intensity drops as $(Q_\perp^{(j)})^{-2}$. In the case of a non-faceted island with a rounded surface, the scattered intensity decreases as Q^{-4} (the Debye-Porod law [34]), so that from the asymptotic intensity decrease it is possible to identify individual facets.

The intensity distribution across the streaks is determined by $\langle |F(\mathbf{Q}_\parallel)|^2 \rangle$, where the average is taken over the distribution of facet sizes. Numerical estimates have revealed that this intensity distribution obeys the asymptotic formula $\langle |F(\mathbf{Q}_\parallel)|^2 \rangle \sim |\mathbf{Q}_\parallel|^{-3}$ for large $|\mathbf{Q}_\parallel|$ for any facet shape and any statistical distribution of the facet sizes of domes. The full-width at half maximum (FWHM) $\Delta Q_\parallel$ of the streak is inversely proportional to the mean facet size $L_0 \equiv \langle L \rangle$, however, the proportionality factor decreases with increasing root mean square (rms) deviation σ_L of L. For $\sigma_L \to 0$, $L_0 \to 2\pi/\Delta Q_\parallel$ holds.

The indirect scattering processes ($n = 2, 3, 4$) give rise to an additional streak for each facet, if $Q_{nz} > 0$. Due to the reflection from the free surface, the additional streak is shifted vertically by $2K \sin \alpha_i$, and its intensity depends on the incidence or exit angles due to the reflectivity coefficients

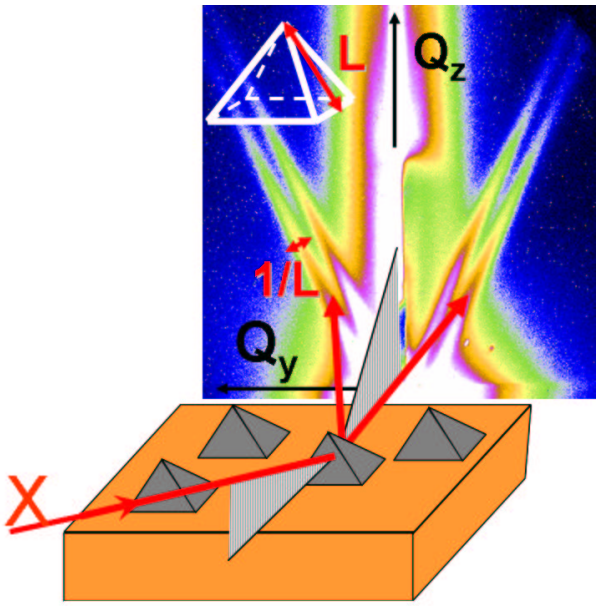

Figure 7.23: Schematic drawing of pyramid islands and their corresponding GISAXS intensity map. The width of the streak is inversely proportional to the facet size L.

$r_{i,f}$. This effect has to be taken into account in the determination of the facet size from the streak width. The influence of the indirect scattering processes is visible in the experimental data taken along [110] and [15 3 0] azimuths in Fig. 7.21 or 7.22 , where the streaks are twofold.

Atomic force microscopy (AFM) measurements were performed *ex situ* on the last deposit after the X-ray measurements. The AFM pictures of the sample surfaces (Fig. 7.24) revealed that the island-size distribution is bimodal, small <100nm wide islands coexisting with islands having a width larger than 400nm. Due to their larger scattering volume, the large islands dominate the GISAXS. In taking only into account the population of large islands, the rms deviation of the island sizes, $\sigma_L/L_0 = 0.17 \pm 0.03$, where L_0 is the mean facet size, was obtained from analysis of the AFM images.

In order to determine the evolution of the facet sizes, we have extracted line scans perpendicular to the streaks from the measured intensity maps and we have fitted the streak profile by a pair of modified Lorentzian functions $f(Q_\parallel) = \text{const}\left[1 + (2Q_\parallel/\Delta Q_\parallel)^2(2^{2/3}-1)\right]^{-3/2}$ ($\Delta Q_\parallel$ is the FWHM of the function), obeying the asymptotic decrease ($|\mathbf{Q}_\parallel|^{-3}$) of the scattered intensity and yielding perfect fits. From direct numerical simulations it follows that, for this value of σ_L, the FWHM of the streak is $\Delta Q_\parallel \approx 2\pi/L_0$ with the accuracy of about 10%. The distance between the peaks stemming from various scattering processes is $\delta Q_\parallel = 2K \sin\alpha_i \sin\beta$, where β is the angle of the facet with (001).

Figure 7.25 shows an example of a fit of a line scan extracted from the GISAXS measurement in the [110] azimuth for a deposit of 10 ML for the growth temperature of 873 K.

This line scan is fitted by the sum of three modified Lorentzian functions, one corresponds to the streak of the top facet (on the right side of the figure), the other two stem from {113} facets. The study was not performed for the {105} facets appearing in the [100] azimuth because the flat facet orientation (11° with respect to the (001) axis) and the small facet size induce a broadening of the {105} diffuse streaks which makes the extraction difficult. Therefore, only the {113} and {15 3 23} facet sizes were characterized. Fig. 7.25 shows the linear scans extracted from the intensity map in the [110] azimuth for θ = 10 ML at a growth temperature of 873 K along and across the intensity streaks. The above predicted $Q_{//}^{-3}$ and $Q_\perp^{-2}$ asymptotic dependences are clearly visible. The values of the mean sizes L_0 for the last deposits deduced from these fits are consistent with those deduced from the *ex situ* AFM measurements performed after growth (Fig. 7.24).

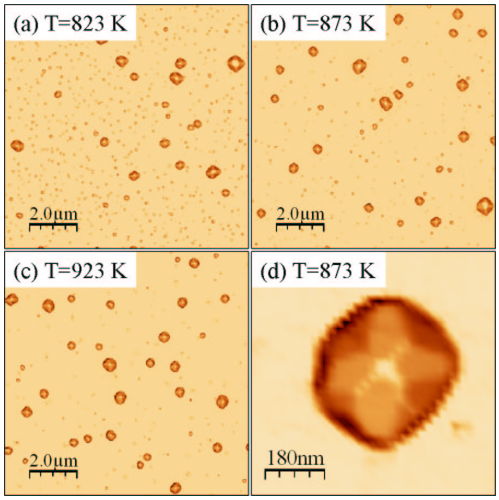

Figure 7.24: (a) AFM images of samples obtained upon deposition of 10-11 ML of Ge at 823 K (a), 873 K (b) and 923 K (c), on a large scale. The presence of two island "families" with different mean sizes is obvious. (d) AFM zoom of a superdome island grown at 873 K. $\sim$ 145nm and $\sim$ 92nm are the measured mean facet sizes of {113} and {15 3 23} facets respectively. They correspond to the simulated values observed on Fig. 7.32 (a) and (b).

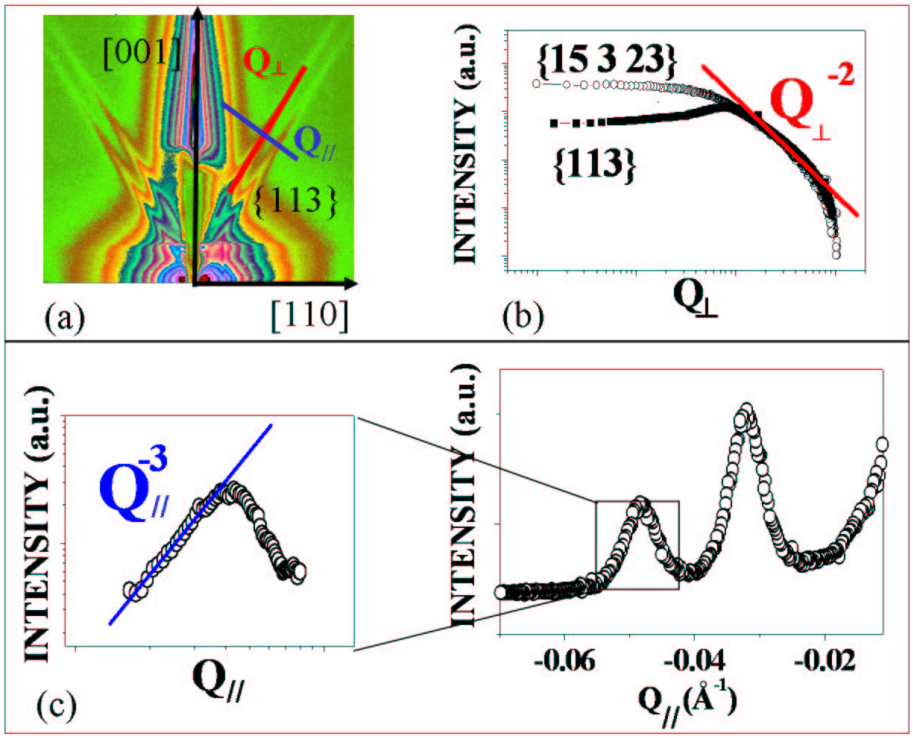

Figure 7.25: Figure (a) shows a GISAXS image (azimuth [110], $\theta = 10$ ML), from which the line scans in panels (b), (c) are extracted along the $Q_\perp$ and $Q_\parallel$ axes. (b) The line scan along the facet streak. (c) The linear scan extracted from the GISAXS intensity map across the {113} facet streak (points); the inset shows the tail of this line scan in a loglog representation. From figures (b) and (c), the $Q_\perp^{-2}$ and $Q_\parallel^{-3}$ slopes are clearly visible.

7.5.4 Analysis and discussion

Below 2.6-3.4 ML, depending on the growth temperature, both GIXD and GISAXS measurements remain unchanged. This reveals the growth of a perfectly strained, flat Ge(001) two-dimensional wetting layer. For larger deposits, diffuse scattering appear in GIXD radial scans below the Si(400) Bragg peak, as well as faint changes of the GISAXS maps. These are signatures of the 2D-3D transition, with the formation of 3D islands on top of the wetting layer. These islands develop to release the stress due to the 4.2% lattice parameter mismatch between Si and Ge. Hence, depending on the growth temperature, the formation of 3D islands is observed after a deposition of 3-4 ML of Ge. These results show that GIXD is very sensitive to the onset of islands nucleation by detecting the very first stages of relaxation of the crystal lattice.

Interpreting our GIXD and GISAXS results, we can state that for T=773 K, the relaxed volume does not increase rapidly until a coverage of about 5.1 ML is reached. At this stage, no dome facets ({113} and {15 3 23}) are detected on the GISAXS images. {105} facets can be detected but their signal is too broad to be analyzed. Pyramid islands have thus been formed. These small islands are almost fully strained by the substrate: they have an in-plane lattice parameter, i.e. parallel to the surface, very close to the Si one, and the measured diffuse scattering mostly arises because of their small size. The scattered intensity is modulated by the form factor of pyramids.

At 6 ML, a huge increase of the diffuse scattering is observed on the GIXD scan (see Fig. 7.20 (a)). Due to the larger lattice parameter of Ge, the partially relaxed component due to germanium shifts to lower values of h and adopts a position close to that of bulk germanium. The signal can be attributed to much more relaxed islands. This coincides with the appearance of weak rods on the GISAXS pictures, corresponding to scattering by {113} and {15 3 23} facets, which are known to be present on Ge domes, barns or superdomes on Si(001). The large lattice parameter of these islands, close to the value for bulk Ge, can only be explained by large, plastically relaxed islands, because coherent islands such as domes or barns are much more strained by the Si substrate [35]. To demonstrate this, we performed finite element method (FEM) simulations, using a program developed by C. Priester [36]. Assuming a coherent ∼100nm (as measured by GISAXS) dome-shaped island of pure Ge (hence having the highest relaxation) , the in-plane relaxation ϵ_{xx}^{Si} was calculated (see Fig. 7.26 (a)), and the scattered intensity simulated (see Fig. 7.26).

The majority of the simulated scattering signal is positionned around h=3.945. Only a weak shoulder is found around h=3.89, at the position of the experimental scattering intensity maximum. The average relaxation of the simulated island is far from being centered at the position of the experimental data and is shifted towards the position of the Si bulk Bragg peak. This demonstrates that the experimentally observed relaxation cannot be achieved by coherent elastic relaxation. These large relaxed islands can thus be identified as large superdomes, exposing the above mentioned side facets ({113} and {15 3 23} facets). The GISAXS signal emanating from the {111} facets of the superdomes is so small compared to the {113} ones that it is hardly detectable in the feet of the rods emanating from {113} facets. Compared to previous works [8, 9], superdomes for a lower coverage can be explained by the slow growth rate. Rastelli *et al.* [9] observed the formation of superdomes after a deposit of 8 ML of Ge at 823 K and at a rate of 0.3 ML/s. As our growth rate is more than one order of magnitude smaller and since a slow growth rate leads to a more complete relaxation [37] by the introduction of dislocations, this can explain why dislocated islands are observed earlier (at 6-6.9 ML for a growth temperature of 773 K) in our case. Besides, a simple energetic model (see section 5.0.14) confirms that a slow growth rate can fasten the introduction of dislocations. In GIXD scans, the pyramid- or dome-to-superdome transition is thus characterized by a strong strain relief with a rapid increase of the relaxed volume.

In Fig. 7.27 we have plotted the dependence of the mean vertical sizes L_0 of the {113} and {15 3 23} facets, for the growth temperature of 773 K, 823 K, 873 K and 923 K as a function of the deposited thickness θ.

Between 6 and 6.9 ML, a significant enlargement of the {113} and {15 3 23} facet sizes (Fig. 7.27) is observed. For instance, the mean size of the {113} facets increases from (0±10)nm to (50±5)nm between 6 and 6.9 ML deposits. Such a sudden increase has been previously observed by Williams

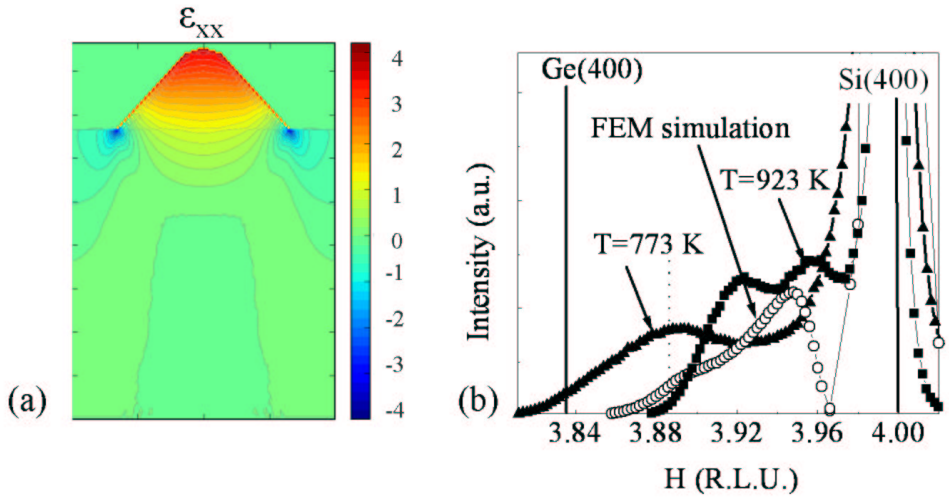

Figure 7.26: (a) FEM simulation of the in-plane deformation ϵ_{xx}^{Si} (with respect to the Si substrate) in a 100nm large dome of pure Ge without dislocations. $\epsilon_{xx}^{Si} = 4.2\%$ means that Ge atoms are no more strained. In the region of the Si substrate, when $\epsilon_{xx}^{Si} < 0\%$, the Si lattices are compressed, and when $\epsilon_{xx}^{Si} > 0\%$, the Si lattices are expanded. (b) Experimental and simulated scattered intensities. Finite element simulations of the strain state of coherent, dome-shaped islands show that their lattice parameter is much closer to that of Si than experimentally observed.

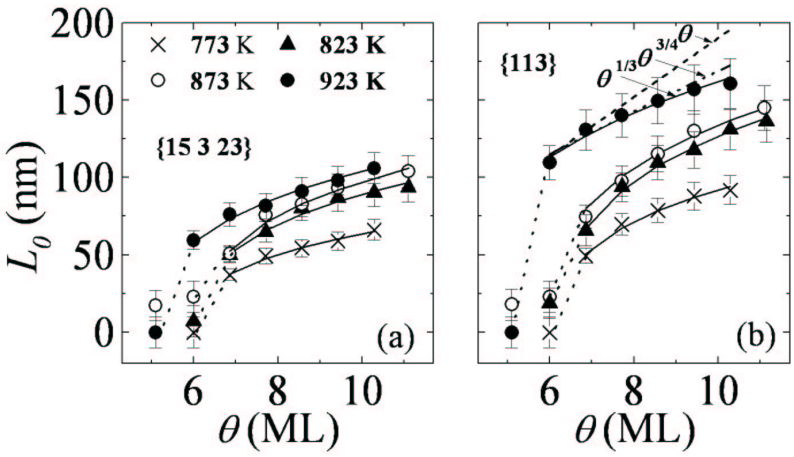

Figure 7.27: (a) and (b) the dependence of the mean facet sizes L_0 on the nominal coverage θ of the deposited Ge layer. Above 6 ML at 923 K and 6.9 ML at the three other temperatures, the data for the {15 3 23} (a) and {113} (b) facets were fitted to a $B(\theta - \theta_c)^{1/3}$ function (full lines).

et al. [37]. In doing reflectivity measurements on a sample grown at 823 K with a very slow growth rate, they extracted the evolution of the island height as a function of deposit. They observed a nonlinearity and sudden increase in island height at ∼6 ML coverage. Besides, it has been observed that islands grown at 773 K and with a height above 50nm, are no more dislocation free [38]. This confirms that at 6-6.9 ML, superdomes can be formed. At the transition, a huge amount of material is transferred into dislocated islands, either by island coalescence or by anomalous coarsening.

For T=773 K, above 6.9 ML, the 1/3 power evolution of the different facet sizes implies that the island volume V is proportional to the deposited thickness θ, neglecting the apparent shape anisotropy of the superdomes and small volume variations possibly induced by a different size variation of the {105}, {111} or {20 4 23} facet areas. The first hypothesis, which postulates that the apparent anisotropy of the superdomes does not influence the analysis of the GISAXS data with respect to the 1/3 power law is justified as GISAXS measurements average the facet size. The second hypothesis is almost valid because the area limited by the {105} facets is negligible with respect to that limited by the other dome or superdome facets [9, 8]. Furthemore, AFM images show that the area limited by the steep superdome facets ({111} and {20 4 23}) is almost negligible compared to the {113} and {15 3 23} superdome facets. The 1/3 power law observation can exclude the possibility of Ostwald ripening for which, according to Lifshitz−Slyozov [39], Wagner [40] and Chakraverty [41, 42], the island size should increase as $t^{3/4}$ or t^1. Our results suggest thus that island coalescence occurs at the transition, and once dislocated islands are formed the coalescence of islands is rare [43, 44]. This is consistent with AFM images, which reveal a large separation of superdome islands. Besides, no depletion region is evident around the dislocated islands. This was previously observed by Merdzhanova *et al.* [28] for a fast growth rate and for a growth temperature around 843 K. This was the signature of the relative non-efficiency of anomalous coarsening at low temperatures. Note that the 1/3 power evolution of superdome facet sizes is valid supposing that the population of domes remain constant with increasing deposit and after the coherent-to-incoherent growth transition. This is justified by the GIXD data. In Fig. 7.20 (b)-(c), it can be observed that the signal from domes, located in-between the signal from superdomes and the Si Bragg peak, does not evolve after a deposit of 7 ML, suggesting that, in average, the quantity of atoms inside domes reamins constant. As no decrease or no increase of the intensity of the scattering from domes is observed, dome coalescence is a rare event and in average, domes do not increase in size. This implies that, when superdomes are formed, the deposited Ge atoms will preferentially attach to superdomes and their mean facet sizes will follow a 1/3 power evolution. Nevertheless, island capture or anomalous coarsening cannot be excluded as it corresponds to a small amount of captured material compared to the volume of superdomes. During the superdome growth, it can also be seen that the maximum of relaxation stays constant but that the corresponding intensity increases (see Fig. 7.20 (a), between 6 and 10.3 ML). The increase of intensity suggests the formation of larger superdomes with increasing deposition as shown by the increase of the {113} and {15 3 23} facet sizes.

We define ϵ^{Ge} as the residual strain of a Ge island (with respect to the Ge lattice parameter) and ϵ_0 (4.16%) the misfit between Si and Ge. In a one dimensional model of an island of width w, relaxed by n dislocations of Burgers vector b, one has $\epsilon^{Ge}=\epsilon_0$-nb/w [45]. The above results show that, at all temperatures, ϵ^{Ge} is constant above θ=6 ML, while w increases with $\theta^{1/3}$ and n increases with θ (see part 5.0.11 C). Thus, the residual strain decreases during growth. This implies that during the superdome growth, the introduction of dislocations is prevalent compared to the coalescence of islands and it reduces the need for strain energy relief by elastic deformation.

The same phenomena are observed for the other studied temperatures. The strong strain relief and the shift of the island relaxation towards the position of the Ge bulk Bragg peak in GIXD can be correlated to the introduction of dislocations inside the islands and to the formation of superdomes. The Ge deposit for the dome-to-superdome transition decreases when temperature increases.

If we consider the growth temperature of 923 K, at the dome-to-superdome transition (between 5.1 and 6 ML), the mean size of the {113} and {15 3 23} facets evolves from (0±10)nm to (110±11)nm and to (60±6)nm, respectively. From literature [46], the mean {113} facet size is around 30nm for a dome-like island. The transition from domes to superdomes does not only explain the significant increase of the facet sizes: a large amount of material is transferred into dislocated islands at the

transition as seen by the huge increase of the scattered intensity. In Fig. 7.27 (b), dashed lines are plotted, corresponding to a $\theta^{1/3}$, $\theta^{3/4}$ and θ power -laws. The best fit is obtained for the $\theta^{1/3}$ power-law.

The superdome growth is thus characterized by two phenomena. *First, at the transition, the coalescence of domes is the dominant pathway towards the formation of dislocated islands. Second, during the growth of superdomes, superdome coalescence is a rare event, the introduction of dislocations prevails, and the superdomes are characterized roughly by a self-similar increase. The {113} and {15 3 23} facets continue to grow and are not suppressed by the introduction of the steeper {111} and {20 4 23} facets.*

From the fit of the experimental data to the $\theta^{1/3}$ power-law of the type: $L_0 = B(\theta - \theta_c)^{\frac{1}{3}}$, where B and θ_c are constant, we determined the temperature dependence of the constant B for both investigated facet types. The value of $B_{\{113\}}/B_{\{15\ 3\ 23\}}$ is found to be constant, around (1.5±0.1) in the investigated temperature range. The almost absent temperature dependence implies that the superdome shape does not strongly depend on temperature.

From GIXD on the last deposit, the average lattice parameter of the superdomes can be estimated as a function of temperature: 5.62Å at 773 K, 5.58Å at 823 K, 5.57Å at 873 K and 5.55Å at 923 K. With increasing temperature, the average lattice parameter of the 3D islands decreases. This can be related to the increase of the Si content [47, 48, 10], when the growth temperature increases. As superdomes are formed at 6 ML at T=923 K and 6-6.9 ML at T=773 K, it appears that for a slow growth rate, the nucleation of dislocation is almost temperature independent and is not delayed by the Si-Ge intermixing. From simple energy considerations it follows that it becomes energetically favorable to incorporate a dislocation for an island with the mean Ge concentration x_{Ge}, if (see chapter 5)

$$x_{Ge}L > \frac{b(c\xi + 2G)}{2\xi c f} = const., \tag{7.8}$$

where ξ is the aspect ratio $h = \xi L$ (h, L are the island height and diameter, respectively), f is the Si/Ge misfit (0.042), N the number of dislocations of Burgers vector b, c the elastic coefficient and G the shear modulus. With increasing growth temperature, the mean island size L increases while the Ge content x_{Ge} decreases. There is thus a competition between intermixing and island size to incorporate a dislocation. For a same Ge deposit θ, the island volume depends on the growth temperature. The higher the growth temperature, the higher the island volume, and the lower the Ge content. As already reported in the previous chapter, assuming that the critical volumes for which it becomes energetically favorable for an island to incorporate a dislocation is proportional to x_{Ge}^{-6} [49, 46, 28], the $x_{Ge}L$ product is roughly proportional to $\frac{1}{x_{Ge}}$. The slower the growth rate, the smaller the Ge concentration and thus the smaller the criterion ($x_{Ge}L \propto \frac{1}{x_{Ge}}$) for which a dislocation is introduced. Thus the condition $x_{Ge}L > const.$ can be fulfilled for smaller deposit compared to a fast growth rate.

Since the mean island size depends on the island density ϱ roughly as $w \propto (\theta/\varrho)^{1/3}$, the critical coverage for the dome-to-superdome transition can be estimated to

$$\theta_c \propto \varrho \left(\frac{b(c\xi + 2G)}{2\xi c f x_{Ge}} \right)^3 .$$

For a slow growth rate, with increasing growth temperature, x_{Ge} decreases due to the intermixing, but ϱ decreases as well, so that the critical coverage is almost temperature independent.

The strength of the present work lies in the direct determination,* in situ*, during the MBE growth under UHV, of the evolution of the statistical average of the facet sizes as a function of deposited material. This direct observation is all the more important as surface preparation, growth temperature, and deposition rate may be slightly different from one sample to another.* In situ *UHV-GISAXS during growth appears as a complementary technique to microscopies and allows a systematic study of the statistical average of the facet sizes as a function of deposited thickness and growth temperatures. Combined with* in situ *GIXD, it allows a more complete understanding of both strain and morphology of the islands.

7.5.5 Conclusion

We have studied the evolution of the size of crystallographic superdome facets during a slow growth of Ge on Si(001) using* in situ *GISAXS. From the evolution of the widths of intensity streaks in reciprocal space we have determined the kinetics of the growth of the superdome {113} and {15 3 23} facets. At the transition, a huge amount of material is transferred into dislocated islands, either by dome coalescence or anomalous coarsening. Superdomes are thus stabilized by the insertion of dislocations during their growth. The 1/3 power law dependence indicates that once dislocated islands are formed, the coalescence of islands is at least a rare event. Ostwald ripening and anomalous coarsening can not be excluded. The next section will deal with the coalescence of domes and superdomes which results in the formation of new shaped superdomes. The coalescence of superdomes is almost a rare event.

7.6 Coalescence of domes or superdomes: towards the formation of "flat-top superdomes".

In this section, we report the formation of superdomes with a new shape. They are observed at low growth rates and result from the complex evolution of domes and superdomes: coarsening and intermixing. These results provide new insight into mechanisms governing shape transformations of incoherent faceted semiconductor islands.

The samples were grown by molecular-beam epitaxy (MBE) in a devoted ultra-high vacuum chamber equipped with large beryllium windows and coupled to a surface diffractometer for X-ray diffraction, on the BM32 synchrotron beamline at the ESRF. The Si(001) substrates were deoxidized by annealing at 1200 K until a sharp, 2x1 reconstructed, Reflection High Energy Electron Diffraction (RHEED) pattern was observed. Germanium was deposited with a Knudsen cell whose slow deposition rate (170 sec for one Ge monolayer (ML)) was *in situ* calibrated using both a quartz microbalance and X-ray reflectivity. Ge was deposited monolayer after monolayer at three growth temperatures (823 K, 873 K and 923 K). Ten to eleven monolayers (ML) of Ge were deposited. As annealing modifies the island morphology [11], after completion of each monolayer, the samples were immediately cooled to 723 K where neither Si-Ge intermixing nor island evolution occurs [32]. In order to investigate annealing effects, another sample was grown at 823 K with 8 ML of Ge deposited. It was then kept at 823 K for one day before cooling to room temperature. The surface morphology of all these samples was next investigated *ex situ* by means of atomic force microscopy (AFM) in tapping mode.

Figure 7.28 shows AFM images of samples obtained upon deposition of 10-11 ML Ge at 823 K, 873 K and 923 K.

A bimodal growth is observed with the coexistence of domes (small islands with a diameter of ∼100 nm) and barns or superdomes (large islands with a size of ∼400-600 nm) which are observed for all growth temperatures. With increasing temperature, the island density clearly decreases for the small islands (domes) (Figs. 7.28 (d)-(f)) and increases for barns or superdomes as an effect of surface diffusion and anomalous coarsening which are enhanced at high temperatures. To discriminate between coherent barns and dislocated superdomes, a study of the island volume and island shape has been performed. Most islands which present {111} facets are no longer regularly shaped and some island volumes are even higher than 1E7 nm^3, which is larger than the critical volume (∼0.4E6 nm^3) of the transition from coherent to dislocated islands [12]. This confirms the presence of dislocated superdomes on each sample. Superdomes present much larger diameters than domes: as observed by LeGoues *et al.* [45], once a dislocation has been introduced, dislocated islands become more relaxed and are thus preferred with respect to domes for Ge attachment. Superdomes then grow much faster than the surrounding domes.

Figure 7.29 shows the morphology of two types of superdome islands, named *A* [Fig. 7.29 (a)-(c)] and *B* [Fig. 7.29 (d)-(f)] and observed on all samples.

We have analyzed their facets following the procedure given in the literature [50, 51] in performing

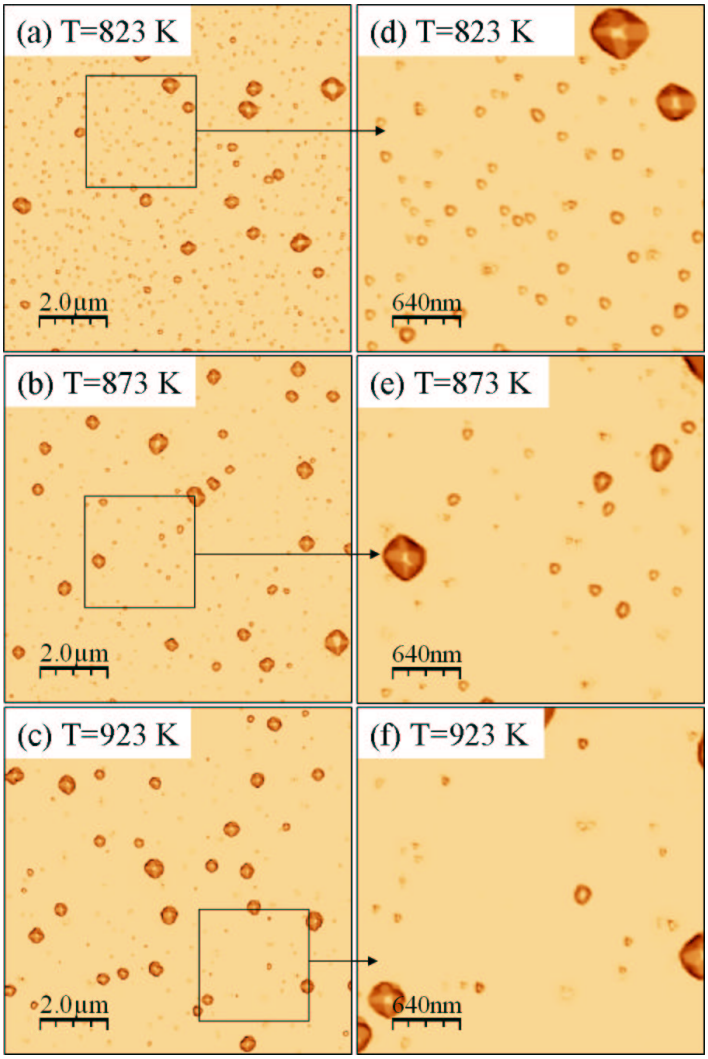

Figure 7.28: AFM images of samples obtained upon deposition of 10-11ML of Ge at 823 K (a, d), 873 K (b, e) and 923 K (c, f). Figures on the right side correspond to zooms.

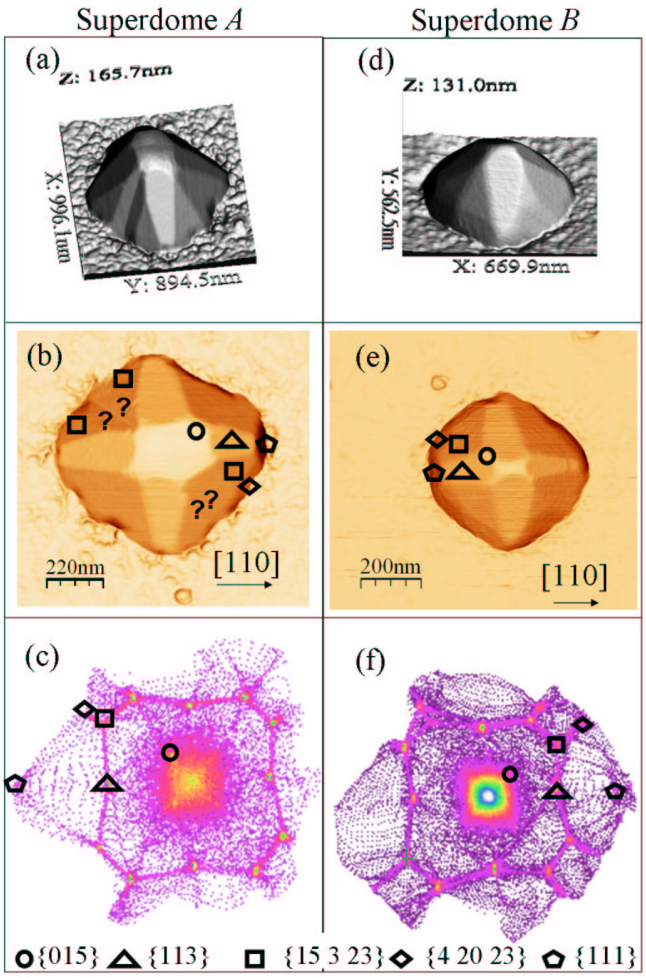

Figure 7.29: (a) and (b) Perspective and top AFM views of a superdome island (10-11 ML of Ge deposited), named A, observed for all growth temperatures. (c) Corresponding facet plot according to the method given in Refs [50, 51]. Representative facets are labelled at the bottom. Unknown facets (labelled '?') are observed. They partially suppress {15 3 23} facets. (d) and (e) Perspective and top AFM views of another superdome island (10-11 ML of Ge deposited), named B, also observed for all growth temperatures. (f) Corresponding facet plot.

facet orientation plot averaged over many islands observed in AFM images (see Fig. 7.29 (c) and (g)). The conventional {105}, {113} and {15 3 23} facets of dome islands [25] appear for both A and B islands. Additional spots can be recognized as arising from steeper facets. They correspond to facets usually observed at the base of superdome islands [9]: {111} and {20 4 23} facets. The superdome, named B, has the usual superdome shape showing these five facets: {105} shallow facets at the top, medium steepness facets ({113}, {15 3 23}) and steep facets ({111}, {20 4 23}) at the bottom of the island. The other superdome-island, named A [Fig. 7.29 (a)-(c)] presents additional facets, which appear as surface indentation and partially suppress the {15 3 23} facets along the [±100] directions. The unknown facets are labelled '?' in Fig. 7.29(b).

To determine the nature of these additional facets, we measured the facet contact angles using AFM. From the knowledge of the crystallographic orientation of the line defined by the intersection of the facet plane and the substrate plane, this contact angle allows the facets of Ge superdomes to be indexed. A cross-sectional line scan through the island center along the [100] direction and passing along the intersection of the two additional facets was performed and showed a contact angle of (33±1)° (see Fig. 7.30 (a)). The possible additional facets which appear along the [100] direction can be either {15 3 23}, {20 4 23} or {4 20 23} facets as no other additional spots are observed on the facet plot [Fig. 7.29 (c)]. They correspond to contact angles of 33°, 41° and 10°, respectively. The measured contact angle thus corresponds to {15 3 23} facets. We can conclude that the two same size additional facets in the left-hand corner of Figs. 7.29 (b) and 7.30 (a) are additional {15 3 23} facets. A similar observation can be performed on the opposite side of the superdome, where, contrary to the other side, the two additional facets do not have the same area. They present a contact angle of (32±1)° with the [-100] direction. We can thus index them as {15 3 23} facets too. What is remarkable is that the {15 3 23} additional facets are only observed along the [±100] direction and not along the [0±10] direction for this island.

The shape and symmetry of this island are thus different from the generally observed superdome shape. Usual superdomes [Fig. 7.29 (d)-(e)] exhibit a steep morphology [Fig. 7.29 (d)-(e)], while the top of this new island is mainly bounded by shallow {105} facets, as observed on Fig. 7.29 (a)-(b). Due to their large {105} facets which give the impression of a superdome-island bounded by a plateau-like facet, we will call them in the following "flat-top superdomes". As observed in references [9, 12], the area of {105} facets decreases at the pyramid-to-dome and dome-to-barn transitions, but it remains approximatively constant with increasing volume for domes, barns and superdomes outside the transitions. This implies that the transition from dome or superdome-to-"flat-top superdome" is not similar to the previous island transitions. Nevertheless, the increase of {105} facets of superdomes has been just recently observed after 360 min annealing of a sample containing dislocated islands at a temperature of 1013 K [11]. We find here that this phenomenon not only occurs during annealing at high temperatures, but also during a slow growth rate.

Figure 7.30 (c)-(d) display side view AFM images of a "flat-top superdome" and a superdome.

To make a comparison and for clarity, the two islands have been rescaled to have identical in-plane size, and their height has been multiplied by two. (In fact, the "flat-top superdome" has a larger diameter than the observed superdome.) The measured aspect ratio of the "flat-top superdome" is (0.19±0.1), significantly smaller than that of the superdome (0.24±0.1). These values can be understood by the increase of shallow facets ({105}) and the presence of additional facets in-between the {15 3 23} facets for the "flat-top superdome"-shaped island. As observed in reference [12], the transitions from pyramid-to-dome, from dome-to-barn and from barn-to-superdome occur via an increase of the island volume and height. With increasing volume, the aspect ratio values of coherent islands (pyramids, transitional pyramids, domes and barns) increase. For dislocated islands, the aspect ratio values are scattered between 0.25 and 0.3 [12]. This means that the aspect ratio value of the superdome [Fig. 7.30 (c)] is in agreement with the aspect ratio of dislocated islands. This is not the case for the "flat-top superdome" whose aspect ratio is largely inferior to the one of barns or superdomes. Thus, contrary to the previous transitions, the transition from dome or superdome to "flat-top superdome" occurs via a decrease of the island aspect-ratio. This suggests that domes or superdomes do not transform into "flat-top superdomes" via accumulation of material at their top but at their corner.

This differs from the previous transitions. The "flat-top superdome" height does not increase

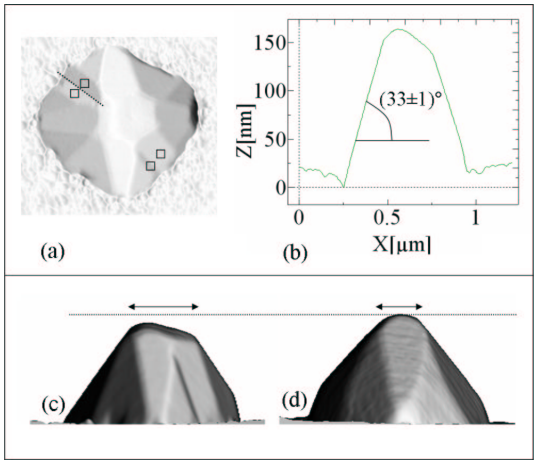

Figure 7.30: (a) Top-view AFM image of a "flat-top superdome" island. The square labels mention the additional facets. (b) Profile of the island along the [100] direction (see line drawn in figure (a)). AFM scans of a "flat-top superdome" island (c) and a superdome-island (d) of same size. The height of each island has been multiplied by two. The superdome-island has a higher aspect-ratio. The {105} facet area of the "flat-top superdome" island is larger.

monotonically with increasing base area contrary to superdomes which present a complex cyclic growth mode [28, 45]. As observed by LeGoues [45], superdome islands grow vertically at constant width until it becomes energetically favourable to introduce another dislocation. At this point, the superdome height drops discontinuously, though never becoming as low as at the beginning of the previous cycle. When fast lateral growth is observed (when each dislocation is introduced), the island must be growing laterally by the transport of atoms from its top to its edge, in order to optimize its shape. After that, lateral growth stops, and the height of the island again begins to slowly increase, until another dislocation is introduced. The drop of the height could suggest that "flat-top superdomes" are the result of this complex cyclic growth. But the ratio of the height to width is lower than the expected aspect ratio for dislocated islands [12]. This means that the drop of the height observed at a value lower than the previous cycle are unlikely to originate from this cyclic growth.

Besides, in looking carefully at figures 7.29 (a) and 7.30 (c), we can observe that the top of the "flat-top superdome" is not flat but presents two maxima. These two maxima can be understood as the result of the coalescence of two domes or superdomes of different heights. This is in good agreement with what has been observed by Merdzhanova *et al.* [see Fig. 7.30 [28]] using a selective etching technique. They demonstrated that coalescence plays an important role at the lowest growth temperature investigated in their work (893 K). The additional {15 3 23} facets which are observed only in one direction are thus the result of the coalescence of domes and maybe superdomes. During growth, "flat-top superdomes" are the evidence of island coalescence. It can be noticed in Ref. [28], that the superdome generated by the coalescence of two islands does not show additional {15 3 23} facets. Thus, the coalescence of two islands does not always result in the formation of "flat-top superdomes".

Coarsening and coalescence have been previously observed in the presence of shape transition for coherent islands [25, 49, 54]. For instance, Floro *et al.* [49] have demonstrated the correlation between hut impingement and the transformations to domes. For the three growth temperatures (823 K, 873 K and 923 K), AFM images show the presence of "flat-top superdomes". In the investigated temperature range, coalescence of domes is prevalent.

The island shape is mainly determined by its size and the misfit with the substrate, which is linked to the composition. In order to determine the composition, we performed multiwavelength anomalous [17] scattering measurements. A mean Ge composition of (58-55±15)% has been determined for both growth temperatures (873 K and 923 K). This indicates a strong Si-Ge intermixing at the origin of

the presence of the {20 4 23} and {111} facets at the bottom of the islands as they are major stable surfaces for Si [52, 55].

To look whether "flat-top superdomes" are obtained after annealing, 11ML of Ge were deposited on a Si(001) sample at a growth temperature of 823K, and **the sample was kept at its growth temperature during one day**. Asymmetric "flat-top superdomes" with several additional {15 3 23} facets were observed on the AFM image [see Fig. 7.31 (a)].

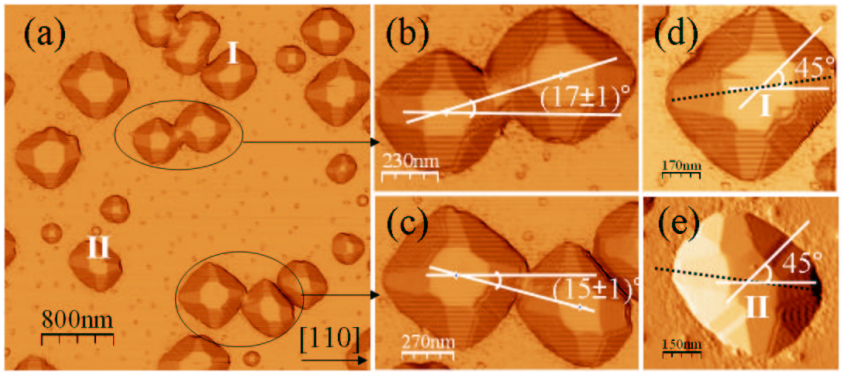

Figure 7.31: (a) AFM image of Ge islands grown at 823 K and annealed at 823 K during one day. (b) and (c) AFM images of superdomes which are in contact. (d) and (e) represent the "flat-top superdomes" named I and II on image (a).

Besides, surprisingly, the AFM image shows the different processes of the coalescence of superdomes towards the formation of "flat-top superdomes". Figures 7.31 (b) and (c) display superdomes in contact. For both cases, the angle between the [110] direction and the center of the two touching islands is about (16±2)°. A statistical analysis on different AFM images shows that there is no prevalent direction along which islands should get into contact. Figures 7.31 (d) and (e) show "flat-top superdomes" which result from the coalescence of superdomes. At the end of the coalescence process, the angle between the [110] direction and the center of the two islands evolves and reaches 45°. The AFM images show that "flat-top superdomes" are elongated along one direction as they present additional {15 3 23} facets along this direction. Their shape is thus asymmetric. It can be clearly observed that the opposite {113} facets are shifted from each other (see black dotted line in Fig. 7.31 (d)-(e)). This suggests that the area of the inserted {15 3 23} facets is not the same on each side of the island.

In the following, we mainly focus on the formation of the "flat-top superdomes". At low temperatures, atomic diffusion is less important so that the inter-island distance is reduced. The probability of coalescence is enhanced. When neighboring islands touch, they tend to ripen to optimize their surface and to reduce the overall surface energy. During annealing, figure 7.31 shows that the coalescence of superdomes is prevalent. As dislocated islands are more relaxed, they are a preferential site for Ge attachment, so they grow faster than coherent islands [56, 57], thus presenting a high probability of static coalescence. Islands grow simultaneously and merge when they touch due to their size increase.

Once islands get into contact, one possibility which can explain the formation of a unique "flat-top superdome" island is that the two neighboring islands continue to grow *self-similarly* until the formation of one island with precisely four {113} facets. In looking at figure 7.31 (b), the distance between the center of the two superdomes is about 500nm so that the radius of each island should increase by a factor of two to displace the center of mass of each island towards the position of the center of mass of the resulting "flat-top superdome"-shaped island. This does not seem to be the prevalent phenomenon, as it needs a high quantity of matter which can not be provided by Si intermixing or anomalous coarsening. Alternatively, the formation of "flat-top superdomes" could tentatively be explained by the strain-mediated *lateral movement* of domes or superdomes. Indeed, strain-mediated lateral motion of coherent islands has been recently observed during annealing [58, 59,

60] and explained theoretically by simple thermodynamic driving forces [61]. As the recently observed lateral motion is produced by strain repulsion applied by neighbouring islands [60], which thus delays coalescence; this phenomenon can be discarded to explain the formation of "flat-top superdomes". A last possibility could be that after contact, the atoms of each island move inside or along the periphery of the islands to quickly form one unique island. It has been shown [62] that there is a probability of detachment of atoms from the island perimeter and reattachment at another place, without moving the facets.

The coalescence stops when only four {113} facets remain out of the eight {113} facets during the coalescence. After growth, only additional {15 3 23} facets and no additional {113} facets are always observed. Besides, island coalescence can be a pathway towards dislocation nucleation. Dislocations may be nucleated at the junction of two growing domes or superdomes. When two strained islands are close together, the distance between the edge atoms is modified compared to that between inner atoms due to edge relaxation. Thus, it is favorable for adatoms to nucleate a dislocation at the trough between two islands. Moreover, it has been found that dislocations are most likely formed at the corners of the islands, where the strain is most concentrated. This has been confirmed by theoretical modeling [63, 64]. The introduction of dislocations when islands meet can possibly anchor the island, making improbable island motion but not atomic diffusion. Besides, this can explain why on one side, two additional {15 3 23} facets remain. This suggests that it is possible that this configuration is stabilized by the introduction of dislocations at the beginning of coalescence. The dislocation will prevent the total recovery of the {15 3 23} facets. We can envisage that when a dislocation is not introduced during island coalescence, the {15 3 23} facets of the two meeting islands will totally recover. That's maybe why, in Ref. [28], the superdome generated by the coalescence of two islands does not show additional {15 3 23} facets.

To understand the shape of 'flat-top superdomes' and the formation of the additional {15 3 23} facets, we build up a morphological model of the 'flat-top superdome'-shaped island in three dimensions (3D) (see Fig. 7.32).

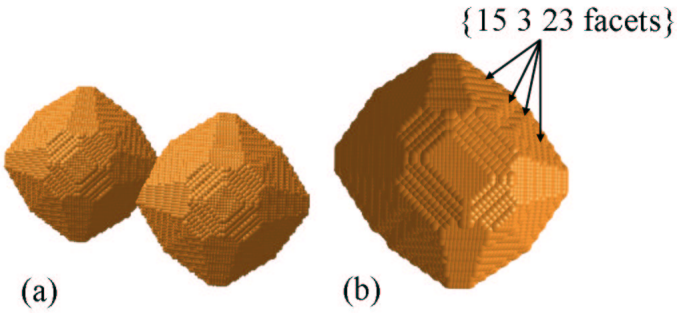

Figure 7.32: 3D morphological models of two islands in contact (a) and after coalescence (b). Aditionnal {15 3 23} facets can be observed.

If the two islands in contact have the same size, this leads to the formation of symmetric additional {15 3 23} facets (Fig. 7.32 (b)). Assymetric {15 3 23} facets appear if the islands have different sizes.

In conclusion, we have characterized the morphological evolution of dislocated SiGe islands. In the investigated temperature range, we demonstrated that island coalescence and consequent dislocation introduction may appear and lead to the formation of a new kind of island, named "flat-top superdomes". They are characterized by the presence of additional {15 3 23} facets and of large {105} and {001} facet area on their top compared to as-known superdomes. As compared to the hut-to-dome transition, the dome- or superdome-to-"flat-top superdome" transition is marked by coalescence which is the motor of the shape transition.

7.7 Conclusion

In this chapter, superdomes are shown to be less intermixed than domes or pyramids as Ge atoms preferentially attach to superdomes. During the in situ growth at 500° C and 650° C, a strong intermixing is observed in pyramids. Integrating the intensity in the region of relaxed Ge during the growth allows to determine and evaluate the participation of the wetting layer at the formation of islands. The evolution of the size of superdome facets was studied during a slow growth rate. It is shown that a slow growth rate fastens the apparition of dislocated islands. At the coherent-to-incoherent growth transition, a huge amount of material is transfered into dislocated islands either by dome coalescence or anomalous coarsening. Superdomes are then stabilized by the insertion of dislocations during their growth. Finally, we presented a new type of dislocated islands resulting from coalescence.

Bibliography

[1] V.A. Shchukin, N.N. Ledentsov and D. Bimberg,*Epitaxy of Nanostructures*, Springer, Berlin (2003).

[2] C. Teichert, Physics Reports **365**, 335 (2002).

[3] G. Medeiros-Ribeiro, A. M. Bratkowski, T. I. Kamins, D. A. A. Ohlberg, and R. S. Williams, Science **279**, 353 (1998).

[4] www.fujitsu.com (2005).

[5] J. Stangl, V. Holy, and G. Bauer, Rev. Mod. Phys. **76**, 725 (2004).

[6] E. J. Smith, D. Chandrasekhar, S. A. Chaparro, P. A. Crozier, J. Drucker, M. Floyd, M. R. McCartney, and Y. Zhang, J. Cryst. Growth **259**, 232 (2003).

[7] E. Sutter, P. Sutter, and J. E. Bernard, Appl. Phys. Lett. **84**, 2100 (2004).

[8] M. Stoffel, A. Rastelli, J. Tersoff, T. Merdzhanova and O. G. Schmidt, Phys. Rev. Lett. **95**, 155326 (2006).

[9] A. Rastelli, H. von Känel, Surf. Sci. **515**, L493 (2002).

[10] T. U. Schulli, J. Stangl, Z. Zhong, R. T.Lechner, M. Sztucki, T. H. Metzger, G. Bauer, Phys. Rev. Lett. **90**, 066105 (2003);T. U. Schülli, M. Stoffel, J. Stangl, R. T. Lechner, E. Wintersberger, M. Sztucki, T. H. Metzger, O. G. Schmidt and G. Bauer, Phys. Rev. B. **71**, 035326 (2005).

[11] M. Stoffel, A. Rastelli, J. Stangl, T. Merdzhanova, G. Bauer, and O. G. Schmidt, Phys. Rev. B **75**, 113307 (2007).

[12] M. Stoffel, A. Rastelli, J. Tersoff, T. Merdzhanova, and O. G. Schmidt, Phys. Rev. B **74**, 155326 (2006).

[13] R. Magalhães-Paniago, G. Medeiros-Ribeiro, A. Malachias, S. Kycia, T. I. Kamins, and R. Stanley Williams, Phys. Rev. B. **66**, 245312 (2002).

[14] J.-M. Baribeau, X. Wu, and D.J. Lockwood, J. Vac. Sci. Technol. A **24**, 663 (2006).

[15] G. Katsaros, G. Costantini, M. Stoffel, R. Esteban, A. M. Bittner, A. Rastelli, U. Denker, O. G. Schmidt and K. Kern, Phys. Rev. B. **72**, 195320 (2005).

[16] G. Capellini, M. De Seta, and F. Evangelisti, Appl. Phys. Lett. **78**, 303 (2001).

[17] A. Letoublon ,V. Favre-Nicolin, H. Renevier, M.G. Proietti, C. Monat, M. Gendry, O. Marty, C. Priester, Phys. Rev. Lett. **92**, 186101 (2004).

[18] M. Rauscher, R. Paniago, H. Metzger, Z. Kovats, J. Domke, J. Peisl, H.-D. Pfannes, J. Schulze, I. Eisele, J. Appl. Phys. **86**, 6763 (1999).

[19] G. Renaud, R. Lazzari, Ch. Revenant, A. Barbier, M. Noblet, O. Ulrich, F. Leroy, J. Jupille, Y. Borensztein, C. R. Henry, J.-P. Deville, F. Scheurer, J. Mane-Mane, and O. Fruchart, Science **300**, 1416 (2003).

[20] W.A. Hendrickson, Trans. Am. Crystallogr. Assoc. **21**, 11 (1985).

[21] A. V. Osipov, F. Schmitt, S. A. Kukushkin, P. Hess, Appl Surf. Sci. **188**, 156 (2002).

[22] Y. Zhang, J. Drucker, J. Appl. Phys. **93** 9583 (2003).

[23] V. G. Dubrowskii, G. E. Cirlin, V. M. Ustinov, Phys. Rev. B **68**, 075409 (2003).

[24] A. Rastelli, M. Stoffel, J. Tersoff, G. S. Kar, and O. G. Schmidt, Phys. Rev. Lett. **95**, 026103 (2005).

[25] F. M. Ross, R. M. Tromp, and M. C. Reuter, Science **286**, 1931 (1999)

[26] U. Denker, M. Stoffel, and O. G. Schmidt, Phys. Rev. Lett., **90**, 196102 (2003).

[27] A. Malachias, S. Kycia, G. Medeiros-Ribeiro, R. Magalhães-Paniago, T. I. Kamins, and R. Stanley Williams, Phys. Rev. B., **91**, 176101 (2003).

[28] T. Merdzhanova, S. Kiravittaya, A. Rastelli, M. Stoffel, U. Denker, and O. G. Schmidt, Phys. Rev. Lett. **96**, 226103 (2006).

[29] D. J. Eaglesham and R. Hull, Mater. Sci. Eng. B **30**, 197 (1995).

[30] M. Takahasi, T. Kaizu, and J. Mizuki, Appl. Phys. Lett. **88**, 101917 (2006).

[31] O. Kirfel, E. Müller, D. Grützmacher, K. Kern, A. Hesse, J. Stangl, V. Holý, and G. Bauer, Appl. Surf. Sci. **224**, 139 (2004).

[32] T. U. Schülli, M.-I. Richard, G. Renaud, V. Favre-Nicolin, E. Wintersberger and G. Bauer, Appl. Phys. Lett., **89**, 143114 (2006).

[33] G. Medeiros-Ribeiro, T. I. Kamins, D. A. A. Ohlberg, and R. Stanley Williams, Physical Review B, **58** , 7 (1998).

[34] A. Guinier and G. Fournet, *Small Angle Scattering of X-rays*, Wiley, New York (1955).

[35] M.-I. Richard, T. U. Schülli, C. Priester, V. Favre-Nicolin and G. Renaud, *unpublished*.

[36] V. Ranjan, G. Allan, C. Priester and C. Delerue, Phys. Rev. B **68**, 115305 (2003).

[37] A. A. Williams, J. M. C. Thornton, J. E. Macdonald, R. G. van Silfhout, J. F. van der Veen, M.S. Finney, A. D. Johnson, and C. Norris, Phys. Rev. B. **43**, 5001 (1991).

[38] D. J. Eaglesham and M. Cerullo, Phys. Rev. Lett. **64**, 1943 (1990).

[39] I. M. Lifshitz and V. V. Slyozov, J. Phys. Chem. Solids **19**, 35 (1961).

[40] C. Wagner, Z. Elektrochem. **65**, 581 (1961).

[41] B. K. Chakraverty, J. Phys. Chem. Solids **28**, 2401 (1967).

[42] B. K. Chakraverty, J. Phys. Chem. Solids **28**, 2413 (1967).

[43] P. Meakin, Rep. Prog. Phys. **55**, 157-240 1992

[44] J. L. Viovy, D. Beysens, C. M. Knobler, Phys. Rev. A **37**, 12 1988

[45] F.K. LeGoues, M.C. Reuter, J. Tersoff, M. Hammar, and R. M. Tromp, Phys. Rev. Lett. **73**, 300 (1994).

[46] A. Rastelli, M. Kummer and H. von Kaenel, Phys. Rev. Lett. **87**, 256101 (2001).

[47] D. J. Smith, D. Chandrasekhar, S. A. Chaperro, P. A. Crozier, J. Drucker, M. Floyd, M. R. McCartney, and Y. Zhang, J. Cryst. Growth **259**, 232 (2003).

[48] M. Floyd and Y. Zhang, Appl. Phys. Lett. **82**, 1473 (2003).

[49] J. A. Floro, G. A. Lucadamo, E. Chason, L. B. Freund, M. Sinclair, R. D. Twesten, and R. Q. Hwang, Phys. Rev. Lett. **80**, 4717 (1998).

[50] C. Teichert, J. C. Bean, and M. C. Lagally, Appl. Phys. A **67**, 675 (1998).

[51] A. Rastelli, H. Von Kanel, B. J. Spencer, and J. Tersoff, Phys. Rev. B **68**, 115301 (2003).

[52] Z. Gai, X. Li, R. G. Zhao, and W. S. Yang, Phys. Rev. B **57**, R15060 (1998).

[53] F. K. LeGoues, M. Hammar, M. C. Reuter, and R. M. Tromp, Surf. Sci. **349**, 249 (1996).

[54] C. J. Huang, Y. H. Zuo, D. Z. Li, B. W. Cheng, L. P. Luo, J. Z. Yu, and Q. M. Wang, Appl. Phys. Lett. **78**, 3881 (2001).

[55] Z. Gai, R. G. Zhao, W. Li, Y. Fujikawa, T. Sakurai, and W. S. Yang, Phys. Rev. B **64**, 125201 (2001).

[56] M. Hammar, F. K. LeGoues, J. Tersoff, M. C. Reuter and R. M. Tromp, Surf. Sci. **349**, 129 (1996).

[57] M. Krishnamurthy, J. S. Drucker and J. A. Venables, J. Appl. Phys. **69**, 6461 (1991).

[58] U. Denker, A. Rastelli, M. Stoffel, J. Tersoff, G. Katsaros, G. Constantini, K. Kern, N. Y. Jin-Philip, D. E. Jesson, and O. G. Schmidt, Phys. Rev. Lett. **94**, 216103 (2005).

[59] G. Katsaros, A. Rastelli, M. Stoffel, G. Isella, H. von Kaenel, A. M. Bittner, J. Tersoff, U. Denker, O. G. Schmidt, G. Costantini, and K. Kern, Surf. Sci. **600**, 2608 (2006).

[60] M. Stoffel, A. Rastelli, S. Kiravittaya, and O. G. Schmidt, Phys. Rev. B **72**, 205411 (2005).

[61] Y. Tu and J. Tersoff, Phys. Rev. Lett. **98**, 096103 (2007).

[62] V. M. Kaganer, K. H. Ploog and K. K. Sabelfeld, Phys. Rev. B **73**, 115425 (2006).

[63] H. T. Johnson and L. B. Freud, J. Appl. Phys. **81**, 6081 (1997).

[64] B. J. Spencer and J. Tersoff, Appl. Phys. Lett. **77**, 2533 (2000).

Chapter 8

In situ study of the growth of Ge islands on pre-patterned Si(001) substrates.

Laterally ordered nanostructures obtained by self-organization during growth are expected to play an increasing role in devices design, as an alternative to conventional microelectronics. To steer lateral organization, two general methods have been proposed, using either an inhomogeneous strain field or a specific morphology at the surface. In this chapter, the organized growth of Ge quantum dots on nano-patterned Si(001) surfaces obtained either by lithography or direct wafer bonding will be studied in situ by X-rays.

8.1 Laterally ordered growth of Ge islands on a nano-patterned Si(001) surface obtained by lithography: An *in situ* study.

A challenge for the development of nano-electronics is to elaborate semiconductor quantum dots (QDs) that are homogeneous in shape, size, strain and composition, thus resulting in well-defined electronic and optical properties [1]. This is obtained by *e.g.* the growth of Ge islands on lithographically prepatterned Si(001) substrates in the form of ordered pits [2, 3]. The growth of ordered Ge islands on lithographically pre-patterned Si(001) substrates has been intensively investigated by *ex situ* techniques like AFM [5], STM and *ex situ* X-rays [6]. These techniques do not allow to determine the chemical composition and the variation of relaxation prior to and during island formation. In contrast *in situ* X-Ray scattering during growth allows to understand and investigate the growth process. For these reasons, three X-ray techniques (GISAXS, GIXD and Anomalous Scattering) were combined to follow *in situ* the growth of ordered Ge islands on a Si(001) prepatterned substrate. The Grazing Incidence Small Angle X-ray Scattering (GISAXS) technique provides information on size, shape and ordering of the QDs and Grazing Incidence X-ray Diffraction (GIXD) measurements allows to determine their strain and composition. A different growth behaviour is foreseen for the growth on these corrugated surfaces as compared to nominal ones: the wetting layer could have a different thickness or even be suppressed; the islands relaxation, composition, shape and size could also differ widely. Our aim is to establish these parameters on a firm ground, and hopefully relate them to the local substrate curvature [7].

8.1.1 Sample preparation and X-ray characterization.

The samples investigated in this work were Si(001) substrates which were prepared in the group of Pr. Bauer at Linz University. They were pre-patterned by holographic lithography [2]. The pits form

a regular two-dimensional grid ordered along two orthogonal $< 110 >$ or $< 100 >$ directions with a periodicity of ∼400nm.

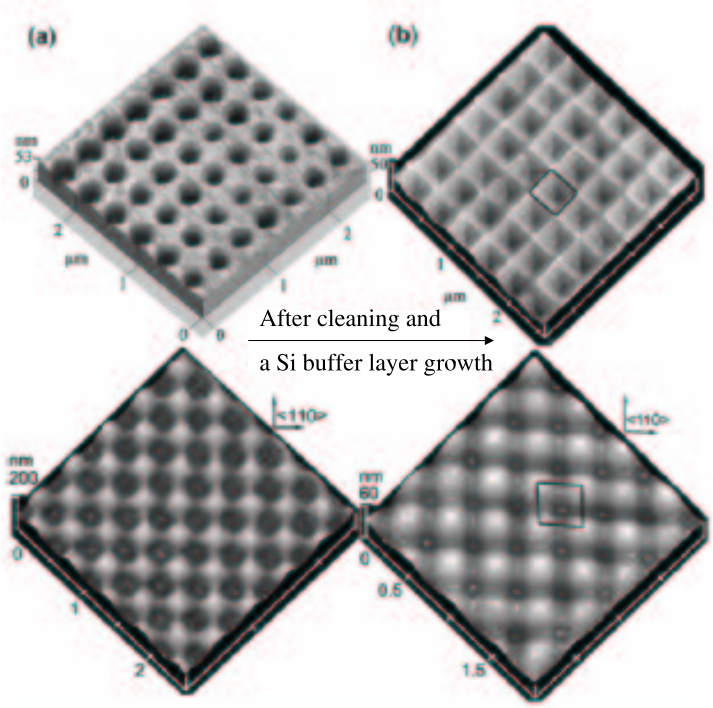

Figure 8.1: AFM images of two different patterned Si(001) substrates just after RIE (a), and after cleaning and Si buffer layer growth (b) [3].

After a chemical cleaning process, including a HF dip, and a thermal treatment in UHV at ∼900°C during 5 min, a 100 nm thick Si buffer layer was grown at a rate of 0.5Å/s while ramping the substrate temperature from 450°C to 520°C in a Riber SIVA 45 reactor (Linz University). This procedure allows to protect the samples before transferring them in the MBE chamber of the BM32 beamline, which is coupled to a diffractometer [9]. Then, a final dip in HF vapours is performed before transferring the samples in the SUV (Surface and Ultra high Vacuum) instrument of the BM32 beamline. To eliminate possible damage and HF residues and to improve the homogeneity of the pattern, the samples undergo a thermal treatment in UHV at ∼725°C, and a final 60-nm-thick Si buffer layer was grown on the Si substrate while ramping the substrate temperature from 420°C to 650°C. Examples of the surface morphology just after RIE and after the buffer layer growth of 2D pit-patterned substrate are depicted in Fig. 8.1. After the buffer layer growth, the surface of the patterned substrate becomes much smoother. The geometrical properties of the 2D pit pattern are changed. The depth is decreased and the slope of the sidewalls become shallower, particularly during the buffer layer growth.

The surface quality was characterized with GIXD and reflection of high energy electron diffraction (RHEED), showing a well-ordered (2x1) reconstructed Si(001) surface. The germanium deposition was performed by molecular beam epitaxy with a rate of 1Å/min, as *in situ* calibrated with a quartz microbalance. A total of 7 monolayers (ML) of Ge were deposited monolayer by monolayer on the Si(001) pre-patterned substrate at a temperature of 650°C. *In situ* X-Ray measurements, GISAXS and GIXD, were performed on the bare substrate and for each added monolayer. Between depositions, the temperature was decreased to 400°C to avoid Si interdiffusion during the X-ray measurements.

GISAXS (Grazing Incidence X-Ray Scattering) measurements provide the detailed evolution of the morphology such as the facetted pits and shape of the QDs during growth and allow characterizing the degree of ordering between islands, at the nm to μm scale [10]. The scattered intensity is recorded

as a function of the exit angle α_f with respect to the surface plane and as a function of the in-plane scattering angle $2\theta_f$. These angles allow to define the reciprocal space coordinates $q_\perp(=q_z)$ and $q_{//}(=q_y)$, respectively perpendicular and parallel to the surface. As these two angles are small: the scattered intensity is measured around the direct and reflected beams. Two-dimensional GISAXS patterns were recorded using a 16 bit, 1Mpixel CDD detector with 56.25μm pixel size. In order to determine the structural characteristics of the Ge islands and ordered pits on the patterned samples, GIXD measurements were performed. The X-ray photon energy was set at 11 keV. The incident angle was set at 0.16°, close to the critical angle of total external reflection (α_c = 0.163° at 11keV) in order to enhance the amplitude of the evanescent wave at the surface. The X-ray scattering was measured in radial and angular directions around Si Bragg peaks. A radial scan is sensitive to the strain, relaxation and epitaxial orientation of the sample, since each q value of the scan corresponds to different interplanar spacing or strain state in direct space. Angular scans are size sensitive. The regions of interest were mapped by a series of angular scans perpendicular to the radial direction over a range between the corresponding reciprocal lattice points of pure Ge and Si, in order to separate the contributions of size and strain broadening in reciprocal space [11]. The Miller indexes (h k l) are expressed in reciprocal lattice units (r.l.u.) of Si, using the bulk fcc unit cell (a_{Si}=5.4309$\mathring{A}$). The l index is the component of the momentum transfer perpendicular to the surface. GI-MAD (Grazing Incidence Multiwavelength Anomalous Diffraction) was performed to probe for possible intermixing. This method allows for a separation of the contributions from Ge and Si and to determine the composition in reciprocal space.

Finally, atomic force microscopy (AFM) and scanning electron microscopy (SEM) were performed after the Si-buffer layer growth and the last Ge deposit.

8.1.2 Morphology of the ordered pits after the growth of a Si buffer layer.

A homoepitaxial Si buffer layer is deposited with a thickness comparable to the depth of the pattern. This buffer layer has a dramatic influence on the geometry of the pits. It removes damages but more importantly, converts the pits into inverted pyramids exposing {11n} facets with 5≤n≤11 [5]. This faceting is attributed to thermodynamic instabilities.

To determine the type of facets of these inverted pyramids, GISAXS images were performed along the $< 110 >$ and $< 100 >$ azimuths. The scattered intensity was measured as a function of Q_y and Q_z, coordinates of the scattering vector parallel and perpendicular to the sample surface, respectively. This is shown in figure 8.2 (a) and (b).

In both azimuths, rods of scattering are measurable. The sidewalls are found to be composed of {1 1 11} and {107} planes, which are inclined by 7±1° (for {1 1 11} planes) and by 8±1° (for {107} planes) relative to the (001) plane. The Si buffer layer converts the etch pits into inverted pyramids composed of {11n} (n=11) and {10m} (m=7) planes. Such facets are not related to known low-energy facets of macroscopic Si crystals. As observed by Zhong [12], the sidewalls of the pits are composed of steps. In analogy to the growth of Ge on stripe-patterned substrates [12], Ge (or Ge-Si) ad-atoms on the terraces between the pits readily migrate to the edges and tend to diffuse to the sidewalls. This phenomenon is attributed to the kinetics of step flow and to the Erhlich-Schwöbel barrier. Thus, it appears that kinetic/energetic effects and microscopic mechanisms associated to steps play an important role in surface pattern morphology. The growth rate anisotropies of the different kind of facets forming the inverted pyramids will thus have to be taken into account in the island growth process.

The size of the facets can be determined by fitting the intensity profile across the facet streak. In the Born approximation, *i.e.* to first order, the intensity is proportional to $\left|\Omega^{FT}(\mathbf{q}_{//}, q_\perp = cst)\right|^2$, where $\mathbf{q}_{//}$ and $q_\perp$ are the components of $\mathbf{q}$ parallel and perpendicular to the facet streak, respectively, and Ω^{FT} is the three-dimensional Fourier transform of the shape function of the facetted pits. Therefore, the width of the streak equals approximately $2\pi/L$, where L is the mean facet size of the pits. The mean facet size of the {11n} and {10m} sidewalls are (42±8)nm and (35±5)nm, respectively, which is in good agreement with the AFM images.

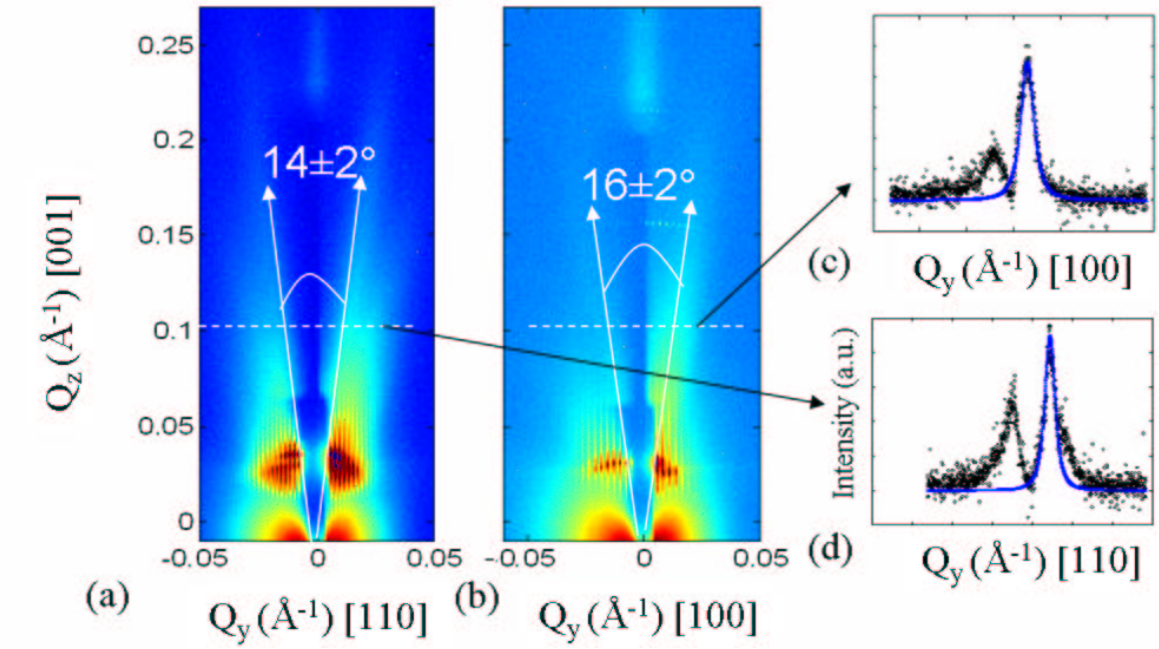

Figure 8.2: GISAXS images along the $< 110 >$ (a) and $< 100 >$ (b) azimuths after the Si-layer growth. Intensity profiles across the facet streaks along the $< 100 >$ (c) and $< 110 >$ (d) azimuths (see corresponding line cuts).

8.1.3 Degree of ordering of the pits after the growth of the Si buffer layer.

The pit morphology after the Si buffer layer growth needs to be highly uniform to obtain an efficient fabrication of ordered Ge islands with a high degree of size homogeneity. GISAXS is a privileged technique to study the degree of organization of such systems. Figure 8.3 (a) shows a GISAXS image centred on the direct beam and along the $< 110 >$ azimuth after the Si buffer layer growth. No intensity is observed around Q_x=0 as the direct beam is blocked by a beam stop. The perfectly periodic lattice of Dirac peaks confirms the uniformity of the pit morphology and the long-range ordering of the pits. The periodicity of the ordered pits, 350nm along the [110] direction, can be deduced from a scan at constant Q_z (see Fig. 8.3 (b)). The width of these satellites does not increase with satellite order, which proves a true long-range ordering of the patterned pits over the macroscopic area (0.35mmx5mm) probed by the X-ray beam in GISAXS.

8.1.4 Morphology and strain state of the Ge deposit during the initial stage of Ge growth on the pre-patterned substrate.

During the very first stage of Ge growth, GIXD measurements were performed mostly along the $[hh\epsilon]$ direction (ϵ being small: ϵ=0.05) in the vicinity of the Si(220) and Ge(220) Bragg peaks (see figure 8.4 (a)). These radial scans were recorded *in situ* for each added monolayer. No significant evolution of the scattering around the (220) peak is found up to 4ML. This reveals the growth of a perfectly two-dimensional pseudomorphic wetting-layer on the pre-patterned pits. No lateral partial strain relaxation occurs during the formation of the wetting-layer. Figure 8.4 (b) represents line scans across the oscillations of the GISAXS image (Fig. 8.5) at constant Q_z for different deposits of Ge. The periodicity of the system remains constant with increasing Ge deposit, but the intensity decreases because the height of the periodic surface shape decreases.

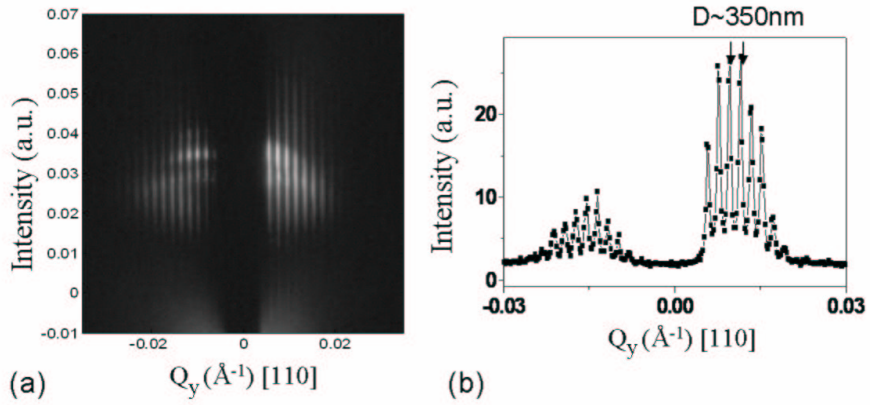

Figure 8.3: (a) GISAXS image along the $< 110 >$ azimuth and centred on the direct beam. (b) Horizontal scan of the GISAXS image after the Si-layer growth on the pre-patterned sample. Note the asymmetry of the signal due to a small misalignement of the X-ray beam.

To study the evolution of the type of pit facets during the growth of the pseudomorphic wetting-layer (from 1 to 4ML of Ge), GISAXS images were performed along the $< 110 >$ and $< 100 >$ azimuths for each added monolayer.

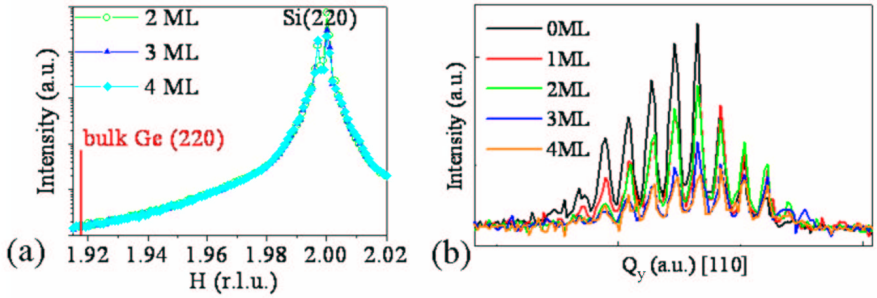

Figure 8.4: (a) Radial scan in the vicinity of the (220)Si Bragg peak from 2 to 4 ML, (b) Constant Q_z cross sections of GISAXS patterns along Q_y for different deposits of Ge: from 0 to 4ML of Ge. The periodicity remains. The intensity is modulated by the Fourier transform of the island and pit shapes.

The preliminary facets of the Si(001) pre-patterned substrate are energetically unfavourable, and the pit facets break up into a rather complex pattern of {10n} and {11m} facets with n>7 and m>11. GISAXS experiments (Fig. 8.5) give the sidewalls inclination averaged over the whole X-ray beam size. With increasing deposition, the angles of the facetted pits relative to the (001) plane decrease ($n_1 < n_2 < n_3 < n_4$ and $m_1 < m_2 < m_3 < m_4$, the index corresponds to the deposited ML). The variation of the sidewalls inclination shows that up to 4ML, Ge atoms preferentially fill the etched pits. Those at the sidewalls prefer to migrate downwards due to a Schwöbel barrier for atoms migrating down rather than up (the activation energy an atom has to overcome to climb a step is larger than to go down the steps; *i.e.* the probability to go down is larger than that to go up). Ge atoms tend to accumulate at the bottom of the pits, facilitating the nucleation of Ge-rich islands. These {11m} and {10n} sidewalls do not correspond to known low-energy facets of Si or Ge crystals. AFM studies have recently shown that the facets of the pits have a complex morphology consisting exclusively of {105} and (001) facets [5] (see Fig. 8.6). Indeed, the {10n} sidewalls are not composed of a single {10n}

facet, but by a staircase of facets consisting of short (001) terraces connected by {105} facets. Besides, the {11m} sidewalls are composed by zigzag arrays of adjacent energetically favourable {105} facets. The conversion of {105} facets could be related to step-meandering instability. As the wetting-layer shows no relaxation compared to the Si(001) substrate, these instabilities are strain-driven. Such {105} faceted structures usually develop during the growth of fully strained SiGe on Si(001) surface [13].

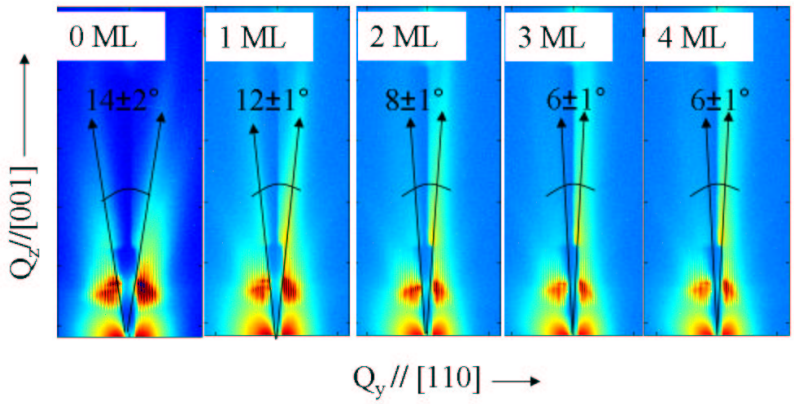

Figure 8.5: GISAXS images along the $< 110 >$ azimuth for θ=0, 1, 2, 3 and 4ML of Ge.

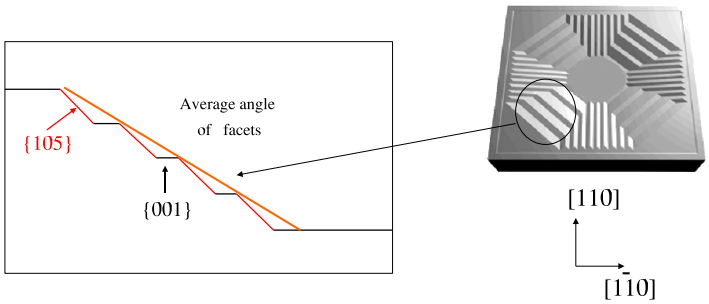

Figure 8.6: Schematic drawing of a facetted pit showing a complex morphology of {105} and (001) facets. GISAXS measurements only give access to the mean facet angle.

Besides, the surface reconstruction has been observed by GIXD and *in situ* reflection high-energy electron diffraction (RHEED) during this first stage of Ge growth. They show a (2x1) reconstructed surface. It has been proposed that anisotropic diffusion induced by the (2x1) reconstruction of Si(001) surface may destabilize the surface towards step-bunching [14]. This can explain the formation of steps on the pit sidewalls.

8.1.5 Formation of 3D islands

Figure 8.7(a) shows GIXD measurements performed mostly along the $[hh\epsilon]$ direction (ϵ being small: ϵ=0.05) in the vicinity of the Si(220) and Ge(220) Bragg peaks. Between 4 and 5 deposited ML, diffuse scattering appears around the Si(220) Bragg peak, made of two components: one centered below the Si Bragg peak at h=2 and one centered at a lower h value, ∼1.987. The shoulders in the left and right side of the Si Bragg peak increase in intensity until the last deposit (θ=7 ML), and evolve towards

positions centered around h=1.97 and h=2.01 respectively. Figure 8.7(b) shows a radial scan in the vicinity of the Si(220) Bragg peak for a deposit of 6ML of Ge at a growth temperature of 550°C (black curve) and after a fast increase of temperature up to 650°C followed by a decrease down to the previous growth temperature, 550°C (red curve). The two curves are not superimposed, indicating that the strain state depends on kinetics (intermixing).

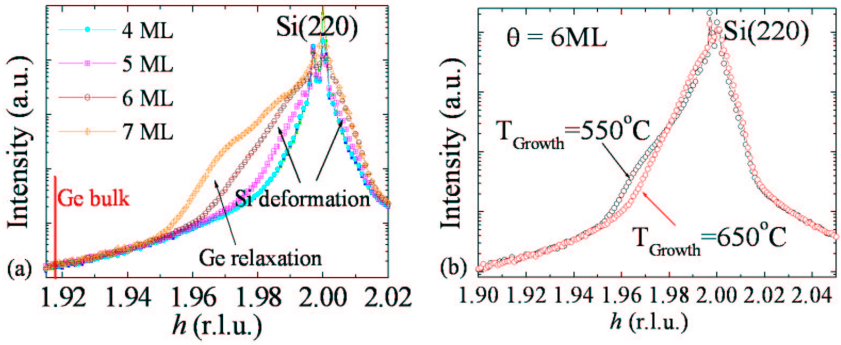

Figure 8.7: (a) Radial scans in the vicinity of the (220)Si Bragg peak from 4 to 7 ML of Ge, (b) Radial scans in the vicinity of the (220)Si Bragg peak for a deposit of 6ML and for two different growth temperatures.

In parallel, GISAXS pictures (see figure 8.8) were recorded for a variety of azimuths of the $\mathbf{q}_{//}$ scattering vector: the $< 110 >$, $< 100 >$ and $< 15\ 3\ 23 >$ azimuths, in which rods of scattering by possible {113}, {105} and {15 3 23} facets are measured.

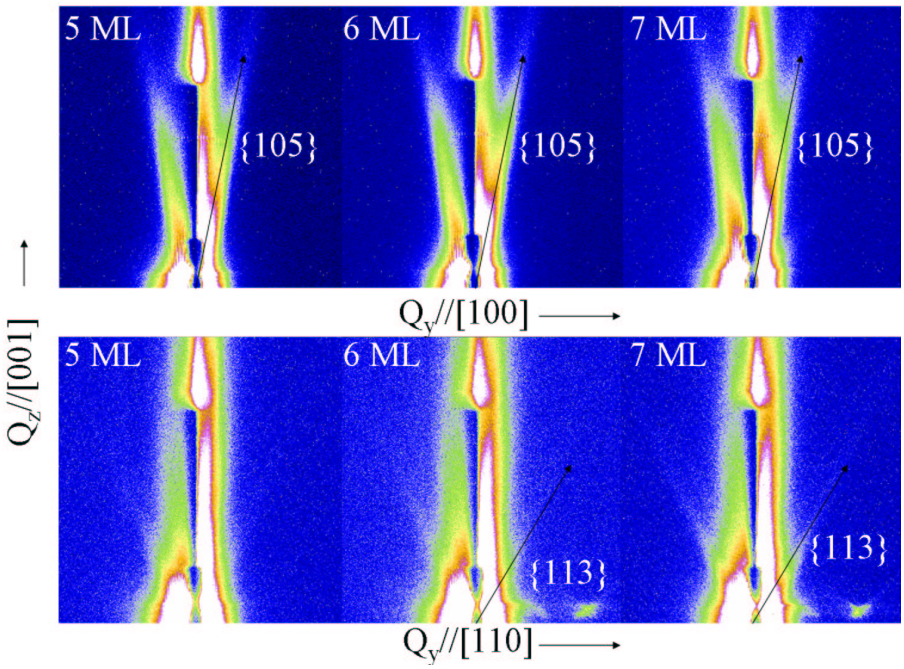

Figure 8.8: GISAXS images along the $< 110 >$ and $< 100 >$ azimuth for θ=5, 6 and 7ML of Ge.

The GISAXS images show features from {105} facets after a deposit of 5ML of Ge. {113} and

{15 3 23} facets (not shown here) are observed after a deposit of 6ML. The rods get narrower with increasing deposit, indicating an increase of the facet size. The appearance of diffuse scattering below the Si(220) Bragg peak and the formation of {105} facets at 5ML is the signature of the 2D-3D transition, with the formation of {105} facetted pyramids. These islands develop to release the stress due to the 4.2% lattice parameter mismatch between Si and Ge. No islands are observed for a deposit of 4ML. This coincides with what has been observed previously [3] : islands appear at 5ML for a growth temperature of 600°C and at 4ML for a higher growth temperature (700°C). Above 5ML, the intensity of the satellite in the left side of the Si(220) Bragg peak (see Fig. 8.7) increases and its maximum moves towards the position of the Ge(220) bulk position. This coincides with the appearance of rods on the GISAXS pictures, arising from scattering by {113} facets, which are known to be present on Ge domes grown on Si(001). The h position of the island's satellite for the last deposit, h ∼1.97 is far from that of relaxed Ge (h ∼1.92). This is attributed to strained domes of mixed composition, Ge_xSi_{1-x}. To determine possible Si interdiffusion inside the Ge domes, GI-MAD experiments (not shown here) were performed. They reveal the formation of intermixed domes composed of ∼ (50 ± 10)% of Ge at 6ML and ∼ (60±10)% of Ge at 7ML. SiGe intermixing has been previously observed by photoluminescence for patterned islands grown at a temperature of 700°C. The average Ge content was about 45% [2]. In our case, the lower temperature growth explain the higher Ge composition inside the dome-shaped islands. The intermixing value of ∼50-60% of Ge corresponds to values obtained in the case of a nominal growth at the same growth temperature (T=650°C). The increase of the Ge content between 6 and 7 ML is explained by the increase of the deposit amount of Ge. Moreover, above 5ML, there is an increase of the diffuse scattering around h=2 which broadens the Si Bragg peak. This is linked to the formation of large domes of mixed composition, Ge_xSi_{1-x}, which strongly distort the Si substrate below them, leading to the Si substrate deformation signal. At this pyramid to dome transition, an increase of the Ge content (from 40 to 50%) inside the islands is observed by anomalous GIXD (not shown here). This finding is in agreement with what is observed in the case of a nominal growth and with the work of Baribeau [4] who observed that pyramids grown at 650° on nominal substrates are more Si intermixed than domes. At the end of the growth (*i.e.* after a deposit of 7 ML of Ge), no superdomes are formed. For the same growth conditions (temperature, growth interruption), we observed the formation of superdomes after a deposit of 6ML of Ge (see chapter 7). As previously observed [3], larger coherent islands can be grown on the patterned substrates as compared to island growth on flat substrates.

8.1.6 Summary of the growth on the lithographically pre-patterned substrate.

AFM and SEM measurements performed after the X-ray measurements (see figure 8.9) clearly confirm that well-ordered islands were grown by this procedure in the SUV/BM32 instrument. They nucleate at the bottom of the pits. They have a height of (30±5)nm and a base width of (155±10)nm. Note that not all the pits are filled by an island.

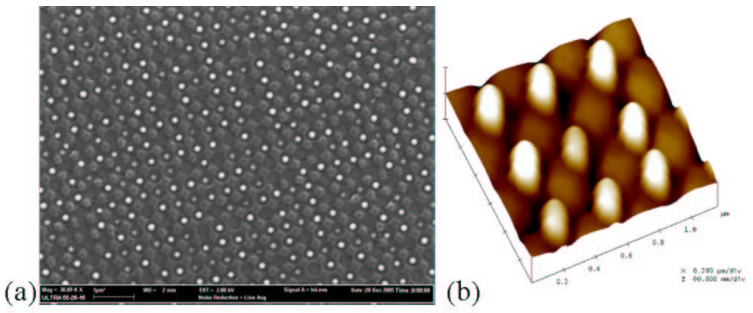

Figure 8.9: SEM (a) and AFM (b) scans performed after the *in situ* growth.

Figure 8.10 summarizes the growth process. During the very first stages of Ge growth ($\theta < 4$ML: growth of the pseudomorphic wetting layer), the preliminary facets of the Si substrate are energetically unfavourable, and the pit facets break up into a rather complex pattern of {10n} and {11m} facets with n>7 and m>11. With increasing deposit, the angles of the facetted pits relative to the (001) plane decrease. The variation of the sidewalls inclination shows that Ge atoms preferentially fill the etched pits. Between 4 and 5 deposited ML, diffuse scattering appears around the Si(220) Bragg peak revealing the nucleation of 3D islands. These results show that GIXD is very sensitive to the onset of islands nucleation by detecting the very first stages of relaxation of the crystal lattice. At 5 ML, rods of scattering by {105}-type facets appear in the GISAXS image revealing the formation of pyramids. After 5ML, intense periodic rods arising from the ordered Ge QDs are evidenced by GISAXS and an increase of the relaxation state is observed by GIXD. Then, after a deposit of 6ML, {113} and {15 3 23} facets are found, corresponding to the formation of domes. At this pyramid to dome transition, a decrease of the Si interdiffusion inside the islands is observed by anomalous GIXD.

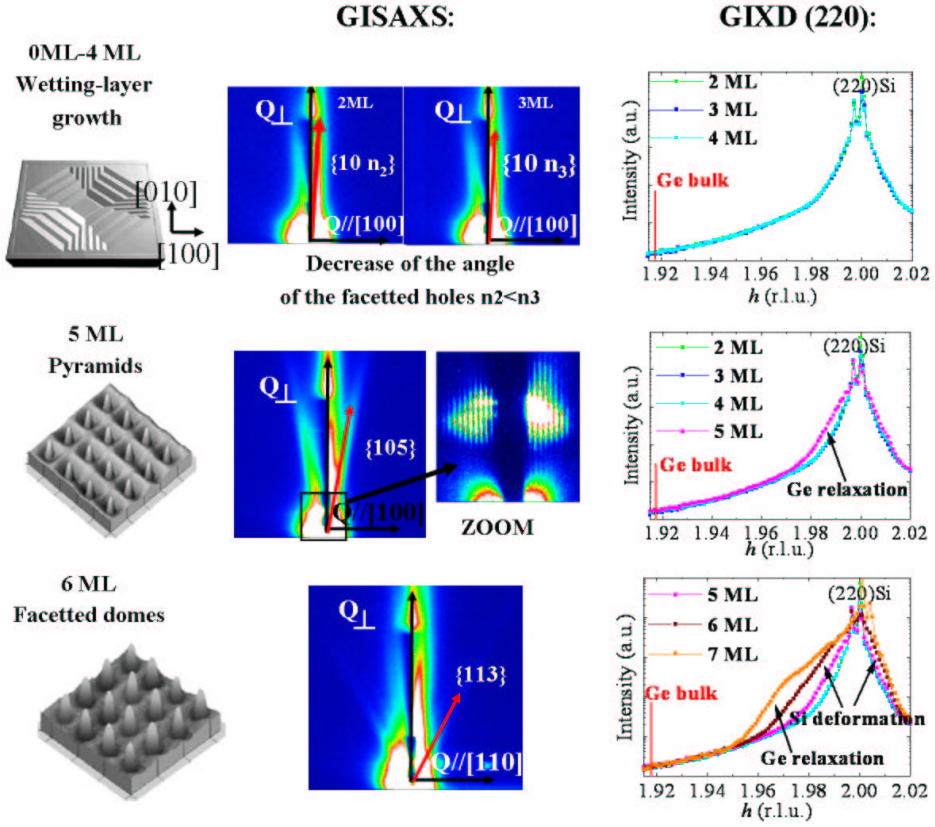

Figure 8.10: Summary of the growth. The left part of the figure shows drawings of the sample. In the middle, GISAXS images can be observed along the $< 100 >$ and $< 110 >$ azimuths. The right part of the figure shows GIXD scans recorded during the growth.

To understand the formation of a single island at the pit bottom, a growth mechanism has been proposed [3, 15]. From an energetic point of view, the pit bottom should not be the favorable position for the compressively strained SiGe islands. In view of the surface curvature (which is one of the term of the chemical energy potential), the concave bottom part of the pits is favoured. This explains thus

the position of the Ge islands inside the pits. At this position, however, the possibility of lateral strain relaxation is rather limited, which explains why with increasing deposit, secondary islands at the top corner of the pits develop, in addition to primary ones that form at the pit bottoms [15, 16]. Another explanation of the localization of islands at the pit bottom is the asymmetrical migration of adatoms over steps of the sidewalls of patterned pits. Provided that the sidewalls of patterned structures are composed of steps and the activation barrier for adatoms migrating downwards over step is smaller than upwards, a net flux of adatoms at the sidewalls can be formed [3].

In the following, we discuss the growth of Ge quantum dots on surfaces obtained by direct wafer bonding and compare it to the growth on surfaces obtained by lithography.

8.2 Organized growth of Ge quantum dots on a nano-patterned Si(001) surface obtained by direct wafer bonding followed by chemical etching: An *in situ* X-ray study.

The simultaneous control of the localization, density and size uniformity of epitaxial nanostructures is a key parameter for future nanoelectronics devices. To fulfil these requirements, Si(001) substrates with a periodic nanometre scale patterning have been developed using wafer bonding and preferential chemical etching techniques. This work presents an *in situ* X-ray study of the growth of Germanium Quantum Dots (QDs) on this template. The combination of Grazing Incidence Small Angle X-ray Scattering (GISAXS), X-ray Diffraction (GIXD) and Anomalous Scattering performed *in situ*, during growth in an Ultra High Vacuum chamber, allows for the characterization of the Ge QDs regarding their shape and organization (GISAXS) as well as their strain and composition (GIXD).

8.2.1 Sample preparation and X-ray characterization.

The Si template is obtained by combining the Smart Cut (Trade Mark of Soitec S.A.) technology [17], wafer bonding and chemical etching of the surface (see Fig. 8.11).

Using direct wafer bonding, a thin monocrystalline silicon layer of ∼200 nm is transferred to a bare silicon or SOI (silicon on insulator) substrate. The in-plane rotation angle ϕ between the bonded crystals defines a square network of screw dislocations. The periodicity d of this network is given by Frank's formula $d = a/(2\sqrt{2}sin(\phi/2))$, where a is the silicon lattice parameter. As the dislocation network is at the interface of the two bonded wafers, it is necessary to perform a preferential etching to transfer the dislocation network symmetry (and period) to the surface [18]. Depending on the etching time, the dislocation network can be removed. In all cases, the periodic surface morphology remains (see Fig. 8.12). Two etching solutions were used: the $Y7$ etching solution, a modified version of the Yang etch [19] (CrO_3 (0.01 g): HF 49% (0.3 mL):H_20 (100 mL)) and the $MD2(70\%)$ solution, generally called Dash etch solution ($MD2(70\%) = CH_3COOH(99\%) : HNO_3(69.5\%) : HF(49\%) = 700 : 298 : 2$) [20].

Two Si nano-patterned substrates were studied: one presenting small square mesa with a periodicity λ of 20 nm and another presenting a periodicity of 50 nm. Table 8.1 shows the aspect ratio (h/λ) of the pre-patterned mesa after the first ($Y7$) and second (MD2(70%)) chemical etchings. The resulting aspect ratio varies from 0.2 to 0.08.

Preferential chemical etching	λ=20nm	λ=50nm
$Y7$ ($h_{max} \sim$ 2nm)	0.1	0.04
MD2(70%) ($h_{mean} \sim$ 4nm)	0.2	0.08

Table 8.1: Aspect ratio of the surface morphology after chemical etching.

The resulting surface morphology was investigated by means of scanning electron microscopy (SEM) and atomic force microscopy (AFM) in tapping mode. Figure 8.13 shows SEM and AFM

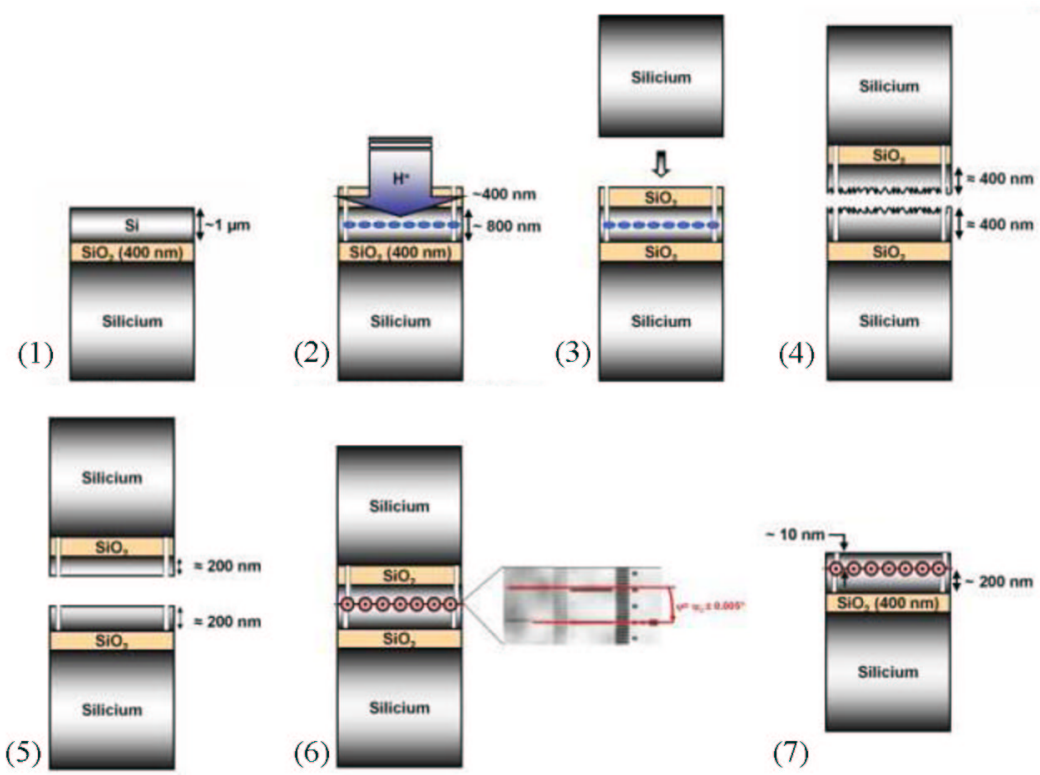

Figure 8.11: The different steps towards the fabrication of a twisted bonded wafer: (1) Starting with a SOI (Silicon On Insulator) substrate with a 1 μm Si film. (2) Thermal oxidation followed by a photolitography process to etch graduated scales (for the control of the rotation of the two bonded substrates) and H^+ implantation. (3) A silicon layer is transferred to the SOI substrate. (4) Fracture at the maximum of the implantation profile. (5) Polishing. (6) In-plane rotation between the bonded crystals and annealing at high temperature. (7) Removal of one Si substrate and of the oxide layer by chemical thinning. From [20].

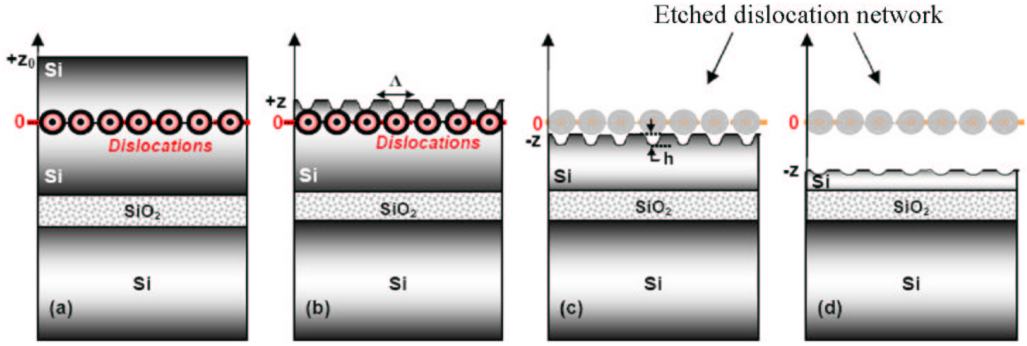

Figure 8.12: (a) Before etching: no surface structuration. Surface morphology when the preferential etching is stopped before the dislocation network (b) or after (c)-(d). Far from the bonded interface, the depth of the trenches decreases. From [20].

scans of the studied Si template which presents a square 50nm surface-patterning of periodic mesa separated by 2.5 to 3 nm deep trenches.

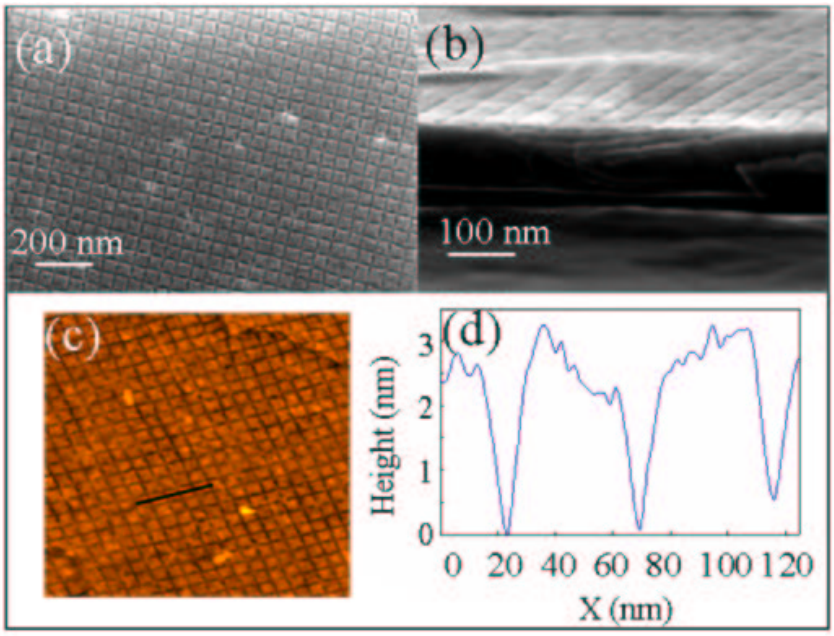

Figure 8.13: In-plane (a) and transverse (b) SEM images of the surface morphology before Ge growth. The Si template presents a square 50nm surface-patterning of periodic mesa. (c) In-plane AFM image of the sample and corresponding depth profile (d).

After a chemical cleaning process, including a final deoxidation in HF vapours, the samples were introduced in a ultra-high vacuum molecular-beam epitaxy (MBE) chamber equipped with large beryllium windows and coupled to a surface diffractometer for GIXD and GISAXS measurements, on the BM32 synchrotron beamline at the ESRF, Grenoble [9]. The Si(001) template was deoxidized by a dip in HF vapours. It was next cleaned *in situ* by annealing. For the 20 and 50 nm Si(001) template, a 3-3.5-nm thick Si buffer layer was first grown on the surface at 923 K. The surface quality was characterized by GIXD and Reflection High Energy Electron Diffraction (RHEED). The formation of a sharp, 2x1 reconstructed RHEED pattern was the signature of a well deoxidized surface. Germanium was deposited with a Knudsen cell with a slow deposition rate of 170 sec for one Ge monolayer (ML) ($\sim$0.008 ML/s), which was *in situ* calibrated using both a quartz microbalance and X-ray reflectivity. Ge was deposited monolayer after monolayer at a growth temperature of 773 K until a deposit of 6-7 ML.

For all X-ray measurements, the X-ray beam energy was set around the Ge K-edge, 11.103 keV, and the incident angle fixed at the critical angle for total external reflection, α_i=0.163°. For GISAXS measurements, in vacuum slits and beam-stop were used to avoid background scattering by the beryllium windows. The scattered intensity was detected by a two-dimensional low-noise CCD detector from Princeton (1152x1242 pixels of 56.25 μm x 56.25 μm) placed 1.68 m away from the sample. All direct- or reciprocal space notations refer to the bulk Si unit cell (a=b=c=5.4309Å, α=β=γ=90°). The Miller indexes (h, k, l) are expressed in reciprocal lattice units (r.l.u.) of Si.

GIXD measurements were performed mostly along the [hkl] direction (h=k) (l being small: l=0.03), with finer measurements in the vicinity of the Si(220) and Ge(220) Bragg peaks. These radial scans

were recorded *in situ* for each added monolayer. GISAXS measurements consisted in recording two-dimensional GISAXS intensity distributions with the X-ray beam aligned along the substrate's [100], [110] and [15 3 0] directions. The GISAXS maps represent cuts of the three-dimensional intensity distribution in reciprocal space with the Ewald sphere.

8.2.2 Experimental results

A. In situ grazing incidence diffraction (GIXD)

Figure 8.14 shows GIXD measurements which were performed around the Si(220) Bragg peak for the 50nm- and 20nm patterned templates.

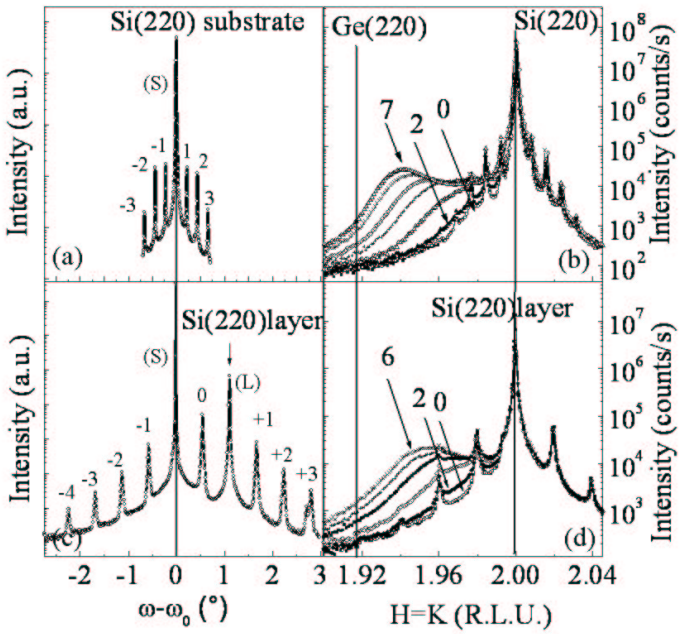

Figure 8.14: (a) and (c) X-ray diffraction data from the templates presenting a periodicity of 50 nm and 20 nm, respectively. Transverse scans around the (220) Bragg peak, obtained with the GIXD geometry. The vertical line indicates the position of the substrate peak and the arrow in figure (c) indicates the position of the layer peak. The other peaks are satellite peaks of diffraction by the periodic surface morphology and, in the 20 nm case, by the square network of buried screw dislocations. (b) and (d) Radial scans along the (hkl) direction, with h=k and l=0.03, in the vicinity of the Si(220) reflection, for different Ge deposits (in equivalent monolayers ML). Some Ge deposits are indicated on the graphs. The vertical lines show the position of the bulk Si(220) and Ge(220) Bragg peak.

GIXD measures the periodic displacement field in both substrate and layer. Figs. 8.14 (a) and (c) display angular scans across the layer and substrate (220) Bragg peaks. The first observation is that there is no more bonded layer peak for the 50 nm patterned template. Only the Bragg peaks of the substrate and the diffraction satellites induced by the nanostructuration of the surface morphology remain. Contrary to the 50 nm patterned template, the bonded layer and substrate peaks are observed on the 20 nm patterned sample (Fig. 8.15).

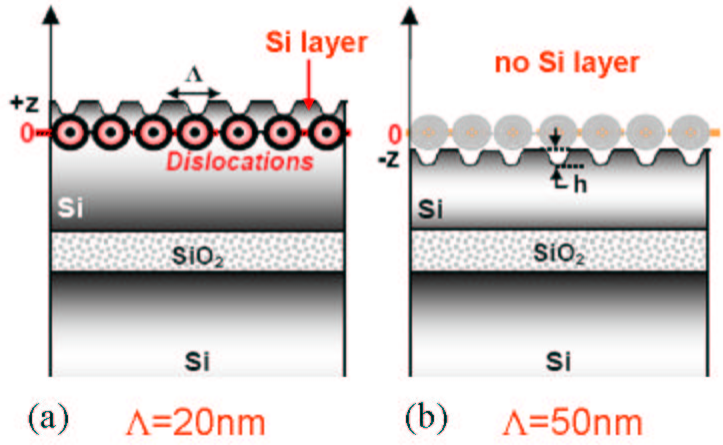

Figure 8.15: (a) The dislocation network and the twisted bonded Si layer above the dislocation network are still present in the 20 nm patterned template. (b) This is not the case for the 50 nm patterned template.

In that case, the satellite peaks arise both from the dislocation network and from the surface morphology. For this sample, the angle between the two Bragg peaks is 1.1°. This angle corresponds to the rotation angle between the substrate and the bonded layer and it refers to a 20 nm periodicity of the square screw dislocation network. In both cases, a large number of satellites are observed. This indicates a very long-range coherent network and/or surface morphology, highly periodic overall the illuminated area (around 1 cm^2). For both samples, the scattering around the substrate (220) Bragg peak (Figs. 8.14 (b) and (d)) is found unchanged between 0 and 2 ML, which shows the growth of a fully strained wetting layer in this regime. After a deposit of 2 ML, a small diffuse scattering appears on the left-hand side of the substrate (220) Bragg peak. With increasing deposit, the maximum of intensity is displaced towards lower h values. At the end of the growth (*i.e.* at 6 or 7 ML), the scattered intensity is centered at h=1.94 and h=1.95 for the 50 nm and 20 nm patterned templates, respectively.

B. In situ grazing incidence small-angle X-ray scattering (GISAXS).

GISAXS measurements were combined with GIXD to have access to the morphology of the growing nanoparticles. Figures 8.16 and 8.17 show the measured data for the 50 nm and 20 nm patterned templates as a function of the Q_y and Q_z coordinates of the scattering vector, *i.e.*, parallel and perpendicular to the sample surface, respectively for Q_y along the $< 100 >$ and $< 110 >$ crystallographic axis. In fact, the sample is oriented so that the crystallographic axis investigated is exactly in between that of the substrate and that of the layer.

For all maps, periodic rods that are narrow in the Q_y direction are observed. They reveal an in-plane bidimensional periodic patterning of the surface. The rod elongation along Q_z is the signature of the small vertical extension of the surface patterning. In Fig. 8.16, the distance ΔQ_y between two rods is about 0.0121 $Å^{-1}$ and 0.0168 $Å^{-1}$ along the [110] and [100] directions, respectively. This indicates a periodicity of $(2\pi/\Delta Q_y)$ ∼51 nm along the [110] direction and ∼37 nm along the [100] direction. In Fig. 8.17, a periodicity of ∼20 nm along the [110] direction and ∼14.7 nm along the [100] direction is deduced. In order to characterize the 2D network of the patterning, a mapping of the reciprocal space has been performed close to the center of reciprocal space by GISAXS for the 20 nm patterned template. In the figure 8.18, a map of the reciprocal space in the surface plane is shown before deposition. This map results from 90 GISAXS patterns measured at different azimuths and for

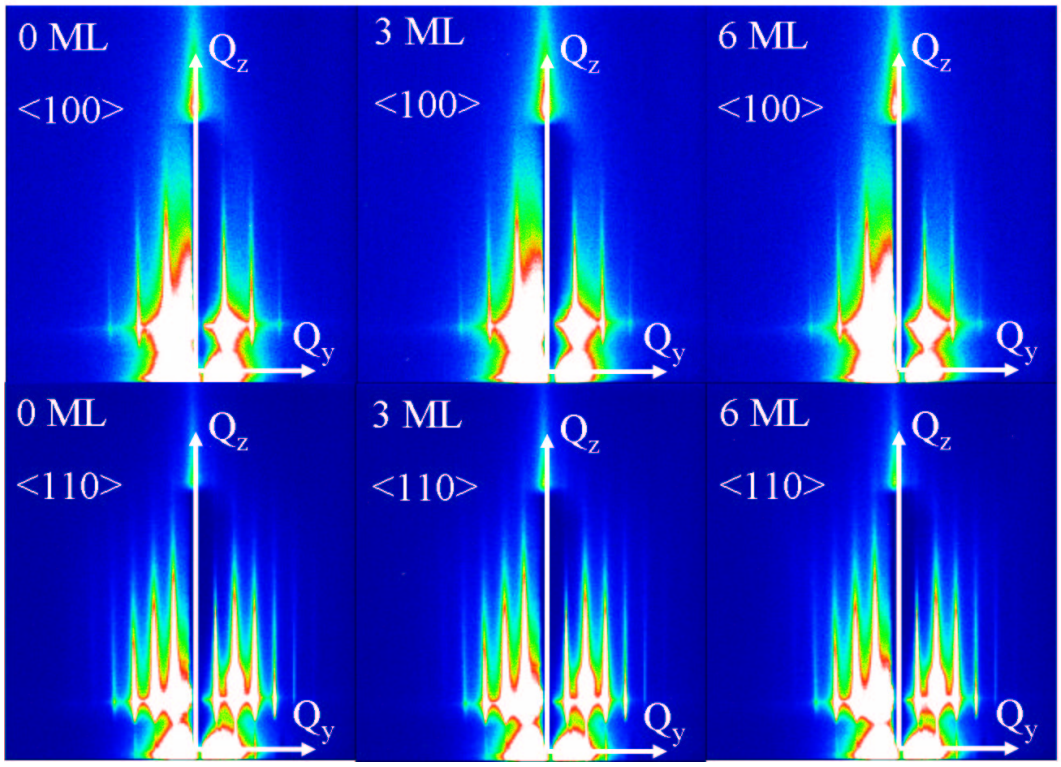

Figure 8.16: GISAXS intensity maps along the $< 100 >$ and $< 110 >$ azimuths obtained at a growth temperature of 773 K for the 50 nm patterned template. The numbers denote the Ge thickness in ML.

which the intensity at $Q_z \sim 0$ (*i.e.* at the Yoneda peak) has been extracted. The fourfold symmetry is in agreement with the fourfold symmetry of the patterned surface. This shows that the etching process directly transfers the fourfold symmetry of the dislocation network to the surface morphology.

With increasing Ge deposit, the periodic rods remain and only weak changes are observed in Figs. 8.16 and 8.17. At first sight, no scattering streaks are visible along the $< 110 >$ and $< 100 >$ azimuths. Nevertheless, very weak scattering streaks along $< 113 >$ directions can be observed in the [110] azimuth for deposits larger than 4 ML for the 50 nm patterned template. The weak scattering streaks can only be observed after substraction with the GISAXS image collected before deposition, at 0 ML (see Fig. 8.19). The existence of $< 113 >$ streaks reveals the formation of {113} facetted Ge islands after a deposit of 4ML for the 50 nm patterned template. No facet streaks are observed during the growth on the 20 nm patterned template. This implies that no facetted islands are grown on the 20 nm patterned template. Pre-patterning changes the morphology of the grown islands. It has been theoretically demonstrated [21] that on such nanomesa, there is no driving force for 3D island nucleation. The usual 2D-3D transition is hence inhibited, simply due to the elastic relaxation allowed by the edges of the mesa. However, it has to be noted that these 'pseudo-2D wetting layers' at the mesa tops are to a certain extent 3D shaped (they look like square base pastilles), due to their small (nanometer range) lateral dimensions, and thus can be viewed as 3D shaped dots. The observed {113} facetted Ge islands on the 50 nm patterned template correspond to islands grown on a flat surface, which implies that some islands are not sensitive to the surface morphology of the 50 nm patterned template.

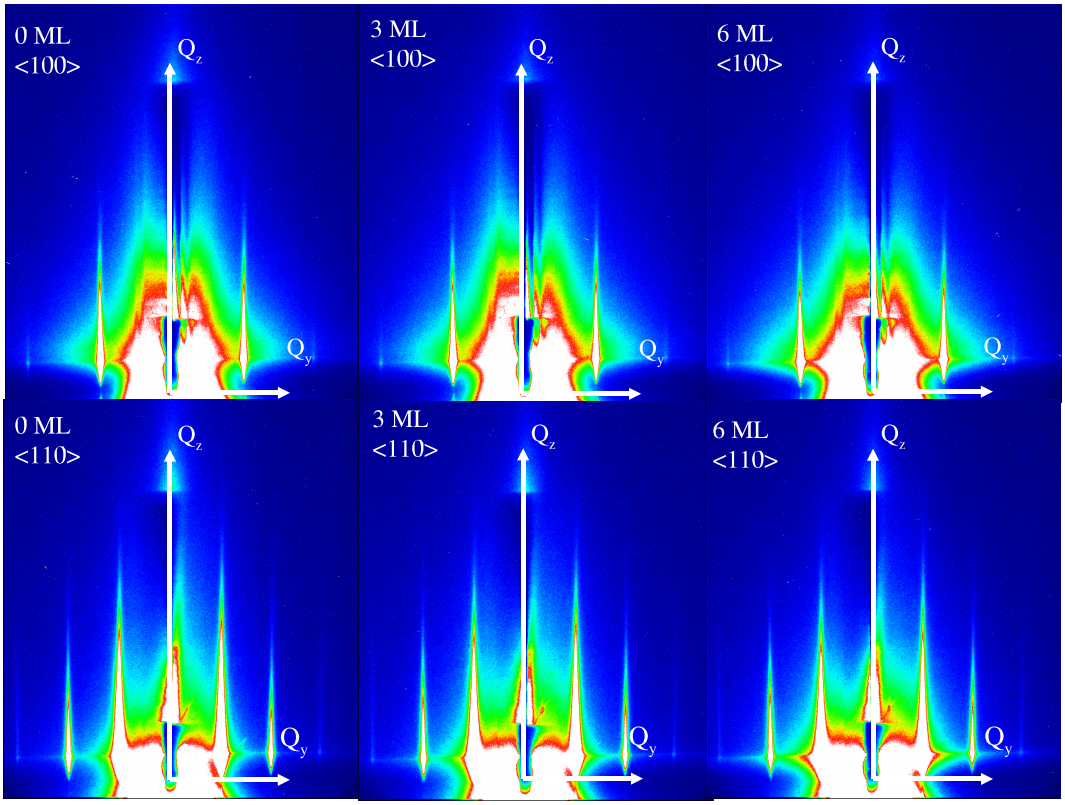

Figure 8.17: GISAXS intensity maps along the $< 100 >$ and $< 110 >$ azimuths obtained at a growth temperature of 773 K for the 20 nm patterned template. The numbers denote the Ge thickness in ML.

B. GISAXS ANALYSIS

B.1. Morphology of the surface

The GISAXS formalism described in the second chapter has been used, within the DWBA and the LMA (neighboring mesa are assumed to have the same shape and size over the coherent area of the X-ray beam), to analyze the experimental data. Within this framework, the IsGISAXS software was used to simulate the scattering data. The GISAXS data and analysis of the 50 nm patterned template before Ge deposition are presented in Fig. 8.20. Good fits were obtained by representing the mesa by cones showing an angle of α=84.5° between the mesa basis and one side (see Fig. 8.20 (a)). Models based on the shape of truncated pyramids with a square-basis failed in this case as no diffuse scattering rods from facets are observed on GISAXS images. The sides of the mesa are not flat and show a non-negligible roughness. The mean lateral size of the Si mesa is 49.4 nm, with a rms width for the Gaussian distribution of sizes of σ_R/R =0.2. The height to lateral size ratio of the mesa is 0.21, with a rms width of the Gaussian distribution of height of σ_H/H =0.35. The height was determined by fitting the intensity cross-section along Q_z (see Fig. 8.20 (d)). Note that the region above the critical angle and below Q_z= 0.6 nm^{-1} is not perfectly fitted. The DWBA formalism used here is only valid for isolated particles. The model did not take into account the multiple scattering by the dense system of correlated mesa. The fit could be improved by including the exact profile of the electronic density of the substrate and mesa and by including the size spacing correlation approximation (SSCA) [22] in the DWBA formalism. This region corresponds to the scattering by the interface. Nevertheless, the interesting Q_z region which allows to determine the height of the mesa, *i.e.* the depth of the trenches, is above Q_z= 0.6 nm^{-1}. Variations of height will drastically affect the

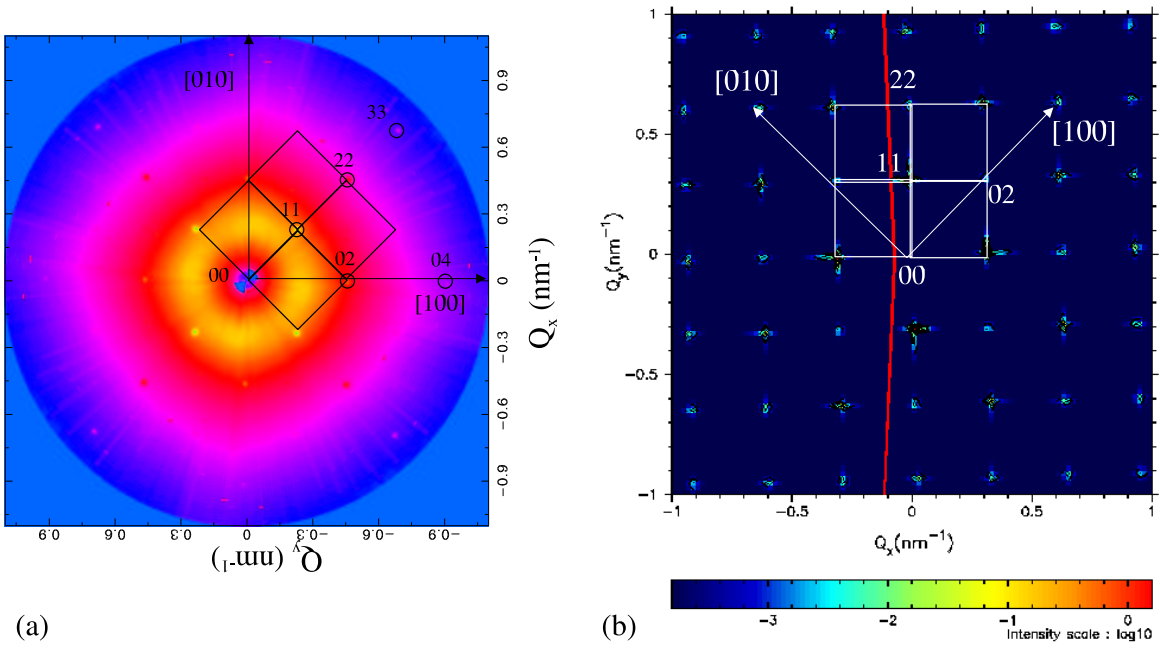

Figure 8.18: (a) 2D mapping of the reciprocal space of the 20 nm Si template at Q_z ∼0. One can define the square elementary unit cell of the reciprocal space. (b) Simulated 2D periodic interference function.

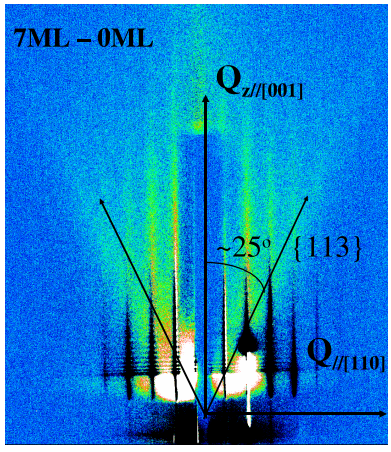

Figure 8.19: GISAXS intensity maps along the < 110 > azimuth resulting from the substraction of the GISAXS map collected at 7ML with the one collected at 0ML.

Q_z region above Q_z=0.6 nm^{-1}. The depth of the trenches is (5±2)nm, which is higher than the depth measured by AFM. This can be explained by the finite size of the AFM tip which minimizes the depth value. Simulated GISAXS patterns reproduce the general features of the experimental GISAXS images, especially the correlation peaks. The spatial correlation between mesa has been well fitted by a square two-dimensional paracrystal of periodicity (51±3) nm. The low disorder factor (ω=3 nm) shows that the Si mesa are highly periodic overall the illuminated area.

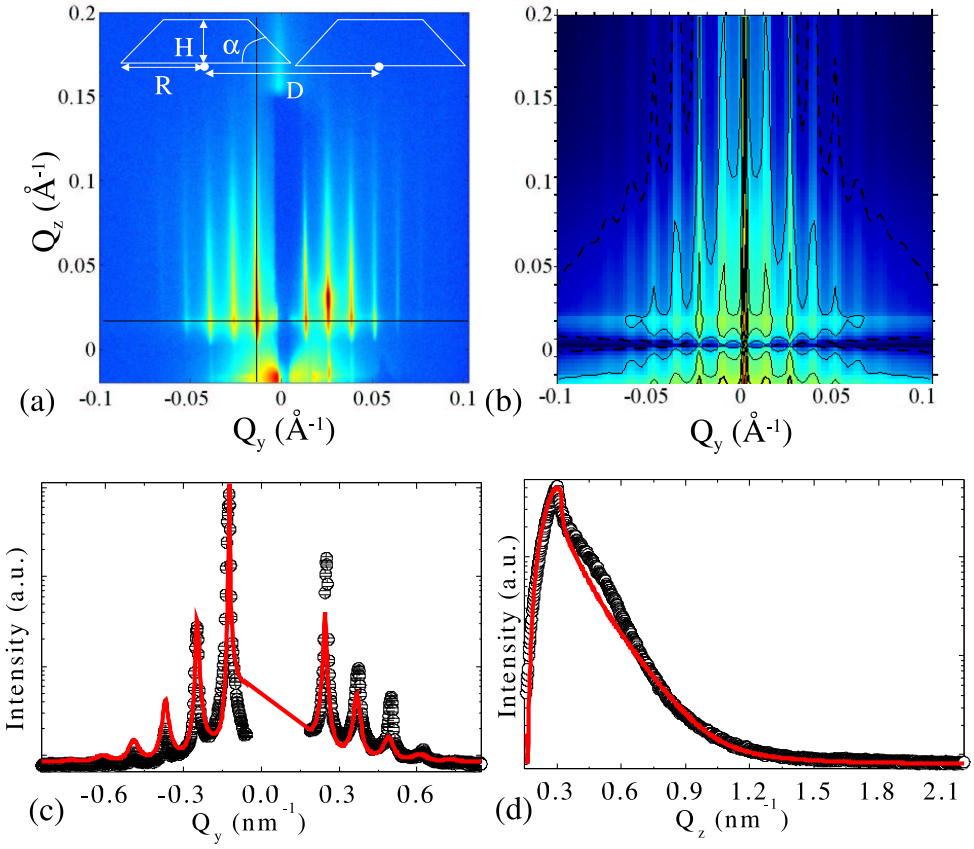

Figure 8.20: 2D GISAXS intensity for a 50nm patterned template after the Si buffer layer growth and before Ge deposition: (a) experimental patterns with the incident beam along the [110] direction of the intermediate referential of the Si(001) substrate and the Si(001) bonded layer. The black lines show the positions of the two cuts used to fit the data, parallel and perpendicular to the surface. (b) Simulated 2D GISAXS patterns of (a) obtained after fitting the experimental cuts (c) and (d) and using a cone to represent the shape of the mesa. The intensities are represented with a logarithmic scale. Cuts parallel (c) and perpendicular (d) to the surface corresponding to the vertical black lines in (a).

B.2. Ordered growth.

The Ge growth was studied monolayer by monolayer by GISAXS as already mentioned. In the case of the 20 nm patterned template, and after a deposit of 2 ML (*i.e.* when 3D islands are formed), the substraction of the intensity measured before and after deposit reveals variations of intensity along the scattering rods of the dislocation network (see Fig. 8.21). The positive and negative variations of intensity along the rods in Fig. 8.21 (a) are noted '+' and '-'. Note that this is not the case for the 50 nm patterned template.

In Fig. 8.21 (b), two lobes of intensity can be observed in addition to the rods. This corresponds to the diffuse scattering from islands. Such signal is not observed below a deposit of 3 ML. Below 3ML, the grown islands are thus smaller. In this case, the collected GISAXS image clearly reveals the interference function.

In the following, one hypothesis, which needs to be confirmed, is given to explain the variations of intensity along the rods.

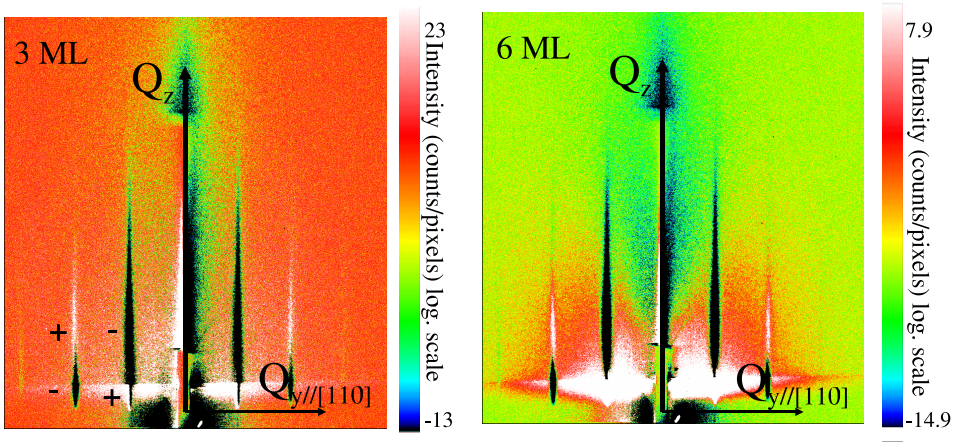

Figure 8.21: Substraction of the scattered intensity before and after deposit for a deposit of 3 ML and 6 ML. The incident beam is parallel to the [110] direction for the 20 nm patterned template.

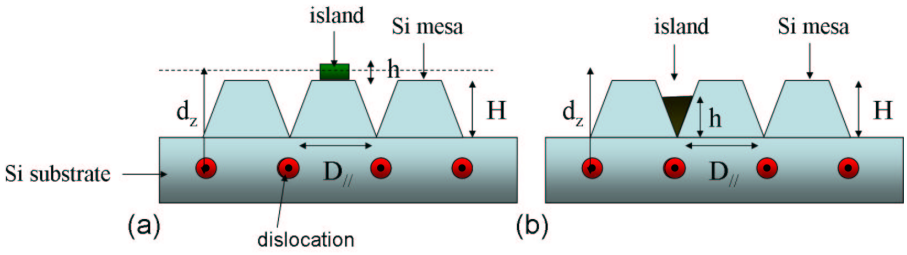

Figure 8.22: (a) Ordered islands on the Si mesa. (b) Ordered islands in the trenches. d_z is the perpendicular coordinate of the Ge islands respectively to the intersection of the dislocations lines, $D_{//}$ is the lateral size of the mesa, h and H are the heights of the islands and of the mesa.

Variations of intensity along rods can appear when the phase between the waves scattered by the Ge islands and the waves scattered by the surface morphology and by dislocations are well defined, *i.e.*, when the position of the Ge islands is correlated with that of the dislocations and surface morphology. The scattered intensity can be written as the sum of six terms: the intensity scattered by the dislocation network, that scattered by the Ge islands and the surface morphology and the interference terms [23].

$$I = |F_D|^2+|F_{Ge}|^2+|F_M|^2+2|F_D||F_{Ge}|cos(\mathbf{q}_{//}\cdot\mathbf{d}_{//}+q_z d_z)+2|F_M||F_{Ge}|cos(\phi_{M,Ge})+2|F_M||F_D|cos(\phi_{M,D}), \quad (8.1)$$

where F_D, F_M and F_{Ge} are the form factors of the dislocations network, the surface morphology and the Ge islands, respectively; $\mathbf{q}_{//}$ (resp. d_z) are the parallel and perpendicular coordinates of the Ge islands respectively to the intersection of the dislocations lines, and $\phi_{M,Ge}$ (resp. $\phi_{M,D}$) are the phases between the waves scattered by the islands and the surface morphology (resp. by the dislocation network and surface morphology). For a deposit of 3 ML of Ge, the Ge islands are small ($|F_{Ge}| << |F_D|$), the $|F_{Ge}|$ term is thus negligible. The interference terms ($2|F_D||F_{Ge}|cos(\mathbf{q}_{//}\cdot\mathbf{d}_{//} + q_z d_z) + 2|F_M||F_{Ge}|cos(\phi_{M,Ge})$) which contain the informations on the localization of the islands is thus simply obtained by substracting the GISAXS measurements after and before deposit. Before deposit, the above scattered intensity can be written as:

$$I = |F_D|^2 + |F_M|^2 + 2|F_M||F_D|cos(\phi_{M,D}), \quad (8.2)$$

Two sites can be considered to locate the Ge islands (see Fig. 8.22): in the trenches, *i.e.* along the dislocation lines ($|\mathbf{d}_{//}| = nD_{//}$, $n \in \aleph$), or on the middle of the mesa $|\mathbf{d}_{//}| = (n+1/2)D_{//}$, $n \in \aleph$). $D_{//}$ is the lateral size of the mesa. If the Ge island of height h is located on the middle of the mesa of height $H \sim 4nm$, then $\phi_{M,Ge} = \phi_{Ge} - \phi_M = q_z(h+H)/2$. In the other case (Ge island in the trenches), $\phi_{M,Ge} = q_{//}(n+1/2)D_{//} + q_z(h-H)/2$. The correlation rod near $\mathbf{q}_{//}$=0 is located at $\mathbf{q}_{//} = 2\pi/D_{//}$ and the other one at $\mathbf{q}_{//} = 4\pi/(D_{//})$. If the organized Ge atoms are localized in the middle of the mesa (resp. in the trenches), the interference terms along the first correlation rod (near $\mathbf{q}_{//}$=0) can be written as $2|F_D||F_{Ge}|cos(2\pi(n+1/2)+q_zd_z)+2|F_{Ge}||F_M|cos(q_z(h+H)/2)$ (Eq. I) (resp. $2|F_D||F_{Ge}|cos(2\pi n+q_zd_z)+2|F_{Ge}||F_M|cos(2\pi(n+1/2)+q_z(h-H)/2)$ (Eq. II)). A minimum of intensity should be observed at q_z=0 for the first correlation rod. Supposing an island height of 3-5 nm as oberved in TEM, and $d_z \sim$ 15-20 nm (this value corresponds roughly to the height of the twisted bonded layer), the intensity along q_z is always negative if islands are positioned in the trenches (see Eq. II) and first positive then negative if islands are positioned in the middle of the mesa (Eq. I). The last case explains the observed features along the first correlation rod. Along the second correlation rod, if islands are laterally ordered on the mesa, the intensity along the rod should verify: $2|F_D||F_{Ge}|cos(q_zd_z)+2|F_{Ge}||F_M|cos(q_z(h+H)/2)$. The intensity is first positive and then negative along q_z, as observed experimentally. Thus, the Ge adatoms will preferentially nucleate on the mesa, *i.e.* on expanding zones than on compressive zones (trenches). The trenches are almost not filled by the Ge atoms.

B.3. Anomalous GISAXS and GIXD during the *in situ* growth.

1. Experimental method

Multiwavelength anomalous diffraction (MAD) measurements were performed to distinguish the Ge contribution from the Si one. Scattered intensities were measured *in situ* for each added monolayer, at 12 energies across the Ge K edge, taking advantage of the Ge anomalous effect to quantify the Ge contribution. For these measurements, the Ge partial structure factor F_{Ge} of phase ϕ_{Ge}, which includes the Thomson scattering of all anomalous atoms (Ge), can be retrieved. In principle, the retrieval should be run in the framework of the distorted wave born approximation (DWBA) [25, 28] in order to take into account the grazing incidence and exit effects. In the DWBA, the effective form factor of the Ge islands comes:

$$\Psi(q_z) = \Phi(k_{fz}-k_{iz}) + r(\alpha_i)\Phi(k_{fz}+k_{iz}) + r(\alpha_f)\Phi(-k_{fz}-k_{iz}) + r(\alpha_i)r(\alpha_f)\Phi(-k_{fz}+k_{iz}) \quad (8.3)$$

If the height of the measured islands is much smaller than the measured GISAXS dimensions, the following approximation can be performed:

$$\Psi(q_z) \sim \Phi(0)[1 + r(\alpha_i) + r(\alpha_f) + r(\alpha_i)r(\alpha_f)]) \sim \Phi(0)t(\alpha_i)t(\alpha_f) \quad (8.4)$$

Above α_c, $t(\alpha_i) \longrightarrow 1$ and $t(\alpha_f) \longrightarrow 1$. One can thus discard the energy dependence at the Ge K edge of the reflection and transmission coefficients for exit angle higher than α_c, as a consequence of the small Ge amount (seven equivalent ML). Therefore, the recorded intensity corrected for fluorescence, I_{exp} is proportional to the total squared structure factor $|F|^2$.

$$I_{exp}(E) \propto |F|^2 \propto |F_T|^2 [cos(\phi_T - \phi_{Ge}) + \xi f_{Ge}^{'}]^2 + [sin(\phi_T - \phi_{Ge}) + \xi f_{Ge}^{"}]^2, \quad (8.5)$$

where $\xi = |F_{Ge}|/(f_{Ge,0}|F_T|)$. $f_{Ge,0}$ is the Ge Thomson scattering factor; $f_{Ge}^{'}$ and $f_{Ge}^{"}$ are the Ge anomalous scattering corrections determined from the X-ray absorption spectrum of a plane of uncovered Ge islands. The partial complex structure factor F_T of phase ϕ_T includes the contributions of all nonresonant atoms and the Thomson scattering of the resonant atoms. The modulus $|F_T|$ and $|F_{Ge}|$ and the phase difference $\phi_T - \phi_{Ge}$ are obtained at each h, k and l values, without any structural model, by fitting the equation to the experimental data with the least-squares `NANOMAD` algorithm [26]. The algorithm allows thus to extract the $|F_{Ge}|$ modulus and $|F_{Si}| = |F_T - F_{Ge}|$, the complex structure factor of non-anomalous atoms was retrieved from the extracted values of $|F_T|$, $|F_{Ge}|$ and $\phi_T - \phi_{Ge}$, assuming a diamond crystallographic structure.

2. Interpretation of anomalous GISAXS.

The anomalous measurements have been performed during the growth for each added monolayer. The scattering rods and the scattering signal out of the rods have been analyzed in the direction perpendicular to the surface, while integrating the signal parallel to the surface to increase the signal/noise ratio. From the previous formalism, both contributions of Si and Ge and the phase shift have been extracted as a function of Ge deposit. The main advantage of measuring GISAXS images at several energies around the absorption edge is to reduce the uncertainty on the fitted parameters. Figure 8.23 depicts the evolution of the Ge partial structure factor as a function of the Ge deposit along the correlation rods and outside (in-between) the correlation rods for the growth on the 20 nm patterned template. The Si structure factor has been extracted for all deposits. It remains almost the same for all deposits along and in-between the correlation rods. For all deposits, a maximum is observed corresponding to the Yoneda peak, which is not taken into account. The interesting part is the region above the Yoneda peak where the scattering of nano-particles is well observed and where the previous approximation is valid. Outside the correlation rods, no scattering signal is observed up to a deposit of 3 ML. After a deposit of 3 ML, this diffuse scattering increases. Additional scattering is observed earlier along the correlation rods. After a deposit of 1-2 ML of Ge, a small scattering signal can be observed, which then increases in intensity.

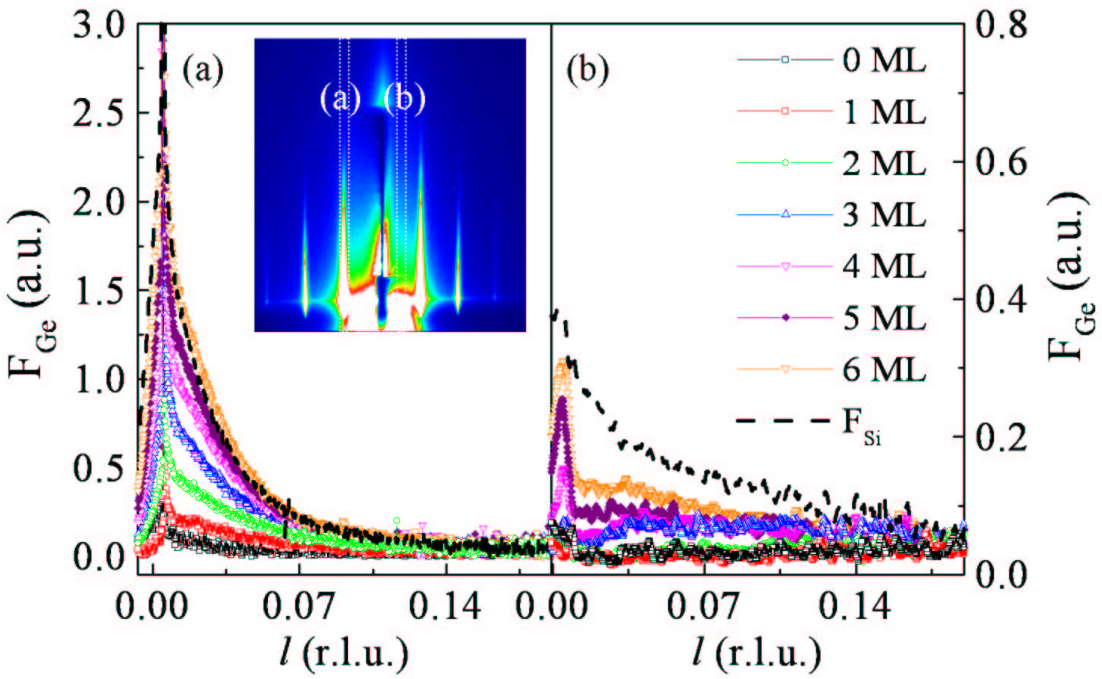

Figure 8.23: Evolution of the structure factors of the Ge atoms as a function of the Ge deposit along the correlation rods and out of the correlation rods.

If we assume that on average the neighbouring islands have the same size, the intensity of the scattered radiation is given by the local monodisperse approximation [27]:

$$I(q) =< |\Phi(q)|^2 > S(q_{//}), \tag{8.6}$$

where $S(q_{//})$ is the structure factor or interference function, *i.e.* the Fourier transform of the autocorrelation function of the particles. The main characteristic of the interference function is its cor-

relation peaks which reveal ordering between neighbouring particles. The small variations along the correlation rods are the signature of the nucleation of small nanostructures on the pre-patterned templates. Laterally ordered islands are thus formed, presenting the same periodicity as the surface morphology. After a deposit of 3 ML, an increase of the partial structure factor of Ge is observed both along and out of the correlation rods. The signal is not restricted to the correlation rods, some non-organized Ge islands are formed. To disentangle the contribution of the organized and non-organized islands, the Ge contribution has been determined along and outside the rods. Qualitatively, the higher the ratio between the F_{Ge} and F_{Si} structure factors (F_{Si} is constant along and out of the rods), the higher the Ge contribution. Figure 8.24 reveals for 3 and 6 ML a different Ge concentration at the position of the correlation peaks and in-between. A higher Ge content is observed at the position of the correlation peaks around $l \sim 0.02$. This means that laterally ordered islands remain. Two contributions are thus found by X-rays one induced by the ordered growth of the Ge nanoparticles and one corresponding to a standard nominal growth. The same behaviour is observed for islands grown on the 50 nm patterned template. This means that a higher Ge contribution is observed along the rods, which reveals that a part of the islands is laterally ordered.

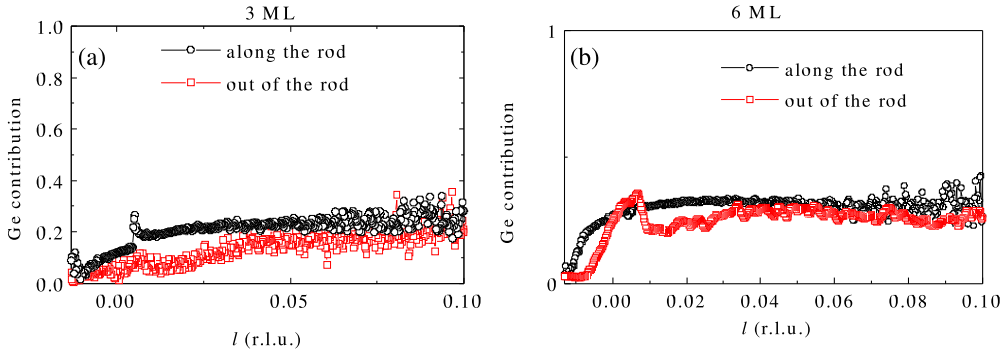

Figure 8.24: Ge contribution along and outside the correlation rods for a deposit of 3 ML (a) and 6ML (b).

3. SEM and TEM analysis of the surface.

Figure 8.25 shows the surface structuration after Ge growth on both 20 nm (Fig. 8.25 (a)-(b)) and 50 nm (Fig. 8.25 (c)-(d)) twisted templates.

On the 20 nm patterned template, two types of islands are observed, depending on the depth of the trenches:

- nanosized ($\sim$ 18 nm) square base Ge islands (one per mesa) on pre-patterned regions,
- large islands on weakly pre-patterned regions.

The study highlights the impact of the depth of the trenches. Not enough deep trenches have a small impact on the lateral ordering of the islands. For deeper trenches, diffusion processes responsible for island coalescence are kinetically blocked by the energetic barrier imposed by the trenches.

The SEM images of the 50 nm patterned template show numerous islands of different sizes and the surface structuration. The cross-section view (Fig. 8.25 (d)) reveals a tiny inflation at the top of the mesa which might be due to the presence of Ge square base islands on top of the mesa.

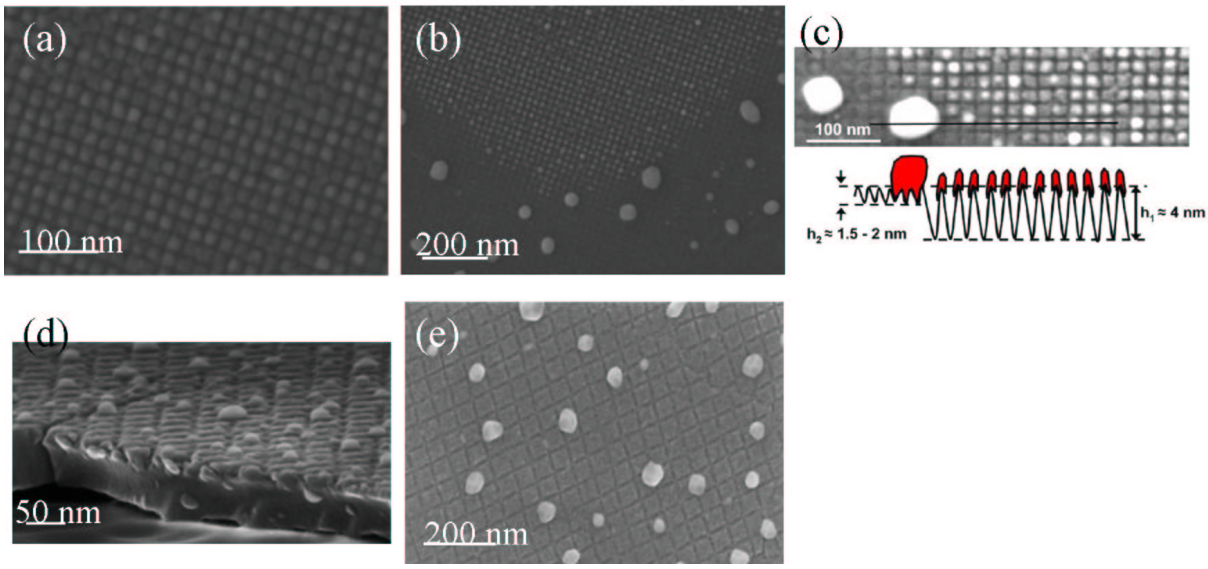

Figure 8.25: (a)-(b)-(c): SEM images obtained after the growth of 6 ML of Ge at 500°C on the 20 nm twisted substrate and schematic drawing of the surface. (d)-(e) Plane-view and cross section SEM images after a growth of 7 ML of Ge at 500°C on the 50 nm twisted substrate.

This study reveals that new shape islands are obtained using a regular array of nanomesas.

To check the preferential sites for Ge dot nucleation, TEM and HRTEM (Fig. 8.26) images have been performed on the 20 nm patterned template. Fig. 8.26 (a) shows the morphology of the surface. On the top of the mesa, a tiny contrast can be observed which can be due to the presence of Ge islands. The HRTEM image displays several mesa with a height of ~ 6 nm. Before growth, the trenches had a height of ~ 4 nm. This implies that the Ge islands preferentially grow on the mesa. A small amount of Ge fills the trenches.

To analyse island positioning as a function of surface morphology, a simple thermodynamic model based on the balance between surface energy and elastic relaxation terms of the chemical potential μ has been implemented [29]. Surface energy anisotropy and intermixing are not considered. The aspect ratio of silicon nanostructures, modelled with a cycloid-like profile can be tuned to separate the influence of the surface curvature and relaxation effects. For a smooth profile (*i.e.* small aspect ratio (α) of the surface morphology, $\alpha \sim 0.1$), the local minimum of energy $\Delta E = \mu(x, \theta) - \mu_0$ (where μ_0 is the chemical potential for the untressed planar surface) changes as a function of deposit θ from a valley ($\theta \sim 0.2nm$), to the top mesa ($\theta \sim 2nm$) and to sidewall positions close to the top mesa ($\theta \sim 10nm$). The 20 nm patterned template shows an aspect ratio of $\alpha \sim 0.2$ close to 0.1, the model suggests that the Ge will be preferentially positioned on top of the mesa and on sidewalls close to the top of the mesa; which is in agreement with the experimental data. The energetic barriers are small and kinetic effects play a major role and explain the development of large islands overlapping trenches. It is also demonstrated [29] that for larger aspect ratio ($\alpha \sim 0.9$), the mesa position is favoured and ΔE is increased to become an effective diffusion barrier.

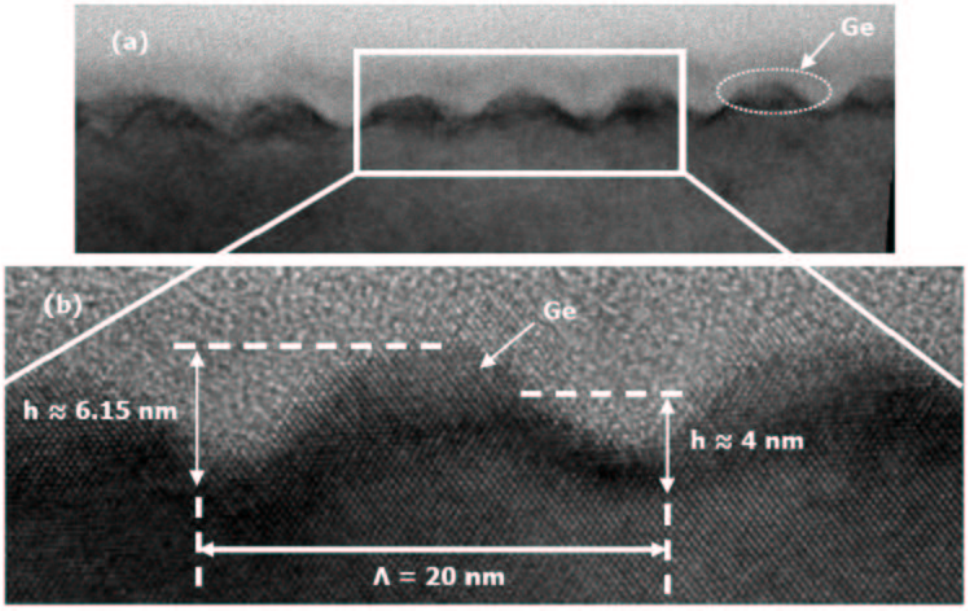

Figure 8.26: TEM (a) and HRTEM (b) cross-section images of the 20 nm patterned template. Courtesy of A. Bavard.

4. Complementary GIXD measurements: analysis of the nucleation process and intermixing

GI-MAD results.

Anomalous GIXD using the MAD method was performed to locate the Ge and Si contributions along the [110] layer direction for each Ge deposit. Fig. 8.27 shows their evolution for the 20 nm patterned template. For a deposit of 2 ML of Ge, an evolution of the Ge partial structure factor is observed. This corresponds to the nucleation of Ge islands. This implies that the wetting layer is only composed of one monolayer. This differs from what is observed on flat substrates. On flat substrates, the wetting layer thickness is about 3-4 ML. An earlier apparition of the 2D-3D transition is thus observed for pre-patterned substrates.

For a deposit of 2 ML, a contribution of Si is found on the left side of the Si Bragg peak in the region of the Ge islands (Fig. 8.27). This may either be attributed to diffusion of Si into the islands or to the scattering from strained Si below the Ge islands. Despite the fact that, at a growth temperature of 500°C, the intermixing of Si into Ge islands is very weak for nominal substrates, intermixing may appear for this temperature in the case of corrugated surfaces.

Why earlier 2D/3D transition on patterned substrates?

In order to explain the earlier apparition of the 2D-3D transition, numerical finite element modelling (FEM) has been performed to calculate the strain field in Ge islands on a flat Si(001) substrate and on a 20 nm wide Si(001) mesa. In both cases, the islands were chosen to be pure Ge islands of 17 nm width and 3 nm height in agreement with HRTEM images. The 20 nm wide Si(001) mesa has a height of 4 nm. The FEM modelling allows to determine the mean strain inside the Ge island and inside the Si substrate along the [110] direction. In the case of the pre-patterned template, the Si substrate is the Si substrate plus the ordered Si mesa. Figure 8.28 compares the relaxation state between two same size islands on a nominal Si(001) substrate and on a Si(001) bonded layer composed of a 20 nm large mesa on a Si substrate. It shows the relative strain $\epsilon_{xx}^{Si} = (a_{ij} - a_{Si})/a_{Si}$ along the [110]

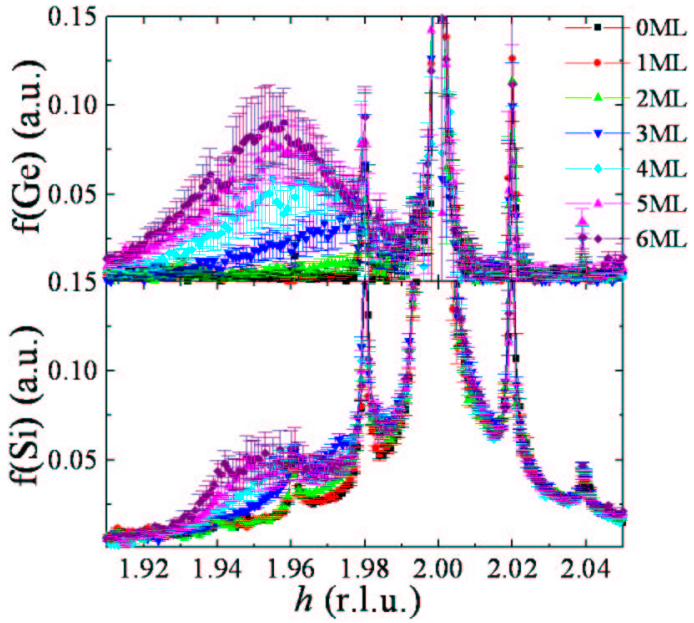

Figure 8.27: Extracted anomalous structure factor F_{Ge} (up) and non-anomalous structure factor F_{Si} (down) for different deposits of Ge during growth. The intensity was collected using radial scans along the [220] direction, in the vicinity of the Ge absorption edge.

direction, where a_{ij} is the lattice parameters of each cell (i,j).

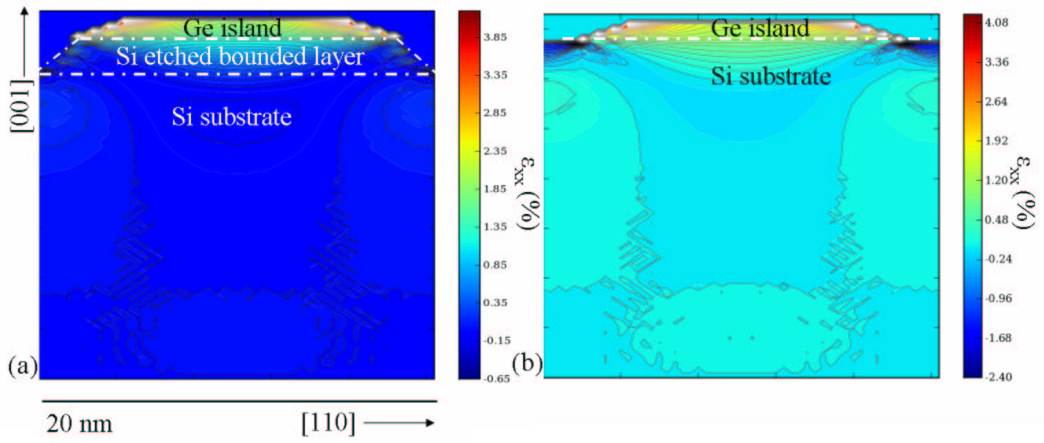

Figure 8.28: FEM simulations of $\epsilon_{xx}^{Si} = (a_{ij} - a_{Si})/a_{Si}$, where a_{ij} is the lattice parameters of the cell (i,j) in the case of a pure Ge island on a twisted wafer (a) or on a nominal Si(001) substrate (b). The strain is relative to the bulk Si cell parameter.

Table 8.2 summarizes the mean ϵ_{xx}^{Si} and ϵ_{zz}^{Si} values inside the Ge islands and the Si substrates for a pure Ge island grown on pre-patterned Si(001) mesa and on Si(001) flat surface.

Pre-patterned mesa	Si(001) flat surface
$\epsilon_{xx}^{Si}(Si) = 0.0301\%$	$\epsilon_{xx}^{Si}(Si) = 0\%$
$\epsilon_{xx}^{Si}(Ge) = 1.9313\%$	$\epsilon_{xx}^{Si}(Ge) = 1.6055\%$
$\epsilon_{zz}^{Si}(Si) = -0.0382\%$	$\epsilon_{zz}^{Si}(Si) = -0.011\%$
$\epsilon_{zz}^{Si}(Ge) = 5.7967\%$	$\epsilon_{zz}^{Si}(Ge) = 6.0431\%$

Table 8.2: $\epsilon_{xx}^{Si}(Si) = \bar{a_{Si}} - a_{Si})/a_{Si}$, $\epsilon_{xx}^{Si}(Ge) = \bar{a_{Ge}} - a_{Si})/a_{Si}$, $\epsilon_{zz}^{Si}(Si) = \bar{c_{Si}} - c_{Si})/c_{Si}$ and $\epsilon_{zz}^{Si}(Ge) = \bar{c_{Ge}} - c_{Si})/c_{Si}$
values, where a_{Si}, c_{Si} are the Si in-plane and out-of-plane lattice parameters and $\bar{a_{Si}}$, $\bar{c_{Si}}$, $\bar{a_{Ge}}$ and $\bar{c_{Ge}}$ are the mean Si and Ge in-plane and out-of-plane lattice parameters inside the Si substrate and pure Ge island for both cases: Ge islands on pre-patterned mesa and on Si(001) flat surface.

Ge islands grown on pre-patterned mesa show a higher mean in-plane relaxation, $\epsilon_{xx}^{Si}(Ge) = 1.93\%$ instead of 1.61% for Ge islands grown on Si(001) flat surface. The elastic relaxation is more efficient on pre-patterned mesa as it is allowed by the edges of the mesa. The edge elastic relaxation may fasten the apparition of the 2D-3D transition. In addition, the Si lattices of the pre-patterned mesa are more expanded than the ones of the flat Si(001) substrate, as the mean in-plane relaxation of pre-patterned Si mesa, 0.0301% instead of 0% for the Si(001) flat surface. This is again due to the elastic relaxation allowed by the edges of the mesa. Note that the simulated $\epsilon_{xx}^{Si}(Ge) = 1.93\%$ value compares well with the experimental value $\sim 2\%$.

Comparison with growth on nominal substrate.

In Fig. 8.27, above 2 ML, the maximum of the scattered intensity progressively shifts to lower h values, indicating the formation of larger islands with Ge deposition. Increasing Ge content, an increase of the Si partial structure factor is observed revealing an increase of Si intermixing during the island growth.

The strain relaxation is found to be considerably smaller than on nominal substrates at the same growth temperature and deposit (see Fig. 8.29 (a)). This may correspond either to a larger diffusion of Si inside the Ge islands, to a modification of the relaxation state of the template generated by the dislocation network or to an earlier formation of superdomes on the nominal template. On the SEM images performed after a deposit of 7 ML and 6ML (see Fig. 8.25), one can find islands whose size reaches 75 nm on the 50 nm pre-patterned template and 55 nm on the 20 nm pre-patterned template, respectively. As a comparison, the average size of Ge islands on nominal Si(001) substrate is about 100 nm. In pre-patterned templates, it appears thus that the trenches prevent large islands coalescence and slow down the formation of dislocated superdomes. Figure 8.29 (b) displays radial scans in the vicinity of the Si(220) Bragg peak for a deposit of 6ML of Ge on the 20 nm twisted substrate at 500°C and after annealing at the same temperature. Only tiny differences are observed. This demonstrates that pre-patterning also acts as an effective diffusion barrier to prevent Ostwald ripening.

Figure 8.30 shows radial scans along the [100] direction in the vicinity of the (400)Si Bragg peak, for different Ge deposits in the case of the 50 nm patterned template. As observed for the 20 nm patterned template, the 2D-3D transition appears for a deposit of 2 ML (earlier compared to a growth on a flat Si(001) substrate). After a deposit of 4 ML, two Ge humps are observed in the left side of the Si Bragg peak, which reveals a bimodal growth. The two Ge contributions can be disentangled at the (400) reflection; this was not the case at the (220) reflection (see Fig. 8.14 (d)). Higher the momentum transfert q ($q_{400} > q_{220}$), the higher the sensitivity to small variations of the lattice parameter a as $\frac{\Delta a}{a} = \frac{\Delta q}{q}$.

The Ge hump located near the position of the Ge bulk Bragg peak corresponds to more relaxed and larger islands and can be identified as being the non ordered large islands overlapping the trenches observed in Fig. 8.25(d)-(e). They develop after a deposit of 4 ML of Ge. The other Ge hump can be related to the smaller and ordered Ge islands which cover the Si mesa. Two contributions are then

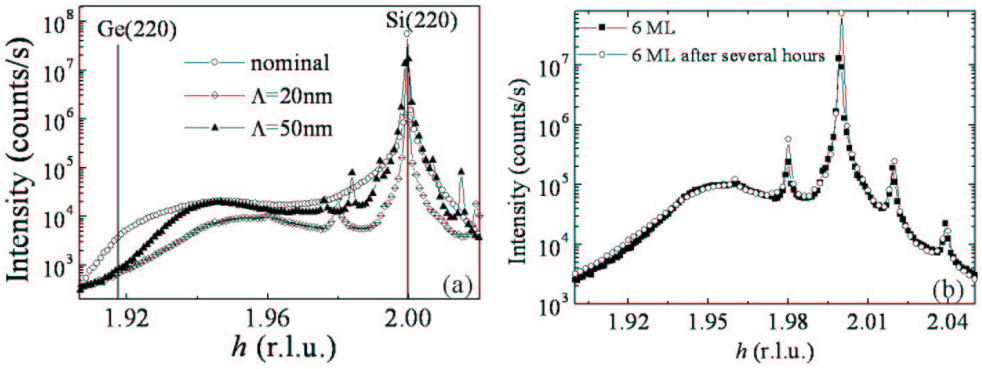

Figure 8.29: (a) Radial scans in the GIXD geometry in the vicinity of the Si(220) Bragg peak for a deposit of 6 ML of Ge at 500°C in the case of nominal and twisted substrates. (b) Radial scans in the GIXD geometry in the vicinity of the Si(220) Bragg peak for a deposit of 6 ML of Ge on the 20 nm twisted substrate at 773 K and after annealing at the same temperature.

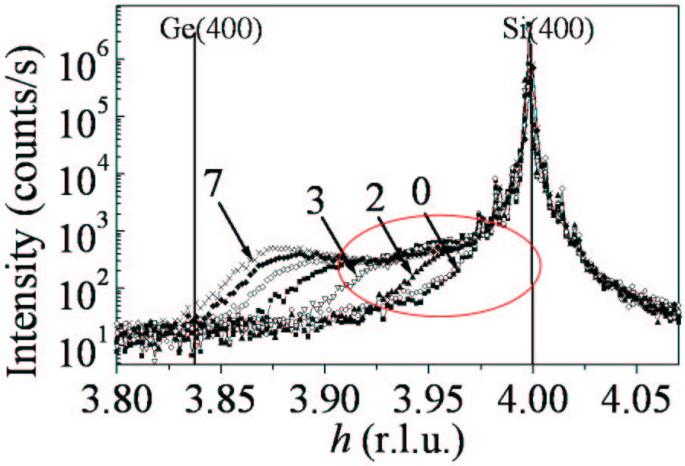

Figure 8.30: (a) Radial scans along the [100] direction in the vicinity of the (400)Si Bragg peak, for different Ge deposits in the case of the 50 nm patterned template. Some Ge deposits are indicated on the graph. The vertical lines show the position of the bulk Si(400) and Ge(400) Bragg peaks.

found by X-rays, one induced by the organized growth of Ge nanoparticles on the well etched regions, and one corresponding to growth on a standard, non-patterned Si(001) surface.

The 20 nm substrate: an inhomogeneous surface.

To understand why the surface patterning was not homogeneous, HRTEM measurements have been performed on the 20 nm patterned template before etching and Ge deposition (see Fig. 8.31). Interfacial oscillations are observed between the two Si layer (Si_1 and Si_2). The heterogeneities of the surface patterning is not due to the etching. Only fluctuations of the grain boundaries can explain this observation. These oscillations are induced by the thermal annealing ($> 1000°C$) which occurs during

the fabrication of the Si nano-patterned template (see Fig. 8.11 (6)). To overcome this problem, the temperature of the thermal annealing has been reduced. Recently, homogeneous 20 nm pre-patterned Si substrates have been obtained.

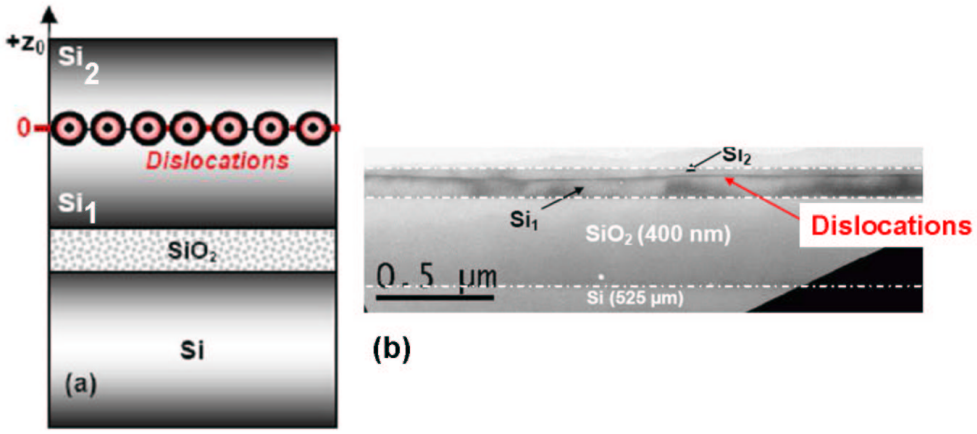

Figure 8.31: (a) Schematic drawing of the pre-patterned template. (b) HRTEM image of the interface between the two Si substrates.

8.2.3 Synthesis on the growth of Ge islands on nano-patterned Si(001) surfaces obtained by wafer bonding.

This study gives a clear indication of the potential of this new substrate for the self-organization of Ge nanostructures. It demonstrates that Ge islands are organized on the well etched fractions of the surface and that grazing incident X-ray scattering allows to characterize the growth by determining for instance the mesa depth, the lateral ordering, and the relaxation of the islands using anomalous GISAXS and GIXD.

It is worth noting that the 20 nm surface-patterning is not homogeneous over the whole surface. The patterned areas are localized on stripes with a width of about 300nm. Two contributions are measured with X-ray: one induced by the organized growth of Ge nanoparticles on the stripes and another contribution which corresponds to a nominal growth. Nevertheless, the organization of Ge QDs on the well-etched parts of the surface is confirmed by GISAXS, as intense periodic rods arising from the ordered Ge QDs are evidenced. GISAXS studies also show that the form factor of the mesa (trench depth, residual roughness, facets) has a strong influence on the germanium quantum dots shape and position, and allows to determine the dots registry with the underlying substrate. In these samples, it appears that the trenches depth acts as an effective diffusion barrier to prevent large island coalescence and the formation of dislocated islands.

8.3 Conclusion

Using nano-patterned Si(001) surfaces obtained either by lithography or direct wafer bonding allows to laterally order Ge islands. Depending on the morphology of the surface, *i.e.* ***on the variation of the chemical potential, Ge islands are located on concave (section 8.1) or convex (section 8.2) morphologies. In both cases, it has been demonstrated in this chapter and in literature that the 2D-3D transition appears earlier compared to a growth on a flat Si(001) substrate and that larger coherent islands can be grown on the patterned substrates as compared to island grown on flat substrates.***

Bibliography

[1] Y. Arakawa and H. Sakaki, Appl. Phys. Lett. **40**, 939 (1982).

[2] Z. Zhong and G. Bauer, Appl. Phys. Lett. **84**, 1922 (2004).

[3] Z. Zhong, A. Halilovic, H. Lichtenberger, F. Schäffler, G. Bauer, Physica E **23**, 243-347 (2004).

[4] J.-M. Baribeau, X. Wu, and D. J. Lockwood, J. Vac. Sci. Technol. A **24**, 663 (2006).

[5] G. Chen, H. Lichtenberger, G. Bauer, W. Jantsch, and F. Schäffler, Cond. Mat. 0602175 (2006).

[6] I. A. Vartanyants, I. K. Robinson, J. D. Onken, M. A. Pfeifer, G. J. Williams, F. Pfeiffer, H. Metzger, Z. Zhong, and G. Bauer, Phys. Rev. B **71**, 245302 (2005).

[7] B. Yang *et al.*, Phys. Rev. Lett. **92**, 025502 (2004).

[8] Z. Zhong, H. Lichtenberger, G. Chen, M. Mühlberger, C. Schelling, J. Myslivecek, A. Halilovic, J. Stangl, G. Bauer, W. Jantsch and F. Schäffler, Micro. Eng. **83**, 1730 (2006).

[9] *http://www.esrf.fr/UsersAndScience/Experiments/CRG/BM32.*

[10] G. Renaud, R. Lazzari, Ch. Revenant, A. Barbier, M. Noblet, O. Ulrich, F. Leroy, J. Jupille, Y. Borensztein, C. R. Henry, J.-P. Deville, F. Scheurer, J. Mane-Mane, and O. Fruchart, Science **300**, 1416 (2003).

[11] I. Kegel, T.-H. Metzger, P. Fratzl, J. Peisl, A. Lorke, J. M. Garcia, and P. M. Petroff, Europhys. Lett. **45**, 222 (1999).

[12] Z. Zhong, A. Halilovic, M. Mühlberger, F. Schäffler, and G. Bauer, J. Appl. Phys. **93**, 6258 (2003).

[13] Y.-W. Mo, D. E. Savage, B. S. Swartzentruber, M. G. Lagally, Phys. Rev. Lett. **65**, 1020 (1990).

[14] J. Myslivecek, C. Schelling, F. Schäffler, G. Springholz, P. Smilauer, J. Krug, B. Voigtländer, Surf. Sci. 520, **193** (2002).

[15] Z. Zhong, O. G. Schmidt, G. Bauer, Appl. Phys. Lett. **87**, 133111 (2005).

[16] M. Borgström, V. Zela, and W. Seifert, Nanotechnology **14**, 264 (2003).

[17] M. Bruel, Electron. Lett. **31**, 1201 (1995).

[18] F. Leroy, J. Eymery, P. Gentile, and F. Fournel, Surf. Sci. **545**, 211-219 (2003).

[19] R. A. Wind, M. J. Murtagh, F. Mei, Y. Wang, M. A. Hines, and S. L. Bass, Appl. Phys. Lett. **78**, 2205 (2001).

[20] A. Bavard, PhD Thesis: University of Grenoble (2007).

[21] M. Bavencoffe, E. Houdart, C. Priester, J. Cryst. Growth **275**, 305 (2005).

[22] R. Lazzari, F. Leroy, G. Renaud, Phys. Rev. B **76**, 125411 (2007).

[23] F. Leroy, G. Renaud, A. Letoublon, R. Lazzari, C. Mottet, and J. Goniakowski, Phys. Rev. Lett. **95**, 185501 (2005).

[24] M. Bavencoffe, E. Houdart, C. Priester, J. Cryst. Growth **275**, 305 (2005).

[25] U. Pietsch, V. Holy, T. Baumbach, *High resolution X-ray scattering from Thin films and lateral Nanostructures (2^{nd} ed.)*, Springer, Berlin (2004).

[26] V. Favre-Nicolin, Computer code, NANOMAD (private communication).

[27] J. S. Pederson, J. Appl. Crystallogr. **27**, 595 (1994). J. S. Pederson, P. Vysckocil, B. Schönfeld, and G. Kortorz, J. Appl. Crystallogr. **30**, 975 (1997).

[28] M. Schmidtbauer, D. Grigoriev, M. Hanke, P. Schäffler, T. Wiebach, and R. Köhler, Phys. Rev. B **71**, 115324 (2005).

[29] A. Bavard, J. Eymery, A. Pascale and F. Fournel, Phys. stat. sol. (b) **243**, 3963 (2006).

Chapter 9

Ex-situ comparison between the growth of Ge islands on pre-patterned and nominal Si(001).

In this chapter, the growth of Ge islands on pre-patterned Si(001) substrate is compared to that of Ge islands on nominal Si(001). The Ge growths on both flat and pre-patterned templates have been performed under similar conditions (growth temperature, growth rate, same Si(001) substrate). Thus, this allows to compare the relaxation state, the elastic energy and the composition between islands grown on flat and pre-patterned templates.

9.1 Introduction

Considerable progress has been achieved in the past decade in the refinement of fabrication methods for self-assembled nanostructures. This imposes the need for a further improvement in characterization methods. In particular, the composition distribution within nanostructures has to be measured precisely in all three dimensions. Whereas several techniques have been used to determine the vertical composition and lateral gradients within islands, precise information on the effect of the scattering by the deformed Si substrate is still lacking. Results have been obtained from TEM and STM, but they are not sufficient to reliably establish the 3D distribution of chemical composition in a nanostructure [1]. X-ray diffraction suffers in this respect from the fact that it investigates the statistical average over many islands, which smears out the fine details of the composition and strain distribution.

The knowledge of strain, vertical and lateral chemical compositions, intermixing at the interfaces, *i.e.* structural properties at the long and short range scale, are of great importance to understand the growth mechanism as well as the electronic and optical properties of the heterostructures and nanostructures. Strain is closely related to the composition, shape and aspect ratio of the nanostructures, and on the mutual stress applied by the nanostructures and the substrate to each other. X-rays are known to be a powerful tool for measuring strain fields and correlations. The combination of MAD that allows to extract the scattering amplitude of the resonant and the non-resonant atoms (chemical mapping in the reciprocal space) and DAFS spectroscopy which allows to determine the local environment of atoms located in an iso-strain volume selected by diffraction is a very powerful approach to disentangle strain and composition.

Samples	Growth temperature	Amount of Germanium
Z576	620°C	7 MLs
Z25	650°C	7.2MLs
Cg267	650°C	6 MLs

Table 9.1: Series of sample

9.1.1 Sample description

Three series of samples were investigated in this work. The three series are named samples Z576, Z25 and Cg267. The samples were grown by solid-source molecular beam epitaxy (MBE) in a Riber SIVA 45 system at the University of Linz.

Sample Z576 corresponds to two different Si(001) substrates: a nominal (Z576N) and a pre-patterned templates (Z576P).

Samples Z25 and Cg267 present a nominal surface which is pre-patterned on one small region of 400μmx400μm for sample Z25 and on two regions of 900μmx900μm for sample Cg576. The pre-patterning was fabricated by holographic lithography for sample Z576P or e-beam lithography and subsequent reactive ion etching (RIE) for samples Z25 and Cg267 [2]. The pit patterns of the pre-patterned samples are two dimensionally ordered with a periodicity of ∼350-400nm.

Thus, each sample consists of a nominal and a pre-patterned surfaces on which a similar growth was performed (Table 9.2). This allows to compare the growth on nanostructured and nominal surfaces. Contrary to samples Z25 and Cg267, sample Z576 presents the difference that the nominal and pre-patterned surfaces do not belong to the same Si(001) template.

After a chemical cleaning process, including a final HF dip, and thermal treatment in UHV at ∼900°C, a thick (≥ 100nm) Si buffer layer was grown on the Si substrate prior to Ge deposition while ramping the substrate temperature from 420°C to 650°C at a rate of 0.5 Angstroms/s. Subsequently, Ge (6-7 MLs) are deposited on the surface at a temperature of 620°C (samples Z576N and Z576P) or 650°C (samples Z25 and Cg267) at a rate of ∼0.05 Angstroms/s. Since the rate is at the lower limit of the flux controller, the migration of the deposited Ge atoms or dimers was further enhanced by growth interruption for 10s after each deposited ML. Afterwards, the substrate temperature was quickly decreased. The surface morphology of the samples was measured by atomic-force microscopy (AFM) and scanning electron microscopy (SEM).

9.1.2 AFM and SEM analysis

Sample Z576N (figure 9.1(a)), which was grown simultaneously with sample Z576P (figure 9.1(b)), presents a bimodal growth. Randomly distributed domes are formed (height: (17.0±1.5)nm, width: (74±5)nm).

A few 130nm-superdomes are observed. Atomic force microscopy and scanning electron microscopy show perfectly ordered Ge islands on sample Z576P (figure 9.1(b)) and on the pre-patterned part of samples Z25 (figure 9.1(d)) and Cg267 (figures 9.2(b), (c)). Sample Z576P (figure 9.1(b)) is formed of {111}-facetted pyramids of about (114±2)nm width and (42±2)nm height. The inter-dot distance is ∼370nm averaged along the [110] and [-110] directions. The patterned part of sample Z25 (figure 9.1(d)) is monomodal composed of domes of about 132nm width and 29nm height. The average inter-dot distance is ∼410nm averaged along the [110] and [-110] directions. Its nominal part (figure 9.1(c)) is quasi-monomodal. A huge part is composed of statistically distributed domes (∼115nm width and ∼18nm height) and few pyramids (∼80nm width and ∼7nm height) are observed. The inter-dot distance is roughly 230nm on the nominal part of sample Z25.

The nominal part of sample Cg267 (figure 9.2(a)) shows a quasi-monomodal growth. A huge part is composed of domes (∼171nm width and ∼19.5nm height) and few pyramids are observed (∼104nm width and ∼6.6nm height). The *square* and *diamond* patterned parts of sample Cg267 are composed of unimodal SiGe islands. On the *square* part of sample Cg267, 186nm-domes (height: ∼26nm) are

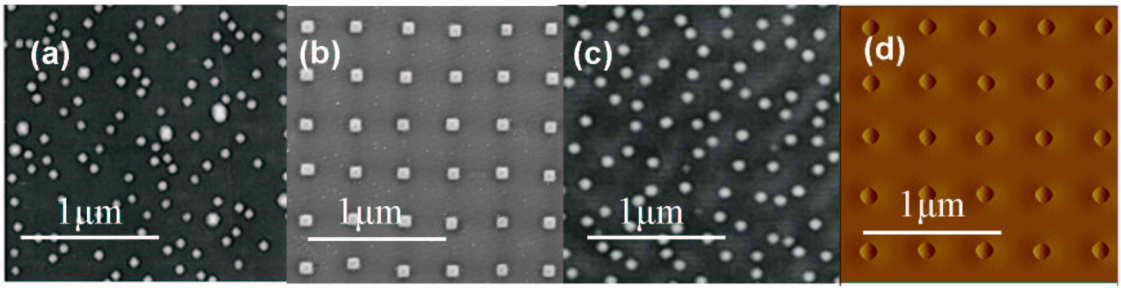

Figure 9.1: AFM or SEM images of samples Z576N (a), Z576P (b), nominal part of sample Z25 (c) and patterned part of sample Z25 (d).

observed; they are separated from each other by a distance of ∼478-482 nm. The depth of the pits for square area was around 40nm before Ge growth. On the *diamond* part, on average, smaller islands (width: ∼166nm) are observed. But, in comparison to islands grown on the *square* patterned part, they are higher (height: ∼30nm) and present a higher inter-dot distance (∼475-490nm). The depth of the pits for *diamond* area was around 36nm before Ge growth. The sizes of domes are not similar on the *square* and *diamond* patterned parts of sample Cg267. But the islands show the same facets: {113}, {105} and {15 3 23} facets (see figure 9.3). Figure 9.4 presents the slope of pit sidewalls for both *square* and *diamond* patterned area which are quite nearly similar. After the Si buffer layer growth, the Si(11n) facetted inverted pyramids could readily form for both cases. Thus, the morphological environment for the *square* and *diamond* patterned parts should be the same. On the other hand, the pit depth must have a certain influence on the amount of Ge which finally is inserted in the pits. The difference of island size can thus be explained by the difference of pit periodicity, pit depth and slope of the pit sidewalls between the *square* and *diamond* parts.

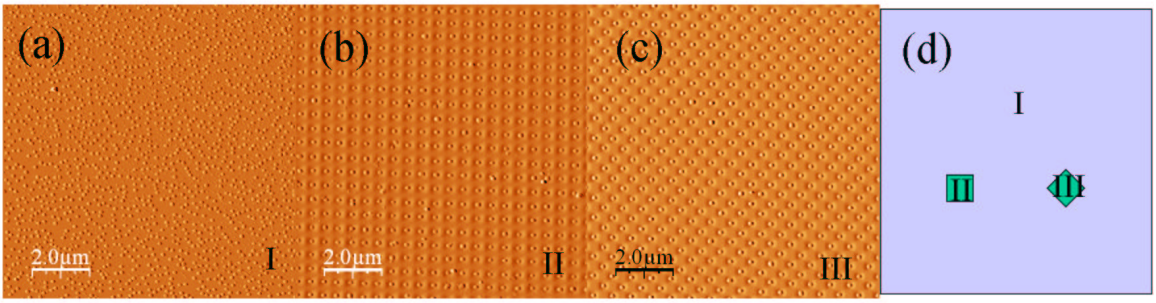

Figure 9.2: AFM images of the nominal part, named I (a), *square* patterned part II (b), *diamond* patterned part III (c) of sample Cg267. (d) represents the localisation of the different parts of sample Cg267 on the whole template.

For both series, *the size and the aspect-ratio of islands on patterned part is larger*, as the inter-dot distance, which is defined by the periodicity of the pits, is higher.

Surface orientation maps and the statistics of the volume of the dots were checked to see whether all the facets in both cases are similar.

Samples	AFM analysis	aspect ratio (height/width)
Z576N	74nm-domes (height:∼ 17nm) and few 130nm-superdomes	0.23 (D)
Z576P	114nm-{111} facetted pyramids (height:∼ 42nm)	0.37
Z25-nominal part	100nm-domes (height:∼ 18nm) and few 80nm-pyramids (height:∼ 7nm)	0.18 (D)
Z25-patterned part	115nm-domes (height:∼ 26nm)	0.23
Cg267-part I	124nm-domes (height:∼ 20nm) and few 104nm-pyramids (height:∼ 6.6nm)	0.16 (D)
Cg267-part II	132nm-domes (height:∼ 33nm)	0.25
Cg267-part III	126nm-domes (height:∼ 33nm)	0.26

Table 9.2: Series of sample

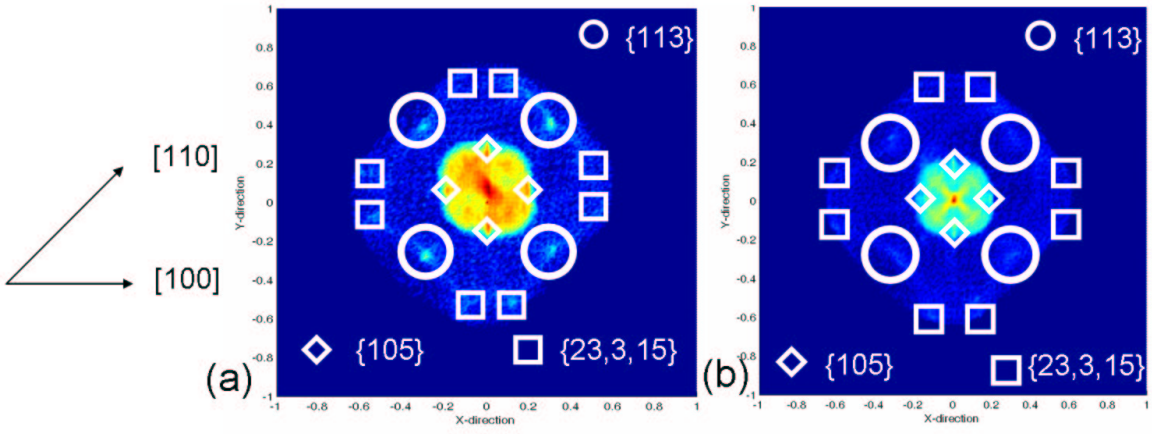

Figure 9.3: Surface orientation map of square (a) and diamond (b) patterned area of Cg267. The islands on both patterned parts show the same facets: {113}, {105} and {15 3 23} facets.

9.1.3 GISAXS analysis

To compare the islands shape, GISAXS experiments were performed on the BM32 beamline at ESRF on sample Z576P. In a first approximation, GISAXS intensity is proportional to the square modulus of the form factor F(**q**) times the interference function S(**q**), where **q** is the momentum transfer. F(**q**) and S(**q**) are the Fourier transforms of the particle shape and the island-island pair correlation function, respectively. GISAXS images (Fig. 9.5) were recorded along the azimuths $< 110 >$ and $< 100 >$ at an incident angle below the critical angle. Rods of scattering are observed along the two azimuths for sample Z576P. Along the $< 110 >$ azimuths, rods arising from facets {111} and {119} are observable. The {111} facets correspond to the island facets. The {119} facets correspond to the mean facets of the ordered pits. As the grazing angle is below the critical angle and as expected by the Distorted Wave Born Approximation (DWBA), a doubling of the truncation rods associated to {111} facets shows up (Fig. 9.5 (b)). In addition, interferences equidistant from each others are found on the GISAXS image (Fig. 9.5 (c)). This is the signature of a perfectly periodic interference function multiplied by the form factor of the islands, revealing well-organized Ge islands. Along the $< 100 >$ azimuth (Fig. 9.5 (a)), rods of scattering making an angle of $(11\pm1)^\circ$ are observed. They are associated with the existence of {105} facets, which are well-known facets for Ge islands on Si(001). Contrary to its reference, sample

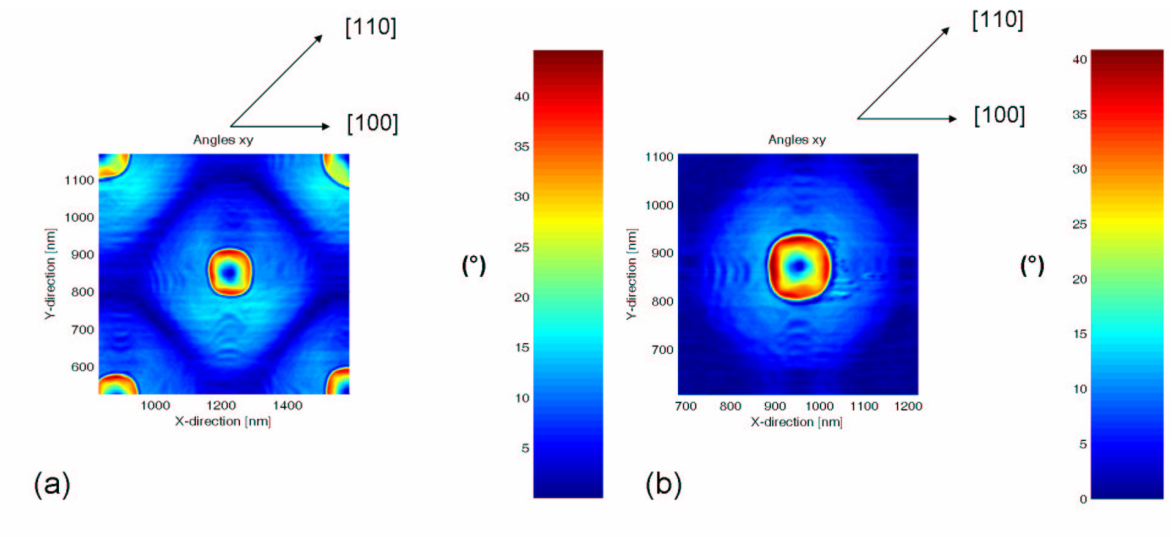

Figure 9.4: Geometrical profile of pits (slope of pit sidewalls) on square (a) and diamond (b) patterned area of Cg267.

Z576P presents the pecularities to be composed of {111}-facetted pyramids. It has been shown [3] that this pre-patterned sample has undergone a dome-to-{111}-pyramid transition. Such islands were only observed for sample Z576P whose reference Z576N presents superdomes. No misfit dislocations were observed by high resolution XTEM in sample Z576P, which demonstrates that {111}-facetted pyramids are coherently grown in the pits. It is not the case for the reference sample which presents dislocated superdomes. On a flat substrate the predicted dome-to-{111}-pyramid transition falls into a volume range where dislocated superdomes are found, *i.e.* dislocation formation is here a more efficient road to strain relaxation. In the pit geometry, however, the volume up to which dislocation-free domes can be observed extends significantly into the volume range where dislocated superdomes are present on flat templates. This can be understood by the fact that dislocation injection is delayed for growth on pit-patterned substrates as demonstrated by Z. Zhong [3].

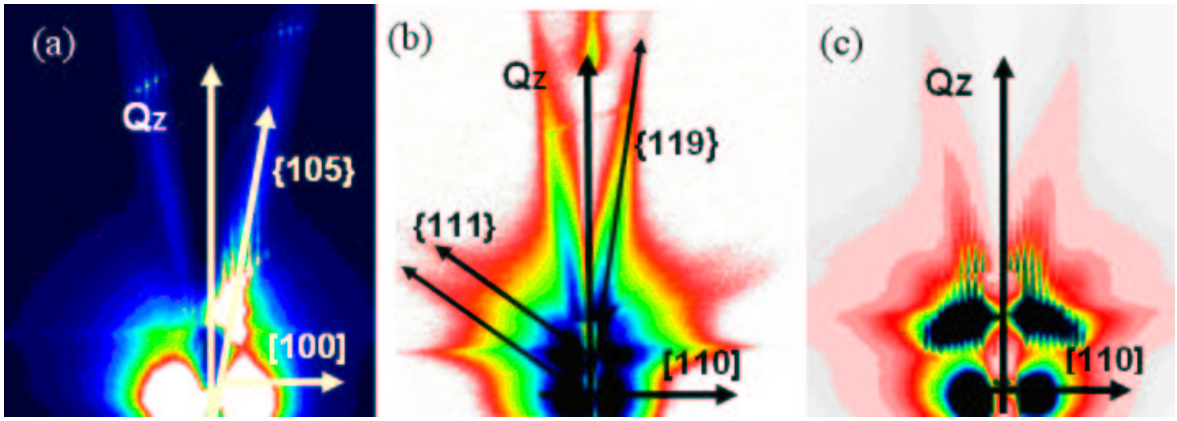

Figure 9.5: GISAXS images of sample Z576P along the $< 100 >$ (a) and $< 110 >$ azimuths (b)-(c).

9.1.4 Strain state analysis

To have access to the relaxation states of the grown Ge islands, radial scans along the [100] direction near the (400) Si Bragg peak or along the [110] direction near the (220) Si Bragg peak were performed for the different series of sample. The radial scans allow determining the strain profiles of the Ge islands.

Figure 9.6(a) shows radial scans along the $< h00>$ direction, around h=4 for samples Z576N and Z576P. In both cases, scattering from Ge is present in the form of a shoulder below the Si Bragg peak. The Ge contribution of diffuse scattering is observed around h ~3.95 for sample Z576N. Two components can be seen for sample Z576P: a dominant one centered at h ~3.97 and a smaller one centered at h ~3.92. For this sample, the in-plane relaxation is found to be reduced for Ge islands grown on the pre-patterned template.

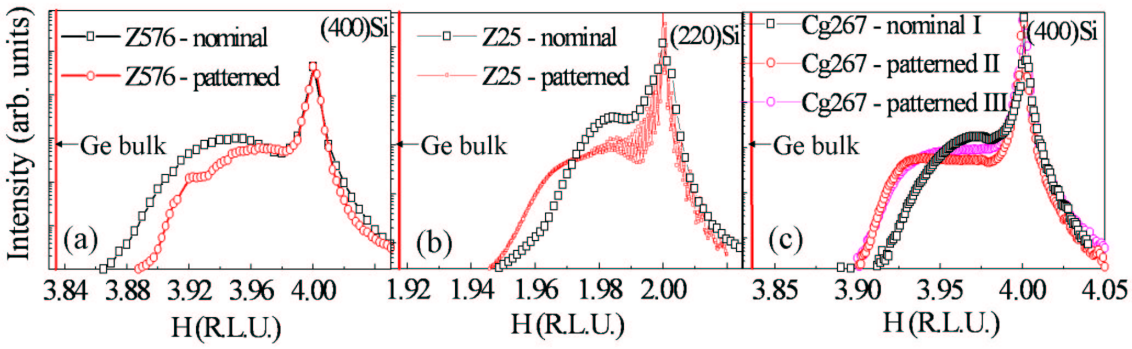

Figure 9.6: Radial scans along the $< h00>$ direction, around h=4 for samples Z576 (a) and Cg267 (c). Radial scans along the $< hh0>$ direction, around h=k=2 for samples Z25 (b). The position of the Ge bulk Bragg peak is indicated by the arrow.

Figure 9.6(b) shows radial scans along $< hh0>$ directions, around h=k=2 for both patterned and nominal parts of sample Z25. To detect only the signal coming from the 400μmx400μm patterned part of sample Z25 and as the beam size is about 180μmx200μm, the exit X-ray slits were closed to collect the intensity arising only from the organized islands. The angular scan 9.7 performed around the (220) Si Bragg peak shows perfectly periodic rods, proving that X-ray measurements can be well-confined on the pre-patterned zone of sample Z25.

On radial scans of figure 9.6(b), partially relaxed Ge is observed for islands on both parts of sample Z25, as revealed by the peaks appearing around h=1.985 for the nominal side and around h=1.965 and h=1.985 for the patterned side. For sample Z25, the in-plane relaxation is found to be significantly smaller for islands grown on the nominal part of the substrate.

On radial scans of figure 9.6(c), only one contribution of diffuse scattering is observed around h=3.97 for the nominal part of sample Cg267. The *diamond* and *square* pre-patterned parts of sample Cg267 show the same relaxation states; their radial scans can be almost super-imposed. The Ge contribution presents a plateau and a maximum of intensity at h=3.93. Like sample Z25, the in-plane relaxation is found to be reduced for Ge islands grown on nominal regions.

For exactly the same growth conditions, a difference of relaxation state is thus observed between islands on nominal and pre-patterned substrates. In addition, depending on the growth conditions and pre-patterning techniques, the in-plane relaxation of Ge islands on patterned substrates compared to nominal substrates varies.

In the case of sample Z576, the in-plane relaxation is larger for islands grown on the nominal sample Z576N. Sample Z576N is composed of domes and a few incoherent superdomes. Incoherent superdomes show dislocations at their interface and undergo plastical relaxation. Sample Z576P shows coherent {111}-facetted pyramids. In the case of sample Z576, the difference of island shape (domes)

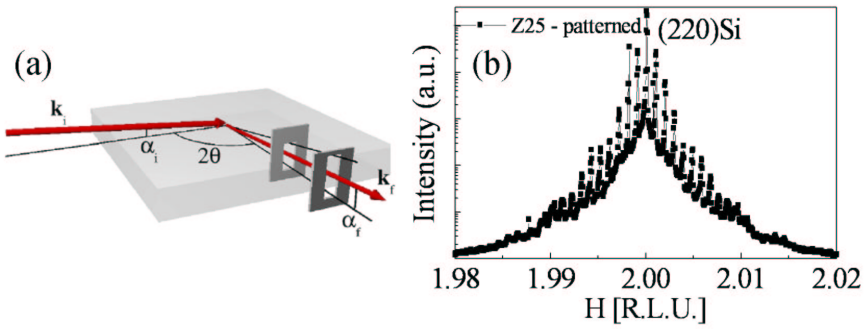

Figure 9.7: (a): Scattering angle, incident and exit angles, and detector slits setup for an in-plane reflection. To collect the intensity arising only from ordered islands, the detector slits should be horizontally closed to 0.2mm with the entrance slits closed to 0.2mm.(b):Rocking scan around the (220)Si Bragg peak of the patterned part of sample Z25. The beam was focused on the 400μmx400μm patterned part of sample Z25.

and the presence of dislocations inside superdomes explains the higher in-plane relaxation of islands grown on nominal surface. Indeed, dislocated islands present a larger relaxation compared to purely elastically relaxed islands.

Contrary to sample Z576, samples Z25 and Cg267 present the same island shape on both patterned and nominal parts (only few pyramids are observed on nominal parts.). The in-plane relaxation is larger for islands grown on pre-patterned substrates. This can be explained by three hypotheses: (1) a higher Si concentration inside islands on nominal substrates, (2) a different strain state at the Si surface induced by patterning which could increase Ge relaxation inside organized islands or (3) different height/shape of islands between nominal and pre-patterned templates. As pre-patterned substrates present larger domes, the third hypothesis could explain the difference of in-plane relaxation. However, the two hypotheses can not be excluded.

On both patterned parts (sample Z576P and sample Z25-patterned), the island scattering is composed of two contributions corresponding to two different relaxed regions. How can this be explained as on the patterned parts, one type of islands is observed?

In figure 9.8(a), radial scans of a bare pre-patterned Si(001) sample, and of samples Z576P, Z25-patterned and Cg267-patterned are plotted around the (220) reflection along the [110] direction. The maximum of relaxation state of the three pre-patterned samples appears nearly similar (especially for samples Z25 and Cg267) despite the different shapes and inter-island distances.

The diffracted intensity around the (220) Bragg peak of the pre-patterned Si(001) sample without grown Ge is symmetric; the relaxation state induced by pre-patterning is thus symmetric. Figure 9.8(b) shows radial scans around the (220) reflection for the nominal parts of samples Z576N, Z25 and Cg267. Sample Z576N presents a different relaxation state compared to the other nominal samples. This can be explained by the presence of incoherent superdomes which are plastically relaxed. Their maximum of relaxation is thus displaced towards the position of Ge bulk Bragg peak. Despite the different growth conditions (growth temperature and amount deposited), samples Z25 and Cg267 presents the same relaxation state as observed in figure 9.9. Note also that the islands which compose sample Z576P are more relaxed in the [100] direction. As observed by GIXD (see Fig. 9.10), the maximum of relaxation along the [100] direction is displaced towards the position of the Ge bulk Bragg peak.

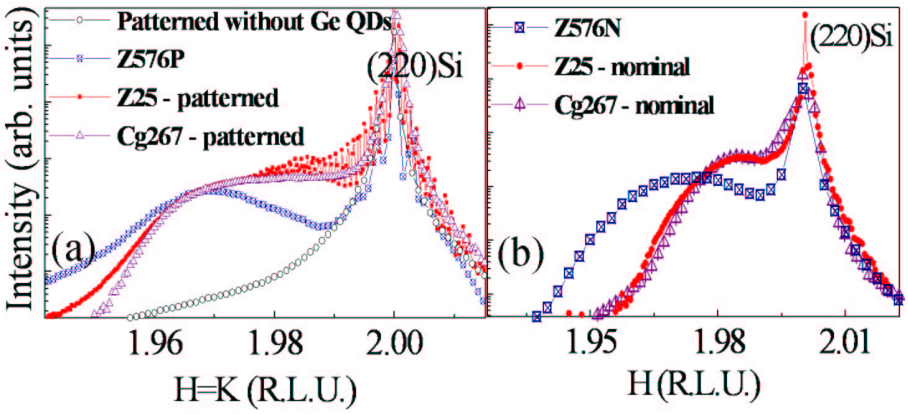

Figure 9.8: (a): Radial scans around the (220)Si Bragg peak for pre-patterned samples: (1) reference without Ge QDs, (2) sample Z576N, (3) sample Z25 and (4) sample Cg267. (b) Radial scans around the (220)Si Bragg peak for all nominal surfaces.

9.1.5 MAD analysis

In the present study, the choice of the critical angle was most often a compromise between surface sensitivity and counting time. To achieve high surface sensitivity, we fixed the incident angle at 0.15° (case of samples Cg267 and Z25), just below the critical angle of total external reflection of bulk Si (α_c=0.163° at 11keV), in order to minimize the scattering by the Si substrate. We also worked in the supercritical regime (α_i=0.25°, case of sample Z576), which is less demanding than the subcritical regime (more stable collected intensity and multiple-scattering effects noticeably limited for incident angle larger than the critical angle) and therefore, is often prefered if possible, *i.e.*, the surface sensitivity is sufficient.

In addition, we measured the scattered intensity around the (602) or (400) reflection as a function of the h reciprocal space direction to characterize the in-plane strain for both patterened and nominal samples. Distinguishing the Ge and Si contributions is made possible using GI-MAD (Grazing Incidence Multiwavelength Anomalous Diffraction) measurements. As the Si substrate is made of non-anomalous atoms, the modulus of the Si and Ge structure factors, $|F_{Si}|$ and $|F_{Ge}|$ and $\Delta\phi = \phi_{Si} - \phi_{Ge}$ can be extracted without including the distorted wave Born approximation (DWBA) [4] in both subcritical and supercritical incident angle regimes. The dependence of the diffracted intensity with the energy of the incident X-ray beam in the vicinity of the Ge K-edge can be written as [4]:

$$I(\mathbf{q},E) \quad \alpha \quad (1+r)^2|F_T|^2 + \left(\frac{|F_{Ge}|}{f^0_{Ge}(\mathbf{q})}\right)^2 \left(f'_{Ge}{}^2(E) + f''_{Ge}{}^2(E)\right) \tag{9.1}$$
$$+2\frac{|F_T F_{Ge}|}{f^0_{Ge}(\mathbf{q})}\left[f'_{Ge}(E)\cos(\varphi_T - \varphi_{Ge}) + f''_{Ge}(E)\sin(\varphi_T - \varphi_{Ge})\right]$$

(9.3)

where $|F_T|$ (resp. φ_T) is the modulus (resp. the phase) of the scattered amplitude from all atoms (excluding the Ge resonant scattering), $|F_{Ge}|$ (resp. φ_{Ge}) is the modulus (resp. the phase) of the non-resonant scattered amplitude from Ge atoms and r the reflectivity coefficient. $f^0_{Ge}(\mathbf{q})$ is the Thomson (non-resonant) scattering factor for germanium, and $f'_{Ge}(E)$ (resp. $f"_{Ge}(E)$) are the real (resp. imaginary) resonant scattering factors for germanium.

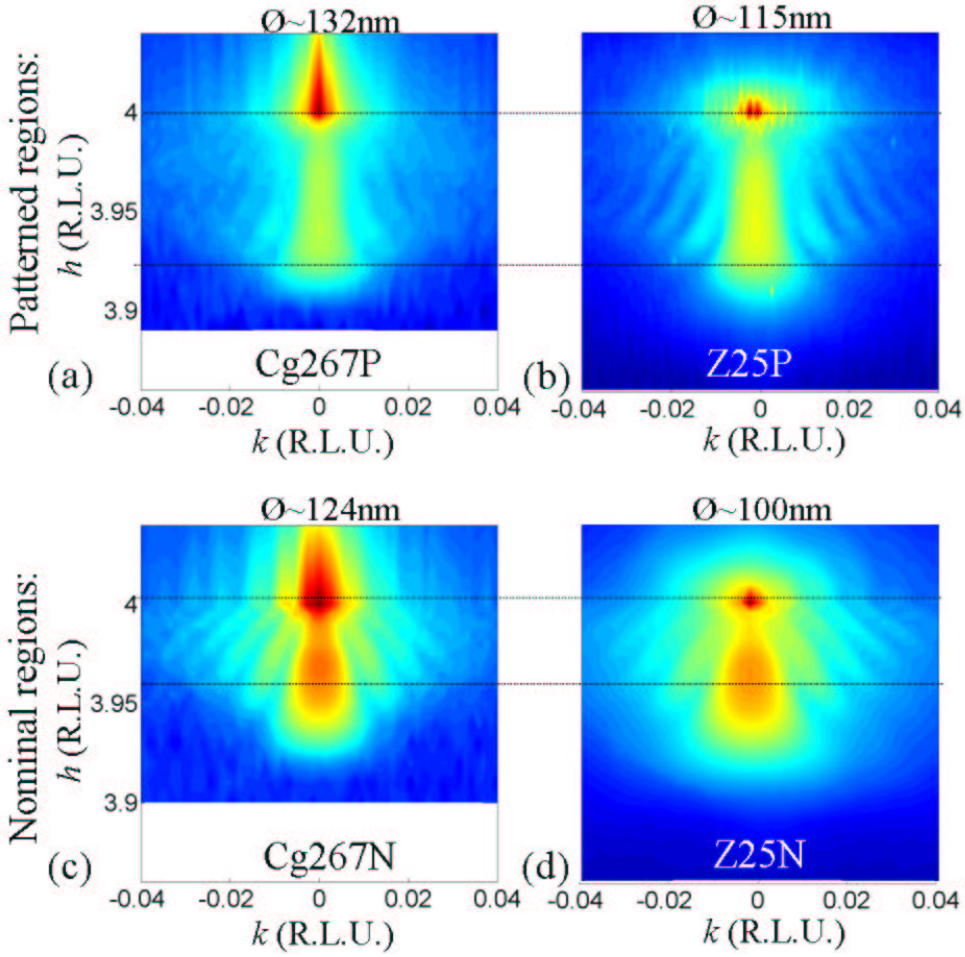

Figure 9.9: (400) reciprocal space maps of the patterned and nominal parts of sample Cg267 (a)-(c) and sample Z25 (b)-(d). The mean diameter of the islands is indicated above each figure.

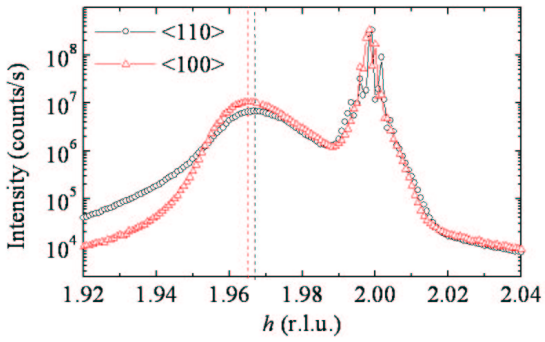

Figure 9.10: (220) and (400) radial scans plotted as a function of h and $h/2$, respectively, in order to determine the relaxation state along the [100] and [110] directions.

The diffracted intensity was measured in the vicinity of the (602) and (400) reflections at 12 energies close to the Ge K-edge. Using the known $f'_{Ge}(E)$ and $f"_{Ge}(E)$, it is then possible to quantitatively extract $|F_{Ge}|$ and $|F_T|$ through a least-square minimization and without any structural model by fitting Eq. 9.2 to the experimental data with the `NANOMAD` algorithm [5]. The retrieval shall be run in the framework of the distorted wave Born approximation, taking into account scattering paths involving the reflection from the layer supporting the islands [6, 7]. We recorded the diffracted intensity integrated over the exit angle α_f, between 0 and $2\alpha_c$, and therefore collected all the scattering paths using a position sensitive detector (PSD). Supposing an homogeneous alloy, the Ge_xSi_{1-x} content can then be deduced using the relation:

$$\frac{|F_{Ge}|}{|F_T|} = \frac{x f^0_{Ge}}{x f^0_{Ge} + (1-x) f_{Si}} \tag{9.4}$$

In order to determine the structural characteristics of the Ge islands on both patterned and nominal samples, X-ray experiments were performed in grazing incidence geometry at Beamline ID01 and BM02 of the European Synchrotron Radiation Facility in Grenoble. The X-ray photon energy was tuned around 11 keV. As observed in chapter 3, the DWBA may affect the collected signal for large islands fulfilling the iso-strain conditions (as it is our case). As an example, the observed maxima in radial directions for in-plane reflections could be mistaken as prevalent strain state inside the islands. This problem is reduced near the critical angle and above it (see Fig. 3.10 (a)). That's why we decided to work above the critical angle or near it and not highly below it.

Sample Z576

The incident angle was fixed at 0.25°, above the critical angle of total external reflection (α_c=0.163° at 11keV). The intensity distribution along the exit angle in a range of about 1.5° was recorded using a position sensitive detector mounted perpendicular to the surface. GI-MAD was performed around the (602) reflection in order to disentangle the contribution of Si inside the Ge nanostructures and the contribution of the Si substrate. Figure 9.11 shows some of the square-root diffracted intensities measured close to the (602)Si reflection and across the Ge K edge for sample Z576P, taking advantage of the Ge anomalous effect to localize the Ge contribution along the [602] direction.

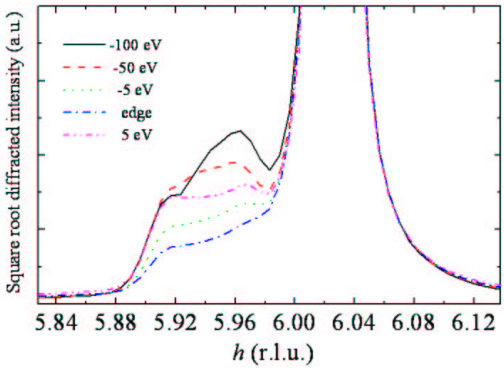

Figure 9.11: Experimental square-root diffracted intensities measured below (-100, -50 and -5 eV), at the edge and above (+5 eV) the Ge K edge for sample Z576P.

Figure 9.12 shows the extracted structure factors and the corresponding vertical composition inside the islands in both patterned and nominal Z576 samples. Note that the extraction is not valid at the position of the Si Bragg peak. The mean composition is $\sim (60 \pm 15)\%$ for sample Z576P and

sample Z576N. In the composition profile of sample Z576N, two shoulders are clearly observed. The one localized at low in-plane lattice values is attributed to domes and the other is attributed to superdomes. Superdomes are less intermixed than domes, as previously explained in chapter 7.

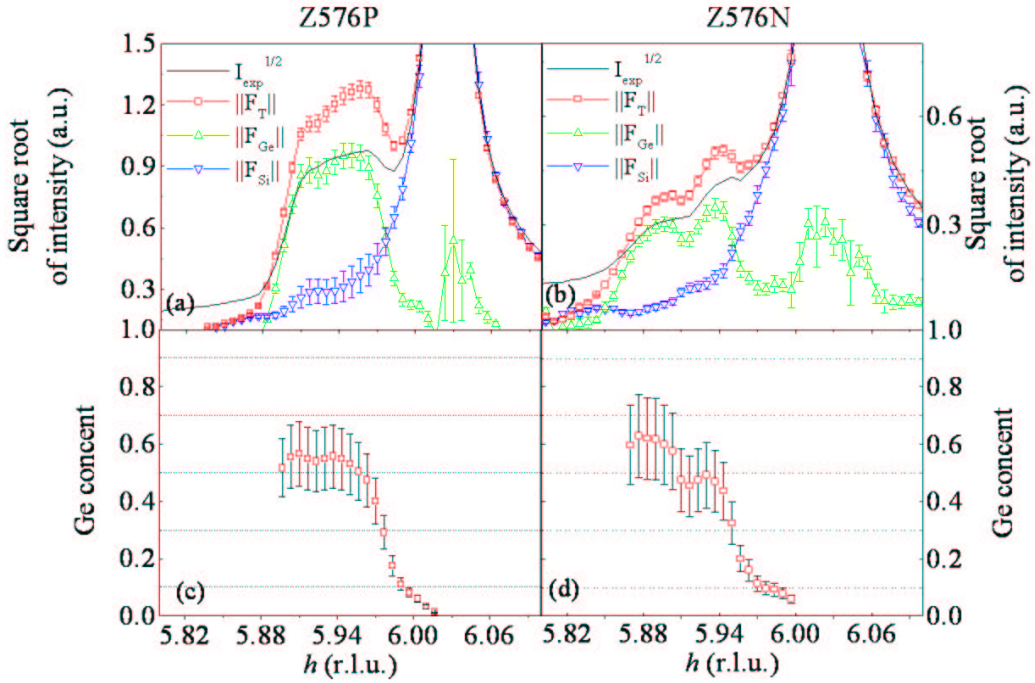

Figure 9.12: (a): $\sqrt{I_{Exp}}$ measured at 11.053keV (50eV below Ge K-edge), $||F_T||$, $||F_{Ge}||$ and $||F_{Si}||$ for sample Z576P and corresponding composition (c). (b): $\sqrt{I_{Exp}}$ measured at 11.053keV (50eV below Ge K-edge), $||F_T||$, $||F_{Ge}||$ and $||F_{Si}||$ for sample Z576N and corresponding composition (d).

Sample Cg267

The incident angle was fixed at 0.15°, below the critical angle of total external reflection (α_c=0.163° at 11keV), in order to minimize the scattering by the Si substrate. GI-MAD was performed around the (400) reflection. Figure 9.13 shows the extracted structure factors for both patterned and nominal parts of sample Cg267. In figure 9.14, the mean Ge composition of the patterned and nominal areas of sample Cg267 is represented. Islands grown on both nominal and patterned areas show nearly the same composition $\sim (57 \pm 15)\%$ (the variations are smaller than the experimental error) for the same in-plane lattice parameter.

Sample Z25

The incident angle was fixed at 0.15°, below the critical angle. GI-MAD was performed around the (400) reflection. Figure 9.15 (a) shows the extracted structure factors for the nominal part of sample Z25. Contrary to sample Z25N, the radial scans around the (400) reflection for the patterned part were only made for three energies instead of twelve. In figure 9.15 (b), the mean Ge composition of the patterned and nominal areas of sample Z25 is represented. The mean composition of sample Z25P has higher error bar values (due to the low number of energies used), which unables to make a

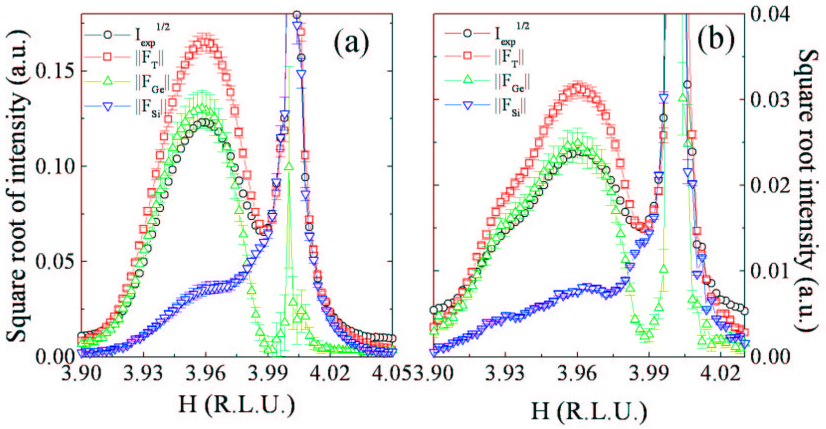

Figure 9.13: (a): $\sqrt{I_{Exp}}$ measured at 11.053keV (50eV below Ge K-edge), $||F_T||$, $||F_{Ge}||$ and $||F_{Si}||$ for sample Cg267-nominal part. (b): $\sqrt{I_{Exp}}$ measured at 11.053keV (50eV below Ge K-edge), $||F_T||$, $||F_{Ge}||$ and $||F_{Si}||$ for sample Cg267-nominal part.

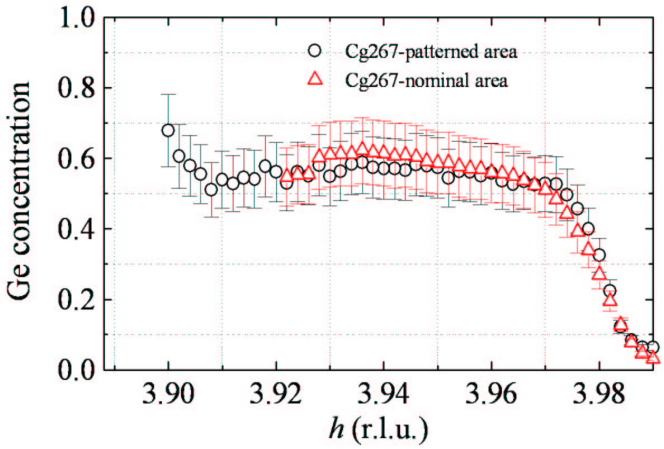

Figure 9.14: Ge composition for sample Cg267-nominal part and sample Cg267-patterned part.

precise comparison of the Ge content between the nominal and patterned areas. As samples Z25 and Cg267 were grown almost with the same conditions, we expect the same composition profiles for both samples. We can observe that the composition of the nominal parts of samples Z25 and Cg267 can be super-imposed. We expect thus that the patterned part of sample Z25 shows the same profile as sample Cg267; this means that we expect that samples Z25N and Z25P show nearly the same mean composition profile as function of the in-plane lattice parameters.

9.1.6 Summary of the GI-MAD analysis

Samples Z25 and Cg267 were grown nearly at the same growth temperature (∼650°C). The mean composition of islands on both patterned and nominal parts is (∼ 57%) of Ge (if we exclude sample

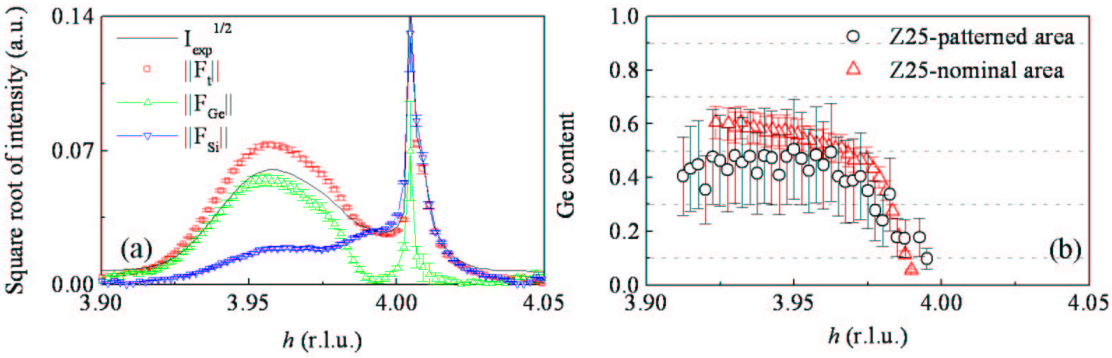

Figure 9.15: (a): $\sqrt{I_{Exp}}$ measured at 11.053keV (50eV below Ge K-edge), $||F_T||$, $||F_{Ge}||$ and $||F_{Si}||$ for sample Z25 patterned part. (b): Ge composition for sample Z25-nominal part and sample Z25-patterned part.

Z25P for which only a rough estimation of the composition is given). *This means that the mean concentration inside Ge islands is mainly or only governed by the growth temperature (thus by diffusion processes).* This is not the case for the relaxation state. Samples grown on pre-patterned templates present a higher relaxation compared to those grown on flat substrates. The relaxation do not only depend on growth temperature but also on the surface curvature of the substrates. It is not possible to determine strain without a simultaneous measurement of both local lattice parameter and composition of islands. This is because the change in lattice parameter can be both due to substrate imposed stress as well as change in composition. The correct value of local in-plane strain with local composition Si_xGe_{1-x} is given by $\epsilon_{//} = \frac{a'}{a(x)} - 1$, where $a(x)$ is the lattice parameter of an unstrained alloy (calculating using the Vegard's law $a(x) = xa_{Si} + (1-x)a_{Ge}$) and a' is the in-plane average lattice parameter which is inversely proportional to the h=h_{Ge} position of the diffuse F_{Ge} peak maximum [8]. The average lateral strain determined at the maximum of relaxation of the radial scans (see Fig. 9.6) is $\epsilon_{//} \sim -1.3\%$ for the nominal part of samples Z25 and Cg267 and is $\epsilon_{//} \sim -0.9\%$ for the patterned part of samples Z25 and Cg267. $\epsilon_{//} < 0$ corresponds to compressive strain. The elastic energy u per unit volume can be calculated at the maximum of relaxation using the formula [9]:

$$u = 2\mu \frac{1+\nu}{1-\nu} \epsilon_{//}^2, \tag{9.5}$$

where μ and ν are the shear modulus and Poisson ratio of the GeSi alloy, and $\epsilon_{//}$ the local strain. The elastic energy is thus proportional to the local strain. This implies that Ge islands forming in the pit have lower elastic energy than if they were forming on a flat substrate. This has been previously observed and demonstrated by Z. Zhong *et al.* [3]. This behaviour was ascribed to the finding that the in-plane strain component for a downward pyramidal pit is already smaller than the one for a flat wetting layer. Besides, they found that pit-patterning causes a redistribution of the elastic energy between island and substrate. In addition, the pit shape has influence on the strain release in the pit, *i.e.* if the pit is truncated the strain release at the center of the pit is lower [3].

We show that by tuning the surface curvature of the surface it is then possible to change the relaxation state and the overall elastic energy of islands without modifying their Ge composition. This is of great importance for technological applications. In addition, due to its high relaxation, the pre-patterned template is ideally suited to strained Si cap layers in order to enhance electron mobility in Si. *Besides, these results show new insight about the intermixing process which does not appear strain-driven but induced by surface-mediated diffusion processes as the same mean composition is observed on both patterned and nominal templates.*

9.1.7 Grazing-incidence diffraction anomalous fine structure (GI-DAFS) analysis

The previous MAD study has been complemented by the analysis of the local environment of the Ge atoms in the islands through the measurements of the fine-structure oscillations in diffraction condition.

Grazing-incidence diffraction anomalous fine structure at the Ge K edge (11.103 keV) was performed at the French Research Group beamline BM2 at ESRF by using a height-circle diffractometer equipment. We measured the diffuse scattering intensity, in grazing incidence and exit, close to the (400) Bragg reflection of the Si substrate (radial scans), at energies close to the Ge K edge. The samples (Cg267N and Cg267P) were mounted in the vertical plane; *i.e.*, the polarization vector $\epsilon_\mathbf{i}$ of the incident photon beam was perpendicular to the sample surface (001). The incident angle was set to α_i=0.2°, above the bulk Si critical angle α_c=0.163° (at 11 keV) for which the total reflection regime takes place. Two kinds of scans were performed: (a) h scans (radial) in the range 3.8-4.04 for 12 energies, from 11.003 to 11.203 keV - *i.e.* close to the Ge K-edge - and (b)energy scans at fixed scattering vector ($\mathbf{Q}$) for different h values along the radial scans in the region of island diffuse scattering. The energy scans were recorded in a large energy interval, typically 1 keV, with an energy step of 1 eV, to allow a quantitative analysis of both the edge and extended oscillations. The MAD analysis, *i.e.* the extraction of the Si, Ge and total structure factors and the determination of the Ge content as a function of h, has been performed in the previous part.

EDAFS analysis

A quantitative analysis of the grazing-incidence diffraction anomalous fine structure oscillations in the extended region above the edge (EDAFS) allows to determine the structural parameters from the first to the second coordination shells around Ge atoms and to precisely determine the Ge content inside the nanostructures. Figure 9.16 shows the diamond structure of crystalline Ge with the representative Ge atoms in the first three shells.

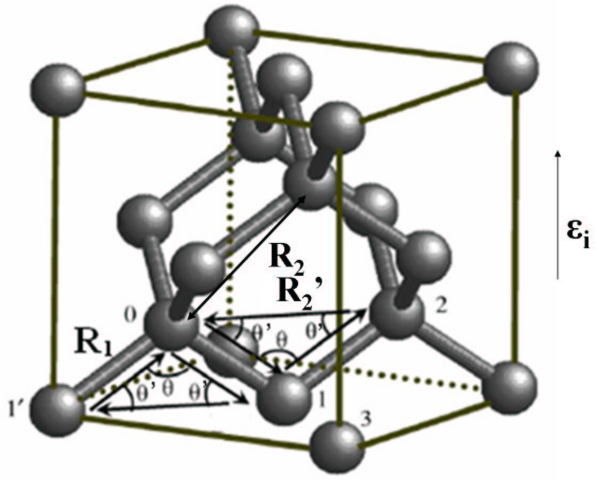

Figure 9.16: The diamond structure of crystalline Ge with the representative Ge atom in the first three shells. $\epsilon_\mathbf{i}$ is the polarization vector. The number 0 refers to the central absorber Ge atom. Numbers 1 to 3 identify corresponding coordination shells atoms and 1' denotes another first coordination shell atom different from atom 1. R_1, R_2 and R_2' correspond to the inter-atomic distances between the central absorber Ge atom (0) and the first and second coordination shell atom, respectively. As the inter-atomic distance R_2' is perpendicular to the polarization vector, this distance is not probed; only R_2 can be determined.

Figure 9.17 (a) shows the oscillatory contribution (χ_{DAFS}) to the DAFS spectrum as a function of the virtual photoelectron wave-vector modulus k. χ_{DAFS} can be written as $\chi_{DAFS} = \frac{1}{S_D}\chi_Q$ where S_D is a normalization factor that depends on crystallography. χ_Q can be written in a form that is similar to the well-known EXAFS formula [10]:

$$\chi_Q = \sum_\gamma A_\gamma(k) sin(2k < R >_\gamma + \phi_\gamma(k) + 2\delta_c(k) + \phi_0 - \phi_{Ge} - \frac{\pi}{2}), \tag{9.6}$$

where γ runs over all possible virtual photoelectron scattering paths, $< R >_\gamma$ is the effective length of path γ, $\phi_\gamma(k) + 2\delta_c(k)$ is the net scattering photoelectron phase shift and ϕ_0 and ϕ_{Ge} are the phase of the smooth structure factor (without oscillations) and the phase of the Ge structure factor, respectively. The EDAFS analysis has been carried out by using the `FEFF8` code [11], taking into account beam polarization. The `ARTEMIS` interface to the `IFEFFIT` package [12] was used to fit theoretical computations to the experimental data.

The EDAFS spectra was Fourier Transformed in the k range 2-10$\AA^-1$, and the fit was performed in R space (real space), using three next-neighboring shells (I-III). Fig. 9.17 shows the best fit curves obtained at h=3.97 for the nominal part of sample Cg267. They are compared to the experimental data. Three multiple-scattering paths were found to be relevant in this range. The possible Ge-Si intermixing makes it necessary to include Ge-Ge and Ge-Si pairs in each coordination shell. The Ge-Si and Ge-Ge distances in three coordination shells are treated as independent adjustable variables.

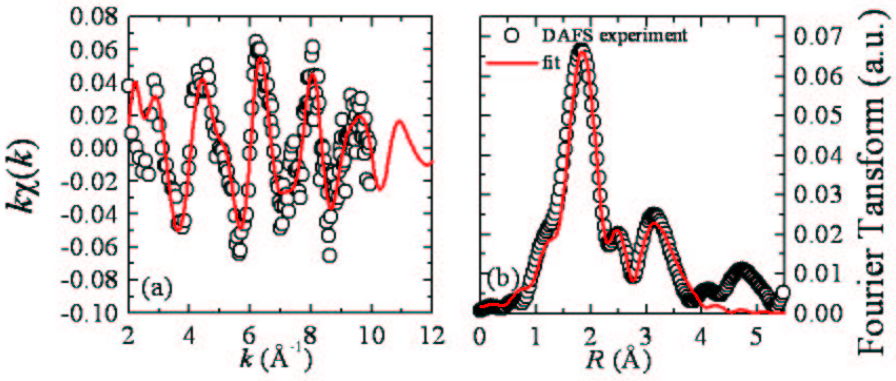

Figure 9.17: (a): Experimental EDAFS for the nominal part of sample Cg267, compared with the best-fit result and (b) R-space experimental curve for the nominal part of sample Cg267 compared with the best fit.

The best-fit parameters at the radial value h=3.97 (sample Cg267N) are shown in Table 9.3, where we also report as a reference, the Si and Ge bulk values. The reported values are in good agreement with literature [13, 14]. The average Ge weighting factor or composition x_{Ge} is obtained using the Ge-Ge (N_{Ge-Ge}) and Ge-Si (N_{Ge-Si}) coordination numbers of each shell. They are related to the total nominal coordination number N_T, $N_{Ge-Ge} = N_T x_{Ge}$ and $N_{Ge-Si} = N_T(1 - x_{Ge})$, respectively. The average Ge weighting factor in the first shell reaches 57%, which is in good agreement with the MAD results obtained at h=3.97 (x_{MAD}=52%). The most stricking result obtained from the EXAFS study is that the average Ge weighting factor (x_{Ge}=33%) is significantly lower in the second shell. To determine if this can be correlated to atomic ordering, we calculate the number of Ge and Si atoms in the first and second shells in the case of the $RS2$ and $RS3$ models.

In the $RS2$ and $RS3$ models, α and β correspond to the probability of finding Ge atoms in (α, β) sites and (δ, γ) correspond to the probability of finding Si atoms in (δ, γ) sites (see the schematic

shell	$R(Ge-Ge)$ Å	N_{Ge-Ge}	N_{Ge-Si}	x_{Ge}	$R(Ge-Si)$ Å	$R(Ge)$ bulk Å	$R(Si)$ bulk Å
1 (R_1)	2.41±0.02	2.3±1	1.7±1	0.57	2.38±0.02	2.447	2.352
2 (R_2)	3.91±0.02	4±1	8±1	0.33	3.9±0.02	3.995	3.841
MS	4.32±0.02				4.28±0.02	4.45	4.27

Table 9.3: EDAFS best-fit values for interatomic distances (R_1, R_2 and multiple scattering (MS) triangular path: Ge-Ge-Ge and Ge-Si-Ge), Ge-Ge (N_{Ge-Ge}) and Ge-Si (N_{Ge-Si}) coordination numbers of each shell and Ge concentration (x_{Ge}) obtained by `IFEFIT` minimization using theoretical fitting standards by the `FEFF8` code.

representation (Fig. 9.18) of the Si/Ge atomic arrangement). In the $RS2$ model, $\alpha = \beta$ and $\gamma = \delta$.

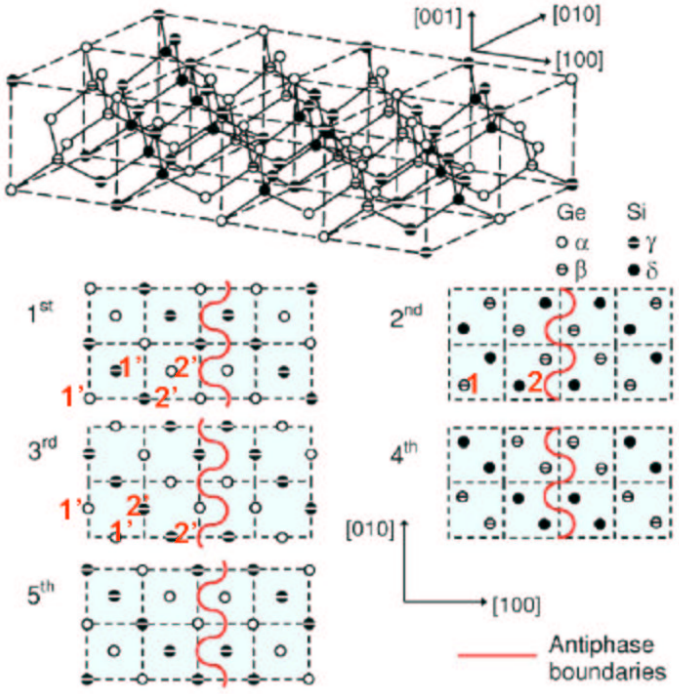

Figure 9.18: Schematic representation of the Si/Ge atomic ordering arrangement in the $RS3$ model. (α, β) and δ, γ) correspond to Ge and Si rich sites, respectively. In the $RS2$ model, α=β and δ=γ.

Supposing the $RS2$ model and that $\alpha = \beta = \gamma = \delta = 1$, for all configurations, the first shell is composed of three Ge atoms and one Si atom. Nevertheless, in the region of antiphase boundaries, the first shell is composed of two Si and two Ge atoms. We can easily suppose that the number of atoms near antiphase boundaries is significantly lower than the total number of atoms belonging to the iso-strain region at h=3.97. In this case, the average Ge weighting factor in the first shell should be $\sim 75\%$, which is higher than the experimental value. In addition, in the $RS2$ model, six Ge and six Si atoms are in the second shell with or without the presence of antiphase boundaries. In this case, the average Ge weighting factor should be $\sim 50\%$, which is again higher than the experimental value. Looking at the (200) forbidden reflection, we observed two intensity lobes that we referred to the signature of ordered domains. The $RS2$ model supposing $\alpha = \beta = \gamma = \delta = 1$ is thus not a correct model to explain atomic ordering in this sample.

We will now take into account the probabilities $\alpha, \beta, \gamma, \delta$ to find a Ge or a Si atom in $(\alpha, \beta, \gamma, \delta)$

sites. If we consider the Ge atom labelled '1' positioned at $(\frac{1}{4},\frac{1}{4},\frac{1}{4})$ in Fig. 9.18, this atom has four first neighbours, labelled '1", located at the positions: (0,0,0), $(\frac{1}{2},\frac{1}{2},0)$,$(\frac{1}{2},0,\frac{1}{2})$ and $(0,\frac{1}{2},\frac{1}{2})$. The number of Ge atoms surrounding it (*i.e.* that belongs to the first shell) is $3\alpha+1(1-\gamma)$. The atom labelled '2' has a probability (1-δ) to be a Ge atom. Its number of first neighbouring Ge atoms is $\alpha+3(1-\gamma)$. This implies that the number of Ge atoms that belong to the first shell is $\beta(3\alpha+(1-\gamma))+(1-\delta)(\alpha+3(1-\gamma))$. From EDAFS experiment, this value equal 2.3. The number of Si atoms in the first shell is then $(1-\beta)(3(1-\alpha)+\gamma)+\delta(3\gamma+(1-\alpha))=1.7$. The same analysis can be performed for the second shell. Whatever the $RS2$ model, it follows that (α, β, γ, δ) are solutions of a non-linear system of four equations:

$$\begin{cases} \beta(3\alpha+1(1-\gamma))+(1-\delta)(\alpha+3(1-\gamma))=2.3 \\ (1-\beta)(3(1-\alpha)+\gamma)+\delta(3\gamma+(1-\alpha))=1.7 \\ \beta(6\beta+6(1-\delta))+(1-\delta)(6\beta+6(1-\delta))=4 \\ (1-\beta)(6(1-\beta)+6\delta)+\delta(6\delta+6(1-\beta))=8 \end{cases}$$

This system has been numerically resolved and no solution has been found.

Contrary to the $RS2$ model, in the $RS3$ model, the α and β sites, and the γ and δ sites are not equivalent. The same analysis as below can be performed in the case of the $RS3$ model. As the number of α, β, γ and δ sites is indentical, it follows that (α, β, γ, δ) are solutions of a non-linear system of four equations:

$$\begin{cases} 0.5(\beta(3\alpha+1(1-\gamma))+(1-\delta)(\alpha+3(1-\gamma))+\alpha(3\beta+1(1-\delta))+(1-\gamma)(\beta+3(1-\delta)))=2.3 \\ 0.5((1-\beta)(3(1-\alpha)+\gamma)+\delta(3\gamma+(1-\alpha))+(1-\alpha)(3(1-\beta)+\delta)+\gamma(3\delta+(1-\beta)))=1.7 \\ 0.5(\beta(6\beta+6(1-\delta))+(1-\delta)(6\beta+6(1-\delta))+\alpha(6\alpha+6(1-\gamma))+(1-\gamma)(6\alpha+6(1-\gamma)))=4 \\ 0.5((1-\beta)(6(1-\beta)+6\delta)+\delta(6\delta+6(1-\beta))+(1-\alpha)(6(1-\alpha)+6\gamma)+\gamma(6\gamma+6(1-\alpha)))=8 \end{cases}$$

This system has been numerically resolved and no solution has been found. Nevertheless, the error bars of the coordination numbers have not been taken into account. A deeper analysis is thus necessary to discard or not the $RS2$, the $RS3$ atomic arrangements or the zinc-blende model (which is a particular case of the $RS3$ model).

In the first shell, the contracted nearest Ge-Ge distance relative to the value of the Ge bulk (2.45 Å), indicates that Ge-Ge bonds in the iso-strain region associated to h =3.97 are subject to compressive strain. It can be also noticed that the Ge-Ge interatomic distances in the second (3.91±0.03Å) and for the triangular multiple scattering path (4.32±0.04Å) are significantly shorter than the corresponding values of $4\mathring{A}$ and $4.45\mathring{A}$ in Ge bulk. From the first shell bond lengths R_{Ge-Ge} (2.41 $\mathring{A}$) and R_{Ge-Si} (2.38 $\mathring{A}$), the local strain in the nearest neighbor around Ge is mainly accomodated by the bond bending. The observed Ge-Ge interatomic distances of the second shell and the triangular multiple scattering path are shorter than the corresponding values in Ge bulk. This indicates that the compressive strain is accomodated by stretching the higher shell Ge-Ge bonds. The Ge-Ge interatomic distances obtained by EDAFS allow us to estimate the strain-induced tetragonal distortion of the Ge lattice in the islands for the iso-strain regions associated to h=3.97. The in-plane strain is calculated, with respect to relaxed bulk Ge, as $\epsilon_{//}=(a_{Ge,GIXD}-a_{Ge,bulk})/a_{Ge,bulk}=-0.031$, where $a_{Ge,GIXD}$ is the lattice parameter obtained from grazing incidence X-ray diffraction (h=3.97). According to the macroscopic elastic theory [15], the out-of-plane strain ($\epsilon_\perp$) is related to $\epsilon_{//}$ by $\epsilon_\perp=(-2c_{12}/c_{11})\epsilon_{//}$=0.0235, where c_{11}=14.75x10^{10} Pa and c_{12}=5.58x10^{10} Pa are elastic constants of $Si_{0.48}Ge_{0.52}$. The in-plane strain calculating using the Vegard's law (x_{Ge} =0.52 from MAD analysis) gives $\epsilon_{//}=-0.018$, which is lower than the obtained experimental value $\epsilon_{//}=-0.031$, demonstrating that the unit cell is in-plane compressed. As the first order approximation, the distortion of Ge-Ge covalent bond due to biaxial compressive strain can be evaluated from the microscopic model proposed by Woicik *et al.* [16]. The contraction of the bond length of the Ge-Ge first shell is $\Delta R_1=(2\epsilon_{//}+\epsilon_\perp)R_1/3=-0.031$Å, and the anisotropical shifts of the tetragonal bond angle are $\Delta\theta=\sqrt{2}(c_{11}+2c_{12})/(c_{11}-c_{12})\Delta R_1/R_1=-2.95°$ and $\Delta\theta'=-\Delta\theta/2=1.46°$, where θ and θ' are the bond angle in- and out-of-plane, respectively. Calculated from the bond angle shifts, the in-plane Ge-Ge interatomic distance in the second shell R_2 is $2R_1 sin(\frac{\theta}{2})$ = 3.863 Å, with $\theta\sim(109.47+\Delta\theta)°$; which is lower than the values obtained by EDAFS. This means that the islands do not follow a biaxial strain behavior. Supposing a biaxial strain behavior, the out-of-plane lattice parameter c follows $c=c_{Ge}(1+\epsilon_\perp)=5.67$ Å. From the first neighbor distance $\sqrt{(\frac{a\sqrt{2}}{4})^2+(\frac{c}{4})^2}$ or from the second neighbor distance $\sqrt{(\frac{a}{2})^2+(\frac{c}{2})^2}$, and keeping in mind that $a=a_{Ge,MAD}$ value provided in MAD, the $c=c_{Ge,EDAFS}$ value can be deduced, either

$c = 5.75$ Å from the first shell distance or $c = 5.59$ Å from the second shell distance. These values are no so far as that obtained supposing a biaxial strain. Compared with Ge bulk, the Ge-Ge interatomic distances in the second (3.91±0.03Å) and for the triangular multiple scattering path (4.32±0.04Å) show remarkable contraction of 0.09 to 0.13 Å, which indicates that the mismatch strain appears mainly in the second and higher Ge-Ge coordination shells as observed by Sun *et al.* [13].

EDGE analysis

Analysis of the DAFS edge shape close to the Ge K edge can give information about the Ge and Si relative composition inside different in-plane iso-strain regions of the Ge islands. The Ge occupation factor is dependent on the curvature and depth of the cusp before and at the edge. Figure 9.19 shows the GIXDAFS spectra measured at different iso-strain values h (*i.e.* at different height inside the islands, as a first approximation) for samples Cg267N and Cg267P. The data were normalized in order to compare the curves. In the two cases (nominal and patterned samples), a clear difference appears between the curves collected at h=3.98 and at lower h values. The curvature and depth of the cusp are totally different. A smaller depth is observed for the signal collected at h=3.98. This is the first GIXDAFS signature which confirms the presence of different iso-strain regions inside Ge islands. The difference observed between h=3.98 and the lower h values shows a different Ge composition inside the islands. The iso-strain regions which scattered at h=3.98 are near the island/substrate interface, whereas the iso-strain region which scattered at lower h values are located inside the Ge nanostructures [17]. We observe the following striking findings:

- The GIXDAFS curves of the nominal and patterned parts of sample Cg267 can be super-imposed for h=3.98 and h=3.97. This implies that the Ge islands on both nominal and patterned parts have the same Ge occupation factor for the same h values. This is in good agreement with the MAD results. Despite their different relaxation states, islands on the nominal and patterned parts of Cg267 have the same mean Ge concentration.

- For all h values lower than 3.98 ($h < 3.98$), the GIXDAFS curves of the nominal and patterned parts of sample Cg267 can be super-imposed. A iso-strain study has shown that the iso-strain regions which scattered at h=3.97 is located around z=5-7nm, where z is the island height; and the iso-strain regions which scatter at h=3.93-3.94 are located at z=15-20nm. Thus different volumes located at different z values inside the islands are probed. The super-imposition of the curves reveals a constant mean Ge occupation factor for z >5-7nm. Contrary to what was previously postulated, after a certain height, the mean Ge composition shows small variations inside the islands.

The GIXDAFS spectrum at h=3.97 (Fig. 9.20) has been fitted using the experimental f'_{Ge} and $f"_{Ge}$ of a Ge thin film and letting a free displacement for Si and Ge atoms inside the unit cell.A good fit has been obtained with x=0.52±0.01 and with Si atoms slightly displaced from Ge atoms ($R_{Si-Ge} < R_{Ge-Ge}$) which confirms MAD results and the compressive strain inside the GeSi unit cells.

Summary

EDAFS has been used to study the local structures of Ge islands grown on nominal and pre-patterned Si(001) substrates. The EDAFS analysis was performed to obtain the structural parameters for the first to third coordination shells around Ge atoms at h=3.97 for sample Cg267N. From the first shell bond lengths R_{Ge-Ge} (2.41 $\mathring{A}$) and R_{Ge-Si} (2.38 $\mathring{A}$) as well as the estimated bond angle distortion $\Delta\theta$ (4.06°) and $\Delta\theta'$ (2.03°), the local strain in the nearest neighbor around Ge is mainly accomodated by the bond bending. The observed Ge-Ge interatomic distances of the second shell and the triangular multiple scattering path are shorter than the corresponding values in Ge bulk. This indicates that the compressive strain is accomodated by stretching the higher shell Ge-Ge bonds. This implies that the mismatch strain appears mainly in the second and higher Ge shells. The islands are strongly

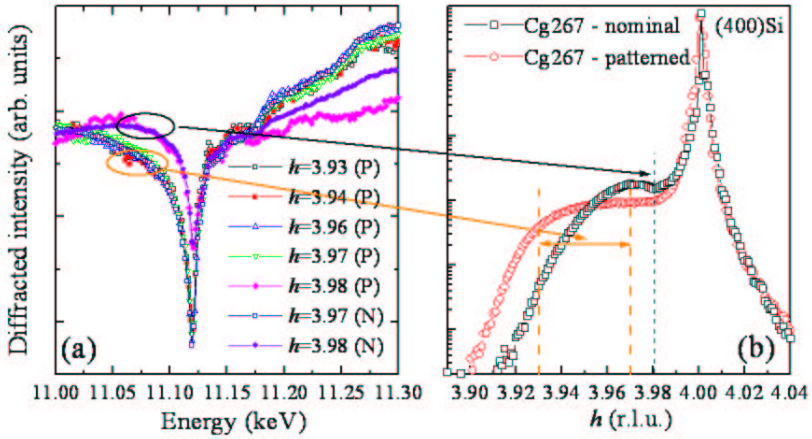

Figure 9.19: (a) GIXDAFS spectra measured at different h values on the nominal and patterned parts of sample Cg267. The letters N and P refer to the nominal and patterned samples. (b) (400) Radial scans of the nominal and patterned parts of sample Cg267. The arrows and lines indicate for which h values the GIXDAFS spectra were measured.

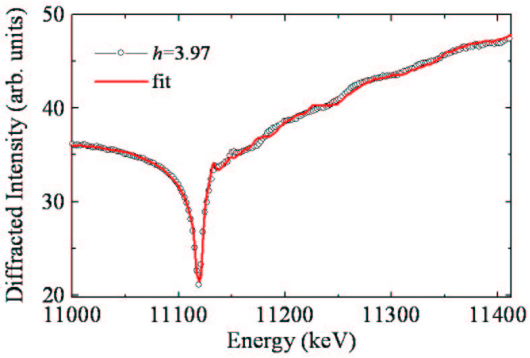

Figure 9.20: Open circle: GIXDAFS spectrum measured at h=3.97 on the nominal part of sample Cg267. Solid line: simulation performed with experimental f'_{Ge} and $f"_{Ge}$ of a Ge thin film.

intermixed with Si. The obtained composition value (57%) at h=3.97 is in agreement with MAD results. This means that no scattering from the Si substrate is observed at this radial position. In addition, we demonstrate that the lower average Ge weighting factor in the second shell cannot be correlated to atomic ordering, supposing an $RS2$ or $RS3$ atomic arrangement.

9.1.8 GI-MAD on asymmetric reflection.

A complete analysis of the strain inside the islands can be outlined by correlating the in-plane strain ($\epsilon_{//}$) and the out-of-plane strain ($\epsilon_{\perp}$). In order to separate these strain contributions in reciprocal space and to analyse the composition of QDs, three dimensional out-of-plane anomalous mapping

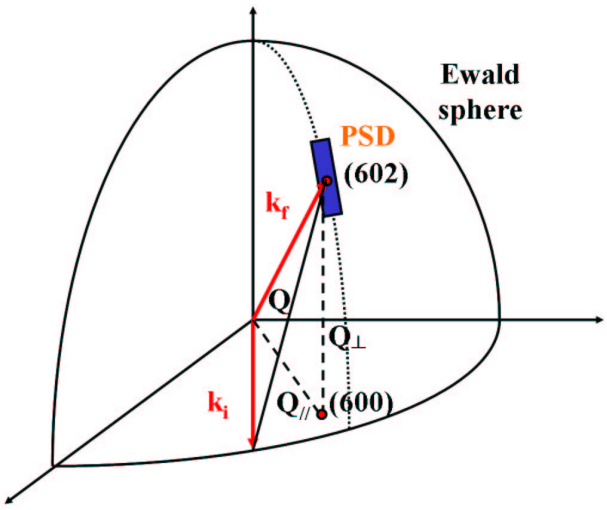

Figure 9.21: Ewald sphere construction for reciprocal-space mapping using a PSD detector.

were performed at the (602) asymmetric reflection [18, 6]. The scattered intensity was collected with a position sensitive detector (PSD) perpendicular to the [602] direction. Radial scans around the (602) reflection were made for twelve energies (using the MAD - Multiwavelength Anomalous Diffraction method [19] around the Ge absorption edge. In this section, grazing incidence diffraction (GIXD) was used in combination with X-ray reciprocal space mapping to infer the three dimensional strain and chemical composition of Ge islands. This technique gives access to the tetragonal distortion of the unit cells inside the islands. The interdiffusion profile was determined by two-dimensional MAD. The incident angle was fixed at 0.28°. The structure factors of the Ge and Si atoms and the Ge composition were extracted with the NANOMAD program at every point of the PSD along the scan direction for samples Z576N, Z576P, Z25. The results (Figs. 9.23, 9.24, 9.25) are shown in (h, k, l) reciprocal lattice units. As the α_f resolution element of the PSD describes a curved line in reciprocal space, the shift of the maximum intensity position along the exit angle α_f versus the h value had to be corrected [20].

It is possible to distinguish different structures in these maps. The Si(001) substrate Crystal Truncation Rod (CTR) [21] is observed along the l direction for h=6. Another line appears due to the saturation of intensity at the (602) reflection. For all maps, no scattered intensity is found at the Ge bulk (*unstrained*) position (h ∼5.76 and l ∼1.92).

A cubic material with lattice constant a, which is compressively strained to the lattice parameter $a_{//}$ in the (100) plane, will react with an expansion in the perpendicular direction to

$$a_\perp = a(1 + \frac{a - a_{//}}{a_{//}} \frac{1 + \nu_{100}}{1 - \nu_{100}}), \tag{9.7}$$

where ν_{100} is the Poisson coefficient along the [100] direction. The Poisson coefficient can be described as

$$\nu_{100} = \frac{3K - 2\tilde{C}}{6K + 2C}, \tag{9.8}$$

where $C = c_{44}$, $\tilde{C} = \frac{c_{11} - c_{12}}{2}$ and $K = \frac{c_{11} + 3c_{12}}{3}$ describe respectively the shear resistance for shearing the (100) plane in the [010] direction, the shear resistance for shearing the (110) plane in the $[1\bar{1}0]$ direction and the resistance against compression under hydrostatic pressure, respectively.

Thus, the biaxial in-plane strain leads to a vertical expansion of the Ge unit cells. Pure pseudomorphic tetragonally distorted Ge is thus localized at h ∼6 and l ∼1.764. The knowledge of the elastic constants of Si and Ge allows to link a position in reciprocal space with a certain composition,

	Elastic constants of Si	Elastic constants of Ge
c_{11}	167.5 GPa	128.9 GPa
c_{12}	63.9 GPa	48.3 GPa
c_{44}	79.6 GPa	67.16 GPa

Table 9.4: Elastic constants of Si and Ge.

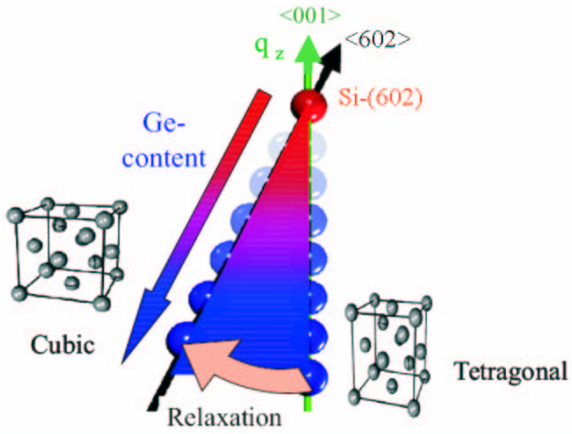

Figure 9.22: Reciprocal lattice points for the (602) reflection of Si (red sphere), relaxed Ge, and pseudomorphic Ge (blue spheres). The transparency of the blue spheres approaching the Si indicate decreasing Ge content. Courtesy of T. Schülli.

according to the native lattice constant of Si and Ge and to their tetragonal distortion. For each sample, two relaxation triangles are plotted, for the alloy composition of $Si_{0.5}Ge_{0.5}$ and for pure Ge. Two mechanims can be responsible for changes in the unit cells volume inside Ge islands: interdiffusion and elastic deformation (strain).

In all cases (see Fig. 9.23, 9.24 and 9.25), the island scattering intensity distribution shows the sign of the tetragonal distortion of the island lattice. At the islands basis, where the in-plane lattice parameter is close to Si ($h = 6$), the tetragonal distortion is stronger and the unit cells exhibit a bigger vertical lattice parameter (the diffuse scattering extends to lower l values). The tetragonal distortion is stronger for islands grown on Z576N compared to the islands grown on Z576P as the Ge structure factor is located at lower l values close to Si. At the basis of the islands, a higher compressive strain is thus observed in islands grown on nominal samples. Inversely, at the top of the islands, *i.e.* for small h values, the in-plane lattice parameter is closed to that of bulk Ge for a pure Ge composition. This leads to a lower expansion of the vertical unit cell dimension.

In Fig. 9.23, scattered intensity from Ge-{111} facetted pyramids (sample Z576P) is observed around (h, l)$\sim$(5.92,1.94). A l-cut in the reciprocal space map through the Ge region for high l value presents more than one intensity peak for sample Z576P. This indicates that the islands are not characterized by a monotonic relaxation of lattice parameter from bottom to top. Fig. 9.24 shows that the (602) Ge structure factor map of sample Z576N clearly presents two relaxation regions. The sample is composed of both domes and superdomes. The scattering from superdomes is localized at low h values ($h \sim$5.87) as dislocated islands present a higher in-plane relaxation. The dome scattering intensity distribution is localized at $h \sim$5.92. Sample Z25N (see Fig. 9.25) is only composed of domes which scatter near the position: (h, l)$\sim$(5.93,1.94).

Regions corresponding to strained Si structures are observed in all Si structure factor maps. In all cases, the Si region at the left side of the (602)Si Bragg peak has a larger in-plane lattice parameter as compared to bulk Si. This type of distortion is found in regions located below Ge islands. The tensile

strain leads to a reduction of the vertical dimension of the Si unit cells. The Si region at the right side of the Si Bragg peak corresponds to compressed Si in the substrate close to the island edge. This has been predicted by finite-element simulations and observed by transmission electron microscopy.

The exact composition and location of each strained region is directly evaluated by multiwavelength anomalous diffraction. Looking at the (602) composition maps, the maximum of Ge concentration of samples Z576P, Z576N and Z25N is about 88%, 67% and 94%, respectively. The composition obtained for sample Z25N may be overestimated due to saturations of the detector. What is important to notice is the variation of composition in the Ge scattering region. The Ge scattering region of the patterned Z576 sample shows small variation of composition ($\sim 55 \pm 15\%$) over a large zone. The same behaviour is observed for the scattering of domes of the nominal Z576 sample and of the nominal part of the Z25 sample. As mentionned above, the nominal Z576 sample is composed of domes and superdomes which scatter at different (h, l) positions. The (602) composition map of Z576N and Z25N (Figs. 9.24 and 9.25) clearly shows an almost constant composition in the scattering region of domes. This is in good agreement with what has been observed with GI-MAD around in-plane reflection (see Figs. 9.14 and 9.15). In all cases, the mean vertical Ge composition is almost constant inside a large volume of the islands, expect at the island basis. This does not exclude the variation of the lateral composition inside islands.

Fig. 9.24 also shows that the superdomes are less Si intermixed than domes. This is explained by the fact that dislocated islands are more relaxed and thus preferred with respect to domes for Ge attachment. It can be observed that the coherent islands of sample Z576N are more Si intermixed than the one of its corresponding patterned part (sample Z576P). Incoherent islands are only observed on sample Z576N. This is explained by the fact that Ge atoms will preferentially attached to dislocated islands, reducing thus the Ge content in coherent islands.

An alternative approach to qualitatively evaluate the Ge composition in these maps have been previously suggested by T. Schülli. The black lines represent the pseudomorphic relaxation of a $Si_{0.5}Ge_{0.5}$ alloy under a biaxial strain and the pseudomorphic relaxation of pure Ge. By using this technique only an average Ge content is obtained. The qualitative approach and MAD estimations are in good agreement for sample Z576P. In constrast, a higher or lower composition is obtained by MAD analysis along the iso-50% Ge line for sample Z25N and Z576P, respectively. This implies that the coherent islands of sample Z25N or Z576N are more strained or more relaxed, respectively compared to those of sample Z576P.

To sum up, anomalous 2D maps reveal that at the basis of the islands higher compressive strain is observed in islands grown on nominal samples. As mentioned above, the higher is the compressive or tensile strain $\epsilon_{//}$, the higher is the elastic energy stored by the deposited elements. This reveals that as early as the beginning of the growth, pre-patterning causes a redistribution of the elastic energy between islands and substrate. Moreover, drastic variations of the composition are not observed inside a large volume of the islands. As previouly mentioned, this does not exclude the possibility of lateral variation of the Ge composition inside the islands.

9.2 Lateral composition of the islands.

Previously, we demonstrate that islands grown on nominal (Z25N, Cg267N) and patterned (Z25P, Cg267P) substrates show the same mean vertical composition. In this section, we will study the variations of lateral composition between islands grown on nominal and pre-patterned substrates. A proper analysis of anomalous X-ray diffraction data collected from a uniformly sized ensemble of epitaxial islands can provide quantitative 3D composition maps. First, we will determine the lateral composition of the new shaped islands ({111} pyramids) observed on sample Z576P.

9.2.1 Lateral composition of the patterned sample Z576.

The pre-patterned template Z576 is composed of {111} facetted pyramids. Complete diffuse scattering maps in (q_r, q_a) space near the (220) and (400) in-plane reflection were performed at two energies:

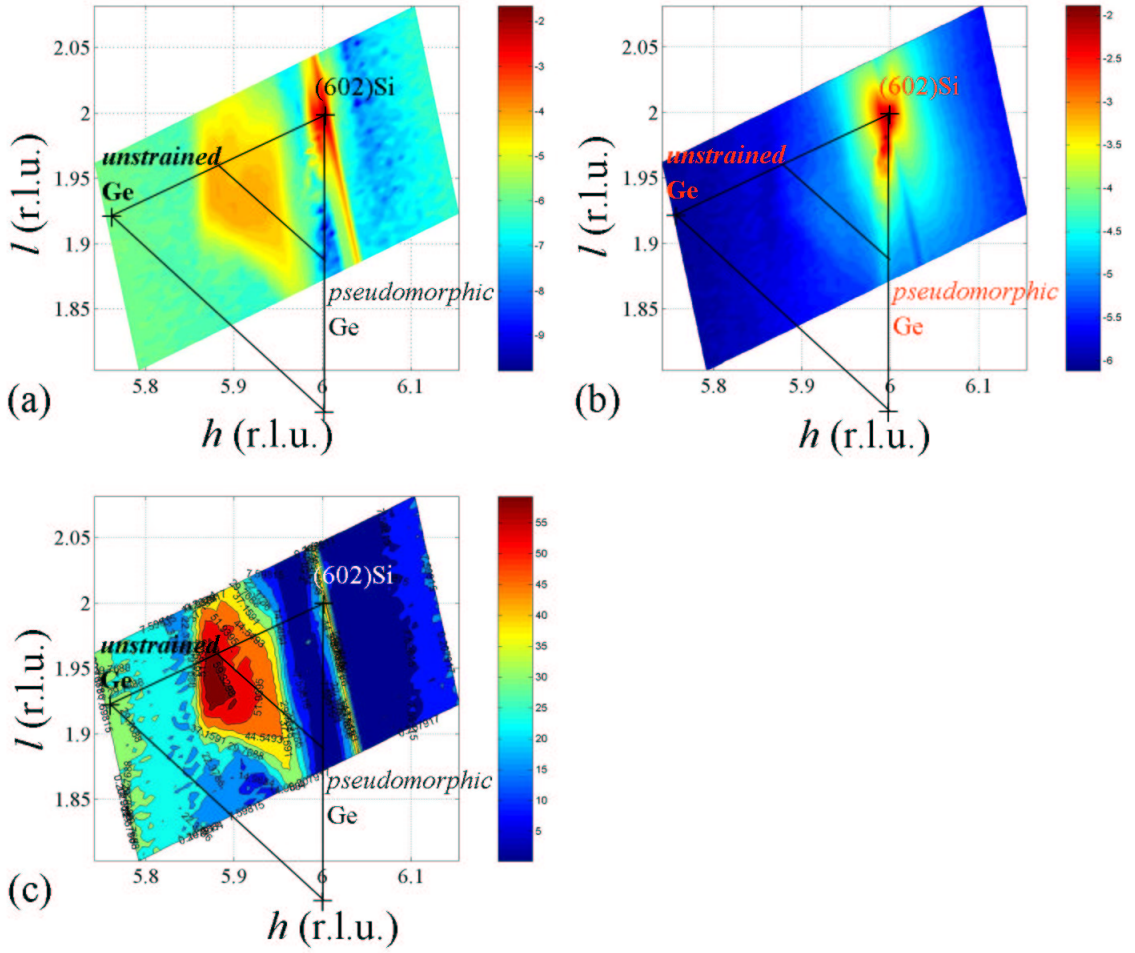

Figure 9.23: Extracted Ge (a) and Si (b) structure factors of sample Z576P and corresponding composition (c). The relaxation triangles for Ge and $Si_{0.5}Ge_{0.5}$ are plotted.

E_1=11.106 keV and E_2=11.061 keV. In the two different energy maps only the scattering power of Ge is changed. Hence any intensity variation from one map to the other is associated with the presence of Ge atoms. The two reciprocal space maps around the (220)Si Bragg peak are shown in figure 9.26. As a first observation, the broad profiles in the h direction indicate a large lattice parameter distribution within the {111} facetted pyramids. The scattering intensity at 11.061 keV is higher than at 11.106 keV, consistent with an energy dependent atomic scattering factor for Ge. The maxima present in both maps indicate a narrow size distribution, as expected from the AFM statistics.

In the (220) maps, large diffuse scattering appears in the [110] and [1$\bar{1}$0] directions as a result of the scattering from the {111} facets which create rods in the $< 110 >$ planes.

As a first approximation, the iso-strain regions of pyramid-shaped islands (Fig. 9.27) are analytically described by cylinders.

The analysis did not take into account the curvature [17] of the iso-strained domains. The simplest composition profile for an equal-lattice parameter disk of radius R, centered at x=0 is

$$C_{Ge}(x) = C_{Ge}(x=0) + (C_{Ge}(x=R) - C_{Ge}(x=0))[\frac{x}{R}]^2 \tag{9.9}$$

where $C_{Ge}(x=0)$ is the Ge concentration at the center of the disk and $C_{Ge}(x=R)$ is the Ge

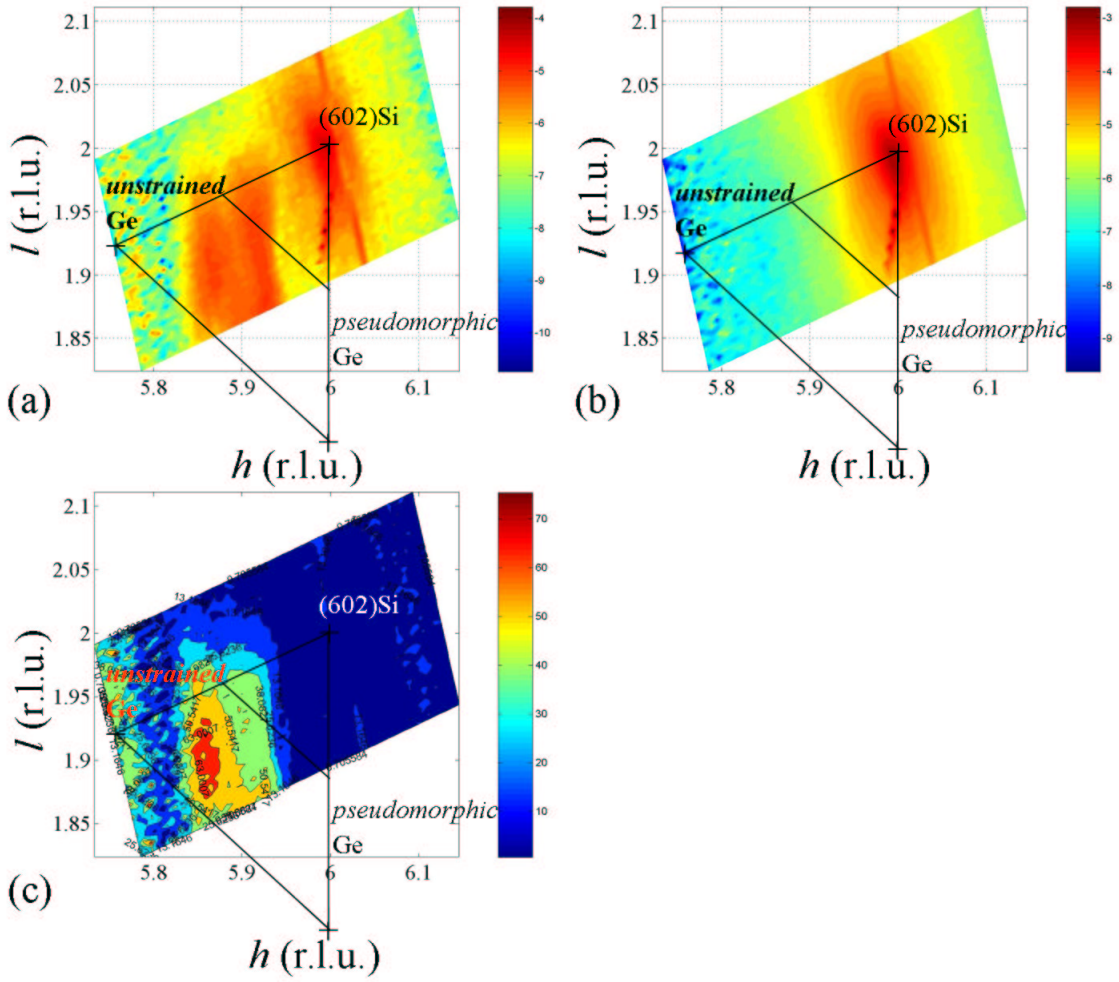

Figure 9.24: Extracted Ge (a) and Si (b) structure factors of sample Z576N and corresponding composition (c). The relaxation triangles for Ge and $Si_{0.5}Ge_{0.5}$ are plotted.

concentration at its border, both varying between 0 and 1. The angular contribution of each iso-strained Ge/Si disk with constant radius R is given by

$$I(q_a, R) \propto \left| \int_{-R}^{R} \frac{\mathrm{e}{-\mathrm{i}q_a x g(x)}}{R^2}\, dx \right|^2 , \tag{9.10}$$

where $g(x) = C_{Ge}(x) \cdot f_{Ge} + [1 - C_{Ge}(x)] \cdot f_{Si}$ is the effective scattering factor of the GeSi alloy at position x. The equal lattice parameter regions of different islands may have different radii. A gate distribution of length σ has been chosen to simulate the angular profile

$$I(q_a, R) \propto \left| \int_{R_1-\frac{\sigma}{2}}^{R_1+\frac{\sigma}{2}} \int_{-R}^{R} \frac{\mathrm{e}{-\mathrm{i}q_a x g(x)}}{\sigma R^2}\, dx \right|^2 dR, \tag{9.11}$$

where $R_1 - \frac{\sigma}{2}$ and $R_1 + \frac{\sigma}{2}$ are the smallest and largest radii of equal-lattice parameter regions.

Several fits with different Ge profiles were performed for a pair of angular scan at $Q_r \sim 3.233\mathring{A}$ in Fig. 9.26. A homogeneous composition will lead to identical line shapes, as represented by black

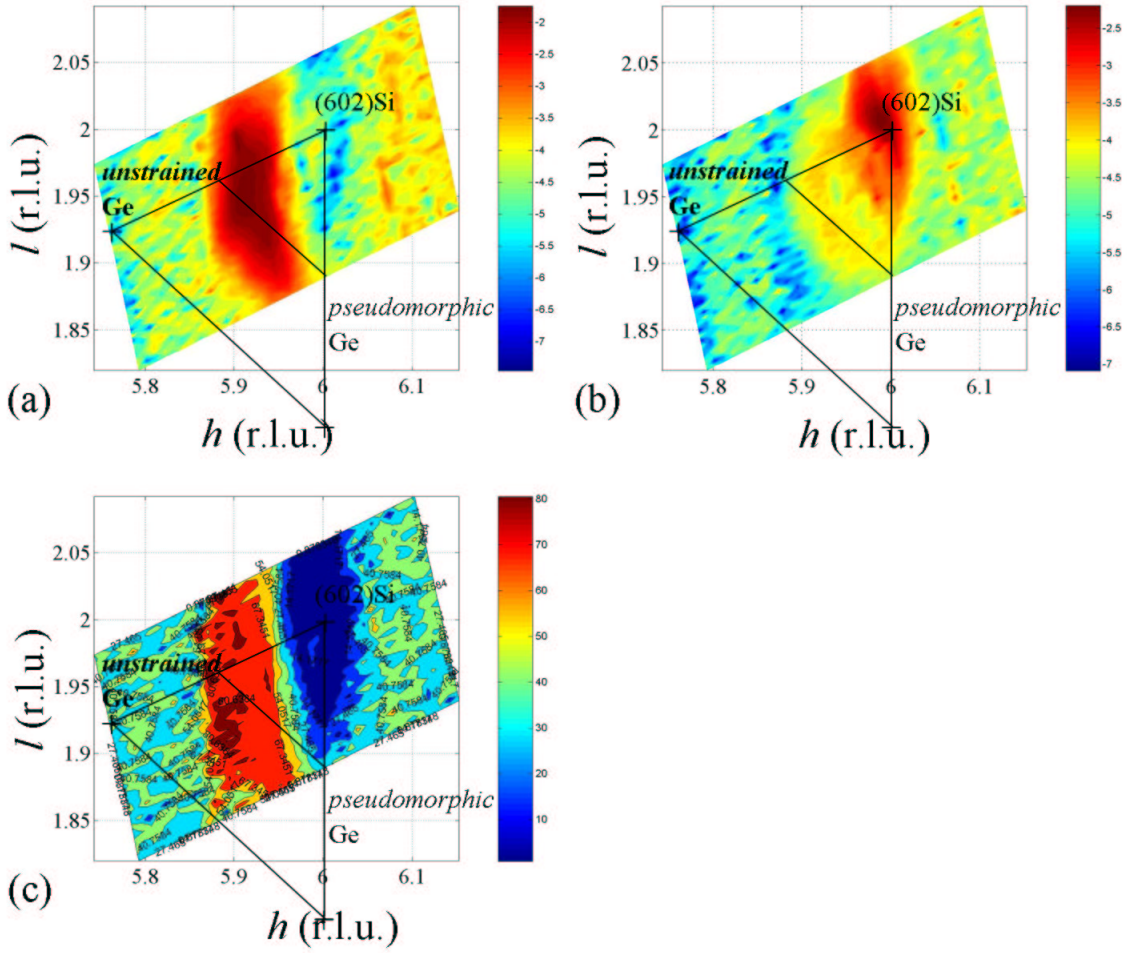

Figure 9.25: Extracted Ge (a) and Si (b) structure factors of sample Z25N and corresponding composition (c). The relaxation triangles for Ge and $Si_{0.5}Ge_{0.5}$ are plotted.

dashed lines in both figures. The sensitivity of the technique is demonstrated by comparing fits with a Si center and a pure Ge border or fits with a Ge center and a pure Si border. Best fits (see red and cyan curves) can be obtained for $C_{Ge}(0)$=0.45 and $C_{Ge}(R) \in [0.5, 1]$. The 3D composition results must agree with the MAD results (see Fig. 9.12 (a)) obtained from radial scans. The scattering intensity measured along the radial line (q_a=0) corresponds to the average concentration of the equal-lattice regions. The integration of the total Ge composition of each equal-lattice parameter by averaging the profiles used to fit angular scans should be comparable to the vertical composition profile (see Fig. 9.29). To be in agreement with the MAD results obtained from radial scans, the best chemical profile is obtained for an alloyed ($C_{Ge}(1)$ =0.85) border and not a pure Ge border.

The fits (cyan lines) in Fig. 9.28 were performed simultaneously for the two energies using the $I(q_a)$ dependence on $R_1 - \frac{\sigma}{2}$, $R_1 + \frac{\sigma}{2}$, $C_{Ge}(R)$ and $C_{Ge}(0)$, which are the fitted parameters. In adjusting these parameters and comparing the results with the MAD results in radial direction (see Fig. 9.12 (a)), the best chemical profile for each equal-lattice parameter region was extracted. Figure 9.28 shows three Ge composition profiles corresponding to different lattice parameters, *i.e.*, different heights within the islands. With increasing height, the island border is more and more Si intermixed. This differs from what has been observed by A. Malachias *et al.* [22] who fixed the composition of the Ge border equal to 1. The Ge concentration at the center varies from 0 to 0.65 from the base to the apex of the islands.

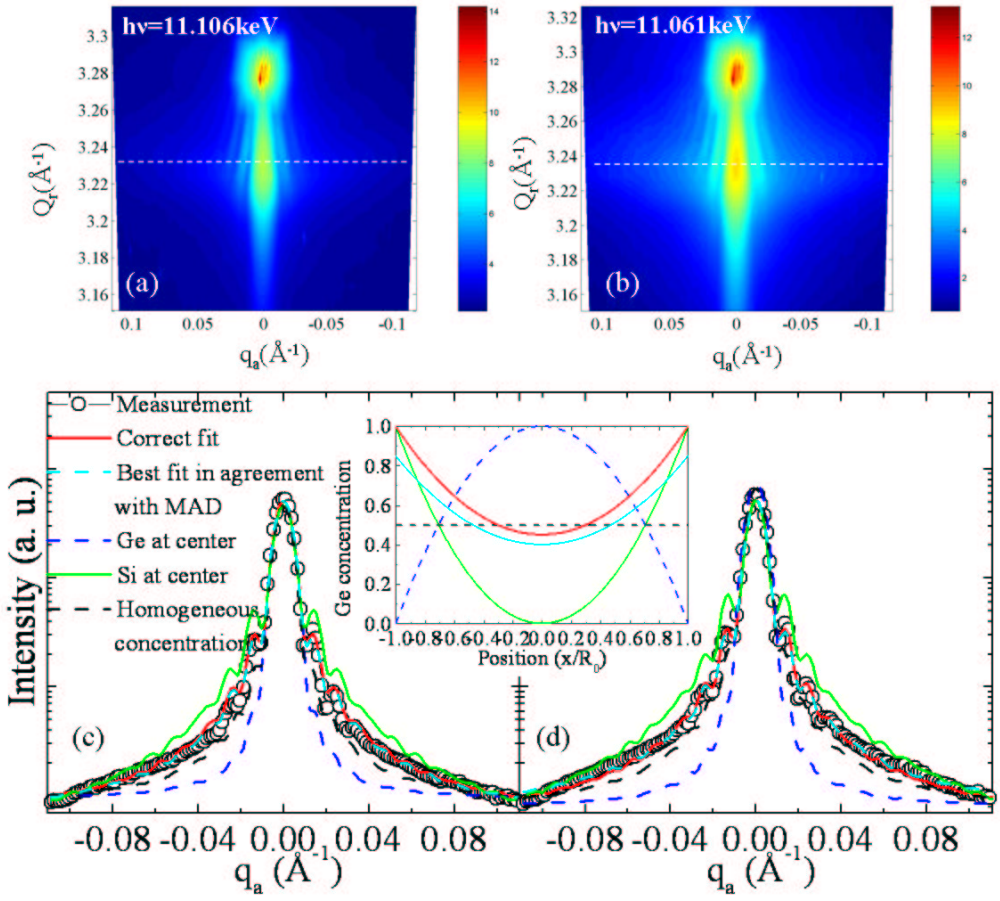

Figure 9.26: (a)-(b) Reciprocal space maps around the (220) reflection using two different X-ray energy: 11.106 keV and 11.061 keV. (c)-(d) Angular scans at constant Q_r corresponding to the dashed line. Several fits corresponding to different lateral profiles are shown. The corresponding Ge profiles are plotted in the inset.

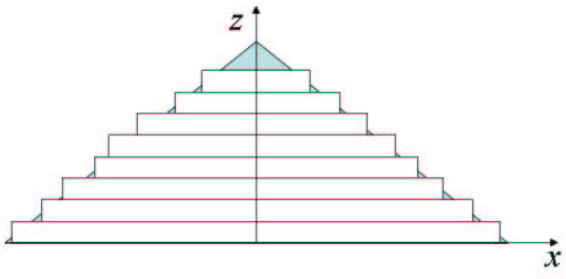

Figure 9.27: Schematic drawing of the iso-strain regions of pyramid-shaped islands. The curvature of the iso-strain domains is not taken into account.

This analytical treatement reveals the presence of a Si-rich core inside the {111} facetted pyramids.

At the pyramid apex, a smearing of the maxima occurs. This has been explained by A. Malachias [22]; the equal-lattice parameter regions within the island ensemble have a broader range of radii. At the reverse, towards the base, the subsidiary maxima sharpen, indicating a narrower range of radii, which is consistent with steeper facets. The integration of the total Ge composition of each equal-lattice parameter by averaging the profiles used to fit angular scans is comparable to the vertical composition profile (see Fig. 9.29)

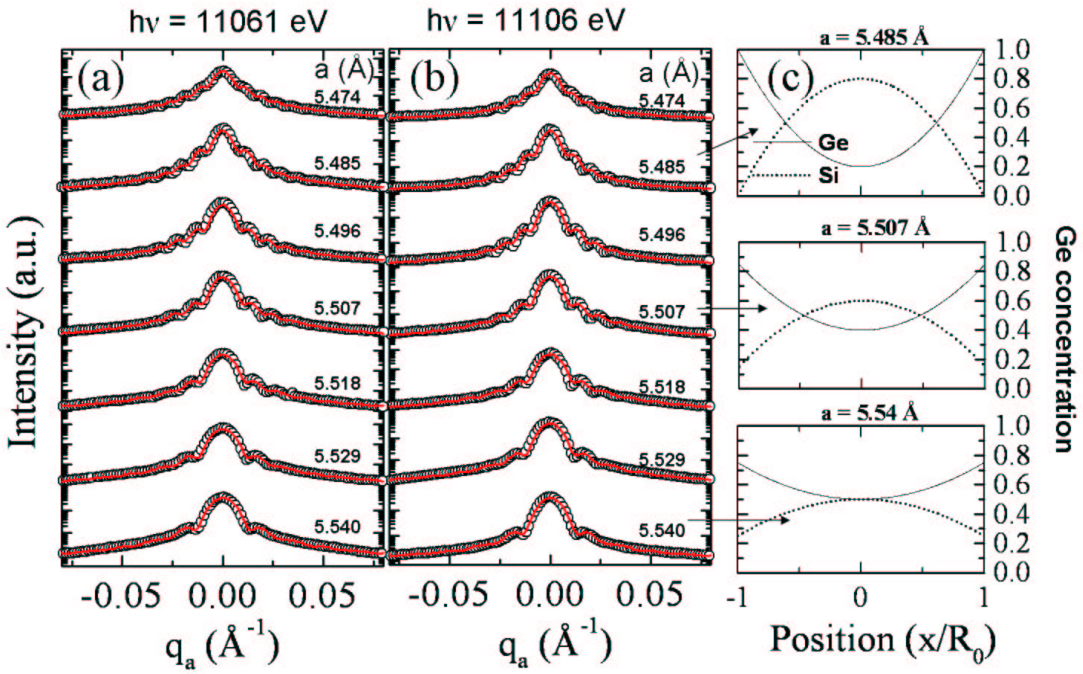

Figure 9.28: (a)-(b) Angular scans performed on sample Z576 around the (220) reflection. The fits were performed to extract the Ge composition profile suited to each equal-lattice parameter region. Some selected profiles are shown in (c).

Fig. 9.32 (a) shows a schematic drawing of the 3D Ge composition profile inside the {111} facetted pyramids. The pyramids present a Si rich core. Ge is observed to segregate towards the surface. The same lateral composition has been observed by Katsaros *et al.* [23] inside pyramids grown at 700°C. This lateral composition was probed to be the result of growth kinetics. Enhancement of diffusion at high enough temperatures may lead to an homogeneous distribution of Si inside the core of the islands. Note that to be consistent with MAD results, the best chemical profile is obtained for an alloyed border and not a pure Ge border.

The analysis was performed around the Si(220) Bragg peak. This allowed to probe the composition profile along the [110] direction, *i.e.* perpendicular to the facets. The same analysis can be performed along the [100] direction by fitting angular scans around the Si(400) Bragg peak. In our case, this was not possible as the $< 111 >$ streaks coming from facets smear the subsidiary maxima of the island form factor (see Fig. 9.30).

In the following, we will perform the same analysis to compare the lateral composition between islands grown on nominal and pre-patterned substrates.

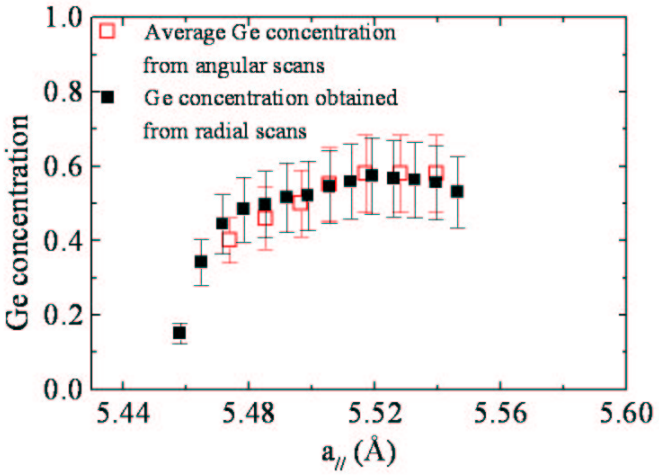

Figure 9.29: Vertical Ge concentration obtained by fitting the angular scans and by the MAD analysis from radial scans.

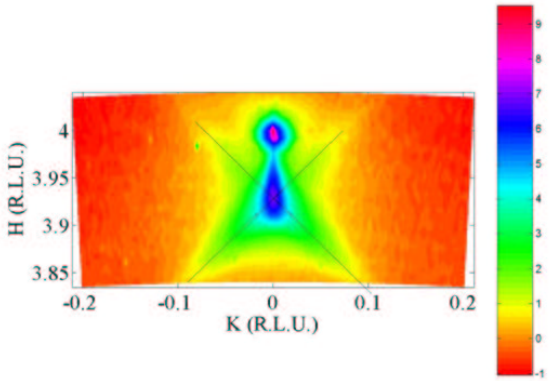

Figure 9.30: Reciprocal space map around the (400) reflection at 11.061 keV. Streaks along the $< 110 >$ directions (see black lines) come from diffuse scattering from {111} facets of the pyramids.

9.2.2 Lateral composition of the nominal and pre-patterned parts of sample $Z25$.

The pre-patterned and nominal parts of sample $Z25$ are composed of domes with {113} and {15 3 23} facets at their basis and {105} facets at their top. Complete diffuse scattering maps in (Q_r, q_a) space were performed near the (400) in-plane reflection for the nominal and pre-patterned parts of sample $Z25$ (see Fig. 9.31). The maxima present in both maps indicate a narrow size distribution, as expected from AFM statistics. The (400) reciprocal space map of the pre-patterned part of sample $Z25$ shows a broader profile in the h direction, indicating that islands are more relaxed in the pre-patterned region.

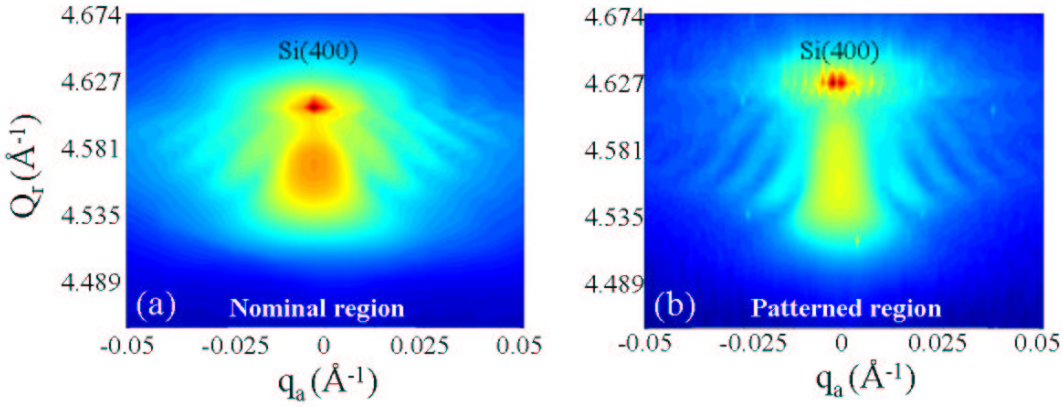

Figure 9.31: Reciprocal space maps around the (400) reflection at 11 keV for the nominal (a) and patterned (b) parts of sample $Z25$.

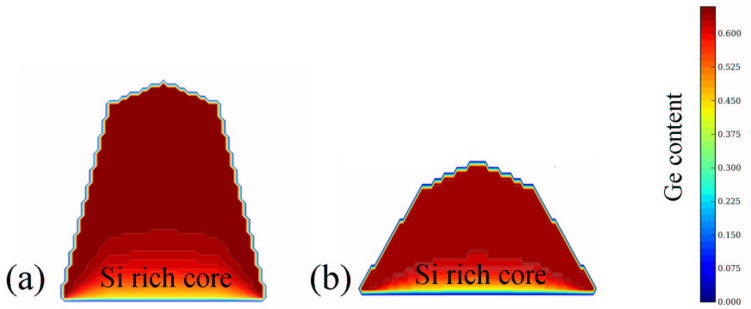

Figure 9.32: Schematic drawing of the composition profile of samples (a) Z576P and (b) Z25P.

A. Lateral composition of the pre-patterned part of sample $Z25$.

Angular fits were performed using the I(q_a) dependence on $R_1 - \frac{\sigma}{2}$, $R_1 + \frac{\sigma}{2}$, $C_{Ge}(R)$ and $C_{Ge}(0)$, which are the fitted parameters (see Fig. 9.33 (a)). Adjusting these parameters and comparing the results with the MAD results in radial direction, the best chemical profile for each equal-lattice parameter region was extracted. Figure 9.33 (b) shows three Ge composition profiles corresponding to different lattice parameters, *i.e.*, different heights within the islands. With increasing height, the island border is more and more Si intermixed. The Ge concentration at the center varies from 0 to 0.65 from the base to the apex of the islands. This analytical treatement reveals the presence of a Si-rich core inside the domes grown in the pre-patterned region, as observed for the {111} facetted pyramids grown on the pre-patterned sample $Z576P$. A qualitatively similar compositional profile was reported for instance by G. Katsaros [23] for domes grown at 620°C, near our growth temperature ($T = 650$°C). This composition profile is explained by a simple model that is of kinetic origin and relies just on surface diffusion phenomenon: the adatom surface diffusivity is enhanced at high temperature. Note that the same profile (*i.e.* Si rich core and Ge enrichment at the island border) is observed for the patterned part of sample Cg267, performed nearly with the same growth conditions as sample Z25P.

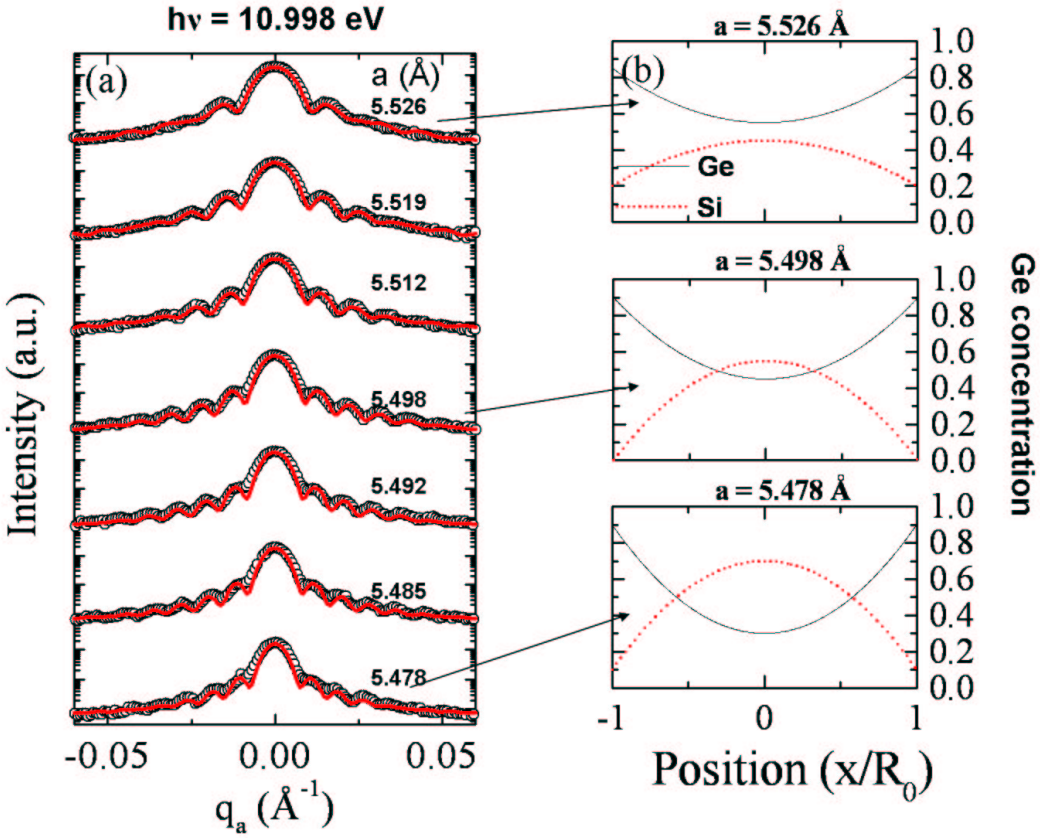

Figure 9.33: (a) Angular scans performed on the patterned part of sample $Z25$ around the (400) reflection. The fits were performed to extract the Ge composition profile suited to each equal-lattice parameter region. (c) Some selected profiles are shown in the right-hand of the figure.

B. Lateral composition of the nominal part of sample $Z25$.

The same analysis was performed for the nominal part of sample $Z25$. Adjusting the $R_1 - \frac{\sigma}{2}$, $R_1 + \frac{\sigma}{2}$, $C_{Ge}(R)$ and $C_{Ge}(0)$ parameters and comparing the results with the MAD results in radial direction, the best chemical profile for each equal-lattice parameter region was extracted.

Several fits with different Ge profiles were performed at a=5.472 Å in Fig. 9.34. Similarly to the patterned part of sample Z25, the best fit is obtained for a Si rich core. But some differences appear: the Si rich core is reduced and some Si enrichment is observed at the island border. The same lateral profile as the one used to simulate the lateral composition of sample Z25P does not perfectly fit the angular scans of the nominal regions. This implies that islands on nominal and pre-patterned templates do not show the same lateral composition, whereas their mean composition is identical.

Figure 9.35 (b) shows three Ge composition profiles corresponding to different lattice parameters, *i.e.*, different heights within the islands. Good fits are observed with a reduced Si rich core and Si enrichment at the island border.

Note that the same profile (*i.e.* a reduced Si rich core and a small Si enrichment at the island border) is observed for the nominal part of sample Cg267, performed nearly with the same growth conditions as sample Z25N (see Fig. 9.36).

The angular scan analysis of the lateral composition reveals that islands on nominal and pre-

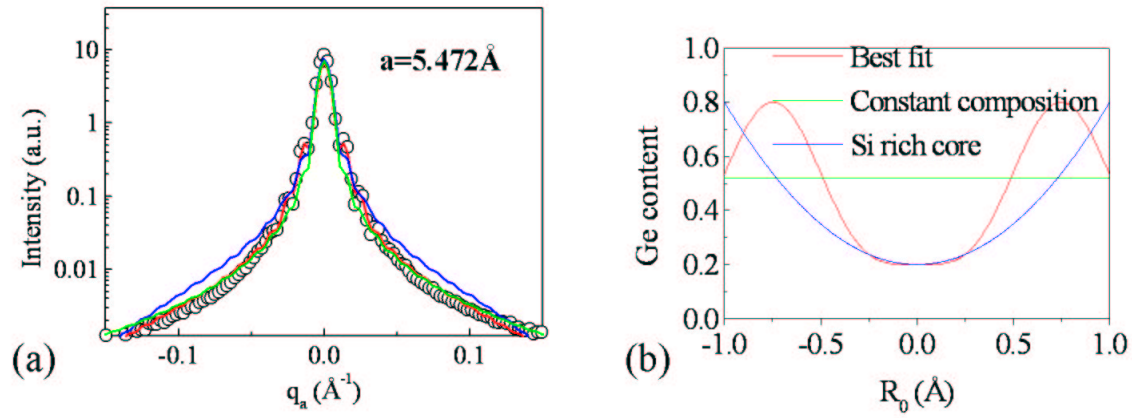

Figure 9.34: (a) Angular scan at constant Q_r corresponding to the island in-plane lattice parameter a=5.472 Å. Several fits corresponding to different lateral profiles are shown. The corresponding Ge profiles are plotted in (b).

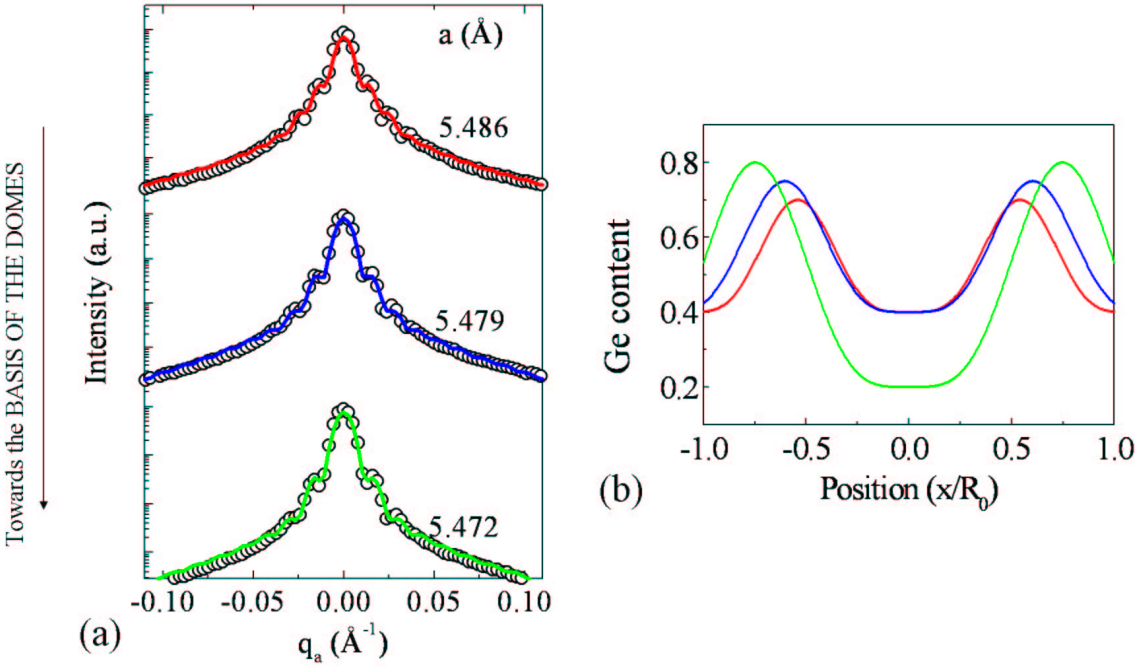

Figure 9.35: (a) Angular scans performed on the nominal part of sample $Z25$ around the (400) reflection. The fit was performed to extract the Ge composition profile (b) suited to each equal-lattice parameter region.

patterned templates do not show the same lateral composition, whereas their mean composition is identical. This has to be confirmed by numerical simulations or selective etching.

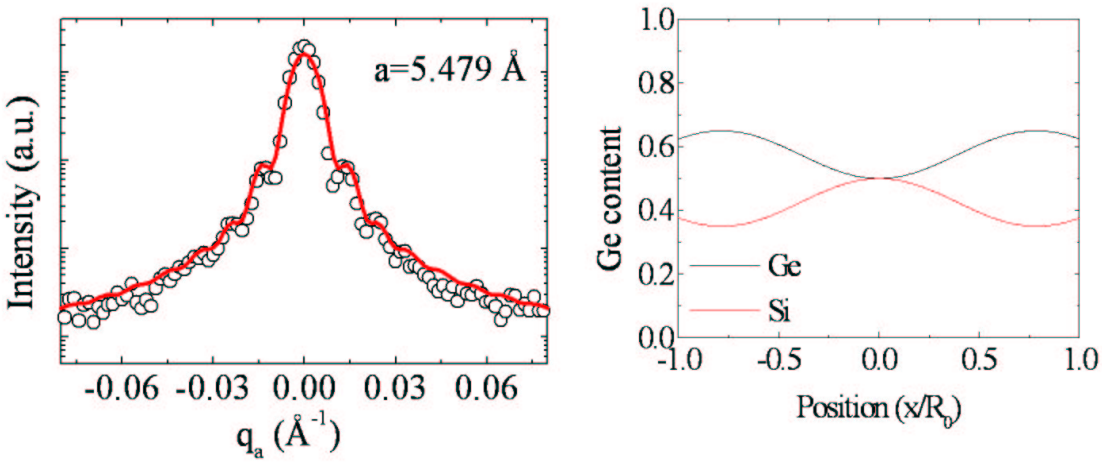

Figure 9.36: Angular scans performed on the nominal part of sample $Cg267$ around the (400) reflection. The fit was performed to extract the Ge composition profile.

9.2.3 Direct evaluation of strain profile and morphology of Ge islands on Si(001) investigated by X-ray scattering

An X-ray scattering method is presented making possible to investigate simultaneously the strain profile, the composition and the shape of uncapped nanocrystals without AFM measurements. The method uses only grazing incidence X-ray diffraction and gives access to the morphology (size and nature of the facetting) of each iso-strain volume composing the nanocrystals.

Grazing incidence X-ray scattering is a well-established method for the investigation of strain, interdiffusion and shape of nanocrystals [1]. The iso-strain scattering method [24] based on grazing incidence X-ray diffraction (GIXD) measurements allows for a direct structural characterization of uncapped nanocrystals without demanding strain field calculations. The anomalous iso-strain scattering technique probes the lateral size, the height and the composition of volume of constant in-plane strain, so-called iso-strain volumes ([25], [26]). In order to fit the data, morphological information from AFM or GISAXS is needed. The data have to be combined with atomic force microscopy (AFM) and/or grazing incidence small-angle X-ray scattering (GISAXS) [27] to determine the morphology (shape and crystallographic facets [28]) of the nano-particles. AFM or GISAXS cannot detect strain.

In this section, we simultaneously profile the strain, composition (see above) and morphology by a single probe, anomalous grazing incidence X-ray scattering (anomalous-GIXD). Without using AFM and/or GISAXS, the nature of crystallographic facets can be determined by GIXD. This means that the morphology of each iso-strain volume and their associated strain and in-plane lattice parameter can be directly evaluated without near field microscopy or other X-ray techniques. Nano-particles are often studied *ex situ*. *Ex situ* AFM or GISAXS are sensitive to the shape of the oxidized particles. As the cristalline properties of nano-objects are most easily measured in the GIXD geometry, anomalous-GIXD allows to measure the cristalline morphology of the nano-particles.

The X-ray scattering experiments were performed at the beamline ID01 at the Synchrotron of Grenoble (ESRF). We use here a reciprocal space coordinate system (q_a, q_r, q_z) connected to the reciprocal space vector $\mathbf{h}$, around which the measurements is performed. The sample is illuminated by the X-ray beam at a shallow incident angle α_i ($\alpha_i \leq \alpha_c$). q_r is the distance from the origin of the reciprocal space in the direction of the $\mathbf{h}$-vector, called radial direction. q_a is the in-plane component of $\mathbf{q} = \mathbf{k}_f - \mathbf{k}_i$ ($\mathbf{k}_{i,f}$ are the wave-vectors of the primary and scattered radiations) perpendicular to q_r and related to the deviation $\Delta\omega$ from the Bragg condition $\omega = 2\theta/2$. q_z is the vertical momentum

tranfer, that defines the distance from the (q_r, q_a) plane. A position sensitive detector (PSD) oriented perpendicular to the sample surface is used to collect all wavevectors $\mathbf{k}_f$ in the vertical (z) direction.

Reciprocal space scans in the directions of these three components have different meanings. Scans in the q_r direction are sensitive to variations in strain. For instance, measurement at fixed $q_r(=q_{r0})$ probes X-rays dominantly scattered from sub-volumes with in-plane lattice parameter

$$a_{//} = 2\pi\sqrt{(h^2+k^2+l^2)}/q_{r0}, \tag{9.12}$$

(h, k, l) are the Miller indexes expressed in reciprocal lattice units (r.l.u.) of Si. The lateral strain with respect to the substrate is

$$\epsilon_0 = (a_{//} - a_{sub})/a_{sub}. \tag{9.13}$$

Scanning the angular component q_a, the size and shape of a region with a fixed lattice parameter can be probed. Finally, scans along q_z can be used to obtain vertical information of the crystalline structure.

The corresponding iso-strain volume can be thus characterized using q_a and q_z scans if the following conditions are fulfilled: (i) the probed iso-strain volume has to spread along a section along the growth direction, which should be small compared to the height of the nanocrystal, H_{nc}. (ii) the change of the island radius along this section should be small a well. (iii) The radius of the iso-strain volume $r(z_0)$ has to be sufficiently large, since the finite size of this volume results in the broadening of the Bragg reflection along the q_r direction. (iv) The strain gradient along the vertical axis $d\epsilon_{//}(z)/dz|_{z=z_0}$ has to be sufficiently large. The iso-strain scattering technique can be applied if the condition [17]

$$r(z)H_{nc}\,|\mathbf{h}|\,d\epsilon_{//}(z)/dz|_{z=z_0} \gg 1 \tag{9.14}$$

is fulfilled for an iso-strain volume at the vertical position z_0.

The lateral size of the selected iso-strain volume is deduced from a fit of the intensity distribution along the angular direction, which is in the kinematical approximation given by

$$I(q_r = q_{r0}, q_a) \propto \left| \int \mathrm{d}^3\mathbf{r}\Omega_i(\mathbf{r})\mathrm{e}^{-\mathrm{i}q_a x_a} \right|^2 \tag{9.15}$$

where x_a is the component of the direct space vector $\mathbf{r}$ along the q_a axis and Ω_i is the shape function of the iso-strain volume i. From fitting of the q_z intensity profiles, the elevation z_i of the selected iso-strain volume above the sample surface is obtained. The intensity distribution along the q_z axis is described by the coherent superposition of waves resulting from four scattering processes of the first order perturbation theory (DWBA). The q_z intensity profiles are usually measured as a function of α_f using a PSD for a fixed incident angle α_i. The intensity distribution exhibits a characteristic maximum. The α_f position of the maxima decreases with increasing z_i, which can be approximatively determined from the equation [17]

$$z_i = \frac{\lambda}{2\pi\alpha_{max}} \arccos(\frac{\alpha_{max}}{\alpha_c}) \tag{9.16}$$

We have used this approach for the investigation of the strain profile and morphology of the nominal part of the sample Z25. As mentionned above, the sample presents a quasi-monomodal growth with statistically distributed domes and few pyramids. To fully characterize the structural properties of nano-objects, a 3D-reciprocal space map of the Ge relaxation around the (400)Si Bragg peak has been collected.

Using equations 9.15 and 9.16, the diameter and the height of each iso-strain domains of the islands have been determined as a function of h and of the in-plane strain with respect to the Si substrate. As observed in figure 9.37, we observe an increase of the lateral size of the dots towards the substrate. It can be noticed that at h=3.93, a change of the height and diameter slopes is observed. The fitted parameters are in good agreement with the AFM measurements.

We have thus determined the in-plane strain profile, the size and height of each iso-strain volume forming the islands. The lateral size of the selected iso-strain volume has been deduced from a fit of

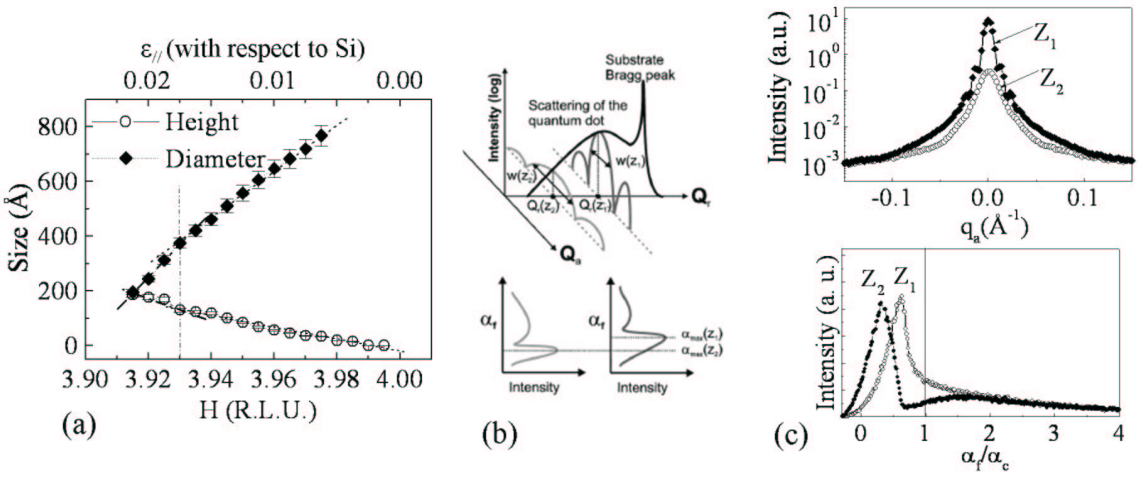

Figure 9.37: (a) Evolution of the diameter and height of the islands as a function of h and in-plane strain with respect to Si. (b) Schematic drawing of the ISS technique and experimental data (c) which are in good agreement with the theory. Z_1 corresponds to an iso-strain region near the Si substrate. Z_2 is the label of an iso-strain region far above the Si substrate.

the intensity distribution along the angular direction done with α_f integrated intensity. The use of the PSD allows not only to record line scan along q_a integrated all over the PSD as shown to determine the size but also to record directly (q_a, q_z) reciprocal space maps. For each selected iso-strain volume, the intensity measured in the (q_a, q_z) plane is given by

$$I(q_r = q_{r0}, q_a, q_z) \propto \left| \int \mathrm{d}^3\mathbf{r}\Omega_i(\mathbf{r})\mathrm{e}^{-\mathrm{i}q_a x_a}\mathrm{e}^{-\mathrm{i}q_z z} \right|^2 \tag{9.17}$$

where x_a and z are the components of the direct space vector $\mathbf{r}$ along the q_a and q_z axis and Ω_i is the shape function of the iso-strain volume i.

Figure 9.38 shows the intensity measured in the (q_a, q_z) or (k, l) plane perpendicular to the [100] direction for two h values near the (400)Si Bragg peak: h=3.925 and h=3.975. On both (k, l) maps, scattering streaks appear. In figure 9.38 (b) and (c), the angles between one streak and the [001] direction is 11±1° and 32±1°, respectively. The splitting of the streaks occurs as a consequence of a fourfold scattering process when working close to the critical angle. Due to the reflection from the free surface, the additional streak is shifted vertically by $2K\sin\alpha_i$, and its intensity depends on the incidence or exit angles due to the reflectivity coefficients $r_{i,f}$. In a direction perpendicular to it, each facet gives rise to a narrow streak in reciprocal space [29]. The streaks are thus the signature of the island facets. The islands are composed of three types of dome facets: {105}, {113} and {15 3 23} facets. As {113} facets will scatter mostly in the {110} planes and as we are looking at {100} planes around the (400)Si Bragg peak, only {105} and {15 3 23} streaks are detectable. The angles between the $<105>$ and $<15\ 3\ 23>$ streaks and the [001] direction are θ_{105} and $\theta_{15\ 3\ 23}$:

$$\theta_{105} = \arccos\left(\frac{<105><100>}{\sqrt{26}}\right) \sim 11.3^\circ \tag{9.18}$$

$$\theta_{15\ 3\ 23} = \arccos\left(\frac{<15\ 3\ 23><100>}{\sqrt{763}}\right) \sim 32.9^\circ \tag{9.19}$$

Hence, the iso-strain volumes located at h=3.925 and h=3.975 present facets. They are bounded by {105} facets and {15 3 23} facets respectively. The nature of the facetting of each iso-strain volume can thus be directly evaluated.

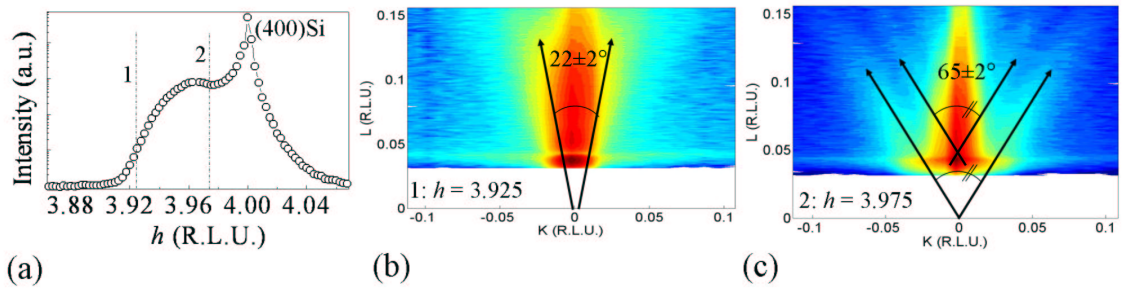

Figure 9.38: (a) Radial scan around the (400)Si Bragg peak. (b) and (c) (k, l) maps at two different iso-strain values 1: h=3.925 and 2: h=3.975 in Figure (a).

The technique has been performed for each iso-strain volume (see Fig. 9.39) and allows the detection of the facetting. {105} facets are observed for low h values which correspond to the top of the islands (see Fig. 9.39 (a). This is in good agreement with AFM. {105} facets alone are observed for values lower than h=3.935. At this h position, a change of the diameter and height of the islands were observed (see Fig. 9.37 (a). This is thus well explained by the transition between the {15 3 23} and {105} facets. For h values lower than the Si Bragg peak, {15 3 23} are also observed (see zone IV in figure 9.39). Numerical simulations using the finite difference method have been performed to understand the presence of {15 3 23} facets for $h > h_{Si}$. This reveals that the {15 3 23} facets come from the Ge islands. Due to their finite size, the {15 3 23} facets extend towards h values above the position of the Si Bragg peak.

We employed the same technique to look whether the ordered domains are facetted. No facet streaks appear in figure 9.40 (a)-(b). The ordered domains are thus not facetted. From the 2D reciprocal space map around the (200) forbidden reflection (see figure 9.40 (c)), the ordered domains scatter at 1.97< h <2. The region of atomic ordering is the region where no {105} facets are present. This can imply that atomic ordering appears during the formation of domes.

In conclusion, we showed that a proper analysis of anomalous X-ray diffraction data associated to grazing incidence data collected from a uniformly sized ensemble of epitaxial islands can provide 3D composition, strain, shape and size maps, including crystalline facets as a function of height and composition.

9.2.4 Observation of the edges of cristallines nano-islands.

The same analysis as reported in Fig. 9.39 has been performed for the {111} facetted pyramids grown on sample Z576P. The sample is illuminated by the X-ray beam at a shallow incident angle α_i ($\alpha_i < \alpha_c$). Figure 9.41 (a) and (b) show the intensity measured in the (q_a, q_z) or (k, l) plane perpendicular to the [100] and [110] direction for h=3.93 near the (400)Si Bragg peak and h=1.98 near the (220)Si Bragg peak. On both (k, l) maps, scattering streaks appear. In figure 9.41 (a), the angles between streaks and the [001] direction is 11±1° and 45±1°, respectively. In figure 9.41 (b), the angle between the streaks and the [001] direction is 55±1° ($\sim (90 - 35)°$). The splitting of the streaks occurs as a consequence of a fourfold scattering process when working close to the critical angle. In a direction perpendicular to it, each facet gives rise to a narrow streak in reciprocal space [29]. The streaks are thus the signature of the island facets. The islands are composed of two types of facets: {105} and {111} facets. The {105} and {111} facets will be observed along the $< 100 >$ and $< 110 >$ azimuths, respectively. The angles between the $< 105 >$ and $< 111 >$ streaks and the [001] direction are θ_{105} and θ_{111}:

$$\theta_{105} = \arccos\left(\frac{< 105 >< 100 >}{\sqrt{26}}\right) \sim 11.3° \tag{9.20}$$

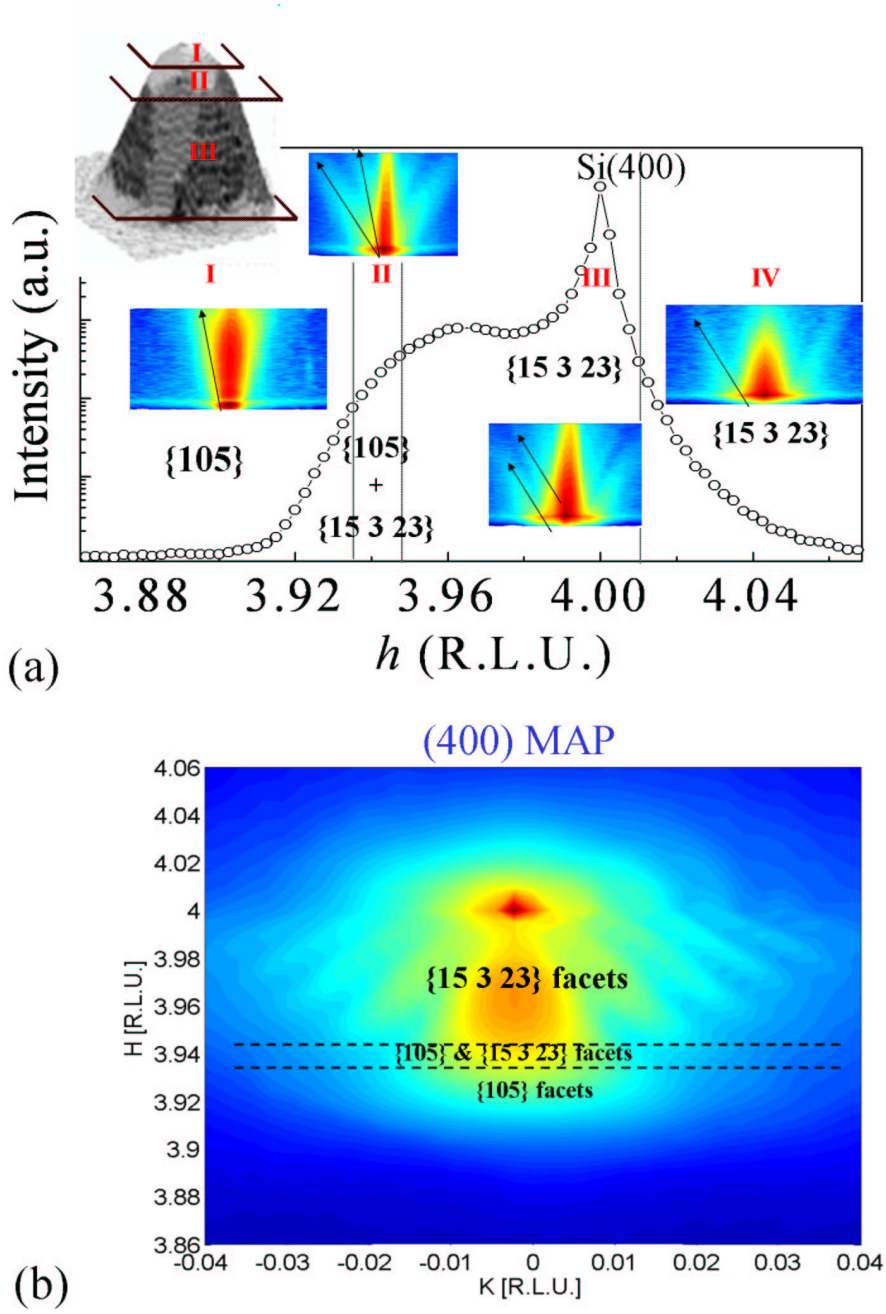

Figure 9.39: Radial scan (a) and recipocal space map (b) around the (400)Si Bragg peak and the associated facetting of each iso-strain domains.

$$\theta_{111} \quad = \quad \arccos(\frac{< 111 >< 100 >}{\sqrt{3}}) \sim 54.7^\circ \tag{9.21}$$

The streaks observed near the (400) reflection (see Fig. 9.41 (b)) come from the scattering by the {111} facets of the pyramids. In Fig. 9.41 (a), the one forming an angle of 11±1° with the [001] direction comes from the {105} facets which are at the top of the pyramids. Near the (400)Si reflection, (*i.e.*) along the < 100 > azimuth, we see again streaks forming an angle of 45±1° with the [001] direction. They can not originate from {111} facets because the position sensitive detector is cutting

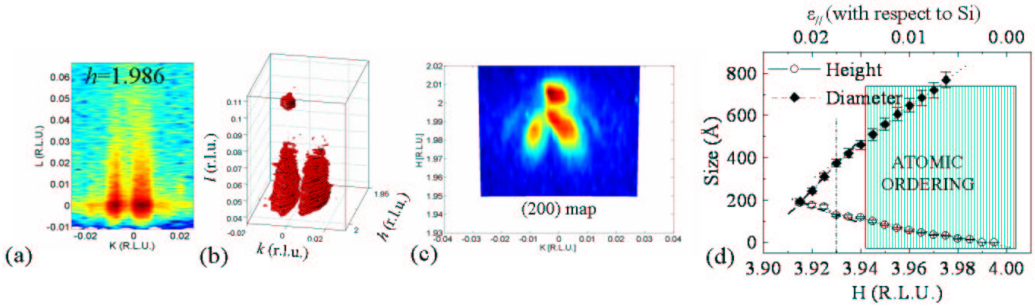

Figure 9.40: (a) (k, l) reciprocal space map at h=1.986. (b) 3D reciprocal space map around the (200) forbidden reflection. (c) In-plane (200) map. (d) Localisation of the atomic ordering as a function of h.

the reciprocal space at the angle 45° off from the direction of the {111} facet streaks and the cut has been chosen at h=3.93, where no signal from the {111} facet streaks are observed in the (400) reciprocal space map (see Fig. 9.30). The angle of 45° observed along the < 100 > azimuth and perpendicular to the [110] corresponds to te direction of the normal to the edge of the SiGe pyramid. These streaks can be attributed to a crystal truncation plane (CTP) perpendicular to an edge of the islands. Scattering from the island edges has been recently observed by Vartanyants *et al.* [30] performing GISAXS experiments. Here, we show that for an homogeneous ensemble of islands, scattering from island edges can also be observed by GIXD using a position sensitive detector.

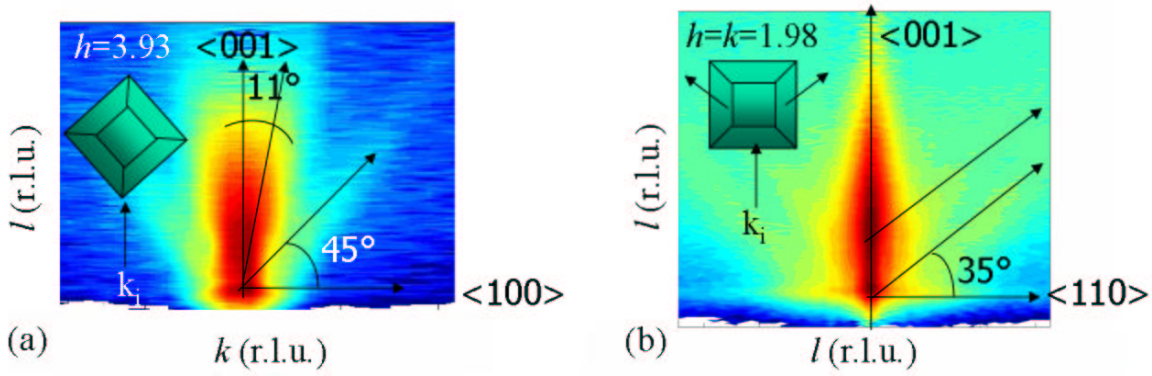

Figure 9.41: (k, l) maps at two different iso-strain values (a): h=1.98 around the (220)Si reflection and (b): h=3.93 around the (400)Si reflection.

In summary, for an homogeneous ensemble of 100 nm wide pyramid shaped islands, crystal truncation planes that are produced by scattering on the edges of the crystalline nano-islands are observed. The possibility to measure these crystal truncation planes (CTP's) will be important for the future applications as soon as they contain information about the atomic structure on the edges of a crystal that can be, in principle, quite different from that of a bulk, or surface. It is well known, for example, that 80% of reactions are going on the surfaces and interfaces. Until now not much information is available about the role of the edges of the crystals in different chemistry and catalytic reaction processes. Careful measurements along CTP's can possibly give this missing information and give explanation to questions in catalysis and surface science [30].

9.3 Conclusion

In this chapter, we have shown that for exactly the same growth conditions, islands grown on pre-patterned templates present a higher relaxation and a lower elastic energy compared to those grown on flat substrates. As the same mean vertical composition has been observed on both nominal and pre-patterned templates, this indicates that the mean Ge concentration is mainly governed by diffusion processes. It has also been revealed by an angular scan analysis of the lateral composition, that islands on nominal and pre-patterned templates do not show the same lateral composition, whereas their mean composition is identical. This has to be confirmed by numerical simulations or selective etching. These results are of great importance for technological applications as they demonstrate that by tuning the surface curvature, it is possible to change the relaxation state and the overall elastic energy of islands without modifying their mean Ge composition. Finally, we have shown that a proper anomalous-GIXD analysis of the grazing incidence data collected from a uniformly sized ensemble can provide 3D composition, strain, shape and size maps, including crystalline facets and island edges as a function of height and composition.

Bibliography

[1] J. Stangl, V. Holý, and G. Bauer, Rev. Mod. Phys. **76**, 725 (2004).

[2] Z. Zhong, H. Lichtenberger, G. Chen, M. Mülberger, C. Schelling, J. Myslivecek, A. Halilovic, J. Stangl, G. Bauer, W. Jantsch, F. Schäffler, Microelectronic Engineering **83**, 1730 (2006).

[3] Z. Zhong, W. Schwinder, F. Schäffler, G. Bauer, G. Vastola, F. Montalenti and L. Miglio, Phys. Rev. Lett. (**98**), 176102 (2007).

[4] J. Coraux, V. Favre-Nicolin, M. G. Proietti, B. Daudin, and H. Renevier, Phys. Rev. B. **75**, 235312 (2007).

[5] V. Favre-Nicolin, Computer code, NANOMAD (private communication).

[6] U. Pietsch, V. Holy, T. Baumbach, *High resolution X-ray scattering from Thin films and lateral Nanostructures (2^{nd} ed.)*, Springer, Berlin (2004).

[7] M. Schmidbauer, D. Grigoriev, M. Hanke, P. Schafer, T. Wiebach, and R. Kohler, Phys. Rev. B **71**, 115324 (2005).

[8] R. Magalhaes-Paniago, G. Meideros-Ribeiro, A. Malachias, S. Kycia, T. I. Kamins, and R. S. Williams, Phys. Rev. B **66**, 245312 (2002).

[9] J. Y. Tsao, *Materials Fundamentals of Molecular Beam Epitaxy*, Academic Press, London (1993).

[10] M. G. Proietti, H. Renevier, J. L. Hodeau, J. Garcia, J. F. Bérar, and P. Wolfers, Phys. Rev. B (**59**), 5479 (1999).

[11] A. L. Ankudinov, B. Ravel, J. J. Rehr, and S. D. Conradson, Phys. Rev. B (**58**), 7565 (1998).

[12] M. Newville, B. Ravel, D. Haskel, J. J. Rehr, E. A. Stern, and Y. Yacobi, Physica B (**208**), 154 (1995).

[13] Z. Sun, S. Wei, A. V. Kolobov, H. Oyanagi and K. Brunner, Phys. Rev. B **71**, 245334 (2005).

[14] L. Incoccia, S. Mobilio, M. G. Proietti, P. Fiorini, C. Evangelisti, Phys. Rev. B **31**, 1028 (1985).

[15] J. Hornsta and W. J. Bartels, J. Cryst. Growth (**44**), 513 (1978).

[16] J. C. Woicik, C. E. Bouldin, K. E. Miyano, and C. A. King, Phys. Rev. B (**55**), 15386 (1997).

[17] I. Kegel, *X-ray diffraction from semiconductor quantum dots*, PhD thesis: Universty of München (2000).

[18] J. Als-Nielson and D. McMorrow, *Elements of modern X-ray physics*, Wiley, New-York (2001).

[19] A. Letoublon, V. Favre-Nicolin, H. Renevier *et al.*, Phys. Rev. Lett. **92**, 186101 (2004).

[20] M. Sztucki, *The Use of Synchrotron Radiation to study Overgrowth Phenomena in InAs/GaAs Nanostructures*, PhD thesis, München (2004).

[21] I. K. Robinson, Phys. Rev. B **33**, 3830 (1986).

[22] A. Malachias, S. Kycia, G. Medeiros-Ribeiro, R. Magalhaes-Paniago, T. I. Kamins, and R. Stanley Williams, Phys. Rev. Lett. **91**, 176101 (2003).

[23] G. Katsaros, G. Costantini, M. Stoffel, R. Esteban, A. M. Bittner, A. Rastelli, U. Denker, O. G. Schmidt, and K. Kern, Phys. Rev. B **72**, 195320 (2005).

[24] I. Kegel, T. H. Metzger, A. Lorke, J. Peisl, J. Stangl, G. Bauer, J. M. García and P. M. Petroff, Phys. Rev. B, **63**, 035318 (2001).

[25] T. U. Schülli, J. Stangl, Z. Zhong, R. T. Lechner, M. Sztucki, T. H. Metzger and and G. Bauer, Phys. Rev. B, **71**, 0353326 (2003).

[26] B. Krause, T. H. Metzger, A. Rastelli, R. Songmuang, S. Kiravittaya and O. G. Schmidt, Phys. Rev. B, **72**, 085339 (2005).

[27] G. Renaud, R. Lazzari, Ch. Revenant, A. Barbier, M. Noblet, O. Ulrich, F. Leroy, J. Jupille, Y. Borensztein, C. R. Henry, J.-P. Deville, F. Scheurer, J. Mane-Mane, and O. Fruchart, Science **300**, 1416 (2003).

[28] T. U. Schülli, M.-I. Richard, G. Renaud, V. Favre-Nicolin, E. Wintersberger and G. Bauer, Appl. Phys. Lett., **89**, 143114 (2006).

[29] R. W. James, *The optical principles of the diffraction of X-rays*, G. Bell and sons LTD, 1954.

[30] I. Vartanyants, *et al.*, *Crystal Truncation Planes Revealed by 3D Tomography of Reciprocal Space*, to be published.

Conclusion and outlook

9.4 Conclusion

The aim of this work was the study of the *in situ* growth of Ge islands on Si(001) during molecular beam epitaxy. Better understanding of the driving forces of QDs and nano-islands formation, the control of their structural properties, and their precise positioning is a prerequisite for their application on a large scale. In this thesis, surface sensitive X-ray scattering techniques *in situ* and post growth, have been combined with element sensitive anomalous scattering in order to reveal decisive structural parameters with great details. In particular, this sheds light on the difference in growth mode on nominal and pre-patterned substrates.

Firstly, were presented the different characterization techniques and especially the different X-ray techniques used to study the atomic and crystallographical properties of Ge nanostructures on Si(001): GISAXS, GIXD and Multiwavelength Anomalous Diffraction (MAD). GISAXS experiments allow to study the morphology and ordering during the *in situ* growth of Ge nanostructures on Si(001). GIXD gives access to the relaxation of the nanostructures. The MAD technique allows to determine the composition distribution within nanostructures. Combining all methods as *in situ* tools, the complete information on the evolution of island morphology and internal crystallographic structure and composition could be followed during island nucleation and growth.

Dynamical diffraction effects and their consequences for the determination of strain profiles were included in the model simulations. The strong influence of the incident angle on the intensity as simulated by the Distorted Wave Born Approximation (DWBA) was modelled for large islands such as domes or superdomes. For large islands fulfilling the iso-strain conditions, the Born approximation is no more valid in the region of exit angles between zero and twice the critical angle. The measurement of the strain state inside domes or superdomes requires extreme accuracy in the adjustment of the angle of incidence.

A novel X-ray method to study the structure of the core of the defects by concentrating on measurements along rods of scattering by defects passing through bulk forbidden reflections was presented. It was first applied to determine the structure of the cores of extrinsic stacking faults in Si [1]. We have shown that the diffuse scattering from the distorted neighborhood of the defects is almost suppressed near a forbidden reflection which makes it possible to study directly the atomic structure of the defect cores. This approach constitutes a pioneer experiment. The method has been revealed as a fine, unique and destruction-free technique to detect stacking faults and characterize their small compression in the defect core. This method was then applied to detect the presence of stacking faults inside Ge nanostructures and allowed to determine the stacking-fault size and the presence of twins inside the Ge islands.

Then, we have presented what can be learnt by looking at a forbidden reflection during the growth of Ge nanostructures on Si(001). Mapping the (200) forbidden reflection allows to detect the presence of atomic ordering inside Ge islands. An X-ray formalism has been developed to evidence that compositional ordering leads to two intensity lobes as those observed at the (200) forbidden reflection. Other models excluding atomic ordering have been tested. Up to now, only atomic ordering explains the observed features at the (200). Nevertheless, further investigations need to be performed to undoubtedly confirm atomic ordering inside Ge islands. Mapping the (200) forbidden reflection

allows also to detect the presence of 111 stacking faults, to determine their sizes perpendicular to the $< 111 >$ directions, to evaluate the number of defects during the *in situ* growth and to determine the mean in-plane distance between interfacial dislocations. The impact of growth temperature, growth rate and annealing on the presence of compositional ordering and/or defects inside Ge nanostructures grown on Si(001) have been discussed. For instance, we evidence that a slow growth rate can fasten the introduction of dislocations inside the nanostructures. This has been confirmed by a simple energetic model.

Despite the wide knowledge acquired in the Ge/Si system, there were still some open questions concerning the evolution of the strain, the elastic to plastic transition, the intermixing and their relations with the different shapes of the island. We have addressed these issues, using scattering methods which do not suffer from restrictions of high temperatures and are thus ideal tools for *in situ* growth studies. The impact of growth interruption and growth rate on island shape and composition has been highlighted. The composition of Ge islands during their *in situ* growth has been determined as a function of growth temperature. Superdomes are shown to be less intermixed than domes or pyramids as Ge atoms preferentially attach to superdomes. During the *in situ* growth at 500°C and 650°C, a strong intermixing is observed in pyramids. Then, the transport of material during the 2D-3D transition is addressed. And we presented the evolution of island morphology and relaxation during a slow growth rate. We have shown that a slow growth rate fastens the appearance of dislocated islands and that, at the coherent-to-incoherent growth transition, a huge amount of material is transfered into dislocated islands either by dome coalescence or anomalous coarsening. Finally, a new shape of superdomes, which is the result of island coalescence, is reported.

An interesting development for devices applications is the positioning of islands and the improvement of size monodispersity. One way to achieve these goals is the growth of regular islands by a combination of patterning techniques and self-assembly. Using nano-patterned Si(001) surfaces obtained either by lithography or direct wafer bonding allows to laterally order Ge islands. The *in situ* evolution of the morphology and relaxation of the pre-patterned surface and ordered islands have been studied by combining (anomalous)-grazing incidence X-ray diffraction (GIXD) and (anomalous)-grazing incidence small angle X-ray scattering (GISAXS). Depending on the morphology of the surface, *i.e.* on the variation of the chemical potential, Ge islands are located on concave or convex morphologies. In both cases, it has been demonstrated that the 2D-3D transition appears earlier compared to a growth on a flat Si(001) substrate and that larger coherent islands can be grown on the patterned substrates as compared to island grown on flat substrates.

Finally, we have compared the growth of Ge islands on pre-patterned and nominal Si(001). The combination of MAD that allows to extract the scattering amplitude of the Ge and Si atoms and diffraction anomalous fine structure (DAFS) spectroscopy allowed to determine the local environment of Ge atoms. Then, we have shown that by tuning the surface curvature it is possible to change the relaxation state and the overall elastic energy of islands without modifying their Ge composition. This is of great importance for technological applications. In addition, due to its high relaxation, the pre-patterned template is ideally suited to strained Si cap layers in order to enhance electron mobility in Si. In addition, these results show new insight about the intermixing process which does not appear to be strain-driven but is rather induced by surface-mediated diffusion processes. Indeed, the same mean composition is observed on both patterned and nominal templates. An angular analysis of the lateral composition has revealed that islands on nominal and pre-patterned templates do not show the same lateral composition, whereas their mean composition is identical. This has to be confirmed by numerical simulations or selective etching.

9.5 Future perspectives.

To confirm the presence of atomic ordering inside Ge islands two experiments are scheduled at the ID03 and BM02 ESRF beamlines. A deep analysis of the wetting layer using surface truncation rods will allow to determine the composition of the wetting layer and its atomic arrangement and then determine if atomic ordering occurs during the formation of the wetting layer. On BM02, GIDAFS

experiments are planned to quantitatively study the local environnement of Ge atoms inside different iso-strain regions of the islands. This will allow to propose a model for atomic ordering or to invalidate atomic ordering.

This work reports the structural properties of 3D nanoislands. Recently, 2D confined structures 'nanowires' have attracted a lot of attention [2, 3]. Structures with typical diameters of 10 to 100 nm, but lengths up to several μm can be fabricated. The same investigations as performed in this thesis can be applied for these nanostructures to reveal their complex structures. *Ex situ* investigations of single wires or *in situ* study of an ensemble of wires during their growth would allow for clues on the growth mechanisms. In this optic, the BM32 MBE chamber will be converted in a (chemical beam epitaxy) CBE chamber to *in situ* study the first mechanisms of the growth of nanowires using gases.

As already mentioned, X-ray scattering is a powerful technique. Nevertheless, it suffers from the fact that real space model assumptions are needed for a direct reconstruction of the structural properties of nanostructures from the measured intensity distribution in reciprocal space. Another limitation of the technique is that the measurements are performed on large nanostructure ensembles. The mean structure is measured rather than the variations of individual structural properties.

To overcome these drawbacks of conventional incoherent scattering experiments as performed in this work, two possible solutions can be exploited: focussing X-rays to submicron dimensions and using the coherence of the beam. In the last years, the focussing of X-rays have progressed to beam diameters less than 100 nm [4]. Coherent diffraction imaging (CDI) has allowed to directly reconstruct strain free nanocrystals using a model free conversion of reciprocal space intensity distribution to the real space sample structure [5].

The combination of these two approaches will offer promising tools for the characterization of single nanostructures and will for instance allow to determine without model the anisotropic strain distribution in a single island and the surrounding substrates. In general, CDI can be anticipated as a versatile tool to determine 3D structural properties of scattering nanomaterials.

Bibliography

[1] M. I. Richard, T. H. Metzger, V. Holý, K. Nordlund, Phys. Rev. Lett., accepted for publication (2007).

[2] A. I. Hochbaum, R. Fan, R. He, and P. Yang, Nano. Lett. **5**, 457 (2005).

[3] J. Goldberger, R. He, Y. Zhang, S. Lee, H. Yan, H. Choi, and P. Yang, Nature **422**, 599 (2003).

[4] C. G. Schroer and B. Lengeler, Phys. Rev. Lett. **94**, 054802 (2005).

[5] G. J. Williams, M. A. Pfeifer, I. A. Vartanyants, and I. K. Robinson, Phys. Rev. Lett. **90**, 175501 (2003).

Abbreviations

2D	bidimensional
3D	tridimensional
AFM	Atomic Force Microscopy
a. u.	arbitrary units
BA	Born Approximation
BM32	32^{nd} bending magnet beamline at the ESRF
CCD	Charge-Coupled Device
CRG	Collaborative Research Group
CVD	Chemical Vapour deposition
DAFS	Diffraction Anomalous Fine Structure
DWBA	Distorted-Wave Born Approximation
EOR	End-Of-Range
ESRF	European Synchrotron Radiation Facility
FDL	Faulted Dislocation Loop
FDM	Finite Difference Method
FT	Fourier Transform
FWHM	Full Width at Half Maximum
GISAXS	Grazing Incidence Small Angle X-ray Scattering
GI-DXS	Grazing Incidence Diffuse X-ray Scattering
GIXD	Grazing Incidence X-ray Diffraction
HDS	Huang Diffuse Scattering
HRTEM	High Resolution Transmission Electron Microscopy
ID01	1^{st} undulator beamline at the ESRF
LED	Light Emitting Diode
MAD	Multiwavelength Anomalous Diffraction
MBE	Molecular Beam Epitaxy
MOCVD	MetalOrganic Chemical Vapour Deposition
ML	monolayer
PAI	Pre-Amorphising Implant
PDL	Perfect Dislocation Loop
PMMA	Polymethylmethacrylate
PSD	Position Sensitive Detector
QD	quantum dot
RHEED	Reflection High-Energy Electron Diffraction
RIE	Reactive Ion Etching
r.l.u.	reciprocal lattice units
SEM	Scanning Electron Microscopy
SF	Stacking Fault
SK	Stranski-Krastanow
SPR	Solid Phase Epitaxial Regrowth
STM	Scanning Tunneling Microscopy
TDS	Thermal Diffuse Scattering
TEM	Transmission Electron Microscopy254

List of symbols

α_i	incident angle
α_c	critical angle for total reflection
α_f	exit angle
β	imaginary part of deviation of refractive index from unity
δ	real part of deviation of refractive index from unity (scattering)
λ	wavelength
ρ	electron density
$F(\mathbf{q})$	scattered amplitude
$g(r)$	pair distribution function
$I(\mathbf{q})$	scattered intensity
$\mathbf{k}$	wave vector
k_0	free-space wave number, $2\pi/\lambda$
n	refractive index (scattering)
$\mathbf{q}$	momentum transfer
q_r	reduced scattering vector in the radial direction
q_a	reduced scattering vector in the angular direction
q_z	reduced scattering vector in the vertical direction
$S(\mathbf{q})$	structure factor of island shape
T	transmission
w_{Ge}	Ge concentration
ϵ^{Ge}	strain with respect to bulk Ge
ϵ^{Si}	strain with respect to bulk Si
(hkl)	plane or set of parallel planes with Miller indices h, k, l
(h,k,l)	Point designed by the Miller indices h, k, l
$[hkl]$	direction with Miller indices h, k, l
hkl	family of planes with Miller indices h, k, l
$< hkl >$	family of directions with Miller indices h, k, l